Investigations of Metal/Organic Interfaces and Metalation Reactions of Organic Semiconductors

Kumulative Dissertationsschrift

zur Erlangung des
Doktorgrades der Naturwissenschaften
(Dr. rer. nat.)

dem Fachbereich Chemie
der Philipps-Universität Marburg

vorgelegt von

Stefan Renato Kachel
Master of Science

aus Erfurt

Marburg
2020

Der praktische Teil der vorliegenden Arbeit wurde unter Leitung von Herrn Prof. Dr. J. Michael Gottfried in der Zeit von Februar 2017 bis April 2020 am Fachbereich Chemie der Philipps-Universität Marburg angefertigt.

Vom Fachbereich Chemie der Philipps-Universität Marburg mit der Hochschulkennziffer 1180 als Dissertation am 29.10.2020 angenommen.

Tag der Einreichung: 24.09.2020

Tag der Disputation: 09.11.2020

Erstgutachter: Prof. Dr. J. Michael Gottfried

Zweitgutachter: Prof. Dr. Gregor Witte

Lizenzierung

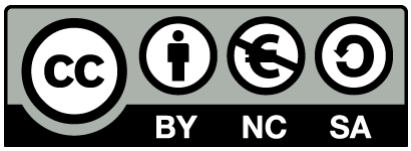

Contents

Selbstständigkeitserklärung

gemäß § 10, Absatz 1 der Promotionsordnung der Mathematisch-Naturwissenschaftlichen Fachbereiche und des Medizinischen Fachbereichs für seine mathematisch-naturwissenschaftlichen Fächer der Philipps-Universität Marburg vom 15.07.2009.

Ich erkläre, dass eine Promotion noch an keiner anderen Hochschule als der Philipps-Universität Marburg, Fachbereich Chemie, von mir versucht wurde und versichere, dass ich meine vorgelegte Dissertation

Investigations of Metal/Organic Interfaces and Metalation Reactions of Organic Semiconductors

selbst und ohne fremde Hilfe verfasst, nicht andere als die in ihr angegebenen Quellen oder Hilfsmittel benutzt, alle vollständig oder sinngemäß übernommenen Zitate als solche gekennzeichnet sowie die Dissertation in der vorliegenden oder einer ähnlichen Form noch bei keiner anderen in- oder ausländischen Hochschule anlässlich eines Promotionsgesuches oder zu anderen Prüfungszwecken eingereicht habe.

Marburg, _____

_____

Stefan Renato Kachel

Abstract

Modern electronic devices are increasingly based on organic semiconductors. The performance of such devices crucially depends on the properties of the interface between the organic semiconductors and the metal contacts. Understanding the influence of the topology of the organic semiconductor's conjugated π-electron system on the interface interaction could greatly improve the device's performance. Furthermore, the knowledge about reactions of heteroatomic organic semiconductors with metal atoms during electrode fabrication may lead to enhanced lifetimes of such devices. This cumulative dissertation comprises several publications and a number of so far unpublished results, addressing metal/organic interface interactions and metalation reactions of heteroatomic organic semiconductors. The properties of the interfaces are tailored by investigating the alternant aromatic molecules naphthalene and pyrene as well as the non-alternant aromatic molecules azulene and azupyrene on different metallic single-crystal surfaces. Investigations by means of temperature-programmed desorption reveal stronger desorption energies for the non-alternant molecules on both Ag(111) and Cu(111). The biggest difference is observed on Cu(111), on which azulene and azupyrene are chemisorbed, whereas naphthalene and pyrene are physisorbed. The enhanced interface interaction of the non-alternant molecules is associated with the formation of surface dipoles that lead to stronger intermolecular repulsion between the adsorbed molecules. These results are supported by additional surface science methods, such as X-ray photoelectron spectroscopy or near-edge X-ray absorption fine structure spectroscopy, as well as density functional theory calculations conducted by group members and external collaboration partners. Detailed quantitative analysis of temperature-programmed desorption data of benzene on Cu(111) and Ag(111) yields experimental desorption energies that can be used as a benchmark for theoretical adsorption energies derived by density functional theory calculations. The interactions of metal/organic interfaces are compared with organic/inorganic interfaces in the case of pentacene and its fluorinated derivative perfluoropentacene on Au(111) as well as on bulk and two-dimensional MoS_2 in a collaboration project. Organic semiconductors often interact weakly with inorganic surfaces, *e.g.*, the

thermal desorption of the first molecular layer is indistinguishable from multilayer desorption. No monolayer desorption peaks are observed as is mostly the case on metal surfaces. However, monolayer desorption of pentacene and perfluoropentacene on MoS_2 occurs at significantly higher temperatures than the multilayer desorption. Detailed analysis reveals that the monolayers of both molecules are entropically stabilized. Codeposition of both molecules results in strong attractive intermolecular interactions on MoS_2, while these interactions are weaker on Au(111). Metalation reactions of organic semiconductors with metal atoms, *e.g.*, Co on tetraphenylporphyrin and Ca on α-sexithiophene, during interface preparation were investigated by means of hard X-ray photoelectron spectroscopy and temperature-programmed desorption mass spectrometry. The thickness of the reaction zone is changed by variation of experimental properties during interface formation. It is found that only the sample temperature during metal atom deposition and the metal atom flux in the case of Ca have an impact on the reaction depth, which is usually limited to few nanometers. In contrast to Co and Ca, Li atoms readily diffuse into the organic bulk and react with tetraphenylporphyrin over several tens of nanometers, forming dilithium tetraphenylporphyrin or monolithium monohydrogen tetraphenylporphyrin depending on the deposited Li amount. Furthermore, the transmetalation reaction of lead(II) tetraphenylporphyrin with Cu atoms on the Cu(111) surface was proven by temperature-programmed desorption. In addition, the Ullmann coupling reaction of bromo- and iodobenzene on Cu(111) was examined. While bromobenzene molecules desorb intact from the Cu(111) surface, iodobenzene molecules dissociate into iodine atoms and phenyl radicals. The latter form biphenyl that desorbs in three distinct desorption peaks at different temperatures. In a collaborative project, the oxidation state and electronic structure of Pb atoms in the newly synthesized Pb_3F_8 were studied by hard X-ray photoelectron spectroscopy and near-edge X-ray absorption fine structure spectroscopy giving evidence for the presence of Pb(II) and Pb(IV) species. The experimental results are complemented by constructional work to improve the temperature-programmed desorption setup. Moreover, two *Igor Pro 8* scripts were written to quickly import data from different experimental setups and speed up the data treatment.

Kurzzusammenfassung

Moderne elektronische Geräte basieren immer häufiger auf organischen Halbleitern. Die Leistung solcher Geräte hängt entscheidend von den Eigenschaften der Grenzfläche zwischen den organischen Halbleitern und den Metallkontakten ab. Das Verständnis über den Einfluss der Topologie des konjugierten π-Elektronensystems des organischen Halbleiters auf die Grenzflächenwechselwirkung kann die Leistungsfähigkeit der Geräte deutlich verbessern. Weiterhin kann das Wissen über Reaktionen von heteroatomaren organischen Halbleitern mit Metallatomen während der Elektrodenherstellung die Lebenszeit solcher Geräte erhöhen. Diese kumulative Dissertationsschrift umfasst einige Publikationen sowie bislang nicht veröffentlichte Ergebnisse, die sich mit metallorganischen Grenzflächenwechselwirkungen und Metallierungsreaktionen von heteroatomaren organischen Halbleitern beschäftigen. Die Eigenschaften der Grenzfläche werden verändert, indem die alternierenden aromatischen Moleküle Naphthalin und Pyren sowie die nicht-alternierenden aromatischen Moleküle Azulen und Azupyren mit verschiedenen metallischen Einkristalloberflächen kombiniert werden. Untersuchungen mittels temperaturprogrammierter Desorption zeigen höhere Desorptionsenergien für die nicht-alternierenden Moleküle auf sowohl Ag(111) als auch Cu(111) auf. Der größte Unterschied ist auf der Cu(111)-Oberfläche zu beobachten, auf der Azulen und Azupyren chemisorbiert und Naphthalin und Pyren physisorbiert sind. Die erhöhte Grenzflächenwechselwirkung der nicht-alternierenden Moleküle is verbunden mit der Ausbildung von Oberflächendipolen, die in einer stärkeren zwischenmolekularen Abstoßung der adsorbierten Moleküle resultieren. Diese Untersuchungen werden durch weitere oberflächenwissenschaftliche Methoden, wie etwa Röntgenphotoelektronenspektroskopie und Röntgen-Nahkanten-Absorption-Spektroskopie, sowie Dichtefunktionaltheorie-Rechnungen unterstützt, die von Gruppenmitgliedern und externen Kooperationspartnern durchgeführt wurden. Aus einer detaillierten quantitativen Analyse von Daten der temperaturprogrammierten Desorption von Benzol auf Cu(111) und Ag(111) sind experimentelle Desorptionsenergien bestimmt worden, die als Maßstab für theoretische Adsorptionsenergien von Dichtefunktionaltheorie-Rechnungen verwendet werden können. Die Wechselwirkungen von metall-

organischen Grenzflächen werden mit organisch-anorganischen Grenzflächen für den Fall des Pentacens und des Perfluoropentacens auf Au(111) sowie auf mehrschichtigem und zweidimensionalem MoS_2 in einem Kollaborationsprojekt verglichen. Organische Halbleiter wechselwirken oft nur schwach mit anorganischen Oberflächen, beispielsweise kann die thermische Desorption der Moleküle in der ersten Lage ununterscheidbar von der Multilagendesorption sein. Es wird dann kein Monolagendesorptionspeak beobachtet, wie es meistens der Fall auf Metalloberflächen ist. Dennoch tritt für Pentacen und Perfluoropentacen auf MoS_2 die Monolagendesorption bei deutlich höheren Temperaturen auf als bei der Multilagendesorption. Eine detailierte Analyse zeigt, dass die Monolagen von beiden Molekülen entropisch stabilisiert sind. Eine Codeposition beider Moleküle resultiert in starken attraktiven intermolekularen Wechselwirkungen auf MoS_2, während diese auf Au(111) schwächer sind. Metallierungsreaktionen von organischen Halbleitern, beispielsweise Co auf Tetraphenylporphyrin und Ca auf α-Sexithiophen, während der Grenzflächenbildung wurden mit harter Röntgenphotoelektronenspektroskopie und temperaturprogrammierter Desorptionsmassenspektrometrie untersucht. Die Dicke der Reaktionsschicht ist durch verschiedene experimentelle Faktoren während der Grenzflächenherstellung verändert worden. Hierbei wurde festgestellt, dass nur die Probentemperatur und die Metallatomaufdampfrate im Falle des Ca eine Auswirkung auf die Reaktionstiefe haben, welche sich meist auf wenige Nanometer beschränkt. Im Gegensatz zu Co und Ca diffundieren Li-Atome sehr tief (mehr als 50 nm) in den organischen Festkörper und reagieren mehrere zehn Nanometer tief mit Tetraphenylporphyrin zu Dilithiumtetraphenylporphyrin oder Monolithiummonowasserstofftetraphenylporphyrin entsprechend der aufgedampften Li-Menge. Des Weiteren wurde die Transmetallierung von Blei(II)-Tetraphenylporphyrin mit Cu-Atomen auf der Cu(111)-Oberfläche mittels temperaturprogrammierter Desorption bewiesen. Außerdem wurde die Ullmann-Kupplungsreaktion von Brom- und Iodbenzol auf Cu(111) untersucht. Während Brombenzolmoleküle intakt von der Cu(111) Oberfläche desorbieren, dissoziieren sich Iodbenzolmoleküle in Iodatome und Phenylradikale. Letztere bilden Biphenyl, das in Form von drei spezifischen Desorptionssignalen bei verschiedenen Temperaturen desorbiert. In einem Kollaborationsprojekt sind die Oxidationsstufen und elektronische Struktur von Pb-Atomen im neu hergestellten Pb_3F_8 mittels harter Röntgenphotoelektronenspektroskopie und die Röntgen-Nahkanten-Absorption-Spektroskopie untersucht worden. Die Untersuchungen liefern den Beweis für die Gegenwart von den Pb(II)- und Pb(IV)-Spezien. Neben der experimentellen

Arbeit wurden von Konstruktionsarbeiten durchgeführt, die das Ziel haben, die Apparatur der temperaturprogrammierten Desorption zu verbessern. Darüber hinaus sind zwei Skripte in *Igor Pro 8* entwickelt worden, mit denen Messdaten verschiedener experimenteller Aufbauten importiert werden können und die die Datenverarbeitung verschnellern.

List of Publications

The following list contains all articles published in scientific journals and manuscripts prepared in the course of the present dissertation.

P1 B. P. Klein, N. J. van der Heijden, **S. R. Kachel**, M. Franke, C. K. Krug, K. K. Greulich, L. Ruppenthal, P. Müller, P. Rosenow, S. Parhizkar, F. C. Bocquet, M. Schmid, W. Hieringer, R. J. Maurer, R. Tonner, C. Kumpf, I. Swart, J. M. Gottfried, "Molecular Topology and the Surface Chemical Bond: Alternant Versus Nonalternant Aromatic Systems as Functional Structural Elements", *Physical Review X* **2019**, *9*(1), 011030, DOI 10.1103/PhysRevX.9.011030.

P2 **S. R. Kachel**, B. P. Klein, J. M. Morbec, M. Schöniger, M. Hutter, M. Schmid, P. Kratzer, B. Meyer, R. Tonner, J. M. Gottfried, "Chemisorption and Physisorption at the Metal/Organic Interface: Bond Energies of Naphthalene and Azulene on Coinage Metal Surfaces", *The Journal of Physical Chemistry C* **2020**, *124*, 8257–8268, DOI 10.1021/acs.jpcc.0c00915.

P3 B. P. Klein, A. Ihle, **S. R. Kachel**, L. Ruppenthal, S. J. Hall, L. E. Sattler, S. M. Weber, J. Herritsch, A. Jaegermann, D. Ebeling, R. J. Maurer, G. Hilt, R. Tonner, A. Schirmeisen, J. M. Gottfried, "Enhanced Interaction of the Stone-Wales Defect at the Metal-Graphene Interface", **2020**, *in preparation.*

P4 **S. R. Kachel**, P.-M. Dombrowski, T. Breuer, J. M. Gottfried, G. Witte, "Engineering of TMDC-OSC Hybrid Interfaces: The Thermodynamics of Unitary and Mixed Acene Monolayers on MoS_2", *Chemical Science* **2020**, *submitted.*

P5 M. Schmid, **S. R. Kachel**, B. P. Klein, N. Bock, P. Müller, R. Riedel, N. Hampp, J. M. Gottfried, "Reactive Metal-Organic Interfaces Studied with Hard X-Ray Photoelectron Spectroscopy: Controlled Formation of Metalloporphyrin Interphase Layers During Metal Vapor Deposition onto Porphyrin Films", *Journal of Physics: Condensed Matter* **2019**, *31*, 094002, DOI 10.1088/1361-648X/aafa2b.

P6 M. Schöniger, **S. R. Kachel**, J. Herritsch, P. Schröder, M. Hutter, J. M. Gottfried, "Direct Synthesis of Dilithium Tetraphenylporphyrin: Facile Reaction of a Free-Base Porphyrin with Vapor-Deposited Lithium", *Chemical Communications* **2019**, *55*, 13665–13668, DOI 10.1039/C9CC07170A.

P7 **S. R. Kachel**, M. Schöniger, J. Herritsch, P. Schröder, J. M. Gottfried, "Synthesis of Partially Metalated Lithium Tetraphenylporphyrin: Characterization of LiHTPP", **2020**, *in preparation.*

P8 **S. R. Kachel**, M. Schöniger, H. Zhou, H.-J. Drescher, C. K. Krug, L. Ruppenthal, B. P. Klein, M. Sachs, K. Gries, J. Hochstraßer, F. Fillsack, R. Riedel, N. Hampp, M. Schmid, J. M. Gottfried, "Examination of the Reaction Zone in a Metal–Organic Semiconductor Interface by Multi-Technique Approach: Characterization and Control of the Ca/6T Interphase", **2020**, *in preparation.*

P9 J. Herritsch, **S. R. Kachel**, Q. Fan, M. Hutter, L. Heuplick, F. Münster, J. M. Gottfried, "Tracking of the Transmetalation Reaction of PbTPP by Cu Adatoms on Cu(111) by Multiple Techniques", **2020**, *in preparation.*

P10 H. L. Deubner, M. Sachs, J. Bandemehr, S. I. Ivlev, A. J. Karttunen, **S. R. Kachel**, B. P. Klein, L. Ruppenthal, M. Schöniger, C. K. Krug, J. Herritsch, J. M. Gottfried, J. N. M. Aman, J. Schmedt auf der Günne, F. Kraus, "Binary Lead Fluoride Pb_3F_8", *Chemistry - A European Journal* **2019**, *25*, 15656–15661, DOI 10.1002/chem.201903954.

Abbreviations

General Acronyms

2D	two-dimensional
AES	AUGER electron spectroscopy
AEY	AUGER electron yield
AFM	atomic force microscopy
ALI	atomic layer injection
ARPES	angle-resolved photoemission spectroscopy
ARUPS	angle-resolved ultraviolet photoelectron spectroscopy
CA	complete analysis
CAW	CHAN-ARIS-WEINBERG
DFT	density functional theory
DOF	degree of freedom
DOS	density of states
EDX	energy dispersive X-ray spectroscopy
ESCA	electron spectroscopy for chemical analysis
FIB	focused ion beam
FY	fluorescence yield
GA	genetic algorithm
HAXPES	hard X-ray photoelectron spectroscopy
HE-SGM	high energy spherical grating monochromator
HIKE	high kinetic energy photoelectron spectroscopy
HRV	heating-rate variation
HZB	*Helmholtz-Zentrum Berlin für Materialien und Energie*
IMFP	inelastic mean free path
IPW	inverted POLANYI-WIGNER
IS	initial state
ISO	International Organisation for Standardisation
LAO	LEED-AES optics
LEA	leading-edge analysis

LEED	low-energy electron diffraction
LUMO	lowest unoccupied molecular orbital
MC	Monte Carlo
mLEA	modified leading-edge analysis
nc-AFM	non-contact atomic force microscopy
NEXAFS	near-edge X-ray absorption fine structure
NI-XSW	normal-incidence X-ray standing wave
NAC	nano-joule adsorption calorimetry
NN	neural network
OLED	organic light-emitting diode
OPVC	organic photovoltaic cell
OSC	organic semiconductor
OTFT	organic thin film transistor
PAH	polycyclic aromatic hydrocarbon
PES	photoelectron spectroscopy
PEY	partial electron yield
PW	Polanyi-Wigner
QCM	quartz crystal microbalance
QMS	quadrupole mass spectrometer
SNR	signal-to-noise ratio
STM	scanning tunneling microscopy
TDS	thermal desorption spectroscopy
TEY	total electron yield
TMDC	transition metal dichalcogenide
TPD	temperature-programmed desorption
TPD-MS	temperature-programmed desorption mass spectrometry
TS	transition state
TST	transition state theory
UHV	ultra-high vacuum
UPS	ultraviolet photoelectron spectroscopy
vdW	van der Waals
XPS	X-ray photoelectron spectroscopy

Chemical Compounds

H_2TPP	*meso*-tetraphenylporphyrin
6T	α-sexithiophene
Az	azulene
AzPyr	azupyrene
BBz	bromobenzene
BP	biphenyl
Bz	benzene
CuTPP	copper(II) tetraphenylporphyrin
IBz	iodobenzene
Li_2TPP	dilithium tetraphenylporphyrin
LiHTPP	monolithium monohydrogen tetraphenylporphyrin
LiTPP	monolithium tetraphenylporphyrin
LN_2	liquid nitrogen
Nt	naphthalene
PbTPP	lead(II) tetraphenylporphyrin
PEN	pentacene
PFP	perfluoropentacene
Ph	phenyl
Pyr	pyrene

1 Introduction

Electronic devices and their applications are a rapidly evolving field in today's society. It is therefore necessary to provide efficient and low-cost technologies to satisfy this demand. In the past years, electronic devices based on organic semiconductors (OSCs),[1,2] *e.g.*, organic light-emitting diodes (OLEDs),[3–5] organic photovoltaic cells (OPVCs)[6,7] and organic thin film transistors (OTFTs),[8,9] have come into focus.[10] Nevertheless, the development of such devices is not at its end yet, since knowledge of the metal/organic interface is incomplete but highly necessary.[11–13] The interface between OSCs and metal atoms is crucial for the device's performance[14–17] because the electronic structure of the interface defines the charge carrier injection kinetics.[18–22] Due to the high complexity of real devices, model systems are often used in fundamental research. Typically, small aromatic compounds with conjugated π-electron systems are investigated instead of large molecules[23,24] or polymers.[25,26] The interaction between monolayers of these OSCs adsorbed on metallic single-crystal surfaces is studied in ultra-high vacuum (UHV) to preserve clean samples. The insights obtained by the model systems can be used to tailor the OSC and surface to achieve certain properties of the interface and improve the device. Ultimately, the gap between model systems and real devices must be bridged.[27] Investigating reactions of OSC bulk materials with metal atoms in buried metal/organic interfaces – a so-called interphase – approaches the conditions in real devices.

This thesis deals with both topics investigated by common surface science techniques in UHV. In the first part, the metal/organic interfaces between monolayers of polycyclic aromatic hydrocarbons (PAHs) on coinage metal surfaces as well as on inorganic VAN DER WAALS (vdW) materials are studied. The second part analyzes the interphase formation of metalated organic bulk material in order to tailor the interphase properties. The third section outlines the motivation for this thesis and gives an overview of the publications presented in Chapter 5 as well as additional projects.

1.1 Properties of Metal/Organic Interfaces and 2D Materials

OSCs represent important components of modern electronics. Most OSCs are aromatic compounds with conjugated π-electron systems due to their functional variety and stability. Organic molecules interact with metal surfaces upon adsorption. Depending on the molecule and surface, the interaction is either a physisorption or a chemisorption. Physisorption is characterized by weak vdW forces between the molecule and the substrate. No charge transfer is observed because the wave function of the molecule does not overlap with electronic states of the substrate. The situation is reversed for chemisorption, *i.e.*, a strong covalent bond is formed between the molecule and the metal. This results in vigorous hybridization and charge transfer at the interface. The discrimination between physisorption and chemisorption, however, is difficult and has to be considered for each adsorbate–substrate system. Using different surface science techniques, experimental parameters such as the desorption energy or the adsorption height can be determined. Physisorbed systems exhibit low desorption energies, high adsorption heights, small hybridization and charge transfers as well as weak disturbances of electronic states, while the opposite is observed for chemisorbed systems. Probing experimental properties gives insight into the bonding situation of certain systems.

Nevertheless, a quick estimation of the bonding situation is often obtained by the desorption energy. The desorption of physisorbed molecules often occurs in a small temperature range. The desorption energies are slightly higher than the multilayer sublimation enthalpy and exhibit a weak coverage dependency. The coverage dependency of the desorption energy stems from intermolecular repulsion related to vertical dipoles formed by the Pauli pushback effect.[28] A stronger bond and, therefore, a stronger charge transfer results in pronounced dipoles and a stronger repulsion. In contrast to physisorbed molecules, desorption of chemisorbed molecules shows considerably higher desorption energies in comparison with corrected sublimation enthalpies. The desorption occurs at significantly higher temperatures in a broader temperature range. Due catalytic effects of the surface, it is possible that certain intramolecular bonds break at elevated temperatures, hence the molecule decomposes before it completely desorbs. It is important to note that physisorption scales with the number of atoms in planar molecules, *i.e.*, in large physisorbed molecules, like polymers or graphene, the interactions add up, resulting in very high desorption energies and

a desorption is not possible. Normalization of the desorption energy with the number of atoms in a molecule yields a good criterion for comparable molecules whether it is physisorbed or chemisorbed. Nevertheless, a full characterization of an adsorbate–substrate system is emphasized for a reliable statement.

Whether an adsorbate–substrate system is physisorbed or chemisorbed does not only depend on the molecule but also on the substrate. For example, benzene (Bz) and naphthalene (Nt) are physisorbed on coinage metal single-crystal surfaces,[29–33] whereas both molecules are chemisorbed on the Pt(111) single-crystal surface.[34,35] Tailoring the molecule as well as finding a matching substrate for the optimized interface interaction is the key to improve organic electronic devices.

Most research is performed on so-called alternant aromatic molecules, like Bz, Nt or even larger molecules. An alternant molecule is described by a certain linking pattern of the conjugated π-electron system according to the topological HÜCKEL matrix.[36] The C atoms of a conjugated π-electron system are alternatingly attributed to two different sets. In case each C atom of the first set is surrounded by C atoms of the second set and *vice versa*, the conjugated system will be called alternant, otherwise it is a non-alternant system.[37] The non-alternant counterpart of Nt is azulene (Az) consisting of a five- and seven-membered ring (see Figure 1.1).

The difference of the two linking patterns becomes obvious when the COULSON-RUSHBROOKE paring theorem is considered.[38] Accordingly, for every occupied

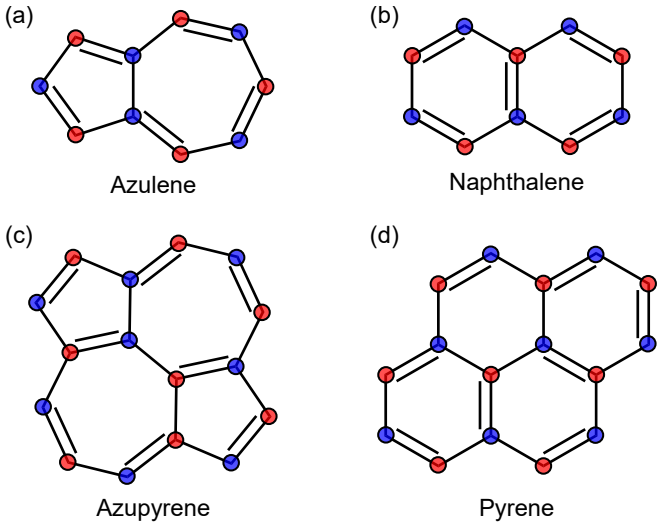

Figure 1.1: Illustration of (a) azulene, (b) naphthalene, (c) azupyrene and (d) pyrene. C atoms are divided into two groups (red and blue). In the non-alternant aromatic molecules (a,c) some C atoms of the same group are placed next to each other. Each C atom is surrounded by C atoms of the other group in the alternant aromatic molecules (b,d).

orbital a corresponding unoccupied orbital exists with an opposite sign of their atomic coefficients. For alternant systems this leads to homogeneous electron distributions and a symmetrical orbital energy distribution. Non-alternant systems, however, disobey the theorem resulting in a high localization of the orbitals. The difference in the electronic structure is expected to influence the metal/organic interaction.

Graphene and graphene-based nanostructures on metal surfaces offer promising properties that can be used in applications.[39,40] Nevertheless, graphene layers suffer from defects that occur during preparation. Common topological defects in graphene emerge when the hexagonal structure is distorted and five- and seven-membered rings are formed. Such defects are often observed at grain boundaries and have an impact on the interaction between the graphene layer and the surface.[41,42] The 5-7 defects distort and build up stress in the graphene lattice. It is possible that two 5-7 defects encounter each other and link together to two five- and two seven-membered rings, resulting in a relief of the tension. Two connected 5-7 defects are called STONE-WALES defects.[43] However, with common surface science techniques it is not possible to investigate the influence of these defects in a graphene lattice on the interface. Therefore, the two non-alternant molecules Az and azupyrene (AzPyr) are used as model molecules. The defect-free counterparts are represented by the alternant molecules Nt and pyrene (Pyr). Within the scope of this thesis, the knowledge about these interfaces is extended on a fundamental level.

Most devices make use of the properties of metal/organic interfaces, however, the interest in two-dimensional (2D) materials is growing since the first successful isolation of graphene.[44,45] A new device generation may evolve from organic and inorganic vdW bound hybrid systems of 2D semiconductors like graphene, hexagonal boron nitride or transition metal dichalcogenides (TMDCs).[46–51] Stacking of different types of 2D materials changes the properties of the interface. In this way, the functionality of a device can be tailored. The materials resemble Lego blocks, thus the stacking is called "VAN DER WAALS Lego".[47] The combination of flat-lying OSC monolayers with inorganic substrates increases the stacking possibilities leading to new devices. However, such systems are not well characterized because the OSCs often dewet these substrates.

Prominent OSCs used for devices based on organic/inorganic interfaces are pentacene (PEN) and the fluorinated derivative perfluoropentacene (PFP) (Figure 1.2).[52–59] In these applications, however, PEN and PFP are often used as bulk materials. Formation of close-packed monolayers combined with a strong

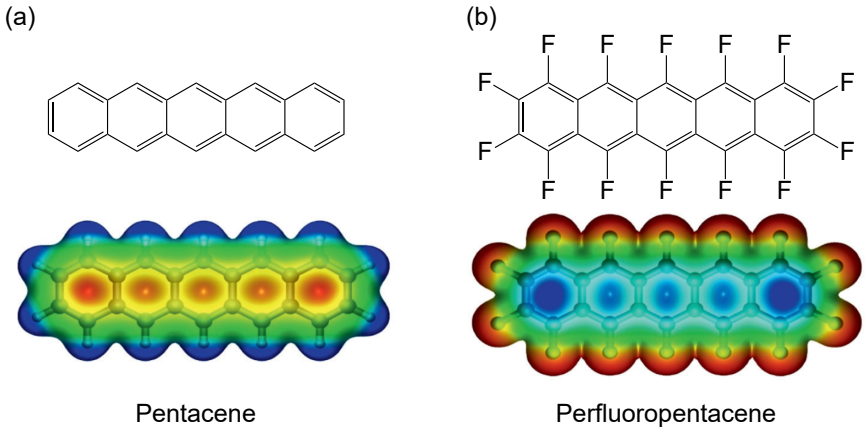

Figure 1.2: Illustration of (a) pentacene and (b) perfluoropentacene. The electrostatic contour plots of both molecules are shown below the molecular structure. Red: electron accumulation, blue: electron depletion. Adapted with permission from ref. [61]. Copyright 2015 John Wiley & Sons, Inc.

interface interaction is not found on most vdW substrates. Due to the weak interface interaction between organic aromatic compounds and the vdW substrates, the molecules often exhibit high mobility. This may lead to a high entropic stabilization in the first molecular layer instead of an enthalpic stabilization observed on metal surfaces.[60] However, close-packed layers do not develop because the mobility, hence the entropic stabilization, would be lost. A possibility to form a close-packed OSC monolayer on inorganic surfaces is the codeposition of PEN and PFP. Since both molecules exhibit reversed electrostatic contours and have opposite quadrupole moments (Figure 1.2), attractive interactions between both molecules should be present. This leads to an additional stabilization in the first layer, resulting in a well-ordered monolayer structure.

1.2 Metal/Organic Interphase Formation

In real devices often thin films, *i.e.*, several tens of nanometers, of OSCs are used. Furthermore, the molecules are often functionalized and more complex containing more elements than C and H like in pure hydrocarbons. A big family of commonly studied molecules are tetrapyrroles. Within this group, porphyrins play an important role. The smallest porphyrin, porphine (Figure 1.3a), consists of four pyrrole units linked *via* methine groups. The nitrogen atoms of the pyrrole units point inside of the macrocycle. The porphine macrocycle can be functionalized by adding groups to either the *meso* positions between the pyrrole units or to the pyrrole units themselves. A common and highly investigated representative is *meso*-tetraphenylporphyrin (H_2TPP) (Figure 1.3b).[62] Porphyrins

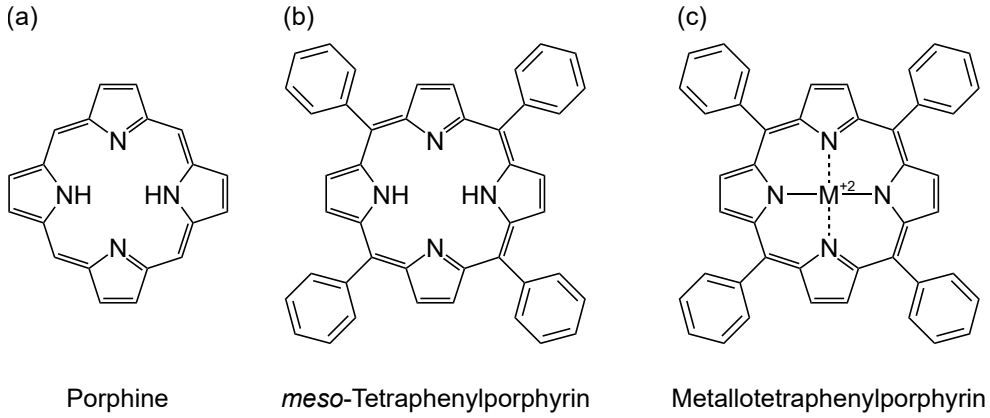

Figure 1.3: Illustration of (a) porphine, (b) H_2TPP and (c) MTPP. Porphine is the smallest representative of the porphyrin group. Substitution of phenyl groups at the *meso* positions yield H_2TPP. Metal atoms may react with H_2TPP to form MTPP.

contain two acidic protons enabling redox reactions, for example, with metal atoms. Afterwards, metal ions are coordinated by four nitrogen atoms in a square-planar coordination geometry (Figure 1.3c). The metalation reactions of porphyrins with several transition metals are well-studied.[62–69]

Besides the direct metalation of porphyrins by deposition of metal atoms onto a porphyrin thin film, self-metalation on metal surfaces[70–73] as well as trans-metalation reactions[74] are reported. Other tetrapyrroles such as corroles gain increasing attention[75–79] but are not the topic of this thesis.

Another often used group of OSCs are poly- and oligothiophenes made of thiophene units (Figure 1.4a). The reaction of poly(3-hexylthiophene) (Figure 1.4b) with Ca has been intensively studied.[80–82] It is found that Ca atoms react with the S atoms of the thiophene units forming CaS. Nevertheless, the reaction products of the residual carbon backbone are unknown. It could be possible that two thiophene units without S atoms form eight-membered ring or that the backbone dimerizes. However, no hard proof has been found until now and polymerization of the residual carbon species could not be excluded. To gain further insight into the reaction, smaller oligothiophenes are investigated.[83] The morphology and the electronic structure of the prominent example 6T (Figure 1.4c) are studied

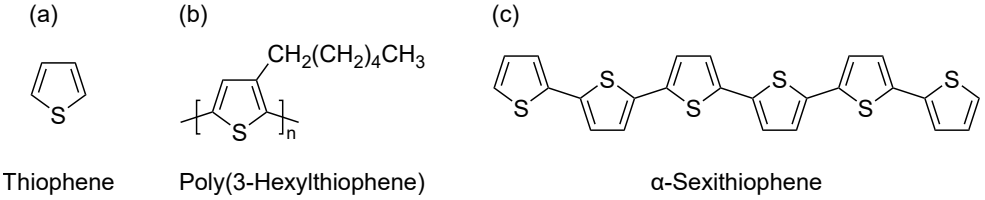

Figure 1.4: Illustration of (a) thiophene, (b) poly(3-hexylthiophene) and (c) 6T. Low-work function metals like Ca may react with the S atom of the thiophene unit forming metal sulfides.

on different metallic single-crystal surfaces.[84–86] Due to application relevance, the metalation reactions of 6T with low-work function metals are still commonly investigated.[87–89]

Devices made of both porphyrins[90,91] and 6T[92] have been reported. As explained above, both OSC families are susceptible to reactions with metal atoms. During fabrication of metal/organic interfaces, metals are sometimes sputter- or vapor-deposited onto organic bulk material. The metal atoms can either form metal clusters, which turns into an electrode after deposition of large amounts of metal during device fabrication, or diffuse into the bulk and react with the organic molecules. The reaction region is then called an interphase, which is buried under the metal layer. The thickness and morphology of the interphase have an impact on the functionality of the device because the interphase influences the charge injection efficiency between the metal and the OSC.[27] Thus, characterization of the internal interphase, diffusion and reaction of the metal atoms in organic bulk materials as well as metal film formation dynamics are crucial.[64,93–98]

Most surface science techniques are highly surface sensitive prohibiting the investigation of the buried interphase. Using X-rays of high energy, however, internal interphases of up to several tens of nanometers can be examined. This method is called hard X-ray photoelectron spectroscopy (HAXPES) and the reaction depths of several systems are studied. The impact of different experimental parameters, such as sample temperature and metal atom flux, on the thickness is investigated by this technique.

1.3 Motivation

The importance of a deeper understanding of interactions and reaction at interfaces led to investigations of several different systems probing metal/organic and organic/inorganic interfaces as well as metal/organic interphases.

The influence of defects in a graphene lattice adsorbed on metals on the interface interaction is not known since investigations of such defects are not possible using techniques that average over a certain region of the sample. In order to circumvent this issue, the defects are modeled by the non-alternant molecules Az and AzPyr and are compared with the alternant molecules Nt and Pyr. In the first study, all four molecules were studied on the Cu(111) surface, while Az and Nt were investigated on the Ag(111) surface as well by means of typical surface science methods, like temperature-programmed desorption (TPD), X-ray pho-

toelectron spectroscopy (XPS), ultraviolet photoelectron spectroscopy (UPS), near-edge X-ray absorption fine structure (NEXAFS) spectroscopy and more. This thesis provides experimental data and detailed analysis in the framework of TPD, whereas the other methods were contributed by other projects within the Gottfried group and external collaboration partners. These investigations gave rise to three publications (P1 to P3). Additionally, the desorption behavior of Bz was investigated on the Cu(111) and Ag(111) surfaces by means of TPD. The data are quantitatively analyzed in order to compare them with adsorption energies derived by density functional theory (DFT) calculations.

As mentioned above, preparation of 2D OSCs on 2D inorganic vdW substrates is difficult due to the weak interaction between them. The second project is a collaboration with P.-M. Dombrowski and other members of the Witte group. Within this project, the successful monolayer formation of the OSCs PEN and PFP on MoS_2 was investigated and preparation techniques of such monolayers were presented. In addition, the interface was investigated qualitatively and quantitatively by means of TPD as well as NEXAFS spectroscopy, Monte Carlo (MC) simulations and scanning tunneling microscopy (STM) contributed by the Witte group. The investigations resulted in publication P4. Furthermore, PEN and PFP were investigated on 2D MoS_2 as well as on Au(111) as a comparison. In addition, multilayers of both molecules were codeposited to study the attractive interaction between both molecules since they exhibit reversed electrostatic contours (Figure 1.2).

Vapor-deposition, as commonly used for device fabrication, often results in a reaction between the organic layer and the metal atoms. However, the resulting interphase may influence the functionality of the device. Control over the interphase formation is crucial, hence the third major topic of this thesis is the characterization of such buried interphases. Here, the well-defined reactions of H_2TPP with Co, Fe and Li gave rise to three publications (P5 to P7). The reaction of 6T with Ca as well as the reaction products were investigated by a multi-technique approach with the help of group members and collaboration partners in publication P8. The transmetalation reaction of lead(II) tetraphenylporphyrin (PbTPP) on the Cu(111) single-crystal surface was studied by TPD and further supported by XPS, STM and DFT calculations performed by members of the Gottfried group. The successful transmetalation and formation of copper(II) tetraphenylporphyrin (CuTPP) in the monolayer resulted in publication P9.

The fourth topic deals with the Ullmann coupling reaction.[99] The Ullmann coupling reaction in solution is a method to form covalent C–C bonds from halogenated aromatic compounds (haloarenes) by the use of Cu ions.[100] In on-surface synthesis, Cu atoms are provided by the surface. The complete mechanism of this reaction is not fully understood until now. It is still unclear, whether the carbon radical binds to the surface or to an adatom.[101–103] TPD experiments of biphenyl (BP), bromobenzene (BBz) and iodobenzene (IBz) will shed light on the mechanism.

In a collaboration project with the Kraus group and other partners, the properties of a newly synthesized compound Pb_3F_8 were analyzed by means of XPS, HAXPES and NEXAFS spectroscopy.

Besides the experimental work that led to this thesis, some parts for improving the experimental setups are invented. Adapter flanges for the LEED-AES optics (LAO) and quartz crystal microbalance (QCM) as well as other smaller parts are constructed. In order to speed up the data processing and especially the treatment of TPD data, two scripts are written in the native language of the software *Igor Pro 8* from Wavemetrics.

2 Experimental Methods and Setups

The results presented in this work were obtained by various surface sensitive techniques but also methods that access bulk properties. These techniques are widely used in modern surface science enabling the investigation of monolayers and thin films including temperature-programmed desorption (TPD), near-edge X-ray absorption fine structure (NEXAFS), AUGER electron spectroscopy (AES) and low-energy electron diffraction (LEED). The bulk properties are probed by hard X-ray photoelectron spectroscopy (HAXPES) and partly TPD. The purpose of this chapter is to explain these techniques and provide necessary physicochemical knowledge in order to fully understand the presented results and publications. The TPD section is explained in more detail since it represents the main method of this work. The other methods will be described on a basic level as there is a variety of literature available, on which this chapter is based.[104–114] In addition, the corresponding experimental setups will be presented, which divide into the TPD chamber in Marburg and the high kinetic energy photoelectron spectroscopy (HIKE) and high energy spherical grating monochromator (HE-SGM) chambers both in Berlin at BESSY II by the *Helmholtz-Zentrum Berlin für Materialien und Energie* (HZB).

2.1 Temperature-Programmed Desorption

The main technique used in this thesis is TPD, also referred to as thermal desorption spectroscopy (TDS). TPD is one of the oldest techniques in surface science studying the interaction between adsorbates and surfaces, but it has been refined and its scope has been substantially widened over the years.

2.1.1 General Introduction

The simplest form of TPD – the so-called flash-filament desorption – consists of a wire of the surface material investigated, which is rapidly heated after ex-

posure to the sample gas. The desorbing species are then simply detected by an ion gauge (total-pressure measurement) or a mass spectrometer set to the corresponding m/z ratio. With such low effort, quantitative information about coverage and kinetic parameters can be obtained, which makes it a common method in the early years of surface science.

However, in order to gain accurate quantitative information about the kinetic parameters like the desorption activation energy (short: desorption energy) and the pre-exponential factor (short: prefactor), a more sophisticated experimental setup using single-crystalline surfaces is mandatory, especially for complex adsorbate–substrate systems and molecule reactions. A schematic drawing of the measuring principle used for modern TPD experiments is shown in Figure 2.1.

It is necessary to conduct the experiments in ultra-high vacuum (UHV) to preserve clean sample surfaces with no contamination as this would heavily influence the outcome of an experiment. A TPD setup needs a sample holder, a detector, an adsorbate source, and high pumping speeds. The focus for high-quality TPD is on the sample holder and the detector. Depending on the investigated adsorbate–substrate systems, the sample holder needs a cooling stage, for example, with liquid nitrogen (LN_2) or helium, a reliable temperature control, *e.g.*, calibrated thermocouples, and a heating system. The cooling is necessary to reach temperatures below the sublimation temperature of the adsorbate so that molecules stick to the surface. Quadrupole mass spectrometers are commonly

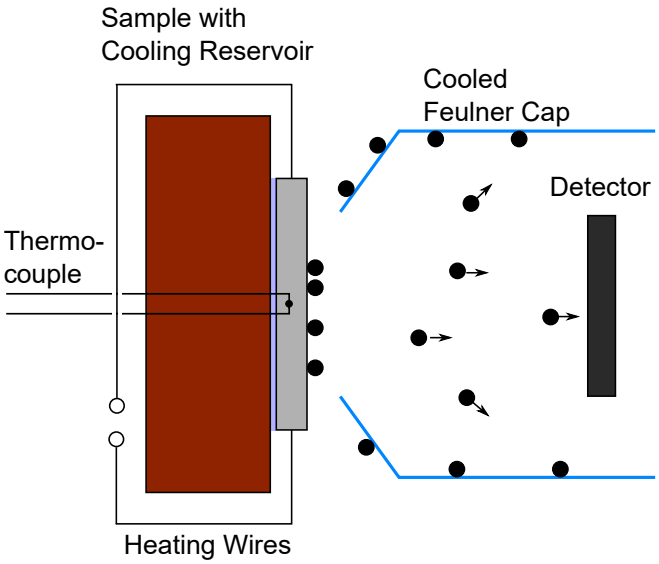

Figure 2.1: Experimental setup for temperature-programmed desorption studies in ultra-high vacuum. Molecules (black dots) are deposited onto the cold sample and desorb if the sample is heated. The sample is electrically insulated from the cooling reservoir. The temperature of the sample is measured by a thermocouple. Molecules can either hit the Feulner cap or the detector.

used as detectors together with a FEULNER cap,[115] which greatly improves TPD traces because background signals are avoided, around the mass spectrometer's ionization source. A cooled FEULNER cap further enhances the data quality. In this way, only desorbing molecules with a direct line-of-sight trajectory hit the detector. Molecules impinging on the walls of the FEULNER cap will condense and stick there without further desorption during the experiment. This greatly reduces high-temperature tails in TPD traces, especially for small organic molecules. Moreover, the mass spectrometer needs differential pumping with high pumping speeds to remove molecules from the detection area, avoiding readsorption on the hot sample surface.

As the name of the method implies, the desorption is the main process and often the rate-limiting step. Hence, the desorbing molecules per time, which are equal to the desorption rate r_{des} measured by mass spectrometry, can be expressed by a simple rate law of n^{th} order with Θ being the surface coverage.

$$r_{\mathrm{des}} = -\frac{\mathrm{d}\Theta}{\mathrm{d}t} = k_n \cdot \Theta^n \tag{2.1}$$

In Equation (2.1) t is the time and k_n the rate constant, which can be described by a simple ARRHENIUS equation

$$k_n = \nu_n \cdot \exp\left(-\frac{\Delta E_{\mathrm{des}}}{RT}\right) \tag{2.2}$$

with the desorption energy E_{des}, the prefactor of n^{th} order ν_n, the universal gas constant R and the temperature T. Inserting Equation (2.2) in Equation (2.1) gives the POLANYI-WIGNER (PW) equation, the fundamental and most important equation in TPD.

$$r_{\mathrm{des}} = -\frac{\mathrm{d}\Theta}{\mathrm{d}t} = \nu_n \cdot \exp\left(-\frac{\Delta E_{\mathrm{des}}}{RT}\right) \cdot \Theta^n \tag{2.3}$$

It is important to note that the coverage Θ represent the residual coverage, defined as $N_{\mathrm{ads}}/N_{\mathrm{surf}}$ with the currently adsorbed particles N_{ads} and the total number of available adsorption sites for the particle N_{surf}. Furthermore, it is common practice to heat the sample with a linear heating rate ($\beta = \mathrm{d}T/\mathrm{d}t$).

The obtained peaks in TPD occur because of two competitive processes: first, the desorption probability exponentially increases with increasing temperature ($\exp(-\Delta E_{\mathrm{des}}/RT)$) and second, at the same time the residual coverage Θ decreases due to desorption, resulting in a decreasing desorption rate until no particles are left on the surface.

Although the fundamental principle is rather simple, real adsorbate–substrate systems may become complex. Often, one or more kinetic parameters are coverage dependent affecting the shape of the peak. In addition, the reaction order corresponds to the rate-limiting step, which is not mandatorily the desorption process; therefore, it is not necessarily equal to one. A comparison of commonly observed reaction orders is shown in Figure 2.2. Coverage series of TPD traces with a reaction order of one (Figure 2.2c), often observed for desorption of intact molecules in the first layer, always share the same peak temperature independent of the initial coverage. The peak shape itself is asymmetric due to the two competing processes discussed above.

For the desorption of intact molecules from multilayers a reaction order of zero is often observed (Figure 2.2a), where no interaction between molecule and substrate exists. The desorption rate in this case is independent of the coverage resulting in an exponential increase of it as long as molecules are available.

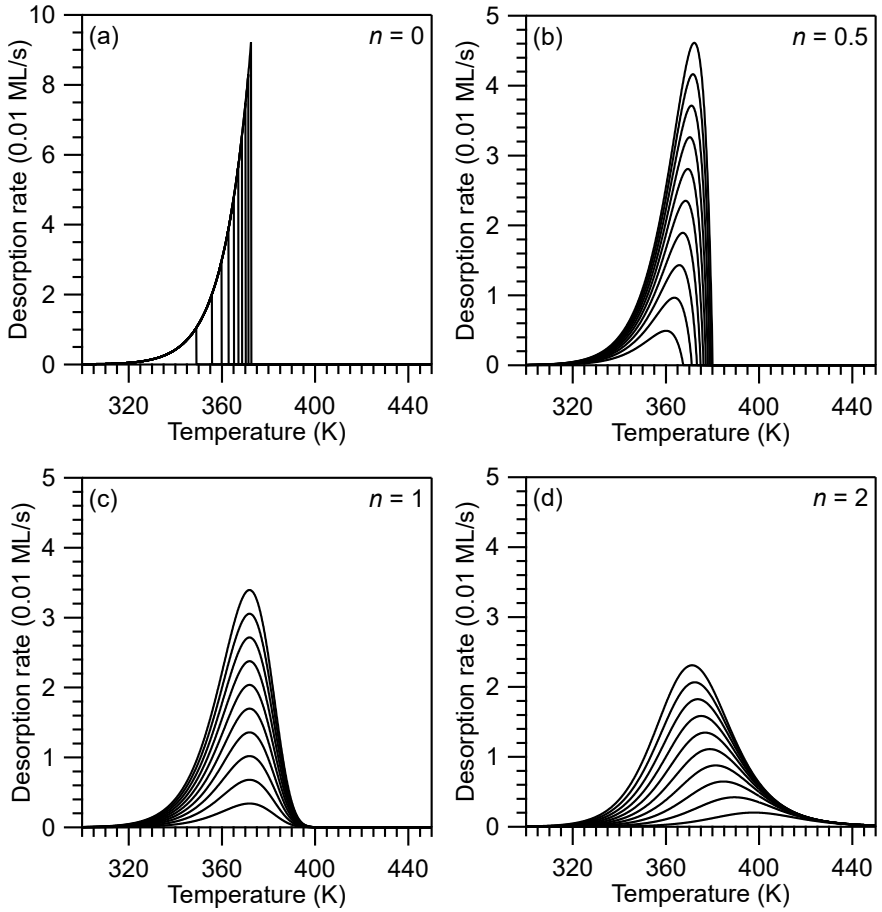

Figure 2.2: Simulated TPD traces for (a) zeroth-, (b) non-integer-, (c) first- and (d) second-order reactions with initial coverages from 0.1 to 1.0 ML in 0.1 ML steps. The heating rate is 1 K/s, the desorption energy 100 kJ/mol and the prefactor $1 \cdot 10^{13}$ s^{-1}. Desorption parameters are independent of the coverage.

The peak suddenly ends with a sharp edge once no molecules are left in the multilayer, however, in real experiments the peaks are slightly broadened due to limited pumping speed and because the final layer often desorbs according to first order. All multilayer traces of a system share the same leading edge independent of the initial coverage. Accordingly, for higher initial coverages the peak maximum temperatures shift to higher temperatures as a larger molecule reservoir lasts longer before it runs empty.

Reaction orders between zero and one often correspond to desorption from islands (Figure 2.2b). Molecules on the edges of the island desorb more easily than the molecules within the island. Nevertheless, these processes are very complex and have to be examined for each system. The TPD peaks are characterized by a peak shift to higher temperatures with increasing coverage.

The last prominent example is the reaction order of two (Figure 2.2d), which often appears in recombination reactions. This is commonly observed for oxygen, where the formation of a bond between two oxygen atoms is the rate limiting step, for example, on Au(110).[116] The desorption rate is proportional to Θ^2, hence the peak maximum temperatures shift to lower temperatures with increasing initial coverages as a higher molecule concentration increases the reaction probability between two atoms.

These considerations of peak shape and peak temperature shift correspond to different reaction orders while the desorption energy and the prefactor are kept constant, *i.e.*, are independent of the coverage. However, real systems often exhibit intermolecular interactions influencing the kinetic parameters. Especially polycyclic aromatic hydrocarbons (PAHs) on metallic single-crystal surfaces show a strong dependence of the desorption energy on the coverage.[29–35,117–122] This dependence originates from intermolecular repulsion between vertical dipoles, which are mainly caused by the Pauli pushback effect.[28,123,124] Information on peak shape and peak temperature shifts for such special cases are important, too. Simulated TPD traces for coverage-dependent kinetic parameters are shown in Figure 2.3.

The intermolecular repulsion is attributed to the repulsion between parallel dipoles on the surface. This interaction occurs between each particle pair on the surface, hence, in a first approximation, the repulsion linearly increases with the surface concentration, *i.e.*, the residual coverage.[125,126] The influence of a linearly decreasing desorption energy on TPD traces is shown in Figure 2.3a. The peak maximum temperature shifts to lower temperatures for increasing coverages. Furthermore, the peak gets significantly broadened. At full monolayer

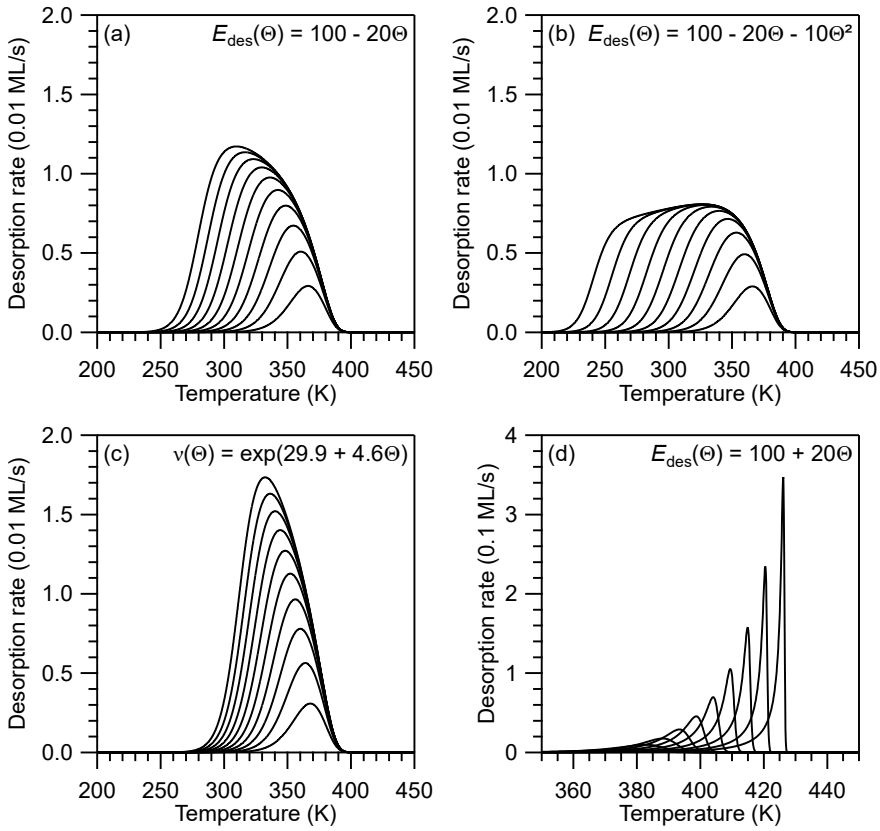

Figure 2.3: Simulated first-order TPD traces for (a) a linear repulsive desorption energy ($E_{\mathrm{des}}(\Theta) = 100-20\Theta$), (b) a linear and quadratic repulsive desorption energy ($E_{\mathrm{des}}(\Theta) = 100-20\Theta-10\Theta^2$), (c) an increasing prefactor of two orders of magnitude ($\nu(\Theta) = \exp(29.9+4.6\Theta)$) and (d) a linear attractive desorption energy ($E_{\mathrm{des}}(\Theta) = 100 + 20\Theta$) with initial coverages from 0.1 to 1.0 ML in 0.1 ML steps. The heating rate is 1 K/s, the zero-coverage desorption energy 100 kJ/mol and the zero-coverage prefactor $1 \cdot 10^{13}$ s^{-1}. The coverage dependencies of the desorption energy (given in kJ/mol) and the prefactor (given in s^{-1}) are shown in the graphs.

coverage (1 ML) the desorption energy is at its minimum resulting in low desorption temperatures. Afterwards, the surface coverage as well as the intermolecular repulsion decreases, while the desorption energy increases. The increased energy lowers the desorption rate at the same time. For lower coverages the repulsion can be neglected leading to a common declining edge of the traces in the coverage series.

The interaction between adsorbed molecules on the surface is not only restricted to linear coverage dependencies. According to a model presented by Persson,[125] the repulsion between two particles on the surface can be lowered if the particles can slightly move away from their preferential adsorption sites. However, this leads to additional interactions with a third particle or a vacancy for submonolayer coverages in the other direction resulting in a quadratic coverage dependence of the energy. This term can be either positive or neg-

ative depending on the energy gain due to decreased repulsion or energy loss due to additional repulsion or incommensurate adsorption motifs. The complex nature of the quadratic term prohibits further quantitative explanation. In a TPD coverage series this term leads to stronger temperature shifts to lower values and more pronounced peak broadening (see Figure 2.3b). Traces are often characterized by a desorption plateau, where the desorption rate nearly stays constant. This behavior is often found for PAHs on metallic single-crystalline surfaces.[31,117]

Intermolecular interactions are not restricted to repulsive forces, *e.g.*, lateral attractive VAN DER WAALS (vdW) interactions. It is possible that the attractive interactions overcompensate the repulsion, resulting in an increasing desorption energy with increasing coverages. In such cases, the desorption energy is at its maximum at high coverage. Therefore, the desorption temperatures as well as the peak maximum temperatures shift to higher temperatures with increasing coverages (Figure 2.3d). Since the desorption energy decreases for decreasing coverages during desorption, the desorption rate rapidly rises until an abrupt end of the TPD trace, which is similar to zeroth-order desorption. Note that this is one rare example where TPD traces of a coverage series cross each other.

Besides intermolecular interactions, mobility and entropy of the adsorbate may vary together with the coverage, however, this will mainly affect the prefactor instead of the desorption energy. A detailed discussion on the prefactor will be given in the next section (2.1.2). An increasing prefactor of two orders of magnitude (Figure 2.3c) leads to peak maximum temperature shifts to lower temperatures as well as peak broadening. Depending on the magnitude of the increase it is hard to distinguish between a linear coverage dependence of the desorption energy or the prefactor (compare a and c in Figure 2.3). This emphasizes the need for sophisticated analysis methods, enabling the determination of coverage-dependent kinetic desorption parameters independent of each other. A variety of common techniques will be presented in Section 2.1.3.

2.1.2 Discussion of Preexponential Factors

The preexponential factor ν, also falsely called frequency factor, is often accounted to molecular vibrations because molecules can only desorb within one vibration. However, this is physically inaccurate as the prefactor is a measure for the standard entropy of activation $\Delta S^{\ddagger}$. This becomes clear if the EYRING equation (2.4) in the framework of the transition state theory (TST) for the rate constant k_{TST} is considered.[127]

$$k_{\mathrm{TST}} = \frac{k_{\mathrm{B}}T}{h} \cdot \exp\left(-\frac{\Delta G^{\ddagger}}{RT}\right) \tag{2.4}$$

Here, k_{B} is the Boltzmann constant, h the Planck constant and $\Delta G^{\ddagger}$ the standard Gibbs free energy of activation. The latter is related to the standard enthalpy of activation $\Delta H^{\ddagger}$ and $\Delta S^{\ddagger}$ by $\Delta G^{\ddagger} = \Delta H^{\ddagger} - T\Delta S^{\ddagger}$. $\Delta H^{\ddagger}$ is thermodynamically related to the activation energy, hence the prefactor correlates with $\Delta S^{\ddagger}$, which can be estimated by the number of degrees of freedom (DOFs) in the initial state (IS) and transition state (TS). Since larger molecules, especially PAHs, are confined on the surface at high coverages, they are losing DOFs on the surface. Upon desorption, they often gain more DOFs manifesting in an increase of the prefactor. This was observed in numerous experiments for organic compounds on graphite as well as on metallic single-crystal surfaces.[35,60,128–135]

In order to calculate the prefactor and compare it with experimental values derived by TPD, the most commonly used approach is the TST.[35,60,127,130,131] In the desorption process the IS can be regarded as the adsorbed molecule, which moves away from the surface upon desorption. Therefore, the TS can be considered as a gas-phase like state, while the final state is the molecule in the gas phase. However, the gas-phase like state is similar to the gas phase without one translational DOF for the critical coordinate in first approximation. According to the TST by Eyring, the prefactor ν_{des} in the TS can be calculated by:[127]

$$\nu_{\mathrm{des}} = \frac{k_{\mathrm{B}}T}{h} \cdot \frac{q^{\ddagger}}{q_{\mathrm{ad}}}. \tag{2.5}$$

In Equation (2.5) $q^{\ddagger}$ is the partition function in the TS (gas-phase like) and q_{ad} the partition function in the IS (adsorbed). Nevertheless, calculations of both partition functions require detailed knowledge of the interaction potentials of the adsorbed molecule and the TS, which is often not known or expensive to calculate albeit not impossible. A much easier approach is to make assumptions simplifying the partition functions. The vibrational contributions to the partition function in the IS and TS are assumed to be very similar, hence they cancel in Equation (2.5). As mentioned above, the TS can be considered as the molecule in the gas phase, where it has three rotational and two translational DOFs. One translational DOF is subtracted as this is the reaction coordinate and considered in the term $k_{\mathrm{B}}T/h$. Accordingly, the partition function in the TS $q^{\ddagger}$ can be expressed as:

$$q^{\ddagger} = q^{\ddagger}_{\mathrm{tr,2D}} \cdot q^{\ddagger}_{\mathrm{rot,3D}}. \tag{2.6}$$

Two limiting cases are considered for the adsorbed molecule. In the first case, the molecule has the highest mobility on the surface, thus the partition function in the mobile state $q_{\mathrm{ad,mob}}$ has two translational DOFs parallel to the surface and one rotational DOF perpendicular to the surface (Equation (2.7)). In the second case, the molecules are completely confined on the surface leading to a partition function in the immobile state $q_{\mathrm{ad,immob}}$ of one.

$$q_{\mathrm{ad,mobile}} = q_{\mathrm{tr,2D}} \cdot q_{\mathrm{rot,1D}} \tag{2.7}$$

Inserting Equations (2.6) and (2.7) into Equation (2.5) enables the calculation of the prefactor. One last assumption is that the translational partition functions of the adsorbed state and in the gas phase are equal, so they cancel in the mobile limit.

$$\nu_{\mathrm{mobile}} = \frac{k_{\mathrm{B}}T}{h} \cdot \frac{q^{\ddagger}_{\mathrm{rot,3D}}}{q_{\mathrm{rot,1D}}} \tag{2.8}$$

$$\nu_{\mathrm{immobile}} = \frac{k_{\mathrm{B}}T}{h} \cdot q^{\ddagger}_{\mathrm{tr,2D}} \cdot q^{\ddagger}_{\mathrm{rot,3D}} \tag{2.9}$$

The translational and rotational partition functions are given by:[35,127,136]

$$q^{\ddagger}_{\mathrm{tr,2D}} = \frac{2\pi m k_{\mathrm{B}} T A}{h^2}, \tag{2.10}$$

$$q^{\ddagger}_{\mathrm{rot,3D}} = \frac{\pi^{1/2}}{\sigma}\left(\frac{k_{\mathrm{B}}T}{hc_0}\right)^{3/2}(B_A B_B B_C)^{-1/2}, \text{ and} \tag{2.11}$$

$$q_{\mathrm{rot,1D}} = \frac{\pi^{1/2}}{\sigma}\left(\frac{k_{\mathrm{B}}T}{hc_0 B_A}\right)^{1/2}. \tag{2.12}$$

Here, m is the molecular mass, A the area, σ the symmetry factor, and B_i the rotational constants around the axes A, B and C. All parameters are now either constants or properties of the molecule making it easy to calculate the prefactor for every adsorbate–substrate system.

There are further approaches to estimate the prefactor, for example, to directly calculate the entropy of activation in the desorption process and derive the prefactor from it.[131,137,138] The prefactor for multilayer desorption can be calculated by assuming detailed balance between a condensed film in equilibrium with its vapor pressure and using the Clausius-Clapeyron equation.[129–131,139–141] As these methods are not used often and exhibit some uncertainties, a detailed explanation is not given here but can be found in publication P2 of this thesis (page 188).

2.1.3 Analysis Methods in Temperature-Programmed Desorption

After a detailed discussion on kinetic parameters and their influence on TPD traces, analytical methods to obtain the desorption energy and the prefactor are now in the focus.

REDHEAD Analysis

A common method is the analysis according to REDHEAD.[142] Starting from the POLANYI-WIGNER Equation (2.3), $\mathrm{d}t$ can be substituted by the heating rate $\beta = \mathrm{d}T/\mathrm{d}t$, yielding:[142]

$$\frac{\mathrm{d}\Theta}{\mathrm{d}T} = -\frac{1}{\beta} \cdot \nu_n \cdot \exp\left(-\frac{\Delta E_{\mathrm{des}}}{RT}\right) \cdot \Theta^n. \tag{2.13}$$

The desorption rate is differentiated at the peak maximum temperature T_{max} leading to:[105,142]

$$\left.\frac{\mathrm{d}r_{\mathrm{des}}}{\mathrm{d}T}\right|_{T_{\mathrm{max}}} = \left.\frac{\mathrm{d}^2\Theta}{\mathrm{d}T^2}\right|_{T_{\mathrm{max}}} = 0. \tag{2.14}$$

To solve this equation, Equation (2.13) is inserted into Equation (2.14) and differentiated resulting in:[105,142]

$$\begin{aligned}\left(\frac{\mathrm{d}^2\Theta}{\mathrm{d}T^2}\right) = {} & \frac{\Theta^n \cdot \nu_n}{\beta} \cdot \frac{\Delta E_{\mathrm{des}}}{RT_{\mathrm{max}}^2} \cdot \exp\left(-\frac{\Delta E_{\mathrm{des}}}{RT_{\mathrm{max}}}\right) \\ & + \frac{\nu_n}{\beta} \cdot n \cdot \Theta^{n-1} \cdot \frac{\mathrm{d}\Theta}{\mathrm{d}T} \cdot \exp\left(-\frac{\Delta E_{\mathrm{des}}}{RT_{\mathrm{max}}}\right) \\ = {} & 0 \end{aligned} \tag{2.15}$$

$$\frac{\Delta E_{\mathrm{des}}}{RT_{\mathrm{max}}^2} = -n \cdot \Theta^{(n-1)/n} \cdot \frac{\mathrm{d}\Theta}{\mathrm{d}T}. \tag{2.16}$$

Equation (2.13) is inserted into Equation (2.16) yielding an expression for the calculation of the desorption energy.[105,142]

$$\frac{\Delta E_{\mathrm{des}}}{RT_{\mathrm{max}}^2} = \frac{n \cdot \nu_n}{\beta} \cdot \Theta^{n-1} \cdot \exp\left(-\frac{\Delta E_{\mathrm{des}}}{RT_{\mathrm{max}}}\right) \tag{2.17}$$

In addition, it is assumed that the activation parameters are independent of the surface coverage and the reaction is proceeding according to first-order kinetics, leading to Equation (2.18).[105,142]

$$\frac{\Delta E_{\mathrm{des}}}{RT_{\mathrm{max}}^2} = \frac{\nu_1}{\beta} \cdot \exp\left(-\frac{\Delta E_{\mathrm{des}}}{RT_{\mathrm{max}}}\right) \tag{2.18}$$

This equation is solved by taking the logarithm of it and rearranging to ΔE_{des}:[105,142]

$$\Delta E_{\mathrm{des}} = RT_{\mathrm{max}}\left[\ln\left(\frac{\nu_1 \cdot T_{\mathrm{max}}}{\beta}\right) - \ln\left(\frac{\Delta E_{\mathrm{des}}}{RT_{\mathrm{max}}}\right)\right]. \tag{2.19}$$

For the condition $10^8\,\mathrm{K}^{-1} < \nu_1/\beta < 10^{13}\,\mathrm{K}^{-1}$, the term $\ln(\Delta E_{\mathrm{des}}/RT_{\mathrm{max}})$ is about 10 % of the first term. An approximation of $\ln(\Delta E_{\mathrm{des}}/RT_{\mathrm{max}}) = 3.64$ only leads to errors less than 1.5 %.[142] Otherwise, the REDHEAD equation has to be graphically or numerically calculated, what is done by programs.

For coverage-independent kinetic parameters and a well-known prefactor, *e.g.*, from TST, this method quickly yields good results from a single TPD trace making it a frequently used technique. However, for more complex systems, as described above, obtained values may not be reliable and often false, because the prefactor is estimated and assumptions must be made. For the calculation of both the desorption energy and the prefactor at the same time, additional methods are necessary.

Heating-Rate Variation Method

The heating-rate variation (HRV) method can be regarded as an enhancement of the REDHEAD analysis method. Again, the peak maximum temperature is of interest, yet a series of traces is used. These should have the same initial coverage but are measured at different heating rates β.[143,144] As a starting point Equation (2.17) can be used. For first-order kinetics, the logarithmic Equation (2.18) is rearranged to $\ln(T_{\mathrm{max}}^2/\beta)$ leading to:[143,144]

$$\ln\left(\frac{T_{\mathrm{max}}^2}{\beta}\right) = \frac{\Delta E_{\mathrm{des}}}{RT_{\mathrm{max}}} + \ln\left(\frac{\Delta E_{\mathrm{des}}}{\nu_1 \cdot R}\right). \tag{2.20}$$

A linear correlation between $\ln(T_{\mathrm{max}}^2/\beta)$ and $1/T_{\mathrm{max}}$ is then found. The desorption energy is calculated from the slope and the prefactor from the y-intercept. According to Equation (2.20), $\widetilde{T}_{\mathrm{max}}\ \exp(\text{-}\widetilde{T}_{\mathrm{max}}^{-1/2})$ is proportional to $\sqrt{\widetilde{\beta}}$, *i.e.*, for increasing values of β the peak maximum temperature is increasing, too.

Moreover, the integral of typical raw TPD curves scale with the heating rate because the desorption rate is plotted against the temperature ($\mathrm{d}\Theta/\mathrm{d}T = \beta \cdot \mathrm{d}\Theta/\mathrm{d}t$). The integral of the time-dependent desorption rate is, however, equal for all heating rates. This change has to be considered due to the conversion

of time into temperature domain using the heating rate β. It is noteworthy that this method is also applicable to second-order kinetics but this will not be further explained here.

Leading-Edge Analysis

Another method to calculate the desorption energy and the prefactor independent of each other is the leading-edge analysis (LEA) by Habenschaden and Küppers.[145] Here, the leading edge of TPD traces is investigated in order to determine coverage- and temperature-dependent activation parameters. Therefore, the PW equation is logarithmized:[145]

$$\ln(r_{\mathrm{des}}) = -\frac{\Delta E_{\mathrm{des}}}{RT} + \ln(\nu) + n \cdot \ln(\Theta). \tag{2.21}$$

The only approximation of this method is that the coverage has to be constant. Using a small section (typically until 1 to 5 % of the initial coverage are desorbed)[145] of the leading edge for the plot, leads to small errors. This enables the determination of kinetic desorption parameters in dependence on the coverage if a coverage series is analyzed. The plot of $\ln(r_{\mathrm{des}})$ *vs.* $1/T$ yields a straight line in this section of the leading edge. The desorption energy can be calculated using the slope of the linear fit and the prefactor using the y-intercept if the initial coverage and the reaction order is known. A special case is given for zeroth-order reactions like the desorption of multilayers. For $n = 0$, Equation (2.21) becomes independent of the coverage, thus it turns into the Arrhenius Equation (2.2).

Due to its simplicity and small amount of assumptions, the LEA is frequently used in TPD studies. However, high-quality data are required because a bad signal-to-noise ratio (SNR) of the leading edge may cause large errors. This method is improved by subtracting the term $n \cdot \ln(\Theta)$ from Equation (2.21),[144,146,147] which is called modified leading-edge analysis (mLEA) in this thesis:

$$\ln\left(\frac{r_{\mathrm{des}}}{\Theta^n}\right) = -\frac{\Delta E_{\mathrm{des}}}{RT} + \ln(\nu). \tag{2.22}$$

The advantage of this method is that the whole TPD trace can be used because the coverage does not have to be constant. Here, Θ is a function of the temperature and is not constant compared with the normal LEA. For the correct choice of the reaction order n, the plot of $\ln(r_{\mathrm{des}}/\Theta^n)$ *vs.* $1/T$ yields a straight line, enabling the determination of the reaction order from experimental data. Otherwise, the plot becomes convex or concave. The desorption energy and the prefactor are averaged over the whole trace. However, if the fit is applied

on a small coverage interval at the beginning of the TPD trace, the coverage-dependent average of the desorption energy and prefactor can be determined. At high coverages, the small coverage interval is related to the leading edge. In contrast, at low coverages nearly the whole trace can be used greatly increasing the statistics and yielding better results compared with the normal LEA.

Complete Analysis

The complete analysis (CA) was first introduced by King[148] and Bauer,[149] providing a method to determine desorption energies and prefactors over a wide coverage range without any assumptions. The disadvantage is that high-quality TPD data and a detailed coverage series with many different initial coverages are necessary.[144,148] In the case of repulsive intermolecular interactions, this method is not suitable because the quality requirements are even higher and are difficult to meet in practice even with the best TPD experiments.[147] The desorption rates and temperatures at a certain residual coverage Θ', with $\Theta' < \Theta_{\text{initial}}$, are determined for all measured TPD traces.[144,148,149] This routine is illustrated in Figure 2.4 for the desorption of Ag on Ru(001).[104]

The Arrhenius plot of these rate–temperature pairs yields a straight line. The desorption energy can be obtained using the slope and the prefactor using

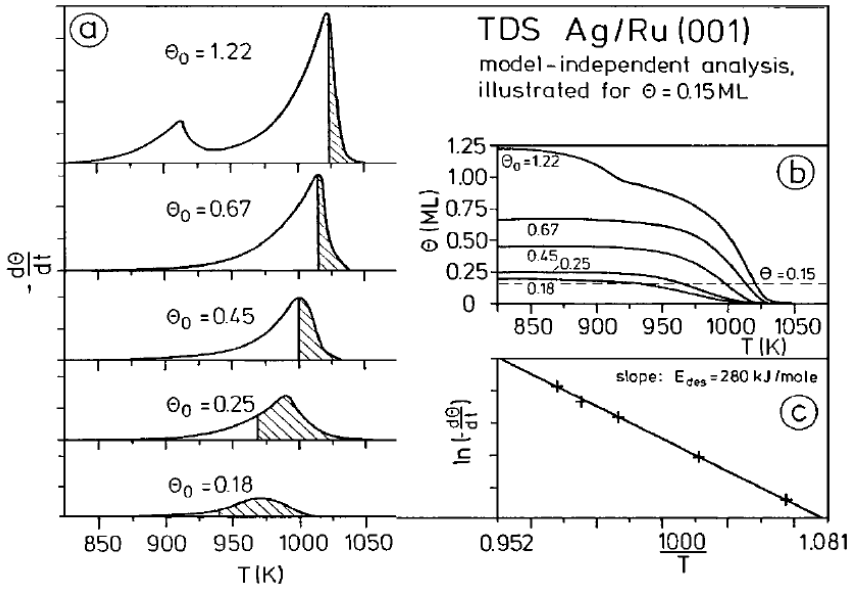

Figure 2.4: Example routine for the CA for the system Ag/Ru(001). (a) Integration of TPD traces to determine desorption rates corresponding to a fixed residual coverage. (b) Plot of Θ *vs.* T indicating the investigated coverage 0.15 ML. (c) Plot of $\ln(r_{\text{des}})$ *vs.* $1/T$ for the coverage–temperature pairs of (b). The slope yields the desorption energy, the y-intercept yields the prefactor corresponding to a fixed coverage of 0.15 ML. Reprinted with permission from ref. [104]. Copyright 2007 John Wiley & Sons, Inc.

the y-intercept for a known reaction order according to $n\ln(\Theta') + \ln(\nu(\Theta'))$. The analysis routine may yield artifacts due to scattering in the coverage series owed to a bad SNR. Furthermore, the CA often shows an artificial or forced compensation effect, *i.e.*, the desorption energy and the prefactor are not independent of each other and follow the same trend.[147,150] Therefore, such data need critical discussion and other methods should be used to verify the results. While repulsive intermolecular interactions result in very dense rate–temperature pairs, reducing the number of points available for the ARRHENIUS plot, this method works especially well for attractive interactions, as shown in the example of Figure 2.4.

Inverted POLANYI-WIGNER Equation

So far, all methods yield kinetic parameters for distinct coverages. Determination of desorption energies and prefactors for the whole coverage range from 0 to 1.0 ML requires a lot of data. NIESKENS developed a method to calculate the desorption energy over the full coverage range only using the monolayer trace, however, the prefactor has to be assumed.[147] For the so-called inverted POLANYI-WIGNER (IPW) equation the PW equation is rearranged to the desorption energy:[147]

$$\Delta E_{\mathrm{des}} = RT \ln\left(\frac{r_{\mathrm{des}} \cdot \beta}{\nu \cdot \Theta^n}\right). \tag{2.23}$$

For each data point of the TPD trace the desorption energy is calculated for a known prefactor. In this way, the coverage dependence of the desorption energy can be obtained from a single monolayer trace. The disadvantage of this method is that the prefactor has to be known or calculated from different approaches like TST.

Fitting of the Desorption Energy

The previously described methods originate from times of slow computers. With the increased computational power of today's computers, it is easily possible to directly fit the TPD curves using the PW equation with mathematical expressions for the coverage-dependent desorption energy. It is shown in the literature[34,35,151,152] that a quadratic equation in the form of $\Delta E_{\mathrm{des}}(\Theta) = \Delta E_{\mathrm{des}}(\Theta = 0) - a\Theta - b\Theta^2$ fits well. In this equation $\Delta E_{\mathrm{des}}(\Theta = 0)$ is the desorption energy at zero coverage and the terms a and b are derived from the PERSSON model explained in Section 2.1.1.[125]

Fitting the parameters a and b to TPD traces yields a continuous description of the desorption energy. In addition, the prefactor can be fitted and does not to be assumed. Due to the compensation effect, many energy–prefactor pairs yield good fitting results, hence the fitting prodecure may get unstable or runs into local minima.

Integral Energies

It is important to note that TPD is a differential method, *i.e.*, the measured rate corresponds to the desorption of single particles. Changes in the TPD traces and in the kinetic parameters are attributed to single particles, too. In contrast to experimental energies, theoretical methods such as density functional theory (DFT) always provide integral energies. This means that in TPD all particles would desorb at once. In order to account for this deviation, the desorption energy must be integrated according to:

$$\Delta E_{\mathrm{des},i}(\Theta_i) = \frac{1}{\Theta_i} \int_0^{\Theta_i} \Delta E_{\mathrm{des}}(\Theta) \mathrm{d}\Theta. \tag{2.24}$$

For reliable results, the desorption energy as a continuous function of the coverage is needed. Therefore, the IPW equation and the fitting of the desorption energy described above are predestined, while the CA would also work.

Comparison of the Analytical Methods

The quantitative calculation of the desorption energy and the prefactor is one of the main purposes of TPD. Therefore, many different analysis methods were developed, some of which were described above. There are more methods, like the Chan-Aris-Weinberg (CAW) method,[153] but they often perform worse than the methods presented above.[144] Each method uses different parts of the TPD trace, *e.g.*, the leading edge or the peak maximum temperature. This leads to various assumptions, advantages and disadvantages of the methods. Under which conditions each method performs best was discussed in literature using simulated TPD traces.[144,147] A comparison of the performances of the methods on real experimental data is a topic of this thesis and published in P2. Nevertheless, there is no perfect analysis, which can calculate the coverage dependence of the desorption energy and the prefactor for every coverage with high precision. It is emphasized to use a variety of different methods and estimate the reliability of the results depending on the quality of the data. Especially the prefactor should be considered when discussing desorption energies since both are needed in the PW Equation (2.3).

Outlook for Improved Methods

As previously mentioned, there is no perfect method for calculating the kinetic parameters for every coverage. That is why research groups still develop new methods until now. This includes optimization of initial values in fitting procedures[154] or a theoretical parameter-free analysis model.[155] However, the perfect solution is yet to be found.

A promising approach is to fit TPD traces using the PW Equation (2.3) as it was proposed above (fitting of the desorption energy). To reduce calculation time, some assumptions were made, for example, a known prefactor and a known reaction order are inserted into the PW equation. An improvement is to nearly keep all parameters free in the PW equation and fit them for best agreement between simulated and experimental TPD traces. However, this would result in a tremendous number of possible parameter sets and a huge computing time. Therefore, sophisticated fitting algorithms are needed. During data analysis, two different approaches were tested – on the one hand a genetic algorithm (GA) and on the other hand a neural network (NN).

The GA generates random parameter sets (individuals) and calculates the error between the simulated and experimental curve in the first generation. Only the best parameter sets survive this generation, for example, the best 10 %. In the next generation new parameter sets are added to the survivors, consisting of random linear combinations of the survivors. Random mutations are added to escape from local minima. Detailed explanations on GAs and implementations in the software *Igor Pro 8* can be found in the literature.[156–159] For a large number of individuals and generations results with low deviation are obtained. The computing time is manageable, although the algorithm sometimes runs into local minima if the number of generations and the mutation probability is too low. Improving this fitting procedure and lowering the run time may be a promising alternative to established analysis methods.

NNs are often used for face recognition algorithms. Information on NNs are widely distributed.[160,161] In a similar way, a NN is used to recognize TPD traces. Therefore, the NN is trained with simulated TPD curves and the corresponding parameter sets. Afterwards a well-trained NN can reproduce every experimental trace in short time and output the corresponding kinetic parameters. A NN was set up using build-in functions of *Igor Pro 8*.[159] Although this approach seems most promising, training a NN well is not easy and takes long computation time. Simple simulated TPD traces with coverage-independent kinetic parameters were well reproduced, however this often failed for real data. Due to limited

computation time and equipment, a working NN could not be trained during this study. Nevertheless, this approach offers great potential. These methods only represent some examples how to improve TPD analysis and may serve as a starting point for future projects.

2.1.4 Temperature-Programmed Desorption Mass Spectrometry

In common TPD experiments only one or just a few masses are recorded, providing high temperature resolution due to a short measuring time. However, this is only possible if the desorbing species and, therefore, their mass is known. Investigating reactions, *e.g.*, the metalation of tetrapyrroles, resulting products are not obvious and many masses are possible. For such cases certain mass ranges or a whole mass spectrum can be recorded while the sample is heated. The combination of mass spectrometry with temperature-programmed desorption is called temperature-programmed desorption mass spectrometry (TPD-MS). This technique was used in literature to study the desorbing reaction products of the coronene oxidation or the dimerization of coronene and fullerenes on graphite – to name just a few examples.[162–165]

The recorded mass spectra are plotted against the temperature with the intensity plotted along the z axis resulting in a 2D or contour plot. The biggest issue of this technique is to reach good temperature and mass resolution as the time of a TPD-MS experiment is limited. Recording a large mass range or with a small mass step width increases acquisition time. For a constant heating rate a longer acquisition time results in larger temperature steps between two duty cycles. A decent mass resolution combined with a low heating rate yields reasonable temperature resolution. Empirically, it was found that the temperature step between two cycles should not be larger than 6 K, but best below 3 K. Considering these restrictions, it is recommended to first record an overview TPD-MS map with a large mass range and step width. Afterwards, when the reaction products are known, TPD-MS maps with a smaller mass range and step width can be recorded.

2.2 Photoelectron Spectroscopy

The previous Section 2.1 dealt with the main topic of this thesis, TPD. In this section the second major topic, the photoelectron spectroscopy (PES), will be

presented. PES makes use of the photoelectric effect, which is one of the possible effects when photons interact with electrons, *e.g.*, if matter is irradiated by electromagnetic radiation. Depending on the photon energy, PES is divided into subgroups, *e.g.*, ultraviolet photoelectron spectroscopy (UPS), X-ray photoelectron spectroscopy (XPS), and HAXPES. UPS is used to investigate the electronic structure in the valence region due to large cross sections of ultraviolet radiation with the valence band. In addition, the work function of the sample can be determined. By variation of the polar ϑ and azimuthal φ angles of the sample, information about the band dispersion of the sample can be obtained. The corresponding method is called angle-resolved photoemission spectroscopy (ARPES) as well as angle-resolved ultraviolet photoelectron spectroscopy (ARUPS) when ultraviolet radiation is used. The methods XPS and HAXPES will be explained in detail in the following.

2.2.1 X-Ray Photoelectron Spectroscopy

Electromagnetic radiation can interact with matter, especially electrons, in different ways. Often, electrons gain the energy of photons $h\nu$ with the frequency ν upon interaction. Electrons are emitted if the photon energy exceeds a certain barrier of the material. This process is well-known as the photoelectric effect, which was first discovered by Hertz[166] and explained later by Einstein.[167] In 1921, Einstein was awarded the Nobel Prize in Physics for the explanation of the photoelectric effect. The barrier is found to be the binding energy E_B of the electron of the corresponding atom and the material specific work function ϕ. Hence, the kinetic energy of the emitted electron can be described by the following equation:

$$E_\mathrm{kin} = h\nu - E_\mathrm{B} - \phi. \tag{2.25}$$

Interestingly, E_B is not constant for each atom of an element, but depends on the electronic state, *i.e.*, the orbital, from which the electron is emitted. Furthermore, the atom's chemical environment, *e.g.*, chemical bonds or its oxidation state, slightly changes E_B. The binding energy is according to the initial state approximation by Koopmans[168] equal to the negative orbital energy ϵ, which can be calculated by Hartree-Fock-based methods. Nevertheless, final state effects occurring in the generated photoion are neglected, *e.g.*, the remaining electrons stay frozen and do not rearrange. Relaxation of the electrons minimizes the energy of the ionized atom resulting in decreasing binding energies.

The precise determination of the binding energy is crucial in all PES techniques as it contains many information about the electronic structure of the sample. Unfortunately, Equation (2.25) cannot simply be used because the work functions of sample and spectrometer are different (Figure 2.5). It is necessary to calibrate the spectrometer in the following way. First, the sample and the spectrometer are placed in electrical contact, often by grounding both. This ensures that the Fermi levels E_F of sample and spectrometer are the same. The actual quantity measured is the kinetic energy of the electrons with respect to the vacuum energy level of the spectrometer $E_\mathrm{kin,Sp}$. The difference between the photon energy $h\nu$ and $E_\mathrm{kin,Sp}$ is, according to Figure 2.5 not the material specific work function of the sample but that of the spectrometer ϕ_Sp. Thus, the binding energy E_B is calculated with the following expression:

$$E_\mathrm{B} = h\nu - E_\mathrm{kin,Sp} - \phi_\mathrm{Sp}. \tag{2.26}$$

The determination of ϕ_Sp is expensive and has to be done for each spectrometer. Nevertheless, placing a grounded and clean standard sample next to the investigated sample, the spectrometer can be referenced to known binding energies. In XPS setups, for example, Au samples are commonly used and spectrometers are calibrated to the Au $4f_{7/2}$ binding energy of 84 eV.[109] In case the Fermi edge is visible, which is often the case for metal samples, the edge is set to $E_\mathrm{B} = 0$

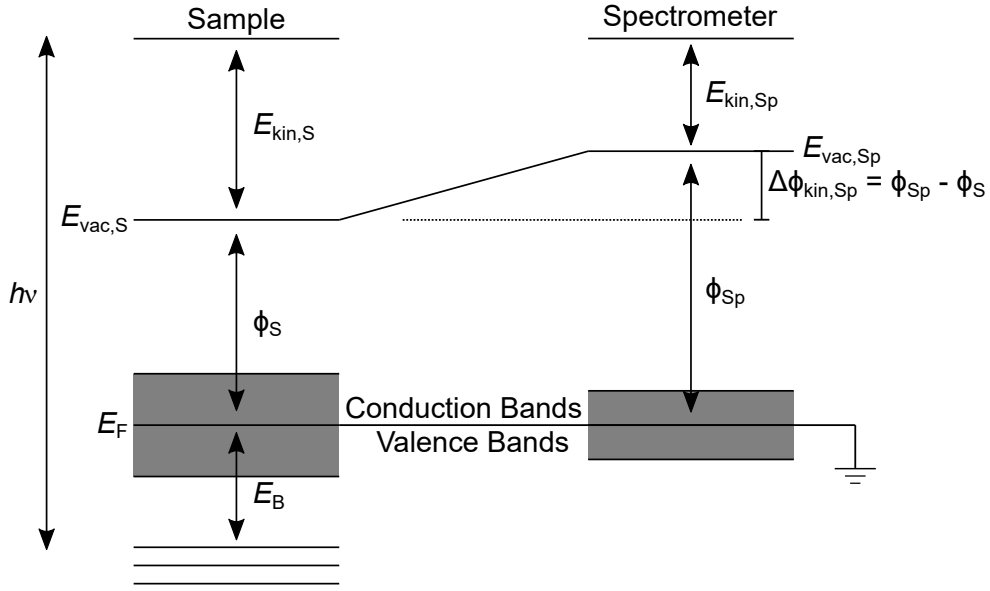

Figure 2.5: Energy level diagram in a photoelectron spectrometer with grounded sample and spectrometer. Fermi levels E_F of sample and spectrometer are aligned due to electrical contact. Calculation of the binding energy E_B from the measured kinetic energy $E_\mathrm{kin,Sp}$ needs the work function of the spectrometer ϕ_Sp. Adapted from [109].

calibrating the XP spectrum. After calibrating the spectrometer, only $E_{\mathrm{kin,Sp}}$ has to be measured, *e.g.*, with a hemispherical analyzer.

Typical analyzers used in PES consist of three components, a collection lens, an energy analyzer and a detector. Most of them reduce the kinetic energy of the incoming electrons to a certain pass energy by ramping voltages inside the lens system. A widely used analyzer is the hemispherical analyzer (Figure 2.6) consisting of two concentric hemispheres, of which the outer one is negatively charged in comparison to the inner one. Electrons emitted under the right angle enter the analyzer through the iris. The lens system accelerates or decelerates electrons to the pass energy E_{pass} of typically 5 to 200 eV. Afterwards, electrons enter the circular path of the hemispherical analyzer through the entrance slit. Only electrons that were accelerated to E_{pass} have the right trajectory to hit the detector. Electrons with different kinetic energies either hit the outer or inner hemisphere. The lens system varies the voltages in such a way that incoming electrons with every kinetic energy reach the detector with the pass energy once. This ensures that for all original kinetic energies the same spectral resolution is achieved depending on the selected E_{pass}. Detectors are often electron-multiplying devices like microchannel plates. Impinging electrons generate a secondary electron cascade, effectively increasing the measured signal that is proportional to the initial photoelectron intensity.

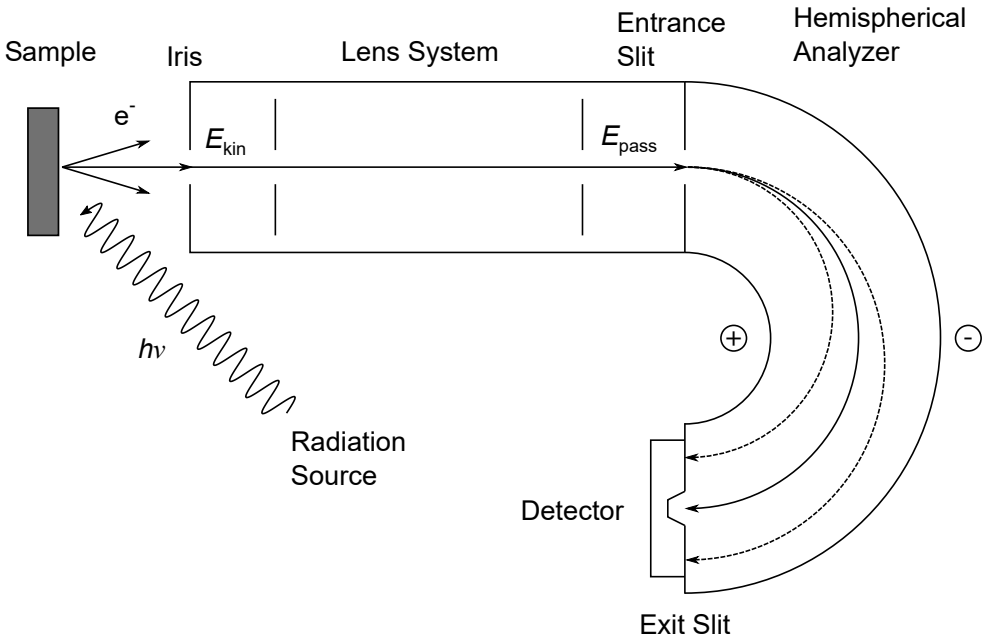

Figure 2.6: Illustration of a hemispherical analyzer system commonly used for PES. Generated photoelectrons enter the system through the iris and are accelerated or decelerated. Only electrons with the correct E_{pass} travel through the hemispheres without collisions and reach the detector. Adapted from [169].

Typical X-ray radiation lines used in laboratories are Mg K_α (1253.6 eV) and Al K_α (1486.6 eV). For higher energies Ag L_α (2984 eV) or Cr K_α (5415 eV) can be used, however, higher photon energies are often accompanied by worse resolution and intensity.[109] At high kinetic energies of the electrons, the resolution of the analyzer gets worse, whereas the broader X-ray lines of high photon energies can be corrected with a monochromator. However, X-ray anodes do not only produce radiation of one distinct energy, but also Bremsstrahlung, satellite X-ray lines and heat radiation disturbing XP spectra. To remove interfering signals, monochromators, *e.g.*, quartz crystals, are applied making use of Bragg's law with the order of reflection n, the wavelength λ, the lattice plane distance d and the incidence angle θ:

$$n\lambda = 2d \sin\theta. \tag{2.27}$$

X-rays interact with core-level electrons, among other electrons, of the atoms of the sample. The binding energy of these core-level electrons is element specific giving rise to study the elemental composition of an unknown sample. Furthermore, small shifts in the binding energy can be monitored, high spectral resolution provided. These shifts originate from the chemical environment of the corresponding element, hence oxidation states and other information can be obtained. Accordingly, those are called chemical shift and were first discovered by Siegbahn.[109,170] The corresponding analysis method was called electron spectroscopy for chemical analysis (ESCA) for which he was awarded the Nobel Prize in Physics in 1981.

2.2.2 Hard X-Ray Photoelectron Spectroscopy

Depending on the used sample, high photon energies are required in XPS to investigate deeper layers of a sample and obtain bulk properties. In the early years of XPS, no high photon energies were available to probe deep layers, hence synchrotron radiation was used, which reached higher photon energies than laboratory sources. However, by this time laboratory X-ray sources with high photon energies are available but the setup is restricted to one energy. In order to investigate the depth profile of a sample, an angle series has to be performed probing different layers of a sample but a high surface roughness can cause high errors. At a synchrotron, the photon energy can be tuned in variable steps over a wide range enabling depth profiling at normal emission, where the surface roughness is not a big problem. Furthermore, a tunable photon energy gives rise to X-ray absorption techniques like NEXAFS.

In a synchrotron charged particles, typically electrons, are forced on a circular path by bending magnets. The electrons are generated by thermionic emission in the microtron and are nearly accelerated to the speed of light in a cyclic synchrotron. Afterwards, they are fed in bunches into the storage ring where they stay on a circular path. When relativistic charged particles are accelerated they emit synchrotron radiation tangentially to their path. Changing the velocity vector of a particle by a bending magnet accounts to an acceleration, leading to the generation of synchrotron radiation. This radiation has a wide electromagnetic spectrum, *e.g.*, from low to high X-ray but also THz, infrared and UV energies, combined with a high brilliance and intensity. Specific energies can be selected by monochromators, *e.g.*, grating monochromators for low energies up to 2000 eV or crystal monochromators above 1500 eV, making use of the Bragg Equation (2.27). Additionally, high spectral resolution and tunable photon energies by changing the geometry of the monochromators can be achieved.

Wigglers and undulators are used to further improve the intensity and quality of the synchrotron radiation replacing normal bending magnets. A wiggler consists of alternatingly polarized dipole magnets in short succession, resulting in much higher intensities. The undulator is a much more sophisticated setup with smaller magnetic fields and an adjusted geometry, resulting in an interference of the radiation lobes. This results in a tunable line spectrum with even higher brilliance and intensity.

Using synchrotron radiation, hard photon energies above 2000 eV, which are used in HAXPES, are easily generated. This technique is used to investigate thick layers of tens of nanometers. By tuning the photon energies, information about the depth profile, *e.g.*, how far a reaction proceeded, can be obtained. The inelastic mean free path (IMFP), which depends on the kinetic energy of the electron and on the material the electrons travel through, plays a key role. The definition of the IMFP according to the International Organisation for Standardisation (ISO) is: "average distance that an electron with a given energy travels between successive inelastic collisions".[171] Besides the IMFP, the effective attenuation length, the mean escape depth and the information depth are important for HAXPES experiments. However, only the IMFP is relevant to understand the conducted experiments and the results presented in this thesis, hence the other three parameters are not discussed (for details see reference [172]).

If a photoelectron is generated, it will travel from the original atom through the sample until it reaches the sample surface and is later detected by an analyzer.

On the way through the sample electrons can be inelastically scattered mainly by excitation of valence electrons from other atoms. This includes plasmon excitation as well as single-electron excitation. Other contributions originate from inner-shell excitations. Electrons with kinetic energies below 20 eV have less possibilities to distribute their energy in the phase space. Therefore, the low-energy electrons are less likely to excite electrons of other atoms then those at higher energies resulting in high IMFP values. Until 100 eV the IMFP strongly decreases as many excitations are possible. Above 100 eV the IMFP increases again due to the high velocity of the electrons. Plotting the IMFP against the kinetic energy of the photoelectron is called the universal curve and reproduces this behavior very well (Figure 2.7). It is called universal curve because the qualitative trend of this curve is the same for each element, although absolute values differ.

The exact determination of the IMFP λ is challenging, hence generally applicable fits are necessary. Many different approaches were developed in the past years, describing different parts of the universal curve better or specializing on organic compounds. Optical data, which contain information on the inelastic scattering probability as a function of the energy loss describing the scattering probability dependence on the momentum transfer, can be used for the calculation of the IMFP.[174–176] Tanuma fitted such optical data by Penn[173] for 41 elements[174] with a modified form of the Bethe equation for inelastic electron scattering in matter:[172,174,177,178]

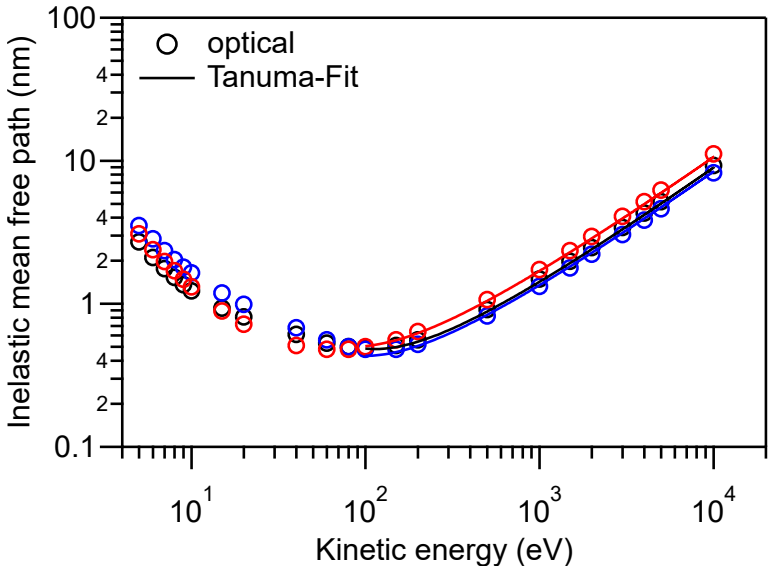

Figure 2.7: Dependence of the IMFP on the kinetic energy for the metals Cu (red), Ag (black) and Au (blue). Cycles: IMFP values taken from the Penn algorithm.[173] Solid lines: Fit according to Tanuma.[172,174]

$$\lambda_i = \frac{E}{E_p^2[\beta \cdot \ln(\gamma E) - (C/E) - (D/E^2)]} \text{ (nm)}. \tag{2.28}$$

In Equation (2.28) E is the kinetic energy of the electron in eV, $E_p = 28.8(N_\mathrm{v}\rho \cdot M^{-1})^{1/2}$ is the bulk plasmon energy in eV, N_v is the number of valence electrons per atom or molecule, ρ is the bulk density in $\mathrm{g \cdot cm^{-2}}$, M is the atomic or molecular mass and β, γ, C and D are fitting parameters. Depending on the investigated system different equations can be used for the calculation of the IMFP.

In Figure 2.7 it is obvious that photoelectrons generated by Al K_α or Mg K_α radiation sources have rather low IMFP values emphasizing the use of hard X-rays for probing large depth ranges. The information depth from where only 5 % of the electrons can escape without loosing some of their kinetic energy is three times the IMFP.[172,179]

Using tunable synchrotron radiation depth profiling is possible, *e.g.*, the reaction depth of metals with organic compounds can be investigated. Depth profiling by angle resolved XPS is possible, too, however, surface defects, such as roughing, crystallization or dewetting, heavily influence the results. These effects especially the roughness are less critical for HAXPES experiments, *i.e.*, experiments at constant angle with a variation of the photon energy. When metals are deposited onto organic compounds, they can either react with reactive centers of the molecules, diffuse deeper into the bulk or form metal clusters. At low photon energies the generated photoelectrons originate from near the surface and correspond in this case mostly to the reaction product and metal clusters. Increasing the photon energy and thus the information depth, more photoelectrons escape from deeper layers associated with unreacted molecules. The reaction depth d can be calculated from the intensity ratios from the reacted I_r to unreacted I_ur species at certain photon energies for a known layer thickness L according to:[64]

$$d = \lambda \ln\left(\frac{(I_\mathrm{r}/I_\mathrm{ur}) + 1}{1 + (I_\mathrm{r}/I_\mathrm{ur}) \cdot \exp(-L/\lambda)}\right). \tag{2.29}$$

The measured peak intensity is proportional to various parameters such as the cross section and the photon flux. The intensities of different orbitals have to be normalized in order to use them in Equation (2.29). However, if the reaction can be traced by a chemical shift of a certain XPS peak, fitting both the reacted and unreacted peak is sufficient because the parameters influencing the XPS peak intensity are equal and cancel.

2.3 Near-Edge X-Ray Absorption Fine Structure Spectroscopy

Another synchrotron-based technique commonly used in surface science is near-edge X-ray absorption fine structure (NEXAFS) spectroscopy. In contrast to XPS and AES that probe occupied electronic states, NEXAFS spectroscopy enables the investigation of unoccupied states by exciting core electrons to higher electronic states but not into the continuum. Normally, X-ray absorption cross sections decrease with the photon energy, though increasing the photon energy over the ionization energy of a specific core level strongly increases the cross section again. This results in an absorption edge visible in the X-ray spectrum. In this method the photon energy is increased in small steps and if the excitation energy fits to the difference between core level and unoccupied state, a peak is visible in the NEXAFS spectrum. Hence, information about the electronic fine structure of a sample can be obtained.

The intensity I of a dipole transition from the initial state i to the final state f is described by Fermi's golden rule (Equation (2.30)).

$$I \propto \left|\langle\phi_f|\vec{E}\cdot\hat{\mu}|\phi_i\rangle\right|^2 \rho(E_{fi}) \tag{2.30}$$

The compliance of the energy conservation is expressed by $\rho(E_{fi})$. The transition is forbidden if no density of states (DOS) ρ at the initial and final states are present. The intensity of the transition depends on the interplay of electric field vector $\vec{E}$ and dipole transition operator $\hat{\mu}$ as well as on the wave functions ϕ_i of the initial and ϕ_f of the final state. Furthermore, the transition is allowed and, therefore, non-zero if the symmetries of the wave functions produce total-symmetric contributions. Using linearly polarized light such as synchrotron radiation, the electric field vector and the transition dipole moment can be separated.

$$I \propto \left|\vec{E}\cdot\langle\phi_f|\hat{\mu}|\phi_i\rangle\right|^2 \rho(E_{fi}) \tag{2.31}$$

$$\propto \left|\vec{E}\vec{\mu}_{fi}\right|^2 \rho(E_{fi}) \tag{2.32}$$

According to Equation (2.30), the symmetries of initial and final state determine the intensity of the transition. The symmetry of the initial state is defined by the excited core-level electron. Excitation from s-orbitals, *e.g.*, the 1s orbital of the K-edge, pose a special case due to their spherical symmetry. In this case, the direction of the transition dipole moment $\vec{\mu}_{fi}$ only depends on the final state's

symmetry. This special case gives rise to the investigation of the orientation of organic compounds on surfaces, since the highest intensity is obtained when the transition dipole moment and the final state orbital orientation are parallel. The electric field vector can be modified by varying the incident angle α of the radiation resulting in changing transition intensities, which is then called X-ray dichroism (Figure 2.8). Irradiation under normal incidence results in the excitation of σ^* and π^* transitions for flat-lying and upright standing molecules, respectively. Grazing incidence yields the opposite transitions, *i.e.*, π^* and σ^* transitions for flat-lying and upright standing molecules, respectively. If transition peaks are observed at both angles, no dichroism is apparent, meaning that the molecules are randomly tilted and have no preferable orientation, which is the case for molecules in a kinetically trapped disordered state at low temperatures.

The measurement of the X-ray absorption is difficult since the samples are often metals or mounted on metallic sample holders. Transmission experiments are not possible due to the experimental setup. Nevertheless, electrons generated by subsequent processes can be detected as secondary probes, which are illustrated in Figure 2.9. In case a core-level electron is excited or emitted, a second electron with higher energy may relax refilling the previously generated core hole. The excess energy is then either released as a photon or transferred to a third electron, which is emitted if the binding energy and work function are overcome. The latter is also known as an Auger electron of the corresponding Auger process. This process will be explained in detail in Section 2.4.

Both processes compete with each other. While the Auger process is dominant for light elements, detection of the fluorescence yield (FY) is emphasized for heavier elements (see Section 2.4 for further details). The FY detection mode is, however, bulk sensitive since photons have far longer mean free paths in matter than electrons and escape from deeper layers. Measurement of the emitted

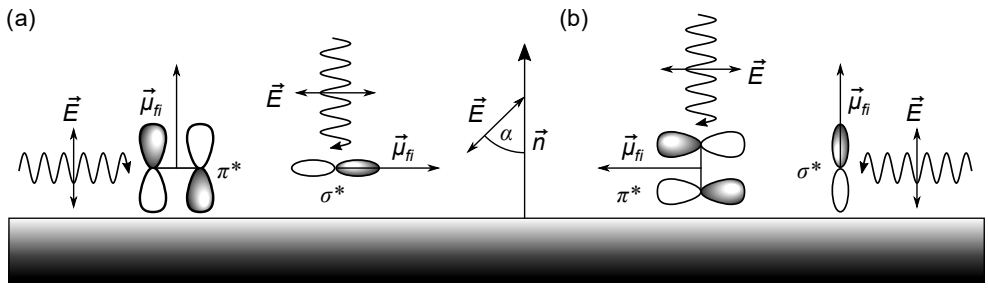

Figure 2.8: Illustration of NEXAFS transitions and the occurrence of X-ray dichroism. (a) Flat-laying molecules: π^* transitions are excited under grazing incidence ($\alpha = 90°$) and σ^* transitions under normal incidence ($\alpha = 0°$). (b) Upright-standing molecules: reversed order. Adapted from [108].

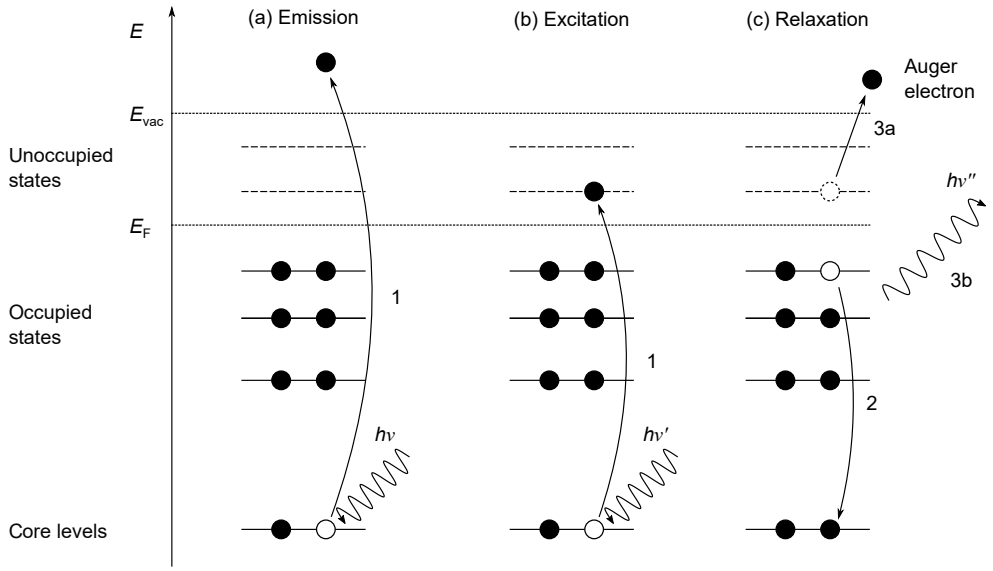

Figure 2.9: Energy level diagram of photoelectron emission and subsequent processes. Upon interaction with a photon an electron is either (a) emitted or (b) excited to an unoccupied state. (c) The generated core hole is refilled by a second electron with higher energy. Excess energy is released either as (3a) an AUGER electron or (3b) a fluorescence photon. Adapted from [110].

electrons is preferred for lighter elements. Here, it can be distinguished between total electron yield (TEY), partial electron yield (PEY) or AUGER electron yield (AEY). Since irradiation with X-rays does not only result in the AUGER process, photoelectrons of other elements, higher electronic states or the substrate, inelastically scattered electrons as well as secondary electrons contribute to the TEY. Detection of slow electrons can be avoided by applying a bias voltage to the sample or a retardation grid in front of the detector (PEY). PEY is more surface sensitive than TEY because electrons from deeper layers are unlikely to escape without inelastic collisions. Measuring only the AUGER electrons in the AEY mode has the highest surface sensitivity due to the discrimination between AUGER electrons and inelastically scattered electrons. However, an electron energy analyzer is necessary to discriminate the AUGER electrons from the other electrons whereas simple retardation grids, an electron multiplier and a collector are sufficient for the other detection methods.

2.4 AUGER Electron Spectroscopy

AUGER electron spectroscopy (AES) was one of the first surface science tools with high surface sensitivity. The basic principle of this technique is the AUGER effect, which was first observed by AUGER in 1923[180,181] and completely explained in his doctoral thesis in 1926.[182] The effect is also referred to as AUGER-

MEITNER effect because MEITNER independently of AUGER described the effect one year earlier.[183,184] The process describes the emission of electrons by irradiation with X-ray photons or electrons. The kinetic energy of the emitted AUGER electrons is independent of the energy of the excitation source. Upon irradiation with X-rays or electrons with energies of typically 2-10 keV core holes are created by emission or excitation of core-shell electrons. A second electron with a higher energy than the core electron refills the core hole and the excess energy is either released as a fluorescence photon or is transferred to a third electron, which is emitted as an AUGER electron (Figure 2.9). Although the basic principle was shortly explained in Section 2.3, a detailed description will follow in this section.

In order to calculate kinetic energies of AUGER electrons, information on the orbital energies of the involved electrons is needed (Figure 2.10). At first, the excitation energy has to be sufficiently high to emit or excite an electron from a core level E_W. An electron from a higher level E_X, which is closer to the FERMI level E_F, relaxes and refills the core. Due to this transition energy corresponding to $\Delta E = E_W - E_X$ is released, which is then transferred to a third electron or released as a photon. The electron is emitted if the energy overcomes the binding energy E_Y as well as the work function ϕ_Sp of the spectrometer according to

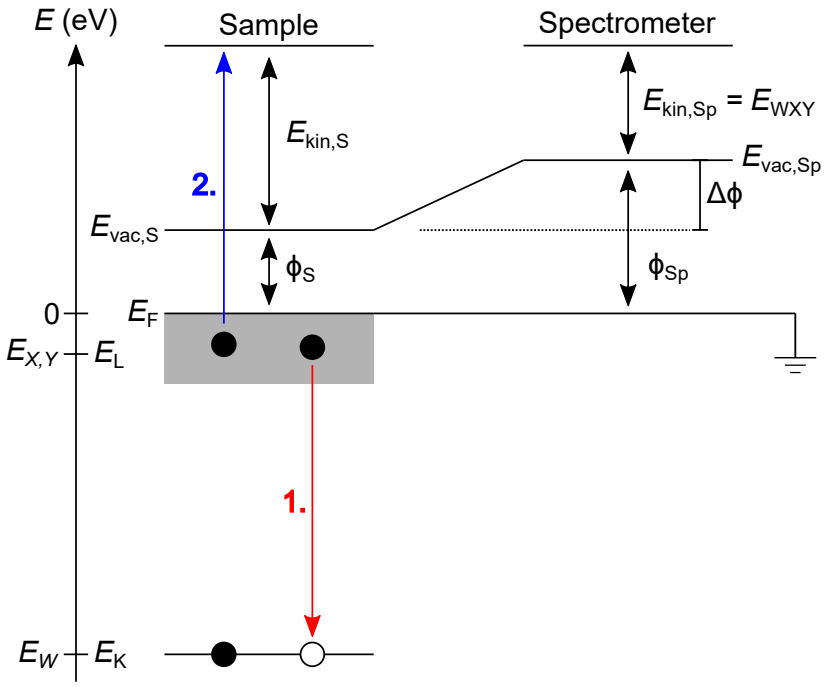

Figure 2.10: Schematic illustration of the AUGER process with energy levels for a KLL transition. Sample and spectrometer are in electrical contact, hence the FERMI energy levels are aligned. After emission of the photoelectron, the generated core hole is refilled by an electron from a higher level (red). The excess energy is transferred to another electron of the same level, which is then emitted (blue). The measured kinetic energy of the AUGER electron is referenced to the work function of the spectrometer ϕ_Sp. Adapted from [109].

Figure 2.5 in Section 2.2. The kinetic energy of an AUGER electron for the WXY transition of the involved energy levels and the atomic number Z can be calculated according to:

$$E_{WXY} = E_W(Z) - E_X(Z + \Delta) - E_Y(Z + \Delta) - \phi_{\mathrm{Sp}}. \tag{2.33}$$

After the emission of electron W, the atom is ionized. The residual electrons of the photoion are shifted to higher binding energies due to the positive charge. This displacement is considered by the term Δ, which takes values between 0 and 1. A good approximation is $\Delta = 0.5$. The AUGER effect is referred to a WXY transition where all energy levels correspond to different shells. Though, WXX transitions are observed more often and are shown in Figure 2.10. Two special cases occur if the photoelectron and, therefore, the core hole as well as the relaxing electron are in the same shell but in different energetic subshells, *e.g.*, L_1L_2M transitions (COSTER-KRONIG). In case the AUGER electron is emitted from a subshell of the same shell as well, then this called a super COSTER-KRONIG transition, *e.g.*, $L_1L_2L_3$. However, these transitions exhibit significant energetic broadening due to shorter lifetimes compared with regular transitions. In XPS, the core hole in the final state can decay according to a super COSTER-KRONIG transition, which reduces the lifetime of the core hole. The reduced lifetime results in a broadening of the XPS peak.

The obtained energy when an electron relaxes and refills the core hole (Figure 2.10, red) may be released as a photon, too. This process is used in the FY detection mode in NEXAFS spectroscopy. Which process is favored depends on quantum mechanical selection rules. Different parameters such as the atomic number Z or the type of the involved shell (K, L, etc.) result in changing cross sections leading to changes in AUGER and X-ray yields. This dependence is illustrated in Figure 2.11.

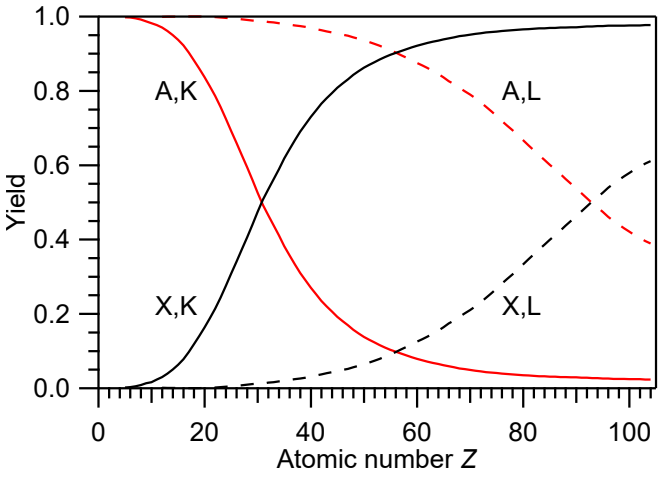

Figure 2.11: Dependence of AUGER (red) and X-ray (black) yield on the atomic number Z for transitions from the K (solid) and L (dashed) shell. Data taken from ref. [185].

2.5 Low-Energy Electron Diffraction

One of the widely used techniques to investigate surface structures is low-energy electron diffraction (LEED). This method makes use of backscattered low-energy electrons from the surface or adsorbate structures. Scattering at periodic surface structures yields specific patterns that can be qualitatively and quantitatively investigated with small effort. Information about cleanliness, impurities and the order of surfaces is obtained. Bright and sharp LEED spots of a blank substrate are widely regarded as evidence of a well-prepared, clean sample by scientists. LEED uses the wave properties of electrons, which are described by the DE BROGLIE relation:

$$\lambda_\mathrm{e} = \frac{h}{p_\mathrm{e}} = \frac{h}{\sqrt{2m_\mathrm{e}E_\mathrm{kin}}}. \tag{2.34}$$

If BRAGG's law (Equation (2.27)) is fulfilled, constructive interference of diffracted electrons is observed at periodic structures. Since low-energy electrons below 200 eV are used in LEED, the IMFPs of the scattered electrons are low making it a highly surface sensitive technique. The periodicity in reciprocal space of the sample is reflected in the diffraction pattern of a LEED experiment. A clean (111) single-crystal surface results, for example, in a hexagonal diffraction pattern. Periodic adsorbate structures would add a new diffraction pattern whereas non-periodic structures would broaden the substrate spots. Small reciprocal lattice vectors of adsorbate structures correspond to large unit cells in real space. The unit cells in real space are described by the lattice vectors $\vec{a}$ and $\vec{b}$. In reciprocal space, they are denoted as $\vec{a}^*$ and $\vec{b}^*$ and are connected to the real space vectors by the following relations, where $\vec{n}$ is a primitive vector perpendicular to the reciprocal lattice.

$$\vec{a}^* = \frac{\vec{b} \times \vec{n}}{\left|\vec{a} \times \vec{b}\right|}; \quad \vec{b}^* = \frac{\vec{a} \times \vec{n}}{\left|\vec{a} \times \vec{b}\right|} \tag{2.35}$$

Using the two-dimensional (2D) MILLER indices h and k, the points of the reciprocal lattice are expressed by $\vec{G}_{hk}$:

$$\vec{G}_{hk} = h \cdot \vec{a}^* + k \cdot \vec{b}^*. \tag{2.36}$$

The wave vector of the backscattered electrons is described by $\vec{k} = \vec{s} \cdot 2\pi/\lambda$, where the waves of incident electrons are expressed by $\vec{k}_0 = \vec{s}_0 \cdot 2\pi/\lambda$. The unit vectors are $\vec{s}$ and $\vec{s}_0$ for backscattered and incident electrons, respectively. Since only elastically scattered electrons contribute to the LEED spots, energy conservation must be given.

$$|\vec{k}| = |\vec{k}_0| \tag{2.37}$$

Since the IMFP of low-energy electrons is small, LEED probes information about the 2D structure of the surface. Diffraction on a 2D surface lacks the crystal periodicity normal to the surface, hence only components of the wave vectors parallel to the surface $\vec{k}^{\parallel}$ and $\vec{k}_0^{\parallel}$ are regarded. Due to the law of conservation, the scattering vector component parallel to the surface $(\vec{k}^{\parallel} - \vec{k}_0^{\parallel})$ must be equal to $\vec{G}_{hk}$:

$$\vec{G}_{hk} = \vec{k}^{\parallel} - \vec{k}_0^{\parallel}. \tag{2.38}$$

For a perpendicular incident beam, $\vec{k}_0^{\parallel}$ should be zero. The 2D EWALD's sphere construction is used for the visualization of the LEED spots and shown for a tilted and normal incident beam in Figure 2.12. 2D lattice spots are observed where the rods intersect the circle.

As mentioned above, periodic adsorbate superstructures form LEED spots, too. Therefore, the real space lattice constants $\vec{a}_{\mathrm{S}}$ and $\vec{b}_{\mathrm{S}}$ are related to the substrate by the matrix $\mathbf{M} = \left(\begin{smallmatrix} M_{11} & M_{12} \\ M_{21} & M_{22} \end{smallmatrix}\right)$:

$$\vec{a}_{\mathrm{S}} = M_{11} \cdot \vec{a} + M_{12} \cdot \vec{b}\,; \quad \vec{b}_{\mathrm{S}} = M_{21} \cdot \vec{a} + M_{22} \cdot \vec{b}. \tag{2.39}$$

This is done analogously for the reciprocal space vectors $\vec{a}_{\mathrm{S}}^*$ and $\vec{b}_{\mathrm{S}}^*$ by the matrix $\mathbf{M}^* = (\mathbf{M}^{-1})^T = \left(\begin{smallmatrix} M_{22} & -M_{21} \\ -M_{12} & M_{11} \end{smallmatrix}\right)$:

$$\vec{a}_{\mathrm{S}}^* = M_{11}^* \cdot \vec{a}^* + M_{12}^* \cdot \vec{b}^*\,; \quad \vec{b}_{\mathrm{S}}^* = M_{21}^* \cdot \vec{a}^* + M_{22}^* \cdot \vec{b}^*. \tag{2.40}$$

Since the unit cell of the adsorbate superstructure is larger than the one of the substrate, the LEED spots in the reciprocal space have shorter distances.

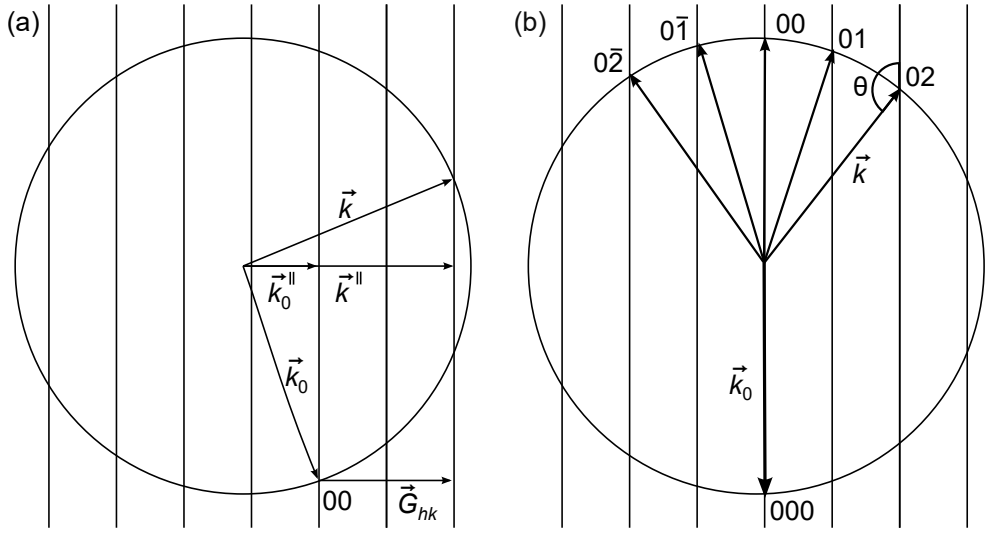

Figure 2.12: EWALD's sphere construction in two dimensions for an electron beam incident (a) tilted and (b) normal to the surface. Scattered wave vectors point to intersections of the rods with the circle. θ is the diffraction angle. Adapted from [110] and [109].

A basic LEED setup is shown in Figure 2.13. The electron gun generates electrons, which are accelerated to the desired energy by a lens system, by thermionic emission. Electrons hitting the grounded sample are either elastically or inelastically scattered. The diffraction pattern corresponds to the elastically scattered electrons whereas the inelastic electrons add to the background signal. The backscattered electrons are accelerated to the fluorescent screen with potentials up to 5 keV. Three grids are mounted between the fluorescent screen and the

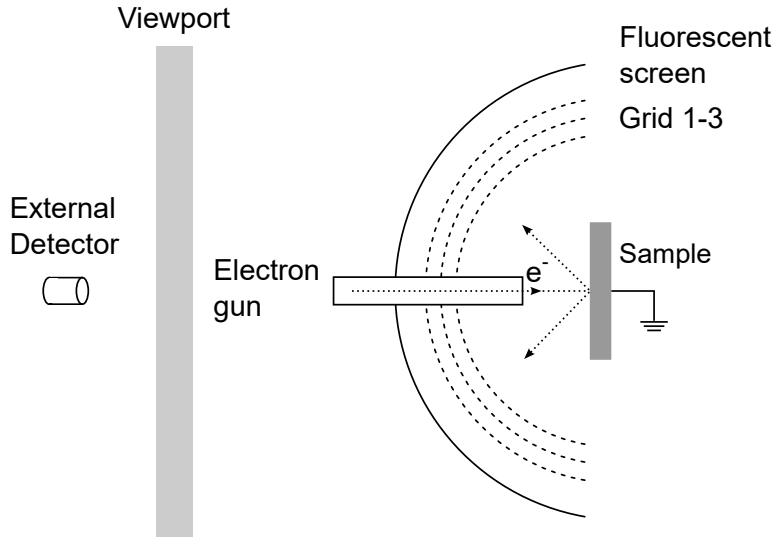

Figure 2.13: Schematic figure of a general LEED setup. The electron gun emits electrons, which are accelerated to the sample, where they are backscattered. The backscattered electrons are accelerated to the fluorescent screen. The diffraction pattern can be observed through a viewport and recorded, *e.g.*, with a camera. Adapted from [109].

sample. The first one is on ground potential to shield all other potentials. The second and third grid have tunable negative potentials to minimize background signals. The LEED pattern is visible on the fluorescent screen through a transparent viewport and can be recorded with a camera.

2.6 Experimental Setups

2.6.1 Temperature-Programmed Desorption Chamber in Marburg

All TPD experiments were conducted in a home-built UHV chamber in the TPD laboratory of the Gottfried group. The base pressure of $2 \cdot 10^{-10}$ mbar is primarily maintained by a turbomolecular pump (*HiPace 300* by Pfeiffer Vacuum), which is backed by a scroll pump (*nXDS6i* by Edwards). The chamber is an asymmetric double cross with one CF100 and five CF160 flanges made of high-grade stainless steel (1.4404) with a low carbon fraction (max. 0.03 % carbon).[186] In addition, several CF40 flanges are welded to the double cross. The base structure is explained in detail elsewhere.[187] An overview of the current status of the chamber is shown in Figure 2.14. A quadrupole mass spectrometer (QMS) (*EPIC series 1000* by Hiden Analytics) is mounted on a T-piece on the right CF160 flange (Figure 2.14a). The QMS is differentially pumped by a turbomolecular pump (*TMU 260* by Pfeiffer Vacuum, backed by the same scroll pump as the *HiPace 300*) and is encased by a cryo shroud, which is a special development of a Feulner cap.[115] The construction of the cryo shroud is described in reference [188]. On the opposite side of the QMS, the LEED-AES optics (LAO) (*BDL450* by OCI Vacuum Microengineering Inc.) is mounted on a specially designed CF160-CF63 reducing piece with a CF40 viewport underneath, which is used for aligning the crystal in front of the QMS. The construction is described in detail in Section 3.1.1. A CF160 cluster flange is attached on the front flange in Figure 2.14. This cluster flange hosts a sputter gun (*IQE 11* operated by an *IQE-A* controller both by Specs Surface Science Nano Analysis) in the center, an evaporator or a dosing valve on the left, a differentially pumped evaporator on the right and a viewport in the top center.

A manipulator with four degrees of freedom is mounted on top of the CF100 flange of the main chamber. The manipulator moves the sample holder flange in the three spatial directions x, y, z and enables rotation of the polar angle θ

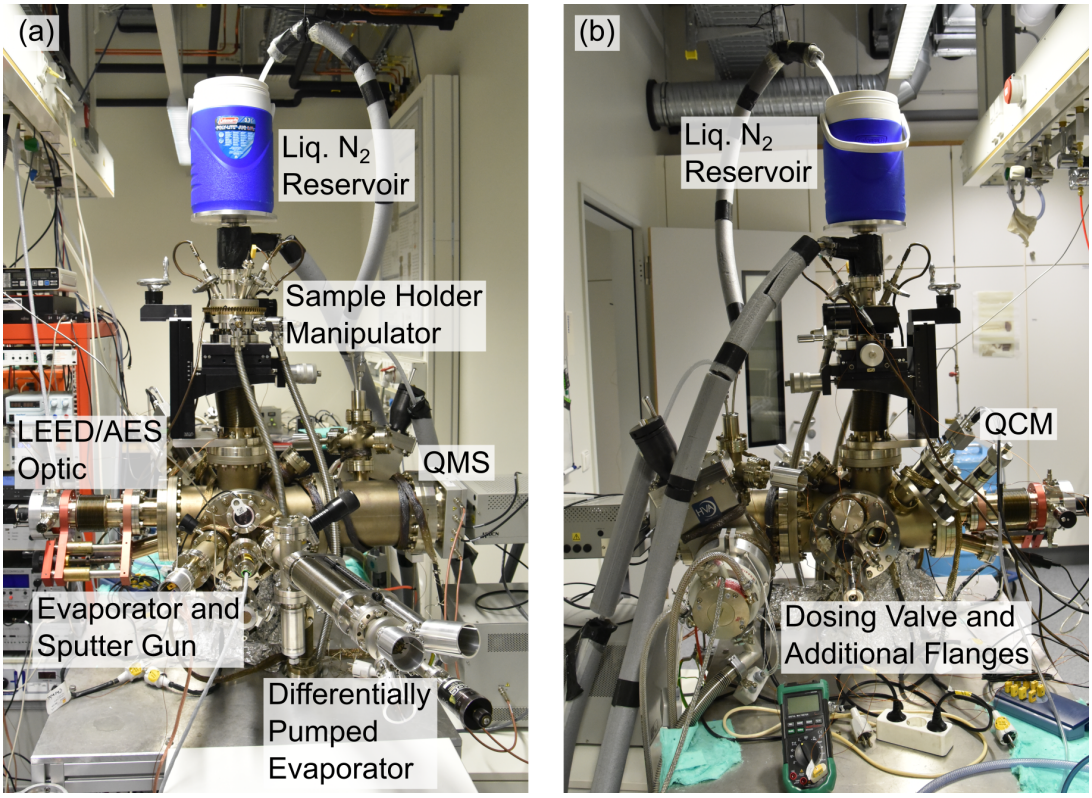

Figure 2.14: Front (a) and back (b) view of the TPD chamber of the GOTTFRIED group.

around the vertical axis z. The rotational feedthrough is differentially pumped by the scroll pump and a third turbomolecular pump (*EXT70* by EDWARDS). The sample holder flange includes electrical feedthroughs for sample heating and measuring its temperature. Furthermore, a cooling finger is located in the center of this flange. The sample holder at the end of the cooling finger contains an LN_2 reservoir and the sample fixed by tungsten wires. A detailed description an be found elsewhere.[189]

On the back side of the chamber (Figure 2.14b) the quartz crystal microbalance (QCM) can be seen on the right. Another cluster flange hosting a viewport and a dosing valve is located in the center. This flange was constructed during the experimental work and details are given in Section 3.1.2. The pump of the cryo shroud with the QMS can be seen on the left of the back view.

2.6.2 High Kinetic Energy Photoelectron Spectroscopy Chamber in Berlin

The high kinetic energy photoelectron spectroscopy (HIKE) endstation (Figure 2.15a) is connected to the KMC-1 beamline, which is a bending magnet beamline, at BESSY II in Berlin. Three different single-crystal pairs can be

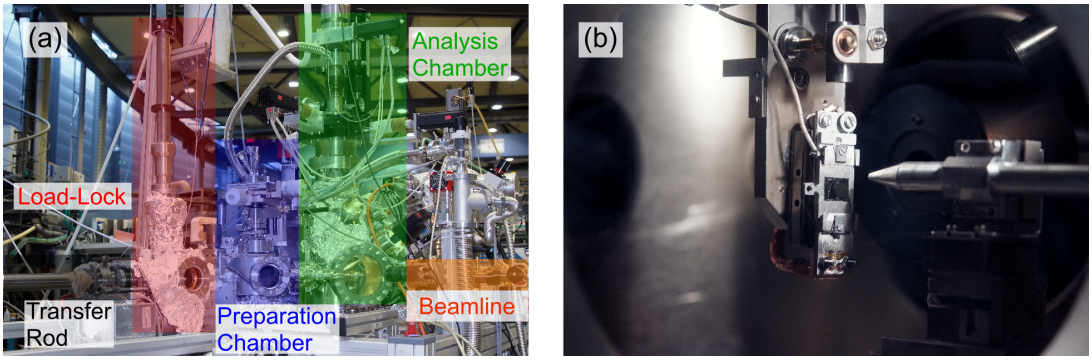

Figure 2.15: Photographs of the HIKE endstation at the KMC-1 beamline at BESSY II in Berlin. (a) Overview of the HIKE endstation showing the load-lock (red), the preparation chamber (blue) and the analysis chamber (green). The hemispherical analyzer is at the backside of the analysis chamber. (b) View into the analysis chamber. The sample stage with a sample is in the center, the beamline capillary is on the right, the fluorescence detector on the top right and the entrance of the electron analyzer in the back right.

used to select a photon energy in the range from 2 to 12 keV in the double-crystal monochromator. The pairs are Si(111), Si(311) and Si(422) crystals with Si(111) reaching the lowest photon energies and highest intensities. However, energy resolution is better for Si(311) and even better for Si(422).[190,191] Smart use of the pairs yields high intensities at high resolution for a broad range of photon energies.

The X-rays are guided in a glass capillary (Figure 2.15b, right) into the analysis chamber (Figure 2.15a, green), where they hit the sample positioned on the manipulator (Figure 2.15b, center). HAXPES measurements are conducted under grazing incidence and near-normal emission to achieve the highest possible information depth. Below the sample holder a Au sheet is mounted, which is used as an internal reference. The manipulator has five DOFs (x, y, z, θ and φ). Rotation around the z-axis is given by the polar angle θ and rotation around the surface normal of the sample by the azimuthal angle φ. Except φ, all degrees are motorized and can be selected by a LabView program. The manipulator can further on be heated and cooled. A *VG Scienta R4000* hemispherical electron energy analyzer with an energy range of 150 to 10 keV is mounted on the analysis chamber for XPS measurements.[190,191] The detector system consists of a 2D micro channel plate detector and a CCD camera, which is appropriate for the investigation of band structures by rotation around φ. A *Bruker XFlash 4010* fluorescence detector (Figure 2.15b, right top) can be used for NEXAFS spectroscopy experiments in the FY detection mode.[190,191] Furthermore, the sample current can be measured for TEY detection. Lastly, a sputter gun for cleaning samples and an electron flood gun for charge compensation of non-conducting samples during irradiation with X-rays are attached to the analysis chamber.

Directly attached to the analysis chamber is the preparation chamber (Figure 2.15a, blue). This chamber is used for *in situ* preparations and is permanently equipped with a QCM. A coolable home-built manipulator[89] with three translational degrees of freedom (x, y and z) is mounted on top of the preparation chamber. Evaporators for organic molecules and metals can be mounted on two residual flanges. On the bottom flange a feed-through for a shutter is mounted.

The last chamber, which is attached to the preparation chamber, is the load-lock (Figure 2.15a, red). Up to six samples can be introduced to the UHV system using the sample garage. Samples can be moved inside the UHV system by the transfer rod.

2.6.3 High Energy Spherical Grating Monochromator Chamber in Berlin

The high energy spherical grating monochromator (HE-SGM) endstation and beamline are specifically designed for NEXAFS spectroscopy measurements. The setup is especially optimized for the investigation of K-edges of carbon, nitrogen and oxygen. The beamline (Figure 2.16, orange) is equipped with a bending magnet (polarization degree $P = 0.91$) and the monochromator includes three different gratings. Typically, the grating with a line density of 1500 1/mm is used to achieve photon energies of 100 to 800 eV with an energy resolution of 0.3 eV at 300 eV kinetic energy.[192]

The analysis chamber (Figure 2.16, green) is mounted at the end of the beamline. In this chamber all NEXAFS spectroscopy and XPS measurements are conducted. The chamber is equipped with a *VG Scienta R3000* analyzer, which enables XPS measurements and the AEY detection mode for NEXAFS spectroscopy. Furthermore, a channelplate detector is mounted for the TEY and PEY detection modes for NEXAFS spectroscopy. Besides the detectors, a sputter gun for cleaning and a dosing valve is attached to the chamber. A manipulator with a sample stage is attached, too. The manipulator can be cooled with LN_2 and specially designed Prevac sample holders can be heated on the manipulator either resistively or with an electron beam. Translation in all three spatial directions x, y and z as well as rotation around the z axis (angle θ) and the azimuthal angle φ is possible. Rotation of the polar angle θ changes the angle of the sample with respect to the radiation beam enabling obseration of X-ray dichroism.

Directly attached to the analysis chamber is the transfer chamber (Figure 2.16, blue) containing a circular transfer system by Prevac. Mounted to the transfer

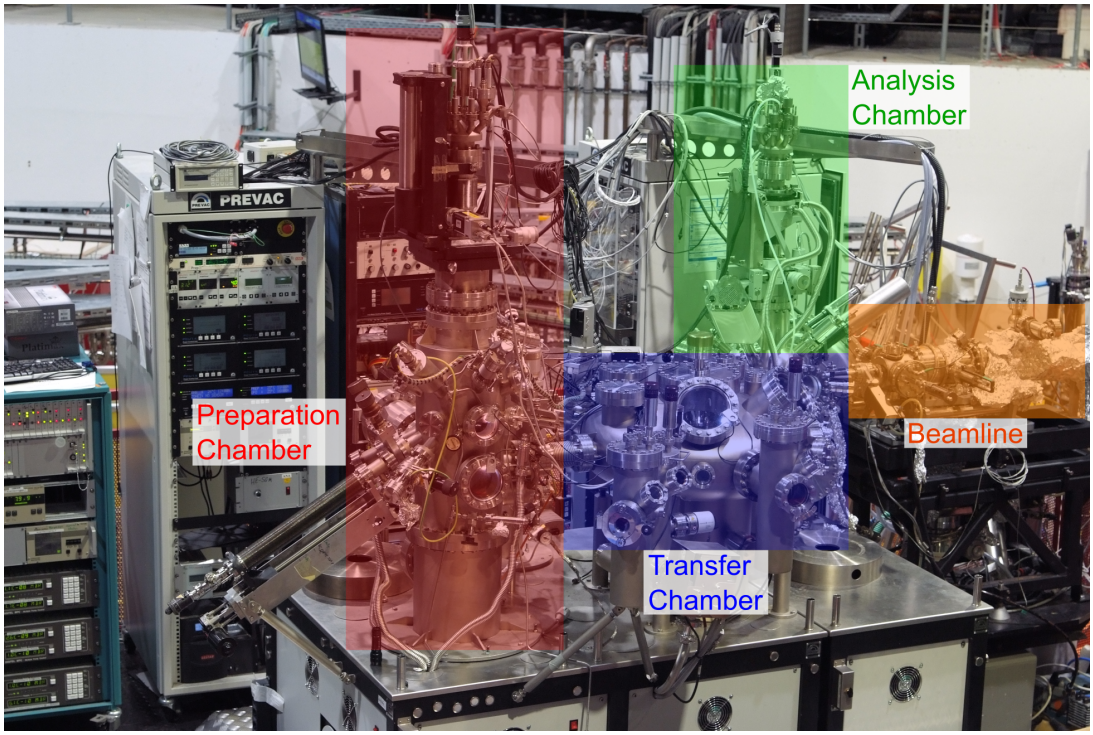

Figure 2.16: Photograph of the HE-SGM endstation at BESSY II in Berlin. The beamline is located at the far right side (orange), the right UHV vessel is the analysis chamber (green) and the left one is the preparation chamber (red). Analysis chamber and preparation chamber are connected by a transfer chamber (blue), on which a load-lock and a sample storage is mounted.

system are a sample storage and a load-lock, which can be used to introduce samples into the UHV system without venting the whole transfer chamber. The preparation chamber (Figure 2.16, red) is attached to the transfer system. This chamber hosts an additional manipulator, which can be cooled and heated as well as moved along four coordinates (x, y, z and θ). Moreover, sputter guns for cleaning and a LEED optics are mounted to the chamber. There are three mounting stages for evaporators or other UHV equipment that can be separately vented and pumped without venting the preparation chamber. These are commonly used to mount evaporators or leak valves for deposition of molecules on the sample. In order to achieve better pressures during preparation a cooling trap is located at the bottom of this chamber.

2.6.4 Pumping Stands

In order to test evaporators, prepare temperature–rate dependences of evaporators for synchrotron beamtimes or other issues, two pumping stands were established in the TPD lab (Figure 2.17). The pumping stand in Figure 2.17a consists of a turbomolecular pump (*TPH 200 S* by Pfeiffer Vacuum), which is backed

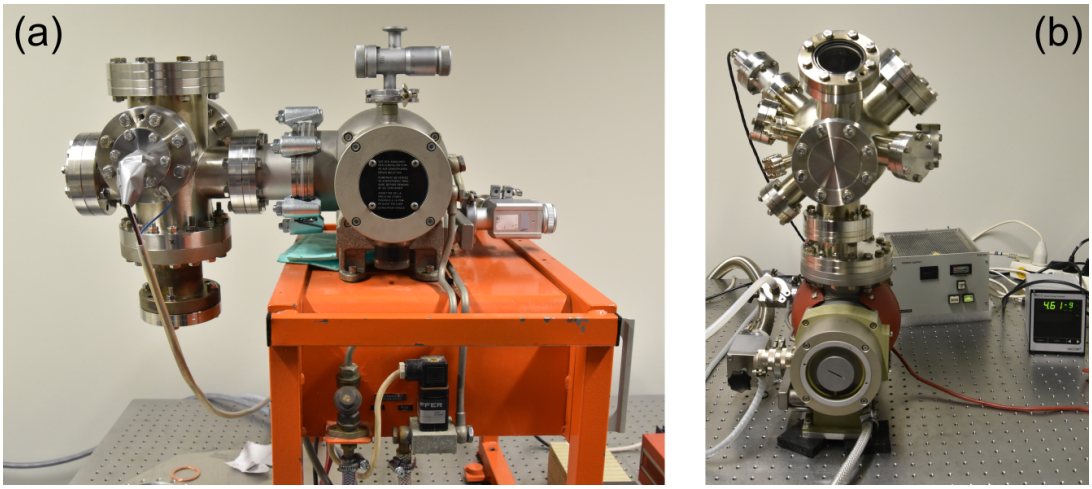

Figure 2.17: Photograph of the pumping stands in the TPD lab of the GOTTFRIED group. (a) High-vacuum pumping stand equipped with a sample holder and a QCM. (b) UHV pumping stand for different setups.

by a rotary vane pump (*DUO 3 M* by PFEIFFER VACUUM). The chamber itself is a double cross with three CF100 and three CF63 flanges. This pumping stand only operates at high vacuum with a minimum pressure of $1 \cdot 10^{-7}$ mbar. Instead of copper gaskets, viton gaskets are used for faster (un)mounting of flanges. The pressure is measured using a home-built and calibrated BAYARD-ALPERT hot ionization gauge. One CF100 flange on top of the double cross hosts a QCM and a sample stage.

The other pumping stand (Figure 2.17b) operates at UHV with a minimum pressure of $5 \cdot 10^{-10}$ mbar. Vacuum is maintained by a turbomolecular pump (*TPU 330* by PFEIFFER VACUUM) backed by a rotary vane pump (*DUO 6* M by PFEIFFER VACUUM). To achieve the minimum pressure the chamber needs to be baked. Only a BAYARD-ALPERT hot ionization gauge by VACOM and a viewport are permanently mounted to the chamber. However, lots of free flanges allow assembly of different setups depending on the purpose the chamber is used for. This pumping stand was used, for example, for the calibration and testing of an atomic layer injection (ALI) device as an alternative deposition method.[169]

3 Instrumental and Script Development

Conducting experiments and analyzing the obtained data was not the only part of this thesis. Maintaining and improving the temperature-programmed desorption (TPD) chamber in the laboratory of the Gottfried group was an additional part. In Section 3.1 constructed parts are shown and explained. All assemblies were created using *Inventor Professional 2017* and rendered using *Autodesk Inventor Professional 2020* both from Autodesk.

Another task was the development of *Igor Pro 8* (from Wavemetrics) scripts to speed up data processing and analysis by automation of routine work. The scripts are presented in Section 3.2.

3.1 Construction Projects

Only a quadrupole mass spectrometer (QMS) was mounted to the TPD chamber at the beginning of the experimental work. Hence, the residual gas and desorbing molecules could be monitored but investigation and characterization of the sample surface and the adsorbates were not possible. To extend the capabilities of the chamber, a LEED-AES optics (LAO) was installed. An adapter flange was necessary to mount the LAO to the TPD chamber. This part is explained in Section 3.1.1.

In the beginning, the TPD chamber was designed for small and light molecules, which are deposited using leak valves. Hence, no quartz crystal microbalance (QCM) was planned for the current setup. However, TPD experiments with heavy molecules, such as porphyrins, became interesting; therefore, a QCM needed to be mounted. The development of an adapter flange for the QCM and its final design are presented in Section 3.1.2.

Throughout the experimental work, it was necessary to construct smaller parts for convenience and smaller improvements. Some of them are shown in Section 3.1.3. The constructional drawings for manufacturing of all parts are attached in Chapter C in the appendix.

3.1.1 LEED-AES Flange

The LAO is mounted on a CF63 flange. Therefore, the adapter flange (Figure 3.1) needs to be a reducing piece from CF160 to CF63. The CF160 flange opposite of the QMS was chosen for mounting the LAO because of the orthogonal geometry to the cluster flange. This prohibits contamination of parts of the optics during sample preparation. However, a large viewport was attached to this CF160 flange prior to this installation. This viewport was necessary to align the sample crystal in front of the QMS, which would not be possible with a standard reducing piece, hence a CF40 flange was welded to the adapter flange. The angle of the tube was chosen in such a way that the CF40 flange directly points to the center of the chamber enabling the alignment of the sample. Due to a lack of space, the CF63 tube had to be shifted 15 mm off-center away from the CF40 flange.

A linear motion was attached to the CF63 flange and the LAO was mounted on the linear motion. A standard viewport was mounted to the CF40 flange allowing the alignment of the sample in front of the QMS. The detailed setup as well as the commissioning of the LAO are described elsewhere.[193] Shortly, the LAO (Figure 3.2) is mounted on a CF63 flange and consists of a miniature electron gun, a fluorescence screen and four grids enabling LEED and Auger

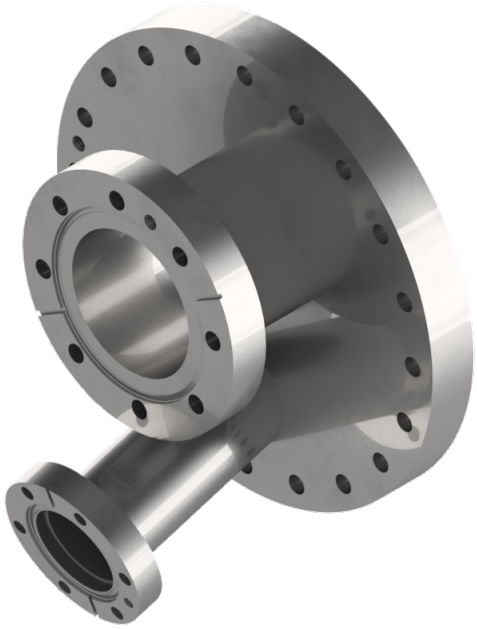

Figure 3.1: Rendered image of the LEED adapter flange. The CF63 flange is off-center and below it there is a CF40 flange, which is aligned to the center of the chamber.

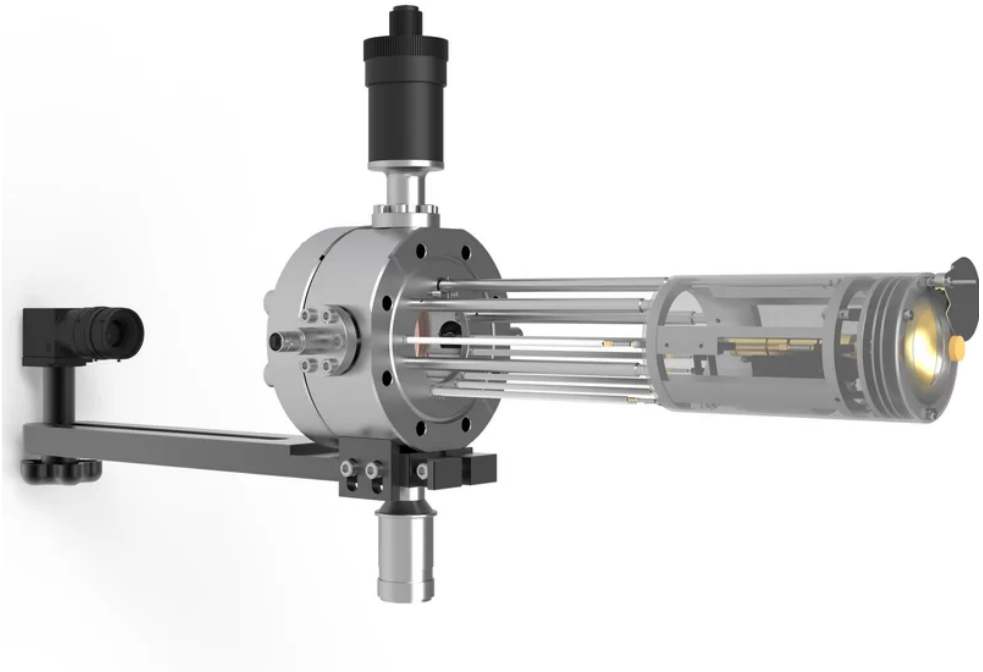

Figure 3.2: Image of the LAO mounted on the LEED adapter flange.[194]

electron spectroscopy (AES) measurements. The beam size is between 1 and 0.25 mm and the energy resolution is 0.8 % at low modulation voltages.[194] The LAO can be moved in by the linear motion until the working distance of 10 mm from the sample is reached.

3.1.2 Cluster Flange for a Quartz Crystal Microbalance

The QCM was planned to be mounted on the opposite side of the cluster flange as this was the only place left. Therefore, the adapter flange had to be a basic CF160 flange with a CF40 flange for the QCM. In addition, a viewport in the direction of the center of the chamber for alignment is necessary. However, this CF160 tube is off-center in comparison to the other three tubes. This asymmetry is used for a another setup of the TPD chamber, called cross-beam geometry.[187] Hence, the viewport had to be placed on the far right side of the adapter flange. Because the window is directly opposite of the evaporators and dosing valves, the viewport needs a shutter to prevent contamination. Accordingly, a CF16 flange was directly placed next to the viewport to mount a rotary feedthrough with a shutter. Additional CF40 and CF16 flanges were welded to the adapter for possible future projects. A rendered image is shown in Figure 3.3.

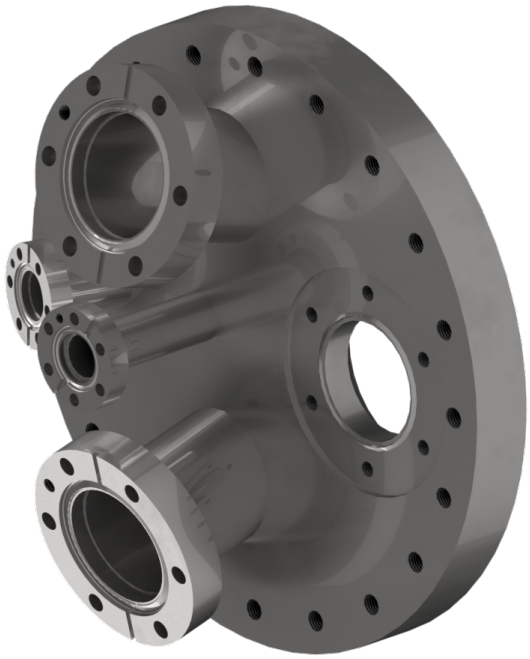

Figure 3.3: Rendered image of the QCM adapter flange. A viewport is mounted on the zero-length CF40 flange, which points directly to the center of the chamber. The center CF16 flange is used for a shutter. The other three flanges are spare for possible applications in the future.

Due to the asymmetry the QCM had to be bend in such a way that it did not hit the LAO or anything else inside the chamber but it needed to be at the crystal position if the QCM is fully moved inside (see Figure 3.4). This led to a long QCM curve, which exhibited strong vibrations during moving in and out. The strong vibration resulted in a loosening of the screws and a malfunction of the QCM after only a few experiments. The idea of mounting the QCM at this CF160 flange was discarded and a new QCM was mounted on the previous sputter gun position. In addition, the sputter gun was mounted on the center CF40 flange of the cluster flange. The QCM adapter flange is now used for additional dosing valves and for possible future projects.

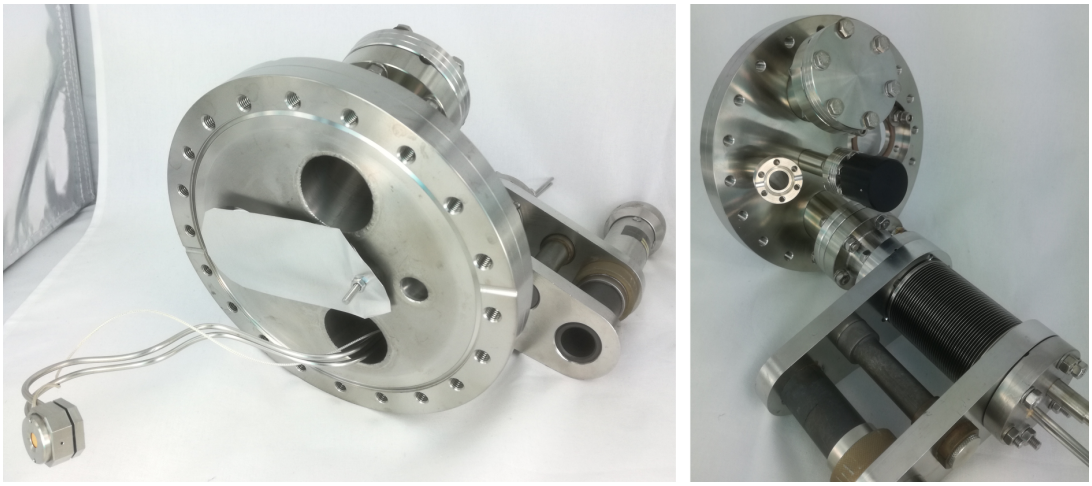

Figure 3.4: Photographs of the QCM adapter flange with the mounted QCM in front (left) and back (right) view. Due to strong vibrations the QCM malfunctioned and was mounted elsewhere. A dosing valve is attached to the former QCM position. A home-built shutter made of aluminum is used to protect the viewport against contamination.

3.1.3 Miscellaneous Parts

Besides the two adapter flanges, other smaller pieces were constructed. Most of them are standard pieces that needed little adjustment for specific purposes, thus they are not further described in this part. Two more specific parts are a heating sleeve for the *TMU 260* turbomolecular pump by Pfeiffer Vacuum and special barrel connectors for the heating connection of the sample holder flange.

The heating sleeve (Figure 3.5, left) is made of aluminum and consists of two half circles, which are wrapped around the turbo pump. The two halves are mounted together with two screws at each end. Each part has three holes, where heating cartridges fit in. The cartridges are fixed by slugs. If the TPD chamber is baked, the sleeve is heated up to bake the turbo pump to remove more contaminants and to achieve even better pressures.

The barrel connectors are specifically designed to connect heating cables to the electrical feedthroughs of the sample holder flange. If the electrical contact is bad, high temperatures can result because currents up to 30 A are used for heating the sample. The connectors are made of copper beryllium (CuBe), which is a alloy that is harder than copper but still has a high electrical conductivity. Steel is not used as the conductivity is too low, which would result in a strong heating of the connectors.

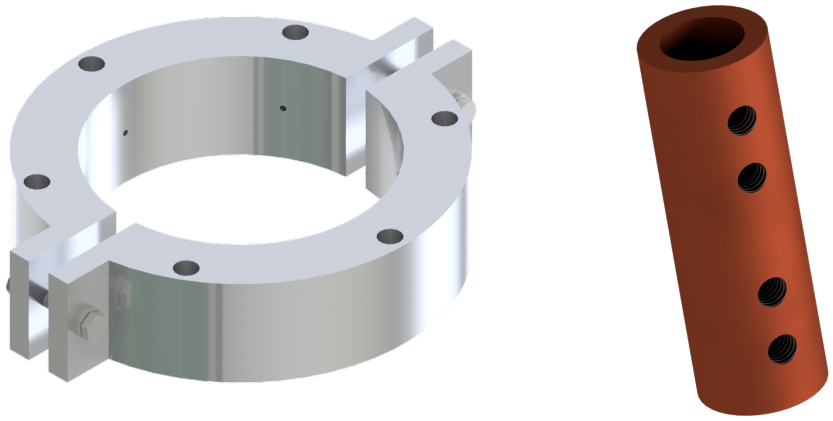

Figure 3.5: Rendered images of the heating sleeve (left) and the barrel connector (right). The heating sleeve is made of aluminum and heating cartridges are placed inside the holes. The barrel connector is made of CuBe due to the high electrical conductivity.

3.2 Programming in Igor Pro

The conducted experiments yielded a lot of data from different techniques. Data import, treatment and processing was often highly repetitive, hence auxiliary scripts were written in *Igor Pro*'s native language to shorten these processes, resulting in two modules. The first one is called *TPD-Analyzer* (Section 3.2.1) and is used for TPD data treatment. The second one contains import macros (Section 3.2.2) for the data obtained from temperature-programmed desorption mass spectrometry (TPD-MS), AES and near-edge X-ray absorption fine structure (NEXAFS) spectroscopy. Both modules are explained in detail in the following sections.

3.2.1 TPD-Analyzer

The *TPD-Analyzer* module incorporates tools for processing and analyzing of TPD data in order to speed up repetitive work. The naming of TPD data output by the QMS converter is >*filename*E*sequence-number*_*measurement*<, where the filename is given prior to the experiment and the measurement is either the mass, temperature or pressure. This naming procedure gives rise to an automatic access of a series of data. Afterwards, data can be duplicated and the logarithm can be taken, data traces can be averaged or normalized or the temperature can be calibrated by an automatic fit. Furthermore, all analysis methods presented in Section 2.1.3 and more are included in this module. Below a list of all implemented functions is given in alphabetical order:

- Albano Fit
- Average TPD Traces
- Complete Analysis
- Exponential Fit of the Polanyi-Wigner Equation
- Genetic Algorithm Fit
- Integral Energies
- Inverted Polanyi-Wigner Equation
- Leading-Edge Analysis
- Modified Leading-Edge Analysis
- Normalization of Traces
- Peak Picking
- Persson Fit
- Plotting of Multiple Graphs
- Ratio Calculation
- Redhead Analysis
- Reduction of Data Points
- Reverting Waves
- Schlichting-Menzel Plot
- Simulation of TPD Traces
- Temperature Calibration

Although there is a main menu of the *TPD-Analyzer*, of which several functions can be accessed, not all functions are implemented in it so far. Therefore, some functions have to be called from *Igor Pro*'s console by entering >tpd#*Function-Name*(*Parameters*)<. Which parameters are necessary can be found in the module script. However, this script can be overwhelming for people that are not experienced with programming. Thus, a manual, which is attached in the appendix (Section D.1), was written for the *TPD-Analyzer*. This manual is not

complete, as well, because the module is always growing and is a project that will be continued even after this thesis. The program code of the current status is attached in the appendix, too (Section D.2).

3.2.2 Import Macros

The module *Import-Procedures* is a collection of functions for importing data files of TPD-MS and AES from the TPD chamber and NEXAFS spectroscopy data from the high kinetic energy photoelectron spectroscopy (HIKE). The functions can be called using the console with >import#AES_TPD()<, >import#NEX AFS_HIKE()< or >import#Survey_ TPD()<. They can also be accessed from the *Macros* dropdown menu in *Igor Pro*, where they are called *Load AES Spectra from TPD*, *Load NEXAFS Spectra from HIKE* and *Load Surveys from TPD*. Using the AES and NEXAFS spectroscopy functions, a new window pops up and the desired data files can be selected. All data columns are imported and saved as waves in the current folder afterwards. A window pops up, too, using the TPD-MS function. However, the names of the data waves corresponding to intensity, mass and temperature have to be provided to the function by the user. The function will then extract TPD traces, mass spectra and a 2D map from the data. The user has to copy the data from the file into *Igor Pro* by hand. The programming code is attached in the appendix (Section D.3).

4 Results and Discussion

The data and results obtained during the experimental work that led to this thesis are presented and discussed. As mentioned in Section 1.3, most of the data are already published or summarized in manuscripts. More projects were addressed besides those, however, these data are not published yet. The additional data are discussed in detail together with the published results. The first part deals with the investigations on the interface of alternant and non-alternant molecules adsorbed on coinage metal surfaces. The second project addresses organic/inorganic interfaces and compares them with metal/organic interfaces. Metalation reactions of heteroatomic organic semiconductors (OSCs) are discussed in the third section. Finally, the Ullmann coupling reaction mechanism is investigated in the fourth section.

4.1 Investigations on the Interface between Alternant and Non-Alternant Molecules and Coinage Metal Surfaces

This section investigates the influence of alternant and non-alternant π-electron systems on the metal/organic interface. In order to characterize the interface interaction of an adsorbate–substrate system, many different surface science techniques can be used to probe various properties. One of these properties is the activation energy of desorption (desorption energy) that is a measure of the bonding strength. The desorption energy was obtained by means of temperature-programmed desorption (TPD), which is the mainly used method of this thesis. Further properties, *e.g.*, electronic states or adsorption heights, were probed by X-ray photoelectron spectroscopy (XPS), ultraviolet photoelectron spectroscopy (UPS), near-edge X-ray absorption fine structure (NEXAFS) spectroscopy, normal-incidence X-ray standing wave (NI-XSW) experiments, non-contact atomic force microscopy (nc-AFM) and density functional theory (DFT) calculations. These data were provided by other group members or col-

laboration partners and will not be discussed in great detail. As model systems, the alternant molecules naphthalene (Nt) and pyrene (Pyr) are compared with the non-alternant molecules azulene (Az) and azupyrene (AzPyr) adsorbed on Cu(111) and Ag(111), resulting in publications P1, P2, and P3. Additionally, a detailed quantitative analysis of TPD data of benzene (Bz) adsorbed on the Cu(111) and Ag(111) surface was performed to provide desorption energies as a benchmark for adsorption energies derived by DFT calculations. The TPD experiments were supported by J. Hochstrasser and L. Hellweg.

4.1.1 Adsorption and Desorption of Azulene and Naphthalene on Cu(111) and Ag(111)

The comparison of the non-alternant Az with the alternant Nt reveals the impact a non-alternant structure has on the bonding situation on the surface. This knowledge is important to gain further insight into the 5-7 defect structure of graphene, which is comparable to Az. A single defect in graphene cannot be probed on its own by many techniques, hence Az is used as a model system for the defect; Nt represents intact graphene. A detailed quantitative TPD study supported by DFT calculations using four different dispersion correction schemes gives insight into the bonding strength of both molecules on Ag(111) and Cu(111). In addition, to characterize the bonding situation on Cu(111), a multi-technique approach was used including XPS, UPS, NEXAFS spectroscopy, the NI-XSW technique, TPD, nc-AFM, scanning tunneling microscopy (STM) and DFT calculations.

TPD experiments (Figure 4.1a) reveal much higher desorption temperatures for Az (550 K) than for Nt (370 K) on Cu(111), which points toward a stronger interaction for Az. On the Ag(111) surface both molecules interact weaker with the surface than on Cu(111). Again, Az desorbs at slightly higher temperatures than Nt (400 K *vs.* 350 K) indicating that Az binds stronger on both surfaces than Nt. All TPD traces exhibit substantial peak broadening to lower temperatures for increasing coverages. Connected to this, the peak maximum temperatures shift to lower temperatures, as well. The strong peak broadening at high coverages is attributed to intermolecular repulsion between upright-standing dipoles due to the Pauli push back effect. This effect is stronger for higher interface interactions. Hence, the strongest interaction is found for Az on Cu(111) followed by Az on Ag(111), Nt on Cu(111) and Nt on Ag(111). Another unique characteristic of Az on Cu(111) is a second peak at coverages above 0.6 ML, which is attributed to a compressed phase. In this phase the Az molecules are densely packed, losing their mobility.

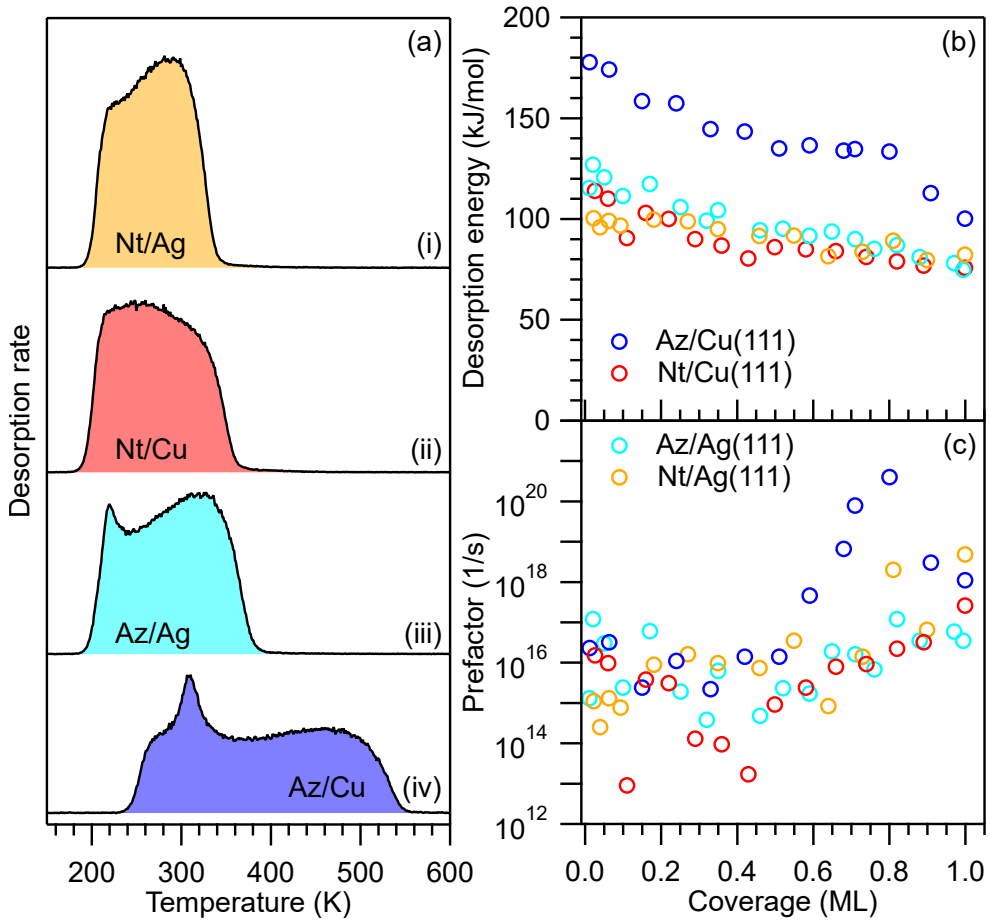

Figure 4.1: (a) Monolayer TPD traces of Az and Nt on Ag(111) and Cu(111). The heating rates were 1 K/s and both molecules were detected at $m/z = 128$ amu. (b) Desorption energies and (c) prefactors obtained by the mLEA for blue: Az on Cu(111), red: Nt on Cu(111), cyan: Az on Ag(111) and orange: Nt on Ag(111).

The TPD traces are quantitatively analyzed using different techniques including the heating-rate variation (HRV) analysis, the inverted Polanyi-Wigner (IPW) equation, fitting of the TPD traces and a mLEA. The derived desorption energies agree well with the qualitative suggestion made before (Figure 4.1b). However, a special focus is put on the pre-exponential factor (prefactor). While the prefactor derived by the HRV analysis is in good agreement with the transition state theory (TST) for Az on Cu(111) and Ag(111) as well as Nt on Ag(111), far too low values are obtained for Nt on Cu(111). This leads to low desorption energies for Nt on Cu(111) in the first place. By using the TST prefactor in the IPW equation and the TPD fits, reasonable energies are obtained. Similar results are found for the mLEA, emphasizing the importance of a thorough discussion and choice of the prefactor within TPD. Furthermore, the mLEA reveals that the second peak in the monolayer trace of Az on Cu(111) is attributed to a strong increase of the prefactor by 5 orders of magnitude (Figure 4.1c), which

is explained by a drastic reduction of the mobility of the molecules on the surface. In contrast, the prefactors of the other three systems increase only slightly with increasing coverages. The big difference in the desorption kinetics of Az on Cu(111) in comparison with the other three systems suggests chemisorption for Az on Cu(111) in contrast to physisorption for the other systems.

DFT calculations are performed for four different dispersion schemes – DFT-D3 with Becke-Johnson damping function (D3), vdW^{surf} correction based on DFT-Tkatchenko-Scheffler (TS), a many-body dispersion (MBD) correction, and the D3^{surf} scheme. All methods reproduce the qualitative trend of the bond strength but differ in the absolute values. D3 and vdW^{surf} overestimate all adsorption energies, whereas MBD and D3^{surf} show no obvious trend of over- or underestimation. Physisorbed systems are better described by vdW^{surf} and D3^{surf} and chemisorbed systems by D3, while MBD yields lower values for physisorbed and higher ones for chemisorbed systems.

It was shown that Az binds much more strongly to the Cu(111) surface than Nt, for which evidence is found by further techniques. The adsorption height determined by NI-XSW measurements of 2.30 Å for Az points toward chemisorption, while a height of 3.04 Å for Nt is in the range of van der Waals (vdW) distances. nc-AFM force spectra and DFT calculations further support this trend. Due to the strong bond between Az and Cu(111), the electronic structure of Az changes indicated by XPS, UPS and NEXAFS spectroscopy. In the C 1s XP spectrum of Az, the peak is shifted to lower binding energies and exhibits a strong peak asymmetry in comparison with Nt. This is caused by molecular density of states (DOS) near the Fermi edge, which is confirmed by increased intensity between the substrate d-band and the Fermi edge in UP spectra. NEXAFS spectroscopy measurements reveal intense changes in the unoccupied states when reducing the coverage from multilayers to monolayers. Analyses of NEXAFS simulations and DFT-based DOS calculations show a net electron transfer from the surface to the former lowest unoccupied molecular orbital (LUMO) of Az. The shape of the former LUMO is observed experimentally at a negative bias in STM experiments, which means that it partially gets occupied on the Cu(111) surface. Such strong effects are not observed for Nt, hence the non-alternant nature of Az causes the chemisorptive bond. Similar investigations are performed on Ag(111), revealing a stronger bond for Az than for Nt, however, the differences are not as pronounced as on Cu(111).[195]

The comparison between Nt and Az showed that the non-alternant topology of Az yields stronger interaction energies with both metal surfaces, although it is

only physisorbed on Ag(111). Moreover, comparing the Cu(111) and the Ag(111) surfaces reveals that the difference in the bonding strengths between alternant and non-alternant structures is not always as significant as on Cu(111).

4.1.2 Adsorption and Desorption of Azupyrene and Pyrene on Cu(111)

Az was used previously as a model for a 5-7 defect in graphene. However, defects are often larger, spanning over two defect units, which are called Stone-Wales defects. The molecule AzPyr, which consists of two five- and two seven-membered rings, is chosen as the higher analog to Az. The corresponding defect-free molecule is Pyr consisting of four six-membered rings. The adsorption and desorption of both molecules were investigated on Cu(111) because the biggest difference between Az and Nt was observed on this surface.

A multi-technique approach was used for the investigation of the Stone-Wales defects. The desorption behavior was studied by means of TPD, revealing big differences between AzPyr and Pyr. Pyr completely desorbs below 520 K, whereas a monolayer of AzPyr desorbs below 650 K (Figure 4.2). Above 650 K the desorption of AzPyr is followed by formation and desorption of molecular hydrogen. Complementary C 1s XP spectra show that approximately 53 % of the AzPyr monolayer do not desorb and remain on the Cu(111) surface. Above 650 K the C 1s peak shifts and gets broadened, indicating decomposition of the remaining molecules. Quantitative analysis of the TPD data reveals a high desorption energy of AzPyr in the range of 198 to 122 kJ/mol between half and full monolayer coverage. The absolute desorption energy as well as the coverage dependence is much lower for Pyr, ranging from 159 to 96 kJ/mol. The coverage-dependent desorption energy is ascribed to intermolecular repulsion between dipoles perpendicular to the surface, which has already been described previously. The work function change is related to the adsorption-induced charge transfer as well as the strength of the dipoles and takes values of -1.18 eV for AzPyr and -0.86 eV for Pyr. The IPW equation of AzPyr is fitted using a quadratic function ($E(\Theta) = (232.7 - 109.6\Theta^2)$ kJ/mol). Accordingly, the zero-coverage desorption energy of AzPyr is estimated to be approximately 233 kJ/mol. The prefactors of Pyr scatter around values of $2 \cdot 10^{15}$ s^{-1}, whereas the values of AzPyr increase from 10^{14} to 10^{16} s^{-1}. A similar increase of the prefactor was found for Az above 0.6 ML, too, attributed to a compressed phase. The high desorption energy of AzPyr indicate a much stronger bond to the Cu(111) surface than Pyr.

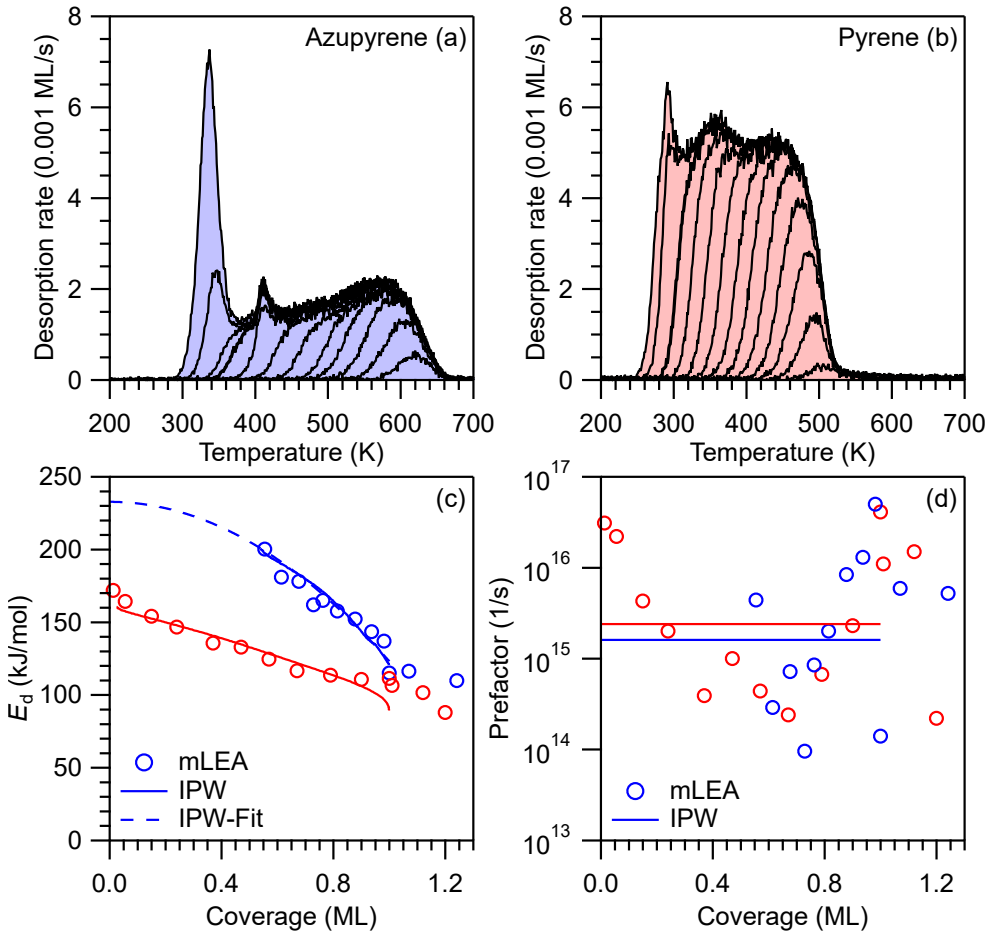

Figure 4.2: Coverage series of (a) AzPyr and (b) Pyr on Cu(111). The initial coverages were prepared by dosing a multilayer coverage and subsequent annealing at certain temperatures. Monolayer traces are indicated by bold lines. The coverages range from 0.53 to 1.26 ML for AzPyr and 0.01 to 1.20 ML for Pyr. The heating rates were 1 K/s and both molecules were detected at m/z = 202 amu. (c) Desorption energies (in kJ/mol) and (d) prefactors (in 1/s) obtained by the mLEA (circles) and IPW equation (solid line) for blue: AzPyr and red: Pyr. The prefactor used for the IPW equation is the average of the mLEA results. The desorption energy of the IPW was fitted ($E(\Theta) = (232.7 - 109.6\Theta^2)$ kJ/mol) determining the zero-coverage desorption energy.

The adsorption height was investigated by nc-AFM and yields a 0.9 Å lower height for AzPyr. Although DFT calculations predict only a 0.5 Å lower height for AzPyr, a stronger bond of AzPyr to the Cu(111) surface than for Pyr is observed. As already noticed for Az on Cu(111), a charge transfer into the former LUMO of AzPyr is indicated by XPS, UPS, and NEXAFS spectroscopy. Pyr does not show according features in the mentioned spectra, which leads to the conclusion that the alternant molecule is again only physisorbed, whereas the non-alternant counterpart is chemisorbed.

DFT calculations were performed on defect structures in graphene adsorbed on Cu(111) to prove the correctness of the model systems. An increased adsorption

energy, a lower adsorption height and a stronger charge transfer are observed for the Stone-Wales defects in a graphene lattice, which point toward a stronger surface interaction.

4.1.3 Quantitative Analysis of TPD Data for Benzene on Cu(111) and Ag(111)

Experimental desorption energies of Az and Nt were compared with theoretical adsorption energies derived by different DFT calculations. It was found that each dispersion correction scheme describes either chemisorption or physisorption better. For an easier comparison of the methods a simpler system than Nt and Az is required as a benchmark. Therefore, the desorption kinetics of Bz adsorbed on the Ag(111) and Cu(111) single-crystal surfaces was quantitatively analyzed by means of TPD. Although these systems have already been investigated in literature, the values are often not reliable because of inappropriate analysis methods or experimental shortcomings.[30,31,117]

The monolayer traces as well as the coverage series of Bz on Ag(111) and Cu(111) are shown in Figure 4.3. The monolayer desorption of Bz on Ag(111) starts at 145 K and ends at 240 K, whereas the desorption on Cu(111) ranges from 140 to 240 K. Above 240 K a high-temperature tail is observed on Cu(111), corresponding to the desorption from defects. At low initial coverages the desorption starts at high temperatures and the peak shifts to lower temperatures for increasing initial coverage. This behavior is attributed to lateral intermolecular repulsion as already discussed in Chapter 2.1.1. Interestingly, the peak shape of the monolayer traces strongly varies between Ag(111) and Cu(111) from a qualitative point of view. Above a temperature of 160 K, the desorption rate decreases nearly linearly on Cu(111) but exhibits a non-linear behavior on Ag(111). This suggests different desorption kinetics in the two systems. The coverage series are in good agreement with recent TPD data from literature.[31]

The thorough choice of the prefactor for a good quantitative analysis was emphasized above. It was shown that the estimation using the TST yields good results. Therefore, the prefactor in the mobile limit of Bz on Ag(111) and Cu(111) is used ($1.53 \cdot 10^{15}$ s^{-1}). The values for the rotational constants are taken from ref. [196]. The coverage series in Figure 4.3b and c are fitted using a quadratic equation for the desorption energy in the Polanyi-Wigner (PW) equation and the TST prefactor of $1.53 \cdot 10^{15}$ s^{-1}. The same prefactor is used for the IPW equation. The fitting results as well as the differential and integral energies are shown in Figure 4.4.

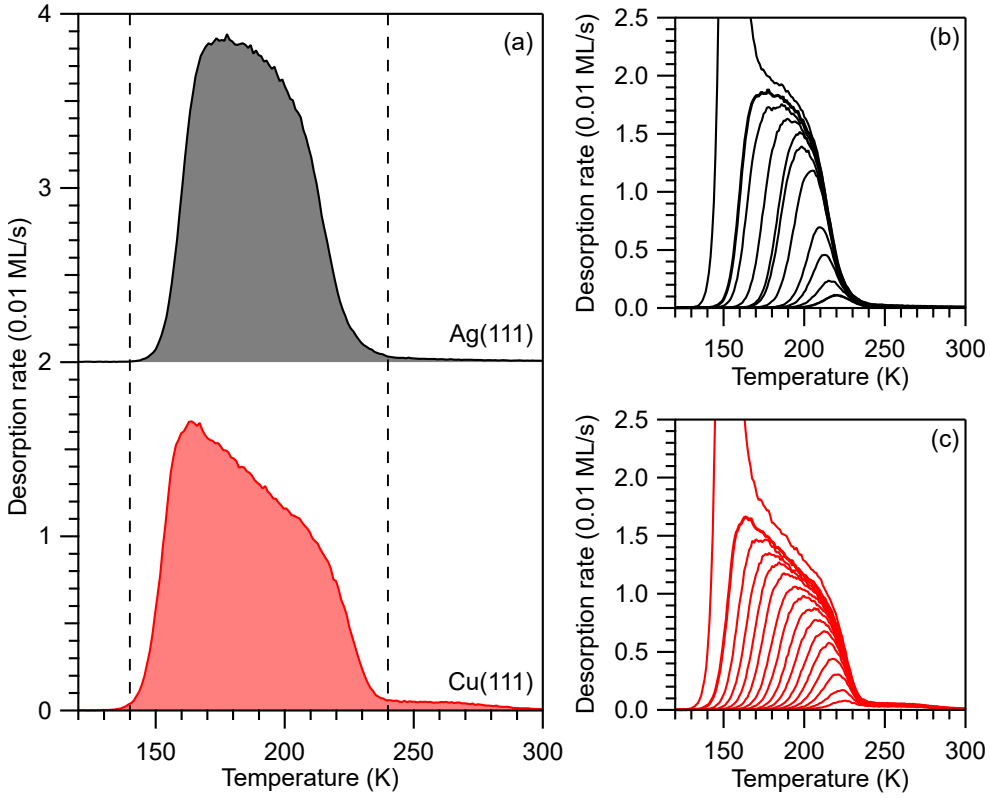

Figure 4.3: (a) Monolayer TPD traces of Bz on Ag(111) and Cu(111). The beginning and ending of the Ag(111) trace is indicated by the dashed lines as a guide to the eye for comparison with Cu(111). (b) and (c) coverage series of Bz on Ag(111) and Cu(111), respectively. The initial coverages were prepared by deposition of an excess of Bz and subsequent annealing of the sample to certain temperatures. Monolayer traces are indicated by bold lines. The heating rate was 1 K/s and Bz was detected at $m/z = 78$ amu.

The simulated TPD traces using the obtained fits (Ag: $E_\mathrm{d} = (66 - 13.8\Theta - 0.8\Theta^2)$ kJ/mol; Cu: $E_\mathrm{d} = (68.7 - 23.3\Theta + 3.7\Theta^2)$ kJ/mol) are in good agreement with the experimental TPD data. Only at low coverages slight deviations are apparent due to desorption from defect sites. The intermolecular repulsion is stronger on Cu(111) indicated by a higher negative value of the linear term for Cu(111) than for Ag(111). Additionally, the quadratic term of the Cu(111) fit is positive in contrast to Ag(111). This results in a linear decrease of the desorption rate on Cu(111) mentioned above. However, the quadratic term cannot be linked to a real phenomenon as the nature of this term is not fully understood.

The results of the IPW equation are in good agreement at intermediate coverages but deviate stronger at low and high coverages (Figure 4.4c). The deviation at low coverages is ascribed to the desorption from defect sites, which is not considered in the fits. The differences at high coverages may arise because of insufficient terms in the fit or a bad signal-to-noise ratio (SNR) in the leading-edge regime of the TPD data. Nevertheless, the integral energies obtained by

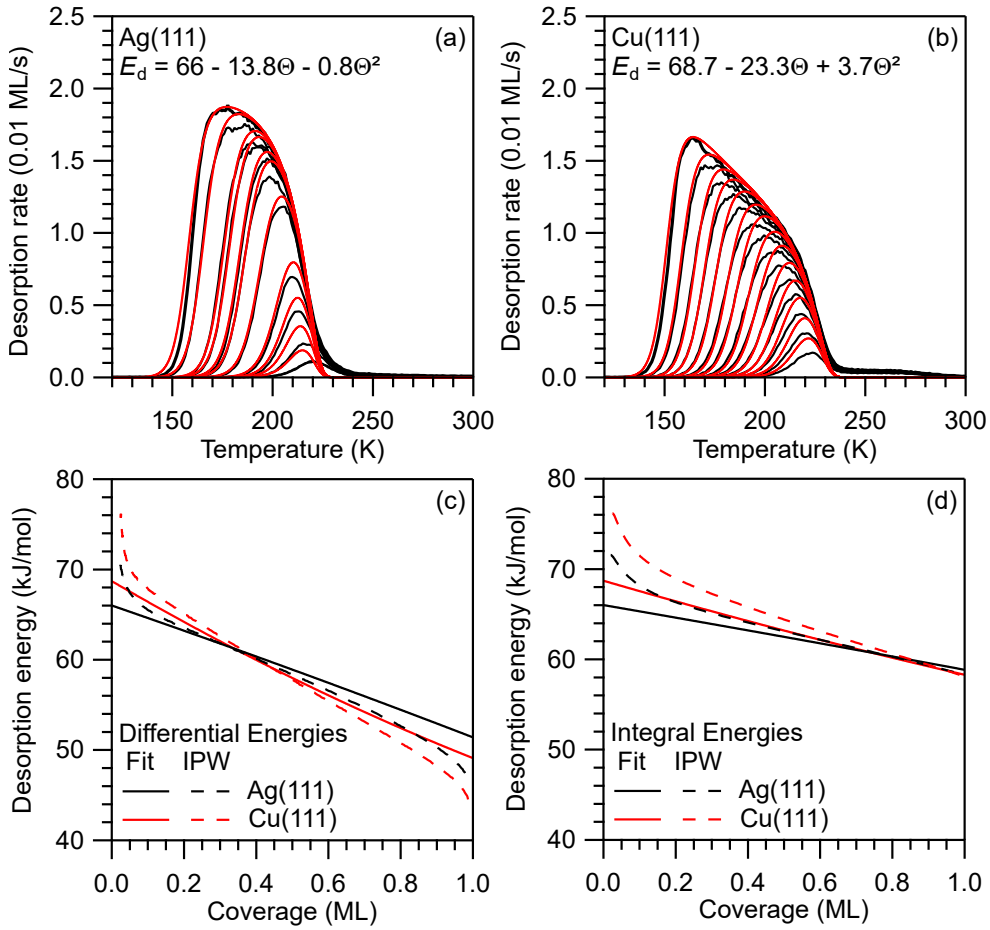

Figure 4.4: The simulated traces (red) compared with experimental data (black) as well as the corresponding fits given in kJ/mol of Bz on Ag(111) and Cu(111) are shown in (a) and (b), respectively. The corresponding energies of the fit together with the results of the IPW equation are plotted in (c). The derived integral energies are given in (d).

both methods are in good agreement with each other except at low coverages (Figure 4.4d). An overall higher energy on Cu(111) is found up to coverages of approximately 0.85 ML. Figure 4.4d is especially useful for comparison with adsorption energies derived by DFT calculations.

As mentioned before, Bz was investigated on coinage metals before.[31] The authors of this publication, however, used the complete analysis (CA), which is not recommended for repulsive systems.[147] A detailed view on the results presented by Maass *et al.*[31] shows an artificial compensation effect, *i.e.*, an increase of the desorption energy is accompanied by an increase of the prefactor. Therefore, they follow the exact same trend. Moreover, some data points correspond to prefactors far below $1 \cdot 10^{12}$ s^{-1}, which is below the physical threshold for a completely mobile particle (all degrees of freedom (DOFs)) at low temperatures. For a better comparison between both data sets, a detailed coverage series of Bz on Ag(111) and Cu(111) was measured and the CA is performed (Figure 4.5).

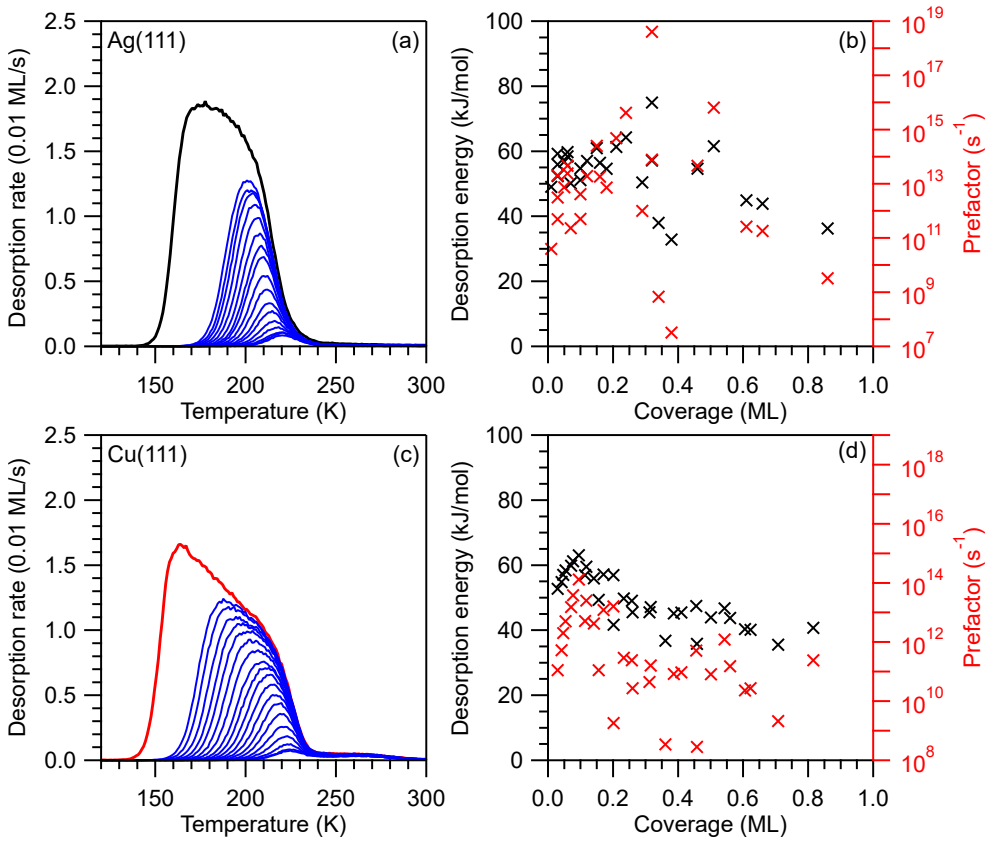

Figure 4.5: Coverage series (blue) in small initial coverage steps and the obtained results using the CA for Bz on (a,b) Ag(111) and (c,d) Cu(111). The monolayer trace (black and red trace) is taken from Figure 4.3. In addition, the traces of the coverage series in Figure 4.3b and c are taken into account in the CA. The results of the CA exhibit an artificial compensation effect.

Taking all measured TPD traces into account, the CA yields lower desorption energies and prefactors in comparison with the fitting procedure and the IPW. The obtained results, however, are in good agreement with the results published in ref. [31]. In both cases an artificial compensation effect is found, stating once more that this method is not applicable to repulsive systems. According to previous results of Az and Nt on Cu(111) and Ag(111), the HRV analysis and mLEA are more reliable. The HRV analysis is performed for four different initial coverages on Ag(111) and for five initial coverages on Cu(111). All recorded TPD traces are analyzed by the mLEA. The results are shown in Figure 4.6 together with the results of the fitting procedure as a comparison.

The results of the mLEA on Ag(111) are in good agreement with the TPD fit in the low coverage regime. Nonetheless, the desorption energy decreases more slowly with increasing coverage than the fit. This is accompanied by an increase of the prefactor by three orders of magnitude, whereas the prefactor is assumed to be constant for the fit. Which method fits better is hard to state because

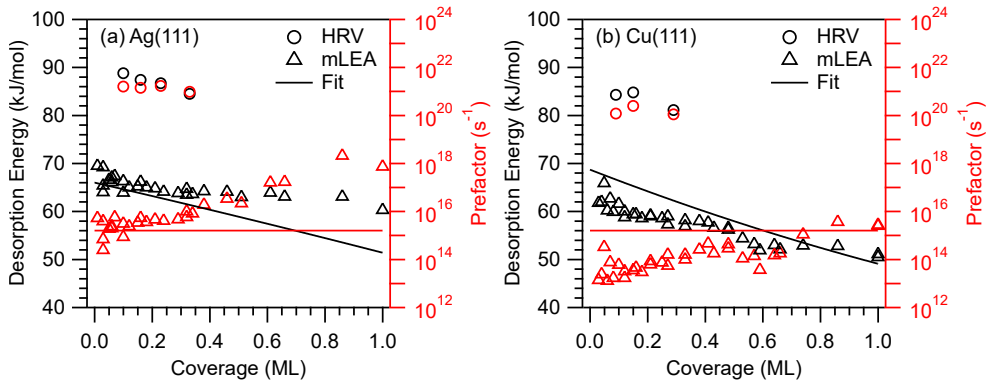

Figure 4.6: Results of the HRV analysis (circles) and mLEA (triangles) of Bz on (a) Ag(111) and (b) Cu(111). The obtained desorption energy by the fitting procedure (solid line) and the TST prefactor are shown for comparison. The desorption energies are presented in black and prefactors in red.

it is difficult to calculate the prefactor dependent on the coverage. The results obtained by the HRV analysis are unreasonably high; therefore, they cannot be taken into consideration. Failure of the HRV analysis has been reported for the system Nt on Cu(111) in Publication P2, too.[197]

Similar findings are observed on Cu(111), however, the best agreement is found for high coverages. Here, the prefactor of the mLEA and the TST are very similar. The prefactor decreases for lower coverages and so does the desorption energy. Again, the HRV analysis yields far too high values for the desorption energy and the prefactor. As a result of the lower prefactor on Cu(111), the desorption energy is lower on Cu(111), as well. Usually, the desorption energy should be higher on Cu(111) because it is the more reactive surface. It is possible that the difference in the prefactors is the reason for the different peak shape of the monolayer traces discussed above. A comparison of the experimental desorption energies with theoretical adsorption energies is difficult since the prefactors depend on the coverage. Therefore, the prefactors have to be calculated by DFT and TST for different coverages and compared with the corresponding experimental ones. A fixed prefactor as in the case of the IPW equation, would lead to false energies.

4.1.4 Summary

The presented results show that a non-alternant aromatic topology increases the interaction of polycyclic aromatic hydrocarbons (PAHs) with metallic single-crystal surfaces. Especially on Cu(111), this leads to a strong chemisorption for Az and AzPyr indicated by high desorption energies, low adsorption heights and large charge transfers. The desorption energies obtained from quantitative

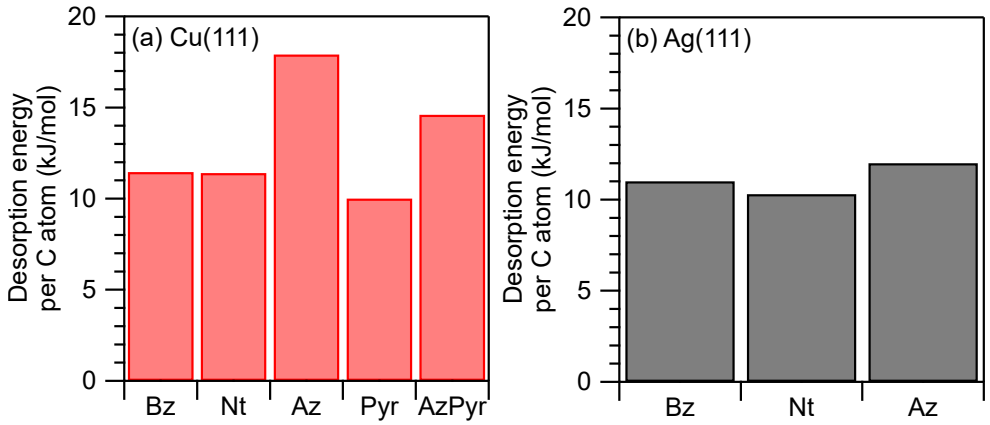

Figure 4.7: Overview of the zero-coverage desorption energies normalized to the number of C atoms of Bz, Nt, Pyr, Az and AzPyr on (a) Cu(111) and (b) Ag(111). No data for Pyr and AzPyr on Ag(111) are available. The desorption energy of AzPyr is estimated by fitting of the IPW equation.

analyses of TPD experiments are summarized in Figure 4.7. The desorption energies on Cu(111) are always higher than those on Ag(111) and increase with the size of the molecule. The highest desorption energy was found for AzPyr on Cu(111), although the zero-coverage energy of AzPyr cannot be determined directly because the molecule does not desorb intact below half monolayer coverage. Normalizing the desorption energies to the number of C atoms in the molecules, reveals 10-12 kJ/mol for physisorbed systems and 15-17 kJ/mol for chemisorbed systems per C atom. Whether an aromatic molecule is physisorbed or chemisorbed on a coinage metal surface, can be roughly estimated by determining the desorption energy per C atom. For values above 15 kJ/mol, the molecule is most likely chemisorbed.

4.2 Analyses of the Interactions of Pristine and Mixed Phases of Pentacene and Perfluoropentacene on MoS_2 and Au(111)

So far, aromatic OSCs were investigated on metal surfaces. On weaker interacting vdW surfaces, such as transition metal dichalcogenides (TMDCs), the formation of flat-lying molecules in the monolayer is rarely observed. This project focuses on the investigation of the monolayer formation and interaction between the OSCs pentacene (PEN) and its fluorinated derivative perfluoropentacene (PFP) on the MoS_2 surface in a multi-method approach. The OSC layer can be considered a two-dimensional (2D) layer when the molecules lie flat on the

surface. The interactions of PEN and PFP with the bulk MoS_2 surface and the surface of a single layer MoS_2 (2D MoS_2) on SiO_2 support are investigated and compared with each other. In addition, experiments on Au(111) were conducted and the desorption kinetics were examined for comparison between organic/inorganic and metal/organic interfaces. Furthermore, the interactions of mixed mono- and multilayers of PEN and PFP were investigated and compared with the pristine deposition. All systems were studied by means of TPD. The TPD experiments were conducted with the help of Dr. T. Breuer, P.-M. Dombrowski and L. Neuhaus. Additional methods include NEXAFS spectroscopy, Monte Carlo (MC) simulations and STM experiments mainly conducted by P.-M. Dombrowski.

4.2.1 Desorption Kinetics of Pentacene and Perfluoropentacene on MoS_2

NEXAFS spectroscopy measurements reveal that after heating of samples with multilayer coverages of PEN and PFP to 410 K small resonances remain, which exhibit X-ray dichroism. These signals are attributed to flat-lying molecules in the monolayer. TPD experiments show a monolayer desorption peak, which can be clearly distinguished from the multilayer desorption for both molecules. Multilayer desorption starts at 350 K for both molecules, whereas the monolayer desorption traces range from 380 to 490 K for PEN and from 390 to 530 K for PFP (Figure 4.8). Moreover, heating of multilayer coverages to 390 and 400 K for 1 min gave rise to the precise preparation of monolayer coverages of PEN and PFP, respectively. Quantitative analysis of the multilayer TPD data yields desorption energies of 141 and 149 kJ/mol for PEN and PFP, respectively, in reasonable agreement with the sublimation enthalpy of (157 ± 14) kJ/mol.[139] Using the HRV analysis on initial coverages of 0.4 ML for both molecules, desorption energies of 122 and 131 kJ/mol for PEN and PFP, respectively, as well as prefactors of $5 \cdot 10^{12}$ s^{-1} are obtained. The mLEA yields similar energies in the range from 105 to 127 kJ/mol for PEN and 121 to 132 kJ/mol for PFP as well as prefactors ranging from 10^{11} to 10^{14} s^{-1}, depending on the coverage. Because the desorption energy of the monolayer is lower than the sublimation enthalpy of the multilayer, the monolayer should dewet the surface. However, the small prefactors indicate a high mobility, which is further proven by STM images, of the molecules on the surface. Analyzing the Gibbs free energy in the multilayer and the monolayer, using the calculated desorption energies and prefactors, it is found that the monolayer is stabilized by 19 kJ/mol with respect

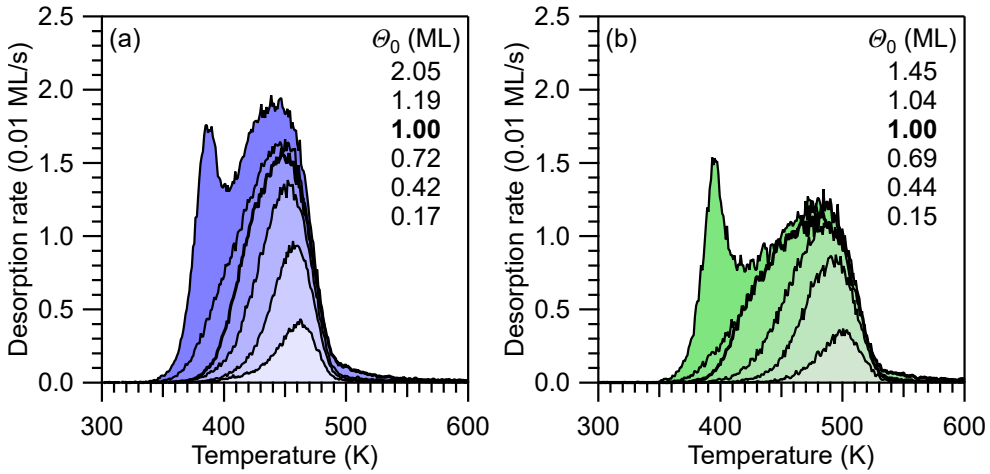

Figure 4.8: Series of TPD traces for different initial coverages of (a) PEN and (b) PFP on bulk MoS_2. Initial coverages range from 0.17 to 2.05 ML for PEN and 0.15 ML to 1.45 ML for PFP starting with the highest coverage at low temperatures. The monolayer traces (1.0 ML) are indicated by bold lines and were prepared by an excess dosage of molecules on the hot MoS_2 surface (390 K for PEN and 400 K for PFP). The heating rates were 1 K/s by mass spectrometric detection of $m/z = 278$ amu and $m/z = 530$ amu for PEN and PFP, respectively.

to the multilayer. This stabilization is mainly driven by a high entropy term resulting from low prefactor values. In addition, MC simulations with electrostatic intermolecular repulsion are performed yielding interaction potentials V of $(8.2\Theta^{2.6})$ kJ/mol and $(12.5\Theta^{2.5})$ kJ/mol for PEN and PFP, respectively, which describe the decreasing desorption energy with increasing coverages. Summarizing these data, PEN and PFP develop an entropically stabilized monolayer on the MoS_2 surface. The monolayer, however, is not close-packed due to the intermolecular repulsion and high mobility of the molecules.

4.2.2 Desorption Kinetics of Pentacene and Perfluoropentacene on 2D MoS_2

In a next step, both molecules were deposited on a single layer (2D) MoS_2 in order to varify whether the same desorption behavior is observed. The TPD measurements on 2D MoS_2 flakes grown on SiO_2 are more difficult than those on bulk MoS_2 because the 2D MoS_2 only covers a part of the SiO_2 surface. Therefore, the total intensity of the desorption signal is reduced by a factor corresponding to the reduced sample area of 2D MoS_2. Furthermore, a smaller orifice of the mass spectrometer entrance was used for these experiments due to a smaller sample, additionally reducing the measured intensity. Since both molecules only bind very weakly to SiO_2, desorption from the SiO_2 surface occurs together with the multilayer desorption from 2D MoS_2 (and SiO_2).[140,198] The

monolayer traces of PEN and PFP on 2D MoS_2 as well as different preparation techniques are shown in Figure 4.9.

Even at (sub-)monolayer coverages, a zeroth-order desorption peak originating from the desorption from SiO_2 occurs at lower temperatures. If the preparation methods M-2 and M-3 are applied (compare Figure 4.9), desorption only occurs from the 2D MoS_2 flakes because desorption from SiO_2 is already complete.[140] Note that the selective adsorption on the 2D MoS_2 flakes enables measurements with laterally integrating spectroscopic techniques without background caused by molecules adsorbed on SiO_2.

Monolayers of PEN and PFP on 2D MoS_2 desorb in the range from 380 K to 480 K and 390 K to 510 K, respectively. The lowest desorption temperature is the same as on bulk MoS_2, however, the desorption ends earlier on 2D MoS_2. This leads to slightly lower peak maximum temperatures, as well. This shift to lower temperatures may be caused by the bad SNR, *i.e.*, the high-temperature edge is not detected due to the low intensity. The adsorption on only one layer of MoS_2 results in a slightly lower interaction energy compared with bulk MoS_2. A thorough quantitative analysis of the TPD traces is not possible due to the extremely bad SNR. Since the desorption temperatures are similar, the desorption kinetics should be qualitatively similar, too.

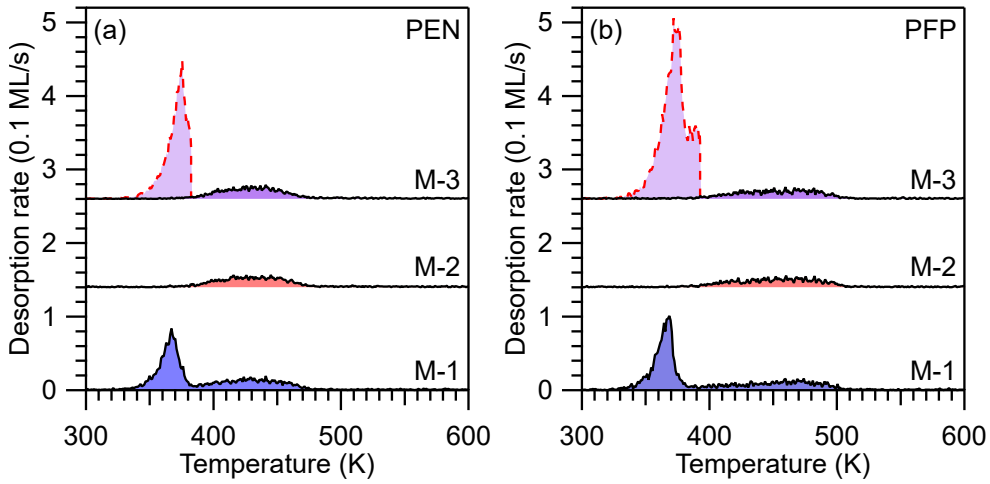

Figure 4.9: Different monolayer preparation techniques of (a) PEN and (b) PFP on 2D MoS_2. M-1, direct deposition of 1 ML at 270 K (blue); M-2, dosing an excess (approx. 3 ML equivalents) at 390 K for PEN and 400 K for PFP (red); M-3, heating an excess deposited at 270 K (approx. 3 ML) to 390 K for PEN and 400 K for PFP (purple). The desorbing multilayer during heating is indicated by the red dashed line. The measurements were performed with a heating rate of 1 K/s by mass spectrometric detection of $m/z = 278$ amu and $m/z = 530$ amu for PEN and PFP, respectively.

4.2.3 Desorption Kinetics of Pentacene and Perfluoropentacene on Au(111)

Besides the MoS_2 surface, the desorption of PEN and PFP on the Au(111) single-crystal surface was investigated. These data are complementary to the data on MoS_2 and pinpoint the differences between metal and inorganic surfaces. The coverage series of both molecules on Au(111) are presented in Figure 4.10. The desorption peak for the smallest initial coverage of PEN occurs at 685 K and strongly shifts to lower temperatures for increasing coverages. Above coverages of 0.75 ML a second peak appears. Similar peaks are observed for several other metal/organic interfaces and are attributed to a compressed phase. Above monolayer coverage the bilayer peak is found at 410 K and at higher coverages multilayer desorption is observed. At 465 K another small peak appears that can be neither assigned to a bilayer nor to a compressed phase. It may originate from a transition region, where molecules in the second layer do not lie parallel to the surface and exhibit weak interactions to the first layer. In contrast, the desorption at small PFP coverages starts at 620 K and shifts to 400 K at full monolayer coverage. Here, neither a compressed peak nor a transition region from bi- to monolayer are found. The peak broadening of 250 K is the same as for PEN. To conclude from its lower desorption temperature that PFP binds more weakly to the Au(111) substrate would be wrong because AES measurements (Figure 4.10c) indicate that PFP decomposes and carbon residues are left on the Au(111) surface. Since no quantitative amounts of the residue can be derived from the AE spectra, complementary XPS data are necessary. Taking the decomposition of PFP at 650 K into account, PFP binds stronger to the Au(111) surface than PEN.

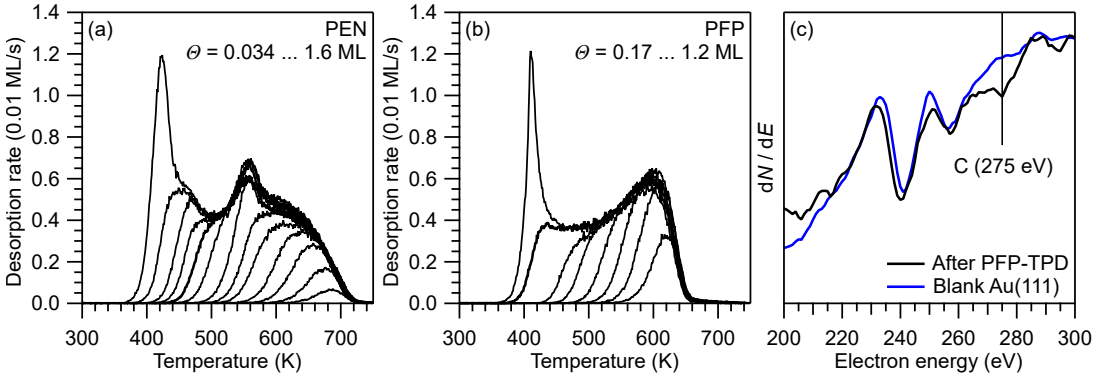

Figure 4.10: Coverage series of (a) PEN and (b) PFP on Au(111). The monolayer trace is indicated by a bold line. The measurements were performed with a heating rate of 1 K/s by simultaneous mass spectrometric detection of $m/z = 278$ amu and $m/z = 530$ amu for PEN and PFP, respectively. (c) AES experiment for the clean Au(111) surface (blue) and after desorption of PFP (black). Spectra were recorded at an electron energy of 2000 eV.

In order to obtain quantitative information on the desorption kinetics of both systems, the mLEA is performed on the coverages series (Figure 4.11). The desorption energies of both molecules slowly decrease with increasing coverage, whereas the prefactors increase at the same time. The desorption energy at zero coverage of PEN is 212 kJ/mol and 219 kJ/mol for PFP. It is important to keep in mind that PFP does not completely desorb, hence the apparent coverage shown here is lower than the real coverage. Furthermore, the prefactors of PFP are higher than those of PEN, which is expected due to the higher mass and moments of inertia of PFP than PEN. Both prefactors increase for increasing coverages. The obtained results clearly illustrate the stronger interaction of PEN and PFP on metal surfaces in comparison with vdW surfaces.

The peak of PEN on Au(111) at 560 K needs a critical discussion because it was found in a previous study,[140] however, in the latest study of this system the peak was not observed.[117] Detailed investigations on the preparation of the Au(111) surface, *e.g.*, varying sputtering and annealing conditions, showed that the peak disappears if the surface is contaminated or defect rich. It was shown above that PFP does not desorb intact and carbon remains on the surface. If PEN is deposited onto a carbon covered surface, the peak disappears (Figure 4.12a, black). In addition, sputtering the surface with Ar^+ ions at high energies results in intercalated Ar atoms in the surface (Figure 4.12a, red). The Ar atoms are only removed at temperatures above 900 K. Otherwise, the surface is defect rich prohibiting the formation of a compressed phase. Thorough preparation and cleaning of the Au(111) surface is mandatory for reliable TPD traces.

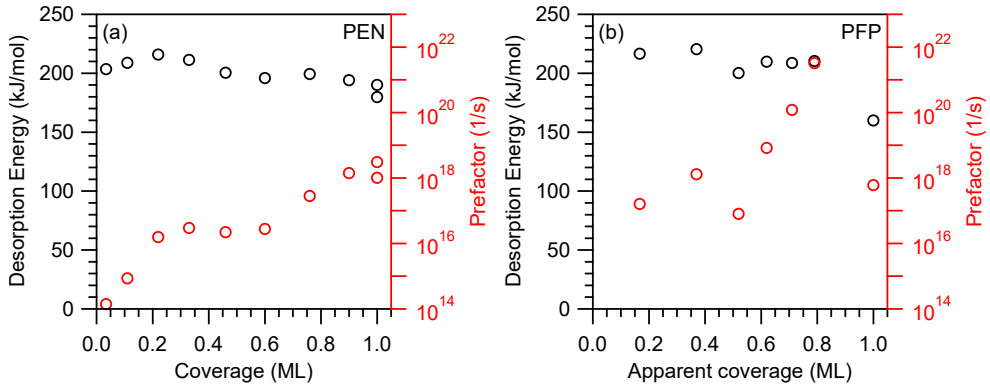

Figure 4.11: Quantitative analysis of the coverage series shown in Figure 4.10 using the mLEA for (a) PEN and (b) PFP on Au(111). For PFP, the apparent coverage, *i.e.*, the integral coverage of the TPD traces, is used since no quantitative information about the residual carbon amount is known. The real coverage is higher than the apparent one. Desorption energies are presented in black and prefactors in red.

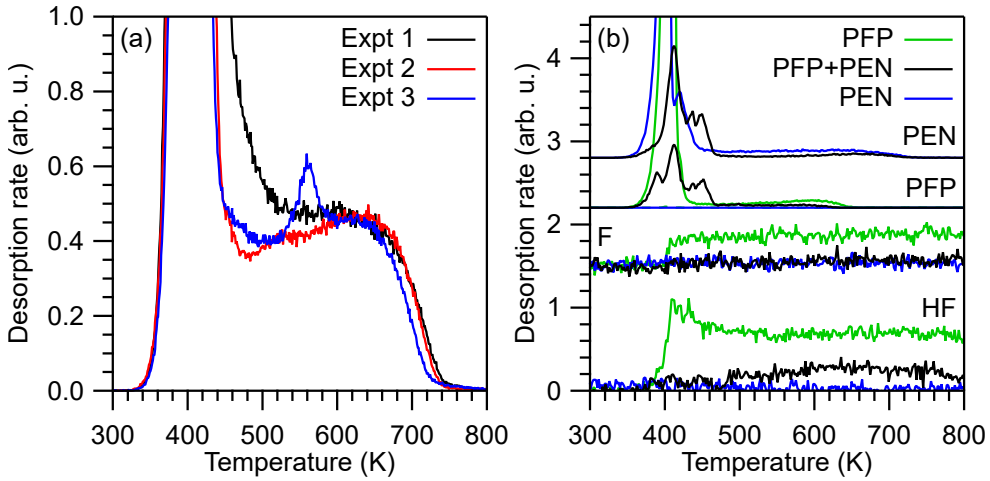

Figure 4.12: (a) TPD traces of PEN on differently prepared Au(111) surfaces. Expt 1 (black): after desorption of PFP without sputtering; Expt 2 (red): after sputtering and annealing to 800 K; Expt 3 (blue): after sputtering and annealing to 1000 K. (b) TPD experiments monitoring the mass-to-charge ratios 278 amu (PEN), 530 amu (PFP), 19 amu (F) and 20 amu (HF). Green: approx. 4 ML pristine PFP on Au(111); black: heterostructure of approx. 2 ML PEN and approx. 2 ML PFP on Au(111); blue: approx. 4 ML pristine PEN on Au(111). The heating rates were 1 K/s.

At the end, monitoring the F and HF masses during the desorption of pristine molecules as well as of a heterostructure gives insight into the decomposition of PFP (Figure 4.12b). In the PEN experiment, no F and HF species are detected, which is expected. The desorption of pristine PFP is accompanied by detection of F and HF in the multilayer regime. Afterwards, an increased background is observed due to the bad pumping speed of F in ultra-high vacuum (UHV) chambers. Since both F and HF are detected and no H should be available on the surface for pristine PFP, F is most probably generated in the ionization source of the mass spectrometer by the decomposition of PFP and HF originates from the reaction of F with H in the residual gas, hence the HF formation is not related to an on-surface reaction. Interestingly, a 1:1 mixture of both molecules results in a pronounced desorption peak of HF ranging from 500 to 800 K, while no desorption of F is observed. The formation of HF is explained by HF-zipping.[199–201] Neighboring PEN and PFP molecules lose their H and F atoms under formation of HF starting at 500 K. This reaction causes PFP molecules to decompose earlier, which is indicated by temperature shift to lower temperatures for the high-temperature edge of PFP by 25 K.

4.2.4 Desorption Kinetics of Heterostructures of Pentacene and Perfluoropentacene

In order to achieve well-ordered and close-packed monolayers especially on MoS_2, an additional enthalpic stabilization is desirable. In a recent study it was found that thin multilayer films of a heterostructure of PEN and PFP resulted in attractive intermolecular interaction.[202] The attractive interactions originate from the reversed quadrupole moments of the two molecules and they could stabilize monolayer coverages of PEN and PFP, developing close-packed layers. Monolayer TPD experiments of heterostructures of PEN and PFP on MoS_2 show peak maximum temperature shifts to higher temperatures of 20 K and a significant change of the peak shape for PEN. The desorption trace of PFP is only slightly affected by codeposited PEN molecules. The change in the PEN trace is attributed to the mentioned attractive interactions between both molecules. Since PEN still desorbs earlier than PFP, above 500 K only PFP molecules remain on the surface, resulting in equal desorption traces for pristine and intermixed PFP. Due to changing stoichiometric ratios of PEN:PFP during desorption, a quantitative analysis of the TPD traces is not meaningful. Nevertheless, MC simulations reproduce the TPD experiments well, using the same desorption parameters and reversed intermolecular interactions. While the pristine systems exhibit high mobility like a 2D gas phase, the heterostructures form close-packed layers at monolayer coverages, which can be imaged by STM experiments. Here, PEN and PFP are arranged alternatingly in a 1:1 ratio yielding the highest attractive stabilization.

Since the attractive interaction between PEN and PFP is a result of the opposite electron density distribution and quadrupole moment, this effect should be observable even in bi- and multilayers. The heterostructures with different deposition orders are shown in Figure 4.13. In the bilayer, a distinct peak shift to higher temperatures of 20 K in comparison with the pristine multilayer coverage is observed. This is the first evidence for an attractive stabilization of the bilayer. The favorable ratio of PEN and PFP is 1:1. An excess of a certain species lies on top of the heterostructure as a pristine bi- or multilayer. This is indicated by a common leading edge of the traces of the codeposition experiment and the pristine experiment. The strong attractive interaction in the monolayer can be seen very clearly at high temperatures in all traces. Interestingly, even at high multilayer coverages a full intermixture of both molecules independent of the deposition order is found. Deposited molecules do not only diffuse in the multilayer but also replace the other species in the monolayer until a 1:1 intermixture is achieved.

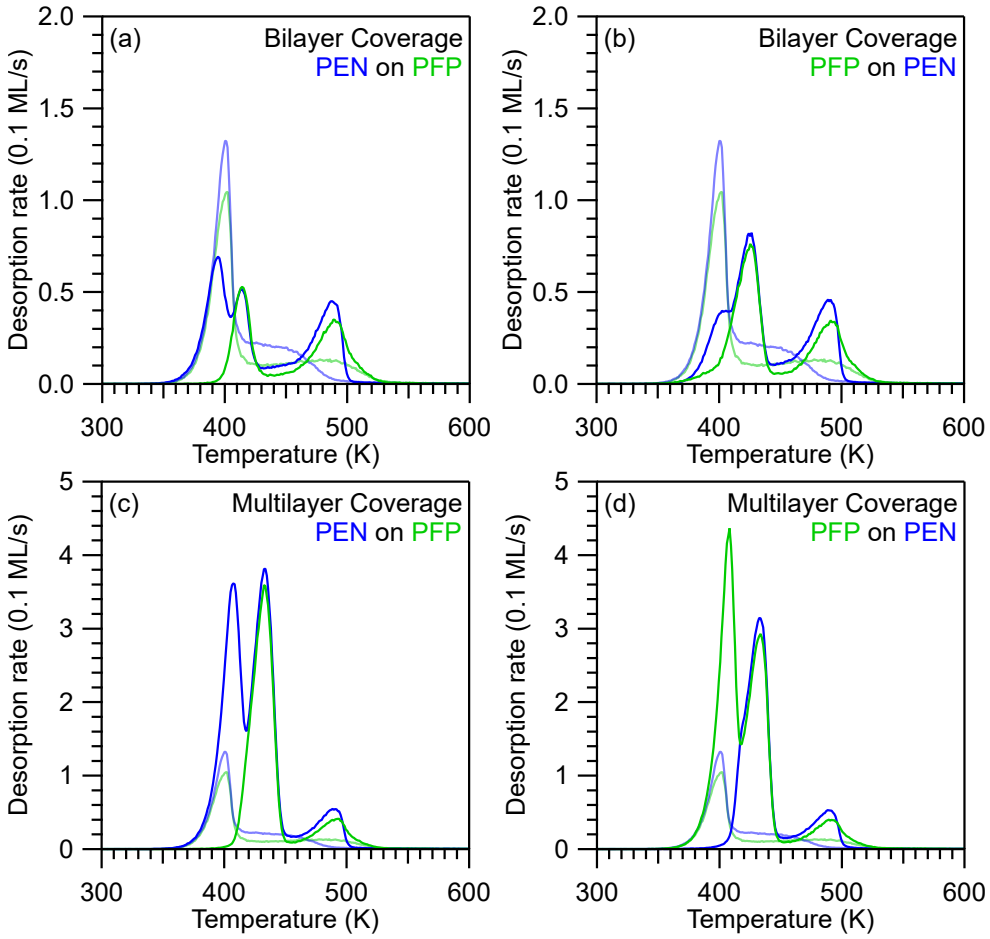

Figure 4.13: Bilayer (a,b) and multilayer (c,d) coverages of the heterostructures of PEN (blue) and PFP (green) on MoS_2. (a,c) PEN is dosed on PFP; (b,d) PFP is dosed on PEN. The pale traces are multilayer traces of the pristine molecules on MoS_2. The measurements were performed with a heating rate of 1 K/s by simultaneous mass spectrometric detection of $m/z = 278$ amu and $m/z = 530$ amu for PEN and PFP, respectively.

Similar experiments were conducted on the Au(111) single-crystal surface showing the same behavior (Figure 4.14). PEN and PFP completely intermix until a 1:1 ratio is achieved. The intermixed multilayer is again stabilized by attractive interactions and excess multilayers of a certain species desorb several kelvin earlier than the intermixed. Interestingly, the monolayer is intermixed, which means that the strong bond of one molecule to the surface is broken, the molecule is replaced by the other species and a new bond is formed. In the monolayer trace the PFP desorption ends at lower temperatures in comparison with the pristine PFP trace due to previously mentioned HF-zipping. In contrast, the PEN desorption peak shifts to slightly higher temperatures in the heterostructure maybe because of residual PFP fragments that stabilize PEN molecules.

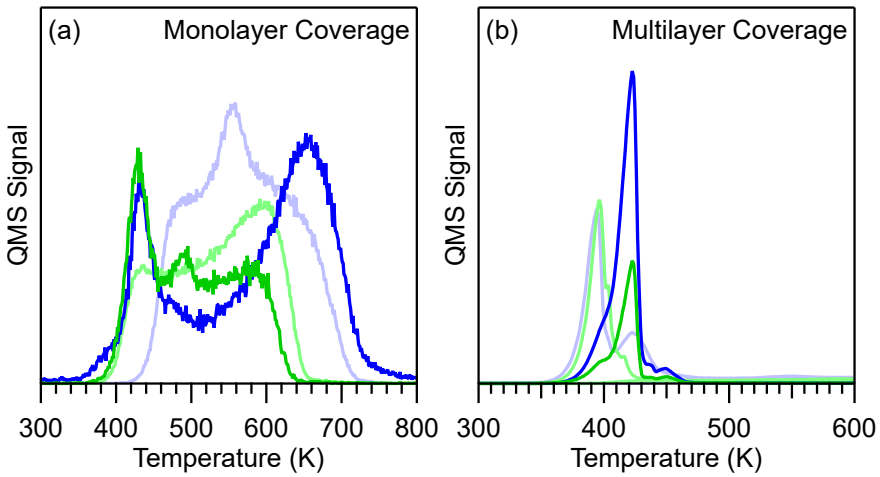

Figure 4.14: TPD traces of (a) monolayer and (b) multilayer coverages of the heterostructures of PEN (blue) and PFP (green) on Au(111). These curves are not normalized and therefore intensities cannot be directly compared. (a) PEN is dosed on PFP; (b) PFP is dosed on PEN. The pale traces are multilayer traces of the pristine molecules on Au(111). The TPD traces in (b) are scaled by a factor of 0.1 for better comparison with the pristine traces. The measurements were performed with a heating rate of 1 K/s by simultaneous mass spectrometric detection of $m/z = 278$ amu and $m/z = 530$ amu for PEN and PFP, respectively.

4.2.5 Summary

The investigations on PEN and PFP on different surfaces have shown that both molecules are entropically stabilized on both MoS_2 surfaces, whereas they are enthalpically stabilized on Au(111). The biggest difference is the stronger adsorbate–substrate interaction on metallic surfaces in contrast to inorganic vdW surfaces. The stronger interaction is represented by higher desorption temperatures (Figure 4.15). The difference between 2D and bulk MoS_2 is only minor as indicated by similar desorption behaviors on both surfaces. By heating multilayer coverages to certain temperatures, well-defined monolayers can be prepared on all surfaces. Codeposition of both molecules results in attractive intermolecular interactions in the monolayer and the multilayer on all surfaces. The attractive effect is more pronounced on MoS_2 due to the smaller repulsive interaction compared with Au(111). Preparation of well-ordered and close-packed monolayer films are possible for pristine PEN and PFP on Au(111) and for an intermixed film of PEN and PFP on MoS_2.

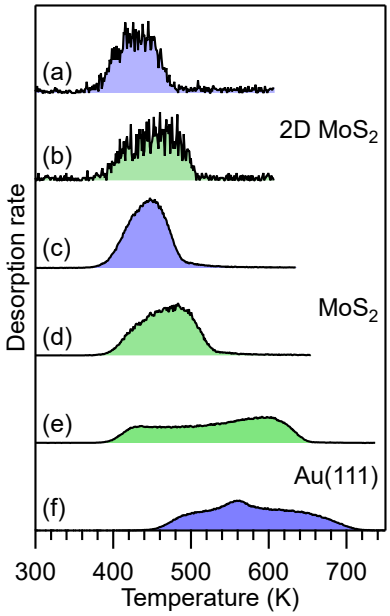

Figure 4.15: Monolayer traces of (a) PEN and (b) PFP on 2D MoS_2, (c) PEN and (d) PFP on MoS_2 as well as (e) PFP and (f) PEN on Au(111). The measurements were performed with a heating rate of 1 K/s by simultaneous mass spectrometric detection of $m/z = 278$ amu and $m/z = 530$ amu for PEN and PFP, respectively.

4.3 Metalation Reactions of Heteroatomic Organic Semiconductors

In this section, the interface between heteroatomic OSCs and metals is investigated. Upon vapor-deposition of metal atoms onto OSC bulk material, metal atoms may react with the molecules. The metal atoms diffuse into the bulk and create an interphase that extends over a certain length. At some point cluster formation exceeds diffusion processes and a metal layer is formed. Because the interphase has an impact on charge-carrier injection rates, the interphase formation of several systems was investigated and characterized in the following studies by means of hard X-ray photoelectron spectroscopy (HAXPES), temperature-programmed desorption mass spectrometry (TPD-MS) and further techniques by group members and collaboration partners. These studies include the metalation of *meso*-tetraphenylporphyrin (H_2TPP) with Co, Fe and Li as well as the reaction of α-sexithiophene (6T) with Ca atoms. The reaction depth is changed by variation of different experimental parameters. Furthermore, the transmetalation reaction of lead(II) tetraphenylporphyrin (PbTPP) with Cu atoms on Cu(111) was examined by TPD measurements as well as XPS and STM experiments performed by members of the Gottfried group.

4.3.1 Metalation of Tetraphenylporphyrin with Co and Fe Atoms

The first metalation study is the well-defined reaction of H_2TPP with Co and Fe atoms investigated by HAXPES. Different experimental parameters, such as sample temperature, metal atom flux, metal atom identity or sample roughness, were varied to change the reaction thickness. The progress of the reaction can be monitored in the N 1s XP spectra. Besides the iminic (398 eV) and the pyrrolic (400.5 eV) nitrogen peaks of pristine H_2TPP, an additional peak between them arises at 399 eV upon reaction (Figure 4.16). Because all nitrogen atoms are chemically equal when they are coordinating a metal atom inside the porphyrin macrocycle, only one peak with a new binding energy is observed. The reaction depth can be calculated from the ratio of reacted to unreacted peak intensities. It was found that only the reduction of the sample temperature during metal atom deposition from 300 K to 90 K reduced the reaction depth from 1 nm to 0.5 nm. Increasing the metal atom flux by a factor of 20, changing the substrate from rough aluminum foil to smooth Si(001) or using Fe instead of Co did not have an influence on the reaction depth. Especially the metal atom flux was considered to have an impact because a higher flux results in a higher concentration of metal atoms on the surface and favors the cluster formation. It is important to note that the spectra were recorded at room temperature, *i.e.*, the sample temperature was only reduced during metal atom deposition and heated up afterwards without increasing the reaction depth.

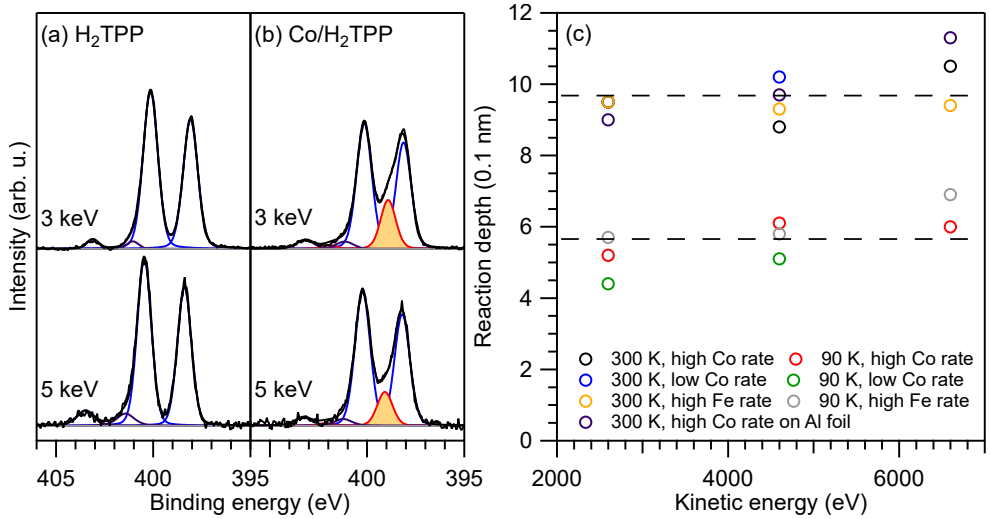

Figure 4.16: N 1s XP spectra of (a) H_2TPP and (b) Co on H_2TPP (300 K, low Co rate) recorded at photon energies of 3 keV and 5 keV. Black trace: experimental data, blue: H_2TPP, red: CoTPP plus satellite, purple: satellite of H_2TPP, grey: background. (c) Calculated reaction depths for all experiments recorded at photon energies of 3, 5 and 7 keV. The color code is given in the graph.

In addition, quantitative simulations using a genetic algorithm showed that the reaction depth can be precisely determined. The exact concentration profile, however, is not accessible. The extent of the concentration profile is far smaller than the information depth, hence HAXPES is not sensitive enough for small reaction zones. Unfortunately, high information depths are necessary to actually obtain information of the reacted species through the metal layer. Thus, analysis of the concentration profile is not possible using XPS or HAXPES.

4.3.2 Multicenter Reaction of α-Sexithiophene with Ca Atoms

This part deals with the reaction of the OSC 6T with the low-work function metal Ca. From studies of polymeric thiophene in the literature it is known that Ca reacts with the S of the thiophene units under formation of CaS.[80–82] However, it is not known what happens to the remaining organic species; cross-linking of the 6T backbone resulting in a dimer or polymer could be possible. After abstraction of the S atom, the two radical C atoms form new C–C bonds. The simplest formation mechanism is a ring closure to cyclobutadiene, which is probably too unstable. Energetically more favorable would be the reaction of C atoms from two nearby thiophene rings to form an eight-membered ring.[80] The interphase formation between the organic bulk and the metal layer was analyzed in a multi-technique approach including energy dispersive X-ray spectroscopy (EDX), atomic force microscopy (AFM), XPS, HAXPES, nano-joule adsorption calorimetry (NAC) and TPD-MS.

The Ca on 6T system was first studied by EDX showing an interphase region containing coexisting Ca and S. The Ca atoms do not fully penetrate the 6T layer but form a metallic layer on top of it before. The reaction zone stretches over 30 nm in a very diffuse manner, although it cannot be excluded that the interphase is perturbed by the preparation with a focused ion beam (FIB). AFM measurements show that the 6T layer can be prepared very smoothly, hence the strong disturbance in the EDX map does not originate from a rough organic layer during metalation. The reaction progress can easily be monitored by XP spectra of the C 1s and S 2p regions. Especially in the S 2p region a new peak appears, which is attributed to the formation of CaS. At high Ca amounts the C 1s peak starts to shift and gets broadened, which is related to side reactions of the Ca with the organic species or formation of new organic species. A detailed HAXPES study for the three S orbitals S 1s, S 2s and S 2p in a wide photon energy range reveals a large reaction depth of 8 nm at room temperature (Fig-

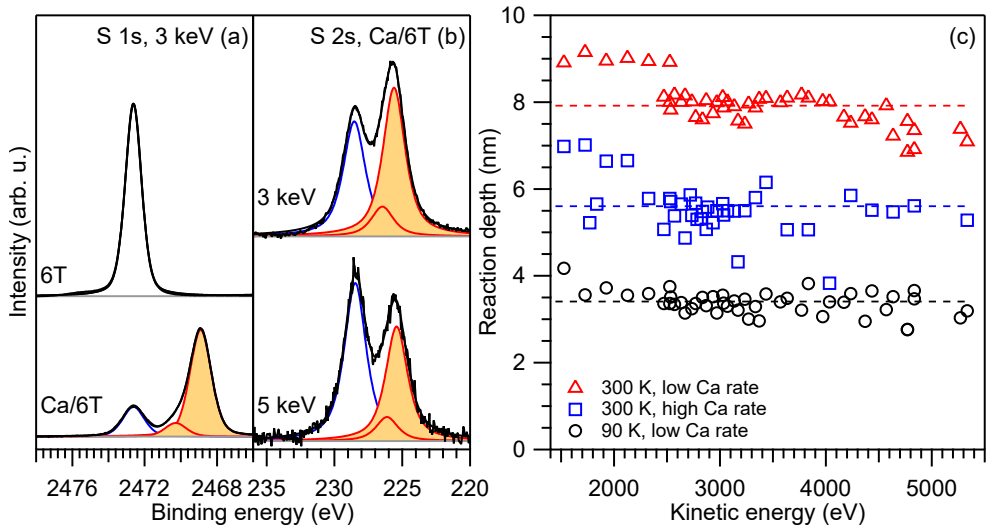

Figure 4.17: (a) S 1s XP spectra of 6T and Ca on 6T (300 K, low Ca rate) recorded at a photon energy of 3 keV. (b) S 2s XP spectra of Ca on 6T (300 K, low Ca rate) recorded at photon energies of 3 and 5 keV. Black trace: experimental data, blue: 6T, red: reacted 6T, grey: background. (c) Calculated reaction depths for all experiments recorded at several photon energies. The color code is given in the graph.

ure 4.17). Reducing the temperature during metal atom deposition decreases the reaction depth by a factor of 2. A similar result is found in the previous section. In contrast to Co on H_2TPP, an increase of the metal atom flux by a factor of 15 decreases the thickness of the interphase by 25 %. This emphasizes the importance of precise control of experimental parameters during preparation. The reaction thickness was also investigated by NAC yielding lower absolute values in comparison with HAXPES data. Nevertheless, cooling the sample reduces the thickness by a factor of 2, which is in perfect agreement with the findings obtained by HAXPES. The interpretation of the measured reaction enthalpy is difficult due to the unknown reaction products besides CaS. In order to shed light onto this issue, TPD-MS experiments were conducted for this system. Increasing the amount of deposited Ca decreases the desorbing amount of 6T until no desorption is observed for an overstoichiometric amount of Ca. No desorption products besides 6T are detected, which means that the remaining organic species polymerize or form large clusters that do not desorb. Dimerization of the 6T backbone or formation of eight-membered rings can be excluded based on these measurements. The investigations on this system reveal that Ca diffuses into and reacts several nanometers with the 6T bulk under formation of CaS. However, the nature of this reaction is still not fully solved.

4.3.3 Metalation of Tetraphenylporphyrin with Li Atoms

The third section reports the solvent free synthesis of dilithium tetraphenylporphyrin (Li_2TPP) formed by the reaction of H_2TPP with Li on surfaces in UHV. Bulk H_2TPP was prepared on Au(111) and Si(001) and metalated *in situ* by Li. Stoichiometric amounts of Li lead to a full conversion of H_2TPP into Li_2TPP up to thicknesses of 50 nm. No other products besides water contaminations are observed in TPD-MS experiments (Figure 4.18). Leading-edge analyses reveal higher desorption energies of Li_2TPP (234 kJ/mol) in comparison with pristine H_2TPP (200 kJ/mol), which is qualitatively observed by a 80 K shift to higher temperatures. HAXPES measurements using photon energies of 2 to 7 keV reveal a full conversion up to information depths of 32.7 nm at room temperature. This indicates that the diffusion of Li into the organic bulk material is highly favored in comparison with the metal cluster formation. DFT calculations of Li_2TPP in the gas phase give insight into the structures and bonding situation

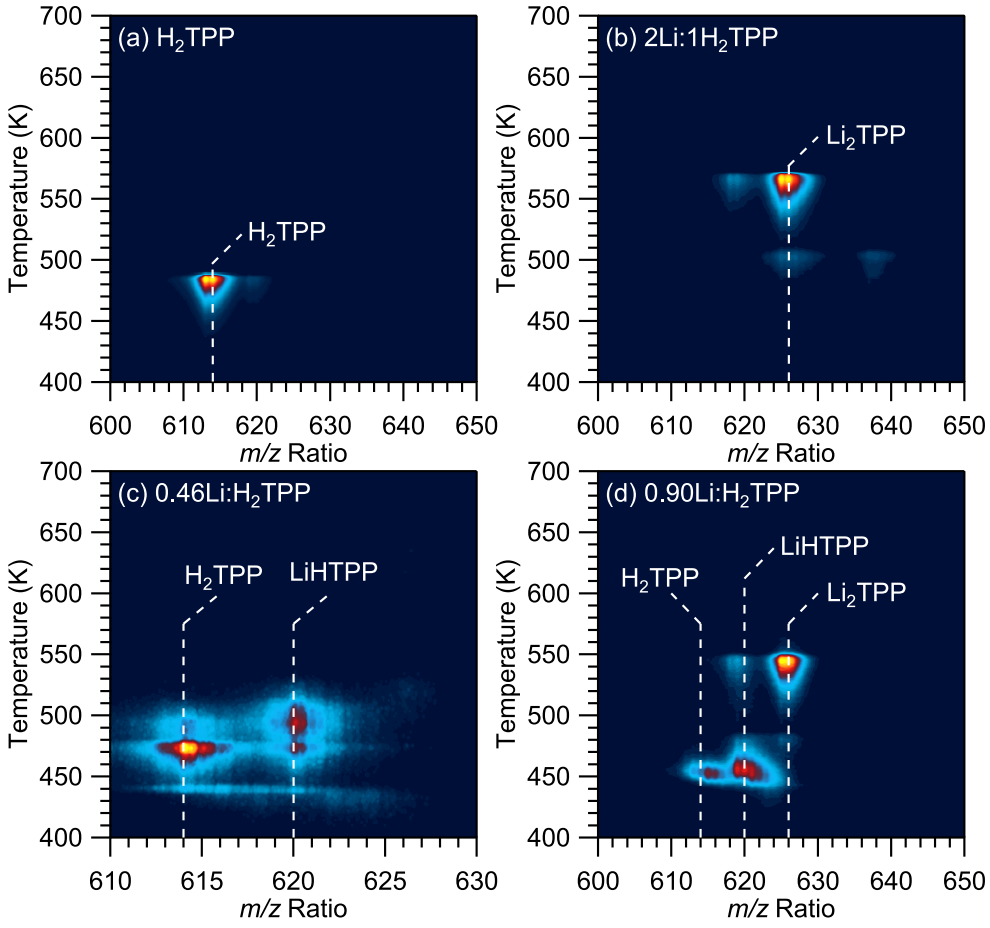

Figure 4.18: TPD-MS maps for (a) pure H_2TPP, (b) 2, (c) 0.46 and (d) 0.9 Li atoms per H_2TPP molecule on Au(111). Recorded with a mass resolution of (a,b,d) 0.5 amu in the range from 600 to 650 amu and (c) 0.1 amu in the range from 610 to 630 amu. All heating rates were 0.1 K/s and Li was dosed at room temperature.

of Li_2TPP. Both Li atoms are located above and below the molecular plane slightly off-center of the macrocycle. This coordination geometry is described by a distorted square-bipyramidal polyhedron. Using the desorption energies obtained by TPD and DFT calculations a BORN-HABER cycle is proposed for this reaction.

The metalation of H_2TPP with low amounts (20 - 45 %) of Li results in the formation of monolithium monohydrogen tetraphenylporphyrin (LiHTPP), which is detected in TPD-MS maps. This species desorbs in the same temperature range as the pristine H_2TPP. The masses 620 and 619 amu, corresponding to LiHTPP and monolithium tetraphenylporphyrin (LiTPP), respectively, are clearly distinguished in a high resolution TPD-MS experiment (Figure 4.18c). Semi-stoichiometric amounts of Li yield a mixed phase with all three species, namely H_2TPP, LiHTPP, and Li_2TPP (Figure 4.18d). Because the final product Li_2TPP desorbs at 80 K higher temperatures, fragmented sublimation was used to isolate LiHTPP. XP spectra of the N 1s and Li 1s regions prove the successful sublimation of LiHTPP, which can be fully metalated afterwards, onto another surface. DFT calculations of the structures in the gas phase give insight into the bonding situation of all intermediate species during the reaction progress. The Li ion in LiHTPP sits inside the macrocycle slightly off-center in the opposite direction of the remaining H atom. The H atom points out of the molecular plane due to steric hindrance by the Li ion.

4.3.4 Transmetalation Reaction of Pb Tetraphenylporphyrin on Cu(111)

So far, metalation reactions of organic molecules with metal atoms were investigated. In this project, the transmetalation reaction of PbTPP on the Cu(111) single-crystal surface was investigated by a variety of different techniques. The Pb ion is too large to fit in the porphyrin macrocycle, hence it is coordinated outside the molecular plane. Placing a Cu atom from the surface inside the porphyrin could be energetically favored, thus a redox reaction of Cu and Pb could be possible. Another driving force of the transmetalation could be the excess of Cu atoms on the Cu(111) surface that shifts the thermodynamic equilibrium to copper(II) tetraphenylporphyrin (CuTPP).

First evidence for the transmetalation is found in TPD measurements (Figure 4.19). Deposition of small amounts of PbTPP on a MTPP-precovered Cu(111) surface results in the desorption of CuTPP (Figure 4.19a). Since no PbTPP desorbs, the desorption of CuTPP can only be attributed to the transmetalation reaction. At higher initial coverages desorption of PbTPP is observed

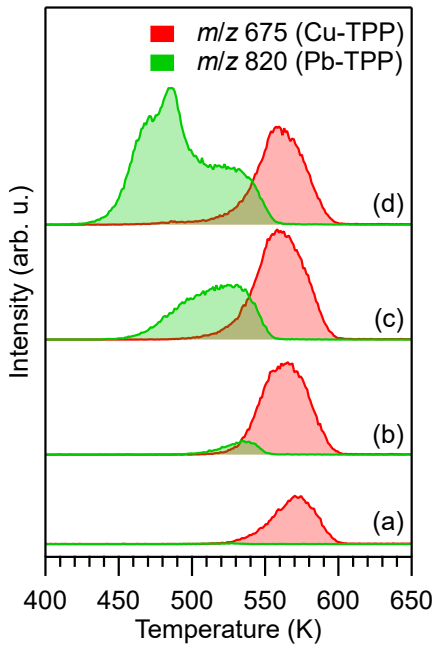

Figure 4.19: TPD traces for increasing initial coverages from (a) to (d) of PbTPP on Cu(111). PbTPP (green) was recorded at $m/z = 820$ amu and CuTPP (red) at $m/z = 675$ amu. A monolayer of PbTPP was deposited on the Cu(111) and annealed to 650 K prior to the experiments in (a) to (d). The heating was 1 K/s.

(Figure 4.19b-d). In the temperature range of multilayer desorption only PbTPP is found, which means that the transmetalation only takes place in the monolayer (Figure 4.19d). Upon annealing of a monolayer of PbTPP the Pb(II) peak in the Pb 4f XP spectrum shifts to lower binding energies. Such a shift is related to a reduction of the metal ion, thus this peak shift is attributed to the transmetalation and the formation of Pb(0). In STM images a deformation of the PbTPP molecules is observed after annealing the sample, which is an indicator for the relaxation of the porphyrin macrocycle upon transmetalation. Furthermore, small dots are visible after annealing to 550 K, which are correlated to Pb(0) atoms on the surface. Statistical analysis of these dots is in good agreement with the corresponding XPS data, adding further proof for the transmetalation reaction.

4.3.5 Summary

The reactions of heteroatomic OSCs with metal atoms were studied and the interphase thickness changed by varying different experimental parameters. The sample temperature during metal deposition influences the interphase formation most and reduces the reaction depth by a factor of two for all systems, except for Li_2TPP because there is no metal layer formation observed. Furthermore, an increased metal atom flux reduced the reaction depth in the case of highly

reactive Ca atoms. In contrast, the Co and Fe fluxes have no impact on the interphase formation. In addition, the choice of the metal species is crucial since low work-function and reactive metals increase the reaction depth and in case of Li it fully penetrates a 50 nm thick organic layer. The interphase formation seems to be independent of other experimental parameters, such as the sample roughness. The study of PbTPP on Cu(111) shows that the transmetalation of PbTPP to CuTPP is possible by annealing the sample to 550 K. This hard proof of a transmetalation is important for other studies where transmetalation reactions is suggested but not totally proven.

4.4 Investigations on the Reaction Mechanism of On-Surface Ullmann Coupling

The Ullmann coupling reaction is a frequently used method to form covalent C–C bonds in solution, but it is also applied to on-surface synthesis. Although there is much literature available on the application of the Ullmann coupling in surface chemistry, the mechanism is still not fully understood.[101,103] While Cu is mostly used in solution chemistry, Ullmann coupling reactions on surfaces are reported on Cu[203–208] as well as on Ag and Au.[209–212] The precursor molecules are halogenated arenes, for example, iodobenzene (IBz). The reaction scheme is shown in Figure 4.20. At a certain temperature, the C–X (X = Cl, Br, I) bond breaks into X and aryl radicals adsorbed on the surface. On the Cu and Ag surfaces an organometallic intermediate with C–M–C bonds is often reported,[213–216] whereas they are rarely observed on Au.[205,217] Still, the true nature of the organometallic species is not completely clarified. The molecule can either bind to the surface or to an adatom on the surface. If the molecule

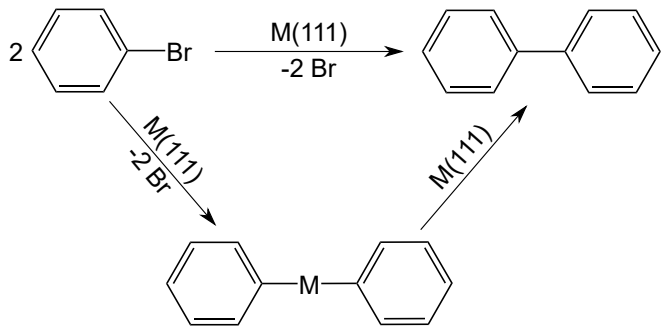

Figure 4.20: Reaction scheme of the Ullmann coupling reaction on coinage metal surfaces (M = Cu, Ag, Au). An organometallic intermediate is often observed for M = Cu, Ag. For M = Au only the direct C–C coupling is often found.

binds to the surface, it should be tilted, however, large molecules should not be able to get tilted because of the strong interaction with the surface. In this project the kinetics of the reaction was investigated using TPD. The reactions of bromobenzene (BBz) and IBz were studied on the Cu(111) surface. Since the reaction product is biphenyl (BP), the desorption of pristine BP on Cu(111) was analyzed, too. M. Cronau conducted some of the presented experiments. The reaction of IBz on Cu(111) was already studied by TPD and NEXAFS spectroscopy in literature.[218–220] Nonetheless, those TPD data were only qualitatively analyzed, hence the system is studied again in this thesis by high-quality TPD and a quantitative analysis is endeavored.

4.4.1 Biphenyl on Cu(111)

The monolayer desorption trace of BP on Cu(111) ranges from 200 to 390 K followed by desorption from defect sites up to 460 K (Figure 4.21a). The desorption temperature at low coverages is 20 K higher than for Nt on Cu(111) and indicates slightly higher desorption energies. Furthermore, the peak shape is very similar to the one of Bz on Cu(111), *i.e.*, after the peak maximum at 250 K the desorption rate decreases nearly linearly with increasing temperature until the end of desorption.

The data are quantitatively analyzed using the HRV analysis, mLEA, quadratic fitting and IPW equation. For the fitting procedure and the IPW equation a constant prefactor derived by TST (Equation (2.8)) was used ($7.8 \cdot 10^{15}$ s^{-1}). The rotational constants of Bz are used for the calculation

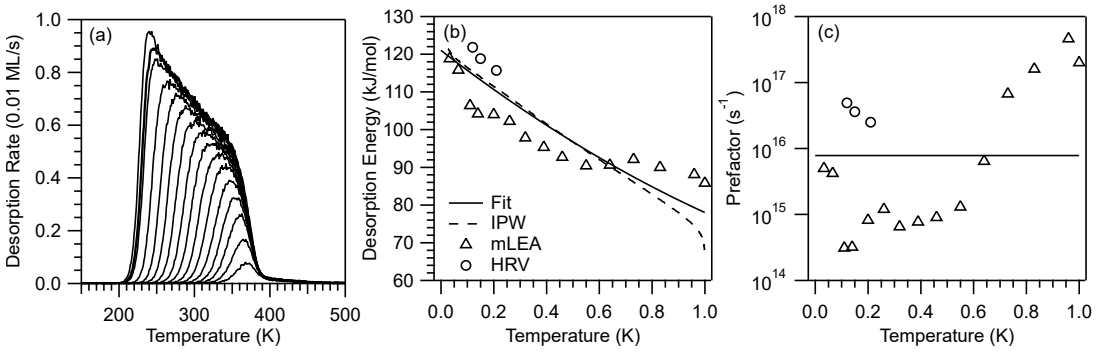

Figure 4.21: (a) Coverage series of BP on Cu(111). The initial coverages were prepared by deposition of an excess of BP and subsequent annealing of the sample to certain temperatures. The monolayer trace is indicated by a bold line. The heating rate was 1 K/s and BP was detected at $m/z = 154$ amu. (b,c) Desorption energies and prefactors, respectively, obtained by HRV analysis (circles), mLEA (triangles), quadratic fitting (solid line) and IPW equation (dashed line). The TST prefactor of $7.8 \cdot 10^{15}$ s^{-1} was used for the fitting procedure and the IPW equation.

because no data for BP are available in literature, hence the prefactor is expected to be slightly higher. The desorption energies derived by the fitting procedure and the IPW equation are in very good agreement with each other and the IPW slightly deviates only at high coverages. The zero-coverage desorption energy is 121 kJ/mol according to the quadratic fit. With respect to the TPD studies presented in the first part, a desorption energy of 10 kJ/mol per C atom indicates physisorption. The HRV analysis yields higher desorption energies than the fit and IPW equation, whereas the mLEA yields lower energies at intermediate coverages. Averaged over all methods, the desorption energy is higher than for Nt adsorbed on Cu(111). Interestingly, above 0.6 ML the desorption energies stay approximately constant in the mLEA but the prefactors increase by two orders of magnitude. A similar behavior was found for Az on Cu(111). This investigation serves as a basis for the following analyses of the Ullmann coupling reaction of BBz and IBz on Cu(111). The desorption of the reacted BP will be compared with the desorption of the as-deposited BP. The differences give insight into the reaction kinetics.

4.4.2 Bromobenzene on Cu(111)

In order to monitor the reaction, the mass-to-charge ratio of a phenyl (Ph) fragment (77 amu), Bz (78 amu), BP (154 amu) and BBz (158 amu) were recorded. It is important to note that Br has two isotopes of the masses 79 and 81 amu with 50 % natural abundance. The mass-to-charge ratio 158 amu of BBz corresponds to the heavier isotope. Nevertheless, due to fragmentation in the ionization source of the mass spectrometer discrimination between BP and BBz may be difficult. The TPD trace for an intermediate coverage is shown in Figure 4.22a. Ranging from 200 K to 270 K, a desorption peak for all masses is detected. This peak is most probably attributed to the desorption from submonolayer coverages of BBz. Since the intensity of BP is low, this trace mostly corresponds to fragmentation of BBz. An additional peak at 175 K for the Ph fragment is observed, which is related to Bz because no other masses are detected there. This Bz peak may originate from a Bz contamination in the BBz source. At 350 K a small Ph peak is followed by the desorption of BP attributed to the Ullmann coupling reaction product. Some Ph radicals may desorb as Bz after the reaction with H atoms in the residual gas of the chamber. The ratio of desorbed BP to deposited BBz is rather low, hence it is possible that only BBz molecules adsorbed on defect sites or step edges stay long enough on the surface that the C–Br bond breaks. To prove this hypothesis, BBz is deposited on a sputtered

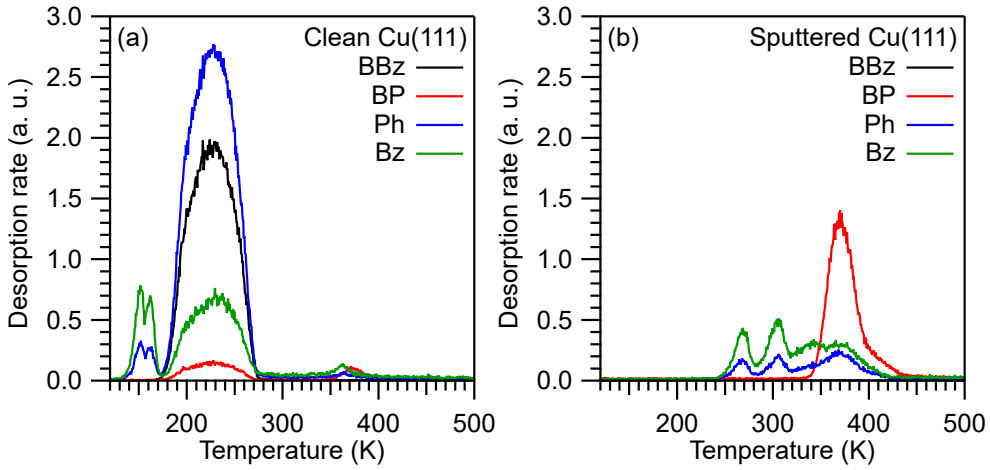

Figure 4.22: TPD experiments of BBz on (a) clean Cu(111) and (b) sputtered Cu(111). The detected mass-to-charge ratios are 77 amu (Ph), 78 amu (Bz), 154 amu (BP) and 158 amu (BBz). The heating rate in both experiments was 1 K/s.

Cu(111) surface without annealing (Figure 4.22b) because on sputtered surfaces the number of defects and step edges is by far higher than on annealed surfaces. Here, no desorption of BBz takes place, instead the main product is BP desorbing at higher temperatures than on annealed Cu(111). These TPD experiments indicate that BBz is not suitable for the investigation of the Ullmann coupling because BBz desorbs at low temperatures and the C–Br bond cannot be broken. Thus, IBz is used as a substitute because the C–I bond is weaker and breaks at lower temperatures.

4.4.3 Iodobenzene on Cu(111)

It is known from literature that the C–I bond on Cu(111) breaks at 175 K and that the adsorbed Ph radicals are thermally stable up to 300 K.[218,219] Two reaction mechanisms are proposed, one at low coverages and one at high coverages.[219] At low coverages, the C–I bond breaks and Ph radicals lie flat on the surface. Above 300 K the Ph radicals form biphenyl desorbing afterwards. When the C–I bond breaks, I atoms and Ph radicals require more space than IBz. At high coverages, the increased area occupied by Ph and I forces intact IBz molecules into an upright-standing position, lowering the intermolecular repulsion.[219] Ph radicals react with upright-standing molecules already at 270 K.

A coverage series of IBz on Cu(111) recording the biphenyl mass was conducted in this project to confirm these findings (Figure 4.23a). At 380 K a first peak α_1 evolves. This peak quickly saturates and a second peak α_2 appears at 320 K for increasing coverages. Interestingly, this peak was not observed in literature until now, since both peaks overlapped due to bad resolution and high heating

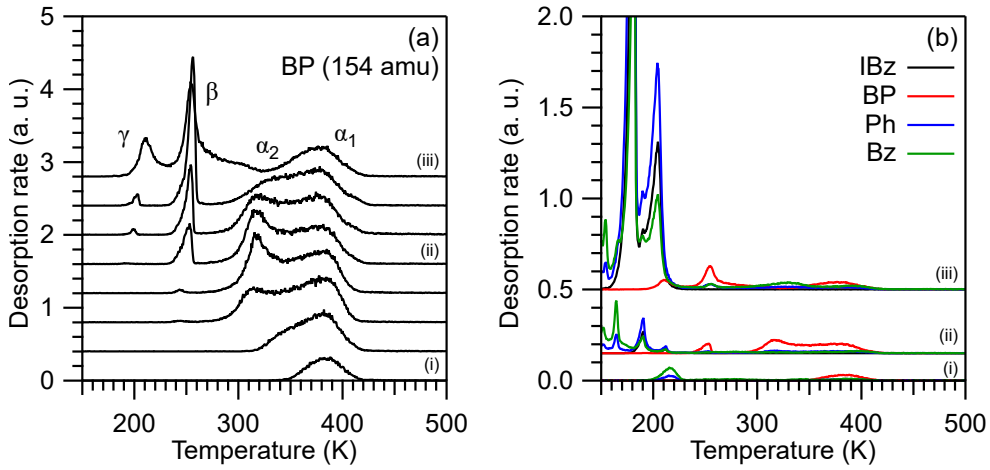

Figure 4.23: (a) Coverage series of IBz on Cu(111) for different initial coverages. The recorded mass-to-charge ratio is 154 amu (BP). The four desorption peaks of BP are labeled as α_1, α_2, β and γ. For the traces marked by (i), (ii) and (iii) all recorded mass-to-charge ratios are shown in (b). (b) TPD experiments of IBz on Cu(111) for different initial coverages. The detected mass-to-charge ratios are 77 amu (Ph), 78 amu (Bz), 154 amu (BP) and 204 amu (IBz). The heating rate in both graphs was 1 K/s.

rates.[218,219] Both peaks are attributed to the reaction of flat-lying Ph radicals to biphenyl, however, the difference in the desorption kinetics is not known and the nature of the second peak remains unclear. When the initial coverage is further increased, peak β evolves at 250 K, corresponding to the second reaction pathway. Peak β increases until it saturates at multilayer coverages. While β increases, the intensity of α_2 decreases and α_1 stays constant. It appears that α_2 is formed by a third mechanism at intermediate coverages that is inhibited at high coverages. The fourth peak γ at 200 K appears only at multilayer coverages and is most probably related to fragmentation of IBz. This peak is not observed in literature either. However, desorption from the second layer is not important for the investigation of the Ullmann coupling reaction mechanism.

In Figure 4.23b all four recorded species are displayed for the TPD experiments labeled with (i), (ii) and (iii). At a low coverage (i) only an additional Bz peak at 215 K is visible. According to Figure 4.3, this corresponds to the desorption of Bz molecules of low to intermediate coverages. Bz originates either from the IBz source as a contamination or from the reaction of Ph radicals with H atoms from the residual gas. At an intermediate coverage (ii) the Bz peak shifts to lower temperatures attributed to desorption from a close-packed monolayer at 170 K. Another peak is visible at 150 K related to the desorption from the second layer. At 190 K the monolayer desorption peak of IBz is observed. Due to intermolecular repulsion a part of the monolayer of IBz desorbs. The residual molecules decompose into I and Ph radicals. Note that the intensity ratios of

mass 77 to 78 amu is lower for the Bz desorption than for Ph and fragmented IBz. This clearly distinguishes between Ph and Bz. At the highest coverage (iii) the monolayer desorption peak of IBz saturates and the multilayer desorption is visible at 180 K. Bz molecules only desorb from multilayers. A small Bz peak appears at 330 K perhaps due to the reaction of Ph radicals with H from the residual gas.

A quantitative analysis of the three BP peaks is currently difficult but could contribute to the clarification of the mechanism. One possibility could be to perform temperature-dependent STM experiments at different coverages imaging upright-standing molecules at high coverages. In another approach, TPD experiments with co-deposited deuterated IBz-d_5 were performed. Nevertheless, such experiments were conducted by Xi and Bent, too.[219] No new insights in comparison with the studies of Xi are obtained from these measurements, thus they are not shown here.[219] The third mechanism forming peak α_2 remains unknown. Performing TPD-MS measurements on mixed IBz and deuterated IBz could answer some open questions, *e.g.*, whether the Bz stems from the reaction of Ph radicals with H of the residual gas.

4.4.4 Summary

The investigations of BP, BBz and IBz on Cu(111) showed that BP is physisorbed and desorbs intact. Since BBz is likewise physisorbed, it desorbs before the C–Br bond breaks. Therefore, IBz is more suitable than BBz for Ullmann coupling reactions on Cu(111). In the monolayer, three distinct desorption peaks of BP are observed, of which two are reported in the literature. Nevertheless, the true nature of the Ullmann coupling reaction mechanism stays unclear. In order to obtain more knowledge further experiments have to be conducted. Larger molecules, such as iodobiphenyl or iodoterphenyl, should not be able to stand upright even at high coverages. Therefore, the second reaction pathway should be inhibited and peak β should vanish. A codeposition experiment of iodobiphenyl and IBz to form bi-, ter- and quarterphenyl is conceivable, too. This might give further insight into the reaction mechanism. Furthermore, NEXAFS spectroscopy and TPD-MS experiments could provide more insight into the orientation on the surface and possible reaction products. If the mechanism is qualitatively described, a quantitative analysis of the IBz experiments might be possible.

5 Cumulative Part

The conducted experiments and the analysis of the data presented in the previous chapter led to several publications during this work. Five of them are already published, two of which I share the first authorship. Additional five publications are in preparation while writing this thesis. Out of these publication I am once the first author and share the first authorship twice. For the rest of the publications I am coauthor and contributed to them by conducting experiments or adding information.

The cumulative chapter of this thesis is divided into three sections. The first part addresses the interaction strength between organic semiconductors (OSCs) and metal as well as transition metal dichalcogenide (TMDC) surfaces. The research of this part focuses on the evaluation of enthalpic and entropic stabilization by determination of desorption energies and pre-exponential factors by means of temperature-programmed desorption (TPD). Detailed discussion of the kinetic parameters gives insight into the bonding situation of various adsorbate–substrate systems. This part is considered as the main topic of the research done in the laboratories of the Gottfried group at the Philipps-Universität Marburg.

The second part deals with metalation reactions of larger organic molecules. Most projects investigate the interphase formation upon metal deposition on *meso*-tetraphenylporphyrin (H_2TPP) and α-sexithiophene (6T) using hard X-ray photoelectron spectroscopy (HAXPES). These data were recorded at the high kinetic energy photoelectron spectroscopy (HIKE) endstation at the Bessy II facility. The reaction products were verified by temperature-programmed desorption mass spectrometry (TPD-MS). One collaboration project, which does not fit into the other parts, is presented in the third part.

The first and second part are opened by a short description of the included publications. In the following, each paper is listed and my contribution is outlined. The publications with the supporting informations are attached in the Appendix A. The permissions of use are added in Appendix B.

5.1 Characterizing the Interactions of Metal/Organic Interfaces

The following four publications investigate the bonding situation of organic aromatic compounds on metallic single-crystal surfaces as well as on MoS_2. Here, the interface was characterized by a variety of common surface science techniques. P1 and P2 compare the interfaces between azulene and naphthalene on coinage metal surfaces. I share the first authorship with Dr. B. P. Klein for P2. The same characterization was done for the larger analogs azupyrene and pyrene on Cu(111) in publication P3. The interaction of pentacene (PEN) and perfluoropentacene (PFP) with the MoS_2 surface is described in publication P4, in which I share the first authorship with P.-M. Dombrowski. The latter manuscript was submitted for publication. I contributed to these publications mainly by conducting TPD experiments and analyzing the obtained data.

P1 Molecular Topology and the Surface Chemical Bond: Alternant Versus Nonalternant Aromatic Systems as Functional Structural Elements

Citation: B. P. Klein, N. J. van der Heijden, **S. R. Kachel**, M. Franke, C. K. Krug, K. K. Greulich, L. Ruppenthal, P. Müller, P. Rosenow, S. Parhizkar, F. C. Bocquet, M. Schmid, W. Hieringer, R. J. Maurer, R. Tonner, C. Kumpf, I. Swart, J. M. Gottfried, *Physical Review X* **2019**, *9*(1), 011030, DOI 10.1103/PhysRevX.9.011030.

Own Contribution

I planned and conducted the TPD experiments in the laboratory of the Gottfried group. The data were analyzed by me, too. I was closely involved in the discussion of the TPD part of this publication and made drafts for figures and the TPD paragraph. The final version of the TPD part was completed by Dr. B. P. Klein and me in cooperation with Prof. Dr. J. M. Gottfried. Dr. B. P. Klein wrote the remaining manuscript and all co-authors contributed to its discussion.

P2

P2 Chemisorption and Physisorption at the Metal/Organic Interface: Bond Energies of Naphthalene and Azulene on Coinage Metal Surfaces

Citation: **S. R. Kachel**[‖], B. P. Klein[‖], J. M. Morbec, M. Schöniger, M. Hutter, M. Schmid, P. Kratzer, B. Meyer, R. Tonner, J. M. Gottfried, *The Journal of Physical Chemistry C* **2020**, *124*, 8257–8268, DOI 10.1021/acs.jpcc.0c00915.

Own Contribution

The publication is divided into an experimental (TPD) and a theoretical (density functional theory (DFT)) part. I planned all experiments and analyzed the data. I was supported by M. Hutter during some experiments and conducted the experiments based on previous work by M. Schöniger, although his measurements are not shown in the publication. Dr. M. Schmid helped implementing some analysis methods in *Igor Pro*. The TPD part was written by me and Prof. Dr. J. M. Gottfried. Dr. B. P. Klein did the DFT-D3 calculations under supervision of Prof. Dr. R. Tonner and merged the DFT parts. The other DFT-based calculations were performed by Dr. J. M. Morbec and Prof. Dr. P. Kratzer (vdW$^{\text{surf}}$ and MBD) and Prof. Dr. B. Meyer (D3$^{\text{surf}}$). Finalization of the manuscript was done by all authors.

[‖]These authors contributed equally to this study and share first authorship.

P3 Enhanced Interaction of the Stone-Wales Defect at the Metal-Graphene Interface

Citation: B. P. Klein, A. Ihle, **S. R. Kachel**, L. Ruppenthal, S. J. Hall, L. E. Sattler, S. M. Weber, J. Herritsch, A. Jaegermann, D. Ebeling, R. J. Maurer, G. Hilt, R. Tonner, A. Schirmeisen, J. M. Gottfried, **2020**, *in preparation*.

Own Contribution

I conducted all TPD experiments and did the quantitative analysis. Furthermore, I contributed to the discussion of the data and gave drafts for figures. Dr. B. P. Klein conducted X-ray photoelectron spectroscopy (XPS), ultraviolet photoelectron spectroscopy (UPS), and near-edge X-ray absorption fine structure (NEXAFS) spectroscopy measurements and analyzed the data. Additionally, he planned and organized the beamtimes at the high energy spherical grating monochromator (HE-SGM) endstation together with L. Ruppenthal. Further members of the experimentalists team were J. Herritsch and A. Jaegermann. Azupyrene was synthesized by L. E. Sattler, S. M. Weber and Prof. Dr. G. Hilt. The non-contact atomic force microscopy (nc-AFM) experiments and their analysis were performed by A. Ihle and D. Ebeling supervised by Prof. Dr. A. Schirmeisen at the University Giessen. DFT calculation were performed by Dr. B. P. Klein under supervision of Prof. Dr. R. Tonner. S. J. Hall and Prof. Dr. R. J. Maurer contributed the NEXAFS simulations. All authors were involved in the finalization of the manuscript.

P4 Engineering of TMDC-OSC Hybrid Interfaces: The Thermodynamics of Unitary and Mixed Acene Monolayers on MoS_2

Citation: **S. R. Kachel**[‡], P.-M. Dombrowski[‡], T. Breuer, J. M. Gottfried, G. Witte, *Chemical Science* **2020**, *submitted*.

Own Contribution

I planned the TPD experiments together with Dr. T. Breuer and P.-M. Dombrowski. Furthermore, I conducted all TPD experiments with the help of Dr. T. Breuer and P.-M. Dombrowski during some measurements. The quantitative TPD analysis was performed by me. P.-M. Dombrowski performed the scanning tunneling microscopy (STM) experiments and the Monte Carlo (MC) simulations under the supervision of Prof. Dr. G. Witte. P.-M Dombrowski was also part of the experimentalists team conducting the NEXAFS spectroscopy experiments at the HE-SGM endstation at BESSY II together with Dr. T. Breuer. I wrote the TPD part of the manuscript and contributed to the introduction of the manuscript. P.-M. Dombrowski wrote the other parts and the finalization of the manuscript involved all authors.

[‡]These authors contributed equally to this study and share first authorship.

5.2 Investigations on Metal/Organic Reactions and Their Interphase Formation

The second part of the cumulative chapter investigates the metalation reactions of *meso*-tetraphenylporphyrin (H_2TPP) with different metals (P5-P7) and the transmetalation of an already metalated porphyrin (P9). In P5 experimental parameters were varied to change the reaction depth of H_2TPP with Co and Fe. Publications P6 and P7 study the reaction of H_2TPP with different amounts of Li. In both publications I share the first authorship with M. Schöniger. P7 is still in preparation and will be submitted for publication soon. In publication P8, of which I am the first author, the reaction of α-sexithiophene (6T) with Ca atoms was examined by a multi-technique approach. The transmetalation of lead(II) tetraphenylporphyrin (PbTPP) with Cu atoms on the Cu(111) surface was explored in publication P9. I added TPD measurements to the project and the manuscript will be finished and submitted by J. Herritsch soon. To the rest of the publications except P9, I mainly contributed by planning and conducting HAXPES experiments as well as analyzing the data. In P6-P8, TPD-MS measurements were conducted to determine the reaction products.

P5 Reactive Metal-Organic Interfaces Studied with Hard X-Ray Photoelectron Spectroscopy: Controlled Formation of Metalloporphyrin Interphase Layers During Metal Vapor Deposition onto Porphyrin Films

Citation: M. Schmid, **S. R. Kachel**, B. P. Klein, N. Bock, P. Müller, R. Riedel, N. Hampp, J. M. Gottfried, *Journal of Physics: Condensed Matter* **2019**, *31*, 094002, DOI 10.1088/1361-648X/aafa2b.

Own Contribution

I organized and planned the HIKE beamtime at BESSY II, where the presented data were measured with the help of Dr. M. Schmid. During the beamtime, I was supported by Dr. M. Schmid, Dr. B. P. Klein and N. Bock. I did the processing of the HAXPES data and analyzed the reaction depths of all samples. Dr. M. Schmid performed the simulations of the concentration profile using a self-written genetic algorithm. The atomic force microscopy (AFM) measurements for checking the surface roughness were carried out by P. Müller under supervision of Dr. R. Riedel and Prof. Dr. N. Hampp. Dr. M. Schmid wrote the manuscript and I contributed to the discussion of the results and finalization of it.

P6 Direct Synthesis of Dilithium Tetraphenylporphyrin: Facile Reaction of a Free-Base Porphyrin with Vapor-Deposited Lithium

Citation: M. Schöniger[‡], **S. R. Kachel**[‡], J. Herritsch, P. Schröder, M. Hutter, J. M. Gottfried, *Chemical Communications* **2019**, *55*, 13665–13668, DOI 10.1039/C9CC07170A.

Own Contribution

I planned the TPD experiments, during which I was supported by M. Hutter and P. Schröder. The quantitative analysis and design of the figures was done by me. Furthermore, I organized the HIKE beamtime at BESSY II, where the HAXPES data were acquired, together with M. Schöniger. M. Schöniger was responsible for the HAXPES data analysis. J. Herritsch performed DFT calculations for the molecules and reactions in the gas phase. Each author wrote his corresponding part and finalization of the manuscript was done by all authors supported by Prof. Dr. J. M. Gottfried.

[‡]These authors contributed equally to this study and share first authorship.

P7 Synthesis of Partially Metalated Lithium Tetraphenylporphyrin: Characterization of LiHTPP

Citation: **S. R. Kachel**[‡], M. Schöniger[‡], J. Herritsch, P. Schröder, J. M. Gottfried, **2020**, *in preparation*.

Own Contribution

The TPD-MS experiments were planned by me and conducted by P. Schröder under my supervision. Analysis of the isotope and fragmentation pattern was done by me. M. Schöniger and J. Herritsch performed the XPS and sublimation experiments. Analysis of the XP spectra was done by M. Schöniger and DFT calculations were performed by J. Herritsch. I wrote the TPD-MS part of the manuscript, M. Schöniger the XPS part and J. Herritsch the DFT part. Finalization of the manuscript was done by all authors with the help of Prof. Dr. J. M. Gottfried.

[‡]These authors contributed equally to this study and share first authorship.

P8 Examination of the Reaction Zone in a Metal–Organic Semiconductor Interface by Multi-Technique Approach: Characterization and Control of the Ca/6T Interphase

Citation: **S. R. Kachel**, M. Schöniger, H. Zhou, H.-J. Drescher, C. K. Krug, L. Ruppenthal, B. P. Klein, M. Sachs, K. Gries, J. Hochstraßer, F. Fillsack, R. Riedel, N. Hampp, M. Schmid, J. M. Gottfried, **2020**, *in preparation*.

Own Contribution

The project was started with nano-joule adsorption calorimetry (NAC) measurements by Dr. H.-J. Drescher, who also did the analysis of these data. The energy dispersive X-ray spectroscopy (EDX) measurements were carried out by Dr. K. Gries with the help of Dr. H. Zhou. He also performed the XPS measurements in the laboratory in Marburg supported by Dr. M. Schmid, who did the in-depth analysis. M. Schöniger performed the AFM measurements with the help of Dr. R. Riedel and Prof. Dr. N. Hampp and analyzed these data. I conducted the TPD-MS experiments and analyzed the data. The HAXPES data were recorded during several HIKE beamtimes, where M. Schöniger, Dr. H. Zhou, Dr. H.-J. Drescher, Dr. C. K. Krug, L. Ruppenthal, Dr. B. P. Klein, M. Sachs, J. Hochstrasser, F. Fillsack, Dr. M. Schmid and me were involved. The final results of the data that are presented in this publication were recorded during the last beamtime, which I planned under supervision of Dr. M. Schmid. Afterwards, I analyzed the HAXPES data. Dr. M. Schmid started the first draft of the manuscript including EDX and XPS data. Afterwards, I continued writing the manuscript and added the parts of AFM, NAC, HAXPES and TPD-MS. Finalization of the manuscript was done by me under the supervision of Prof. Dr. J. M. Gottfried.

P9 Tracking of the Transmetalation Reaction of PbTPP by Cu Adatoms on Cu(111) by Multiple Techniques

Citation: J. Herritsch, **S. R. Kachel**, Q. Fan, M. Hutter, L. Heuplick, F. Münster, J. M. Gottfried, **2020**, *in preparation*.

Own Contribution

The TPD measurements were carried out by M. Hutter supervised by me. Analysis of the data as well as writing the TPD part of the manuscript was done by M. Hutter and me in close cooperation. J. Herritsch conducted the XPS measurements with the help of L. Heuplick and F. Münster. Data analysis and fitting of the XP spectra was done by J. Herritsch. Dr. Q. Fan as well as L. Heuplick performed the STM measurements. J. Herritsch did the statistical evaluation of the STM images. He also wrote most parts of the manuscript with the help of L. Heuplick. All authors contributed to the discussion of the presented data.

5.3 Other Publications

P10 Binary Lead Fluoride Pb_3F_8

Citation: H. L. Deubner†, M. Sachs†, J. Bandemehr, S. I. Ivlev, A. J. Karttunen, **S. R. Kachel**, B. P. Klein, L. Ruppenthal, M. Schöniger, C. K. Krug, J. Herritsch, J. M. Gottfried, J. N. M. Aman, J. Schmedt auf der Günne, F. Kraus, *Chemistry - A European Journal* **2019**, *25*, 15656–15661, DOI 10.1002/chem.201903954.

Summary

In this publication the synthesis and characterization of the new material Pb_3F_8 is described. Pb_3F_8 is the fluorinated analog to the red lead Pb_3O_4 with two Pb(II) and one Pb(IV) species. The crystal structure reveals two different valence states of Pb, which are attributed to [Pb(IV)F_6] octahedra and Pb(II)F_2 ladders in a 2D network.

To gain further insight into the oxidation states of the Pb species XPS and HAXPES measurements were conducted on Pb_3F_8 and reference substances. XP spectra of the valence region of Pb_3F_8 show specific peaks correlated to electron density in sterically active lone pairs. The results are in good agreement with periodic DFT calculations. Fitting of other regions like Pb 4f or Pb 4d is not possible due to strong charging effects of the non-conducting sample. The small differences in the binding energy of Pb(II) and Pb(IV) cannot be resolved in this way. To circumvent issues with charging, NEXAFS spectroscopy measurements of the Pb M_5-edge were performed, demonstrating different pre-edge features for the two species. With the help of reference samples the existence of both Pb(II) and Pb(IV) pre-edge features was proven.

P10

Own Contribution

The synthesis and analysis of the crystal structure was done by the inorganic chemistry group of Prof. Dr. F. Kraus. I started the HAXPES and NEXAFS spectroscopy measurements of this project at the HIKE endstation. Due to unsatisfying results Pb_3F_8 was investigated at more endstations including the HE-SGM and LowDosePES at BESSY II. The final results were obtained during another HIKE beamtime, which was again planned by me. Summarizing all beamtimes, Dr. B. P. Klein, L. Ruppenthal, M. Schöniger, Dr. C. K.

†These authors contributed equally to this study and share first authorship.

Krug and J. Herritsch contributed to finishing this project. Furthermore, Dr. B. P. Klein and L. Ruppenthal conducted valence band XPS measurements in the laboratory in Marburg. I wrote the XPS, HAXPES and NEXAFS spectroscopy part of the publication, while all co-authors contributed to the analysis and discussion of the data. The other parts of the manuscript were written by the first authors Dr. H. L. Deubner and M. Sachs. All authors contributed to the finalization of the publication.

P10

6 Summary

The aim of this thesis is to shed light on metal/organic interfaces. By detailed investigations, fundamental knowledge about the interactions and reactions at such interfaces was obtained. This gives rise to further improvement of modern organic electronic devices. In the presented work, not only the interface between organic semiconductor (OSC) monolayers and different substrates but also the interphase formation upon the reaction of OSC bulk phases with metal atoms was studied. The metal/organic interface was mainly examined by means of temperature-programmed desorption (TPD) yielding desorption energies and prefactors that provide insight into the interaction strength between adsorbate and substrate as well as the mobility of the adsorbate. This was further supported by many common surface science techniques like X-ray photoelectron spectroscopy (XPS), ultraviolet photoelectron spectroscopy (UPS), near-edge X-ray absorption fine structure (NEXAFS) spectroscopy, as well as density functional theory (DFT) calculations provided by group members and various external collaboration partners. The determination of the reaction thickness of the reaction of OSCs with metal atoms was realized by hard X-ray photoelectron spectroscopy (HAXPES) experiments. The reaction products of these reactions were examined by temperature-programmed desorption mass spectrometry (TPD-MS).

An easy way to modify a polycyclic aromatic hydrocarbon (PAH) in order to vary its interaction strength with substrates, is to change the conjugated π-electron system from an alternant to a non-alternant aromatic structure. The smallest practically usable model molecules for this approach are azulene (Az) and naphthalene (Nt). The latter consists of two six-membered conjugated rings (alternant), whereas the former consists of a five- and a seven-membered ring (non-alternant). Their adsorption and desorption behaviors were investigated on the Cu(111) and Ag(111) single-crystal surfaces. The non-alternant topology resulted in an increased interaction with both metal surfaces leading to higher desorption temperatures. The weakest interaction was observed for Nt on Ag(111), followed by Nt on Cu(111), Az on Ag(111) and Az on Cu(111). The TPD traces of all four systems exhibited a substantial peak broadening as

well as a peak maximum temperature shift to lower temperatures for increasing initial coverages. This effect gets more pronounced for stronger interactions between adsorbate and substrate. Vertical dipoles on the surface caused by the PAULI pushback effect induce this effect. Quantitative analysis using the heating-rate variation (HRV) analysis, the inverted POLANYI-WIGNER (IPW) equation, a fitting procedure of the TPD traces and the modified leading-edge analysis (mLEA) supported the qualitative findings. The desorption energy at zero coverage of Az on Cu(111) of 180 kJ/mol is far higher than those of the remaining systems (100-120 kJ/mol). This suggests a chemisorptive bond for Az on Cu(111) and physisorptive bonds for the other three systems. Further proof was found in the adsorption height and the electronic structure of Az and Nt on Cu(111). The adsorption height of 2.30 Å obtained by normal-incidence X-ray standing wave (NI-XSW) measurements for Az is indicative for chemisorption as it is in the range of common chemical bonds. For Nt a value of 3.04 Å points toward a physisorptive bond. NEXAFS spectroscopy and DFT-based density of states (DOS) calculations showed a net electron transfer from the surface to the former lowest unoccupied molecular orbital (LUMO) of Az, whereas no changes were observed for Nt. An interesting observation was found for Az on Cu(111) at coverages above 0.6 ML. The mLEA revealed that above 0.6 ML the desorption energy stays constant but the prefactor increases by five orders of magnitude until full monolayer coverage is reached. In the corresponding monolayer TPD trace a second peak appeared in this coverage range. This peak is related to a compressed phase, where the Az molecules are densely packed with short molecule-molecule distances resulting in prevention of translation and rotation. The reduced mobility manifests in an increased prefactor. The disordered and highly packed structure was revealed by non-contact atomic force microscopy (nc-AFM) experiments. These investigations clearly showed that changing the conjugated π-electron system from alternant to non-alternant can strongly increase the metal/organic interface interaction.

Often observed defects in the graphene lattice are 5-7 defects that are represented by Az. Furthermore, it is common that two 5-7 defects join each other to lower the tension in the graphene lattice induced by the defect. This junction is called a STONE-WALES defect and can be modeled by the non-alternant molecule azupyrene (AzPyr), while the alternant analog is pyrene (Pyr). TPD measurements of both molecules on Cu(111) revealed significantly higher desorption temperatures for AzPyr (650 K) than for Pyr (520 K). Moreover, AzPyr did not completely desorb because above 650 K the molecule decomposes as in-

dicated by a shift in the C 1s XP spectrum. Only 47 % of the AzPyr monolayer desorbed intact. Taking this into account, a desorption energy of 198 kJ/mol at half monolayer coverage was obtained for AzPyr. Even at zero coverage, the desorption energy of Pyr was lower (159 kJ/mol). XPS, UPS and NEXAFS spectroscopy measurements provided further proof for the chemisorptive bond of AzPyr on the Cu(111) surface. In contrast, Pyr is only physisorbed. These results pinpointed the interactions of 5-7 and STONE-WALES defects in the graphene lattice with the Cu(111) surface. The observations can be transferred to other comparably reactive metal surfaces.

The graphene lattice consists of fused six-membered rings, for which benzene (Bz) is the smallest molecular model system. Experimental properties of Bz on metal surfaces can be used as benchmarks for quantum mechanical methods like DFT. Reliable quantitative analyses, however, are rare in the literature, although this system was often studied. In this thesis the desorption energy and the prefactor of Bz on Cu(111) and Ag(111) were obtained from a thorough quantitative analysis of TPD data using the IPW equation, the fitting procedure of TPD traces and the mLEA. It was found that Bz adsorbs stronger on the Cu(111) surface than on Ag(111). On Cu(111) the prefactor is much lower, indicating more degrees of freedom (DOFs) than on Ag(111). This qualitatively expresses in different desorption peak shapes. The obtained desorption energies were converted into integral energies allowing a comparison with adsorption energies delivered by DFT calculations.

Besides metal/organic interfaces, organic/inorganic semiconductor interfaces were used in devices more frequently recently. However, the interaction between OSCs and inorganic semiconductors, such as hexagonal boron nitride or transition metal dichalcogenides (TMDCs), is weaker in comparison with metal substrates. Often, organic molecules do not develop a thermally stabilized monolayer on VAN DER WAALS (vdW) substrates. Their desorption behavior is similar to the desorption of multilayers. Nevertheless, in this thesis a monolayer of flat-lying molecules on MoS_2 was observed. The molecule pentacene (PEN) and its fluorinated derivative perfluoropentacene (PFP) exhibited a monolayer desorption peak at temperatures above the multilayer desorption of 390 and 400 K, respectively. Heating multilayers of PEN and PFP to these temperatures resulted in a highly reproducible preparation method of monolayers on MoS_2. Quantitative analysis of the TPD traces yielded desorption energies of 122 and 131 kJ/mol for PEN and PFP, respectively. The prefactors of both molecules were rather low with values of $5 \cdot 10^{12}$ s^{-1}. This means that both molecules

were highly mobile on the surface leading to similar partition functions in the adsorbed state as well as in the transition state. Interestingly, the sublimation enthalpy of the multilayer was higher than the desorption energy of the monolayer. This would result in a dewetting of the molecules. Because of the high mobility, the molecules were entropically stabilized instead of enthalpically as often observed on metal substrates. Similar desorption behaviors of PEN and PFP were found on two-dimensional (2D) MoS_2. Here, the desorption temperatures were slightly lower but the peak shapes were in good agreement with those on bulk MoS_2. Heating multilayers to 390 K, again resulted in the preparation of monolayers giving rise to further investigations with other methods and future applications. Depositing both molecules on the surface at the same time led to attractive interactions between PEN and PFP, since they have opposite electrostatic contours. The attractive interaction resulted in a peak maximum temperature shift to higher temperatures in the monolayer. Especially the TPD peak shape of PEN drastically changed. In the multilayer the same effect was observable. Even thick layers of several nanometers of PEN and PFP completely intermixed to achieve a 1:1 ratio with the strongest attractive interaction.

PEN and PFP were also investigated on the Au(111) surface to compare it with the MoS_2 surface. PEN desorbed intact from the surface and exhibited a compressed phase on the clean Au(111) surface. In contrast, the PFP desorption ended at lower temperatures because it decomposed on Au(111) at 650 K. Furthermore, no compressed phase was observed for PFP. The desorption temperatures were much higher than on MoS_2 indicating a stronger interaction with the surface as expected. The attractive interaction of the heterostructure in the monolayer was weaker on Au(111) than on MoS_2. On Au(111), the repulsive interaction caused by lateral dipoles reduced the attractive interaction between PEN and PFP. In the mixed monolayer experiment the desorption of PFP ended earlier than in the pristine phase. HF-zipping with PEN molecules resulted in an earlier decomposition of PFP and the formation of HF.

The second part of this thesis dealt with metalation reactions of large heteroatomic OSCs. The special interest was to explore how the thickness of the buried interphase (reaction depth) changes with the preparation parameters such as the temperature of the OSC and the flux of metal atoms. The reaction depth was determined by HAXPES measurements. The first well-defined reaction was the metalation of *meso*-tetraphenylporphyrin (H_2TPP) with Co and Fe atoms. The metal atoms were deposited at room temperature and at liquid nitrogen (LN_2) temperature (approx. 90 K) as well as with different fluxes. H_2TPP was

prepared on smooth Si(001) as well as on rough aluminum foil. It was found that only the sample temperature during metal deposition influenced the reaction depth. By cooling the sample, the reaction depth was reduced from 1 nm to 0.5 nm. No other experimental parameters had an impact, although a dependency of the reaction depth on the metal atom flux was expected.

The investigation of a more reactive system, namely the reaction of α-sexithiophene (6T) with Ca atoms, revealed a larger reaction depth of 8 nm at room temperature. Cooling of the sample to 90 K again reduced the depth by a factor of two. In addition, increasing the Ca atom flux during deposition by a factor of 15 yielded a decrease of the reaction thickness by 25 %. This was attributed to a faster closing metal layer due to a higher Ca atom concentration on the surface. In TPD-MS experiments no desorption of any reaction products, *e.g.*, an eight-membered ring or a dimer without S atoms, was observed. This leads to the conclusion that the remaining carbon species after the formation of CaS polymerized and formed big molecules that do not desorb even at high temperatures.

In a last study, vapor-deposited Li atoms completely diffused into the H_2TPP bulk, forming dilithium tetraphenylporphyrin (Li_2TPP) at stoichiometric amounts of Li. Even at overstoichiometric amounts of Li no metal layer formation was observed on top of the organic film as it is the case for Co and Fe. At photon energies of 7 keV and information depths of about 35 nm only reacted Li_2TPP was found. TPD-MS measurements showed that even a 50 nm thick H_2TPP layer was completely converted into Li_2TPP. Substoichiometric amounts of Li resulted in the formation of monolithium monohydrogen tetraphenylporphyrin (LiHTPP). At semistoichiometric amounts of Li, a mixture of H_2TPP, LiHTPP and Li_2TPP was obtained. Due to the different desorption temperatures, LiHTPP was successfully sublimated onto another single-crystal surface and isolated there.

Several transmetalation reactions of metalated porphyrins on metal surfaces in ultra-high vacuum (UHV) were reported in the literature, however, a hard proof has not been provided. Here, the transmetalation of lead(II) tetraphenylporphyrin (PbTPP) on the Cu(111) single-crystal surface was investigated by TPD. Deposition of PbTPP on a MTPP-precovered Cu(111) surface resulted in the desorption of copper(II) tetraphenylporphyrin (CuTPP). The desorption of PbTPP was observed only at higher initial coverages and in the multilayer. Nevertheless, CuTPP was not recorded in multilayer experiments, hence the transmetalation is limited to the monolayer and no intermixing with molecules

from other layers is possible. The formation of CuTPP was further supported by XPS and scanning tunneling microscopy (STM) conducted by members within the Gottfried group.

In a collaboration project, the electronic structure of Pb_3F_8 was studied by XPS, HAXPES and NEXAFS spectroscopy. Although the oxidation states of the Pb atoms could not be distinguished in HAXPES measurements due to charging of the sample, pre-edge features of Pb(II) and Pb(IV) were observed in the Pb M_5-edge in NEXAFS spectroscopy experiments. In comparison with reference samples, the pre-edge features were attributed to the oxidation states and the existence of both states was proven.

In the last project of this thesis, the mechanism of the Ullmann coupling was investigated. At first, the desorption behavior of pristine biphenyl (BP) was studied by TPD on Cu(111). The desorption behavior was similar to that of Bz but with a higher desorption energy and only a slightly higher prefactor. The desorption energy was even higher than for Nt on Cu(111), but BP is still physisorbed. Deposition of bromobenzene (BBz) did not result in an Ullmann coupling, since the C–Br bond is too strong and BBz desorbed prior to the bond cleavage. Only molecules at step edges and defects remained adsorbed on the surface until sufficient temperatures to induce the C–Br bond cleavage and form BP. The C–I bond in iodobenzene (IBz) is much weaker than the C–Br bond, hence formation and desorption of BP was observed. The TPD trace of BP for high coverages of IBz was somewhat complicated since four different BP peaks were observed. One of them was attributed to multilayers of IBz, but the three remaining peaks originated from the first layer. Although this system was studied by Xi and Bent before, they did not observe the third peak. The results of this thesis establish the basis for further investigations that will provide further insight into the Ullmann coupling mechanism.

As an addition to the experimental work that led to this thesis, various UHV parts, such as two adapter flanges, were successfully designed and constructed for the further improvement of the TPD apparatus. Furthermore, two scripts were written in the native language of *Igor Pro 8* to speed up data processing and treatment as well as importing data from TPD-MS, Auger electron spectroscopy (AES) and NEXAFS spectroscopy.

7 Bibliography

[1] *Organic Electronics II: More Materials and Applications*, (Ed.: H. Klauk), Wiley VCH Verlag GmbH, Weinheim, **2012**.

[2] *Organic Optoelectronics*, (Ed.: W. Hu), Wiley VCH Verlag GmbH, Weinheim, **2013**.

[3] C. W. Tang, S. A. VanSlyke, "Organic electroluminescent diodes", *Applied Physics Letters* **1987**, *51*(12), 913–915, DOI 10.1063/1.98799.

[4] J. H. Burroughes, D. D. C. Bradley, A. R. Brown, R. N. Marks, K. Mackay, R. H. Friend, P. L. Burns, A. B. Holmes, "Light-emitting diodes based on conjugated polymers", *Nature* **1990**, *347*(6293), 539–541, DOI 10.1038/347539a0.

[5] S. Reineke, F. Lindner, G. Schwartz, N. Seidler, K. Walzer, B. Lüssem, K. Leo, "White organic light-emitting diodes with fluorescent tube efficiency", *Nature* **2009**, *459*(7244), 234–238, DOI 10.1038/nature08003.

[6] C. W. Tang, "Two-layer organic photovoltaic cell", *Applied Physics Letters* **1986**, *48*(2), 183–185, DOI 10.1063/1.96937.

[7] M. Grätzel, "Solar cells to dye for", *Nature* **2003**, *421*(6923), 586–587, DOI 10.1038/421586a.

[8] C. Dimitrakopoulos, P. Malenfant, "Organic Thin Film Transistors for Large Area Electronics", *Advanced Materials* **2002**, *14*(2), 99–117, DOI 10.1002/1521-4095(20020116)14:2<99::aid-adma99>3.0.co;2-9.

[9] M. Małachowski, J. Żmija, "Organic field-effect transistors", *Opto-Electronics Review* **2010**, *18*(2), 121–136, DOI 10.2478/s11772-010-0008-9.

[10] S. R. Forrest, M. E. Thompson, "Introduction: Organic Electronics and Optoelectronics", *Chemical Reviews* **2007**, *107*(4), 923–925, DOI 10.1021/cr0501590.

[11] L. Bartels, "Tailoring molecular layers at metal surfaces", *Nature Chemistry* **2010**, *2*(2), 87–95, DOI 10.1038/nchem.517.

[12] N. Koch, A. Vollmer, S. Duhm, Y. Sakamoto, T. Suzuki, "The Effect of Fluorination on Pentacene/Gold Interface Energetics and Charge Reorganization Energy", *Advanced Materials* **2007**, *19*(1), 112–116, DOI 10.1002/adma.200601825.

[13] J. V. Barth, G. Costantini, K. Kern, "Engineering atomic and molecular nanostructures at surfaces", *Nature* **2005**, *437*(7059), 671–679, DOI 10.1038/nature04166.

[14] H. Kroemer, "Quasi-Electric Fields and Band Offsets: Teaching Electrons New Tricks (Nobel Lecture)", *ChemPhysChem* **2001**, *2*(8-9), 490–499, DOI 10.1002/1439-7641(20010917)2:8/9<490::aid-cphc490>3.0.co;2-1.

[15] H. Kroemer, "Nobel Lecture: Quasielectric fields and band offsets: teaching electrons new tricks", *Reviews of Modern Physics* **2001**, *73*(3), 783–793, DOI 10.1103/revmodphys.73.783.

[16] M. Knupfer, H. Peisert, *Physics of organic semiconductors*, (Ed.: W. Brütting), Wiley-VCH, Weinheim Chichester, **2005**.

[17] *The Molecule-Metal Interface*, (Eds.: N. Koch, N. Ueno, A. T. S. Wee), Wiley-VCH, Weinheim, **2013**, 272 pp.

[18] A. Kahn, N. Koch, W. Gao, "Electronic structure and electrical properties of interfaces between metals and π-conjugated molecular films", *Journal of Polymer Science Part B: Polymer Physics* **2003**, *41*(21), 2529–2548, DOI 10.1002/polb.10642.

[19] R. Otero, A. V. de Parga, J. Gallego, "Electronic, structural and chemical effects of charge-transfer at organic/inorganic interfaces", *Surface Science Reports* **2017**, *72*(3), 105–145, DOI 10.1016/j.surfrep.2017.03.001.

[20] J. C. Scott, "Metal–organic interface and charge injection in organic electronic devices", *Journal of Vacuum Science & Technology A: Vacuum Surfaces and Films* **2003**, *21*(3), 521–531, DOI 10.1116/1.1559919.

[21] A. Kumatani, Y. Li, P. Darmawan, T. Minari, K. Tsukagoshi, "On Practical Charge Injection at the Metal/Organic Semiconductor Interface", *Scientific Reports* **2013**, *3*(1), 1026, DOI 10.1038/srep01026.

[22] H. Tajima, K. Yoshida, S. Sato, T. Kadoya, J.-i. Yamada, "Estimation of the Charge Injection Barrier at a Metal/Organic Semiconductor Interface Based on Accumulated Charge Measurement: The Effect of Offset Bias Voltages", *The Journal of Physical Chemistry C* **2017**, *121*(27), 14725–14730, DOI 10.1021/acs.jpcc.7b04456.

[23] J. Anthony, "The Larger Acenes: Versatile Organic Semiconductors", *Angewandte Chemie International Edition* **2008**, *47*(3), 452–483, DOI 10.1002/anie.200604045.

[24] A. Mishra, P. Bäuerle, "Small Molecule Organic Semiconductors on the Move: Promises for Future Solar Energy Technology", *Angewandte Chemie International Edition* **2012**, *51*(9), 2020–2067, DOI 10.1002/anie.201102326.

[25] M. Fahlman, S. Fabiano, V. Gueskine, D. Simon, M. Berggren, X. Crispin, "Interfaces in organic electronics", *Nature Reviews Materials* **2019**, *4*(10), 627–650, DOI 10.1038/s41578-019-0127-y.

[26] A. Pron, P. Rannou, "Processible conjugated polymers: from organic semiconductors to organic metals and superconductors", *Progress in Polymer Science* **2002**, *27*(1), 135–190, DOI 10.1016/s0079-6700(01)00043-0.

[27] J. M. Gottfried, "Quantitative model studies for interfaces in organic electronic devices", *New Journal of Physics* **2016**, *18*(11), 111002, DOI 10.1088/1367-2630/18/11/111002.

[28] G. Witte, S. Lukas, P. S. Bagus, C. Wöll, "Vacuum level alignment at organic/metal junctions: "Cushion" effect and the interface dipole", *Applied Physics Letters* **2005**, *87*(26), 263502, DOI 10.1063/1.2151253.

[29] T. J. Rockey, M. Yang, H.-L. Dai, "Adsorption Energies, Inter-adsorbate Interactions, and the Two Binding Sites within Monolayer Benzene on Ag(111)", *The Journal of Physical Chemistry B* **2006**, *110*(40), 19973–19978, DOI 10.1021/jp062225n.

[30] W. Liu, F. Maaß, M. Willenbockel, C. Bronner, M. Schulze, S. Soubatch, F. S. Tautz, P. Tegeder, A. Tkatchenko, "Quantitative Prediction of Molecular Adsorption: Structure and Binding of Benzene on Coinage Metals", *Physical Review Letters* **2015**, *115*(3), 036104, DOI 10.1103/physrevlett.115.036104.

[31] F. Maass, Y. Jiang, W. Liu, A. Tkatchenko, P. Tegeder, "Binding energies of benzene on coinage metal surfaces: Equal stability on different metals", *The Journal of Chemical Physics* **2018**, *148*(21), 214703, DOI 10.1063/1.5030094.

[32] H. Wang, G. Dutton, X.-Y. Zhu, "Electronic Structure at Organic/Metal Interfaces: Naphthalene/Cu(111)", *The Journal of Physical Chemistry B* **2000**, *104*(44), 10332–10338, DOI 10.1021/jp002257p.

[33] T. Rockey, H.-L. Dai, "Adsorbate–substrate bonding and the growth of naphthalene thin films on Ag(111)", *Surface Science* **2007**, *601*(11), 2307–2314, DOI 10.1016/j.susc.2007.03.024.

[34] H. Ihm, H. M. Ajo, J. M. Gottfried, P. Bera, C. T. Campbell, "Calorimetric Measurement of the Heat of Adsorption of Benzene on Pt(111)", *The Journal of Physical Chemistry B* **2004**, *108*(38), 14627–14633, DOI 10.1021/jp040159o.

[35] J. M. Gottfried, E. K. Vestergaard, P. Bera, C. T. Campbell, "Heat of Adsorption of Naphthalene on Pt(111) Measured by Adsorption Calorimetry", *The Journal of Physical Chemistry B* **2006**, *110*(35), 17539–17545, DOI 10.1021/jp062659i.

[36] K. Ruedenberg, "Quantum Mechanics of Mobile Electrons in Conjugated Bond Systems. III. Topological Matrix as Generatrix of Bond Orders", *The Journal of Chemical Physics* **1961**, *34*(6), 1884–1891, DOI 10.1063/1.1731787.

[37] R. B. Mallion, D. H. Rouvray, "The golden jubilee of the Coulson-Rushbrooke pairing theorem", *Journal of Mathematical Chemistry* **1990**, *5*(1), 1–21, DOI 10.1007/bf01166272.

[38] C. A. Coulson, G. S. Rushbrooke, "Note on the method of molecular orbitals", *Mathematical Proceedings of the Cambridge Philosophical Society* **1940**, *36*(2), 193–200, DOI 10.1017/s0305004100017163.

[39] Z. Chen, Y.-M. Lin, M. J. Rooks, P. Avouris, "Graphene nano-ribbon electronics", *Physica E: Low-dimensional Systems and Nanostructures* **2007**, *40*(2), 228–232, DOI 10.1016/j.physe.2007.06.020.

[40] B. H. Nguyen, V. H. Nguyen, "Promising applications of graphene and graphene-based nanostructures", *Advances in Natural Sciences: Nanoscience and Nanotechnology* **2016**, *7*(2), 023002, DOI 10.1088/2043-6262/7/2/023002.

[41] P. Kim, "Across the border", *Nature Materials* **2010**, *9*(10), 792–793, DOI 10.1038/nmat2862.

[42] O. V. Yazyev, S. G. Louie, "Topological defects in graphene: Dislocations and grain boundaries", *Physical Review B* **2010**, *81*(19), DOI 10.1103/physrevb.81.195420.

[43] A. Stone, D. Wales, "Theoretical studies of icosahedral C60 and some related species", *Chemical Physics Letters* **1986**, *128*(5-6), 501–503, DOI 10.1016/0009-2614(86)80661-3.

[44] K. S. Novoselov, "Electric Field Effect in Atomically Thin Carbon Films", *Science* **2004**, *306*(5696), 666–669, DOI 10.1126/science.1102896.

[45] K. S. Novoselov, A. Mishchenko, A. Carvalho, A. H. Castro Neto, "2D materials and van der Waals heterostructures", *Science* **2016**, *353*(6298), aac9439, DOI 10.1126/science.aac9439.

[46] Y. L. Huang, Y. J. Zheng, Z. Song, D. Chi, A. T. S. Wee, S. Y. Quek, "The organic–2D transition metal dichalcogenide heterointerface", *Chemical Society Reviews* **2018**, *47*(9), 3241–3264, DOI 10.1039/c8cs00159f.

[47] A. K. Geim, I. V. Grigorieva, "Van der Waals heterostructures", *Nature* **2013**, *499*(7459), 419–425, DOI 10.1038/nature12385.

[48] Q. H. Wang, K. Kalantar-Zadeh, A. Kis, J. N. Coleman, M. S. Strano, "Electronics and optoelectronics of two-dimensional transition metal dichalcogenides", *Nature Nanotechnology* **2012**, *7*(11), 699–712, DOI 10.1038/nnano.2012.193.

[49] L. Britnell, R. V. Gorbachev, R. Jalil, B. D. Belle, F. Schedin, A. Mishchenko, T. Georgiou, M. I. Katsnelson, L. Eaves, S. V. Morozov, N. M. R. Peres, J. Leist, A. K. Geim, K. S. Novoselov, L. A. Ponomarenko, "Field-Effect Tunneling Transistor Based on Vertical Graphene Heterostructures", *Science* **2012**, *335*(6071), 947–950, DOI 10.1126/science.1218461.

[50] L. Britnell, R. M. Ribeiro, A. Eckmann, R. Jalil, B. D. Belle, A. Mishchenko, Y. J. Kim, R. V. Gorbachev, T. Georgiou, S. V. Morozov, A. N. Grigorenko, A. K. Geim, C. Casiraghi, A. H. Castro Neto, K. S. Novoselov, "Strong Light-Matter Interactions in Heterostructures of Atomically Thin Films", *Science* **2013**, *340*(6138), 1311–1314, DOI 10.1126/science.1235547.

[51] F. Withers, O. D. Pozo-Zamudio, S. Schwarz, S. Dufferwiel, P. M. Walker, T. Godde, A. P. Rooney, A. Gholinia, C. R. Woods, P. Blake, S. J. Haigh, K. Watanabe, T. Taniguchi, I. L. Aleiner, A. K. Geim, V. I. Fal'ko, A. I. Tartakovskii, K. S. Novoselov, "WSe_2 Light-Emitting Tunneling Transistors with Enhanced Brightness at Room Temperature", *Nano Letters* **2015**, *15*(12), 8223–8228, DOI 10.1021/acs.nanolett.5b03740.

[52] D. Jariwala, S. L. Howell, K.-S. Chen, J. Kang, V. K. Sangwan, S. A. Filippone, R. Turrisi, T. J. Marks, L. J. Lauhon, M. C. Hersam, "Hybrid, Gate-Tunable, van der Waals p–n Heterojunctions from Pentacene and MoS_2", *Nano Letters* **2015**, *16*(1), 497–503, DOI 10.1021/acs.nanolett.5b04141.

[53] J. Dong, F. Liu, F. Wang, J. Wang, M. Li, Y. Wen, L. Wang, G. Wang, J. He, C. Jiang, "Configuration-dependent anti-ambipolar van der Waals p–n heterostructures based on pentacene single crystal and MoS_2", *Nanoscale* **2017**, *9*(22), 7519–7525, DOI 10.1039/c7nr01822c.

[54] S. B. Homan, V. K. Sangwan, I. Balla, H. Bergeron, E. A. Weiss, M. C. Hersam, "Ultrafast Exciton Dissociation and Long-Lived Charge Separation in a Photovoltaic Pentacene–MoS_2 van der Waals Heterojunction", *Nano Letters* **2016**, *17*(1), 164–169, DOI 10.1021/acs.nanolett.6b03704.

[55] J.-K. Kim, K. Cho, T.-Y. Kim, J. Pak, J. Jang, Y. Song, Y. Kim, B. Y. Choi, S. Chung, W.-K. Hong, T. Lee, "Trap-mediated electronic transport properties of gate-tunable pentacene/MoS_2 p-n heterojunction diodes", *Scientific Reports* **2016**, *6*(1), 36775, DOI 10.1038/srep36775.

[56] Q. Ren, Q. Xu, H. Xia, X. Luo, F. Zhao, L. Sun, Y. Li, W. Lv, L. Du, Y. Peng, Z. Zhao, "High performance photoresponsive field-effect transistors based on MoS_2/pentacene heterojunction", *Organic Electronics* **2017**, *51*, 142–148, DOI 10.1016/j.orgel.2017.07.022.

[57] Y. Peng, R. Ding, Q. Ren, S. Xu, L. Sun, Y. Wang, F. Lu, "High performance photodiode based on MoS_2/pentacene heterojunction", *Applied Surface Science* **2018**, *459*, 179–184, DOI 10.1016/j.apsusc.2018.07.197.

[58] S.-T. Pham, Y. Kawasugi, H. Tada, "Magnetic Field Effect on Photoconductivity of Single-Crystalline Pentacene and Perfluoropentacene Field-Effect Transistors", *MRS Proceedings* **2012**, *1402*, DOI 10.1557/opl.2012.501.

[59] Y. Inoue, Y. Sakamoto, T. Suzuki, M. Kobayashi, Y. Gao, S. Tokito, "Organic Thin-Film Transistors with High Electron Mobility Based on Perfluoropentacene", *Japanese Journal of Applied Physics* **2005**, *44*(6A), 3663–3668, DOI 10.1143/jjap.44.3663.

[60] M. Roos, A. Breitruck, H. E. Hoster, R. J. Behm, "Entropic stabilization of large adsorbates on weakly binding substrates—a thermal desorption and scanning tunneling microscopy study", *Physical Chemistry Chemical Physics* **2010**, *12*(4), 818–822, DOI 10.1039/b920481d.

[61] J. Schwaben, N. Münster, M. Klues, T. Breuer, P. Hofmann, K. Harms, G. Witte, U. Koert, "Efficient Syntheses of Novel Fluoro-Substituted Pentacenes and Azapentacenes: Molecular and Solid-State Properties", *Chemistry - A European Journal* **2015**, *21*(39), 13758–13771, DOI 10.1002/chem.201501399.

[62] J. M. Gottfried, "Surface chemistry of porphyrins and phthalocyanines", *Surface Science Reports* **2015**, *70*(3), 259–379, DOI 10.1016/j.surfrep.2015.04.001.

[63] T. E. Shubina, H. Marbach, K. Flechtner, A. Kretschmann, N. Jux, F. Buchner, H.-P. Steinrück, T. Clark, J. M. Gottfried, "Principle and Mechanism of Direct Porphyrin Metalation: Joint Experimental and Theoretical Investigation", *Journal of the American Chemical Society* **2007**, *129*(30), 9476–9483, DOI 10.1021/ja072360t.

[64] M. Chen, H. Zhou, B. P. Klein, M. Zugermeier, C. K. Krug, H.-J. Drescher, M. Gorgoi, M. Schmid, J. M. Gottfried, "Formation of an interphase layer during deposition of cobalt onto tetraphenylporphyrin: a hard X-ray photoelectron spectroscopy (HAXPES) study", *Physical Chemistry Chemical Physics* **2016**, *18*(44), 30643–30651, DOI 10.1039/c6cp05894a.

[65] M. Franke, D. Wechsler, Q. Tariq, M. Röckert, L. Zhang, P. K. Thakur, N. Tsud, S. Bercha, K. Prince, T.-L. Lee, H.-P. Steinrück, O. Lytken, "Interfacial interactions between CoTPP molecules and MgO(100) thin films", *Physical Chemistry Chemical Physics* **2017**, *19*(18), 11549–11553, DOI 10.1039/c7cp00442g.

[66] M. Röckert, M. Franke, Q. Tariq, S. Ditze, M. Stark, P. Uffinger, D. Wechsler, U. Singh, J. Xiao, H. Marbach, H.-P. Steinrück, O. Lytken, "Coverage- and Temperature-Dependent Metalation and Dehydrogena-

tion of Tetraphenylporphyrin on Cu(111)", *Chemistry - A European Journal* **2014**, 8948–8953, DOI 10.1002/chem.201402420.

[67] M. Chen, X. Feng, L. Zhang, H. Ju, Q. Xu, J. Zhu, J. M. Gottfried, K. Ibrahim, H. Qian, J. Wang, "Direct Synthesis of Nickel(II) Tetraphenylporphyrin and Its Interaction with a Au(111) Surface: A Comprehensive Study", *The Journal of Physical Chemistry C* **2010**, *114*(21), 9908–9916, DOI 10.1021/jp102031m.

[68] A. Baklanov, M. Garnica, A. Robert, M.-L. Bocquet, K. Seufert, J. T. Küchle, P. T. P. Ryan, F. Haag, R. Kakavandi, F. Allegretti, W. Auwärter, "On-Surface Synthesis of Nonmetal Porphyrins", *Journal of the American Chemical Society* **2020**, *142*(4), 1871–1881, DOI 10.1021/jacs.9b10711.

[69] M. Röckert, M. Franke, Q. Tariq, D. Lungerich, N. Jux, M. Stark, A. Kaftan, S. Ditze, H. Marbach, M. Laurin, J. Libuda, H.-P. Steinrück, O. Lytken, "Insights in Reaction Mechanistics: Isotopic Exchange during the Metalation of Deuterated Tetraphenyl-21,23D-porphyrin on Cu(111)", *The Journal of Physical Chemistry C* **2014**, *118*(46), 26729–26736, DOI 10.1021/jp507303h.

[70] S. Ditze, M. Stark, M. Drost, F. Buchner, H.-P. Steinrück, H. Marbach, "Activation Energy for the Self-Metalation Reaction of 2H-Tetraphenylporphyrin on Cu(111)", *Angewandte Chemie International Edition* **2012**, *51*(43), 10898–10901, DOI 10.1002/anie.201205464.

[71] B. Cirera, B. de la Torre, D. Moreno, M. Ondracek, R. Zboril, R. Miranda, P. Jelinek, D. Ecija, "On-Surface Synthesis of Gold Porphyrin Derivatives via a Cascade of Chemical Interactions: Planarization, Self-Metalation, and Intermolecular Coupling", *Chemistry of Materials* **2019**, *31*(9), 3248–3256, DOI 10.1021/acs.chemmater.9b00125.

[72] M. Röckert, S. Ditze, M. Stark, J. Xiao, H.-P. Steinrück, H. Marbach, O. Lytken, "Abrupt Coverage-Induced Enhancement of the Self-Metalation of Tetraphenylporphyrin with Cu(111)", *The Journal of Physical Chemistry C* **2014**, *118*(3), 1661–1667, DOI 10.1021/jp412121b.

[73] J. Xiao, S. Ditze, M. Chen, F. Buchner, M. Stark, M. Drost, H.-P. Steinrück, J. M. Gottfried, H. Marbach, "Temperature-Dependent Chemical and Structural Transformations from 2H-Tetraphenylporphyrin to Copper(II)-Tetraphenylporphyrin on Cu(111)", *The Journal of Physical Chemistry C* **2012**, *116*(22), 12275–12282, DOI 10.1021/jp301757h.

[74] D. Hötger, P. Abufager, C. Morchutt, P. Alexa, D. Grumelli, J. Dreiser, S. Stepanow, P. Gambardella, H. F. Busnengo, M. Etzkorn, R. Gutzler, K. Kern, "On-surface transmetalation of metalloporphyrins", *Nanoscale* **2018**, *10*(45), 21116–21122, DOI 10.1039/c8nr04786c.

[75] M. Schmid, M. Zugermeier, J. Herritsch, B. P. Klein, C. K. Krug, L. Ruppenthal, P. Müller, M. Kothe, P. Schweyen, M. Bröring, J. M. Gottfried, "On-Surface Synthesis and Characterization of an Iron Corrole", *The Journal of Physical Chemistry C* **2018**, *122*(19), 10392–10399, DOI 10.1021/acs.jpcc.8b00067.

[76] M. Zugermeier, J. Herritsch, J.-N. Luy, M. Chen, B. P. Klein, F. Niefind, P. Schweyen, M. Bröring, M. Schmid, R. Tonner, J. M. Gottfried, "On-Surface Formation of a Transient Corrole Radical and Aromaticity-Driven Interfacial Electron Transfer", *The Journal of Physical Chemistry C* **2020**, *124*(25), 13825–13836, DOI 10.1021/acs.jpcc.0c04451.

[77] J. Herritsch, J.-N. Luy, S. Rohlf, M. Gruber, B. P. Klein, M. Kalläne, P. Schweyen, M. Bröring, K. Rossnagel, R. Tonner, J. M. Gottfried, "Influence of Ring Contraction on the Electronic Structure of Nickel Tetrapyrrole Complexes: Corrole vs Porphyrin", *ECS Journal of Solid State Science and Technology* **2020**, *9*(6), 061005, DOI 10.1149/2162-8777/ab9e18.

[78] M. M. Kruk, D. V. Klenitsky, W. Maes, "Molecular Structure and Conformation of Free Base Corroles", *Macroheterocycles* **2019**, *12*(1), 58–67, DOI 10.6060/mhc190229k.

[79] H. Lim, K. E. Thomas, B. Hedman, K. O. Hodgson, A. Ghosh, E. I. Solomon, "X-ray Absorption Spectroscopy as a Probe of Ligand Noninnocence in Metallocorroles: The Case of Copper Corroles", *Inorganic Chemistry* **2019**, *58*(10), 6722–6730, DOI 10.1021/acs.inorgchem.9b00128.

[80] J. Zhu, F. Bebensee, W. Hieringer, W. Zhao, J. H. Baricuatro, J. A. Farmer, Y. Bai, H.-P. Steinrück, J. M. Gottfried, C. T. Campbell, "Formation of the Calcium/Poly(3-Hexylthiophene) Interface: Structure and Energetics", *Journal of the American Chemical Society* **2009**, *131*(37), 13498–13507, DOI 10.1021/ja904844c.

[81] F. Bebensee, J. Zhu, J. H. Baricuatro, J. A. Farmer, Y. Bai, H.-P. Steinrück, C. T. Campbell, J. M. Gottfried, "Interface Formation between Calcium and Electron-Irradiated Poly(3-hexylthiophene)", *Langmuir* **2010**, *26*(12), 9632–9639, DOI 10.1021/la100209v.

[82] F. Bebensee, M. Schmid, H.-P. Steinrück, C. T. Campbell, J. M. Gottfried, "Toward Well-Defined Metal-Polymer Interfaces: Temperature-Controlled Suppression of Subsurface Diffusion and Reaction at the Calcium/Poly(3-Hexylthiophene) Interface", *Journal of the American Chemical Society* **2010**, *132*(35), 12163–12165, DOI 10.1021/ja104029r.

[83] L. Sang, J. E. Pemberton, "Penetration and Reaction Depths of Vapor Deposited Ag, Mg, Al, and Ca on Oligothiophene Thin Films", *Chemistry of Materials* **2019**, *31*(17), 6908–6917, DOI 10.1021/acs.chemmater.9b01313.

[84] B. Klett, C. Cocchi, L. Pithan, S. Kowarik, C. Draxl, "Polymorphism in α-sexithiophene crystals: relative stability and transition path", *Physical Chemistry Chemical Physics* **2016**, *18*(21), 14603–14609, DOI 10.1039/c6cp01405d.

[85] W. Bronsch, T. Wagner, S. Baum, M. Wansleben, K. Zielke, E. Ghanbari, M. Györök, A. Navarro-Quezada, P. Zeppenfeld, M. Weinelt, C. Gahl, "Interplay between Morphology and Electronic Structure in α-Sexithiophene Films on Au(111)", *The Journal of Physical Chemistry C* **2018**, *123*(13), 7931–7939, DOI 10.1021/acs.jpcc.8b07280.

[86] T. Wagner, E. Ghanbari, D. Huber, P. Zeppenfeld, "The growth of α-sexithiophene films on Ag(111) studied by means of PEEM with linearly polarized light", *Ultramicroscopy* **2015**, *159*, 464–469, DOI 10.1016/j.ultramic.2015.06.013.

[87] L. Sang, J. E. Pemberton, "Chemistry at the Interface of α-Sexithiophene and Vapor-Deposited Ag, Al, Mg, and Ca: A Molecular View", *The Journal of Physical Chemistry C* **2019**, *123*(31), 18877–18888, DOI 10.1021/acs.jpcc.9b06479.

[88] H.-J. Drescher, *Nanojoule Adsorption Calorimetry. Design, Construction, Novel Evaluation Approach, Software Development, Characterization, and Exemplary Measurements*, Dissertation, Philipps-Universität Marburg, **2016**, DOI 10.17192/z2016.0474.

[89] H. Zhou, *Reactive Metal-Organic Interfaces Studied with Adsorption Calorimetry and Photoelectron Spectroscopy*, Dissertation, Philipps-Universität Marburg, **2018**, DOI 10.17192/Z2018.0513.

[90] P. Gao, Z. Chen, Z. Zhao-Karger, J. E. Mueller, C. Jung, S. Klyatskaya, T. Diemant, O. Fuhr, T. Jacob, R. J. Behm, M. Ruben, M. Fichtner, "A Porphyrin Complex as a Self-Conditioned Electrode Material for High-Performance Energy Storage", *Angewandte Chemie International Edition* **2017**, *56*(35), 10341–10346, DOI 10.1002/anie.201702805.

[91] Z. Chen, P. Gao, W. Wang, S. Klyatskaya, Z. Zhao-Karger, D. Wang, C. Kübel, O. Fuhr, M. Fichtner, M. Ruben, "A Lithium-Free Energy-Storage Device Based on an Alkyne-Substituted-Porphyrin Complex", *ChemSusChem* **2019**, *12*(16), 3737–3741, DOI 10.1002/cssc.201901541.

[92] G. Horowitz, P. Delannoy, H. Bouchriha, F. Deloffre, J.-L. Fave, F. Garnier, R. Hajlaoui, M. Heyman, F. Kouki, P. Valat, V. Wintgens, A. Yassar, "Two-layer light-emitting diodes based on sexithiophene and derivatives", *Advanced Materials* **1994**, *6*(10), 752–755, DOI 10.1002/adma.19940061007.

[93] K. Ozawa, T. Kakubo, K. Shimizu, N. Amino, K. Mase, E. Ikenaga, T. Nakamura, T. Kinoshita, H. Oji, "In situ chemical state analysis of buried polymer/metal adhesive interface by hard X-ray photoelectron spectroscopy", *Applied Surface Science* **2014**, *320*, 177–182, DOI 10.1016/j.apsusc.2014.09.012.

[94] T. Strunskus, M. Kiene, R. Willecke, A. Thran, C. Bechtolsheim, F. Faupel, "Chemistry, diffusion and cluster formation at metal-polymer interfaces", *Materials and Corrosion* **1998**, *49*(3), 180–188, DOI 10.1002/(sici)1521-4176(199803)49:3<180::aid-maco180>3.0.co;2-l.

[95] T. Strunskus, V. Zaporojtchenko, K. Behnke, C. v. Bechtolsheim, F. Faupel, "Tailoring the Morphology of Metal/Polymer Interfaces", *Advanced Engineering Materials* **2000**, *2*(8), 489–492, DOI 10.1002/1527-2648(200008)2:8<489::aid-adem489>3.0.co;2-t.

[96] V. Zaporojtchenko, T. Strunskus, K. Behnke, C. Bechtolsheim, A. Thran, F. Faupel, "Formation of metal–polymer interfaces by metal evaporation: influence of deposition parameters and defects", *Microelectronic Engineering* **2000**, *50*(1-4), 465–471, DOI 10.1016/s0167-9317(99)00316-0.

[97] H. Leidheiser, P. D. Deck, "Chemistry of the Metal-Polymer Interfacial Region", *Science* **1988**, *241*(4870), 1176–1181, DOI 10.1126/science.241.4870.1176.

[98] X.-Y. Zhu, "Electronic structure and electron dynamics at molecule–metal interfaces: implications for molecule-based electronics", *Surface Science Reports* **2004**, *56*(1-2), 1–83, DOI 10.1016/j.surfrep.2004.09.002.

[99] F. Ullmann, J. Bielecki, "Ueber Synthesen in der Biphenylreihe", *Berichte der deutschen chemischen Gesellschaft* **1901**, *34*(2), 2174–2185, DOI 10.1002/cber.190103402141.

[100] F. Ullmann, "Ueber symmetrische Biphenylderivate", *Justus Liebig's Annalen der Chemie* **1904**, *332*(1-2), 38–81, DOI 10.1002/jlac.19043320104.

[101] J. Björk, F. Hanke, S. Stafström, "Mechanisms of Halogen-Based Covalent Self-Assembly on Metal Surfaces", *Journal of the American Chemical Society* **2013**, *135*(15), 5768–5775, DOI 10.1021/ja400304b.

[102] C. Bronner, J. Björk, P. Tegeder, "Tracking and Removing Br during the On-Surface Synthesis of a Graphene Nanoribbon", *The Journal of Physical Chemistry C* **2014**, *119*(1), 486–493, DOI 10.1021/jp5106218.

[103] J. Björk, "Reaction mechanisms for on-surface synthesis of covalent nanostructures", *Journal of Physics: Condensed Matter* **2016**, *28*(8), 083002, DOI 10.1088/0953-8984/28/8/083002.

[104] J. W. Niemantsverdriet, *Spectroscopy in Catalysis*, WILEY-VCH, Weinheim, **2007**, DOI 10.1002/9783527611348.

[105] K. Christmann, *Introduction to Surface Physical Chemistry*, Steinkopff, Heidelberg, **1991**, DOI 10.1007/978-3-662-08009-2.

[106] R. Browning, *Ultraviolet Photoelectron and Photoion Spectroscopy, Auger Electron Spectroscopy, Plasma Excitation in Spectrochemical Analysis*, Elsevier Scientific Pub. Co, Amsterdam, New York, **1979**.

[107] *Hard X-ray Photoelectron Spectroscopy (HAXPES)*, (Ed.: J. Woicik), Springer International Publishing Switzerland, **2016**, DOI 10.1007/978-3-319-24043-5.

[108] *Surface Science Techniques*, (Eds.: G. Bracco, B. Holst), Springer, Berlin, Heidelberg, **2013**, DOI 10.1007/978-3-642-34243-1.

[109] *Surface Analysis – The Principal Techniques*, (Eds.: J. C. Vickerman, I. S. Gilmore), John Wiley & Sons Ltd, Chichester, West Sussex, **2009**, DOI 10.1002/9780470721582.

[110] K. Oura, V. G. Lifshits, A. A. Saranin, A. V. Zotov, M. Katayama, *Surface Science*, Springer-Verlag GmbH, Berlin, Heidelberg, **2003**.

[111] K. Wille, *Physik der Teilchenbeschleuniger und Synchrotronstrahlungsquellen*, Teubner Verlag Stuttgart, **1996**, DOI 10.1007/978-3-663-11039-2.

[112] F. Hinterberger, *Physik der Teilchenbeschleuniger und Ionenoptik*, Springer, Berlin, Heidelberg, **2008**, DOI 10.1007/978-3-540-75282-0.

[113] S. Suga, A. Sekiyama, *Photoelectron Spectroscopy*, Springer, Berlin, Heidelberg, **2014**, DOI 10.1007/978-3-642-37530-9.

[114] S. Hofmann, *Auger- and X-Ray Photoelectron Spectroscopy in Materials Science*, Springer, Berlin, Heidelberg, **2013**, DOI 10.1007/978-3-642-27381-0.

[115] P. Feulner, D. Menzel, "Simple ways to improve "flash desorption" measurements from single crystal surfaces", *Journal of Vacuum Science and Technology* **1980**, *17*(2), 662–663, DOI 10.1116/1.570537.

[116] J. Gottfried, K. Schmidt, S. Schroeder, K. Christmann, "Oxygen chemisorption on Au(110)-(1×2) I. Thermal desorption measurements", *Surface Science* **2003**, *525*(1-3), 184–196, DOI 10.1016/s0039-6028(02)02560-8.

[117] F. Maass, M. Ajdari, F. C. Kabeer, M. Vogtland, A. Tkatchenko, P. Tegeder, "Nonadditivity of the Adsorption Energies of Linear Acenes on Au(111): Molecular Anisotropy and Many-Body Effects", *The Journal of Physical Chemistry Letters* **2019**, *10*(5), 1000–1004, DOI 10.1021/acs.jpclett.9b00265.

[118] M. Xi, M. X. Yang, S. K. Jo, B. E. Bent, P. Stevens, "Benzene adsorption on Cu(111): Formation of a stable bilayer", *The Journal of Chemical Physics* **1994**, *101*(10), 9122–9131, DOI 10.1063/1.468041.

[119] H.-P. Steinrück, W. Huber, T. Pache, D. Menzel, "The adsorption of benzene mono- and multilayers on Ni(111) studied by TPD and LEED", *Surface Science* **1989**, *218*(2-3), 293–316, DOI 10.1016/0039-6028(89)90154-4.

[120] G. Gonella, H.-L. Dai, T. J. Rockey, "Tetracene Monolayer and Multilayer Thin Films on Ag(111): Substrate-Adsorbate Charge-Transfer Bonding and Inter-Adsorbate Interaction", *The Journal of Physical Chemistry C* **2008**, *112*(12), 4696–4703, DOI 10.1021/jp709826q.

[121] S. Lukas, S. Vollmer, G. Witte, C. Wöll, "Adsorption of acenes on flat and vicinal Cu(111) surfaces: Step induced formation of lateral order", *The Journal of Chemical Physics* **2001**, *114*(22), 10123–10130, DOI 10.1063/1.1370936.

[122] J. Götzen, C. H. Schwalb, C. Schmidt, G. Mette, M. Marks, U. Höfer, G. Witte, "Structural Evolution of Perfluoro-Pentacene Films on Ag(111): Transition from 2D to 3D Growth", *Langmuir* **2011**, *27*(3), 993–999, DOI 10.1021/la1022664.

[123] I. Fernandez-Torrente, S. Monturet, K. J. Franke, J. Fraxedas, N. Lorente, J. I. Pascual, "Long-Range Repulsive Interaction between Molecules on a Metal Surface Induced by Charge Transfer", *Physical Review Letters* **2007**, *99*(17), 176103, DOI 10.1103/physrevlett.99.176103.

[124] G. Tomba, M. Stengel, W.-D. Schneider, A. Baldereschi, A. D. Vita, "Supramolecular Self-Assembly Driven by Electrostatic Repulsion: The 1D Aggregation of Rubrene Pentagons on Au(111)", *ACS Nano* **2010**, *4*(12), 7545–7551, DOI 10.1021/nn101884p.

[125] B. N. J. Persson, "On the nature of adsorbate phase diagrams: beyond lattice gas models", *Surface Science* **1991**, *258*(1-3), 451–463.

[126] E. M. Karp, T. L. Silbaugh, C. T. Campbell, "Energetics of Adsorbed CH3 on Pt(111) by Calorimetry", *Journal of the American Chemical Society* **2013**, *135*(13), 5208–5211, DOI 10.1021/ja400899p.

[127] H. Eyring, "The Activated Complex in Chemical Reactions", *The Journal of Chemical Physics* **1935**, *3*(2), 107–115, DOI 10.1063/1.1749604.

[128] K. A. Fichthorn, R. A. Miron, "Thermal Desorption of Large Molecules from Solid Surfaces", *Physical Review Letters* **2002**, *89*(19), 196103, DOI 10.1103/physrevlett.89.196103.

[129] R. Zacharia, H. Ulbricht, T. Hertel, "Interlayer cohesive energy of graphite from thermal desorption of polyaromatic hydrocarbons", *Physical Review B* **2004**, *69*(15), 155406, DOI 10.1103/physrevb.69.155406.

[130] H. Ulbricht, R. Zacharia, N. Cindir, T. Hertel, "Thermal desorption of gases and solvents from graphite and carbon nanotube surfaces", *Carbon* **2006**, *44*(14), 2931–2942, DOI 10.1016/j.carbon.2006.05.040.

[131] J. D. Thrower, E. E. Friis, A. L. Skov, L. Nilsson, M. Andersen, L. Ferrighi, B. Jørgensen, S. Baouche, R. Balog, B. Hammer, L. Hornekær, "Interaction between Coronene and Graphite from Temperature-Programmed Desorption and DFT-vdW Calculations: Importance of Entropic Effects and Insights into Graphite Interlayer Binding", *The Journal of Physical Chemistry C* **2013**, *117*(26), 13520–13529, DOI 10.1021/jp404240h.

[132] S. L. Tait, Z. Dohnálek, C. T. Campbell, B. D. Kay, "*n*-alkanes on MgO(100). I. Coverage-dependent desorption kinetics of *n*-butane", *The Journal of Chemical Physics* **2005**, *122*(16), 164707, DOI 10.1063/1.1883629.

[133] S. L. Tait, Z. Dohnálek, C. T. Campbell, B. D. Kay, "*n*-alkanes on MgO(100). II. Chain length dependence of kinetic desorption parameters for small *n*-alkanes", *The Journal of Chemical Physics* **2005**, *122*(16), 164708, DOI 10.1063/1.1883630.

[134] B. Scherwitzl, R. Resel, A. Winkler, "Film growth, adsorption and desorption kinetics of indigo on SiO_2", *The Journal of Chemical Physics* **2014**, *140*(18), 184705, DOI 10.1063/1.4875096.

[135] B. Scherwitzl, R. Lassnig, M. Truger, R. Resel, G. Leising, A. Winkler, "Adsorption, desorption, and film formation of quinacridone and its thermal cracking product indigo on clean and carbon-covered silicon dioxide surfaces", *The Journal of Chemical Physics* **2016**, *145*(9), 094702, DOI 10.1063/1.4961738.

[136] T. L. Hill, *Statistical Thermodynamics*, Addison-Wesley Publishing Company, Inc., Reading, MA, **1960**, DOI 10.1002/aic.690090133.

[137] C. T. Campbell, J. R. V. Sellers, "The Entropies of Adsorbed Molecules", *Journal of the American Chemical Society* **2012**, *134*(43), 18109–18115, DOI 10.1021/ja3080117.

[138] D. A. McQuarrie, *Statistical Mechanics*, University Science Books, Sausalito, CA, **2000**.

[139] V. Oja, E. M. Suuberg, "Vapor Pressures and Enthalpies of Sublimation of Polycyclic Aromatic Hydrocarbons and Their Derivatives", *Journal of Chemical & Engineering Data* **1998**, *43*(3), 486–492, DOI 10.1021/je9702221.

[140] D. Käfer, C. Wöll, G. Witte, "Thermally activated dewetting of organic thin films: the case of pentacene on SiO_2 and gold", *Applied Physics A* **2008**, *95*(1), 273–284, DOI 10.1007/s00339-008-5011-3.

[141] C. Antoine, "Des Vapeurs: Nouvelle Relation Entre Les Tensions Et Les Temperatures", *Comptes Rendus des Séances de l'Académie des Sciences. Paris.* **1888**, 681–684, 778–780, 836–837.

[142] P. Redhead, "Thermal desorption of gases", *Vacuum* **1962**, *12*(4), 203–211, DOI 10.1016/0042-207x(62)90978-8.

[143] J. Falconer, R. Madix, "Flash desorption activation energies: DCOOH decomposition and CO desorption from Ni(110)", *Surface Science* **1975**, *48*(2), 393–405, DOI 10.1016/0039-6028(75)90414-8.

[144] A. de Jong, J. Niemantsverdriet, "Thermal desorption analysis: Comparative test of ten commonly applied procedures", *Surface Science* **1990**, *233*(3), 355–365, DOI 10.1016/0039-6028(90)90649-s.

[145] E. Habenschaden, J. Küppers, "Evaluation of flash desorption spectra", *Surface Science* **1984**, *138*(1), L147–L150, DOI 10.1016/0039-6028(84)90488-6.

[146] D. H. Parker, M. E. Jones, B. E. Koel, "Determination of the reaction order and activation energy for desorption kinetics using TPD spectra: Application to D_2 desorption from Ag(111)", *Surface Science* **1990**, *233*(1-2), 65–73, DOI 10.1016/0039-6028(90)90176-9.

[147] D. Nieskens, A. van Bavel, J. Niemantsverdriet, "The analysis of temperature programmed desorption experiments of systems with lateral interactions; implications of the compensation effect", *Surface Science* **2003**, *546*(2-3), 159–169, DOI 10.1016/j.susc.2003.09.035.

[148] D. A. King, "Thermal desorption from metal surfaces: A review", *Surface Science* **1975**, *47*(1), 384–402, DOI 10.1016/0039-6028(75)90302-7.

[149] E. Bauer, F. Bonczek, H. Poppa, G. Todd, "Thermal desorption of metals from tungsten single crystal surfaces", *Surface Science* **1975**, *53*(1), 87–109, DOI 10.1016/0039-6028(75)90118-1.

[150] J. Niemantsverdriet, K. Markert, K. Wandelt, "The compensation effect and the manifestation of lateral interactions in thermal desorption spectroscopy", *Applied Surface Science* **1988**, *31*(2), 211–219, DOI 10.1016/0169-4332(88)90062-1.

[151] J. T. Stuckless, D. E. Starr, D. J. Bald, C. T. Campbell, "Calorimetric measurements of the energetics of Pb adsorption and adhesion to Mo(100)", *Physical Review B* **1997**, *56*(20), 13496–13502, DOI 10.1103/physrevb.56.13496.

[152] J. Zhu, S. Diaz, L. Heeb, C. T. Campbell, "Adsorption of Pb on NiAl(110): energetics and structure", *Surface Science* **2005**, *574*(1), 34–42, DOI 10.1016/j.susc.2004.10.014.

[153] C.-M. Chan, R. Aris, W. Weinberg, "An analysis of thermal desorption mass spectra. I.", *Applications of Surface Science* **1978**, *1*(3), 360–376, DOI 10.1016/0378-5963(78)90038-7.

[154] C. Pirola, A. D. Michele, "Nonlinear desorption activation energy from TPD curves: Analysis of the influence of initial values for the regression procedure", *The Canadian Journal of Chemical Engineering* **2020**, *98*(5), 1115–1123, DOI 10.1002/cjce.23700.

[155] J. Xu, J. Deng, "Theoretical Parameter-Free Analysis Model for Temperature-Programmed Desorption (TPD) Spectra", *ACS Omega* **2020**, *5*(8), 4148–4157, DOI 10.1021/acsomega.9b03867.

[156] H. Mühlenbein, D. Schlierkamp-Voosen, "Predictive Models for the Breeder Genetic Algorithm I. Continuous Parameter Optimization", *Evolutionary Computation* **1993**, *1*(1), 25–49, DOI 10.1162/evco.1993.1.1.25.

[157] M. C. South, G. B. Wetherill, M. T. Tham, "Hitch-hiker's guide to genetic algorithms", *Journal of Applied Statistics* **1993**, *20*(1), 153–175, DOI 10.1080/02664769300000013.

[158] D. Whitley, "A genetic algorithm tutorial", *Statistics and Computing* **1994**, *4*(2), 65–85, DOI 10.1007/bf00175354.

[159] M. Schmid, *Programming in Igor Pro: A Comprehensive Introduction*, CreateSpace, Middletown, DE, **2018**.

[160] J. Jordan, *Neural networks: training with backpropagation*, https://www.jeremyjordan.me/neural-networks-training/, last visited 28.08.2020, **2017**.

[161] H. Li, Z. Xu, G. Taylor, C. Studer, T. Goldstein, "Visualizing the Loss Landscape of Neural Nets", **2017**, arXiv: 1712.09913v3 [cs.LG].

[162] J. Weippert, S. Ulas, D. Strelnikov, A. Böttcher, M. M. Kappes, "Formation of Sublimable Nanographene Oxides by Reacting Coronene Films with Atomic Oxygen", *The Journal of Physical Chemistry C* **2018**, *122*(50), 28588–28600, DOI 10.1021/acs.jpcc.8b01655.

[163] J. Weippert, V. Gewiese, A. Böttcher, M. M. Kappes, "Graphite-Mediated Oxidation of Coronene Adsorbates: A UHV Study", *The Journal of Physical Chemistry C* **2018**, *122*(50), 28601–28612, DOI 10.1021/acs.jpcc.8b08637.

[164] J. Weippert, L. Hohmann, D. Strelnikov, P. Weis, M. L. Pop, A. Böttcher, M. M. Kappes, "Desorption of Fullerene Dimers upon Heating Non-IPR Fullerene Films on HOPG", *The Journal of Physical Chemistry C* **2019**, *123*(9), 5721–5730, DOI 10.1021/acs.jpcc.8b12113.

[165] J. Weippert, J. Hauns, J. Bachmann, J.-F. Greisch, A. Narita, K. Müllen, A. Böttcher, M. M. Kappes, "Oligomerization of Dehydrogenated Polycyclic Aromatic Hydrocarbons on Highly Oriented Pyrolytic Graphite", *The Journal of Physical Chemistry C* **2020**, *124*(15), 8236–8246, DOI 10.1021/acs.jpcc.0c00883.

[166] H. Hertz, "Ueber einen Einfluss des ultravioletten Lichtes auf die electrische Entladung", *Annalen der Physik und Chemie* **1887**, *267*(8), 983–1000, DOI 10.1002/andp.18872670827.

[167] A. Einstein, "Über einen die Erzeugung und Verwandlung des Lichtes betreffenden heuristischen Gesichtspunkt", *Annalen der Physik* **1905**, *322*(6), 132–148, DOI 10.1002/andp.19053220607.

[168] T. Koopmans, "Über die Zuordnung von Wellenfunktionen und Eigenwerten zu den Einzelnen Elektronen Eines Atoms", *Physica* **1934**, *1*(1-6), 104–113, DOI 10.1016/s0031-8914(34)90011-2.

[169] C. K. Krug, *Structure and Reactivity of Aromatic Molecules on Metal Single-Crystal Surfaces and at Metal/Organic Interfaces*, Dissertation, Philipps-Universität Marburg, **2020**, DOI 10.17192/z2020.0486.

[170] K. M. G. Siegbahn, "A Discussion on photoelectron spectroscopy - Electron spectroscopy for chemical analysis (e.s.c.a.)", *Philosophical Transactions of the Royal Society of London. Series A Mathematical and Physical Sciences* **1970**, *268*(1184), 33–57, DOI 10.1098/rsta.1970.0060.

[171] ISO 18115-1, Chemical Analysis-Vocabulary-Part 1. General terms and terms used in spectroscopy, International Organization for Standardization, **2010**.

[172] C. J. Powell, S. Tanuma in *Springer Series in Surface Sciences*, Springer International Publishing Switzerland, **2015**, pp. 111–140, DOI 10.1007/978-3-319-24043-5_5.

[173] D. R. Penn, "Electron mean-free-path calculations using a model dielectric function", *Physical Review B* **1987**, *35*(2), 482–486, DOI 10.1103/physrevb.35.482.

[174] S. Tanuma, C. J. Powell, D. R. Penn, "Calculations of electron inelastic mean free paths. IX. Data for 41 elemental solids over the 50 eV to 30 keV range", *Surface and Interface Analysis* **2011**, *43*(3), 689–713, DOI 10.1002/sia.3522.

[175] S. Tanuma, C. J. Powell, D. R. Penn, "Calculations of electron inelastic mean free paths for 31 materials", *Surface and Interface Analysis* **1988**, *11*(11), 577–589, DOI 10.1002/sia.740111107.

[176] S. Tanuma, C. J. Powell, D. R. Penn, "Calculations of electron inelastic mean free paths. II. Data for 27 elements over the 50-2000 eV range", *Surface and Interface Analysis* **1991**, *17*(13), 911–926, DOI 10.1002/sia.740171304.

[177] C. J. Powell, A. Jablonski, "Evaluation of Calculated and Measured Electron Inelastic Mean Free Paths Near Solid Surfaces", *Journal of Physical and Chemical Reference Data* **1999**, *28*(1), 19–62, DOI 10.1063/1.556035.

[178] H. Bethe, "Zur Theorie des Durchgangs schneller Korpuskularstrahlen durch Materie", *Annalen der Physik* **1930**, *397*(3), 325–400, DOI 10.1002/andp.19303970303.

[179] A. Jablonski, C. J. Powell, "Practical expressions for the mean escape depth, the information depth, and the effective attenuation length in Auger-electron spectroscopy and x-ray photoelectron spectroscopy", *Journal of Vacuum Science & Technology A: Vacuum Surfaces and Films* **2009**, *27*(2), 253–261, DOI 10.1116/1.3071947.

[180] P. Auger, "Sur l'effet photoélectrique composé", *Journal de Physique et le Radium* **1925**, *6*(6), 205–208, DOI 10.1051/jphysrad:0192500606020500.

[181] P. Auger, "L'effet photoélectrique composé", *Annales de Physique* **1926**, *10*(6), 183–253, DOI 10.1051/anphys/192610060183.

[182] P. Auger, "The Auger effect", *Surface Science* **1975**, *48*(1), 1–8, DOI 10.1016/0039-6028(75)90306-4.

[183] L. Meitner, "Über die β-Strahl-Spektra und ihren Zusammenhang mit der γ-Strahlung", *Zeitschrift für Physik* **1922**, *11*(1), 35–54, DOI 10.1007/bf01328399.

[184] O. H. Duparc, "Pierre Auger – Lise Meitner: Comparative contributions to the Auger effect", *International Journal of Materials Research* **2009**, *100*(9), 1162–1166, DOI 10.3139/146.110163.

[185] M. O. Krause, "Atomic radiative and radiationless yields for K and L shells", *Journal of Physical and Chemical Reference Data* **1979**, *8*(2), 307–327, DOI 10.1063/1.555594.

[186] Deutsche Edelstahlwerke, *Werkstoffdatenblatt: X2CrNiMo17-12-2, 1.4404*, **2016**.

[187] B. P. Klein, *Untersuchungen zur Adsorption von Azulen und Naphthalin auf Cu(111) und Ag(111)*, Master's Thesis, Philipps-Universität Marburg, **2016**.

[188] S. R. Kachel, *Temperature-Programmed Desorption of Azulene and Naphthalene on Cu(111)*, Master's Thesis. Philipps-Universität Marburg, **2017**.

[189] M. Schöniger, *Investigations of Naphthalene and Azulene on Ag(111) and Cu(111) with Temperature-Programmed Desorption*, Master's Thesis, Philipps-Universität Marburg, **2016**.

[190] F. Schaefers, M. Mertin, M. Gorgoi, "KMC-1: A high resolution and high flux soft x-ray beamline at BESSY", *Review of Scientific Instruments* **2007**, *78*(12), 123102, DOI 10.1063/1.2808334.

[191] M. Gorgoi, S. Svensson, F. Schäfers, G. Öhrwall, M. Mertin, P. Bressler, O. Karis, H. Siegbahn, A. Sandell, H. Rensmo, W. Doherty, C. Jung, W. Braun, W. Eberhardt, "The high kinetic energy photoelectron spectroscopy facility at BESSY progress and first results", *Nuclear Instruments and Methods in Physics Research Section A: Accelerators Spectrometers Detectors and Associated Equipment* **2009**, *601*(1-2), 48–53, DOI 10.1016/j.nima.2008.12.244.

[192] M. Surman, I. Cragg-Hine, J. Singh, B. J. Bowler, H. A. Padmore, D. Norman, A. L. Johnson, W. K. Walter, D. A. King, R. Davis, K. G. Purcell, G. Thornton, "A high-energy spherical grating monochromator for soft x rays at the Daresbury SRS", *Review of Scientific Instruments* **1992**, *63*(10), 4349–4353, DOI 10.1063/1.1143735.

[193] M. Hutter, *Reactions of Tetraphenylporphyrin with Lithium and Lead on Coinage Metal Surfaces*, Master's Thesis, Philipps-Universität Marburg, **2019**.

[194] Scienta Omicron GmbH, *LEED 450 - Compact LEED to fit any UHV System*, https://scientaomicron.com/en/Components/LEED-RHEED/MiniLEED-450, last visited 07.09.2020, **2020**.

[195] B. P. Klein, J. M. Morbec, M. Franke, K. K. Greulich, M. Sachs, S. Parhizkar, F. C. Bocquet, M. Schmid, S. J. Hall, R. J. Maurer, B. Meyer, R. Tonner, C. Kumpf, P. Kratzer, J. M. Gottfried, "Molecule–Metal Bond of Alternant versus Nonalternant Aromatic Systems on Coinage Metal Surfaces: Naphthalene versus Azulene on Ag(111) and Cu(111)", *The Journal of Physical Chemistry C* **2019**, *123*(48), 29219–29230, DOI 10.1021/acs.jpcc.9b08824.

[196] G. Herzberg, *Electronic spectra and electronic structure of polyatomic molecules (Molecular spectra and molecular structure Volume III)*, National Research Council of Canada, D. Van Nostrand Co., Inc., Princeton, New Jersey, **1966**.

[197] S. R. Kachel, B. P. Klein, J. M. Morbec, M. Schöniger, M. Hutter, M. Schmid, P. Kratzer, B. Meyer, R. Tonner, J. M. Gottfried, "Chemisorption and Physisorption at the Metal/Organic Interface: Bond Energies of Naphthalene and Azulene on Coinage Metal Surfaces", *The Journal of Physical Chemistry C* **2020**, *124*(15), 8257–8268, DOI 10.1021/acs.jpcc.0c00915.

[198] T. Breuer, M. Klues, G. Witte, "Characterization of orientational order in π-conjugated molecular thin films by NEXAFS", *Journal of Electron Spectroscopy and Related Phenomena* **2015**, *204*, 102–115, DOI 10.1016/j.elspec.2015.07.011.

[199] A.-K. Steiner, K. Y. Amsharov, "The Rolling-Up of Oligophenylenes to Nanographenes by a HF-Zipping Approach", *Angewandte Chemie International Edition* **2017**, *56*(46), 14732–14736, DOI 10.1002/anie.201707272.

[200] M. Kolmer, R. Zuzak, A. K. Steiner, L. Zajac, M. Engelund, S. Godlewski, M. Szymonski, K. Amsharov, "Fluorine-programmed nanozipping to tailored nanographenes on rutile TiO_2 surfaces", *Science* **2019**, *363*(6422), 57–60, DOI 10.1126/science.aav4954.

[201] M. Kolmer, A.-K. Steiner, I. Izydorczyk, W. Ko, M. Engelund, M. Szymonski, A.-P. Li, K. Amsharov, "Rational synthesis of atomically precise graphene nanoribbons directly on metal oxide surfaces", *Science* **2020**, *369*(6503), 571–575, DOI 10.1126/science.abb8880.

[202] T. Breuer, G. Witte, "Thermally activated intermixture in pentacene-perfluoropentacene heterostructures", *The Journal of Chemical Physics* **2013**, *138*(11), 114901, DOI 10.1063/1.4795004.

[203] E. A. Lewis, M. D. Marcinkowski, C. J. Murphy, M. L. Liriano, A. J. Therrien, A. Pronschinske, E. C. H. Sykes, "Controlling selectivity in the Ullmann reaction on Cu(111)", *Chemical Communications* **2017**, *53*(55), 7816–7819, DOI 10.1039/c7cc02901b.

[204] W. Wang, X. Shi, S. Wang, M. A. V. Hove, N. Lin, "Single-Molecule Resolution of an Organometallic Intermediate in a Surface-Supported Ullmann Coupling Reaction", *Journal of the American Chemical Society* **2011**, *133*(34), 13264–13267, DOI 10.1021/ja204956b.

[205] T. A. Pham, F. Song, M.-T. Nguyen, Z. Li, F. Studener, M. Stöhr, "Comparing Ullmann Coupling on Noble Metal Surfaces: On-Surface Polymerization of 1,3,6,8-Tetrabromopyrene on Cu(111) and Au(111)", *Chemistry - A European Journal* **2016**, *22*(17), 5937–5944, DOI 10.1002/chem.201504946.

[206] M.-T. Nguyen, C. A. Pignedoli, D. Passerone, "An ab initio insight into the Cu(111)-mediated Ullmann reaction", *Physical Chemistry Chemical Physics* **2011**, *13*(1), 154–160, DOI 10.1039/c0cp00759e.

[207] A. Rastgoo-Lahrood, J. Björk, W. M. Heckl, M. Lackinger, "1,3-Diiodobenzene on Cu(111) – an exceptional case of on-surface Ullmann coupling", *Chemical Communications* **2015**, *51*(68), 13301–13304, DOI 10.1039/c5cc04453g.

[208] S. Zint, D. Ebeling, T. Schlöder, S. Ahles, D. Mollenhauer, H. A. Wegner, A. Schirmeisen, "Imaging Successive Intermediate States of the On-Surface Ullmann Reaction on Cu(111): Role of the Metal Coordination", *ACS Nano* **2017**, *11*(4), 4183–4190, DOI 10.1021/acsnano.7b01109.

[209] J. Dai, W. Zhao, L. Xing, J. Shang, H. Ju, X. Zhou, J. Liu, Q. Chen, Y. Wang, J. Zhu, K. Wu, "Dechlorinated Ullmann Coupling Reaction of Aryl Chlorides on Ag(111): A Combined STM and XPS Study", *ChemPhysChem* **2019**, *20*(18), 2367–2375, DOI 10.1002/cphc.201900264.

[210] J. Eichhorn, T. Strunskus, A. Rastgoo-Lahrood, D. Samanta, M. Schmittel, M. Lackinger, "On-surface Ullmann polymerization via intermediate organometallic networks on Ag(111)", *Chemical Communications* **2014**, *50*(57), 7680–7682, DOI 10.1039/c4cc02757d.

[211] R. Gutzler, L. Cardenas, J. Lipton-Duffin, M. E. Garah, L. E. Dinca, C. E. Szakacs, C. Fu, M. Gallagher, M. Vondráček, M. Rybachuk, D. F. Perepichka, F. Rosei, "Ullmann-type coupling of brominated tetrathienoanthracene on copper and silver", *Nanoscale* **2014**, *6*(5), 2660–2668, DOI 10.1039/c3nr05710k.

[212] A. Basagni, L. Ferrighi, M. Cattelan, L. Nicolas, K. Handrup, L. Vaghi, A. Papagni, F. Sedona, C. D. Valentin, S. Agnoli, M. Sambi, "On-surface photo-dissociation of C–Br bonds: towards room temperature Ullmann coupling", *Chemical Communications* **2015**, *51*(63), 12593–12596, DOI 10.1039/c5cc04317d.

[213] C. J. Judd, S. L. Haddow, N. R. Champness, A. Saywell, "Ullmann Coupling Reactions on Ag(111) and Ag(110); Substrate Influence on the Formation of Covalently Coupled Products and Intermediate Metal-Organic Structures", *Scientific Reports* **2017**, *7*(1), DOI 10.1038/s41598-017-13315-1.

[214] Q. Fan, C. Wang, Y. Han, J. Zhu, J. Kuttner, G. Hilt, J. M. Gottfried, "Surface-Assisted Formation, Assembly, and Dynamics of Planar Organometallic Macrocycles and Zigzag Shaped Polymer Chains with C–Cu–C Bonds", *ACS Nano* **2013**, *8*(1), 709–718, DOI 10.1021/nn405370s.

[215] Q. Fan, C. Wang, L. Liu, Y. Han, J. Zhao, J. Zhu, J. Kuttner, G. Hilt, J. M. Gottfried, "Covalent, Organometallic, and Halogen-Bonded Nanomeshes from Tetrabromo-Terphenyl by Surface-Assisted Synthesis on Cu(111)", *The Journal of Physical Chemistry C* **2014**, *118*(24), 13018–13025, DOI 10.1021/jp5037475.

[216] Q. Fan, T. Wang, L. Liu, J. Zhao, J. Zhu, J. M. Gottfried, "Tribromobenzene on Cu(111): Temperature-dependent formation of halogen-bonded,

organometallic, and covalent nanostructures", *The Journal of Chemical Physics* **2015**, *142*(10), 101906, DOI 10.1063/1.4906214.

[217] T. A. Pham, B. V. Tran, M.-T. Nguyen, M. Stöhr, "Chiral-Selective Formation of 1D Polymers Based on Ullmann-Type Coupling: The Role of the Metallic Substrate", *Small* **2017**, *13*(13), 1603675, DOI 10.1002/smll.201603675.

[218] M. Xi, B. E. Bent, "Iodobenzene on Cu (111): formation and coupling of adsorbed phenyl groups", *Surface Science* **1992**, *278*(1-2), 19–32, DOI 10.1016/0039-6028(92)90580-Y.

[219] M. Xi, B. E. Bent, "Mechanisms of the Ullmann coupling reaction in adsorbed monolayers", *Journal of the American Chemical Society* **1993**, *115*(16), 7426–7433, DOI 10.1021/ja00069a048.

[220] M. X. Yang, M. Xi, H. Yuan, B. E. Bent, P. Stevens, J. M. White, "NEXAFS studies of halobenzenes and phenyl groups on Cu (111)", *Surface Science* **1995**, *341*(1-2), 9–18, DOI 10.1016/0039-6028(95)00737-7.

[221] B. P. Klein, N. J. van der Heijden, S. R. Kachel, M. Franke, C. K. Krug, K. K. Greulich, L. Ruppenthal, P. Müller, P. Rosenow, S. Parhizkar, F. C. Bocquet, M. Schmid, W. Hieringer, R. J. Maurer, R. Tonner, C. Kumpf, I. Swart, J. M. Gottfried, "Molecular Topology and the Surface Chemical Bond: Alternant Versus Nonalternant Aromatic Systems as Functional Structural Elements", *Physical Review X* **2019**, *9*(1), 011030, DOI 10.1103/physrevx.9.011030.

[222] B. P. Klein, A. Ihle, S. R. Kachel, L. Ruppenthal, S. J. Hall, L. E. Sattler, S. M. Weber, J. Herritsch, A. Jaegermann, D. Ebeling, R. J. Maurer, G. Hilt, R. Tonner, A. Schirmeisen, J. M. Gottfried, "Enhanced Interaction of the Stone-Wales Defect at the Metal-Graphene Interface", **2020**, *in preparation.*

[223] S. R. Kachel, P.-M. Dombrowski, T. Breuer, J. M. Gottfried, G. Witte, "Engineering of TMDC-OSC Hybrid Interfaces: The Thermodynamics of Unitary and Mixed Acene Monolayers on MoS_2", *Chemical Science* **2020**, *submitted.*

[224] M. Schmid, S. R. Kachel, B. P. Klein, N. Bock, P. Müller, R. Riedel, N. Hampp, J. M. Gottfried, "Reactive metal-organic interfaces studied with hard x-ray photoelectron spectroscopy: controlled formation of metalloporphyrin interphase layers during metal vapor deposition onto porphyrin

films", *Journal of Physics: Condensed Matter* **2019**, *31*(9), 094002, DOI 10.1088/1361-648x/aafa2b.

[225] M. Schöniger, S. R. Kachel, J. Herritsch, P. Schröder, M. Hutter, J. M. Gottfried, "Direct synthesis of dilithium tetraphenylporphyrin: facile reaction of a free-base porphyrin with vapor-deposited lithium", *Chemical Communications* **2019**, *55*(91), 13665–13668, DOI 10.1039/c9cc07170a.

[226] S. R. Kachel, M. Schöniger, J. Herritsch, P. Schröder, J. M. Gottfried, "Synthesis of Partially Metalated Lithium Tetraphenylporphyrin: Characterization of LiHTPP", **2020**, *in preparation*.

[227] S. R. Kachel, M. Schöniger, H. Zhou, H.-J. Drescher, C. K. Krug, L. Ruppenthal, B. P. Klein, M. Sachs, K. Gries, J. Hochstraßer, F. Fillsack, R. Riedel, N. Hampp, M. Schmid, J. M. Gottfried, "Examination of the Reaction Zone in a Metal–Organic Semiconductor Interface by Multi-Technique Approach: Characterization and Control of the Ca/6T Interphase", **2020**, *in preparation*.

[228] J. Herritsch, S. R. Kachel, Q. Fan, M. Hutter, L. Heuplick, F. Münster, J. M. Gottfried, "Tracking of the Transmetalation Reaction of PbTPP by Cu Adatoms on Cu(111) by Multiple Techniques", **2020**, *in preparation*.

[229] H. L. Deubner, M. Sachs, J. Bandemehr, S. I. Ivlev, A. J. Karttunen, S. R. Kachel, B. P. Klein, L. Ruppenthal, M. Schöniger, C. K. Krug, J. Herritsch, J. M. Gottfried, J. N. M. Aman, J. S. auf der Günne, F. Kraus, "Binary Lead Fluoride Pb 3 F 8", *Chemistry - A European Journal* **2019**, *25*(68), 15656–15661, DOI 10.1002/chem.201903954.

8 Acknowledgment / Danksagung

Acknowledgment

In the following, I want to thank everyone, who contributed to the success of this thesis. To begin with, I would like to thank my supervisor Prof. Dr. J. Michael Gottfried for accompanying me during my whole chemistry studies. He supervised me during my PhD, masters, and bachelors thesis, a mentoring program and he gave several lectures. I want to thank him for the opportunity to study such an interesting topic because I dealt with organic LEDs since my high-school diploma. Additionally, I want to thank Prof. Gottfried for the numerous scientific discussions and the great personal advancement.

I want to thank Prof. Dr. Gregor Witte for being the second assessor of this thesis. Furthermore, I want to thank him for several inspiring discussions on surface science and the successful cooperation projects.

I would like to thank Prof. Dr. Seubert for leading the assessment commission as the third member.

I give my thanks to all collaboration partners for the nice publications. These partners include all members of the Gottfried group and the chemical department of the Philipps University Marburg, Dr. Tobias Breuer, Pierre-Martin Dombrowski as well as the collaboration partners from the research center Jülich and the universities from Duisburg, Erlangen and Warwick.

A special contribution to this thesis has Dr. Martin Schmid, whom I want to thank for the very good supervision during my master's thesis and the beginning of my doctorate. He gave me advice in daily lab work, teached me a lot of basics and the programming in *Igor Pro*. In addition, I want to thank him for all scientific and non-scientific discussions during that time.

Furthermore, I would like to say a big thank you to the whole working group of Prof. Gottfried. Since beginning my master's thesis, there was always a pleasant and entertaining working atmosphere in the office and in the lab. I made friends with you apart from work. I give a special thanks to Dr. Claudio Krug, who helped me a lot when I was new in the group. I am owing thanks to

Dr. Benedikt Klein, Maik Schöniger and Jan Herritsch for the support in many research projects and publications.

Since the beamtimes at Bessy II are an important part of this thesis, I want say thank you to all beamtime participants as well as the HZB for the opportunity to conduct experiments at Bessy II.

During the experimental work in the lab, I was supported by numerous students, which I want to thank a lot. These include my master students Mark Hutter and Leonard Neuhaus. Both did an internship supervised by me, too. Furthermore, I want to thank Janika Hochstraßer, who worked as an student assistant and did two internships. Moreover, I want to thank all other internship students, namely Philipp "Flippo" Müller, Janosch Kettner, Florian Fillsack, Lukas Hellweg, Marvin Cronau, Philipp Schröder and Markus Pyschik.

I want to give a special thanks to Marco Hill and Rigobert Donner. Marco Hill did a lot technical work for me and always gave advice if needed. Rigobert Donner quickly finished and helped with bureaucratic matters.

I want to thank the mechanical and the electrical workshop of the chemistry department as well as the computer workshop of the HRZ for the production and the repair of vacuum components, measuring and office devices.

Without the financial support by the SFB 1083 and the DFG, a lot beamtimes, business trips and lab devices would not be affordable.

I thank Dr. Claudio Krug, Mark Hutter, Lukas Ruppenthal, Jan Herritsch and Katharina Rausch for proof reading.

I want to thank all my friends, with whom I spent a great time in the past years apart from work. I want to emphasize my fiancee Regina Schimpf and want to gratefully thank her for the great eight years until now.

Finally, the greatest thanks goes to my mother Sabine Kachel. She supported and promoted me during my whole education. A lot of things would not be possible without her. For this I thank her from the bottom of my heart.

Danksagung

Ich möchte mich im Folgenden bei allen Personen bedanken, die zum Gelingen dieser Arbeit wesentlich beigetragen haben.

Zuerst möchte ich meinen Betreuer Prof. Dr. J. Michael Gottfried herzlich dafür danken, dass er mich durch mein gesamtes Studium in unterschiedlichen Funktionen begleitet hat. Dazu gehören neben der Promotionsbetreuung und den Mentorengesprächen zu Beginn des Bachelorstudiums, die Betreuung der

Bachelor- und Masterarbeit sowie viele Vorlesungen. Ich möchte mich für die Möglichkeit bedanken an dem Thema der organischen Elektronik zu forschen, da ich mich bereits während des Abiturs mit organischen LEDs beschäftigt habe. Zudem danke ich Prof. Gottfried für die zahlreichen wissenschaftlichen Diskussionen und die sehr gute persönliche Förderung.

Prof. Dr. Gregor Witte möchte ich dafür danken, dass er das Zweitgutachten dieser Dissertation übernommen hat. Des Weiteren möchte ich ihm für viele anregende Diskussionen über Themen der Oberflächenchemie und -physik sowie erfolgreiche Kooperationsprojekte danken.

Prof. Dr. Andreas Seubert möchte ich dafür danken, dass er die Prüfungskommission als drittes Mitglied geleitet hat.

Ich möchte mich zudem bei allen Kooperationspartnern bedanken, die großen Beitrag zu dem Gelingen der Publikationen geleistet haben. Dabei sollen die Mitglieder der Arbeitsgruppe Gottfried und des Fachbereichs Chemie sowie Dr. Tobias Breuer, Pierre-Martin Dombrowski und die Kooperationspartner aus dem Forschungszentrum Jülich, der Universität Duisburg, Erlangen und Warwick nicht unerwähnt bleiben.

Einen großen Beitrag zu dieser Arbeit hat Dr. Martin Schmid, dem ich für die Betreuung während meiner Masterarbeit und den Anfängen meiner Promotionen herzlich danke. Er stand mir mit Rat und Tat im Laboralltag zur Seite, hat mir viele wichtige Grundlagen vermittelt und mir das Programmieren in Igor Pro beigebracht. Zudem möchte ich ihm für die vielen wissenschaftlichen, aber auch alltäglichen Gespräche danken.

Weiterhin möchte ich der gesamten Arbeitsgruppe Gottfried meinen Dank aussprechen. Seit Beginn meiner Masterarbeit herrschte immer eine angenehme und unterhaltsame Arbeitsatmosphäre. Auch über die gemeinsame Arbeit hinaus haben sich Freundschaften entwickelt. Ich möchte an dieser Stelle Dr. Claudio Krug hervorheben, der mir besonders während der Masterarbeit und dem Beginn meiner Promotionen im Laboralltag geholfen hat, damit ich mich besser in der Arbeitsgruppe zurecht finde. Dr. Benedikt Klein, Maik Schöniger und Jan Herritsch möchte ich für die tatkräftige Unterstützung bei vielen Forschungsprojekten und Veröffentlichungen danken.

Da die Strahlzeiten am Bessy II ein wichtiger Bestandteil dieser Arbeit sind, möchte ich mich bei allen Mitfahrenden sowie dem HZB für die Bereitstellung der Messzeit danken.

Während der praktischen Arbeit im Labor wurde ich von zahlreichen Studenten unterstützt, bei denen ich mich herzlich bedanken möchte. Dazu gehören

die Masterstudenten Mark Hutter und Leonard Neuhaus, die beide auch Vertiefungspraktika bei mir absolvierten. Ein besonderer Dank gilt Janika Hochstraßer, die neben zwei Vertiefungspraktia auch für mehrere Monate als studentische Hilfskraft mich im Labor unterstützt hat. Weiterhin bedanke ich mich bei Philipp “Flippo” Müller, Janosch Kettner, Florian Fillsack, Lukas Hellweg, Marvin Cronau, Philipp Schröder und Markus Pyschik.

Einen besonderen Dank möchte ich Marco Hill und Rigobert Donner aussprechen. Marco Hill stand mir im Laboralltag immer hilfreich zur Seite und hat mir viele handwerkliche Nebenaufgaben abgenommen. Rigobert Donner möchte ich für die schnelle und unkomplizierte Hilfe bei bürokratischen Angelegenheiten danken.

Des Weiteren möchte ich mich bei der feinmechanischen und elektrischen Werkstatt am Fachbereich Chemie sowie der PC-Werkstatt des HRZs für die schnelle und kompetente Bearbeitung und Reparatur von Vakuumbauteilen, Mess- und Bürogeräten bedanken.

Ohne die finanzielle Unterstützung durch den SFB 1083 und die DFG, wären die vielen Strahlzeiten, Dienstreisen, teuren Laborgeräte und damit das Gelingen dieser Arbeit nicht möglich gewesen.

Ich möchte mich bei Dr. Claudio Krug, Mark Hutter, Lukas Ruppenthal, Jan Herritsch und Katharina Rausch für das Korrekturlesen meiner Arbeit bedanken.

Ich möchte mich bei all meinen Freunden bedanken, die mich abseits der Promotion auf andere Gedanken gebracht haben und mit denen ich eine tolle Zeit in den letzten Jahren verbracht habe. Ich möchte mich bei meiner Verlobten Regina Schimpf herzlich für die nun mehr als acht schönen Jahre bedanken. Danke für die tolle Zeit!

Der größte Dank gilt zu guter Letzt meiner Mutter Sabine Kachel. Sie hat mich während meiner gesamten Ausbildung tatkräftig unterstützt, gefördert und mir den bestmöglichen Bildungsweg ermöglicht. Ohne sie wäre vieles nicht möglich gewesen. Dafür bedanke ich mich vom tiefsten Herzen.

Appendix

A Presented Publications

All presented publications in Chapter 5 are listed in the following. The full text together with the supporting information of each publication is appended afterwards and the corresponding pages are noted.

Part I: Characterizing the Interactions of Metal/Organic Interfaces

P1 **p. 145** B. P. Klein, N. J. van der Heijden, **S. R. Kachel**, M. Franke, C. K. Krug, K. K. Greulich, L. Ruppenthal, P. Müller, P. Rosenow, S. Parhizkar, F. C. Bocquet, M. Schmid, W. Hieringer, R. J. Maurer, R. Tonner, C. Kumpf, I. Swart, J. M. Gottfried, "Molecular Topology and the Surface Chemical Bond: Alternant Versus Nonalternant Aromatic Systems as Functional Structural Elements", *Physical Review X* **2019**, *9*(1), 011030, DOI 10.1103/PhysRevX.9.011030.

P2 **p. 188** **S. R. Kachel**, B. P. Klein, J. M. Morbec, M. Schöniger, M. Hutter, M.. Schmid, P. Kratzer, B. Meyer, R. Tonner, J. M. Gottfried, "Chemisorption and Physisorption at the Metal/Organic Interface: Bond Energies of Naphthalene and Azulene on Coinage Metal Surfaces", *The Journal of Physical Chemistry C* **2020**, *124*, 8257–8268, DOI 10.1021/acs.jpcc.0c00915

P3 **p. 221** B. P. Klein, A. Ihle, **S. R. Kachel**, L. Ruppenthal, S. J. Hall, L. E. Sattler, S. M. Weber, J. Herritsch, A. Jaegermann, D. Ebeling, R. J. Maurer, G. Hilt, R. Tonner, A. Schirmeisen, J. M. Gottfried, "Enhanced Interaction of the Stone-Wales Defect at the Metal-Graphene Interface", **2020**, *in preparation.*

P4 **p. 273** **S. R. Kachel**, P.-M. Dombrowski, T. Breuer, J. M. Gottfried, G. Witte, "Engineering of TMDC-OSC Hybrid Interfaces: The Thermodynamics of Unitary and Mixed Acene Monolayers on MoS_2", *Chemical Science* **2020**, *in preparation.*

Part II: Investigations on Metal/Organic Reactions and Their Interphase Formation

P5 **p. 304** M. Schmid, **S. R. Kachel**, B. P. Klein, N. Bock, P. Müller, R. Riedel, N. Hampp, J. M. Gottfried, "Reactive Metal-Organic Interfaces Studied with Hard X-Ray Photoelectron Spectroscopy: Controlled Formation of Metalloporphyrin Interphase Layers During Metal Vapor Deposition onto Porphyrin Films", *Journal of Physics: Condensed Matter* **2019**, *31*, 094002, DOI 10.1088/1361-648X/aafa2b.

P6 **p. 315** M. Schöniger, **S. R. Kachel**, J. Herritsch, P. Schröder, M. Hutter, J. M. Gottfried, "Direct Synthesis of Dilithium Tetraphenylporphyrin: Facile Reaction of a Free-Base Porphyrin with Vapor-Deposited Lithium", *Chemical Communications* **2019**, *55*, 13665–13668, DOI 10.1039/C9CC07170A.

P7 **p. 329** **S. R. Kachel**, M. Schöniger, J. Herritsch, P. Schröder, J. M. Gottfried, "Synthesis of Partially Metalated Lithium Tetraphenylporphyrin: Characterization of LiHTPP", **2020**, *in preparation.*

P8 **p. 341** **S. R. Kachel**, M. Schöniger, H. Zhou, H.-J. Drescher, C. K. Krug, L. Ruppenthal, B. P. Klein, M. Sachs, K. Gries, J. Hochstraßer, F. Fillsack, R. Riedel, N. Hampp, M. Schmid, J. M. Gottfried, "Examination of the Reaction Zone in a Metal–Organic Semiconductor Interface by Multi-Technique Approach: Characterization and Control of the Ca/6T Interphase", **2020**, *in preparation.*

P9 **p. 358** J. Herritsch, **S. R. Kachel**, Q. Fan, M. Hutter, L. Heuplick, F. Münster, J. M. Gottfried, "Tracking of the Transmetalation Reaction of PbTPP by Cu Adatoms on Cu(111) by Multiple Techniques", **2020**, *in preparation.*

Part III: Other Publications

P10 **p. 377** H. L. Deubner, M. Sachs, J. Bandemehr, S. I. Ivlev, A. J. Karttunen, **S. R. Kachel**, B. P. Klein, L. Ruppenthal, M. Schöniger, C. K. Krug, J. Herritsch, J. M. Gottfried, J. N. M. Aman, J. Schmedt auf der Günne, F. Kraus, "Binary Lead Fluoride Pb_3F_8", *Chemistry - A European Journal* **2019**, *25*, 15656–15661, DOI 10.1002/chem.201903954.

PHYSICAL REVIEW X **9,** 011030 (2019)

Molecular Topology and the Surface Chemical Bond: Alternant Versus Nonalternant Aromatic Systems as Functional Structural Elements

Benedikt P. Klein,[1] Nadine J. van der Heijden,[2] Stefan R. Kachel,[1] Markus Franke,[3] Claudio K. Krug,[1] Katharina K. Greulich,[1] Lukas Ruppenthal,[1] Philipp Müller,[1] Phil Rosenow,[1] Shayan Parhizkar,[3] François C. Bocquet,[3] Martin Schmid,[1] Wolfgang Hieringer,[4] Reinhard J. Maurer,[5] Ralf Tonner,[1] Christian Kumpf,[3] Ingmar Swart,[2] and J. Michael Gottfried[1,*]

[1]*Philipps-Universität Marburg, Fachbereich Chemie, Hans-Meerwein-Straße 4, 35032 Marburg, Germany*
[2]*Condensed Matter and Interfaces, Debye Institute for Nanomaterials Science, Utrecht University, P.O. Box 80000, 3508 TA Utrecht, The Netherlands*
[3]*Peter Grünberg Institut (PGI-3), Forschungszentrum Jülich, 52425 Jülich, Germany and Jülich Aachen Research Alliance (JARA), Fundamentals of Future Information Technology, 52425 Jülich, Germany*
[4]*Lehrstuhl für Theoretische Chemie, Universität Erlangen-Nürnberg, Egerlandstraße 3, 91058 Erlangen, Germany*
[5]*Department of Chemistry and Centre for Scientific Computing, University of Warwick, Gibbet Hill Road, Coventry, CV4 7AL, United Kingdom*

(Received 15 August 2018; revised manuscript received 22 November 2018; published 13 February 2019)

The interaction of carbon-based aromatic molecules and nanostructures with metals can strongly depend on the topology of their π-electron systems. This is shown with a model system using the isomers azulene, which has a nonalternant π system with a 5-7 ring structure, and naphthalene, which has an alternant π system with a 6-6 ring structure. We found that azulene can interact much more strongly with metal surfaces. On copper (111), its zero-coverage desorption energy is 1.86 eV, compared to 1.07 eV for naphthalene. The different bond strengths are reflected in the adsorption heights, which are 2.30 Å for azulene and 3.04 Å for naphthalene, as measured by the normal incidence x-ray standing wave technique. These differences in the surface chemical bond are related to the electronic structure of the molecular π systems. Azulene has a low-lying LUMO that is close to the Fermi energy of Cu and strongly hybridizes with electronic states of the surface, as is shown by photoemission, near-edge x-ray absorption fine-structure, and scanning tunneling microscopy data in combination with theoretical analysis. According to density functional theory calculations, electron donation from the surface into the molecular LUMO leads to negative charging and deformation of the adsorbed azulene. Noncontact atomic force microscopy confirms the deformation, while Kelvin probe force microscopy maps show that adsorbed azulene partially retains its in-plane dipole. In contrast, naphthalene experiences only minor adsorption-induced changes of its electronic and geometric structure. Our results indicate that the electronic properties of metal-organic interfaces, as they occur in organic (opto)electronic devices, can be tuned through modifications of the π topology of the molecular organic semiconductor, especially by introducing 5-7 ring pairs as functional structural elements.

DOI: 10.1103/PhysRevX.9.011030

Subject Areas: Chemical Physics, Condensed Matter Physics, Materials Science

I. INTRODUCTION

Carbon-based materials with aromatic π-electron systems, such as π-conjugated molecular solids [1,2], polymers [3,4], and low-dimensional nanostructures [5,6], have attracted considerable attention as organic semiconductors [7–9]. A crucial aspect for the application of these materials in (opto) electronic devices is their interface formation with metal surfaces at the contacting electrodes. The electronic properties of the resulting metal-organic interfaces determine important performance parameters such as charge carrier injection rates [10,11]. Precise control over various interface properties, especially the wave-function overlap and the energy-level alignment, is therefore critical for the rational improvement of organic electronic devices [12].

*michael.gottfried@chemie.uni-marburg.de

The properties of a π-electron system are largely determined by its topology, i.e., the connectivity pattern as expressed through the topological matrix in the Hückel molecular orbital (HMO) theory [13]. Most organic semiconductors have carbon backbones with alternant topology because they consists of six-membered rings [1,7]. Only very recently has increased interest in so-called *nonalternant* aromatic structures [14] arisen in the field of graphene nanoribbons [15], nanographenes [16], and polycyclic aromatic hydrocarbons [17,18]. These nonalternant structures often contain linked 5- and 7-membered rings. It has been recognized that their unique electronic structure makes nonalternant aromatic systems highly interesting as novel (opto)electronic semiconductor materials for organic field-effect transistors (OFET) and photovoltaic cells (OPVC) [19,20]. Nonalternant structural elements also occur in graphene in the form of 5-7 defects [21,22]. Theoretical studies have predicted that various properties of graphene depend on the presence of these nonalternant structural elements, including electron transport properties [23,24], mechanical stability [25,26], magnetism [27], and chemical reactivity [28].

While interfaces between metals and alternant organic semiconductor materials have been widely studied [29–33], up until now it has not been known how the surface chemical bond is influenced by nonalternant structural elements. To address this fundamental question, we perform a direct comparison between two isomeric aromatic molecules on a Cu(111) surface. One of these isomers, azulene, is a prototypical nonalternant aromatic system with a 5-7 ring structure, while naphthalene, with its 6-6 ring structure, serves as its alternant counterpart (Fig. 1). Some previous work exists for naphthalene on Cu(111) [34–38] but not for azulene. Copper was chosen as a model substrate because of its frequent use for the epitaxial growth of graphene [39–41] or the on-surface synthesis of carbon-based nanostructures [42].

Below, we show that the topology of the molecular π system drastically influences its electronic interaction with a metal surface. It is therefore proposed that the incorporation of nonalternant structural elements in molecular semiconductors can be used to control and to optimize performance-related properties of functional metal-organic interfaces. Recent achievements in the synthesis on novel, structurally complex, nonalternant, aromatic molecules [16,19,20,43] show that this is a feasible and promising approach.

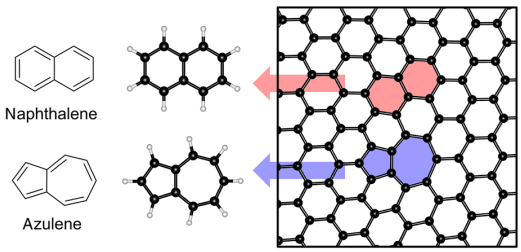

FIG. 1. Right, graphene lattice with an embedded nonalternant 5-7 defect, highlighted in blue. If this structural element is cut out of graphene and terminated with hydrogen atoms, the resulting molecule is azulene, shown on the left. Its isomer naphthalene serves as the complementary model system for the regular, alternant 6-6 structure, highlighted in red.

For a quantitative comparison of the adsorbate-metal bonds of aromatic 5-7 and 6-6 carbon skeletons, we determine the adsorbate-substrate bond distances with the normal incidence x-ray standing wave (NIXSW) technique and noncontact atomic force microscopy (nc-AFM), while adsorbate-substrate bond energies are measured by temperature-programmed desorption (TPD). The electronic structures are analyzed by x-ray and UV photoelectron spectroscopy (XPS/UPS) in combination with near-edge x-ray absorption fine-structure (NEXAFS) measurements. Complemented by dispersion-corrected density functional theory (DFT) calculations, our results provide a detailed understanding of the surface chemical bond and its dependence on the π topology.

II. METHODS

A. Experimental methods

The interaction of azulene and naphthalene with Cu(111) was studied under ultrahigh vacuum (UHV) conditions. Azulene (Sigma-Aldrich, purity $> 99.0\%$) and naphthalene (Sigma-Aldrich, purity $> 99.7\%$) were introduced into the vacuum systems through leak valves after initial pump-freeze-thaw cycles of the reservoirs. A polished Cu(111) single-crystal surface (purity $> 99.9999\%$, roughness $< 0.03\ \mu$m, orientation accuracy $< 0.1°$, from MaTecK/Germany) was prepared by iterated sputtering with Ar^+ ions (0.5–1 keV, 5–15 μA, 30 min) and annealing (800–830 K, 15 min). Surface cleanliness and structure were confirmed by XPS, low energy electron diffraction, and scanning tunneling microscopy (STM). Sample temperatures were measured with a type K thermocouple directly mounted to the Cu single crystal. Coverages are given in monolayers (ML). The coverage was determined by a consistent routine using XPS, nc-AFM, and TPD measurements. For a detailed description, see the Supplemental Material [44].

NIXSW measurements were performed at the undulator beam line I-09 at Diamond Light Source in Didcot, UK, using a VG Scienta EW4000 HAXPES hemispherical electron analyzer for photoelectron detection, which is mounted at 90° with respect to the incident x-ray beam. Nondipolar effects were neglected in the data analysis, which was performed using the software package Torricelli [45]. The sample temperature was approximately 150 K, which led to a Bragg energy of 2980 eV for the Cu(111) lattice planes.

TPD measurements were carried out with a HIDEN EPIC 1000 mass spectrometer mounted inside a differentially pumped cryoshroud cooled to 80 K with l-N_2. This

setup is a variant of line-of-sight mass spectrometry [46] and ensures that molecules hitting the inner wall of the cryoshroud stick there, such that the mass spectrometer detects only molecules with a straight trajectory between sample and detector. This leads to improved quality of the TPD traces and is the basis for their quantitative analysis.

XPS was performed with monochromatic Al-K_α radiation using a SPECS XR 50 M x-ray anode, a FOCUS 500 monochromator, and a PHOIBOS 150 electron energy analyzer equipped with an MCD-9 multichanneltron detector. Work functions were measured with He-I radiation from a UVS 10/35 gas discharge lamp. UPS was performed at the PM4 dipole beam line with the LowDosePES end station at the synchrotron radiation facility BESSY II (Helmholtz-Zentrum Berlin) using a Scienta ArTOF angle-resolved time-of-flight spectrometer. A photon energy of 16.5 eV was used.

NEXAFS spectroscopy was also performed at BESSY II using the HE-SGM dipole beam line, which provides linearly polarized radiation with a polarization factor of 0.91 and an energy resolution of 300 meV at the carbon K-edge. The partial electron-yield (PEY) mode was used with a retarding field of −150 V and a channeltron detector voltage of 2.2 keV. Further information on the data treatment can be found in the Supplemental Material [44].

For variable-temperature scanning tunneling microscopy (VT-STM), a SPECS 150 Aarhus STM with SPC 260 electronics was used. VT-STM measurements were performed at a sample temperature of 150 K using an etched tungsten tip conditioned by initial Ar^+ sputtering and pulsing. The reported bias voltages refer to the sample. The STM images were recorded in constant-current mode and were processed with WSxM v5.0 D8.4 [47] by carefully using flatten and plane tools, scale adjustment, and slightly filtering with a Gaussian filter.

The nc-AFM images were taken with an Omicron NanoTechnology LT-STM/AFM with a commercially available qPlus sensor, operating at approximately 4.6 K in UHV with an average pressure of 5×10^{-10} mbar. The baked qPlus sensor (3 h at 120 °C) had a quality factor of $Q \approx 30\,000$, a resonance frequency of $f_0 = 21\,922$ Hz, and a peak-to-peak oscillation amplitude of less than 1 Å. Tip conditioning was accomplished with controlled crashes into the copper surface and bias pulses until the STM resolution was satisfactory. The tip apex was functionalized with a CO molecule. The AFM was operated in constant-height mode, and AFM images show the frequency shift (Δf) with respect to the resonance frequency. During the AFM scan, the tunneling current was also measured, which gives a constant-height STM scan.

B. Density functional theory calculations

Periodic density functional theory calculations of azulene and naphthalene on Cu(111) were performed with the Vienna *Ab Initio* Simulation Package (VASP) [48–51]. The PBE functional [52] was used in combination with the third-generation van der Waals dispersion correction by Grimme (DFT-D3) [53] and the projector-augmented wave (PAW) ansatz [54,55] for the atomic cores. Further details can be found in the Supplemental Material [44].

XP and x-ray absorption spectra were calculated using the pseudopotential plane-wave code CASTEP-17.1 [56]. For the XPS chemical shifts, the delta self-consistent field (DeltaSCF) method of constraining electronic occupations to resemble full core-hole excitations was used. NEXAFS simulations were performed using on-the-fly generated USPPs and the CASTEP module ELNES [57] and the transition-potential approach [58,59]. For more details on the computational settings, analysis, and implementation, see the Supplemental Material [44] and Diller *et al.* [60] as well as Maurer and Reuter [61]. Furthermore, the Supplemental Material [44] contains additional NEXAFS simulations obtained by a more approximate method.

III. RESULTS

A. Adsorbate-substrate bond distances (adsorption heights)

The vertical distance of an adsorbed molecule from the surface is an important parameter for the quantitative characterization of the adsorbate-substrate bond. To measure the adsorption heights of azulene and naphthalene over the Cu(111) surface [Fig. 2(a)], we used the NIXSW technique. This method utilizes the standing x-ray wave field generated by a crystalline substrate when near-normal incidence x rays undergo Bragg diffraction on a set of lattice planes $H = (hkl)$ with a distance of d^H [62]. The standing wave field can be vertically shifted by $d^H/2$ by scanning the photon energy E through the Bragg energy [62].

At any certain adsorption height, the photon field intensity will therefore change in a characteristic way during such a scan. Hence, one expects characteristic x-ray absorption profiles for different adsorption heights since the atomic absorption is proportional to the local photon intensity. By recording the photoelectron yield of any core level of this species, which is (within the dipole approximation) proportional to the atomic absorption, one can measure the x-ray absorption profile at the position of the adsorbate atom and obtain the height D^H of this atomic species relative to the substrate diffraction plane locations. The variation of the atomic absorption $I(E)$ can be calculated with dynamical diffraction theory and follows the equation

$$I(E) = 1 + R + 2\sqrt{R} \cdot F^H \cdot \cos(\Phi + 2\pi \cdot P^H), \quad (1)$$

where $R = R(E)$ is the reflectivity and $\Phi = \Phi(E)$ is the phase of the standing wave field [63,64].

Data analysis on the basis of Eq. (1) provides the coherent position P^H and the coherent fraction F^H. The coherent position P^H equals D^H modulo d^H, i.e., $D^H/d^H = n + P^H$ ($n = 0, 1, 2\ldots$) In the case of single-site adsorption,

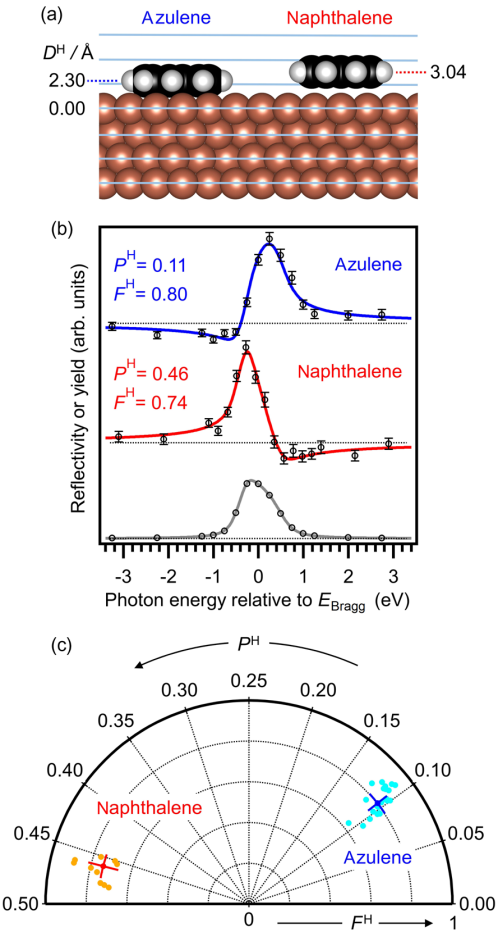

FIG. 2. Adsorption heights from NIXSW measurements for azulene and naphthalene on Cu(111), coverage 1 ML. (a) Space-filling adsorbate models with the heights true to scale as obtained from NIXSW. (b) C 1s photoelectron yields for azulene (top) and naphthalene (center) along with the x-ray reflectivity $R(E)$ (bottom) as a function of the photon energy around the Bragg energy E_{Bragg}. The yield data are shown as open circles (with error bars); the solid blue and red lines are fits with Eq. (1). (c) Argand diagram with the results of the individual measurements in light colors and the averaged value in bold colors, with error bars.

i.e., when each atomic species occupies only one adsorption height (this is the relevant case for the systems discussed here), F^H is a measure for the scattering of the real heights around the coherent position. A coherent fraction of $F^H = 1$ means that all contributing atoms have exactly the same height D^H, whereas a fraction of $F^H = 0$ means that they have a random height distribution. Note that the latter is not necessarily true if (at least) two clearly different adsorption heights occur. In this case, averaging of coherent positions and fractions has to be performed in an Argand vector diagram [62–65].

For our systems, we used the background corrected total intensity of the C 1s spectral region to obtain the photoelectron yield curve for each individual NIXSW scan. A typical yield curve is shown in Fig. 2(b). A distinction between the different carbon atoms within one molecule was not possible because the core level shifts were too small compared to the available energy resolution. Note that we have not performed any correction for nondipolar parameters in our analysis since the NIXSW data were recorded close to grazing emission geometry (90° between incident x-ray beam and the analyzer). In this geometry, nondipolar effects are minimal.

The results of the analysis are summarized in the Argand diagram in Fig. 2(c). The coherent position for azulene at monolayer coverage is $P^H = 0.11 \pm 0.01$, which yields an adsorption height of $D^H = 2.30 \pm 0.03$ Å. This number was derived using $d^H = 2.08$ Å for the Cu(111) surface at the measurement temperature of 150 K. The corresponding coherent fraction of $F^H = 0.80 \pm 0.06$ is in a typical range for a rather homogeneous contribution of the adsorption heights. For the naphthalene monolayer, the analysis gives a coherent position of $P^H = 0.46 \pm 0.01$, from which an adsorption height of 3.04 ± 0.03 Å is obtained. The coherent fraction is similar, with $F^H = 0.74 \pm 0.08$.

Comparison of these values [see also Fig. 2(a)] reveals a much lower adsorption height for azulene. A shorter adsorbate-substrate bond distance typically indicates a stronger bond [66], which agrees with the higher desorption energy of azulene as discussed below. The adsorption height for naphthalene is quite similar to the sum of the van der Waals radii of a carbon and a copper atom (3.10 Å) [67]. In contrast, the adsorption height of azulene, 2.30 Å, is closer to known organometallic carbon-copper bond lengths of approximately 2.10 Å [67]. All these considerations lead to the conclusion that naphthalene engages only in dispersive interaction with the Cu(111) surface, whereas azulene forms a chemical bond.

NIXSW as a laterally integrating technique averages over a large number of molecules. Later, we present nc-AFM data that qualitatively confirm the height difference between azulene and naphthalene on the single-molecule level.

B. Adsorbate-substrate bond energies

Another quantitative parameter describing the strength of the adsorbate-substrate interactions is the activation energy for desorption, which can be derived from temperature-programmed desorption (TPD) data [68–70]. At low submonolayer coverages, the TPD traces of both molecules are governed by first-order desorption kinetics [Figs. 3(a) and 3(b)]. As can be seen, the low-coverage desorption maxima occur at 520 K for azulene and at 340 K for naphthalene. Qualitatively, this large temperature difference shows that the adsorbate-substrate interaction is substantially higher for the 5-7 isomer.

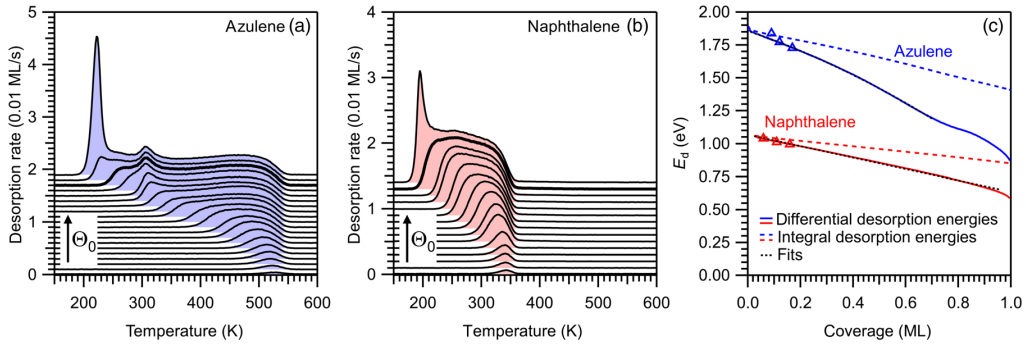

FIG. 3. TPD traces of (a) azulene and (b) naphthalene on Cu(111), with a heating rate 1.0 K/s. Curves with different initial coverage Θ_0 are shifted along the vertical axis for clarity, but we start with a zero desorption rate in each case. The monolayer coverages are marked by bold lines. The other initial coverages are listed in Tables S II in the Supplemental Material [44]. (c) Desorption activation energies as a function of coverage for azulene (blue) and naphthalene (red). Solid lines: Differential desorption energies. Dashed lines: Integral energies for comparison with DFT calculations. Black dotted lines: Fits of the differential desorption energies with the equations mentioned in the text. Triangles: Energies from HRV analysis. Note that HRV is only possible at low coverages, where the peaks have a regular first-order shape.

With increasing coverage, the TPD traces of both molecules broaden towards lower temperatures. The effect, which is attributed to lateral intermolecular repulsion, is more pronounced for azulene. Its monolayer TPD trace reaches a width of 330 K, compared to 180 K for naphthalene (bold lines). Lateral intermolecular repulsion in adsorbates on metal surfaces is usually dominated by a dipole-dipole interaction between vertical dipoles created by electron transfer between molecules and surface, as well as by the pillow (or pushback) effect. This effect is caused by Pauli repulsion between the electrons in the molecule and those in the metal [71–74]. Apparently, these effects play a larger role for azulene than for naphthalene. The vertical dipole moments are also related to the adsorbate-induced work-function change. We show below that azulene causes a larger work-function change than naphthalene, in line with the stronger lateral repulsion of the former.

The high-coverage TPD traces of azulene show an additional desorption maximum at 300 K, which is attributed to a compressed phase occurring close to monolayer saturation (above 0.7 ML). This phase can also be observed in the nc-AFM images discussed below. Above monolayer coverage, narrow second-layer peaks occur at 220 K (azulene) and 190 K (naphthalene).

Quantitative analysis of the TPD spectra gives access to the desorption activation energy E_d as a measure of the adsorbate-substrate bond energy [68–70]. The most rigorous analyses, the so-called complete methods [75,76], are not suitable here because of the strong lateral repulsion [70]. Instead, we use an alternative approach, which provides the coverage-dependent desorption energy from a single TPD trace [70,77]. The resulting curves for azulene and naphthalene are shown in Fig. 3(c) (solid lines). The desorption energies in the zero-coverage limit, E_d^0, are 1.86 eV for azulene and 1.07 eV for naphthalene. This confirms that azulene forms a much stronger bond to the metal surface than naphthalene. While both curves show a substantial decrease of E_d with increasing coverage as a result of the lateral repulsion, the effect is more pronounced for azulene. In the case of naphthalene, E_d decreases nearly linearly with coverage following the equation $E_d = (1.07 - 0.44\Theta)$ eV, where Θ is in units of monolayers. In contrast, the desorption energy of azulene is well described by the second-order polynomial $E_d = (1.86 - 0.67\Theta - 0.40\Theta^2)$ eV for coverages up to 0.75 ML. Figure 3(c) also shows the integral desorption energies necessary for comparison with DFT results (dashed lines).

The desorption prefactors used for the analysis are determined by heating rate variation (HRV) analysis [68], which is only meaningful for the regular first-order peaks in the low-coverage range. The related data are presented in the Supplemental Material [44]. For the respective coverages, the HRV analysis also provides the desorption energies [triangles in Fig. 3(c)], which agree well with the other data.

C. Occupied electronic states: Photoelectron spectroscopy

The very different adsorption energies and heights of azulene and naphthalene are expected to correspond to characteristic differences in the electronic structure. First, we focus on the molecules in a thick multilayer, i.e., without the influence of the metal surface. The multilayer C 1s XP spectra of azulene and naphthalene are compared in Fig. 4(a). The C 1s signal of azulene has a broader shape with a distinct shoulder at the low binding energy side. This shape can be understood by theoretical modeling. For this aim, we calculate the relative peak positions for the different carbon atoms in the molecule by DFT. The details of the calculation and the theoretical modeling can be found in the Supplemental Material [44]. The results are in agreement with previously reported values [78]. While these calculations are performed for the isolated molecules, this

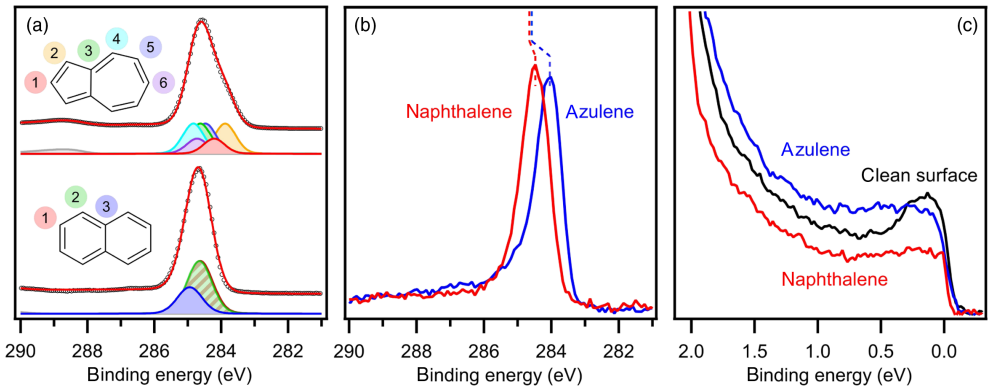

FIG. 4. Photoelectron spectra: (a) Multilayer C 1s XP spectra of azulene and naphthalene, compared with a theoretical model based on DFT calculations. Black circles are experimental data; red lines are fitted results from DFT-based model calculations. The colors of the component peaks correspond to the colors of the labels on the molecular formulas. The shake-up satellite of azulene is shown in grey. (b) C 1s XP spectra of monolayers of azulene and naphthalene on Cu(111). The dotted lines indicate the shifts relative to the multilayer peak positions. (c) UP spectra of azulene and naphthalene monolayers and of the clean Cu(111) surface, taken with a photon energy of 16.5 eV.

simplification appears to be justified considering that the intermolecular interactions in the multilayer are relatively weak and thus have only little influence on the electronic energies and transitions. The resulting theoretical model agrees well with the experimental data for azulene. It further reveals that the shoulder at low binding energies is associated with the five-membered ring. For naphthalene, the calculations of the C 1s spectrum are performed in the same way and confirm the narrower peak shape of the experimental spectrum. In the azulene multilayer spectrum [Fig. 4(a)], a shake-up satellite at 289 eV is shown in grey. The corresponding satellite for naphthalene appears above 290 eV and is thus not visible in this plot. However, it can be seen in an extended plot in Fig. S3 of the Supplemental Material [44].

In the monolayer, the differences between the XP spectra of azulene and naphthalene are even more pronounced. As can be seen in Fig. 4(b), the naphthalene signal is shifted by only −0.2 eV relative to its multilayer position and is only slightly asymmetric. In contrast, the azulene peak shifts by −0.5 eV and develops a strong asymmetry. The asymmetric peak shape is attributed to the interaction of the C 1s core hole with electron density close to the Fermi edge [79]. This is an indication for a distinctly different electronic valence structure of azulene compared to naphthalene when adsorbed on Cu(111). In an initial-state picture, the shift of the C 1s signal of azulene towards lower binding energies suggests a transfer of negative charge from the surface to the molecule. Further evidence for a negative charging of the molecule will be presented below. In addition, the closer distance of the azulene molecule to the surface will likely cause increased final-state screening, which would also lead to a shift to lower binding energy.

Synchrotron-based valence photoelectron spectroscopy (PES) was used for the direct probing of the occupied valence electronic structure. In the PE spectra, the molecular states already occupied in the free molecules cannot be identified because they have binding energies above 2 eV and thus are obscured by the d-band of the substrate. Nevertheless, the important changes in the valence electronic structure close to the Fermi edge are quite visible [Fig. 4(c)]. For azulene/Cu(111), the entire range between the Cu d-band and the Fermi edge experiences a massive rise in intensity with a broad maximum around 0.3–0.4 eV. In contrast, naphthalene only causes attenuation of the region between 0 and 2 eV, including the surface state. The occurrence of broad, adsorbate-related features for azulene, but not for naphthalene, is consistent with the calculated densities of states, as will be discussed later.

Adsorbate-induced work-function changes were extracted from He-I UPS data and show that both azulene and naphthalene lower the work function of the Cu(111) surface. The change is larger for azulene with −1.07 eV than for naphthalene with −0.73 eV, both at full monolayer coverage. Apparently, azulene causes a larger vertical surface dipole upon adsorption than naphthalene, in agreement with the stronger intermolecular repulsion of azulene observed in TPD. The negative sign of the work-function change indicates that the pillow effect is dominant and overcompensates for any contributions by the charge transfer from the surface to the molecule.

D. Unoccupied electronic states: NEXAFS

Information about the unoccupied valence electronic structure of the adsorbed molecules is obtained from carbon K-edge NEXAFS spectra. Multilayers of both molecules show a distinct set of π^* and σ^* resonances, which are well reproduced by the theoretical calculations, as shown in Fig. 5.

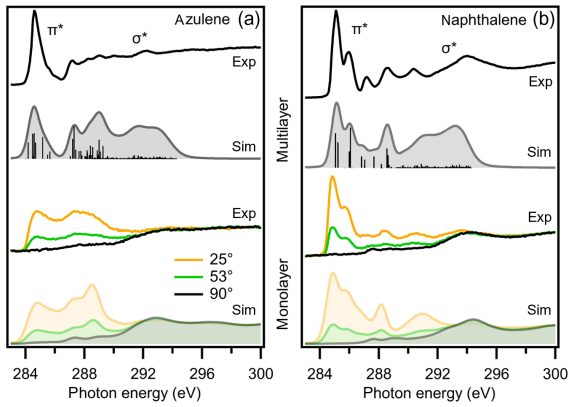

FIG. 5. Experimental carbon K-edge NEXAFS spectra and corresponding DFT simulations for (a) azulene and (b) naphthalene. Upper part: Multilayer spectra and simulations for the free molecule. The multilayer spectra were taken with the electric field vector oriented 90° relative to the surface normal. Lower part: Monolayer spectra and simulations for different angles of the electric field vector relative to the surface normal as indicated. The simulations for the free molecules are displayed both as isolated excitations and after broadening; the simulations for the monolayers are only shown in broadened form. For the broadening, each excitation is represented by a pseudo-Voigt peak with an increasing width and Lorentzian contribution at higher photon energies. The simulated spectra were shifted by −6.1 eV to match the experimental data.

In the monolayer spectra, the π^* resonances disappear when the electric field vector of the incident x rays is parallel to the surface (i.e., 90° relative to the surface normal). This shows that the molecular planes are parallel to the surface for both azulene and naphthalene.

In the case of naphthalene, the monolayer spectrum taken with the electric field vector oriented 25° relative to the surface normal closely resembles the multilayer spectrum; only a slight signal broadening is visible. This result confirms that the unoccupied valence electronic states of naphthalene are only weakly influenced by the metal surface.

For azulene, however, the shape of the π^* resonance is very different in the monolayer and multilayer spectra. The narrow π^* peak in the multilayer spectrum, resulting from the excitation into the LUMO and LUMO+1 of the azulene molecule, turns into a very broad monolayer feature, which is lower in intensity and covers a broad range of 5 eV. For both systems, the NEXAFS spectra are correctly reproduced by DFT-based transition potential simulations, which are discussed in detail later. A simpler approach for simulating NEXAFS spectra based only on ground-state properties can be found in the Supplemental Material [44].

E. Geometric structure: Scanning probe microscopies

Local information about the bonding situation of azulene as the model 5-7 structural element is obtained by scanning probe microscopies. These methods also provide valuable input for the DFT calculations discussed further below because there is no information in the literature about the adsorbate structure of azulene on Cu(111), in stark contrast to naphthalene [34–36,38,80]. In the low submonolayer range, azulene avoids the formation of ordered islands, in line with the strong lateral repulsion seen in TPD. Corresponding submonolayer STM and nc-AFM images are shown in Fig. S4 of the Supplemental Material [44]. When the coverage is increased, azulene eventually forms a long-range-ordered, commensurate $(2\sqrt{3}\times 2\sqrt{3})$-R30° superstructure [Fig. 6(a)]. This structure does not represent the saturated monolayer but has a coverage of only 0.65 ML. (Note that 1 ML is defined here as the coverage in the saturated monolayer as determined by TPD.) Upon deposition of additional molecules onto this commensurate structure, the molecules are even more closely packed but lose the long-range order. This case is illustrated in the nc-AFM image in Fig. 6(b), which still shows one unit cell of the commensurate $(2\sqrt{3}\times 2\sqrt{3})$-R30° structure in the image center. The molecules surrounding this unit cell, however, are more densely packed and break the translational symmetry.

Formation of a commensurate phase, which is followed by a more densely packed, incommensurate phase without long-range order at full monolayer coverage, has previously been found for other organic molecules with lateral intermolecular repulsion and preference of a certain adsorption

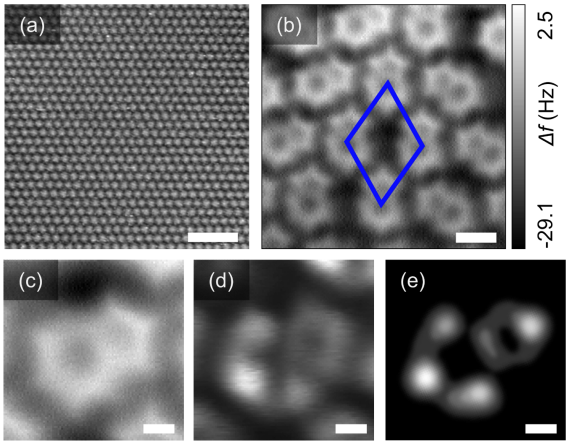

FIG. 6. STM and nc-AFM images of azulene on Cu(111). (a) Large-scale STM image of azulene on Cu(111), commensurate $(2\sqrt{3}\times 2\sqrt{3})$-R30° structure (0.65 ML), $I_t = -0.06$ nA $U_t = -1.28$ V, scale bar = 5 nm. (b) nc-AFM image of azulene on Cu(111), partially compressed phase (total coverage 0.78 ML), with an overlaid unit cell of the $(2\sqrt{3}\times 2\sqrt{3})$-R30° structure, scale bar = 0.5 nm. Note the disordered structure with higher density around the central unit cell of the commensurate structure. (c) nc-AFM image of an azulene molecule, (d) corresponding STM constant-height image, (e) DFT Tersoff-Hamann simulation of azulene adsorbed on Cu(111) within an energy range of 0 to 0.1 V below E_F. Scale bar for (c-e) = 0.1 nm.

site, such as porphine on Ag(111) [81]. The transition from the compressed quasidisordered phase to the commensurate $(2\sqrt{3} \times 2\sqrt{3})$-R30° phase during desorption is associated with the small maximum around 300 K in the TPD curve [Fig. 3(a)].

In the nc-AFM images, the two rings of the azulene molecule can clearly be distinguished, and thus its azimuthal orientation on the surface can be determined. In the $(2\sqrt{3} \times 2\sqrt{3})$-R30° unit cell, all molecules point along the $[1\bar{1}0]$ direction (and symmetry equivalent directions) of the substrate.

During the nc-AFM scans, naphthalene showed a higher tendency for tip-induced lateral displacements, whereas azulene was more resistant to accidental manipulation and only occasionally showed rotation by a 60° angle. Example images for both phenomena are shown in Figs. S5 and S6 of the Supplemental Material [44]. The reduced susceptibility of azulene for tip-induced displacement probably also means that it has a higher barrier for spontaneous diffusion.

In Figs. 6(c)–6(e), we compare an nc-AFM image of an adsorbed azulene molecule with the corresponding constant-height STM scan and with a DFT Tersoff-Hamann simulation [82]. The nc-AFM image in Fig. 6(c) shows the molecular structure with the five- and seven-membered rings. The STM current map in Fig. 6(d) was taken during the nc-AFM scan with negative sample bias (i.e., with electrons flowing from the sample to the tip) and shows well-defined features with lobes and nodes. Considering the bias voltage, these features must be attributed to an occupied state of the adsorbed azulene. They are well reproduced by a Tersoff-Hamann simulation using the DFT density of states (DOS) in the energy range from 0 to 0.1 eV below the Fermi energy [Fig. 6(e)]. The shape of this occupied state closely resembles that of the LUMO of the free molecule, as will be discussed in more detail below.

The difference in adsorption height between azulene and naphthalene as found by NIXSW was also measured on the single-molecule level by comparing the positions of the minima of frequency shift distance, i.e., $\Delta f(z)$ curves [83]. The inset of Fig. 7(a) shows a STM image of codeposited azulene and naphthalene molecules. Naphthalene appears as a single bright white feature, whereas azulene is imaged as a two-segmented grey shape. The vertical and lateral position at which the feedback loop was interrupted is the same for both molecules (above the metal, the STM set point of $V = 100$ mV and $I = 10$ pA corresponds to $z = 0$ Å). The minimum z_{min} in the $\Delta f(z)$ curve for azulene occurs 0.92 ± 0.08 Å closer to the substrate than for naphthalene. This difference is highly reproducible for different tip terminations and molecules. Considering the margins of error, this value is only slightly larger than the difference in the NIXSW heights of 0.74 ± 0.06 Å. The deviation between NIXSW and AFM values is possibly a temperature-related effect or due to small influences of the AFM tip.

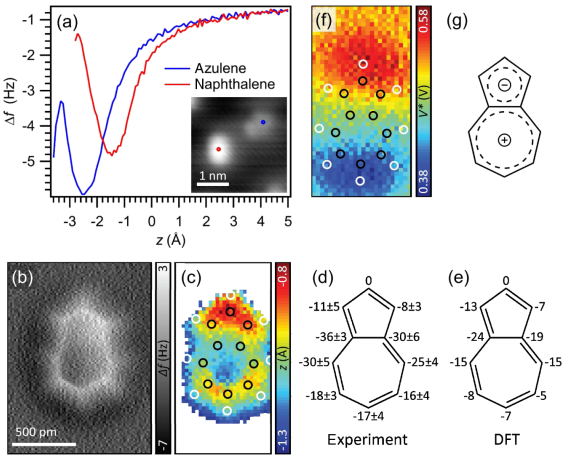

FIG. 7. (a) $\Delta f(z)$ spectra over azulene and naphthalene molecules illustrating the difference in z_{min}, which is indicative of the difference in adsorption height. The inset is an STM image, where the blue and red dots indicate the positions at which the $\Delta f(z)$ spectra were taken. The STM image was acquired with $I_t = 10$ pA at $U_t = 100$ mV. (b) Constant-height nc-AFM image of a single azulene molecule at −180 pm w.r.t. an STM set-point of 10 pA at 100 mV. (c) z_{min} map of azulene, overlaid with carbon (black) and hydrogen (white) atom positions. (d) Experimentally obtained z_{min} height of all C atoms with respect to the C atom at the apex of the 5-membered ring, in pm. (e) z_{min} heights of all C atoms with respect to the nose-C atom calculated by DFT, in pm. (f) KPFM map of a single azulene molecule, overlaid with carbon (black) and hydrogen (white) atom positions. (g) Model of the azulene molecule indicating the direction of the dipole moment.

The AFM-based height measurements also reveal a substantial adsorption-induced deformation of the azulene molecule. Figure 7(b) shows a constant-height nc-AFM image of azulene, in which the 5-7-ring structure is clearly resolved. The corresponding Fig. 7(c) shows a map with the lateral variation of z_{min}, indicating that the apices of the 5- and 7-membered rings are located farther away from the surface than the C─C bond that joins the two rings. This V-shaped adsorption geometry is later confirmed by DFT calculations [Figs. 7(e) and 8]. A detailed comparison of the relative heights as extracted from the AFM experiments and DFT calculations is given in Figs. 7(d) and 7(e). The value for the atom with the highest position is set to zero. Both in the experiment and in theory, one long side of the molecule is located somewhat closer to the surface than the other. These results demonstrate that AFM can be used to detect vertical relaxations in single molecules in the range of a few pm.

The free azulene molecule has a considerable in-plane dipole moment of 0.8 D [67]. To establish whether azulene adsorbed on Cu(111) still has an in-plane dipole moment, we performed Kelvin probe force microscopy (KPFM) experiments [83–85]. The maps extracted from these experiments show how the local contact potential

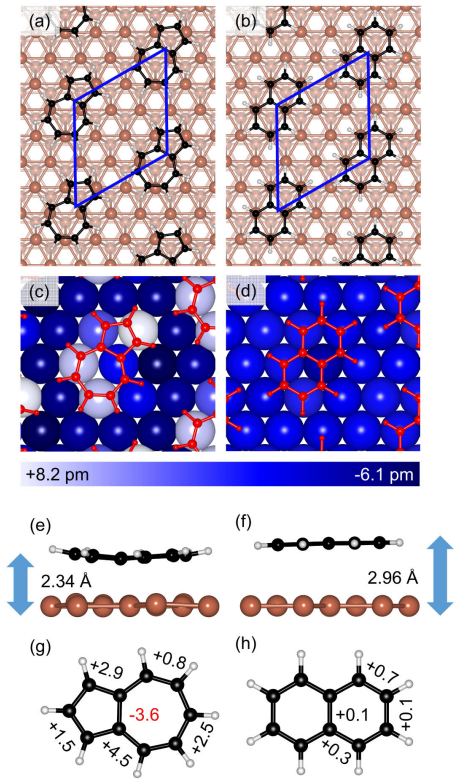

FIG. 8. Structural data for azulene and naphthalene on Cu(111) from dispersion-corrected DFT-D3 calculations. (a,b) Top view of the optimized $(2\sqrt{3}\times 2\sqrt{3})$-R30° structure. The most favorable adsorption site for both molecules is hcp-hcp. (c,d) Vertical displacements (in pm) of the copper atoms in the topmost layer, compared to the relaxed surface without a molecule. Positive values mean a displacement towards the molecule. (e,f) Side view of the molecule in the optimized $(2\sqrt{3}\times 2\sqrt{3})$-R30° structure. Azulene shows a large distortion and is much closer to the surface than naphthalene (average adsorption height 2.34 Å vs 2.96 Å). (g,h) Changes of the in-plane bond lengths relative to the gas phase structure (in pm).

difference varies. This quantity is related to the electrostatic potential above the sample [84]. The KPFM maps presented here are obtained from finding the maximum (V^*) of $\Delta f(V)$ curves extracted from a set of constant-height AFM images at increasing bias [85]. Figure 7(f) presents a V^* map of a single azulene molecule. The V^* for the 5-membered ring is about +0.52 V, while for the 7-membered ring, it is +0.42 V. The value of V^* represents the voltage needed to minimize the electrostatic interaction between the tip and the molecule. Above the 5-membered (7-membered) ring, a larger (smaller) positive voltage is needed to compensate for the presence of the negative (positive) charge. From the V^* data shown in Fig. 7(f), it is evident that the adsorbed molecule has an in-plane dipole along the long molecular axis, pointing from the 5- to the 7-membered ring. The magnitude of the retained dipole moment cannot be extracted from such experiments [86].

F. Theoretical analysis

For additional insight into the surface chemical bond of azulene and naphthalene, dispersion-corrected periodic density functional theory calculations (DFT-D3) [53] were performed for the ordered $(2\sqrt{3}\times 2\sqrt{3})$-R30° structure, which was found in the STM images of azulene/Cu(111) [Fig. 6(a)]. This structure is not observed for naphthalene/Cu(111), but as the $(2\sqrt{3}\times 3)$-Rect structure known in the literature has the same coverage, it is also used here for better comparability [34,36]. For both molecules, the same preferential adsorption site is found. In this geometry, the molecules adsorb with each ring above an hcp hollow site, as shown in Figs. 8(a) and 8(b). This result is in agreement with the nc-AFM data, which show that the molecules are aligned along a principal direction of the surface, which is also the case with this adsorption site.

Closer inspection of the adsorbate geometries reveals that the azulene molecule and the top layer of the surface undergo substantial adsorption-induced deformations. The surface copper atoms in the unit cell differ in height by up to 0.14 Å, as is visualized in Fig. 8(c). For comparison, naphthalene does not cause any significant deformation of the surface [Fig. 8(d)]. Azulene experiences an out-of-plane deformation, which brings the bridging carbon atoms closer to the surface than the apex atoms of the rings [Fig. 8(e)]. This was also observed with nc-AFM [Figs. 7(c) and 7(d)]. In addition, azulene shows extensive changes of the in-plane bond lengths, in particular, a shortening of the bridging bond (−3.6 pm) and elongations of the other bonds (up to +4.5 pm). This can be explained by electron donation into the LUMO [as shown in Fig. 9(a)] because its bonding and antibonding contributions agree with the pattern in the bond length changes. In the case of naphthalene, the adsorption-induced deformations are much smaller [Figs. 8(d), 8(f), and 8(h)].

The adsorption height was calculated as the distance between the average height of the carbon atoms and the relaxed height of the first substrate layer without a molecule. For naphthalene, this approach gives a height of 2.96 Å, which is only slightly smaller than the sum of the van der Waals radii of a carbon and a copper atom (3.10 Å) and thus is consistent with the van der Waals character of the naphthalene-copper interaction. In the case of azulene, the calculated distance of 2.33 Å is closer to the sum of the covalent radii of a carbon and a copper atom (2.20 Å), in line with the much stronger bond of azulene. Both calculated values are in excellent agreement with the NIXSW results of 2.30 Å for azulene and 3.04 Å for naphthalene.

In this comparison, we have considered that the standing x-ray wave is formed by the bulk lattice planes, and therefore, the experimental height value is the distance

between the carbon atoms of the molecule and the ideal, unrelaxed surface layer. For Cu(111), the vertical relaxation of the adsorbate-covered first layer proved to be very small in our calculations (less than 0.01 Å), and thus the relaxation correction is actually negligible.

In the electronic adsorption energies yielded by the DFT-D3 calculations, azulene shows a much higher value than naphthalene, $E_{ads} = -1.79$ eV and -1.40 eV, respectively. When zero-point vibrational energy (ZPVE) corrections are taken into account, the energy for azulene increases to $E_{ads} = -1.87$ eV, while there is no change for naphthalene (because its vibrational frequencies are much less influenced by the adsorption). To compare these DFT results with TPD data, we must use the integral desorption energy at the coverage of the $(2\sqrt{3} \times 2\sqrt{3})$-R30° structure used in the DFT calculations (0.65 ML) and make the (here very reasonable) assumption that the adsorption of azulene and naphthalene has no activation barrier. The corresponding experimental energies are 1.58 eV for azulene and 0.93 eV for naphthalene [see Fig. 3(c), dashed lines]. In comparison, theory overestimates the adsorption energy by 0.29 eV for azulene and by 0.47 eV for naphthalene, which is in the range of expected deviations of current DFT methods [87]. In particular, dispersion-corrected DFT adsorption energies of molecules on metal surfaces are typically overestimated and usually show errors of this magnitude [88,89].

DFT also provides additional insight into the valence electronic structure of the adsorbed molecules. For azulene/Cu(111), the carbon-projected DOS in Fig. 9(e) shows a substantial density of states spread out over a large energy window around E_F, with only small variations in magnitude. In contrast, naphthalene has a clear gap in the carbon-projected DOS between -1.4 and $+0.5$ eV [Fig. 9(f)]. Both findings are in agreement with the UPS data in Fig. 4(c). The reason for this different behavior is related to azulene's low-lying LUMO, which is very close to the Fermi edge of Cu(111), as shown in Fig. 9(e). As a result, the LUMO is pulled below E_F and is partially filled with electrons from the surface, as can be seen in the charge density difference plot [Figs. 9(a) and 9(b)]. Comparison with a related plot for naphthalene using the same isosurface value shows no visible charge transfer [see Figs. 9(c) and 9(d)]. If a much lower isosurface value is chosen, the so-called pillow effect (i.e., the pushback of electron density between the molecule and surface caused by Pauli repulsion [71]) can be seen for both molecules, but it is much larger for azulene. These additional charge density difference plots are shown in Fig. S7 of the Supplemental Material [44].

The participation of the frontier orbitals in the surface chemical bond is illustrated in Figs. 10(a) and 10(b), which show the DOS projected onto the molecular orbitals of the free molecules. Again, drastic differences can be seen between azulene and naphthalene. The frontier orbitals of azulene [Fig. 10(a)] undergo substantial energetic broadening in the adsorbed state. As a result, the LUMO and

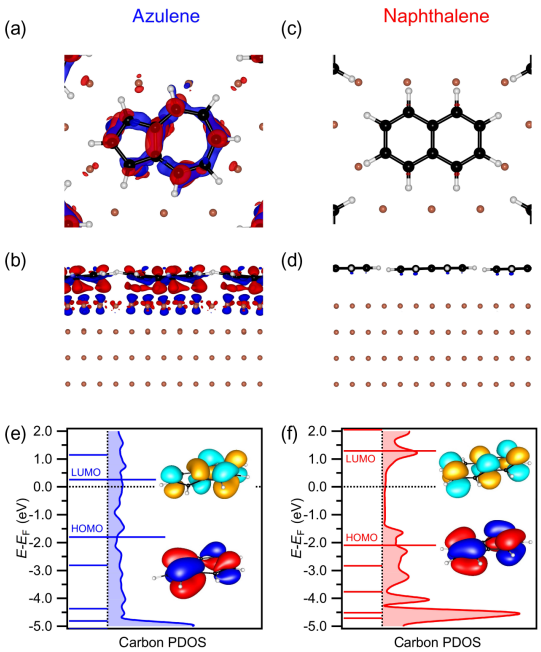

FIG. 9. Electronic structure of azulene and naphthalene on Cu(111) from DFT calculations. (a,b) Charge density difference plots for azulene. (c,d) Charge density difference plots for naphthalene. The isosurface value is 0.003 $e^-/$Å; electrons flow from blue to red. In panel (a), electron enrichment in the shape of the LUMO is clearly visible. (e,f) Carbon partial density of states of the adsorbed species. The horizontal bars represent the energies of the frontier orbitals of the free molecules. These energy levels are shifted to align the lowest valence orbitals for the free and the adsorbed molecules. The figure also shows images of the HOMO and LUMO as calculated by DFT.

LUMO+1 levels show large contributions below the Fermi energy. In the case of naphthalene, the frontier orbitals are much less broadened and the LUMO remains well above the Fermi energy.

The adsorption-induced changes in the valence electronic structure also have important consequences for the NEXAFS spectra, as can be seen in the MO-projected NEXAFS simulations [Figs. 10(c)–10(f)]. The LUMO and LUMO+1 contributions are greatly reduced for azulene, when adsorbed on Cu(111), because these orbitals are now partially occupied and therefore are not fully available for an excitation anymore. For naphthalene, adsorption does not result in substantial spectral changes. Note that the MO contributions do not seem to add up to the total spectrum for azulene on Cu(111) [Fig. 10(e)]. Because of the strong hybridization between the molecular orbitals and the surface, as well as final-state screening effects, the spectral contributions from states with ground-state molecular orbital character are much smaller than for the weakly interacting naphthalene.

The hybridization of the frontier orbitals also has consequences for the charge redistribution between the

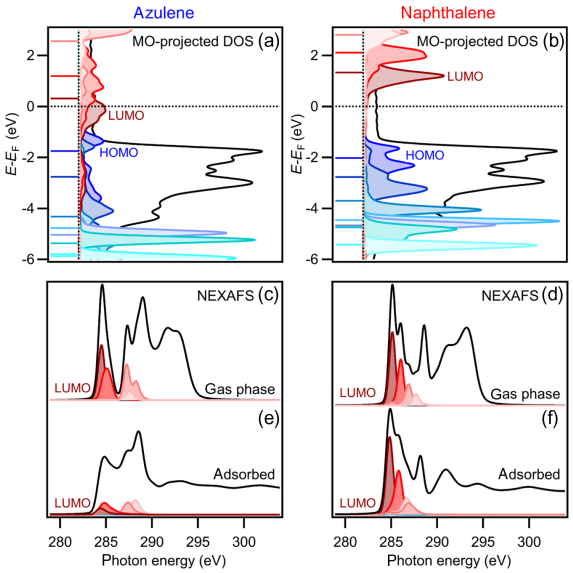

FIG. 10. MO projection analysis, left azulene, right naphthalene. Contributions of the LUMO are shown in dark red and of the HOMO in blue; higher and lower orbitals are shown in incrementally lighter colors. Total DOS and total spectrum are shown in black. (a,b) TDOS and MO-projected density of states of the adsorbed species with the energies of the molecular frontier orbitals. The nonvanishing TDOS around the Fermi energy is caused by the metal substrate. (c,d) MO-projected NEXAFS simulations of the free molecules. (e,f) MO-projected NEXAFS simulations of the adsorbed molecules. The simulated spectra are shifted by −6.1 eV to match the experimental data in Fig. 5.

surface and the molecule. The charge transfer is quantified using two different methods. The Bader analysis method [90] predicts that azulene receives 0.49 negative elementary charges (e^-) from the surface, resulting in a net negative charge at the molecule. In contrast, naphthalene shows only a very small charge transfer of 0.06 e^- from the molecule to the surface, i.e., in the opposite direction. Using an alternative approach, we integrate the MO projection in Figs. 10(a) and 10(b) up to E_F, including the pulled-down contributions of LUMO and LUMO+1. The resulting excess charges (negative charges) on the molecules are 1.39 e^- for azulene and 0.13 e^- for naphthalene, respectively. Both methods thus indicate a significant surface-to-molecule charge transfer. The partial charge is not an observable property, and it is well known that different methods give different absolute values. The chemisorbed character of azulene on Cu(111) means that separation of molecule and surface electronic states is not straightforward, either in real or in orbital space. However, the considerable effects observed in the NEXAFS spectrum of azulene upon adsorption indicate that the magnitude of charge transfer is probably larger than predicted by the Bader analysis method.

IV. DISCUSSION

The combined TPD, NIXSW, PES, NEXAFS, nc-AFM, and DFT results provide a consistent picture of the surface chemical bond of azulene and naphthalene on Cu(111). Azulene, as a prototypical 5-7 system, forms a strong chemical bond to the copper surface, whereas naphthalene as a 6-6 system is only physisorbed. This difference is related to the topology of the π-electron system. In naphthalene, the π system has an alternant topology, which means that all carbon atoms can be divided into two disjoint sets, such that an atom of one set binds only to atoms of the other set [14]. All aromatic systems with 6-membered rings, the benzoid systems, are alternant. In contrast, the 5-7π system of azulene has a nonalternant topology [Fig. 11(a)].

Alternant and nonalternant π systems show fundamental differences in the electronic structure. The Coulson-Rushbrooke theorem, which states that the energy levels of the aromatic π system are symmetrically distributed, is

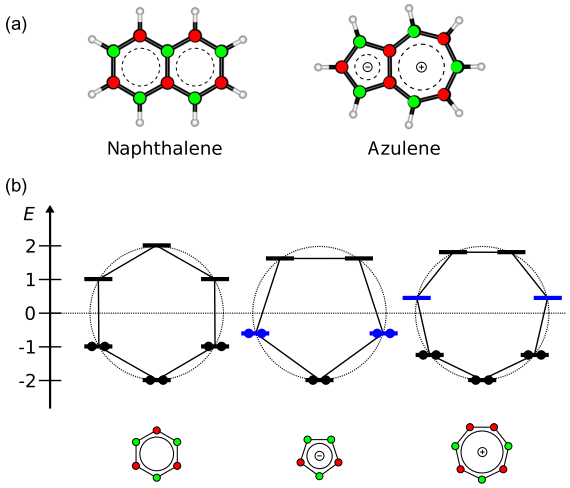

FIG. 11. (a) Alternating labeling of the carbon atoms (red, green), illustrating that the 6-6 system has an alternant and the 5-7 system has a nonalternant π system. The dipole moment of the 5-7 system can also be understood as a consequence of the Hückel $4n+2$ rule for aromatic systems [91], which requires transfer of one electron from the heptagon to the pentagon, such that an aromatic sextet (Clar sextet) can be formed [92]. (b) Frost-Musulin diagrams [93] for 6-, 5-, and 7-membered cyclic π systems. The HOMO level of the 5-membered ring and the LUMO level of the 7-membered ring are highlighted in blue. All π-MO energies lie on a circle, which is centered at the Coulomb integral α and has the radius of 2 times the Hückel exchange integral β. The energy scale is in units of x, with $x \equiv (\alpha - \varepsilon)/\beta$, where ε is the π-MO energy. Only the 6-membered ring is alternant and fulfills the Coulson-Rushbrooke theorem. In the 5-membered system, the HOMO is lifted, and in the 7-membered system, the LUMO is lowered. The hexagon has a neutral closed-shell state, whereas the pentagon and the heptagon form a closed-shell anion and cation, respectively.

violated by nonalternant species [14,94]. While alternant aromatic molecules have highly delocalized π orbitals, these orbitals are more localized in nonalternant molecules.

The concept of alternant and nonalternant cyclic π-conjugated systems is visualized in Fig. 11(b), which compares the Frost-Musulin energy diagrams for 5-, 6-, and 7-membered cyclic π systems [93]. As can be seen, the 6-membered ring is alternant, and its π-orbital energies are paired, such that each occupied bonding orbital with energy $-E$ has an empty antibonding counterpart with energy $+E$. This symmetry is broken for nonalternant 5- and 7-membered π systems. As one of the consequences, the HOMO of the 5-membered ring is lifted, whereas the LUMO of the 7-membered ring is lowered, compared to the 6-membered, alternant system.

Qualitatively, the electronic structure of azulene can be viewed as a combination of 5- and 7-membered π systems. From this consideration, one would expect that the HOMO-LUMO gap of azulene is considerably smaller than that of the corresponding system with two 6-membered rings, naphthalene. The increased HOMO energy should make azulene a better donor, and the reduced LUMO energy a better acceptor, than naphthalene. In addition, the frontier orbitals should be somewhat localized, with increased contributions of the 5-membered ring to the HOMO and of the 7-membered ring to the LUMO.

These anticipated properties are in agreement with the experimental observations. The localization of HOMO and LUMO in azulene causes a molecular dipole moment of 0.8 D [67], which is a very large value for a simple hydrocarbon without heteroatoms. In contrast, naphthalene has no dipole moment. The HOMO-LUMO gap of azulene is 2.1 eV, compared to 3.5 eV for naphthalene, as calculated by DFT.

With respect to the adsorption behavior of azulene, the energetic shift of the frontier orbitals, especially the down-shift of the LUMO, leads to the described accessibility for electron donation from the surface into the LUMO and thus to the much stronger chemical bond to the Cu(111) surface. The partial occupation of the LUMO also explains some of the adsorption-induced deformations, especially the striking shortening of the bridging bond [see Fig. 8(g)] because the LUMO is bonding while the HOMO is antibonding between the two shared C atoms [see Fig. 9(e)].

As pointed out above, the special electronic structure of azulene and the resulting strong surface chemical bond are by no means a coincidence but a consequence of the topology of its π system, which is fundamentally different from that of naphthalene. We expect this to hold true wherever this structural element occurs, whether it be in a molecule, a graphene nanoribbon, or another π-electron system. The limitations of this molecular model system are discussed in the following for a system that is, in many ways, furthest removed from the molecules investigated: defects in an infinite graphene lattice.

The 5-7 defects embedded in the graphene lattice have the same topology as azulene, whereas the regular graphene lattice has the same topology as naphthalene (Fig. 1). Therefore, we expect the 5-7 defects in graphene to have a much stronger and more localized interaction with a metal substrate than the regular graphene. It is also possible that metal atoms deposited onto graphene bind more strongly to 5-7 defects than to regular lattice sites. In addition, electron transfer from the substrate is more likely to occur at the 5-7 defects than at defect-free areas.

Compared to a 5-7 defect in substrate-supported graphene, our molecular system, azulene, differs in two important points. First, the π system in azulene is terminated by hydrogen atoms, and thus the area of π-electron delocalization is spatially confined. In contrast, the 5-7 defect in a graphene layer is embedded in the π system of graphene, making the area of delocalization much larger. However, it is important to keep in mind that the effect of the topological symmetry break caused by the 5-7 defect is a spatial localization and energetic lowering of electronic states. These effects should also occur in the extended structure because the symmetry break is also present there. To verify this assumption, we performed periodic DFT calculations for a 5-7 defect embedded in a freestanding graphene layer. As can be seen in a section through the charge density, the defect interrupts the homogeneous charge distribution present in the defect-free graphene [Fig. 12(a)] and accumulates negative charge at the 5-membered ring and positive charge at the 7-membered ring [Fig. 12(b)]. The local charge accumulation on the embedded 5-7 defect, as quantified by the Hirshfeld charge analysis [95], has a similar magnitude as in the isolated 5-7 system of azulene (see the Supplemental Material [44] for details). The graphene with the embedded defect also shows additional DOS in the vicinity of the Fermi energy [Fig. 12(c)].

Another difference between the molecular nonalternant system and a 5-7 defect in an adsorbed graphene layer will be apparent in the adsorption height. While azulene can always adopt its equilibrium height, the 5-7 defect embedded in the graphene lattice (or in another extended aromatic system) will be pulled closer to the surface, but it will also be held back by the surrounding regular graphene lattice (or other alternant structure), which resides at a larger distance. This competition may further influence the electronic interaction with the substrate and related effects, such as electron transfer. Nevertheless, the molecular nonalternant system of azulene represents a highly valuable model for extended aromatic systems with embedded nonalternant structural elements because reliable quantitative information such as local interaction energies and adsorption heights are very difficult to obtain for defects in extended π-conjugated systems with the presently available experimental and theoretical methods.

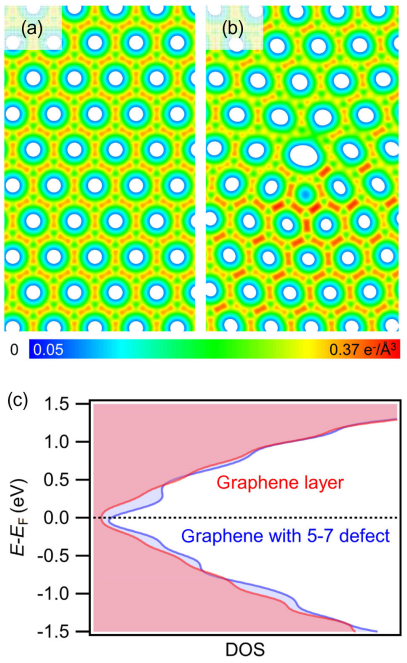

FIG. 12. Results of periodic DFT calculations for a freestanding graphene layer with and without 5-7 defects. (a) The section through the charge density for the planar ideal graphene layer and (b) the section through the charge density for the planar graphene layer with a 5-7 defect. As can be seen, the 5-7 defect accumulates negative charge (red) at the 5-membered ring and positive charge (blue/white) at the 7-membered ring. Only part of the unit cell is shown. For a complete view, see Fig. S9 of the Supplemental Material [44]. (c) Total density of states for both systems. The DOS of the defect structure shows new states around the Fermi energy. The nonzero DOS at E_F for both systems is caused by the employed electronic smearing and is a known artifact of the method [96,97].

V. CONCLUSIONS

Azulene as a nonalternant aromatic hydrocarbon forms a much stronger chemical bond to the Cu(111) surface than naphthalene as its alternant isomer. This result follows from the very different low-coverage TPD peak temperatures (520 K for azulene vs 340 K for naphthalene) and from the resulting zero-coverage desorption energy, which is much higher for azulene (1.86 eV) than for naphthalene (1.07 eV). The same trend is seen in the vertical bonding distances (adsorption heights) as measured by NIXSW and nc-AFM. The NIXSW value of 2.30 Å for azulene is much smaller than the sum of the van der Waals radii and agrees with the formation of a real chemical bond. In contrast, the height of 3.04 Å found for naphthalene is consistent with pure physisorption. The distances calculated by dispersion-corrected DFT agree very well with the measured heights. The calculations also show that both azulene and the surface underneath undergo substantial distortion (as is confirmed by AFM experiments), while naphthalene remains almost undistorted. Repulsive interactions between the adsorbed azulene molecules lead to a strongly coverage-dependent desorption energy, which follows the equation $E_d = (1.86 - 0.67\Theta - 0.40\Theta^2)$ eV. Naphthalene shows less repulsion, and its desorption energy is well described by the equation $E_d = (1.07 - 44\Theta)$ eV. Effects of the intermolecular repulsion are also visible in the submonolayer STM images. The work-function change at monolayer coverage is higher for azulene (−1.07 eV) than for naphthalene (−0.73 eV), indicating that azulene forms the larger surface dipole. The higher intermolecular repulsion seen for azulene is therefore likely related to increased dipole-dipole repulsion.

The differences in the surface chemical bonds of azulene and naphthalene can be rationalized on the basis of the different topologies of the molecular π systems. Because of its violation of the Coulson-Rushbrooke theorem, azulene has a low-lying LUMO, which is close to the Fermi energy of copper. This fact leads to a strong hybridization between the LUMO and electronic states of the surface, as well as electron transfer from the surface into the LUMO. This electron transfer is confirmed by various experimental data: Probing the occupied states, the UP spectra of azulene on Cu(111) show an adsorption-induced, broad feature below the Fermi edge. Complementary NEXAFS studies of the unoccupied states reveal strong changes in the π^* resonance, which is attenuated and broadened. Theoretical analysis shows that the new broad feature in the occupied range is related to the former LUMO and other formerly unoccupied orbitals, while the changes in the NEXAFS are due to the partial occupation of the LUMO and LUMO+1 orbitals. In addition, submolecularly resolved STM images of azulene show the shape of the former LUMO at negative bias, which confirms that this orbital is filled with electrons. This finding is also supported by STM simulations. Theoretical analysis indicates a pronounced redistribution of charge in the case of azulene and a substantial charge transfer from the surface to the molecule. In contrast, the electronic structure of naphthalene is only slightly influenced by the surface, in line with its weaker and longer surface chemical bond.

Our results show that the topology of an aromatic π system greatly influences its interaction with a metal surface. In particular, structural elements with the nonalternant 5-7 topology can form much stronger surface chemical bonds than elements with the regular, alternant 6-6 topology. This may be true not only for aromatic molecules but also for all occurrences of nonalternant topology in carbon-based nanostructures on surfaces, in graphene nanoribbons or, in the form of 5-7 defects, in graphene itself. For all of these structures, we predict a localized surface chemical bond and local electron transfer between the substrate and adsorbate. In addition, our findings may be relevant for the optimization of the

metal-organic interfaces that occur at electrodes in organic electronic devices. They suggest that modifying the topology of the molecular π system represents a possible way to tune performance-related parameters such as wave-function overlap and energy-level alignment at the electrode-semiconductor interface.

ACKNOWLEDGMENTS

Funded by the Deutsche Forschungsgemeinschaft (DFG, German Research Foundation)-Projektnummer 223848855-SFB 1083. We thank the synchrotron radiation facilities BESSY-II of the Helmholtz-Zentrum für Materialien und Energie, Berlin, for allocation of beam time at the beam lines HE-SGM and PM4/LowDosePES and for financial support. The experimental support by E. Giangrisostomi and R. Ovsyannikov is gratefully acknowledged. Furthermore, we thank Diamond Light Source for access to beam line I09 (Proposal No. SI16259), and the I09 beam-line staff (T.-L. Lee, P. K. Thakur, and D. McCue) for their support during the experiment. We acknowledge computational resources from HLR Stuttgart, CSC-LOEWE Frankfurt, and HRZ Marburg.

[1] J. E. Anthony, *The Larger Acenes: Versatile Organic Semiconductors*, Angew. Chem. Int. Ed. **47**, 452 (2008).

[2] A. Mishra and P. Bäuerle, *Small Molecule Organic Semiconductors on the Move: Promises for Future Solar Energy Technology*, Angew. Chem. **51**, 2020 (2012).

[3] J. H. Burroughes, D. D. C. Bradley, A. R. Brown, R. N. Marks, K. Mackay, R. H. Friend, P. L. Burns, and A. B. Holmes, *Light-Emitting Diodes Based on Conjugated Polymers*, Nature (London) **347**, 539 (1990).

[4] A. Pron and P. Rannou, *Processible Conjugated Polymers: From Organic Semiconductors to Organic Metals and Superconductors*, Prog. Polym. Sci. **27**, 135 (2002).

[5] Z. Chen, Y.-M. Lin, M. J. Rooks, and P. Avouris, *Graphene Nano-ribbon Electronics*, Physica E **40**, 228 (2007).

[6] B. H. Nguyen and V. H. Nguyen, *Promising Applications of Graphene and Graphene-based Nanostructures*, Adv. Nat. Sci. Nanosci. Nanotechnol. **7**, 023002 (2016).

[7] *Concepts in Molecular and Organic Electronics*, MRS Proceedings, edited by N. Koch, E. Zojer, S.-W. Hla, and X. Zhu (Cambridge University Press, Cambridge, England, 2014).

[8] *Organic Electronics: Materials, Manufacturing, and Applications*, edited by H. Klauk (Wiley-VCH, Weinheim, 2006).

[9] *Organic Electronics II: More Materials and Applications*, edited by H. Klauk (Wiley-VCH, Weinheim, 2012).

[10] J. M. Gottfried, *Quantitative Model Studies for Interfaces in Organic Electronic Devices*, New J. Phys. **18**, 111002 (2016).

[11] A. Kahn, N. Koch, and W. Gao, *Electronic Structure and Electrical Properties of Interfaces between Metals and π-conjugated Molecular Films*, J. Polym. Sci. B **41**, 2529 (2003).

[12] N. Koch, *Organic Electronic Devices and Their Functional Interfaces*, Chem. Phys. Chem. **8**, 1438 (2007).

[13] K. Rüdenberg, *Quantum Mechanics of Mobile Electrons in Conjugated Bond Systems. III. Topological Matrix as Generatrix of Bond Orders*, J. Chem. Phys. **34**, 1884 (1961).

[14] R. B. Mallion and D. H. Rouvray, *The Golden Jubilee of the Coulson-Rushbrooke Pairing Theorem*, J. Math. Chem. **5**, 1 (1990).

[15] M. Liu, M. Liu, Z. Zha, J. Pan, X. Qiu, T. Li, J. Wang, Y. Zheng, and D. Zhong, *Thermally Induced Transformation of Nonhexagonal Carbon Rings in Graphene-like Nanoribbons*, J. Phys. Chem. C **122**, 9586 (2018).

[16] J. Hieulle, E. Carbonell-Sanrom, M. Vilas-Varela, A. Garcia-Lekue, E. Guitin, D. Peña, and J. I. Pascual, *On-surface Route for Producing Planar Nanographenes with Azulene Moieties*, Nano Lett. **18**, 418 (2018).

[17] A. Shiotari, T. Nakae, K. Iwata, S. Mori, T. Okujima, H. Uno, H. Sakaguchi, and Y. Sugimoto, *Strain-induced Skeletal Rearrangement of a Polycyclic Aromatic Hydrocarbon on a Copper Surface*, Nat. Commun. **8**, 16089 (2017).

[18] S. Mishra, T. G. Lohr, C. A. Pignedoli, J. Liu, R. Berger, J. I. Urgel, K. Müllen, X. Feng, P. Ruffieux, and R. Fasel, *Tailoring Bond Topologies in Open-Shell Graphene Nanostructures*, ACS Nano, **12**, 11917 (2018).

[19] H. Xin and X. Gao, *Application of Azulene in Constructing Organic Optoelectronic Materials: New Tricks for an Old Dog*, Chem. Plus Chem. **82**, 945 (2017).

[20] Y. Yamaguchi, M. Takubo, K. Ogawa, K.-i. Nakayama, T. Koganezawa, and H. Katagiri, *Terazulene Isomers: Polarity Change of OFETs through Molecular Orbital Distribution Contrast*, J. Am. Chem. Soc. **138**, 11335 (2016).

[21] P. Y. Huang, C. S. Ruiz-Vargas, A. M. van der Zande, W. S. Whitney, M. P. Levendorf, J. W. Kevek, S. Garg, J. S. Alden, C. J. Hustedt, Y. Zhu, J. Park, P. L. McEuen, and D. A. Muller, *Grains and Grain Boundaries in Single-Layer Graphene Atomic Patchwork Quilts*, Nature (London) **469**, 389 (2011).

[22] F. Banhart, J. Kotakoski, and A. V. Krasheninnikov, *Structural Defects in Graphene*, ACS Nano **5**, 26 (2011).

[23] J. Červenka and C. F. J. Flipse, *Structural and Electronic Properties of Grain Boundaries in Graphite: Planes of Periodically Distributed Point Defects*, Phys. Rev. B **79**, 195429 (2009).

[24] N. M. R. Peres, F. Guinea, and A. H. C. Neto, *Electronic Properties of Disordered Two-Dimensional Carbon*, Phys. Rev. B **73**, 125411 (2006).

[25] R. Grantab, V. B. Shenoy, and R. S. Ruoff, *Anomalous Strength Characteristics of Tilt Grain Boundaries in Graphene*, Science **330**, 946 (2010).

[26] Y. Wei, J. Wu, H. Yin, X. Shi, R. Yang, and M. Dresselhaus, *The Nature of Strength Enhancement and Weakening by Pentagon-Heptagon Defects in Graphene*, Nat. Mat. **11**, 759 (2012).

[27] J. Červenka, M. I. Katsnelson, and C. F. J. Flipse, *Room-Temperature Ferromagnetism in Graphite Driven by Two-dimensional Networks of Point Defects*, Nat. Phys. **5**, 840 (2009).

[28] S. Malola, H. Häkkinen, and P. Koskinen, *Structural, Chemical, and Dynamical Trends in Graphene Grain Boundaries*, Phys. Rev. B **81**, 165447 (2010).

[29] K. Müller, A. P. Seitsonen, T. Brugger, J. Westover, T. Greber, T. Jung, and A. Kara, *Electronic Structure of an Organic/Metal Interface: Pentacene/Cu(110)*, J. Phys. Chem. C **116**, 23465 (2012).

[30] F. S. Tautz, *Structure and Bonding of Large Aromatic Molecules on Noble Metal Surfaces: The Example of PTCDA*, Prog. Surf. Sci. **82**, 479 (2007).

[31] E. Umbach, *Characterization of Organic Overlayers on Well-Defined Substrates*, Prog. Surf. Sci. **35**, 113 (1990).

[32] K. Seki, N. Hayashi, H. Oji, E. Ito, Y. Ouchi, and H. Ishii, *Electronic Structure of Organic/Metal Interfaces*, Thin Solid Films **393**, 298 (2001).

[33] *The Molecule-Metal Interface*, edited by N. Koch, N. Ueno, and A. T. S. Wee (Wiley-VCH, New York, 2013).

[34] T. Yamada, M. Shibuta, Y. Ami, Y. Takano, A. Nonaka, K. Miyakubo, and T. Munakata, *Novel Growth of Naphthalene Overlayer on Cu(111) Studied by STM, LEED, and 2PPE*, J. Phys. Chem. C **114**, 13334 (2010).

[35] L.-J. Wan and K. Itaya, *In Situ Scanning Tunneling Microscopy of Benzene, Naphthalene, and Anthracene Adsorbed on Cu(111) in Solution*, Langmuir **13**, 7173 (1997).

[36] R. Forker, J. Peuker, M. Meissner, F. Sojka, T. Ueba, T. Yamada, H. S. Kato, T. Munakata, and T. Fritz, *The Complex Polymorphism and Thermodynamic Behavior of a Seemingly Simple System: Naphthalene on Cu(111)*, Langmuir **30**, 14163 (2014).

[37] S. Lukas, S. Vollmer, G. Witte, and C. Wöll, *Adsorption of Acenes on Flat and Vicinal Cu(111) Surfaces: Step Induced Formation of Lateral Order*, J. Chem. Phys. **114**, 10123 (2001).

[38] H. Wang, G. Dutton, and X. Y. Zhu, *Electronic Structure at Organic/Metal Interfaces: Naphthalene/Cu(111)*, J. Phys. Chem. B **104**, 10332 (2000).

[39] H. Tetlow, J. P. de Boer, I. J. Ford, D. D. Vvedensky, J. Coraux, and L. Kantorovich, *Growth of Epitaxial Graphene: Theory and Experiment*, Phys. Rep. **542**, 195 (2014).

[40] L. Gao, J. R. Guest, and N. P. Guisinger, *Epitaxial Graphene on Cu(111)*, Nano Lett. **10**, 3512 (2010).

[41] X. Li, C. W. Magnuson, A. Venugopal, J. An, J. W. Suk, B. Han, M. Borysiak, W. Cai, A. Velamakanni, Y. Zhu, L. Fu, E. M. Vogel, E. Voelkl, L. Colombo, and R. S. Ruoff, *Graphene Films with Large Domain Size by a Two-Step Chemical Vapor Deposition Process*, Nano Lett. **10**, 4328 (2010).

[42] Q. Fan, J. M. Gottfried, and J. Zhu, *Surface-Catalyzed C–C Covalent Coupling Strategies Toward the Synthesis of Low-Dimensional Carbon-Based Nanostructures*, Acc. Chem. Res. **48**, 2484 (2015).

[43] M. Murai, S. Iba, H. Ota, and K. Takai, *Azulene-fused Linear Polycyclic Aromatic Hydrocarbons with Small Bandgap, High Stability, and Reversible Stimuli Responsiveness*, Org. Lett. **19**, 5585 (2017).

[44] See Supplemental Material at http://link.aps.org/supplemental/10.1103/PhysRevX.9.011030 for details of the coverage determination, the NIXSW, TPD, and NEXAFS data treatment, as well as additional XPS, STM, and nc-AFM data, and further details of the DFT calculations.

[45] F. C. Bocquet, G. Mercurio, M. Franke, G. van Straaten, S. Wei, S. Soubatch, C. Kumpf, and F. S. Tautz, *Torricelli: A Software to Determine Atomic Spatial Distributions from Normal Incidence X-ray Standing Wave Data*, Comput. Phys. Commun. **235**, 502 (2019).

[46] S. G. Hessey and R. G. Jones, *Line-of-Sight Mass Spectrometry: Principles and Practice*, Surf. Interface Anal. **47**, 587 (2015).

[47] I. Horcas, R. Fernandez, J. M. Gomez-Rodriguez, J. Colchero, J. Gomez-Herrero, and A. M. Baro, *WSXM: A Software for Scanning Probe Microscopy and a Tool for Nanotechnology*, Rev. Sci. Instrum. **78**, 013705 (2007).

[48] G. Kresse and J. Hafner, *Ab Initio Molecular Dynamics for Liquid Metals*, Phys. Rev. B **47**, 558 (1993).

[49] G. Kresse and J. Hafner, *Ab Initio Molecular-Dynamics Simulation of the Liquid-Metal-Amorphous-Semiconductor Transition in Germanium*, Phys. Rev. B **49**, 14251 (1994).

[50] G. Kresse and J. Furthmüller, *Efficiency of Ab-Initio Total Energy Calculations for Metals and Semiconductors Using a Plane-Wave Basis Set*, Comput. Mater. Sci. **6**, 15 (1996).

[51] G. Kresse and J. Furthmüller, *Efficient Iterative Schemes for Ab Initio Total-Energy Calculations Using a Plane-Wave Basis Set*, Phys. Rev. B **54**, 11169 (1996).

[52] J. P. Perdew, K. Burke, and M. Ernzerhof, *Generalized Gradient Approximation Made Simple*, Phys. Rev. Lett. **77**, 3865 (1996).

[53] S. Grimme, J. Antony, S. Ehrlich, and H. Krieg, *A Consistent and Accurate Ab Initio Parametrization of Density Functional Dispersion Correction (DFT-D) for the 94 Elements H-Pu*, J. Chem. Phys. **132**, 154104 (2010).

[54] P. E. Blöchl, *Projector Augmented-Wave Method*, Phys. Rev. B **50**, 17953 (1994).

[55] G. Kresse and D. Joubert, *From Ultrasoft Pseudopotentials to the Projector Augmented-Wave Method*, Phys. Rev. B **59**, 1758 (1999).

[56] S. J. Clark, M. D. Segall, C. J. Pickard, P. J. Hasnip, M. I. J. Probert, K. Refson, and M. C. Payne, *First Principles Methods Using CASTEP*, Z. Kristallogr. Cryst. Mater. **220**, 567 (2009).

[57] M. Teruyasu, T. Isao, G. Shang-Peng, and J. P. Chris, *First-Principles Calculation of Spectral Features, Chemical Shift and Absolute Threshold of ELNES and XANES Using a Plane Wave Pseudopotential Method*, J. Phys. Condens. Matter **21**, 104204 (2009).

[58] L. Triguero, L. G. M. Pettersson, and H. Ågren, *Calculations of Near-Edge X-Ray-Absorption Spectra of Gas-Phase and Chemisorbed Molecules by Means of Density-Functional and Transition-Potential Theory*, Phys. Rev. B **58**, 8097 (1998).

[59] M. Klues, K. Hermann, and G. Witte, *Analysis of the Near-Edge X-Ray-Absorption Fine-Structure of Anthracene: A Combined Theoretical and Experimental Study*, J. Chem. Phys. **140**, 014302 (2014).

[60] K. Diller, R. J. Maurer, M. Müller, and K. Reuter, *Interpretation of X-Ray Absorption Spectroscopy in the Presence of Surface Hybridization*, J. Chem. Phys. **146**, 214701 (2017).

[61] R. J. Maurer and K. Reuter, *Excited-State Potential-Energy Surfaces of Metal-Adsorbed Organic Molecules from Linear Expansion Δ-Self-Consistent Field Density-Functional Theory (ΔSCF-DFT)*, J. Chem. Phys. **139**, 014708 (2013).

[62] D. P. Woodruff, *Normal Incidence X-Ray Standing Wave Determination of Adsorbate Structures*, Prog. Surf. Sci. **57**, 1 (1998).

[63] D. P. Woodruff, *Surface Structure Determination Using X-Ray Standing Waves*, Rep. Prog. Phys. **68**, 743 (2005).

[64] J. Zegenhagen, *Surface Structure Determination with X-Ray Standing Waves*, Surf. Sci. Rep. **18**, 202 (1993).

[65] The issue of unrealistically high coherent fractions, recently observed in several measurements performed at the I09 beam line, did not occur in our case. This is possibly due to the moderate maximum count rates we allowed during data acquisition, in order to avoid a possible nonlinearity of the multichannel plate detector.

[66] B. Stadtmüller, S. Schröder, and C. Kumpf, *Heteromolecular Metalorganic Interfaces: Electronic and Structural Fingerprints of Chemical Bonding*, J. Electron Spectrosc. Relat. Phenom. **204**, 80 (2015).

[67] D. R. Lide, *CRC Handbook of Chemistry and Physics*, 90th ed. (CRC Press, Boca Raton, FL, 2010).

[68] K. Christmann, *Introduction to Surface Physical Chemistry* (Steinkopff Verlag, Springer-Verlag, Darmstadt, New York, 1991).

[69] A. M. de Jong and J. W. Niemantsverdriet, *Thermal Desorption Analysis: Comparative Test of Ten Commonly Applied Procedures*, Surf. Sci. **233**, 355 (1990).

[70] D. L. S. Nieskens, A. P. van Bavel, and J. W. Niemantsverdriet, *The Analysis of Temperature Programmed Desorption Experiments of Systems with Lateral Interactions; Implications of the Compensation Effect*, Surf. Sci. **546**, 159 (2003).

[71] G. Witte, S. Lukas, P. S. Bagus, and C. Wöll, *Vacuum Level Alignment at Organic/Metal Junctions: Cushion Effect and the Interface Dipole*, Appl. Phys. Lett. **87**, 263502 (2005).

[72] I. Fernandez-Torrente, S. Monturet, K. J. Franke, J. Fraxedas, N. Lorente, and J. I. Pascual, *Long-Range Repulsive Interaction between Molecules on a Metal Surface Induced by Charge Transfer*, Phys. Rev. Lett. **99**, 176103 (2007).

[73] S. Lukas, G. Witte, and C. Wöll, *Novel Mechanism for Molecular Self-Assembly on Metal Substrates: Unidirectional Rows of Pentacene on Cu(110) Produced by a Substrate-Mediated Repulsion*, Phys. Rev. Lett. **88**, 028301 (2001).

[74] G. Tomba, M. Stengel, W. D. Schneider, A. Baldereschi, and A. De Vita, *Supramolecular Self-Assembly Driven by Electrostatic Repulsion: The 1D Aggregation of Rubrene Pentagons on Au111*, ACS Nano **4**, 7545 (2010).

[75] E. Bauer, F. Bonczek, H. Poppa, and G. Todd, *Thermal Desorption of Metals from Tungsten Single Crystal Surfaces*, Surf. Sci. **53**, 87 (1975).

[76] D. A. King, *Thermal Desorption from Metal Surfaces: A Review*, Surf. Sci. **47**, 384 (1975).

[77] S. L. Tait, Z. Dohnálek, C. T. Campbell, and B. D. Kay, *n-Alkanes on MgO(100). I. Coverage-Dependent Desorption Kinetics of n-Butane*, J. Chem. Phys. **122**, 164707 (2005).

[78] D. P. Chong, *Density Functional Theory Study on the Electron Spectra of Naphthalene and Azulene Vapours*, Can. J. Chem. **88**, 787 (2010).

[79] S. Doniach and M. Šunjić, *Many-Electron Singularity in X-Ray Photoemission and X-Ray Line Spectra from Metals*, J. Phys. C **3**, 285 (1970).

[80] W. Zhao, W. Wei, and J. M. White, *Two-Photon Photoemission Spectroscopy: Naphthalene on Cu(111)*, Surf. Sci. **547**, 374 (2003).

[81] F. Bischoff, K. Seufert, W. Auwärter, S. Joshi, S. Vijayaraghavan, D. Écija, K. Diller, A. C. Papageorgiou, S. Fischer, F. Allegretti, D. A. Duncan, F. Klappenberger, F. Blobner, R. Han, and J. V. Barth, *How Surface Bonding and Repulsive Interactions Cause Phase Transformations: Ordering of a Prototype Macrocyclic Compound on Ag (111)*, ACS Nano **7**, 3139 (2013).

[82] J. Tersoff and D. R. Hamann, *Theory of the Scanning Tunneling Microscope*, Phys. Rev. B **31**, 805 (1985).

[83] B. Schuler, W. Liu, A. Tkatchenko, N. Moll, G. Meyer, A. Mistry, D. Fox, and L. Gross, *Adsorption Geometry Determination of Single Molecules by Atomic Force Microscopy*, Phys. Rev. Lett. **111**, 106103 (2013).

[84] F. Mohn, L. Gross, N. Moll, and G. Meyer, *Imaging the Charge Distribution within a Single Molecule*, Nat. Nanotechnol. **7**, 227 (2012).

[85] L. Gross, F. Mohn, P. Liljeroth, J. Repp, F. J. Giessibl, and G. Meyer, *Measuring the Charge State of an Adatom with Noncontact Atomic Force Microscopy*, Science **324**, 1428 (2009).

[86] B. Schuler, S.-X. Liu, Y. Geng, S. Decurtins, G. Meyer, and L. Gross, *Contrast Formation in Kelvin Probe Force Microscopy of Single p-conjugated Molecules*, Nano Lett. **14**, 3342 (2014).

[87] J. Wellendorff, T. L. Silbaugh, D. Garcia-Pintos, J. K. Nørskov, T. Bligaard, F. Studt, and C. T. Campbell, *A Benchmark Database for Adsorption Bond Energies to Transition Metal Surfaces and Comparison to Selected DFT Functionals*, Surf. Sci. **640**, 36 (2015).

[88] R. J. Maurer, V. G. Ruiz, and A. Tkatchenko, *Many-body Dispersion Effects in the Binding of Adsorbates on Metal Surfaces*, J. Chem. Phys. **143**, 102808 (2015).

[89] R. J. Maurer, W. Liu, I. Poltavsky, T. Stecher, H. Oberhofer, K. Reuter, and A. Tkatchenko, *Thermal and Electronic Fluctuations of Flexible Adsorbed Molecules: Azobenzene on Ag(111)*, Phys. Rev. Lett. **116**, 146101 (2016).

[90] R. F. W. Bader, *Atoms in Molecules—A Quantum Theory* (Oxford University Press, Oxford, 1990).

[91] E. Hückel, *Quantentheoretische Beiträge Zum Problem der Aromatischen und Ungesättigten Verbindungen. III*, Z. Phys. **76**, 628 (1932).

[92] E. Clar, *The Aromatic Sextet*, 2nd ed. (John Wiley & Sons, London, New York, Sydney, Toronto, 1972).

[93] A. A. Frost and B. Musulin, *A Mnemonic Device for Molecular Orbital Energies*, J. Chem. Phys. **21**, 572 (1953).

[94] C. A. Coulson and G. S. Rushbrooke, *Note on the Method of Molecular Orbitals*, J. Phys. Condens. Matter **36**, 193 (1940).

[95] F. L. Hirshfeld, *Bonded-Atom Fragments for Describing Molecular Charge Densities*, Theor. Chim. Acta **44**, 129 (1977).

[96] H. Vita, S. Böttcher, K. Horn, E. N. Voloshina, R. E. Ovcharenko, T. Kampen, A. Thissen, and Y. S. Dedkov, *Understanding the Origin of Band Gap Formation in Graphene on Metals: Graphene on* Cu/Ir(111), Sci. Rep. **4**, 5704 (2014).

[97] H. S. Moon, J. H. Lee, S. Kwon, I. T. Kim, and S. G. Lee, *Mechanisms of Na Adsorption on Graphene and Graphene Oxide: Density Functional Theory Approach*, Carbon Lett. **16**, 116 (2015).

P1

XV10333

Molecular Topology and the Surface Chemical Bond: Alternant vs. Non-Alternant Aromatic Systems as Functional Structural Elements

SUPPORTING INFORMATION

Benedikt P. Klein[1], Nadine J. van der Heijden[2], Stefan R. Kachel[1], Markus Franke[3], Claudio K. Krug[1], Katharina K. Greulich[1], Lukas Ruppenthal[1], Philipp Müller[1], Phil Rosenow[1], Shayan Parhizkar[3], François C. Bocquet[3], Martin Schmid[1], Wolfgang Hieringer[4], Reinhard J. Maurer[5], Ralf Tonner[1], Christian Kumpf[3], Ingmar Swart[2], and J. Michael Gottfried[1]

[1]Philipps-Universität Marburg, Fachbereich Chemie, Hans-Meerwein-Str. 4, 35032 Marburg, Germany
[2]Condensed Matter and Interfaces, Debye Institute for Nanomaterials Science, Utrecht University, P.O. Box 80000, 3508 TA Utrecht, The Netherlands
[3]Peter Grünberg Institut (PGI-3), Forschungszentrum Jülich, 52425 Jülich, Germany and Jülich Aachen Research Alliance (JARA) Fundamentals of Future Information Technology, 52425 Jülich, Germany
[4]Lehrstuhl für Theoretische Chemie, Universität Erlangen-Nürnberg, Egerlandstr. 3, 91058 Erlangen, Germany and
[5]Department of Chemistry and Centre for Scientific Computing, University of Warwick, Gibbet Hill Road, Coventry, CV4 7AL, United Kingdom

(Dated: November 22, 2018)

1

I. COVERAGE DETERMINATION

The absolute monolayer coverage (*i.e.* the number of molecules per area) was determined from a large-scale nc-AFM image of a saturated, compressed layer (with partial second layer) prepared by careful dosing at low temperature. For the XPS, UPS and NIXSW measurements, the relative coverage (in ML) was checked by the XPS intensity. The monolayer XPS intensity was beforehand established with an XPS temperature series monitoring peak intensity and position. The thus conceived temperature at which a monolayer is formed by desorption of a multilayer is in accordance with the monolayer trace as measured by TPD. At 300 K a self limiting adsorption of azulene to a coverage of 0.65 ML takes place. This was used as an additional, internal calibration standard.

II. XPS SPECTRA USED FOR THE GENERATION OF NIXSW YIELD CURVES

Examples for the C 1s XP spectra used for the generation of the NIXSW yield curves are shown in Fig. S1. To fully avoid any beam damage, the measurement time was chosen very short, at the expense of increased noise levels. The spectra were fitted using CASA XPS, the resulting yield curves can be found in the main text. The NIXSW analysis was performed with Torricelli [1].

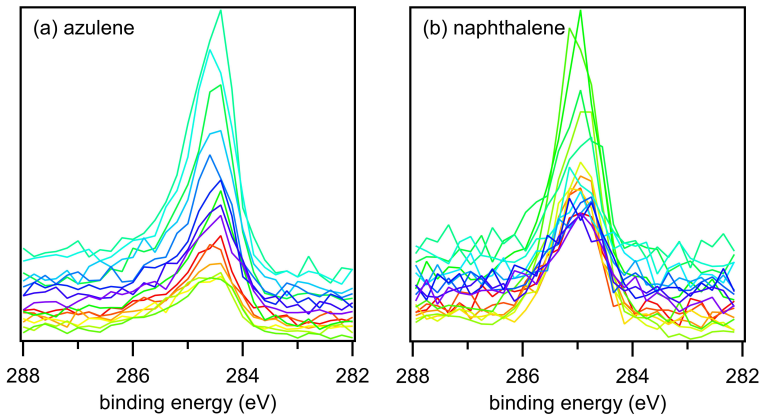

FIG. S1. (a) Examples for the C 1s XP spectra used for the generation of the NIXSW yield curves. (a) 1 ML azulene, (b) 1 ML naphthalene on Cu(111), color scheme from red (lowest photon energy) to blue (highest photon energy) in the order of the visible spectrum.

P1

III. TEMPERATURE PROGRAMMED DESORPTION (TPD)

A. Estimation of desorption activation energies

Quantitative analysis of the TPD spectra based on the Polanyi-Wigner rate equation [2–4], gives access to the desorption activation energy E_d as a measure of the adsorbate-substrate bond energy:

$$\text{rate} = -\frac{\mathrm{d}\Theta}{\mathrm{d}t} = \nu_\mathrm{d}\Theta \exp\left(-E_\mathrm{d}/RT\right) \tag{1}$$

In Eq. (1), Θ is the coverage, ν_d is the desorption prefactor, T is the temperature, and R is the universal gas constant. The most rigorous approach for TPD analysis, the so-called complete methods [5, 6], are not suitable here because of the strong lateral repulsion [4]. Instead, we use an alternative approach as proposed by Nieskens *et al.* [4] and Tait *et al.* [7] and rewrite Eq. (1) as follows:

$$E_\mathrm{d}(\Theta) = -RT \ln\left[\frac{-\mathrm{d}\Theta/\mathrm{d}t}{\nu_\mathrm{d}\Theta}\right] \tag{2}$$

Eq. (2) provides the coverage-dependent desorption energy $E_\mathrm{d}(\Theta)$ from a single TPD trace. The prefactors used in Eq. (2) were determined by heating rate variation (HRV) analysis [2], which is only meaningful for the regular first-order peaks in the low-coverage range. The related data are presented in Fig. S2 and Table SI below. It should be noted that Eq. (2) is strictly applicable only if the prefactor does not change with coverage. However, small changes of ν_d have a negligible effect on the estimate of E_d: Even if ν_d varies by one order of magnitude, E_d changes by only a few percent [4].

B. TPD heating rate variation series

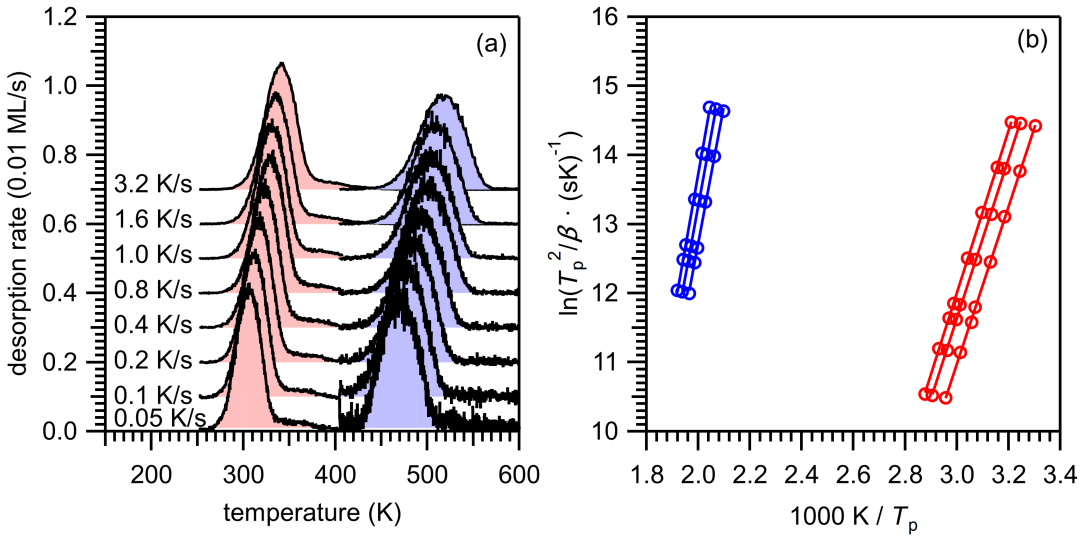

FIG. S2. (a) Examples for heating rate variation (HRV) series for azulene and naphthalene (both initial coverages 0.16 ML). (b) Analysis of the heating rate variation series for coverages of 0.07, 0.11 and 0.16 ML for azulene and 0.04, 0.08 and 0.16 ML for naphthalene, providing desorption activation energies and pre-exponential factors.

TAB. SI. Desorption energies and prefactors for each heating rate variation series for azulene and naphthalene on Cu(111).

Experiment	ΔE_{des} (eV)	ν_{d} (s^{-1})
Azulene/Cu 0.07 ML	1.83	$7.7 \cdot 10^{16}$
Azulene/Cu 0.11 ML	1.77	$2.6 \cdot 10^{16}$
Azulene/Cu 0.16 ML	1.73	$1.6 \cdot 10^{16}$
Naphthalene/Cu 0.04 ML	1.04	$2.3 \cdot 10^{14}$
Naphthalene/Cu 0.08 ML	1.02	$1.4 \cdot 10^{14}$
Naphthalene/Cu 0.16 ML	0.99	$1.5 \cdot 10^{14}$

C. TPD dosing series coverages

TAB. SII. Initial coverages of the TPD spectra for azulene and naphthalene on Cu(111) (shown in Fig. 3 in the main paper) starting from low coverages to high coverages (from bottom to top).

Azulene (ML)	Naphthalene (ML)
0.015	0.015
0.015	0.015
0.030	0.021
0.044	0.031
0.065	0.037
0.079	0.078
0.12	0.16
0.17	0.20
0.24	0.30
0.29	0.39
0.39	0.49
0.45	0.60
0.56	0.75
0.58	0.78
0.73	1.0
0.76	1.3
0.79	
0.92	
1.0	
1.1	
1.6	

D. Estimation of desorption prefactors from transition state theory

The precise quantitative analysis of TPD data requires careful treatment of the prefactor ν_d . To estimate desorption energies on the basis of single desorption maxima, the prefactor is often assumed to be $1 \cdot 10^{13}\mathrm{s}^{-1}$. For atoms or small molecules, this is a sufficiently accurate approximation in many cases [8]. However, the prefactor can be much higher for larger molecules. It can be derived by various methods from high-quality TPD data using various analysis methods [3], but it can also be estimated using the transition state theory (TST) [9, 10]. Within the framework of TST, the desorption prefactor can be calculated by (3):

$$\nu_\mathrm{d} = \frac{kT}{h} \cdot \frac{q^{\neq}}{q_\mathrm{ad}} \tag{3}$$

5

(with the Boltzmann constant k, the Planck constant h, and the partition functions $q^{\neq}$ and q_{ad} of the transition state and the adsorbed state, respectively.) An accurate calculation of $q^{\neq}$ and q_{ad} would require detailed knowledge of the interaction potentials of the adsorbed molecule and the transition state [11]. These data are not available. Nevertheless, upper and lower limits for ν_{d} can be estimated on the basis of reasonable assumptions about the degrees of freedom in the adsorbed state and in the transition state. First, we neglect any vibrational partition functions, which are small and mostly cancel in Eq. (3). Second, the transition state is approximated as a free gas-phase molecule with two translational and three rotational degrees of freedom. (The third translational degree of freedom represents the critical coordinate and is therefore omitted in $q^{\neq}$.) The partition function of the transition state is therefore given by:

$$q^{\neq} = q^{\neq}_{\mathrm{tr,2D}} \cdot q^{\neq}_{rot,\mathrm{3D}} \tag{4}$$

The two-dimensional translational partition function per area A is given by [12]:

$$\frac{q^{\neq}_{\mathrm{tr,2D}}}{A} = \frac{2\pi mkT}{h^2} \tag{5}$$

where m is the mass of the molecule. The three-dimensional rotational partition function is [12]:

$$q^{\neq}_{rot,3D} = \frac{\pi^{1/2}}{\sigma}\left(\frac{kT}{hc_0}\right)^{3/2}(B_{\mathrm{A}}B_{\mathrm{B}}B_{\mathrm{C}})^{-1/2} \tag{6}$$

with the symmetry factor σ, the velocity of light c_0, and the rotational constants B_{A}, B_{B} and B_{C} (in m^{-1}).

In the following, we consider the two limiting cases for the degrees of freedom of the adsorbate. In the mobile limit, the adsorbed molecule possesses two translational degrees of freedom parallel to the surface and one rotational degree of freedom around an axis perpendicular to the molecular plane, which is assumed to be parallel to the surface. The partition function for this rotation with the rotational constant B_{A} is given by:

$$q_{rot,1D} = \frac{\pi^{1/2}}{\sigma}\left(\frac{kT}{hc_0B_{\mathrm{A}}}\right)^{1/2} \tag{7}$$

The translational partition function for the mobile adsorbate equals $q^{\neq}_{\mathrm{tr,2D}}$ (Eq. (5)).

P1

TAB. S III. Desorption prefactors in the mobile and immobile limit for azulene and naphthalene, and parameters necessary for the calculation. See the text for further details.

Adsorbate	Azulene on Cu(111)	Naphthalene on Cu(111)
Overlayer Structure	$(2\sqrt{3} \times 2\sqrt{3})$-R30°	$(2\sqrt{3} \times 2\sqrt{3})$-R30°
A (10^{-19} m^{-2})	6.79	6.79
	B_{A}: 0.0948	B_{A}: 0.104
Rotational Constants [14, 15]	B_{B}: 0.0419	B_{B}: 0.0411
(cm^{-1})	B_{C}: 0.0290	B_{C}: 0.0295
$\nu_{\mathrm{d,mobile}}$ (s^{-1})	$1.0 \cdot 10^{16}$	$9.9 \cdot 10^{15}$
$\nu_{\mathrm{d,im}}$ (s^{-1})	$1.3 \cdot 10^{22}$	$6.4 \cdot 10^{21}$

Hence, the translations contributions cancel in Eq. (3) and the prefactor for the mobile limit depends only on the rotational partition functions:

$$\nu_{\mathrm{d,mobile}} = \frac{kT}{h} \cdot \frac{q^{\neq}_{\mathrm{rot,3D}}}{q_{\mathrm{rot,1D}}} \tag{8}$$

In the immobile limit, the adsorbed molecule has no rotational or translational degrees of freedom. The corresponding prefactor $\nu_{\mathrm{d,im}}$ therefore depends only on the partition function of the transition state:

$$\nu_{\mathrm{d,im}} = \frac{kT}{h} \cdot q^{\neq}_{\mathrm{tr,2D}} \cdot q^{\neq}_{\mathrm{rot,3D}} \tag{9}$$

The resulting prefactors are shown in Table SIII. The mass m is $2.13 \cdot 10^{-25}$ kg for both azulene and naphthalene. For A, the area per molecule in the saturated layer is used. (This area is difficult to estimate, because it depends essentially on the lateral mobility of the molecule in the transition state. Some authors use the full area of the crystal here [13].) The symmetry factor σ counts the number of rotational operations ($\mathrm{C_n}$) plus the identity operation. For the free molecules, the values are 4 for naphthalene ($\mathrm{D_{2h}}$) and 2 for azulene ($\mathrm{C_{2v}}$). For the adsorbed molecules, the values are 2 for naphthalene ($\mathrm{C_{2v}}$) and 1 for azulene ($\mathrm{C_s}$). B_{A}, B_{B} and B_{C} are rotational constant for the molecules. The index A denotes the axis perpendicular to the molecule plane. For an exact treatment, the prefactor has to be calculated for each temperature. However, calculating it only for 300 K leads to a small error.

IV. XPS MULTILAYER SPECTRA

Fig. S3 shows the multilayer C 1s XP spectra for azulene and naphthalene in a wider range than depicted in Fig. 3 of the main paper. Here, the shake-up satellites for both molecules are visible. The main satellite for azulene is at lower binding energy and thus closer to the regular C 1s peak.

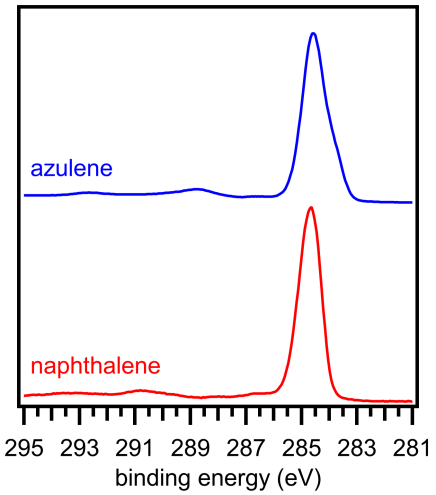

FIG. S3. Multilayer C 1s XP spectra for azulene (top, blue) and naphthalene (bottom, red). The main shake-up satellites are at a binding energy of 289 eV for azulene and 291 eV for naphthalene.

V. SIMULATION OF THE XPS MULTILAYER SPECTRA

The C 1s signal of a azulene multilayer has a broad shape with a distinct shoulder at the low binding energy side (see Fig. 4(a) of the main text and Fig. S3). To understand this shape we calculated the relative peak positions for the different carbon atoms in the free molecule by DFT using the core level shift method described by Chong [16]. The results were found to be in agreement with previously reported values for azulene and naphthalene [17]. The DFT calculations give the relative peak positions for each carbon atom. From these calculations, we derived a fit model by creating a group of pseudo-Voigt peaks linked to each other in accordance with the relative peak positions and the stoichiometry. The resulting model has now six peaks (three for naphthalene), but only four fitted parameters (the position of the combined peak, the total intensity, the peak width and the Gauß-Lorentz ratio). This model was then fitted to the experimental data together with a background function and peaks for the satellites, yielding the good agreement as shown in Fig. 4(a) of the main text.

VI. NEXAFS DATA TREATMENT

This section shortly explains the data treatment used to obtain the shown NEXAFS spectra. The incident photon flux was monitored with a gold grid. Calibration of the photon energy was performed by means of the carbon-related absorption on the gold grid, as previously described [18]. The NEXAFS spectra were treated according to standard procedures [19]. All spectra of the samples and the clean Cu(111) substrate were corrected for a photon energy shift and normalized in the pre-edge region at 282 eV. For background correction, spectra of the clean Cu(111) substrate were fitted and then subtracted from the sample spectra. In a last step, the sample spectra were normalized in the range behind the absorption edge (300 eV).

P1

VII. STM AND NC-AFM IMAGES OF AZULENE ON CU(111) AT LOW COVERAGES

Fig. S4 shows a very low coverage and an intermediate coverage of azulene on Cu(111). It can clearly be seen that no islands are formed. Instead, the molecules tend to avoid each other.

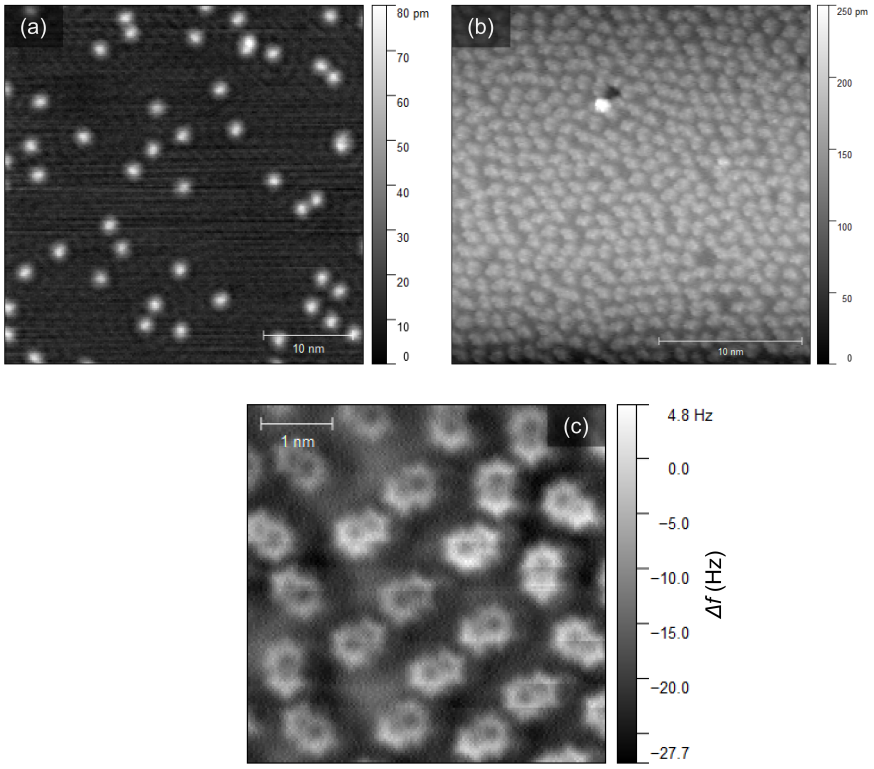

FIG. S4. (a) STM and nc-AFM images of azulene on Cu(111) at various submonolayer coverages. (a) STM image of a very low coverage of 0.01 ML. (b) STM image of an intermediate coverage of 0.4 ML, (c) nc-AFM image of the intermediate coverage of 0.4 ML. The molecules were adsorbed above room temperature, measurements were taken at 4.5 K. The formation of the disordered structure is therefore not caused by limited diffusion. Rather, it likely represents the equilibrium structure.

VIII. NC-AFM IMAGES OF A ROTATION OF AN AZULENE MOLECULE

Fig. S5 shows the tip-induced rotation of an azulene molecule by a 60° angle

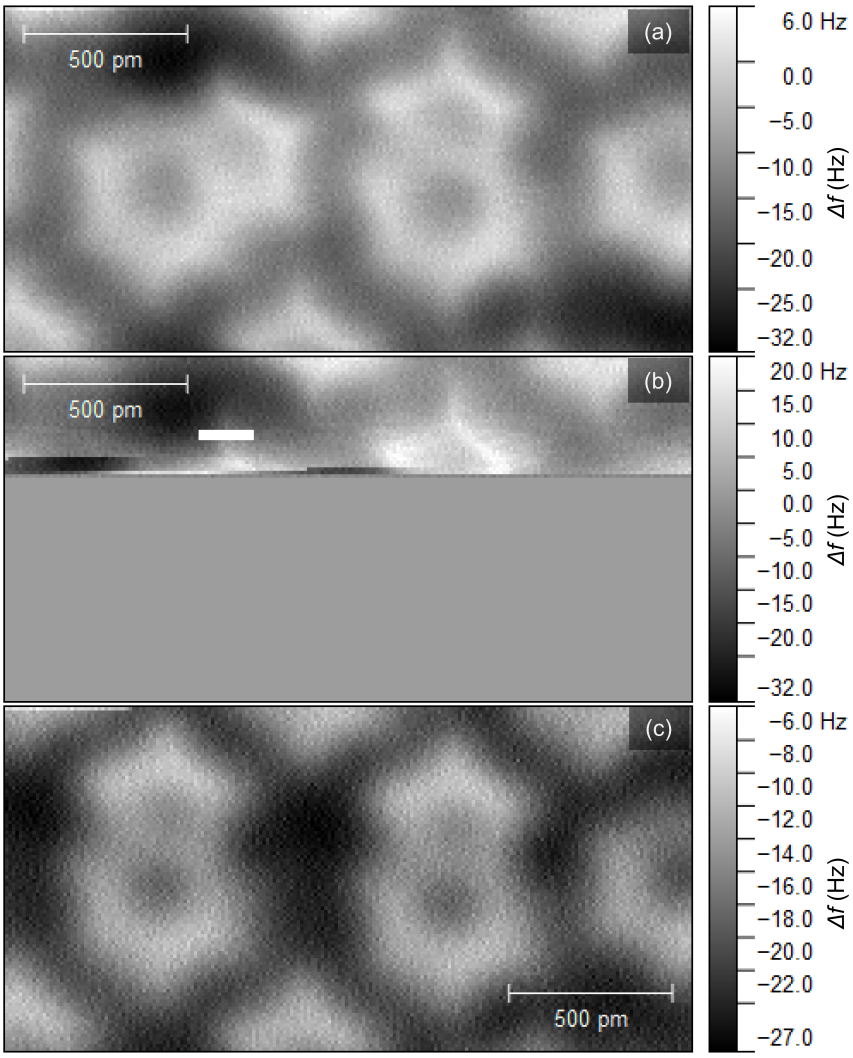

FIG. S 5. nc-AFM images illustrating the tip-induced rotation of an azulene molecule by 60°. (a) nc-AFM image before the rotation. (b) Interrupted nc-AFM scan during which the rotation occurred. (c) nc-AFM image after the rotation.

P1

IX. NC-AFM AND STM IMAGES OF NAPHTHALENE

Fig. S6 shows STM and nc-AFM images of naphthalene adsorbed on Cu(111). In Fig. S6(c), a naphthalene molecule is laterally manipulated by the tip, something that has never been observed for azulene under otherwise identical conditions.

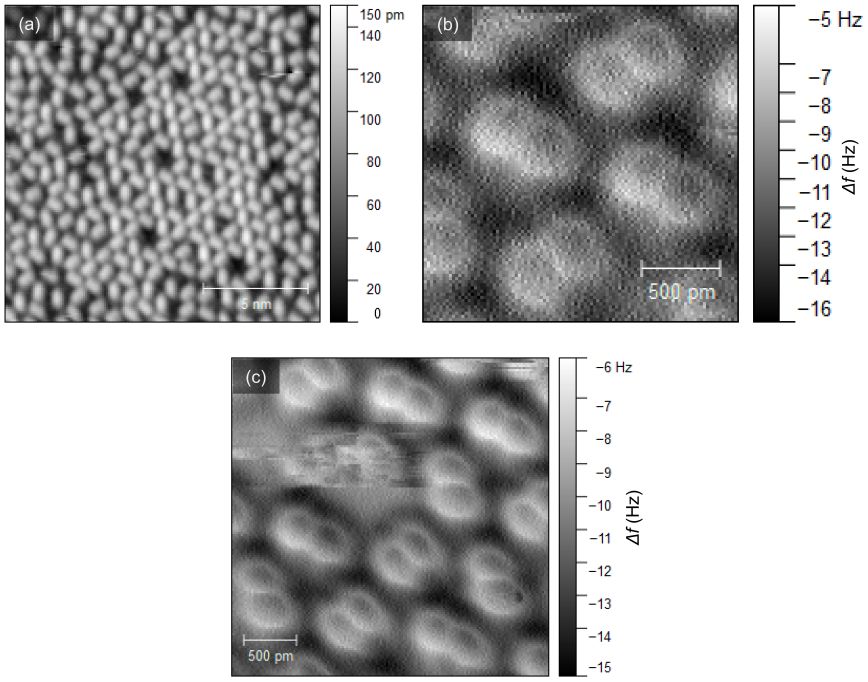

FIG. S 6. STM and nc-AFM images of naphthalene on Cu(111) at a coverage of approximately 0.6 ML: (a) STM image, (b) nc-AFM image, (c) nc-AFM image showing the higher mobility of the naphthalene molecules.

X. CHARGE DENSITY DIFFERENCE PLOTS SHOWING THE PUSH-BACK EFFECT

Fig. S7 shows charge density difference plots for azulene and naphthalene adsorbed on copper. The plots show the same charge density difference calculations as Fig. 9 of the main text, but have a smaller isosurface value, so that the small changes in the case of naphthalene become visible. The images clearly show the operation of the so-called pillow effect, *i.e.*, the push-back of electron density between molecule and surface caused by Pauli repulsion [20]. The effect is more pronounced for azulene (Fig. S7(a,b)) than for naphthalene (Fig. S7(c,d)), in line with the larger work function change and the stronger lateral repulsion in the case of azulene.

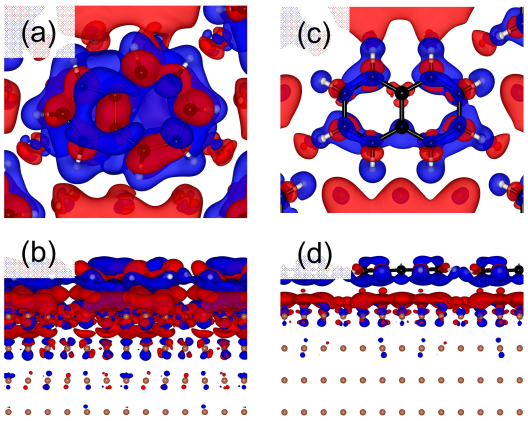

FIG. S 7. (a,b) Charge density difference plots for azulene. (c,d) Charge density difference plots for naphthalene. The isosurface value for all plots is 0.0007. Electrons flow from blue to red.

XI. FURTHER COMPUTATIONAL DETAILS

A. General parameters and optimizations

Periodic density functional theory calculations of azulene and naphthalene on Cu(111) were performed with the Vienna Ab Initio Simulation Package (VASP) [21–24]. The PBE functional [25] was used in combination with the third-generation van der Waals dispersion correction by Grimme (DFT-D3) [26] and the projector-augmented wave (PAW) ansatz [27, 28] for the atomic cores. A plane-wave cutoff energy of 350 eV was employed. The Cu(111) surface was modeled as a 4-layer, $(2\sqrt{3} \times 2\sqrt{3})$-R30° copper atom slab (48 Cu atoms in total) in an hexagonal unit cell. Only the topmost two layers were freely optimized together with the adsorbed molecule, while the bottom two Cu layers were kept frozen at their optimized bulk positions. A vacuum layer of 30 Å was introduced to isolate the repeated slabs from each other. For all calculations, final geometry optimization with a $24 \times 24 \times 1$ Monkhorst-Pack k-point mesh was used, which was adjusted to the unit cell size. Geometries were optimized until the forces on the active atoms dropped below 0.01 eV/Å. Coordinates of the final optimized geometry are attached. STM simulations were visualized with the p4vasp program 0.3.29 based on the Tersoff-Hamann model [29]. The Bader charge analysis [30] was performed in ADF-BAND 2017 [31–35] on the level PBE-D3(BJ)/TZ2P [36–38]. Visualization was done with the program VESTA 3 [39].

B. 7.2 XPS and NEXAFS simulations

All calculations were performed with the PBE functional [25], a plane-wave cutoff of 350 eV, and an $8 \times 8 \times 1$ Monkhorst Pack k-point grid sampling. We calculated the ground-state electronic structure as well as the density of states (DOS) and the molecular-orbital projected DOS [40], which reflects the interaction of the free molecular orbitals (MO) with the metal substrate using standard library ultra-soft pseudopotentials (USPPs) [41]. MO projections and core-level spectra are processed using a self-written post-processing tool for CASTEP [40]. We calculated XPS chemical shifts using the delta self-consistent field (DeltaSCF) method of constraining electronic occupations to resemble full core-hole excitations. NEXAFS simulations were performed using on-the-fly generated USPPs and the CASTEP module ELNES [42] and the transition-potential approach [43, 44], where the occu-

pation of the initial state orbital (here C 1s) is set to 0.5 and the corresponding Kohn-Sham eigen-energies are taken to reflect the NEXAFS spectrum. Atom-wise projected NEXAFS spectra result from XAS calculations for each individual C 1s center in the corresponding molecule. MO-projected spectra have been generated by multiplying XAS intensities with the absolute overlap matrix element of free azulene and naphthalene frontier molecular orbitals and the band structure of the corresponding adsorbed molecules on the surface. For more details on the computational settings and analysis see Diller *et al.* [45]. For more details on the implementation, see Maurer and Reuter [40].

P1

XII. APPROXIMATE C 1S NEXAFS SPECTRA FROM A CORE-LEVEL SHIFTED, SITE- AND ANGULAR MOMENTUM PROJECTED WAVE FUNCTION CHARACTER

In addition to the CASTEP/ELNES transition potential simulations of the NEXAFS (XAS) spectra shown in the main text and the previous section [40], we also used a more approximate way to simulate NEXAFS spectra that resorts to ground-state properties of the system only (*cf.* Bauer *et al.*, J. Phys. Chem. C, in press (2018); DOI: 10.1021/acs.jpcc.8b03746). This scheme employs occupied-unoccupied Kohn-Sham (PBE) orbital energy differences and the site- and angular momentum projected wave function character of each band obtained from standard periodic DFT calculations using the VASP program and the PAW method implemented in VASP. Specifically, excitation energies from a C 1s core level at a specified atom (*i.e.*, all carbon atoms in the present case of naphthalene and azulene) to an unoccupied band $\Phi_{a,k}$ (with band index a and k-point index k) were approximated as the difference $\Delta\varepsilon_{i,a,k}$ between the 1s core level energy $\varepsilon_{1s,i}$ at atom i (ICORELEVEL=1 tag of the VASP program) and the single-particle energy of $\varepsilon_{a,k}$ of the unoccupied band. The obtained $\Delta\varepsilon_{i,a,k}$ are uniformly shifted (by +17.8 eV) such that the onset of the simulated spectrum approximately matches the onset of the experimental spectrum. Approximate intensity information is obtained from the site- and (p_x,p_y,p_z)-projected wave function character of each band at the corresponding carbon atom as provided in the standard VASP PROCAR file. These data (multiplied with appropriate prefactors [46]) are interpreted as approximate dipole intensities for electronic transitions from the C 1s core levels to the unoccupied bands. The resulting line spectra were subsequently convoluted using a standard broadening procedure to obtain the continuous spectrum (*cf.* Fig. 5 of the main text). These simulated spectra, shown in Fig. S8, qualitatively reproduce salient features of the experimental NEXAFS spectra of free and adsorbed naphthalene and azulene, thereby allowing assignment of the dominant features. However, larger uncertainties in relative intensities compared to experiment and those found with the more sophisticated ELNES simulation method (see Fig. 5 of the main paper) are observed.

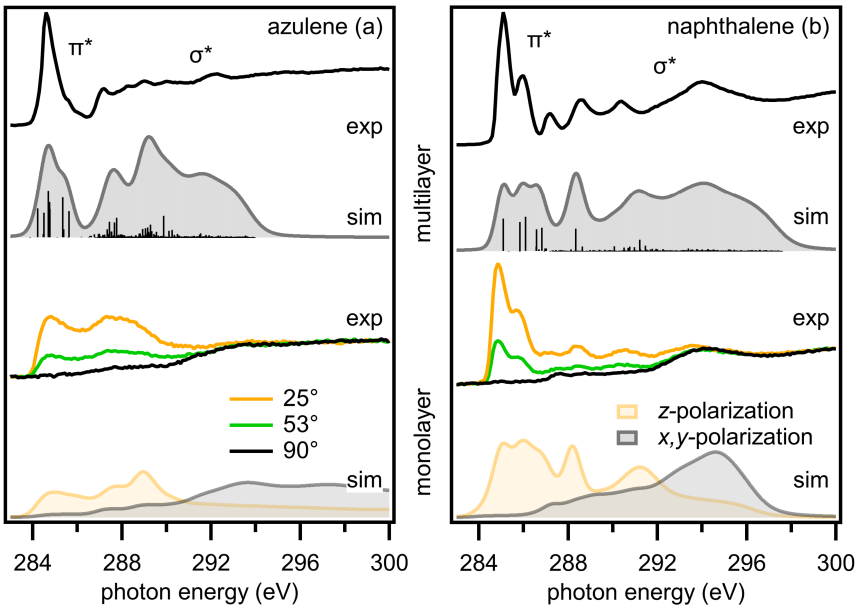

FIG. S 8. Comparison of the approximate NEXAFS with the experimental K-edge spectra of (a) azulene and (b) naphthalene using ground state core orbital energies and local DOS information from the VASP program as described in the text (PBE functional, $8 \times 8 \times 1$ MP k-point mesh, 400 eV plane wave cutoff); upper part: experimental multilayer spectra *vs.* simulated spectra of the isolated molecules; bottom part: experimental and simulated monolayer spectra on Cu(111); simulated spectra for x,y and z-polarization, respectively.

XIII. DFT CALCULATIONS OF THE 5-7 DEFECTS IN GRAPHENE

The calculations for the 5-7 defect in free standing graphene were also performed in VASP on the level PBE-D3(BJ)/PAW with a plane-wave cutoff energy of 350 eV and 30 Å vacuum, the k-grid consisted only of the Γ-Point. The unit cell with 456 carbon atoms was chosen large enough to contain two 5-7 defects isolated by a quite large distance. The size of the cell was optimized for the regular graphene sheet with the same number of carbon atoms. Afterwards the positions of all atoms were allowed to relax. For the sake of simplicity, the local, planar minimum structure was used. In the absolute minimum, the defective graphene sheet distorts out of the plane, but the influence of this on the shown results is negligible. In Figure S9, sections through the charge density are shown for the complete unit cells.

To quantify the charge separation, the partial charges by the Hirshfeld method [47] were calculated using ADF-BAND 2017, PBE-D3(BJ)/TZ2P. In Table SIV, the Hirshfeld charges for all atoms of a 5-7 defect in a free standing graphene layer are compared to the corresponding atoms in a free azulene molecule (H/Cix labels the carbon or hydrogen bonded to the atom i). The higher charges of single carbon atoms in azulene are due to the positive hydrogens bonded to them. The charge separation between 5- and 7-membered ring is approximately the same.

TAB. SIV. Hirshfeld charges for all atoms in the free azulene molecule and the corresponding atoms in a 5-7 defect in a free standing graphene layer. The charges were calculated with ADF-BAND, PBE-D3(BJ)/TZ2P and are given in units of the elementary charge.

	Azulene molecule	5-7 defect in graphene
C1	−0.05	−0.02
C2	−0.08	−0.02
C3	−0.01	−0.01
C4	−0.02	0.01
C5	−0.05	0.01
C6	−0.03	0.02
H/C1x	0.05	0.00
H/C2x	0.04	0.00
H/C4x	0.05	0.00
H/C5x	0.04	0.00
H/C6x	0.05	0.00
5-7 charge difference	−0.13	−0.11

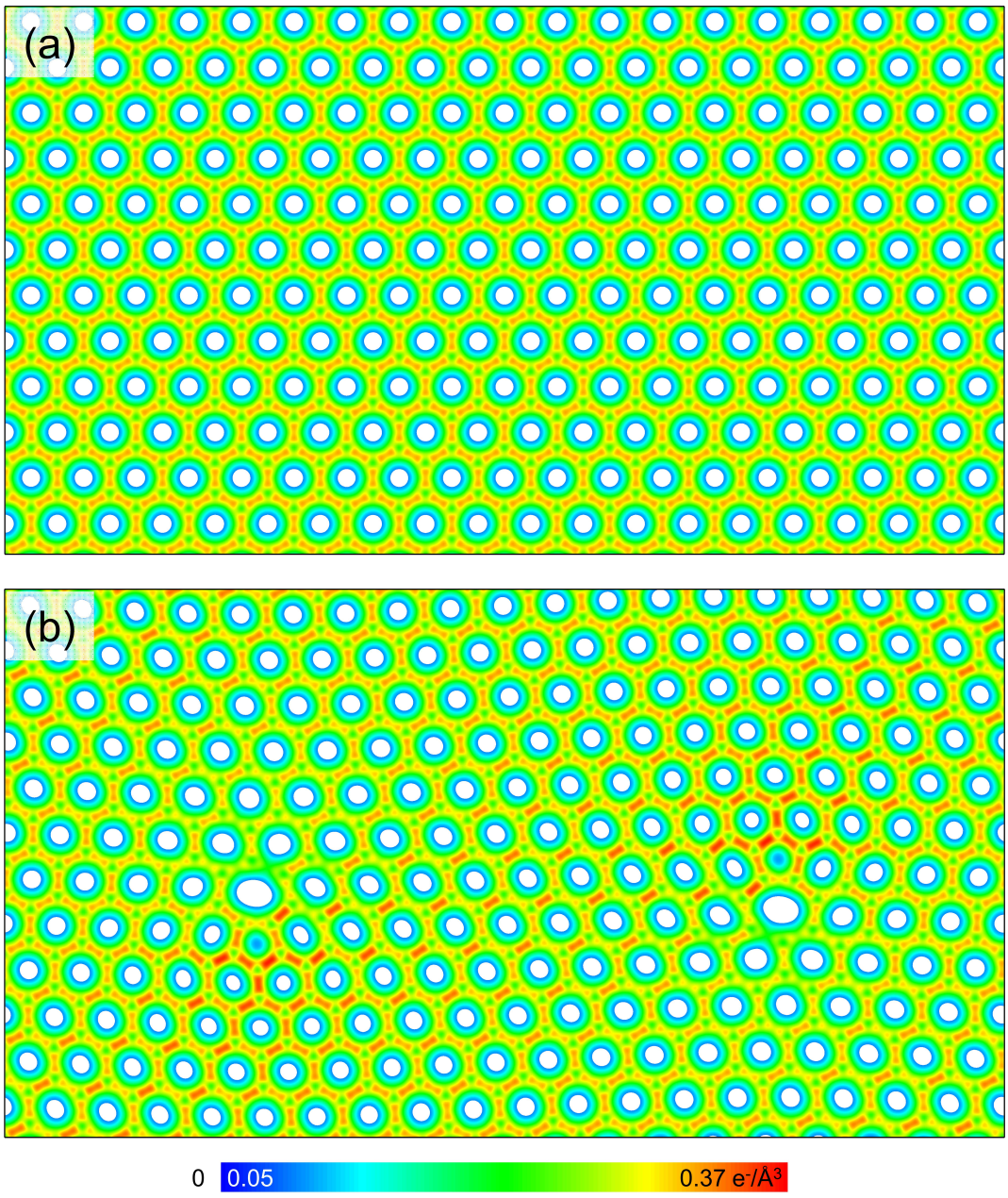

FIG. S 9. Section through the charge density for the pristine graphene layer and (b) Section through the charge density for the graphene layer with two isolated 5-7 defects.

P1

XIV. COORDINATES OF THE OPTIMIZED STRUCTURES

Azulen/Cu(111) 2r3x2r3
1
7.568022460000000 -4.36939980000000 0.000000000000000
0.000000000000000 8.738799610000000 0.000000000000000
0.000000000000000 0.000000000000000 36.17926446000000
Cu C H
48 10 8
Selective dynamics
Direct

0.000000000000000	0.000000000000000	0.000000000000000	F	F	F
0.000000000000000	0.499999999427843	0.000000000000000	F	F	F
0.166666667107115	0.833333332599956	0.000000000000000	F	F	F
0.166666667107115	0.333333333172121	0.000000000000000	F	F	F
0.333333332892884	0.666666665683557	0.000000000000000	F	F	F
0.500000000000000	0.999999998855678	0.000000000000000	F	F	F
0.333333332892884	0.166666666255722	0.000000000000000	F	F	F
0.500000000000000	0.499999999427843	0.000000000000000	F	F	F
0.666666667107116	0.833333332599956	0.000000000000000	F	F	F
0.666666667107116	0.333333333172121	0.000000000000000	F	F	F
0.833333332892885	0.666666665683557	0.000000000000000	F	F	F
0.833333332892885	0.166666666255722	0.000000000000000	F	F	F
0.166666666618220	0.166666666508938	0.056931920279290	F	F	F
0.166666666618220	0.666666666302959	0.056931920279290	F	F	F
0.333333333236432	0.999999999413717	0.056931920279290	F	F	F
0.333333333236432	0.499999999619696	0.056931920279290	F	F	F
0.499999999841435	0.833333332723853	0.056931920279290	F	F	F
0.666666666459655	0.166666665834612	0.056931920279290	F	F	F
0.499999999841435	0.333333332929826	0.056931920279290	F	F	F
0.666666666459655	0.666666666040584	0.056931920279290	F	F	F
0.833333333077874	0.999999999151349	0.056931920279290	F	F	F
0.833333333077874	0.499999999357328	0.056931920279290	F	F	F
0.999999999696087	0.833333332468087	0.056931920279290	F	F	F
0.999999999696087	0.333333332674059	0.056931920279290	F	F	F
0.332848711742287	0.333142756485644	0.115767323384702	T	T	T
0.333944399347891	0.832252702573379	0.113583903438455	T	T	T
0.498776372726573	0.166722705301642	0.113970767316169	T	T	T
0.501236861790010	0.668019641089215	0.115075713986626	T	T	T
0.667309831488595	0.998890268402075	0.113608791035716	T	T	T
0.832682011849006	0.333056974937810	0.113025798858840	T	T	T
0.665866673764026	0.499652492344268	0.113412947856192	T	T	T
0.832657730001803	0.834493081026438	0.113620190128857	T	T	T
0.002377596951953	0.168702220403079	0.113641836261603	T	T	T
0.000648103772099	0.667219879417994	0.112747953509676	T	T	T
0.168723734918125	0.001553169781761	0.113521702475958	T	T	T
0.168293010209529	0.500101450888521	0.114192038788208	T	T	T
0.003542273969833	0.001397470270254	0.169515963191732	T	T	T
0.995586853201696	0.500229855557409	0.169684726246360	T	T	T
0.165816383748964	0.831261752870134	0.169641244571653	T	T	T
0.159907314083559	0.333063839345017	0.172632769537454	T	T	T
0.331102659512075	0.667935048678675	0.171536118234579	T	T	T
0.501899698384467	0.998335449466040	0.169684178695577	T	T	T
0.333157804904178	0.160171403137508	0.172617922787023	T	T	T
0.507770488664965	0.503244288153981	0.170720991328150	T	T	T
0.675543946421775	0.839583902330302	0.173041228333131	T	T	T
0.667931338531516	0.332903474198991	0.170467986700450	T	T	T
0.839844480335912	0.670092729863831	0.169091286764352	T	T	T
0.831932316391765	0.168382887005345	0.169447936628823	T	T	T
0.579150628447997	0.846922841596637	0.238213382312439	T	T	T
0.661194912187147	0.743196461287479	0.234599557762096	T	T	T
0.392078272030375	0.732046934184569	0.236339065353324	T	T	T
0.525374801494527	0.559346948401690	0.231686756385074	T	T	T
0.355654026144500	0.554099499562656	0.232825407110018	T	T	T
0.559967827167044	0.415662707310815	0.233959990837919	T	T	T
0.181098159666244	0.400682195732401	0.234100593555557	T	T	T
0.436114046979300	0.233542716514849	0.236820659109727	T	T	T
0.137134919600026	0.222939891065926	0.236042706789866	T	T	T
0.249081647991366	0.146834949914951	0.236399578945025	T	T	T
0.646391816086344	0.987768549140986	0.244327445121005	T	T	T
0.800096080941010	0.787169649528222	0.239706778955689	T	T	T
0.292568557229814	0.769477232050355	0.241878871827307	T	T	T
0.698849323161297	0.453851576019774	0.238166120244715	T	T	T
0.073311283341860	0.427837557284057	0.239074065223796	T	T	T
0.492486739387064	0.148316813279354	0.241903987723039	T	T	T
0.996472152732013	0.128599843958274	0.240284084407146	T	T	T
0.181365811112745	0.004844530493394	0.242065023580986	T	T	T

Naphthalene 2r3x2r3
1
7.568022460000000 -4.36939980000000 0.000000000000000
0.000000000000000 8.738799610000000 0.000000000000000
0.000000000000000 0.000000000000000 36.17926446000000
Cu C H
48 10 8
Selective dynamics
Direct
0.000000000000000 0.000000000000000 0.000000000000000 F F F
0.000000000000000 0.499999999427843 0.000000000000000 F F F
0.166666667107115 0.833333332599956 0.000000000000000 F F F
0.166666667107115 0.333333333172121 0.000000000000000 F F F
0.333333332892884 0.666666665683557 0.000000000000000 F F F
0.500000000000000 0.999999998855678 0.000000000000000 F F F
0.333333332892884 0.166666666255722 0.000000000000000 F F F
0.500000000000000 0.499999999427843 0.000000000000000 F F F
0.666666667107116 0.833333332599956 0.000000000000000 F F F
0.666666667107116 0.333333333172121 0.000000000000000 F F F
0.833333332892885 0.666666665683557 0.000000000000000 F F F
0.833333332892885 0.166666666255722 0.000000000000000 F F F
0.166666666578578 0.166666666431901 0.056931920279290 F F F
0.166666666578578 0.666666666317468 0.056931920279290 F F F
0.333333333289289 0.999999999405816 0.056931920279290 F F F
0.333333333289289 0.499999999634682 0.056931920279290 F F F
0.499999999867868 0.833333332771396 0.056931920279290 F F F
0.666666666446439 0.166666665793670 0.056931920279290 F F F
0.499999999867868 0.333333332885829 0.056931920279290 F F F
0.666666666446439 0.666666666022536 0.056931920279290 F F F
0.833333333025017 0.999999999159250 0.056931920279290 F F F
0.833333333025017 0.499999999388116 0.056931920279290 F F F
0.999999999735728 0.833333332476464 0.056931920279290 F F F
0.999999999735728 0.333333332705322 0.056931920279290 F F F
0.332853113624547 0.332599895405494 0.114047050022079 T T T
0.333408318363100 0.833226313668926 0.113757018622032 T T T
0.500109256437448 0.166731575001489 0.113745891982721 T T T
0.500098248591397 0.667144598396518 0.113993013851469 T T T
0.666916045222523 -0.000183624304412 0.113726726184362 T T T
0.833638754575209 0.333262306512019 0.113572061878632 T T T
0.667146000612182 0.499890820378755 0.113672170602830 T T T
0.833208673483383 0.833001319905958 0.113722053177966 T T T
0.000072793715471 0.166610771843711 0.113762069106949 T T T
0.000200138767617 0.666530949754057 0.113566733009820 T T T
0.167015983198996 0.000022467842902 0.113762374730593 T T T
0.166669903654652 0.499943185568165 0.113898793080459 T T T
0.000328343677067 -0.000314455216769 0.170612160919380 T T T
-0.001190657166005 0.499807971140068 0.171002959553344 T T T
0.165988803420421 0.832339604467639 0.170853169087652 T T T
0.165424635346845 0.332951872830138 0.170977086515402 T T T
0.332542300071236 0.666711505774503 0.171021337847523 T T T
0.500546866581887 -0.000464614945201 0.170678715040574 T T T
0.334058582206586 0.165116531697342 0.171159078139636 T T T
0.501408422316647 0.500022346982154 0.170098764044209 T T T
0.668461735647842 0.834357243272314 0.171147210280296 T T T
0.667706093225853 0.332900229885767 0.170808810793530 T T T
0.834578403257074 0.666837218162010 0.170871328095671 T T T
0.832974045049519 0.166894125259719 0.170890761074688 T T T
0.165249064813437 0.329305182828500 0.251750690542174 T T T
0.166406854650206 0.171634319065875 0.251004044155810 T T T
0.327953293681096 0.171036611508222 0.251113839613198 T T T
0.486953710800903 0.328505866913074 0.252075202811573 T T T
0.326327528732237 0.493259927387571 0.252978374836590 T T T
0.490624816823994 0.492871090330571 0.253052936363472 T T T
0.329983680861787 0.657604572740771 0.253183523039333 T T T
0.489101908859226 0.814830260278483 0.253858301239660 T T T
0.650726266770028 0.814621051706984 0.253989088229004 T T T
0.651670325338827 0.656894671677769 0.253503904280052 T T T
0.040375533745838 0.329921042325217 0.251374689909797 T T T
0.042582101683431 0.045650639056368 0.249762828573744 T T T
0.325237836556824 0.044818593300200 0.250240623151760 T T T
0.612300883327786 0.328689720265213 0.251744463530555 T T T
0.776540064929746 0.656131959529495 0.253113943341222 T T T
0.774546771255215 0.940584700673086 0.254262293884787 T T T
0.491813036306483 0.941154031429324 0.253812969493004 T T T
0.204767310826226 0.657499944033975 0.252712377762836 T T T

P1

[1] F. C. Bocquet, G. Mercurio, M. Franke, G. van Straaten, S. Wei, S. Soubatch, C. Kumpf, and F. S. Tautz, "Torricelli: A software to determine atomic spatial distributions from normal incidence x-ray standing wave data," Comput. Phys. Commun. **235**, 502–513 (2018).

[2] K. Christmann, *Introduction to Surface Physical Chemistry* (Steinkopff Verlag, Springer-Verlag, Darmstadt, New York, 1991).

[3] A. M. de Jong and J. W. Niemantsverdriet, "Thermal desorption analysis: Comparative test of ten commonly applied procedures," Surf. Sci. **233**, 355–365 (1990).

[4] D. L. S. Nieskens, A. P. van Bavel, and J. W. Niemantsverdriet, "The analysis of temperature programmed desorption experiments of systems with lateral interactions; implications of the compensation effect," Surf. Sci. **546**, 159–169 (2003).

[5] E. Bauer, F. Bonczek, H. Poppa, and G. Todd, "Thermal desorption of metals from tungsten single crystal surfaces," Surf. Sci. **53**, 87–109 (1975).

[6] D. A. King, "Thermal desorption from metal surfaces: A review," Surf. Sci. **47**, 384–402 (1975).

[7] S. L. Tait, Z. Dohnálek, C. T. Campbell, and B. D. Kay, "n-alkanes on mgo(100). i. coverage-dependent desorption kinetics of n-butane," J. Chem. Phys. **122**, 164707 (2005).

[8] P. A. Redhead, "Thermal desorption of gases," Vacuum **12**, 203–211 (1962).

[9] R. I. Masel, *Principles of adsorption and reaction on solid surfaces, Wiley series in chemical engineering* (1996).

[10] H. Eyring, "The activated complex in chemical reactions," J. Chem. Phys. **3**, 107–115 (1935).

[11] J. M. Gottfried, E. K. Vestergaard, P. Bera, and C. T. Campbell, "Heat of adsorption of naphthalene on pt(111) measured by adsorption calorimetry," J. Phys. Chem. B **110**, 17539–17545 (2006).

[12] T. L. Hill, *An Introduction to Statistical Thermodynamics* (Addison-Wesley Publishing Company, Inc., Reading, MA, 1960).

[13] A. Redondo, Y. Zeiri, J. J. Low, and W. A. Goddard, "Application of transition state theory to desorption from solid surfaces: Ammonia on ni(111)," J. Chem. Phys. **79**, 6410–6415 (1983).

[14] M. Goubet and O. Pirali, "The far-infrared spectrum of azulene and isoquinoline and supporting anharmonic density functional theory calculations to high resolution spectroscopy of

polycyclic aromatic hydrocarbons and derivatives," J. Chem. Phys. **140**, 044322 (2014).

[15] O. Pirali, M. Goubet, T. R. Huet, R. Georges, P. Soulard, P. Asselin, J. Courbe, P. Roy, and M. Vervloet, "The far infrared spectrum of naphthalene characterized by high resolution synchrotron ftir spectroscopy and anharmonic dft calculations," Phys. Chem. Chem. Phys. **15**, 10141–50 (2013).

[16] D. P. Chong, "Localized and delocalized 1s core-holes in dft calculations," J. Electron Spectrosc. Rel. Phenom. **159**, 94–96 (2007).

[17] D. P. Chong, "Density functional theory study on the electron spectra of naphthalene and azulene vapours," Can. J. Chem. **88**, 787–796 (2010).

[18] S. Reiß, *Spektroskopische Untersuchungen verschiedener molekularer Adsorbate auf der Titandioxid(110)-Oberfläche*, Thesis (2001).

[19] J. Stöhr, *NEXAFS Spectroscopy* (Springer-Verlag, 1992).

[20] G. Witte, S. Lukas, P. S. Bagus, and C. Wöll, "Vacuum level alignment at organic/metal junctions: cushion effect and the interface dipole," App. Phys. Lett. **87**, 263502 (2005).

[21] G. Kresse and J. Hafner, "Ab initio molecular dynamics for liquid metals," Phys. Rev. B **47**, 558–561 (1993).

[22] G. Kresse and J. Hafner, "Ab initio molecular-dynamics simulation of the liquid-metal-amorphous-semiconductor transition in germanium," Phys. Rev. B **49**, 14251–14269 (1994).

[23] G. Kresse and J. Furthmüller, "Efficiency of ab-initio total energy calculations for metals and semiconductors using a plane-wave basis set," Comput. Mat. Sci. **6**, 15–50 (1996).

[24] G. Kresse and J. Furthmüller, "Efficient iterative schemes for ab initio total-energy calculations using a plane-wave basis set," Phys. Rev. B **54**, 11169–11186 (1996).

[25] J. P. Perdew, K. Burke, and M. Ernzerhof, "Generalized gradient approximation made simple," Phys. Rev. Lett. **77**, 3865–3868 (1996).

[26] S. Grimme, J. Antony, S. Ehrlich, and H. Krieg, "A consistent and accurate ab initio parametrization of density functional dispersion correction (dft-d) for the 94 elements h-pu," J. Chem. Phys. **132**, 154104 (2010).

[27] P. E. Blöchl, "Projector augmented-wave method," Phys. Rev. B **50**, 17953–17979 (1994).

[28] G. Kresse and D. Joubert, "From ultrasoft pseudopotentials to the projector augmented-wave method," Phys. Rev. B **59**, 1758–1775 (1999).

[29] J. Tersoff and D. R. Hamann, "Theory of the scanning tunneling microscope," Phys. Rev. B

31, 805–813 (1985).

[30] R. F. W. Bader, *Atoms in Molecules - A Quantum Theory* (Oxford University Press, Oxford, 1990).

[31] G. te Velde and E. J. Baerends, "Precise density-functional method for periodic structure," Phys. Rev. B **44**, 7888 (1991).

[32] G. Wiesenekker and E. J. Baerends, "Quadratic integration over the three-dimensional brillouin zone," J. Phys.: Condens. Matter **3**, 6721 (1991).

[33] M. Franchini, P. H. T. Philipsen, E. van Lenthe, and L. Visscher, "Accurate coulomb potentials for periodic and molecular systems through density fitting," J. Chem. Theory Comput. **10**, 1994–2004 (2014).

[34] M. Franchini, P. H. T. Philipsen, and L. Visscher, "The becke fuzzy cells integration scheme in the amsterdam density functional program suite," J. Comput. Chem. **34**, 1819–1827 (2013).

[35] BAND2017, SCM, Theoretical Chemistry, Vrije Universiteit, Amsterdam, The Netherlands, http://www.scm.com.

[36] G. te Velde, F. M. Bickelhaupt, S. J. A. van Gisbergen, C. Fonseca Guerra, E. J. Baerends, J. G. Snijders, and T. Ziegler, "Chemistry with adf," J. Comput. Chem. **22**, 931–967 (2001).

[37] C. Fonseca Guerra, J. G. Snijders, G. te Velde, and E. J. Baerends, "Towards an order-n dft method," Theor. Chem. Acc. **99**, 391–403 (1998).

[38] E. van Lenthe and E. J. Baerends, "Optimized slater-type basis sets for the elements 1-118," J. Comput. Chem. **24**, 1142–1156 (2003).

[39] K. Momma and F. Izumi, "Vesta 3 for three-dimensional visualization of crystal, volumentric and morphology data," J. Appl. Cryst. **44**, 1272–1276 (2011).

[40] R. J. Maurer and K. Reuter, "Excited-state potential-energy surfaces of metal-adsorbed organic molecules from linear expansion -self-consistent field density-functional theory (scf-dft)," J. Chem. Phys. **139**, 014708 (2013).

[41] D. Vanderbilt, "Soft self-consistent pseudopotentials in a generalized eigenvalue formalism," Phys. Rev. B **41**, 7892–7895 (1990).

[42] M. Teruyasu, T. Isao, G. Shang-Peng, and J. P. Chris, "First-principles calculation of spectral features, chemical shift and absolute threshold of elnes and xanes using a plane wave pseudopotential method," J. Phys.: Condens. Matter **21**, 104204 (2009).

[43] L. Triguero, L. G. M. Pettersson, and H. Ågren, "Calculations of near-edge x-ray-absorption

spectra of gas-phase and chemisorbed molecules by means of density-functional and transition-potential theory," Phys. Rev. B **58**, 8097–8110 (1998).

[44] M. Klues, K. Hermann, and G. Witte, "Analysis of the near-edge x-ray-absorption fine-structure of anthracene: A combined theoretical and experimental study," J. Chem. Phys. **140**, 014302 (2014).

[45] K. Diller, R. J. Maurer, M. Müller, and K. Reuter, "Interpretation of x-ray absorption spectroscopy in the presence of surface hybridization," J. Chem. Phys. **146**, 214701 (2017).

[46] M. Cohen and R. P. McEachran, "Length and velocity formulae in approximate oscillator strength calculations," Chem. Phys. Lett. **14**, 201–204 (1972).

[47] F. L. Hirshfeld, "Bonded-atom fragments for describing molecular charge densities," Theor. Chim. Acta **44**, 129–138 (1977).

THE JOURNAL OF PHYSICAL CHEMISTRY C

P2

pubs.acs.org/JPCC Article

Chemisorption and Physisorption at the Metal/Organic Interface: Bond Energies of Naphthalene and Azulene on Coinage Metal Surfaces

Stefan R. Kachel,[‖] Benedikt P. Klein,[‖] Juliana M. Morbec, Maik Schöniger, Mark Hutter, Martin Schmid, Peter Kratzer, Bernd Meyer, Ralf Tonner, and J. Michael Gottfried*

Cite This: *J. Phys. Chem. C* 2020, 124, 8257−8268 Read Online

ACCESS | Metrics & More | Article Recommendations | Supporting Information

ABSTRACT: Organic/inorganic hybrid interfaces play a prominent role in organic (opto)electronics, heterogeneous catalysis, sensors, and other current fields of technology. The performance of the related devices and processes depends critically on the nature and strength of interfacial interaction. Here, we use the molecular isomers naphthalene (Nt) and azulene (Az) on the Ag(111) and Cu(111) surfaces as model systems that cover different bonding regimes from physisorption to chemisorption. Az also serves as a model for nonalternant molecular electronic materials and for topological 5−7 defects in graphene. The interaction energies are determined from the quantitative analysis of temperature-programmed desorption data. On both surfaces, Az binds more strongly than Nt, with zero-coverage desorption energies (in kJ/mol) of 120 for Az/Ag and 179 for Az/Cu, compared to 103 for Nt/Ag and 114 for Nt/Cu. The integrated experimental energies are compared with adsorption energies from density-functional theory (DFT) calculations, which include van der Waals contributions using four different correction schemes for the PBE functional: (1) the DFT-D3 scheme with Becke−Johnson damping, (2) the vdW^{surf} correction based on DFT-TS, (3) a many-body dispersion correction scheme, and (4) the D3^{surf} scheme. Differences in the performance of these methods are discussed. Periodic energy decomposition analysis reveals details of the surface chemical bond and confirms that Az/Cu forms a chemisorptive bond, while the other systems are physisorbed. The variation of the adsorbate−substrate interaction with the topology of the π-electron system and the type of surface can be employed to modify the interface properties in graphene-based and organic electronic devices.

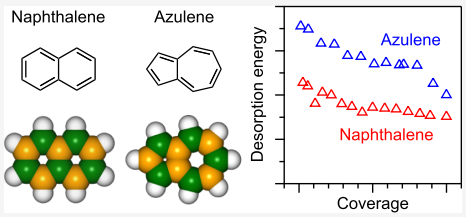

INTRODUCTION

Hybrid interfaces between organic and inorganic materials play a prominent role in modern technology and the related fundamental research.[1,2] These interfaces carry multiple functionalities and possess properties different from those of the adjacent pristine phases.[1,3] With the advent of organic (opto)electronics,[4,5] interfaces between organic semiconductors (OSCs) and metals have come into focus, because they control charge injection as a crucial performance-determining process at the metal/OSC contacts. However, the fundamental understanding of these interfaces is still lacking, because reliable quantitative investigations are methodologically challenging.

The nature of the metal/organic interaction depends on the electronic structure of the OSC, especially its frontier orbitals, which are typically part of the π-electron system. Within the framework of Hückel molecular orbital theory, the electronic structure of a π-electron system is related to its topology, as expressed by the topological matrix, which reflects the connectivity pattern of the atoms within the π-system.[6,7] Molecular OSCs usually contain benzenoid aromatic π-systems (i.e., their aromatic backbone consists of hexagonal benzene rings), and thus have alternant (or bipartite[8]) topologies. In contrast, aromatic backbones with nonalternant (or nonbipartite) topologies have only recently gained interest in the context of organic (opto)electronics.[9] Nonalternant structural elements are also used for the topological design of graphene derivatives.[10]

Recently, it has been shown that the strength of the surface chemical bond can depend on the topology of the π-electron system: while naphthalene (Nt) on Cu(111) is physisorbed, its nonalternant isomer azulene (Az) forms a chemisorptive bond.[7] Even when both Az and Nt are chemisorbed onto the more reactive Pt(111) surface, there remains a large difference in the interaction strength.[11] The observation that these two closely related molecules—both are bicyclic aromatic hydrocarbons with the same number of carbon and hydrogen atoms—bind so differently to surfaces makes them a very

Received: February 1, 2020
Revised: February 27, 2020
Published: April 2, 2020

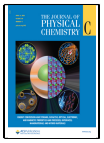

https://dx.doi.org/10.1021/acs.jpcc.0c00915
J. Phys. Chem. C 2020, 124, 8257−8268

The Journal of Physical Chemistry C pubs.acs.org/JPCC Article

interesting model system for quantitative studies of the metal/organic interfacial interaction, both in experiment and theory.

As an extension of previous work,[7,12] we study here the interaction of both molecules with the (111) surfaces of silver and copper for various coverages in the submonolayer regime. The four different systems (and different coverages) provide us with a gradational change of the molecule−metal interaction from physisorption to chemisorption. Because both isomers desorb as intact molecules from both surfaces, temperature-programmed desorption (TPD, Figure 1) is the method of

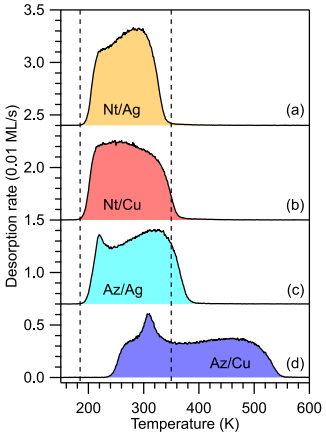

Figure 1. Monolayer TPD traces for (a) Nt/Ag(111), (b) Nt/Cu(111), (c) Az/Ag(111), and (d) Az/Cu(111), measured with a heating rate of 1 K/s by mass spectrometric detection of m/z = 128 amu. The vertical dashed lines indicate the desorption range for Nt/Ag(111) and also serve as a guide to the eye and for comparison with the three other systems.

choice to assess the strength of the adsorbate−substrate bond. To obtain reliable and reproducible data, a dedicated setup including a Feulner cup cryo shroud for line-of-sight conditions, along with precise temperature calibration and sample positioning,[13] was employed. The resulting data were subjected to extended analysis with several suitable methods.

Different bond strengths of the isomer pair make it especially suitable for benchmarking current methods for the correction of dispersion interaction within the density-functional theory (DFT) approach. Therefore, we compare here four different correction schemes for the Perdew, Burke, and Ernzerhof (PBE) functional: (1) the DFT-D3 scheme[14] with the Becke−Johnson damping function,[15,16] (2) the vdW^{surf} correction[17] based on DFT−Tkatchenko-Scheffler (TS),[18−20] (3) a many-body dispersion (MBD) correction scheme,[21,22] and (4) the D3^{surf} scheme.[12]

Our results reveal the critical role of topology of the conjugated π-electron system in controlling the chemical bond at the metal/organic interface and show that the dispersion correction schemes perform quite differently with respect to the metal−organic bond energies.

METHODS

Experimental Methods. TPD was carried out in a dedicated ultrahigh-vacuum (UHV) apparatus with base pressure in the low 10^{-10} mbar regime. The apparatus hosts a HIDEN EPIC 1000 quadrupole mass spectrometer mounted inside a differentially pumped cryo shroud cooled to 80 K with l-N_2. This setup is a variant of line-of-sight mass spectrometry,[23] and ensures that molecules impinging upon the inner wall of the cryo shroud are permanently adsorbed (or condensed) there, such that the mass spectrometer mainly detects molecules with a straight trajectory from the sample. This leads to improved quality of the TPD traces, and is the basis for their quantitative analysis. Temperatures were precisely measured inside the sample using a calibrated type K thermocouple. Azulene (Sigma-Aldrich, purity >99.0%) and naphthalene (Sigma-Aldrich, purity >99.7%) were introduced into the UHV system through leak valves after repeated freeze−pump−thaw cycles of the reservoirs. Polished Ag(111) and Cu(111) single-crystal surfaces (purity >99.9999%, roughness <0.03 μm, orientation accuracy <0.1°, from MaTecK/Germany) were prepared by iterated sputtering with Ar^+ (0.5 keV, 5−7 μA, 30 min) and annealing (850 K, 15 min). For each system, monolayer coverage (1 ML) corresponds to the integral of the saturated first-layer desorption trace. For the adjustment of different (sub)-monolayer coverages, partial thermal desorption of an initial excess dosage was used, as described in the Supporting Information (SI), Figure S1. A coverage of 1 ML corresponds to 2.28 × 10^{14} molecules/cm^2, according to previous work.[7,12]

Density Functional Theory Calculations. DFT calculations with periodic boundary conditions were performed to compute the adsorption energies of Az and Nt on Ag(111) and Cu(111). We used the PBE generalized gradient approximation[24] for the exchange−correlation functional in combination with four different methods to treat the van der Waals (vdW) interactions: (1) the DFT-D3 scheme[14] with Becke−Johnson damping function,[15,16] (2) the vdW^{surf} correction[17] based on DFT-TS,[18−20] (3) a MBD correction scheme,[21,22] and (4) the D3^{surf} scheme.[12]

The DFT-D3 scheme proposed by Grimme et al. uses atomic pairwise contributions to the dispersion interaction energy based on the polarization of the respective atoms in the chemical environment of the system.[14] The energy contributions are based on tabulated C_6 coefficients taking into account the fractional coordination number of the atom under consideration and a damping function for close interatomic distances following a proposal by Becke and Johnson.[15,16]

The vdW^{surf} approach[17] includes the collective electronic response of the substrate in the determination of vdW parameters (C_6 coefficients, polarizabilities, and vdW radii) by combining the pairwise TS method[18] with Lifshitz−Zaremba−Kohn theory.[19,20]

The MBD method[21,22] accounts for collective vdW effects beyond the pairwise approximation by representing the atomic response functions (within the random phase approximation) by a set of quantum harmonic oscillators interacting via the dipole−dipole interaction potential.

The D3^{surf} scheme is an extension of the original DFT-D3 method proposed by Grimme et al., in which the parameter set of coordination-dependent C_6 coefficients is extended by additional values for Cu and Ag at higher coordination numbers of the surface and bulk atoms.

Calculations with the DFT-D3 scheme were performed with the Vienna ab Initio Simulation Package (VASP).[25−28] The PBE functional,[24] the projector-augmented wave (PAW) ansatz[29,30] for the atomic cores, a plane-wave cutoff energy of 350 eV, and a vacuum layer of 30 Å were used. For all calculations, a 24 × 24 × 1 Monkhorst−Pack k-point mesh was

https://dx.doi.org/10.1021/acs.jpcc.0c00915
J. Phys. Chem. C 2020, 124, 8257−8268

The Journal of Physical Chemistry C pubs.acs.org/JPCC Article

adjusted to the supercell of a 4-layer slab. The fcc bulk lattice parameters were obtained with the same method and were 4.072 Å for Ag and 3.568 Å for Cu. The frequency calculations for the thermodynamic corrections were also performed in VASP using a finite differences approach, where only the atoms of the molecule and the first surface layer were displaced. The calculation of enthalpies follows the literature.[31]

Calculations with the vdW^{surf} and the MBD methods were performed using the FHI-aims code,[32] an all-electron code that uses numeric atom-centered orbitals as basis functions. We used "tight-tier2" basis sets for the Ag, Cu, and H atoms, and the "tight-tier3" basis set for the C atoms. Convergence criteria of 10^{-5} electrons/Å^3 and 10^{-5} eV were applied for the charge density and the total energy, respectively. Both Cu(111) and Ag(111) surfaces were modeled using a $(2\sqrt{3} \times 2\sqrt{3})$-*R*30° unit cell, with a five-layer slab and a vacuum region of 130 Å. In geometry optimizations, the molecules and the top two metal layers were allowed to relax, while the remaining bottom layers were constrained to their bulk positions; a force convergence criterion of 10^{-2} eV/Å was applied for structural relaxations. We used a 4 × 4 × 1 Monkhorst−Pack *k*-point mesh to sample the Brillouin zone. The fcc bulk lattice parameters obtained with vdW^{surf} were also used for the MBD calculations and were 4.014 Å for Ag and 3.601 Å for Cu. The vibrational frequencies for the calculation of zero-point energies and thermodynamic corrections were computed using the PHONOPY package[33] in conjunction with the FHI-aims code.

The D3^{surf} calculations were performed with the PWscf code of the Quantum Espresso software package.[34] As in the D3 calculations, we use the PBE functional[24] and the Becke−Johnson damping function within the dispersion correction scheme.[15,16] Atomic cores were represented by Vanderbilt ultrasoft pseudopotentials,[35] and the wave functions were expanded in a plane wave basis with a cutoff energy of 30 Ry. With this setup and the D3^{surf} dispersion correction scheme, we obtained fcc bulk lattice constants of 4.101 and 3.606 Å for Ag and Cu, respectively. Surfaces were represented by periodically repeated slabs with a thickness of 5 atomic layers and a $(2\sqrt{3} \times 2\sqrt{3})$-*R*30° surface unit cell. The optimized bulk lattice constants were used for the lateral dimensions of the slabs. In the structure optimization, the force convergence criterion was set to 0.003 eV/Å. Only the upper three surface layers and the adsorbate were allowed to relax, while the bottom two layers were kept frozen in their bulk positions. The *k*-point sampling was done with a Γ-centered 7 × 7 × 1 Monkhorst−Pack mesh. Further details can be found in Tables S5 and S6 in the Supporting Information.

The energy decomposition analysis using periodic boundary conditions (pEDA) was performed using the PBE functional,[24] the DFT-D3 dispersion correction scheme,[14] a TZ2P basis set,[36] and considering relativistic effects with the zeroth order regular approximation,[37] as implemented in the ADF-BAND package 2017.[38−40] The optimized $(2\sqrt{3} \times 2\sqrt{3})$-*R*30° structures were taken from the PBE-D3 calculations in VASP. In ADF-BAND, a 7 × 7 *k*-grid and 2-dimensional periodic boundary conditions were used. The integration accuracy of the used Becke-grid was set to quality "normal".[41] The charge transfer was derived via Bader's atoms-in-molecules (AIM) scheme and was calculated in ADF-BAND 2017. The same values were already reported in previous work.[7,12]

The pEDA method allows decomposition of the bond energy into several physically well-defined terms, thus permitting a more detailed interpretation of the character of the chemical bond between two fragments.[42] In our case, the fragments are chosen to be the molecule and the surface in their respective singlet electronic states. The convergence of the pEDA values with the *k*-space sampling density is nontrivial for metal surfaces[38] and has been checked thoroughly, as explained in detail in Tables S7 and S8 in the Supporting Information. Further details of all DFT calculations can be found in the Supporting Information. A comparison of the calculation parameters of all employed DFT methods can be found in Table S9.

RESULTS AND DISCUSSION

TPD Coverage Series. TPD traces of all four systems at complete monolayer coverage are compared in Figure 1. Depending on the pairing of the adsorbate (Az, Nt) and the substrate (Ag, Cu), desorption occurs over different temperature ranges. Nt on Ag(111) has the narrowest desorption range from 190 to 350 K, whereas Az on Cu(111) has the widest range from 240 to 550 K. The temperatures, at which desorption is complete, also vary considerably. On both surfaces, Az requires a higher temperature for complete desorption than Nt (550 K vs 370 K on Cu; 400 K vs 350 K on Ag), suggesting that the nonalternant isomer Az binds more strongly to both metal surfaces.

To gain further insights into the coverage dependence of the desorption rate and to acquire data for the quantitative analysis, desorption traces for different initial coverages Θ_0 were measured, as shown in Figures 2 and 3. All systems

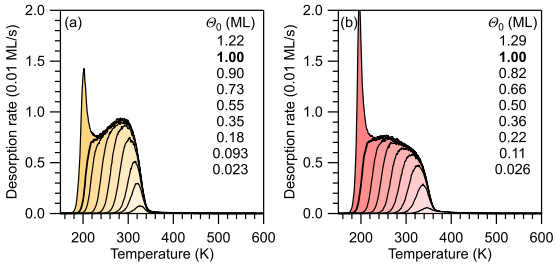

Figure 2. Series of TPD traces for different initial coverages Θ_0 of Nt on (a) Ag(111) and (b) Cu(111). Initial coverages listed in the graphs from top to bottom correspond to the TPD traces from left to right. The monolayer spectra (1.00 ML) are indicated by bold lines. The measurements were performed with a heating rate of 1 K/s by mass spectrometric detection of m/z = 128 amu.

experience substantial peak broadening toward lower temperatures with increasing Θ_0. This effect is frequently observed in the TPD curves of organic molecules, and can be attributed to coverage-dependent lateral repulsion between surface dipoles.[43] The vertical dipoles mainly arise from the "pillow," "cushion," or Pauli push-back effect, which describes the redistribution of electron density near the surface because of the Pauli repulsion with electrons in the molecule.[12,44,45] Additional dipole contributions may result from electron transfer between the molecules and the surface[46] or deformation of the molecule in the case of chemisorption.

The TPD traces of Az on Cu(111) in Figure 3b show a peak around 300 K, which appears at initial coverages between 0.7 and 0.9 ML. This peak is attributed to desorption from a compressed, incommensurate submonolayer Az phase, which

https://dx.doi.org/10.1021/acs.jpcc.0c00915
J. Phys. Chem. C 2020, 124, 8257−8268

The Journal of Physical Chemistry C pubs.acs.org/JPCC Article

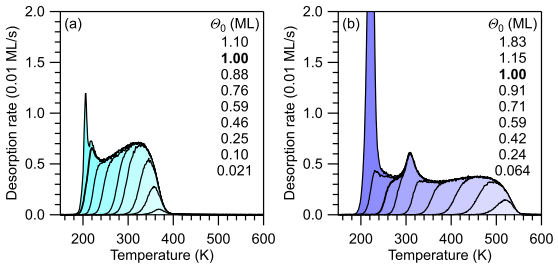

Figure 3. Series of TPD traces for different initial coverages Θ_0 of Az on (a) Ag(111) and (b) Cu(111). Initial coverages listed in the graphs from top to bottom correspond to the TPD traces from left to right. The monolayer spectra (1.00 ML) are marked by bold lines. The measurements were performed with a heating rate of 1 K/s by mass spectrometric detection of m/z = 128 amu.

was previously observed by nc-AFM.[7] Being less pronounced, this decompression peak also occurs for Az/Ag(111) around 220 K, but it is absent in the spectra of Nt. Apparently, the occurrence of the decompression peak correlates with the strength of the adsorbate−substrate interaction. Above the monolayer coverage, second- and multilayer desorption peaks occur, of which only the onsets of the second-layer peaks are displayed.

Quantitative Analysis of TPD Data. The desorption activation energy E_d as a measure of the adsorbate−substrate bond energy is obtained by quantitative analysis of the TPD data using the Polanyi−Wigner rate equation[47−49]

$$r_d = -\frac{d\Theta}{dt} = \nu_d \Theta \exp(-E_d/RT) \quad (1)$$

Here, r_d is the desorption rate, Θ is the coverage, t is the time, ν_d is the pre-exponential factor for desorption (prefactor), T is the temperature, and R is the universal gas constant.

If the adsorption is nonactivated for all Θ, E_d can be equated in good approximation with the negative differential adsorption energy.[50] For comparison with DFT calculations, which provide integral adsorption energies, the experimental energies must be integrated

$$E_{d,i}(\Theta_i) = -\frac{1}{\Theta_i}\int_0^{\Theta_i} E_d(\Theta)d\Theta \quad (2)$$

The so-called "complete" methods for TPD analysis[50,51] are not suitable here because of the strong lateral repulsion.[49] Instead, we use alternative and, in combination, similarly effective methods. A straightforward approach that provides the coverage-dependent desorption activation energy $E_d(\Theta)$ from a single TPD trace was first proposed by Nieskens et al., and is based on rewriting eq 1 as follows[49,52]

$$E_d(\Theta) = -RT \ln\left[\frac{-d\Theta/dt}{\nu_d \Theta}\right] \quad (3)$$

It should be noted that eq 3 is strictly applicable only when the prefactor is independent of the coverage, which is not necessarily the case.[53,54] In practice, moderate changes of the prefactor have a small effect on the estimate of E_d. Even if the prefactor varies by as much as one order of magnitude over the coverage range, E_d changes by only a few percent.[49] In addition to this analysis, we employ here heating-rate variation (HRV) analysis,[55] a direct fitting procedure of the TPD data, and a modified leading-edge analysis (LEA) method that provides coverage-dependent prefactors.[56,57]

Desorption Prefactors. The prefactors required for application in eq 3 were determined by HRV analysis according to[47]

$$\ln\left(\frac{T_{max}^2}{\beta}\right) = \frac{E_d}{RT} + \ln\left(\frac{E_d}{\nu_d R}\right) \quad (4)$$

In this equation, β is the heating rate, which is defined as dT/dt. This method can be used in the low-coverage range, where the peaks have a regular first-order shape because the broadening due to intermolecular repulsion is small. A representative data set for Az on Ag(111) is shown in Figure 4; the data for the three other adsorbate systems are shown in the Supporting Information, Figures S2−S5. The obtained experimental prefactors are shown in Table 1 (mean values) and Table S1 in the Supporting Information (individual values). The prefactors are the highest for Az on Cu(111) and the lowest for Nt on both surfaces. A higher prefactor can indicate a reduced mobility of the desorption precursor because of a more localized surface chemical bond.[58,59] According to eq 4, the HRV analysis also provides the desorption energies E_d, which will be discussed later.

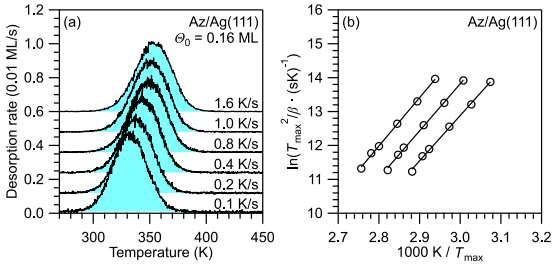

Figure 4. (a) HRV series for Az on Ag(111) for heating rates from 0.1 to 1.6 K/s and an initial coverage of 0.16 ML. (b) Analysis of the HRV series for coverages of 0.08, 0.16, and 0.28 ML, according to eq 4, yields desorption activation energies and pre-exponential factors. Corresponding data for the other systems can be found in the Supporting Information.

Table 1. Desorption Prefactors (in s^{-1}) for (Sub)monolayer and Multilayer Regimes[a]

	Az/Cu(111)	Az/Ag(111)	Nt/Cu(111)	Nt/Ag(111)
expt. (HRV)	3.2×10^{16}	1.5×10^{16}	1.7×10^{14}	3.4×10^{15}
TST $\nu_{d,mobile}$	3.2×10^{16}	1.6×10^{16}	1.3×10^{16}	1.2×10^{16}
TST $\nu_{d,im}$	6.1×10^{22}	1.8×10^{22}	7.1×10^{21}	5.8×10^{21}
entropy ν_d	1.3×10^{18}	1.0×10^{17}	7.5×10^{16}	5.4×10^{16}
multilayer ν_d	1.6×10^{18}		3.2×10^{17}	

[a](Sub)monolayer prefactors from the experiment (HRV mean values, for detailed data, see Table S1 in the Supporting Information), from TST in the mobile and immobile limits, and from entropy considerations. Multilayer prefactors from the Clausius−Clapeyron equation (see Tables S2−S4 in the Supporting Information).

In the literature, analysis of TPD data is frequently performed with estimated, not measured, prefactors ν_d. For a rough estimate of the desorption energy from a single desorption maximum, the prefactor is usually assumed to be 1×10^{13} s^{-1}, which can be reasonably accurate for atoms or diatomic molecules.[60] However, much higher prefactors have

https://dx.doi.org/10.1021/acs.jpcc.0c00915
J. Phys. Chem. C 2020, 124, 8257−8268

been reported for the desorption of larger molecules.[61,62] In such cases, estimates on the basis of transition state theory (TST) are more reasonable.[62−64]

As shown in detail in the Supporting Information, we have used TST to calculate prefactors for two limiting cases of the translational and rotational degrees of freedom (DOFs) of the adsorbate (Table S2). In the mobile limit, the adsorbed molecule possesses two translational DOFs parallel to the surface and one rotational DOF around an axis perpendicular to the molecular plane, which is assumed to be parallel to the surface. In the immobile limit, the adsorbed molecule has no rotational or translational DOF. At the desorption temperature, especially in the low-coverage regime, the mobile limit is more realistic. The resulting TST prefactors are shown in Table 1.

Another approach, which is also based on the TST, uses the activation entropy of the desorption process to calculate the prefactor.[54,65] The entropy in the transition state is approximated by the gas-phase entropy minus the entropy of the one-dimensional translation perpendicular to the surface.[65] This is equivalent to the mobile limit considered above. The adsorbate entropy can be estimated from the gas-phase entropy by a relation that was originally proposed for alkanes, but was later successfully applied to larger aromatic molecules such as coronene.[54] Detailed calculations are presented in the Supporting Information, Table S3. As expected, the resulting prefactors (Table 1) are similar to those obtained with TST in the mobile limit. Prefactors for multilayer desorption were estimated by another method based on the Clausius−Clapeyron equation [see Table 1 and the Supporting Information (Table S4) for details of the calculation]. Note that the limitations inherent in TST in the calculation of prefactors cannot be overcome by using normal mode frequencies calculated using DFT, thus DFT turns out not to be helpful in determining reliable prefactors.[65,66]

Desorption Energies. Inverted Polanyi−Wigner Equation. The inverted Polanyi−Wigner (IPW) equation (eq 3) provides coverage-dependent differential desorption energies from a single TPD trace. Here, we used the monolayer TPD traces of all four systems and employed the average experimental prefactors obtained by HRV as well as the TST prefactors (Table 1). The energies obtained by IPW analysis are presented in Figure 5 (solid lines). Since HRV and TST deliver almost identical prefactors for Az, only one energy curve is shown, while for Nt, two separate energy curves are shown corresponding to the HRV and TST prefactors. On both surfaces, Az shows higher desorption energies than Nt over the whole coverage range up to one monolayer. The desorption energies of Az also drop faster with increasing coverage, indicating a stronger intermolecular repulsion. These differences between the two isomers are especially pronounced on Cu(111).

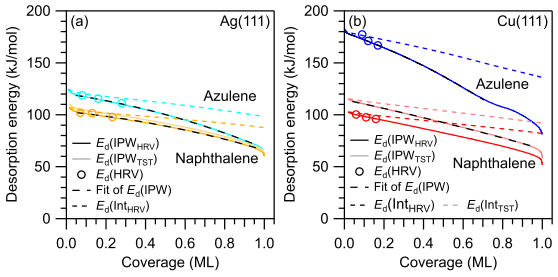

Figure 5. Desorption activation energies as a function of coverage for Az (cyan and blue) and Nt (orange and red) on (a) Ag(111) and (b) Cu(111). Solid lines: differential desorption energies [opaque: ν_d(HRV), pale: ν_d(TST)]; colored dashed lines: integral energies (for comparison with DFT calculations); black dashed lines: fits of differential desorption energies with the polynomials described in the text; and circles: desorption energies from HRV.

The coverage dependencies of differential desorption energies E_d based on the HRV prefactors are well described by the following second-order polynomial fits (in kJ/mol, Θ in ML): Az/Cu: $179 - 65\Theta - 39\Theta^2$, Az/Ag: $120 - 27\Theta - 25\Theta^2$, and Nt/Ag: $103 - 18\Theta - 19\Theta^2$. (The Nt/Cu case will be discussed separately below.) These polynomial fits are shown as black dashed lines in Figure 5. This figure also shows the energies obtained from the HRV analysis as open circles in the low-coverage range. The agreement with the IPW results is very good. For later comparison with the integral adsorption energies calculated by DFT, the integral desorption energies are needed. They were obtained by integration (eq 2) of the corresponding IPW curves, and are included as colored dashed lines in Figure 5.

For Nt, the DFT methods discussed below predict a stronger bonding to Cu(111) than to Ag(111), contrary to the experimental energies based on the HRV prefactors. This disagreement requires special consideration and a critical discussion of the desorption prefactors used in the analysis. As can be seen in Table 1, Nt on Cu(111) is the only system with a very substantial deviation between the experimental prefactor (from HRV) and the TST prefactor for the mobile limit. Interestingly, the experimental HRV prefactor (1.7×10^{14} s^{-1}) is here almost two orders of magnitude lower than its theoretical TST counterpart (1.3×10^{16} s^{-1}). This is a rather unusual finding, because the prefactor in the mobile limit represents the smallest possible prefactor (within the framework of TST). Using the TST prefactor instead of the HRV prefactor for the IPW analysis results in substantially higher energies, which are well described by the second-order polynomial $114 - 40\Theta - 7\Theta^2$ (in kJ/mol, Θ in ML, see also Figure 5b). Later, we will show that the TST prefactor agrees better with that obtained from a modified LEA methods. Therefore, we will use the TST prefactor for Nt on Cu(111) in the following.

Fit of the TPD Traces. Using the IPW method, we found that the coverage dependence of the desorption energy is well described by a second-order polynomial. However, this method uses only one TPD trace for the analysis (here, the trace corresponding to monolayer coverage). To use the full data sets shown in Figures 2 and 3, the TPD data were fitted using the Polanyi−Wigner equation (eq 1) with a second-order polynomial for the desorption energy, $E_d = a - b\Theta - c\Theta^2$. The prefactors obtained from the HRV analysis were used, except for Nt on Cu(111), for which the TST prefactor was used (see above). The computed TPD traces are shown in Figure 6 along with the experimental TPD data. The desorption energies obtained by the fit are in excellent agreement with the results of the IPW analysis, especially for coverages below 0.6 ML, as can be seen in direct comparison in Figure 7.

The simulated TPD traces in Figure 6 show a good agreement with the experimental data in the leading-edge range, especially at higher coverages. However, the high-

https://dx.doi.org/10.1021/acs.jpcc.0c00915
J. Phys. Chem. C 2020, 124, 8257−8268

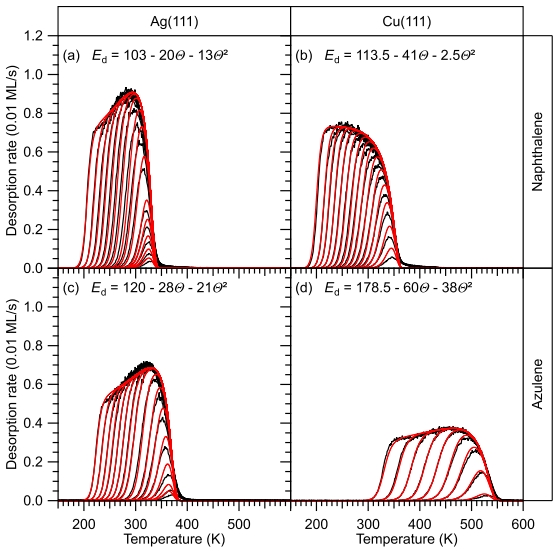

Figure 6. TPD coverage series of (a,b) Nt and (c,d) Az on (a,c) Ag(111) and (b,d) Cu(111) (black lines) and simulated TPD traces (red lines) using a quadratic function for the desorption energy (shown in graphs, in kJ/mol). Constant prefactors, as obtained by the HRV, were used, except for Nt on Cu(111), where the TST prefactor was used (see Table 1). Coverage ranges: (a) 0.03−1.0 ML, (b) 0.01−1.0 ML, (c) 0.01−0.88 ML, and (d) 0.01−0.68 ML.

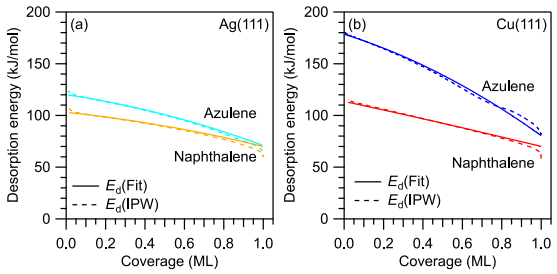

Figure 7. Desorption activation energies as a function of coverage for Az (cyan, blue) and Nt (orange, red) on (a) Ag(111) and (b) Cu(111). Solid lines: desorption energies obtained by fitting of the TPD spectra according to Figure 6; dashed lines: desorption energies obtained by IPW for comparison. The energies are based on the TST prefactor for Nt on Cu(111) and HRV prefactors otherwise.

temperature (low-coverage) sides of the peaks are broader in reality than in the fits. This can be attributed to the presence of defect sites, which lead to higher desorption temperatures at very low coverages, but are not considered in the fits.

Note that second-order polynomials $a - b\Theta - c\Theta^2$ have been used in previous work to describe the coverage dependence of adsorption energies.[62,67,68] The constant a is the desorption energy at zero coverage, while b is qualitatively related to the intermolecular repulsion, which depends linearly on the coverage. The constant c is related to relaxation, which occurs when the molecules move away from their preferred adsorption sites to lower the repulsion.[62,67−69]

Modified Leading-Edge Analysis for Coverage-Dependent Prefactors. The above analysis is based on the assumption of coverage-independent prefactors. In the following, we will use a modified LEA to obtain coverage-dependent prefactors, and thus more reliable coverage-dependent energies. In the original work by Habenschaden and Küppers,[56] the analysis uses only a small section on the low-temperature side of each TPD trace. For this section, ln r_d is plotted versus $1/T$. According to the rearranged eq 1

$$\ln r_d = -\frac{E_d}{RT} + \ln \nu_d + n \ln \Theta \tag{5}$$

this procedure should result in a straight line with the slope $-E_d/R$ and an intercept that depends on ν_d. This only holds true if the relative coverage change is negligible, that is, if the term n·ln Θ is approximately constant in the analyzed section. A clear disadvantage of the original LEA lies in the low signal/noise (S/N) ratio in the low-rate range used for the analysis. Extension of the analyzed region to the range of higher rates improves the S/N ratio, but introduces more errors because of the neglected temperature dependence of the coverage.

A complementary approach was suggested by Parker et al.[57] According to the rearranged eq 1

$$\ln \frac{r_d}{\Theta^n} = -\frac{E_d}{RT} + \ln \nu_d \tag{6}$$

plotting a single TPD trace as $\ln(r_d/\Theta^n)$ versus $1/T$ results in a straight line if the correct value for the desorption order n is chosen. The slope and the intercept of this line provide E_d and ν_n, respectively. A disadvantage is that these values are only mean values averaged over the whole coverage range of the TPD trace. In the case of strong coverage dependence of E_d and ν_n, not even a straight line is obtained. As an advantage, statistical errors are much lower than in the case of LEA, because the entire TPD trace is used.

To combine the advantages of both approaches while avoiding their disadvantages, we explicitly take the coverage dependence of Θ into account using eq 6, but consider a reasonably small part of the leading edge. In this way, we avoid errors from neglecting the temperature dependence of Θ, while achieving a good balance between statistics and coverage resolution. In practice, coverage variations between 0.2 and 4% (absolute up to 0.006 ML) were allowed. If the four lowest initial coverages are excluded, the allowed coverage variations are even smaller and in the range of 0.2−1%.

The results of this analysis (in short: LNR) are shown in Figure 8 (triangles) along with the results of IPW (dashed line) and HRV (circles). All methods show remarkably good agreement up to 0.7 ML for Nt and 0.5 ML for Az. These coverage ranges coincide for the most part with those for which theoretical adsorption energies calculated by DFT are available (ranges illustrated by grey arrows in Figure 8). At higher coverages, the LNR energies exceed the IPW energies, and the desorption prefactors increase. Increased prefactors can generally be attributed to the reduced lateral mobility of the desorption precursor at high coverages.

The most pronounced deviations between IPW and LNR energies in the high-coverage range are found for Az on Cu(111). For this system, the LNR energy decreases up to 0.6 ML. In the range from 0.6 to 0.8 ML, the energy remains nearly constant (Figure 8c), while the prefactor increases and reaches almost 10^{21} s^{-1} (Figure 8d). This value is in agreement with that of the immobile limit of the TST (Table 1), and thus agrees with a densely-packed adsorbate structure. A corresponding compressed incommensurate phase has previously been observed by nc-AFM.[7] The same effect, but less

https://dx.doi.org/10.1021/acs.jpcc.0c00915
J. Phys. Chem. C 2020, 124, 8257−8268

The Journal of Physical Chemistry C pubs.acs.org/JPCC Article

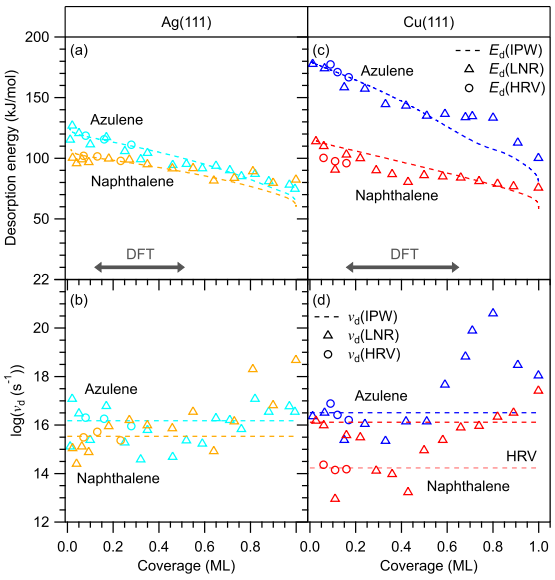

Figure 8. Coverage-dependent desorption energies and prefactors obtained by the modified LEA (LNR). (a,c) Desorption energies E_d and (b,d) prefactors ν_d for Az (cyan and blue triangles) and Nt (orange and red triangles) on (a,b) Ag(111) and (c,d) Cu(111). The results of HRV (circles) and IPW (dashed lines) are shown for comparison. IPW energies were derived with the HRV prefactor, except for Nt on Cu(111), where the TST prefactor was used. The HRV prefactor for Nt is indicated as a faint dashed line. The dark grey arrows indicate the coverage ranges for which DFT calculations were performed (Ag: 0.12–0.51 ML; Cu: 0.16–0.65 ML).

pronounced, is also visible for the three other systems. The steeply increasing prefactor for Az on Cu also seems to be related to the appearance of the additional peak in the monolayer spectrum above 0.7 ML.

For Nt on Cu(111), note that the IPW energy curve based on the TST prefactor (see Figure 5b and related discussion of the prefactors) is in good agreement with the LNR values in the low-coverage range of up to 0.25 ML, while the HRV energies are too low (Figure 8c). In addition, the prefactors from the LNR analysis in this coverage range are substantially higher than the HRV prefactor and closer to the TST prefactor for the mobile limit. This retrospectively justifies our choice of the TST prefactor in the above-presented IPW and TPD-fit analyses. Apparently, the HRV analysis does not provide a reliable value for Nt on Cu(111). The reason for this apparent failure of the HRV analysis for this system is unclear, but the case shows that a critical consideration of the desorption prefactors and the application of several independent analysis methods is indispensable for obtaining reliable desorption energies from TPD experiments.

DFT Calculations. We will now compare the experimental energies with theoretical adsorption energies obtained from DFT calculations. Because DFT provides integral adsorption energies, denoted E_{ads} here, while the energies derived from the TPD data are differential desorption energies E_d, it is necessary to integrate the latter using eq 2 up to the coverage used in the DFT calculation. As noted above, E_d can be equated to the negative differential adsorption energy if the adsorption is nonactivated.[50] It is reasonable to assume that this is the case here because the molecules stay intact and no intramolecular bonds are dissociated. For the experimental energies, we use here the IPW values, which mostly agree well with the values from the other methods in the relevant coverage range. Note that desorption energies are positive, while adsorption energies are negative. Therefore, we compare here the negative integral desorption energy $-E_{d,i}$ (eq 2) and E_{ads}. In the DFT calculations, the following methods were used to treat vdW interactions: (1) the DFT-D3 scheme[14] with the Becke–Johnson damping function,[15,16] (2) the vdW^{surf} correction[17] based on DFT-TS,[18−20] (3) a MBD correction scheme,[21,22] and (4) the D3^{surf} scheme.[12] All methods were combined with the PBE exchange–correlation functional. In Table 2 and

Table 2. Comparison of the DFT Adsorption Energies E_{ads} (in kJ/mol) with Different Methods for the vdW Corrections[a]

	Nt/Ag	Nt/Cu	Az/Ag	Az/Cu
experiment	-97	-100^{TST}	-111	-153
D3	-118	-135	-128	-173
vdW^{surf}	-104	-118	-119	-194
MBD	-74	-81	-88	-166
D3^{surf}	-97	-97	-108	-141

[a]The coverage for the experimental energies $-E_{d,i}$ (from TPD, integrated IPW results, and HRV prefactors) is 0.65 ML on Cu(111) and 0.51 ML on Ag(111) corresponding to the $(2\sqrt{3} \times 2\sqrt{3})$-R30° structure used for both surfaces in the DFT calculations. The value for Nt/Cu marked with "TST" is based on the TST prefactor.

Figure 9, the electronic adsorption energies from all four DFT methods are compared with each other and with the experimental energies. Qualitatively, all DFT methods correctly predict the larger adsorption energy of Az compared to Nt on both surfaces, as well as a larger adsorption energy for both molecules on Cu(111) than on Ag(111). On a quantitative level, the D3 and vdW^{surf} schemes substantially overestimate all adsorption energies, whereas the MBD and the D3^{surf} methods overestimate the energies for some systems and underestimate them for others. A comparison of the D3 and vdW^{surf} schemes reveals that D3 shows a smaller deviation for the strongly bonded system Az/Cu and larger deviations for the other three systems, which are more weakly bonded. In contrast, vdW^{surf} produces the larger deviation for the strongly bonded system and a better agreement for the weakly bonded systems. The MBD scheme leads to a slightly smaller overestimation for the strongly bonded Az/Cu and even an underestimation for the other weakly bonded systems. D3^{surf} shows a good agreement for the weakly bonded systems, but a small underestimation for Az/Cu. Overall, D3^{surf} comes closest to the experimental values with an average deviation of 5 kJ/mol, whereas D3 deviates the most by an average of 23 kJ/mol. The agreement of D3^{surf} with the experimental values is even better if thermodynamic corrections are included (see below). Very recently, an extension to the D3 scheme (termed DFT-D4) was put forward that could lead to an improvement of the DFT-D values in future investigations.[70,71]

The adsorption heights calculated for the same systems with the same dispersion correction methods were already discussed in previous work.[12] There, all methods showed comparable

https://dx.doi.org/10.1021/acs.jpcc.0c00915
J. Phys. Chem. C 2020, 124, 8257–8268

The Journal of Physical Chemistry C pubs.acs.org/JPCC Article

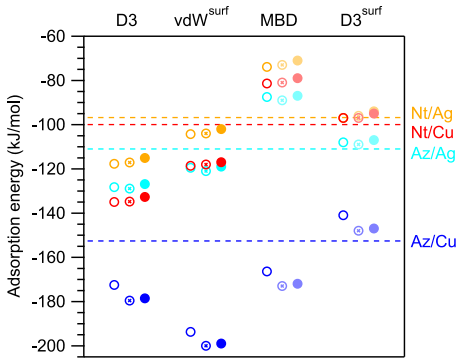

Figure 9. Comparison of the DFT adsorption energies E_{ads} obtained with different methods for the vdW corrections with the experimental values $-E_{d,i}$ (eq 2) derived by TPD (included as dotted lines). For Nt/Cu, the experimental value based on the TST prefactor was used. The coverage for the experimental energies is 0.65 ML on Cu(111) and 0.51 ML on Ag(111) corresponding to the $(2\sqrt{3} \times 2\sqrt{3})$-*R*30° structure used for both surfaces in the DFT calculations. Open circles are electronic adsorption energies, half-filled circles include a harmonic zero-point vibrational energy (ZPVE) correction, and filled circles include harmonic thermodynamic corrections; both are in the mobile limit. For MBD and D3^{surf}, no calculations for thermodynamic corrections were performed, but the ZPVE and thermodynamic corrections obtained for D3 (in light colors) were included for better comparability.

average errors of 0.04−0.07 Å.[12] The vdW^{surf} method consistently produced smaller adsorption heights than the other methods, while MBD and D3^{surf} yielded larger values.[12] This finding is in agreement with the performance regarding the adsorption energies discussed above.

To include corrections for the finite temperature during the measurements, harmonic thermodynamic corrections were performed for the D3 and vdW^{surf} calculations (Table 3). The simplest correction is the inclusion of the differences in the harmonic zero-point vibrational energy (ZPVE). Somewhat more complicated is the conversion to the standard enthalpy of adsorption ΔH_{ads}.[31] For both corrections, assumptions about the molecular DOFs in the adsorbed state are necessary. In the following, we consider only two limiting cases: first, the mobile limit with two translational DOFs and one rotational DOF on the surface, then the immobile limit with only vibrational DOFs. For thermodynamic corrections, a pressure of 1 bar and a temperature of 298 K were used to get the standard enthalpies; the area available for the translation of the molecule on the surface was chosen to be the size of one unit cell at the corresponding coverage.

It is noteworthy that the corrections lead to a minor improvement for the weakly bonded systems, whereas larger effects are found for the strongly bonded system Az/Cu. In the latter case, the corrections lead to an improvement only for D3^{surf}. Only harmonic corrections were performed, but as the molecule-surface potential is anharmonic, additional anharmonic finite temperature effects may contribute.[72] However, because of the stiffness of the molecules, only very small effects are expected.

To evaluate whether the DFT calculations reproduce the coverage dependency of the adsorption energies, calculations for six different coverages were performed with the DFT-D3 scheme. In Figure 10, these calculated energies are compared

Table 3. Compilation of the D3 and vdW^{surf} Adsorption Energies E_{ads} (in kJ/mol) with ZPVE Correction and Harmonic Thermodynamic Corrections[a]

	Nt/Ag	Nt/Cu	Az/Ag	Az/Cu
experiment	-97	-100	-111	-153
E(D3)	-118	-135	-128	-173
E(D3) + ZPVE	-117 (-117)	-135 (-135)	-129 (-129)	-180 (-180)
ΔH(D3)	-115 (-114)	-133 (-131)	-127 (-126)	-179 (-177)
E(vdW^{surf})	-104	-119	-120	-194
E(vdW^{surf}) + ZPVE	-104 (-104)	-118 (-118)	-121 (-121)	-200 (-200)
ΔH(vdW^{surf})	-102 (-101)	-117 (-115)	-119 (-118)	-199 (-198)

[a]The coverage for the experimental energies $-E_{d,i}$ is 0.65 ML on Cu(111) and 0.51 ML on Ag(111) corresponding to the $(2\sqrt{3} \times 2\sqrt{3})$-*R*30° structure used for both surfaces in the DFT calculations. The experimental TPD energies were obtained using the integrated IPW with HRV prefactors, except for Nt/Cu, where the TST prefactor was used. The values for the ZPVE-corrected energies and enthalpies are given in the mobile limit; the values obtained for the immobile limit are given in parentheses. For all thermodynamic corrections, a temperature of 298 K was used.

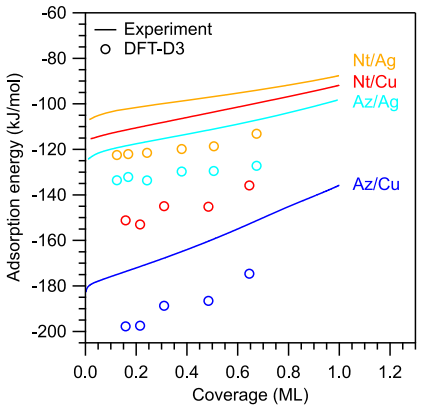

Figure 10. Experimental coverage-dependent integral desorption energies $-E_{d,i}$ (lines) compared with DFT-D3 adsorption energies (open circles).

to the coverage-dependent integral energies from TPD, $-E_{d,i}$ (eq 2). As expected for this type of vdW correction, the DFT-D3 results show an overestimation for all coverages. The deviation is especially large in the case of Nt/Cu(111) with an average of 39 kJ/mol, while the energies of the three other systems are overestimated by averages of 17−24 kJ/mol. Nevertheless, the general coverage dependency, especially the decrease of adsorption energy with increasing coverage, is reproduced well for all four adsorbate systems. The largest gradient is observed for the most strongly bonded system Az/Cu. When the experimental and theoretical data for Az/Cu are each fitted with a linear function, the gradients of these linear fits differ by only 2%. For the more weakly bonded systems, the

https://dx.doi.org/10.1021/acs.jpcc.0c00915
J. Phys. Chem. C 2020, 124, 8257−8268

The Journal of Physical Chemistry C pubs.acs.org/JPCC Article

adsorption energies are less dependent on the coverage, the gradients are smaller and the relative deviations between theoretical and experimental gradients are larger (12−53%).

Energy Decomposition Analysis. Further information on the nature of the surface chemical bond was obtained from a periodic energy decomposition analysis (pEDA) on the PBE-D3 level of theory. In this method, the adsorbate structure is divided into two fragments, one containing the molecule and the other the surface. The total interaction energy can then be divided into different terms, which reveal the details of surface−adsorbate bonding (Table 4).[38]

Table 4. Compilation of the pEDA Results for all Four Adsorbate Systems; Energies in kJ/mol and Charges in Elementary Charges (e)[a]

	Nt/Ag	Nt/Cu	Az/Ag	Az/Cu
ΔE_{int}	-123	-146	-137	-233
ΔE_{int} (disp)	-129	-154	-140	-181
ΔE_{int} (elec)	+6	+8	+3	-52
ΔE_{Pauli}	+280	+392	+426	+2044
ΔE_{elstat}	-164	-213	-251	-1138
ΔE_{orb}	-110	-171	-172	-958
ΔE_{prep}(mol,in cell)	-3	-7	-2	+24
ΔE_{prep}(mol,free)	+0	+1	+2	+35
ΔE_{prep}(surf)	+0	+1	+1	+12
ΔE_{bond}	-126	-153	-138	-196
ΔE_{bond} (PAW)	-119	-136	-130	-175
q_{mol} (AIM)	+0.06	+0.06	+0.01	-0.49

[a]A negative value of q_{mol} derived via Bader's AIM scheme indicates charge transfer from the surface to the molecule. To check the consistency of the pEDA calculations, the total bond energies ΔE_{bond} are compared to results obtained by a plane-wave code ΔE_{bond} (PAW); in this case, the PBE-D3 calculations used above. The pEDA terms for the total bond energy follow the same trend as the plane-wave results, but show an error of about 20 kJ/mol on Cu(111) and 10 kJ/mol on Ag(111).

The bond of Az with the Cu(111) surface is qualitatively different from the bonds in other systems. Only for Az/Cu, the electronic interaction energy is attractive with ΔE_{int} (elec) = −52 kJ/mol, which is the result of large attractive electrostatic (ΔE_{elstat} = −1138 kJ/mol) and orbital (ΔE_{orb} = −958 kJ/mol) terms, partly counterbalanced by a large Pauli repulsion term (ΔE_{Pauli} = +2044 kJ/mol). Remarkably, these terms are almost fivefold larger than in the other three adsorbate systems. Although the dispersion term [ΔE_{int} (disp) = −181 kJ/mol] makes up a large part of the total interaction energy (ΔE_{int} = −233 kJ/mol), it would be misleading to conclude that the Az−Cu bond is mainly of dispersive nature. In a more appropriate interpretation, the molecule is attracted by both dispersive and electronic contributions until it gets so close to the surface that the Pauli repulsion balances both attractive forces, and an equilibrium is established. The electronic interaction energy then includes both attraction and repulsion, whereas the dispersive interaction energy includes only the (necessarily) attractive contribution of the semi-empirical vdW correction. Further indications of a chemisorptive bond include the large positive preparation energies ΔE_{prep}, which are caused by the considerable distortion of both the Az molecule and the Cu surface in the adsorbed state, and the substantial charge transfer from the surface to the molecule (0.49 elementary charges).

The other three systems (Nt/Ag, Nt/Cu, and Az/Ag) show weaker bonds between the surface and the molecule, in line with previous work on Nt/Cu.[12] The constituent electrostatic, orbital, and Pauli terms of the interaction energy are again larger than the total interaction energy and compensate each other, but their magnitude is much smaller than in the case of Az/Cu(111). For all three systems, the total electronic interaction energy is now repulsive. In addition, the preparation energies are very small; in fact, they are even slightly negative, which is an artefact of the calculations and discussed in the Supporting Information. The overall conclusion is that the molecule−surface bonds in these three systems should be classified as purely physisorptive, in accordance with the negligible charge transfer and the large adsorption heights as described in previous work.[12] It should be noted, however, that the orbital and electrostatic interaction energies are the largest for the Az/Ag(111) system, even as the overall bond is predicted to be stronger for Nt/Cu(111). Thus, even on the less reactive Ag(111) surface, the nonalternant π-topology of the Az molecule gives rise to an increased, if still weak, involvement of the molecular orbitals in the bond with the surface.

CONCLUSIONS

The interaction of the molecular isomers Nt and Az with the (111) surfaces of Ag and Cu was studied using TPD and dispersion-corrected DFT calculations. The different π-topologies of the molecules result in different bonding energetics to the two metal surfaces. On both surfaces, the nonalternant Az forms a stronger bond than the alternant Nt, in line with previous structural data showing shorter adsorption heights for Az.[12] Detailed quantitative TPD analysis with several complementary methods provides reliable coverage-dependent desorption energies and pre-exponential factors. The latter are shown to play a critical role in assessing the reliability of the experimental energies. In the monolayer range, the differential desorption energies are well described by the following second-order polynomials (in kJ/mol, Θ in ML): Nt/Ag: $103 - 18\Theta - 19\Theta^2$, Nt/Cu: $114 - 40\Theta - 7\Theta^2$, Az/Ag: $120 - 27\Theta - 25\Theta^2$, and Az/Cu: $179 - 65\Theta - 39\Theta^2$. Slightly different coverage-dependencies were found by a modified leading-edge analysis. The DFT calculations qualitatively reproduce the general trends in the adsorption energies and their coverage dependencies. In particular, they correctly predict the substantially larger adsorption energy of Az on both metals and the larger adsorption energies of both isomers on Cu(111) than on Ag(111). On a quantitative level, the D3 and vdW^{surf} schemes overestimate all adsorption energies, with D3 performing better for the chemisorbed system and vdW^{surf} performing better for the physisorbed systems. MBD underestimates the adsorption energy in the physisorbed systems, and shows only a slight overestimation for the chemisorbed system. The D3^{surf} method is in good agreement with the

https://dx.doi.org/10.1021/acs.jpcc.0c00915
J. Phys. Chem. C 2020, 124, 8257−8268

physisorbed systems, and only very slightly underestimates the adsorption energy for the chemisorbed system. Overall, D3^{surf} shows the smallest deviation in absolute values. The pEDA analysis provides a detailed picture of the surface chemical bond and confirms the interpretation that Az on copper forms a chemisorptive bond, while the other three systems are physisorbed.

■ ASSOCIATED CONTENT

Supporting Information

The Supporting Information is available free of charge at https://pubs.acs.org/doi/10.1021/acs.jpcc.0c00915.

Details of TPD measurements and analysis, HRV analysis, estimation of desorption prefactors, and details of DFT calculations (PDF)

■ AUTHOR INFORMATION

Corresponding Author

J. Michael Gottfried − *Fachbereich Chemie, Philipps-Universität Marburg, 35032 Marburg, Germany;* orcid.org/0000-0001-5579-2568; Email: michael.gottfried@chemie.uni-marburg.de

Authors

Stefan R. Kachel − *Fachbereich Chemie, Philipps-Universität Marburg, 35032 Marburg, Germany*

Benedikt P. Klein − *Fachbereich Chemie, Philipps-Universität Marburg, 35032 Marburg, Germany;* orcid.org/0000-0002-6205-8879

Juliana M. Morbec − *Fakultät für Physik, Universität Duisburg-Essen, 47048 Duisburg, Germany;* orcid.org/0000-0002-1672-3575

Maik Schöniger − *Fachbereich Chemie, Philipps-Universität Marburg, 35032 Marburg, Germany*

Mark Hutter − *Fachbereich Chemie, Philipps-Universität Marburg, 35032 Marburg, Germany*

Martin Schmid − *Fachbereich Chemie, Philipps-Universität Marburg, 35032 Marburg, Germany*

Peter Kratzer − *Fakultät für Physik, Universität Duisburg-Essen, 47048 Duisburg, Germany;* orcid.org/0000-0001-5947-1366

Bernd Meyer − *Interdisciplinary Center for Molecular Materials (ICMM) and Computer-Chemistry-Center (CCC), Friedrich-Alexander-Universität Erlangen-Nürnberg, 91052 Erlangen, Germany;* orcid.org/0000-0002-3481-8009

Ralf Tonner − *Fachbereich Chemie, Philipps-Universität Marburg, 35032 Marburg, Germany;* orcid.org/0000-0002-6759-8559

Complete contact information is available at: https://pubs.acs.org/10.1021/acs.jpcc.0c00915

Author Contributions

‖S.R.K. and B.P.K. contributed equally to this work.

Notes

The authors declare no competing financial interest.

■ ACKNOWLEDGMENTS

This work was funded by the Deutsche Forschungsgemeinschaft (DFG) via 223848855-SFB 1083. J.M.M. gratefully acknowledges the computing time granted by the John von Neumann Institute for Computing (NIC) and provided on the supercomputer JURECA at Jülich Supercomputing Centre (JSC). We further acknowledge computational resources from HLR Stuttgart, CSC-LOEWE Frankfurt, RRZ Erlangen, and HRZ Marburg. We thank Reinhard J. Maurer for discussion.

■ REFERENCES

(1) Gottfried, J. M. Quantitative Model Studies for Interfaces in Organic Electronic Devices. *New J. Phys.* **2016**, *18*, 111002.

(2) Liu, W.; Maaß, F.; Willenbockel, M.; Bronner, C.; Schulze, M.; Soubatch, S.; Tautz, F. S.; Tegeder, P.; Tkatchenko, A. Quantitative Prediction of Molecular Adsorption: Structure and Binding of Benzene on Coinage Metals. *Phys. Rev. Lett.* **2015**, *115*, 036104.

(3) Kroemer, H. Nobel Lecture: Quasielectric Fields and Band Offsets: Teaching Electrons New Tricks. *Rev. Mod. Phys.* **2001**, *73*, 783−793.

(4) *Organic Electronics II: More Materials and Applications*; Klauk, H., Ed.; Wiley-VCH: Weinheim, 2012.

(5) *Organic Optoelectronics*; Hu, W., Ed.; Wiley-VCH: Weinheim, 2013.

(6) Ruedenberg, K. Quantum Mechanics of Mobile Electrons in Conjugated Bond Systems. III. Topological Matrix as Generatrix of Bond Orders. *J. Chem. Phys.* **1961**, *34*, 1884−1891.

(7) Klein, B. P.; van der Heijden, N. J.; Kachel, S. R.; Franke, M.; Krug, C. K.; Greulich, K. K.; Ruppenthal, L.; Müller, P.; Rosenow, P.; Parhizkar, S.; et al. Molecular Topology and the Surface Chemical Bond: Alternant Versus Nonalternant Aromatic Systems as Functional Structural Elements. *Phys. Rev. X* **2019**, *9*, 011030.

(8) Trinajsti, N. Graph Theory and Molecular Orbitals. In *Chemical Graph Theory: Introduction and Fundamentals*; Bonchev, D., Rouvray, D. H., Eds.; Gordon and Breach Science Publishers: New York, Philadelphia, London, Paris, Montreux, Tokyo, Melbourne, 1991.

(9) Xin, H.; Gao, X. Application of Azulene in Constructing Organic Optoelectronic Materials: New Tricks for an Old Dog. *ChemPlusChem* **2017**, *82*, 945−956.

(10) Ni, B.; Zhang, T.; Li, J.; Li, X.; Gao, H. Topological Design of Graphene. In *Handbook of Graphene*; Celasco, E., Chaika, A. N., Stauber, T., Zhang, M., Ozkan, C., Ozkan, C., Ozkan, U., Palys, B., Harun, S. W., Eds.; Wiley: New York, 2019.

(11) Klein, B. P.; Harman, S. E.; Ruppenthal, L.; Ruehl, G. M.; Hall, S. J.; Carey, S. J.; Herritsch, J.; Schmid, M.; Maurer, R. J.; Tonner, R.; et al. Enhanced Bonding of Pentagon−Heptagon Defects in Graphene to Metal Surfaces: Insights from the Adsorption of Azulene and Naphthalene to Pt(111). *Chem. Mater.* **2020**, *32*, 1041−1053.

(12) Klein, B. P.; Morbec, J. M.; Franke, M.; Greulich, K. K.; Sachs, M.; Parhizkar, S.; Bocquet, F. C.; Schmid, M.; Hall, S. J.; Maurer, R. J.; et al. Molecule-Metal Bond of Alternant Versus Nonalternant Aromatic Systems on Coinage Metal Surfaces: Naphthalene Versus Azulene on Ag(111) and Cu(111). *J. Phys. Chem. C* **2019**, *123*, 29219−29230.

(13) Schlichting, H.; Menzel, D. Techniques for Wide Range, High Resolution and Precision, Thermal Desorption Measurements: I. Principles of Apparatus and Operation. *Surf. Sci.* **1993**, *285*, 209−218.

(14) Grimme, S.; Antony, J.; Ehrlich, S.; Krieg, H. A Consistent and Accurate Ab Initio Parametrization of Density Functional Dispersion Correction (DFT-D) for the 94 Elements H-Pu. *J. Chem. Phys.* **2010**, *132*, 154104.

(15) Becke, A. D.; Johnson, E. R. A Density-Functional Model of the Dispersion Interaction. *J. Chem. Phys.* **2005**, *123*, 154101.

(16) Grimme, S.; Ehrlich, S.; Goerigk, L. Effect of the Damping Function in Dispersion Corrected Density Functional Theory. *J. Comput. Chem.* **2011**, *32*, 1456−1465.

(17) Ruiz, V. G.; Liu, W.; Zojer, E.; Scheffler, M.; Tkatchenko, A. Density-Functional Theory with Screened Van Der Waals Interactions for the Modeling of Hybrid Inorganic-Organic Systems. *Phys. Rev. Lett.* **2012**, *108*, 146103.

(18) Tkatchenko, A.; Scheffler, M. Accurate Molecular Van Der Waals Interactions from Ground-State Electron Density and Free-Atom Reference Data. *Phys. Rev. Lett.* **2009**, *102*, 073005.

https://dx.doi.org/10.1021/acs.jpcc.0c00915
J. Phys. Chem. C 2020, 124, 8257−8268

(19) Lifshitz, E. M. The Theory of Molecular Attractive Forces between Solids. *J. Exp. Theor. Phys. Lett.* **1956**, *2*, 94−110.
(20) Zaremba, E.; Kohn, W. Van der Waals Interaction between an Atom and a Solid Surface. *Phys. Rev. B: Condens. Matter Mater. Phys.* **1976**, *13*, 2270−2285.
(21) Tkatchenko, A.; DiStasio, R. A.; Car, R.; Scheffler, M. Accurate and Efficient Method for Many-Body Van Der Waals Interactions. *Phys. Rev. Lett.* **2012**, *108*, 236402.
(22) Ambrosetti, A.; Reilly, A. M.; DiStasio, R. A.; Tkatchenko, A. Long-Range Correlation Energy Calculated from Coupled Atomic Response Functions. *J. Chem. Phys.* **2014**, *140*, 18A508.
(23) Hessey, S. G.; Jones, R. G. Line-of-Sight Mass Spectrometry: Principles and Practice. *Surf. Interface Anal.* **2015**, *47*, 587−600.
(24) Perdew, J. P.; Burke, K.; Ernzerhof, M. Generalized Gradient Approximation Made Simple. *Phys. Rev. Lett.* **1996**, *77*, 3865−3868.
(25) Kresse, G.; Hafner, J. Ab Initio Molecular Dynamics for Liquid Metals. *Phys. Rev. B: Condens. Matter Mater. Phys.* **1993**, *47*, 558−561.
(26) Kresse, G.; Hafner, J. Ab Initio Molecular-Dynamics Simulation of the Liquid-Metal-Amorphous-Semiconductor Transition in Germanium. *Phys. Rev. B: Condens. Matter Mater. Phys.* **1994**, *49*, 14251−14269.
(27) Kresse, G.; Furthmüller, J. Efficient Iterative Schemes for Ab Initio Total-Energy Calculations Using a Plane-Wave Basis Set. *Phys. Rev. B: Condens. Matter Mater. Phys.* **1996**, *54*, 11169−11186.
(28) Kresse, G.; Furthmüller, J. Efficiency of Ab-Initio Total Energy Calculations for Metals and Semiconductors Using a Plane-Wave Basis Set. *Comput. Mater. Sci.* **1996**, *6*, 15−50.
(29) Blöchl, P. E. Projector Augmented-Wave Method. *Phys. Rev. B: Condens. Matter Mater. Phys.* **1994**, *50*, 17953−17979.
(30) Kresse, G.; Joubert, D. From Ultrasoft Pseudopotentials to the Projector Augmented-Wave Method. *Phys. Rev. B: Condens. Matter Mater. Phys.* **1999**, *59*, 1758−1775.
(31) Pecher, J.; Tonner, R. Precursor States of Organic Adsorbates on Semiconductor Surfaces Are Chemisorbed and Immobile. *ChemPhysChem* **2017**, *18*, 34−38.
(32) Blum, V.; Gehrke, R.; Hanke, F.; Havu, P.; Havu, V.; Ren, X.; Reuter, K.; Scheffler, M. Ab Initio Molecular Simulations with Numeric Atom-Centered Orbitals. *Comput. Phys. Commun.* **2009**, *180*, 2175−2196.
(33) Togo, A.; Tanaka, I. First Principles Phonon Calculations in Materials Science. *Scr. Mater.* **2015**, *108*, 1−5.
(34) Giannozzi, P.; Baroni, S.; Bonini, N.; Calandra, M.; Car, R.; Cavazzoni, C.; Ceresoli, D.; Chiarotti, G. L.; Cococcioni, M.; Dabo, I.; et al. Quantum Espresso: A Modular and Open-Source Software Project for Quantum Simulations of Materials. *J. Phys.: Condens. Matter* **2009**, *21*, 395502.
(35) Vanderbilt, D. Soft Self-Consistent Pseudopotentials in a Generalized Eigenvalue Formalism. *Phys. Rev. B: Condens. Matter Mater. Phys.* **1990**, *41*, 7892−7895.
(36) van Lenthe, E.; Baerends, E. J. Optimized Slater-Type Basis Sets for the Elements 1-118. *J. Comput. Chem.* **2003**, *24*, 1142−1156.
(37) van Lenthe, E.; Baerends, E. J.; Snijders, J. G. Relativistic Regular Two-Component Hamiltonians. *J. Chem. Phys.* **1993**, *99*, 4597−4610.
(38) Raupach, M.; Tonner, R. A Periodic Energy Decomposition Analysis Method for the Investigation of Chemical Bonding in Extended Systems. *J. Chem. Phys.* **2015**, *142*, 194105.
(39) *BAND 2017, SCM, Theoretical Chemistry*; Vrije Universiteit: Amsterdam, the Netherlands, http://www.scm.com.
(40) te Velde, G.; Baerends, E. J. Precise Density-Functional Method for Periodic Structure. *Phys. Rev. B: Condens. Matter Mater. Phys.* **1991**, *44*, 7888.
(41) Franchini, M.; Philipsen, P. H. T.; Visscher, L. The Becke Fuzzy Cells Integration Scheme in the Amsterdam Density Functional Program Suite. *J. Comput. Chem.* **2013**, *34*, 1819−1827.
(42) Pecher, L.; Tonner, R. Deriving Bonding Concepts for Molecules, Surfaces, and Solids with Energy Decomposition Analysis for Extended Systems. *Wiley Interdiscip. Rev.: Comput. Mol. Sci.* **2019**, *9*, No. e1401.
(43) Winkler, A. Thermal Desorption of Organic Molecules. In *Interface Controlled Organic Thin Films*, Al-Shamery, K.; Horowitz, G.; Sitter, H.; Rubahn, H.-G., Eds.; Springer: Berlin, Heidelberg, 2009; pp 29−36.
(44) Witte, G.; Lukas, S.; Bagus, P. S.; Wöll, C. Vacuum Level Alignment at Organic/Metal Junctions: "Cushion" Effect and the Interface Dipole. *Appl. Phys. Lett.* **2005**, *87*, 263502.
(45) Vázquez, H.; Dappe, Y. J.; Ortega, J.; Flores, F. Energy Level Alignment at Metal/Organic Semiconductor Interfaces: "Pillow" Effect, Induced Density of Interface States, and Charge Neutrality Level. *J. Chem. Phys.* **2007**, *126*, 144703.
(46) Fernandez-Torrente, I.; Monturet, S.; Franke, K. J.; Fraxedas, J.; Lorente, N.; Pascual, J. I. Long-Range Repulsive Interaction between Molecules on a Metal Surface Induced by Charge Transfer. *Phys. Rev. Lett.* **2007**, *99*, 176103.
(47) Christmann, K. *Introduction to Surface Physical Chemistry*; Steinkopff Verlag, Springer-Verlag: Darmstadt, New York, 1991.
(48) de Jong, A. M.; Niemantsverdriet, J. W. Thermal Desorption Analysis: Comparative Test of Ten Commonly Applied Procedures. *Surf. Sci.* **1990**, *233*, 355−365.
(49) Nieskens, D. L. S.; van Bavel, A. P.; Niemantsverdriet, J. W. The Analysis of Temperature Programmed Desorption Experiments of Systems with Lateral Interactions; Implications of the Compensation Effect. *Surf. Sci.* **2003**, *546*, 159−169.
(50) King, D. A. Thermal Desorption from Metal Surfaces: A Review. *Surf. Sci.* **1975**, *47*, 384−402.
(51) Bauer, E.; Bonczek, F.; Poppa, H.; Todd, G. Thermal Desorption of Metals from Tungsten Single Crystal Surfaces. *Surf. Sci.* **1975**, *53*, 87−109.
(52) Tait, S. L.; Dohnálek, Z.; Campbell, C. T.; Kay, B. D. N-Alkanes on MgO(100). I. Coverage-Dependent Desorption Kinetics of N-Butane. *J. Chem. Phys.* **2005**, *122*, 164707.
(53) Roos, M.; Breitruck, A.; Hoster, H. E.; Behm, R. J. Entropic Stabilization of Large Adsorbates on Weakly Binding Substrates − a Thermal Desorption and Scanning Tunneling Microscopy Study. *Phys. Chem. Chem. Phys.* **2010**, *12*, 818−822.
(54) Thrower, J. D.; Friis, E. E.; Skov, A. L.; Nilsson, L.; Andersen, M.; Ferrighi, L.; Jørgensen, B.; Baouche, S.; Balog, R.; Hammer, B.; et al. Interaction between Coronene and Graphite from Temperature-Programmed Desorption and DFT-vdW Calculations: Importance of Entropic Effects and Insights into Graphite Interlayer Binding. *J. Phys. Chem. C* **2013**, *117*, 13520−13529.
(55) Falconer, J. L.; Madix, R. J. Flash Desorption Activation Energies: DCOOH Decomposition and CO Desorption from Ni (110). *Surf. Sci.* **1975**, *48*, 393−405.
(56) Habenschaden, E.; Küppers, J. Evaluation of Flash Desorption Spectra. *Surf. Sci.* **1984**, *138*, L147−L150.
(57) Parker, D. H.; Jones, M. E.; Koel, B. E. Determination of the Reaction Order and Activation Energy for Desorption Kinetics Using TPD Spectra: Application to D_2 Desorption from Ag(111). *Surf. Sci.* **1990**, *233*, 65−73.
(58) Dresser, M. J.; Madey, T. E.; Yates, J. T. The Adsorption of Xenon by W(111), and Its Interaction with Preadsorbed Oxygen. *Surf. Sci.* **1974**, *42*, 533−551.
(59) Gottfried, J. M.; Schmidt, K. J.; Schroeder, S. L. M.; Christmann, K. Oxygen Chemisorption on Au(110)-(1×2) I. Thermal Desorption Measurements. *Surf. Sci.* **2003**, *525*, 184−196.
(60) Redhead, P. A. Thermal Desorption of Gases. *Vacuum* **1962**, *12*, 203−211.
(61) Paserba, K. R.; Gellman, A. J. Kinetics and Energetics of Oligomer Desorption from Surfaces. *Phys. Rev. Lett.* **2001**, *86*, 4338−4341.
(62) Gottfried, J. M.; Vestergaard, E. K.; Bera, P.; Campbell, C. T. Heat of Adsorption of Naphthalene on Pt(111) Measured by Adsorption Calorimetry. *J. Phys. Chem. B* **2006**, *110*, 17539−17545.
(63) Masel, R. I. *Principles of Adsorption and Reaction on Solid Surfaces*; Wiley Series in Chemical Engineering, 1996.
(64) Eyring, H. The Activated Complex in Chemical Reactions. *J. Chem. Phys.* **1935**, *3*, 107−115.

https://dx.doi.org/10.1021/acs.jpcc.0c00915
J. Phys. Chem. C 2020, 124, 8257−8268

(65) Campbell, C. T.; Sellers, J. R. V. The Entropies of Adsorbed Molecules. *J. Am. Chem. Soc.* **2012**, *134*, 18109−18115.
(66) Campbell, C. T.; Árnadóttir, L.; Sellers, J. R. V. Kinetic Prefactors of Reactions on Solid Surfaces. *Z. Phys. Chem.* **2013**, *227*, 1435.
(67) Ihm, H.; Ajo, H. M.; Gottfried, J. M.; Bera, P.; Campbell, C. T. Calorimetric Measurement of the Heat of Adsorption of Benzene on Pt(111). *J. Phys. Chem. B* **2004**, *108*, 14627−14633.
(68) Zhu, J. F.; Diaz, S. F.; Heeb, L. R.; Campbell, C. T. Adsorption of Pb on NiAl(110): Energetics and Structure. *Surf. Sci.* **2005**, *574*, 34−42.
(69) Persson, B. N. J. On the Nature of Adsorbate Phase Diagrams: Beyond Lattice Gas Models. *Surf. Sci.* **1991**, *258*, 451−463.
(70) Caldeweyher, E.; Ehlert, S.; Hansen, A.; Neugebauer, H.; Spicher, S.; Bannwarth, C.; Grimme, S. Generally Applicable Atomic-Charge Dependent London Dispersion Correction. *J. Chem. Phys.* **2019**, *150*, 154122.
(71) Caldeweyher, E.; Ehlert, S.; Hansen, A.; Neugebauer, H.; Spicher, S.; Bannwarth, C.; Grimme, S. Generally Applicable Atomic-Charge Dependent London Dispersion Correction Scheme. **2018**, ChemRxiv; 7430216.v2, DOI: 10.26434/chemrxiv.7430216.v2
(72) Maurer, R. J.; Liu, W.; Poltavsky, I.; Stecher, T.; Oberhofer, H.; Reuter, K.; Tkatchenko, A. Thermal and Electronic Fluctuations of Flexible Adsorbed Molecules: Azobenzene on Ag(111). *Phys. Rev. Lett.* **2016**, *116*, 146101.

https://dx.doi.org/10.1021/acs.jpcc.0c00915
J. Phys. Chem. C 2020, 124, 8257−8268

P2

SUPPORTING INFORMATION

for

Chemisorption and Physisorption at the Metal-Organic Interface: Bond Energies of Naphthalene and Azulene on Coinage Metal Surfaces

Stefan R. Kachel,[‡a] Benedikt P. Klein,[‡a] Juliana M. Morbec,[b§] Maik Schöniger,[a] Mark Hutter,[a] Martin Schmid,[a] Peter Kratzer,[b] Bernd Meyer,[c] Ralf Tonner,[a] J. Michael Gottfried*[a]

[a]*Fachbereich Chemie, Philipps-Universität Marburg, Hans-Meerwein-Straße 4, 35032 Marburg, Germany*

[b]*Fakultät für Physik, Universität Duisburg-Essen, Lotharstraße 1, 47048 Duisburg, Germany*

[c]*Interdisciplinary Center for Molecular Materials (ICMM) and Computer-Chemistry-Center (CCC), Friedrich-Alexander-Universität Erlangen-Nürnberg, Nägelsbachstraße 25, 91052 Erlangen, Germany*

Author Contributions

‡ Stefan R. Kachel and Benedikt P. Klein contributed equally to this work.

Present address

§ School of Chemical and Physical Sciences, Keele University, Keele ST5 5BG, UK.

Contents

I. Additional details of the TPD measurements and analysis

Sample preparation

For the adjustment of the different (sub)monolayer coverages, two different methods were used and critically compared: Method 1 produces the required coverage directly by adsorption of a corresponding amount of the gas-phase molecules onto the cold sample (<150 K). In contrast, method 2 employs an excess dosage of the molecules, which leads to a coverage larger than the required coverage. Thereafter, the sample is heated to an intermediate temperature, resulting in the partial desorption of the initial layer. The sample is then cooled back to <150 K and the TPD experiment is started. Figure S1, which compares two coverage series obtained by the different methods, reveals characteristic differences in the signal shapes: while method 2 (red curves) leads to regular, well defined line shapes, method 1 (black curves) results in deviations in the high-coverage leading edges, which partly extend considerably towards lower temperatures. We attribute these irregular leading edges to metastable phases, in which the molecules have a higher chemical potential than in the corresponding stable phases. Apparently, the phase transition from the metastable to the stable adsorbate phase is partly slower than the desorption into the gas phase. The annealing procedure in method 2 apparently leads to the desorption or transformation of the metastable phases, as indicated by the regular shapes for desorption from a stable thermodynamic equilibrium phase.

The irregular leading edges can lead to erroneous results in the data analysis, especially when leading-edge methods are used, which rely on the range in which the artifacts appear. As an example, we compare the two TPD traces corresponding to initial coverages of 0.9 ML. For the sample prepared by method 2 (annealed), we find a desorption energy of 113 kJ/mol and a realistic prefactor of $4 \cdot 10^{18}$ s^{-1}. In contrast, the sample prepared by method 1 (non-annealed) yields unrealistically low values for the energy (34 kJ/mol) and the prefactor ($3 \cdot 10^{3}$ s^{-1}), which clearly show that the analysis method fails.

The deviations between the annealed and non-annealed layers occur especially in the range of intermediate coverage, where a compressed monolayer phase is formed. According to recent nc-AFM studies on the azulene/Cu(111) system, this phase has no long-range order and thus not all molecules are adsorbed at their most stable adsorption sites.[1] Apparently, this disordered structure shows an increased tendency for the formation of metastable phases. Our results also suggest that there is an activation barrier between the regular and the compressed phase, such that desorption can successfully compete with the transition from the (partly metastable) compressed to the (stable) expanded, commensurate structure. To avoid the above-mentioned problems in the data analysis, only method 2 (annealed sample) was used to obtain the data for the quantitative analysis.

P2

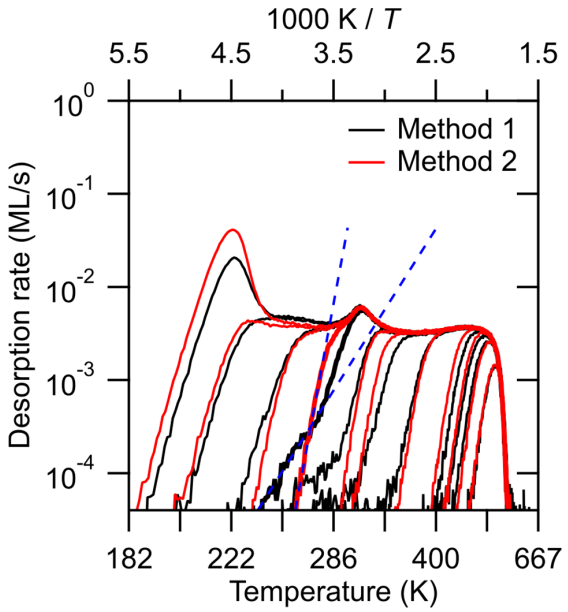

Figure S1. Menzel-Schlichting plot of two coverage series corresponding to two different preparation techniques: method 1 without preannealing (black lines) and method 2 with preannealing (red lines). See the text for further details. The heating rate was 1 K/s. The bold traces correspond to a coverage of 0.9 ML. The different slopes in the leading edge (blue dashed lines) reveal that low-temperature adsorption produces (partly) metastable adsorbate phases, which have disappeared after annealing.

Heating-rate variation

In the following section all data of the heating-rate variations for naphthalene on Ag(111) (Figure S2) and Cu(111) (Figure S3) and for azulene on Ag(111) (Figure S4) and Cu(111) (Figure S5) are shown as well as a table summarizing the results (Table S1).

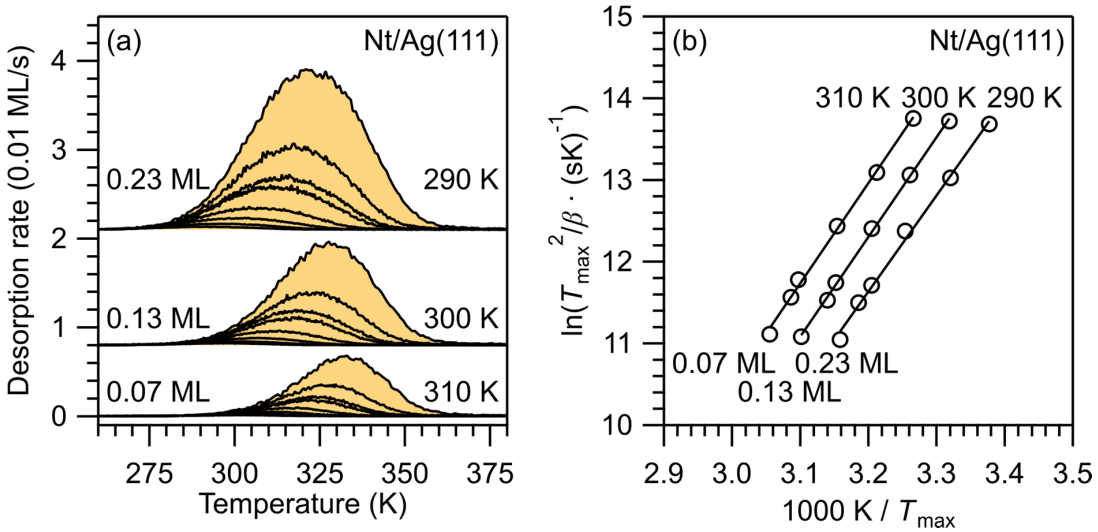

Figure S2. (a) Heating-rate variation (HRV) series for naphthalene on Ag(111) for heating rates from 0.1 to 1.6 K/s. Initial coverages were prepared according to method 2 by annealing to 290, 300 and 310 K, yielding coverages of 0.23, 0.13 and 0.07 ML, respectively. (b) Linear fit of $\ln\left(T_{\max}^2/\beta\right)$ vs. $1/T_{\max}$; the results are shown in the table below.

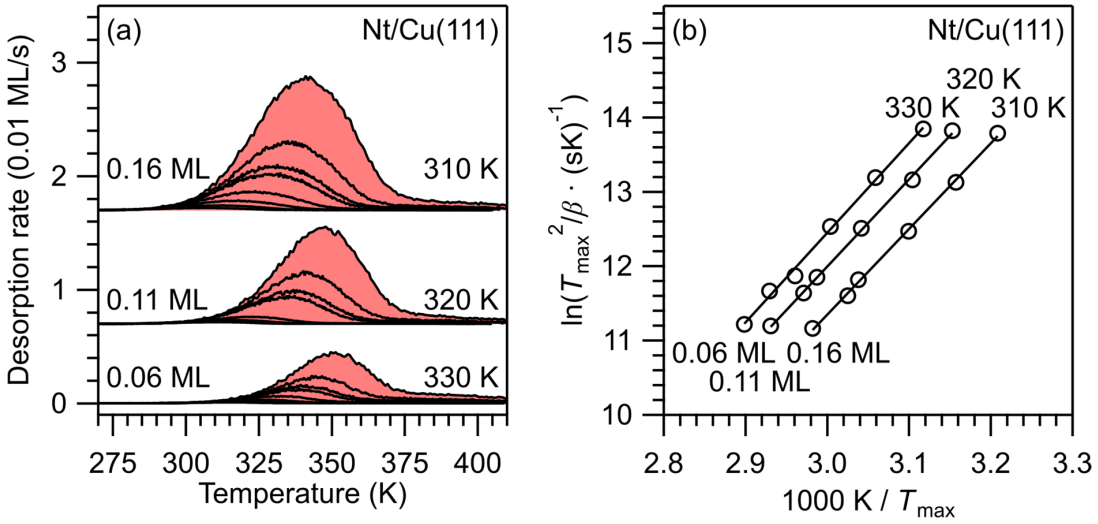

Figure S3. (a) Heating-rate variation (HRV) series for naphthalene on Cu(111) for heating rates from 0.1 to 1.6 K/s. Initial coverages were prepared according to method 2 by annealing to 310, 320 and 330 K, yielding coverages of 0.16, 0.11 and 0.06 ML, respectively. (b) Linear fit of $\ln\left(T_{\max}^2/\beta\right)$ vs. $1/T_{\max}$; the results are shown in the table below.

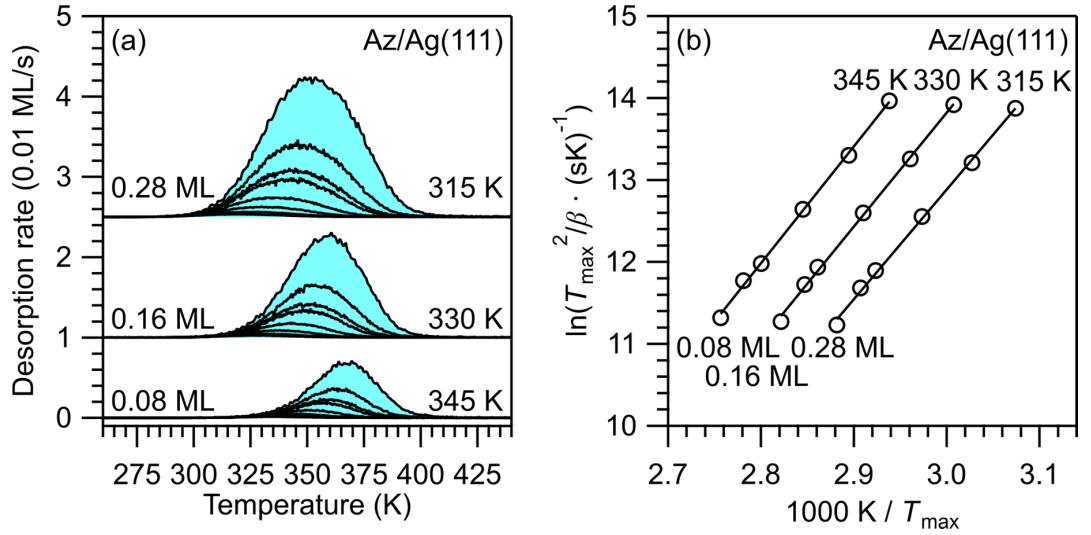

Figure S4. (a) Heating-rate variation (HRV) series for azulene on Ag(111) for heating rates from 0.1 to 1.6 K/s. Initial coverages were prepared according to method 2 by annealing to 315, 330 and 345 K, yielding coverages of 0.28, 0.16 and 0.08 ML, respectively. (b) Linear fit of $\ln\left(T_{\max}^2/\beta\right)$ vs. $1/T_{\max}$; the results are shown in the table below.

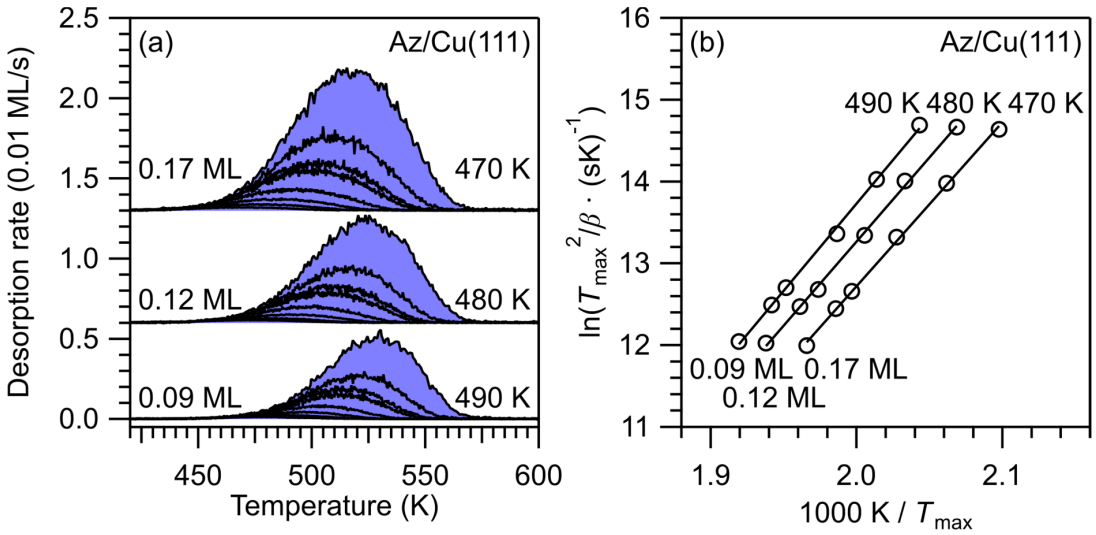

Figure S5. (a) Heating-rate variation (HRV) series for azulene on Cu(111) for heating rates from 0.1 to 1.6 K/s. Initial coverages were prepared according to method 2 by annealing to 470, 480 and 490 K, yielding coverages of 0.17, 0.12 and 0.09 ML, respectively. (b) Linear fit of $\ln\left(T_{\max}^2/\beta\right)$ vs. $1/T_{\max}$; the results are shown in the table below.

Table S1. Desorption activation energies and prefactors of azulene (Az) and naphthalene (Nt) on Ag(111) and Cu(111) obtained by HRV in the low-coverage regime. Energies in kJ/mol, and prefactors in s^{-1}.

System	Coverage	E_d	ν_d
Nt/Ag(111)	0.07	102	$3.1 \cdot 10^{15}$
	0.13	101	$5.2 \cdot 10^{15}$
	0.23	98	$2.3 \cdot 10^{15}$
Nt/Cu(111)	0.06	100	$2.3 \cdot 10^{14}$
	0.11	98	$1.4 \cdot 10^{14}$
	0.16	96	$1.5 \cdot 10^{14}$
Az/Ag(111)	0.08	119	$2.0 \cdot 10^{16}$
	0.16	116	$1.8 \cdot 10^{16}$
	0.28	111	$9.0 \cdot 10^{15}$
Az/Cu(111)	0.09	177	$7.7 \cdot 10^{16}$
	0.12	171	$2.6 \cdot 10^{16}$
	0.17	167	$1.6 \cdot 10^{16}$

P2

Estimation of desorption prefactors

Within the framework of TST, the desorption prefactor is:

$$\nu_{\mathrm{d}} = \frac{kT}{h} \cdot \frac{q^{\neq}}{q_{\mathrm{ad}}} \tag{S1}$$

with the Boltzmann constant k, the Planck constant h, and the partition functions $q^{\neq}$ and q_{ad} of the transition state and the adsorbed state, respectively. An accurate calculation of $q^{\neq}$ and q_{ad} would require detailed knowledge of the interaction potentials of the adsorbed molecule and the transition state.[2] These data are not available from the experiment. Nevertheless, upper and lower limits for ν_{d} can be estimated on the basis of reasonable assumptions about the degrees of freedom in the adsorbed state and in the transition state. First, we neglect any vibrational partition functions, which are small and mostly cancel in Equation S1. Second, the transition state is approximated as a free gas-phase molecule with two translational and three rotational degrees of freedom. (The third translational degree of freedom represent the critical coordinate and is therefore omitted in $q^{\neq}$.) The partition function of the transition state is therefore given by:

$$q^{\neq} = q^{\neq}_{\mathrm{tr,2D}} q^{\neq}_{\mathrm{rot,3D}} \tag{S2}$$

The two-dimensional translational partition function per area A is given by:[3]

$$\frac{q^{\neq}_{\mathrm{tr,2D}}}{A} = \frac{2\pi mkT}{h^2} \tag{S3}$$

where m is the mass of the molecule. The three-dimensional rotational partition function is:[3]

$$q^{\neq}_{\mathrm{rot},3D} = \frac{\pi^{1/2}}{\sigma}\left(\frac{kT}{hc_0}\right)^{3/2}\left(B_{\mathrm{A}}B_{\mathrm{B}}B_{\mathrm{C}}\right)^{-1/2} \tag{S4}$$

with the symmetry factor σ, the velocity of light c_0, and the rotational constants B_{A}, B_{B}, B_{C}, (in m^{-1}).

In the following, we consider the two limiting cases for the degrees of freedom of the adsorbate. In the mobile limit, the adsorbed molecule possesses two translational degrees of freedom parallel to the surface and one rotational degree of freedom around an axis perpendicular to the molecular plane, which is assumed to be parallel to the surface. The partition function for this rotation with the rotational constant B_{A} is given by:

$$q_{\mathrm{rot,1D}} = \frac{\pi^{1/2}}{\sigma}\left(\frac{kT}{hc_0 B_{\mathrm{A}}}\right)^{1/2} \tag{S5}$$

The translational partition function for the mobile adsorbate equals $q^{\neq}_{\mathrm{tr,2D}}$ (Equation S3). Hence, the translational contributions cancel in Equation S6 and the prefactor for the mobile limit depends only on the rotational partition functions:

$$\nu_{\mathrm{d,mobile}} = \frac{kT}{h} \cdot \frac{q^{\neq}_{\mathrm{rot,3D}}}{q_{\mathrm{rot,1D}}} \tag{S6}$$

In the immobile limit, the adsorbed molecule has no rotational or translational degrees of freedom. The corresponding prefactor $\nu_{d,im}$ therefore depends only on the partition function of the transition state:

$$\nu_{d,im} = \frac{kT}{h} \cdot q^{\neq}_{tr,2D} q^{\neq}_{rot,3D} \qquad \text{(S7)}$$

The resulting prefactors are shown in Table S2. The mass m is $2.13 \cdot 10^{-25}$ kg for both azulene and naphthalene. For A, the area per molecule in the saturated layer is used, in case of azulene on Cu(111) the area of the compressed phase obtained by nc-AFM is used.[1] (This area is difficult to estimate, because it depends essentially on the lateral mobility of the molecule in the transition state. Some authors use the full area of the crystal here.[4]) The symmetry factor σ counts the number of rotational operations (C_n) plus the identity operation. For the free molecules, the values are 4 for naphthalene (D_{2h}) and 2 for azulene (C_{2v}). For the adsorbed molecules, the values are 2 for naphthalene (C_{2v}) and 1 for azulene (C_s). The index A denotes the axis perpendicular to the molecule plane.

Table S2. Desorption prefactors in the mobile and immobile limit for azulene (Az) and naphthalene (Nt) on Cu(111) and Ag(111), and parameters necessary for the calculation. All areas are given in 10^{-19} m^2, rotational constants in cm^{-1}, temperatures in K and prefactors in s^{-1}.

Adsorbate	**Az/Cu(111)**	**Az/Ag(111)**	**Nt/Cu(111)**	**Nt/Ag(111)**
Area A	4.40	4.40	4.40	4.40
Rotational Constants[5-6]	B_A: 0.0948	B_A: 0.0948	B_A: 0.104	B_A: 0.104
	B_B: 0.0419	B_B: 0.0419	B_B: 0.0411	B_B: 0.0411
	B_C: 0.0290	B_C: 0.0290	B_C: 0.0295	B_C: 0.0295
Temperature	525	370	350	330
$\nu_{d,mobile}$	$3.2 \cdot 10^{16}$	$1.6 \cdot 10^{16}$	$1.3 \cdot 10^{16}$	$1.2 \cdot 10^{16}$
$\nu_{d,im}$	$6.1 \cdot 10^{22}$	$1.8 \cdot 10^{22}$	$7.1 \cdot 10^{21}$	$5.8 \cdot 10^{21}$

Another approach to obtain the prefactor for (sub-)monolayers is to directly calculate the entropy of activation in the desorption process similar to Equation S8:[7-8]

$$\nu_d = \frac{kT}{h} \cdot \exp\left(\frac{\Delta S^0_{\neq}}{R}\right) \qquad \text{(S8)}$$

where $\Delta S^0_{\neq}$ is the entropy of activation in the desorption process. This entropy is the difference between the entropy of the molecule in the transition state $S^0_{\neq}$ and in the adsorbed state S^0_{ads}. The entropy in the transition state itself can be approximated by the gas phase entropy S^0_{gas} minus the entropy of the one-dimensional translation $S^0_{gas,1D\text{-}trans}$ perpendicular to the surface (Equation S9):[7]

P2

$$\Delta S^0_{\neq} = S^0_{\neq} - S^0_{\text{ads}} = S^0_{\text{gas}} - S^0_{\text{gas,1D-trans}} - S^0_{\text{ads}} \quad \text{(S9)}$$

The gas phase entropy S^0_{gas} can be obtained by interpolating literature values. Campbell and Sellers found a relation for alkanes between the entropies of the gas phase and the adsorbed state if the gas-phase entropy is below $60R$:[7]

$$S^0_{\text{ads}}(T) = 0.7 S^0_{\text{gas}}(T) - 3.3R \quad \text{(S10)}$$

This relation was already applied to larger molecules like coronene yielding good results.[8] Using statistical mechanics and the Sackur-Tetrode equation[9] $S^0_{\text{gas,1D-trans}}$ can be calculated for any molecule if assuming that each translational degree of freedom contributes equally to the 3D translational entropy:[7]

$$S^0_{\text{gas,1D-trans}} = \frac{1}{3}\left(S^0_{\text{Ar,298K}} + R \ln\left[\left(\frac{m}{m_{\text{Ar}}} \right)^{3/2} \left(\frac{T}{298\,\text{K}} \right)^{5/2} \right] \right) \quad \text{(S11)}$$

With these equations the prefactor for submonolayers can be calculated (Table S3). The gas phase entropies for naphthalene were taken from Ref. 10. No entropy data are available for azulene, hence the same data as for naphthalene were used.

Table S3. Desorption prefactors obtained by the activation entropy of desorption for azulene and naphthalene on Cu(111) and Ag(111), and parameters necessary for the calculation. All temperatures in K, all entropies in J/(mol K) and prefactors in s^{-1}.

Adsorbate	**Az/Cu(111)**	**Az/Ag(111)**	**Nt/Cu(111)**	**Nt/Ag(111)**
Temperature	525	370	350	330
S^0_{gas} [10]	434.2	364.7	356.3	347.8
S^0_{ads}	276.5	227.9	222.0	216.0
$S^0_{\text{gas,1D-trans}}$	60.4	57.9	57.6	57.2
ν_{d}	$1.3 \cdot 10^{18}$	$1.0 \cdot 10^{17}$	$7.5 \cdot 10^{16}$	$5.4 \cdot 10^{16}$

The calculated prefactors are in good agreement with the transition state theory, except for azulene on Cu(111). This further proves the possibility of prefactors above $1 \cdot 10^{13}$ s^{-1}.

The two presented methods for calculating the prefactor apply only for (sub-)monolayers. For the multilayer desorption another method has to be used. Because the desorption of multilayers is similar to the process of sublimation, the prefactor can be estimated assuming detailed balance between a condensed film in equilibrium with its vapor pressure and the Clausius-Clapeyron equation:[8, 11-14]

$$\nu_{\text{d}} = p_0 \frac{sA}{\sqrt{2\pi mkT}} \quad \text{(S12)}$$

with the vapor pressure at infinite temperature p_0 and the sticking coefficient s. The vapor pressure at infinite temperature p_0 can be calculated by the Clausius-Clapeyron equation and the Antoine-equation:[15]

$$\ln\left(p(T)\right) = \ln\left(p_0\right) - \frac{\Delta H_{\mathrm{subl}}}{kT} = A_{\mathrm{AE}} - \frac{B_{\mathrm{AE}}}{T + C_{\mathrm{AE}}} \tag{S13}$$

with the sublimation enthalpy ΔH_{subl} and the fit parameters A_{AE}, B_{AE} and C_{AE}. Vapor pressure data can be plotted as ln(p) *vs*. 1/T and fitted with the Antoine equation. To address the temperature dependency of the vapor pressure, the y-intercept of the tangent at the multilayer desorption temperature has to be used instead of the intercept of the Antoine equation (parameter A_{AE}).[13] The results are shown in Table S4.

Table S4. Desorption prefactors obtained by detailed balance for multilayers of azulene and naphthalene on Cu(111) and Ag(111), and parameters necessary for the calculation. Vapor pressure data are taken from Refs. 16-17. All temperatures, B_{AE} and C_{AE} in K, areas in 10^{-19} m^2, vapor pressures in Pa and prefactors in s^{-1}.

Adsorbate	**Az**	**Nt**
Temperature	210	205
Area	4.39	4.39
A_{AE}	21.7	33.5
B_{AE}	4743.5	9625.0
C_{AE}	-56.4	9.9
p_0	$2.2 \cdot 10^{14}$	$4.4 \cdot 10^{13}$
ν_{d}	$1.6 \cdot 10^{18}$	$3.2 \cdot 10^{17}$

P2

II. Details of the DFT calculations

PBE-D3(BJ) calculations

The DFT-D3 scheme proposed by Grimme et al. uses atomic pairwise contributions to the dispersion interaction energy based on the polarization of the respective atoms in their chemical environment.[18] The energy contributions are based on tabulated C_6 coefficients taking into account the fractional coordination number of the atom under consideration and a damping function for close interatomic distances following a proposal by Becke and Johnson.[19-20]

The calculations were performed with the Vienna Ab Initio Simulation Package (VASP) Version 5.4.4.[21-24] The PBE functional[25] was used in combination with the third-generation van der Waals dispersion correction by Grimme (DFT-D3)[18-19] and the projector-augmented wave (PAW) ansatz[26-27] for the atomic cores.

The bulk lattice parameter for silver and copper were optimized with the Birch-Murnaghan approach yielding 4.072 Å for silver and 3.568 Å for copper. Using these lattice parameters a 4-layer slab was constructed.

The plane-wave cutoff energy, the vacuum layer thickness, and the k-mesh were determined by convergence series. The resulting values were a cutoff energy of 350 eV and a vacuum layer thickness of 30 Å. The Γ–centered 24×24×1 Monkhorst-Pack k-point mesh of the 1×1 surface cell was adjusted for the unit cell size, yielding an 7×7×1 mesh for the $(2\sqrt{3} \times 2\sqrt{3})$-*R*30° unit cell. The Methfessel-Paxton scheme of 2nd order for partial occupancies was used in the calculations (ISMEAR = 2) with a width of the smearing of $\sigma = 0.2$ eV to accelerate SCF convergence. The electronic SCF convergence criterion was set to 10^{-5} eV.

All structures were optimized until changes in forces were below 0.01 eV/Å. Only the topmost two surface layers were freely optimized together with the adsorbed molecule, while the bottom two layers were kept frozen at their bulk positions. An extensive search for the best adsorption site was carried out, yielding the on-top-30° site for the (3×3) structures on Ag(111) and the hcp-hcp-0° site for all other structures. The energies of the free molecules were calculated using a cubic unit cell with an edge length of 30 Å at the Γ-point.

PBE-vdW^{surf} calculations

The vdW^{surf} approach[28-29] includes the collective electronic response of the substrate in the determination of the vdW parameters (C_6 coefficients, polarizabilities and vdW radii) by combining the pairwise Tkatchenko-Scheffler (TS) method[30] with the Lifshitz-Zaremba-Kohn theory.[31-32] The TS scheme includes the dependence on the electronic density in the calculation of the vdW parameters by using the local Hirshfeld volume of the atoms in the chemical environment to reweight the free-atom parameters; thus, the TS method accounts for hybridization and other effects of the chemical environment.

Calculations with the vdW^{surf} method were performed using the FHI-aims code,[33] an all-electron code that uses numeric atom-centered orbitals as basis functions. We used "tight-tier2" basis sets for the Ag, Cu and H atoms, and the "tight-tier3" basis set for the C atoms. Convergence criteria of 10^{-5} electrons/Å^3 and 10^{-5} eV were applied for the charge density and

the total energy, respectively. We used the vdW parameters (C_6 coefficients, polarizabilities and vdW radii) computed in Ref. 29. Both Cu(111) and Ag(111) surfaces were modeled using a ($2\sqrt{3} \times 2\sqrt{3}$)-*R*30º unit cell, with a five-layer slab and a vacuum region of 130 Å. In the geometry optimizations, the molecules and the top two metal layers were allowed to relax while the remaining bottom layers were constrained to their bulk positions; a force convergence criterion of 10^{-2} eV/Å was applied for structural relaxations. We used a 4×4×1 Monkhorst-Pack k-point mesh to sample the Brillouin zone. Occupation numbers were determined using a Gaussian broadening function with a broadening width of 0.1 eV.

PBE-MBD calculations

The MBD method[34-35] accounts for collective many-body vdW effects beyond the pairwise approximation by representing the atomic response functions (within the random phase approximation) by a set of quantum harmonic oscillators interacting via the dipole–dipole interaction potential.

Calculations with the MBD methods were performed using the FHI-aims code,[33] an all-electron code that uses numeric atom-centered orbitals as basis functions. We used "tight-tier2" basis sets for the Ag, Cu and H atoms, and the "tight-tier3" basis set for the C atoms. Convergence criteria of 10^{-5} electrons/Å^3 and 10^{-5} eV were applied for the charge density and the total energy, respectively. We used the vdW parameters (C_6 coefficients, polarizabilities and vdW radii) computed in Ref. 29. Both Cu(111) and Ag(111) surfaces were modeled using a ($2\sqrt{3} \times 2\sqrt{3}$)-*R*30º unit cell, with a five-layer slab and a vacuum region of 130 Å. In the geometry optimizations, the molecules and the top two metal layers were allowed to relax while the remaining bottom layers were constrained to their bulk positions; a force convergence criterion of 10^{-2} eV/Å was applied for structural relaxations. We used a 4×4×1 Monkhorst-Pack k-point mesh to sample the Brillouin zone. Occupation numbers were determined using Gaussian broadening function with a broadening width of 0.1 eV.

PBE-D3^{surf}(BJ) calculations

The Grimme D3 dispersion correction scheme is based on coordination-dependent C_6 coefficients.[18] Its main limitation is that for many elements the original parameter tables only contain C_6 values for rather low coordination numbers. For example, for the noble metals Cu, Ag and Au, only C_6 coefficients for coordination number 0 (isolated atoms in the gas phase) and coordination number 1 (derived from the gas phase monohydride molecules) are included. In the bulk or at a surface the polarizability of the noble metal atoms is significantly reduced compared to the gas phase or a hydride molecule, giving rise to lower C_6 values. Thus, applying the original D3 parameter table of Grimme for adsorption studies of molecules on noble metal surfaces often leads to overbinding, especially for the adsorption energies.

The need to adjust C_6 coefficients for adsorption studies was also realized by Tkatchenko and Scheffler (TS) when they applied their TS dispersion correction scheme,[30] which is based on atomic C_6 values, to metal substrates. To remedy the overbinding, they combined the pairwise Tkatchenko-Scheffler (TS) method[30] with the Lifshitz-Zaremba-Kohn (LZK) theory[31-32] to include the collective electronic response of the substrate in the determination of the vdW

parameters (C_6 coefficients, polarizabilities and vdW radii). The TS method with the new vdW parameters was then called vdW^{surf} approach.[28]

Our new D3^{surf} scheme is similar in spirit as the vdW^{surf} method: the dispersion energy is still calculated as a sum of pairwise contributions, but the C_6 coefficients for the surface and the bulk atoms are reduced to reflect the lower polarizability of the atoms in the highly-coordinated environment. However, in contrast to vdW^{surf} we determine the new C_6 coefficients by a different approach. In D3^{surf}, the C_6 coefficients for surface and bulk atoms are obtained by using the older Grimme D2 approach, which only utilizes static polarizabilities.[36] Static polarizabilities are calculated by applying a static electric field of different strength to Cu and Ag slabs and by deducing the slope of the induced dipole moment at zero electric field strength.

Table S5 shows that by using slabs with different thickness, we can nicely entangle the contributions of the surface and bulk atoms to the overall total polarizability of the slab. The obtained values for the atomic polarizabilities also do not differ much for (111)- and (100)-oriented slabs. In the final step, the atomic static polarizabilities are converted to C_6 coefficients by using the relation of Grimme's D2 scheme (see Table S6).

Table S5. Calculated static polarizabilities. α_{tot} is the total polarizability of slabs with N_L layers. α_{surf} is half of α_{tot} of the 2-layer slab. The polarizability of bulk atoms is $\alpha_{bulk} = (\alpha_{tot} - 2\alpha_{surf})/(N_L-2)$. All polarizabilities are given in bohr^3.

	Cu(111)			Ag(111)		
N_L	α_{tot}	α_{surf}	α_{bulk}	α_{tot}	α_{surf}	α_{bulk}
2	15.8636	7.9318		22.2378	11.1189	
3	22.6001		6.7365	32.0558		9.8180
4	28.9980		6.5672	41.8087		9.7855
5	35.5926		6.5763	51.4319		9.7314
	Cu(100)			**Ag(100)**		
N_L	α_{tot}	α_{surf}	α_{bulk}	α_{tot}	α_{surf}	α_{bulk}
2	17.4807	8.7404		24.3232	12.1616	
3	23.9892		6.5085	33.8209		9.4977
4	30.3763		6.4478	43.0346		9.3557
5	36.6466		6.3886	52.3454		9.3407

Table S6. C_6 coefficients used in this work. CN is the result of Grimme's "counting function" for the fractional coordination number and α is the averaged static polarizability for surface and bulk atoms from Table S5.

	CN	α / bohr^3	C_6 / Ry·bohr^6	
Cu	0.0	-	674.4	D3
	1.0	-	350.0	D3
	5.9	8.3361	177.4	D3^{surf}
	8.4	6.5375	139.1	D3^{surf}
Ag	0.0	-	853.5	D3
	1.0	-	537.2	D3
	5.9	11.64025	364.3	D3^{surf}
	8.3	9.5882	300.0	D3^{surf}

These new C_6 coefficients for Cu and Ag surface and bulk atoms are then added to the D3 parameter table at the coordination numbers as determined in our slab calculations by Grimme's "counting function".[18] D3^{surf} is thus a rather simple extension of the original D3 scheme by adding C_6 coefficients for higher coordination number where none were available yet. The D3^{surf} scheme has been applied to several other materials, in particular oxides and halides. These additional benchmark calculations will be presented in a forthcoming publication.

The D3^{surf} calculations were performed with the PWscf code of the Quantum Espresso software package.[37] As in the D3 calculations we use the PBE functional[25] and the Becke-Johnson damping function within the dispersion correction scheme.[19-20] Atomic cores were represented by Vanderbilt ultrasoft pseudopotentials[38] and the wave functions were expanded in a plane wave basis with cutoff energy of 30 Ry.

With this setup and the D3^{surf} dispersion correction scheme we obtain bulk lattice constants for Cu and Ag of 3.606 Å and 4.101 Å, respectively. Surfaces were represented by periodically repeated slabs with a thickness of 5 atomic layers and a $(2\sqrt{3} \times 2\sqrt{3})$-*R*30º surface unit cell. The optimized bulk lattice constants were used for the lateral dimensions of the slabs. In the structure optimization the force convergence criterion was set to 0.003 eV/Å. Only the upper three surface layers and the adsorbate were allowed to relax, while the bottom two layers were kept frozen at their bulk positions. k-point sampling was done with a Γ-centered 7×7×1 Monkhorst-Pack mesh and fractional occupation numbers were determined by a Gaussian smearing with a smearing width of 0.02 Ry.

pEDA in ADF-BAND

The calculations were performed in ADF-BAND Version 2017.104.[39-40] The same DFT functional and dispersion correction PBE-D3(BJ)[18-19, 25] as employed in VASP was used here and scalar relativistic corrections with the ZORA approach were included.[41] A Becke grid with normal accuracy was employed for the numerical integration.[42] For the atom-centered basis set a convergence series was performed (see Table S7) yielding the use of TZ2P.[43-44] The frozen core approximation was used for the metal atoms (setting "small", Cu: 1s,2s,2p; Ag: 1s,2s,2p,3s,3p,3d). Electronic smearing with a width of 10^{-4} a.u. was applied during SCF calculations.

The structures were taken from the VASP optimizations and not further optimized in ADF-BAND. The calculations of the 4-layer slabs were done with 2D periodic boundary conditions (PBC) whereas the free molecules were calculated without PBC. For the molecular fragments calculations both with and without PBC were conducted. The fragments for the pEDA analysis were chosen to be the surface and the molecule in their singlet ground states.

The actual pEDA calculation was performed as implemented in the ADF-BAND package 2017.[39-40, 45] Calculations were conducted with different k-meshs going from Γ-only to the 7×7 mesh to test for the convergence of the pEDA terms (see Table S8).

Table S7. Basis set convergence for the pEDA calculations, k-grid = 7×7. Shown are the energies in kJ/mol and the deviation to the TZ2P value in percent.

ΔE_{int}	DZ		TZP		TZ2P
Az/Ag	-184	35%	-137	1%	-137
Az/Cu	-282	21%	-234	0%	-233
Nt/Ag	-167	35%	-124	1%	-123
Nt/Cu	-190	30%	-148	2%	-146

ΔE_{Pauli}	DZ		TZP		TZ2P
Az/Ag	445	5%	422	-1%	426
Az/Cu	2183	7%	2027	-1%	2044
Nt/Ag	288	3%	277	-1%	280
Nt/Cu	398	1%	386	-2%	392

ΔE_{elstat}	DZ		TZP		TZ2P
Az/Ag	-322	28%	-247	-1%	-251
Az/Cu	-1361	20%	-1129	-1%	-1138
Nt/Ag	-215	31%	-161	-2%	-164
Nt/Cu	-267	25%	-210	-2%	-213

ΔE_{orb}	DZ		TZP		TZ2P
Az/Ag	-167	-3%	-173	0%	-172
Az/Cu	-924	-4%	-951	-1%	-958
Nt/Ag	-111	1%	-111	1%	-110
Nt/Cu	-166	-3%	-171	0%	-171

The negative preparation energies (shown in Table 4 of the main text) should be impossible given the definition of the preparation energy. This unexpected behavior is observed if the preparation energies are calculated by comparing the deformed molecule layer with the free molecule in the ground state. In this case, the mutual attraction of molecules in neighboring cells leads to a decrease in energy of the deformed fragment and thus to a negative preparation energy (ΔE_{prep}(mol,in cell)). By comparing instead the free deformed molecule with the free molecule in the ground state (ΔE_{prep}(mol,free)), this attraction can be avoided, leading to the expected slightly positive preparation energies.

P2

Table S8. k-space convergence for the pEDA calculations, basis set = TZ2P. Shown are the energies in kJ/mol and the deviation to the 7×7 value in percent.

ΔE_{int}	k-grid = 1×1		k-grid = 3×3		k-grid = 5×5		k-grid = 7×7
Az/Ag	-116	-15%	-124	-9%	-132	-3%	-137
Az/Cu	-185	-20%	-205	-12%	-235	1%	-233
Nt/Ag	-111	-10%	-115	-7%	-121	-2%	-123
Nt/Cu	-139	-5%	-137	-6%	-148	1%	-146

ΔE_{Pauli}	k-grid = 1×1		k-grid = 3×3		k-grid = 5×5		k-grid = 7×7
Az/Ag	419	-2%	428	0%	422	-1%	426
Az/Cu	2099	3%	2103	3%	2037	0%	2044
Nt/Ag	273	-3%	281	0%	277	-1%	280
Nt/Cu	405	3%	404	3%	388	-1%	392

ΔE_{elstat}	k-grid = 1×1		k-grid = 3×3		k-grid = 5×5		k-grid = 7×7
Az/Ag	-254	1%	-263	5%	-251	0%	-251
Az/Cu	-1136	0%	-1159	2%	-1122	-1%	-1138
Nt/Ag	-166	1%	-173	5%	-164	0%	-164
Nt/Cu	-214	0%	-220	3%	-207	-3%	-213

ΔE_{orb}	k-grid = 1×1		k-grid = 3×3		k-grid = 5×5		k-grid = 7×7
Az/Ag	-141	-18%	-149	-13%	-163	-5%	-172
Az/Cu	-968	1%	-968	1%	-970	1%	-958
Nt/Ag	-88	-20%	-94	-15%	-104	-5%	-110
Nt/Cu	-177	3%	-167	-3%	-174	2%	-171

Comparison of DFT methods

Finally, in Table S9 the computational details as well as the used parameters of all different DFT methods are compared.

Table S9. Comparison of the calculational details of the different employed DFT methods.

Parameter	**D3(BJ)**	**vdW^{surf}**	**MBD**	**D3^{surf}(BJ)**	**pEDA**
Program package	VASP 5.4.4	FHI-aims 171221	FHI-aims 171221	Quantum Espresso	BAND 2017
Functional	PBE	PBE	PBE	PBE	PBE
Dispersion correction	D3(BJ)	vdW^{surf}	MBD	D3(BJ) / D3^{surf}(BJ)	D3(BJ)
Basis set	plane waves, E_{cut}^{pw} = 350 eV	numeric AOs, tight-tier2, tight-tier3	numeric AOs, tight-tier2, tight-tier3	plane waves, E_{cut}^{pw} = 30 Ry	numeric AOs, TZ2P
Pseudopotentials	PAW	none	none	USPP	frozen core
Slab thickness	4 layers	5 layers	5 layers	5 layers	4 layers
Vacuum layer	30 Å	130 Å	130 Å	about 20 Å	-
k-grid	7×7×1	4×4×1	4×4×1	7×7×1	7×7
Ag fcc lattice parameter (Expt.: 4.079 Å)	4.072 Å	4.014 Å	4.014 Å	4.069 Å / 4.101 Å	4.072 Å
Cu fcc lattice parameter (Expt.: 3.597 Å)	3.568 Å	3.601 Å	3.601 Å	3.566 Å / 3.606 Å	3.568 Å

P2

III. References

1. Klein, B. P.; van der Heijden, N. J.; Kachel, S. R.; Franke, M.; Krug, C. K.; Greulich, K. K.; Ruppenthal, L.; Müller, P.; Rosenow, P.; Parhizkar, S., et al. Molecular Topology and the Surface Chemical Bond: Alternant Versus Nonalternant Aromatic Systems as Functional Structural Elements. *Phys. Rev. X* **2019,** *9*, 011030.
2. Gottfried, J. M.; Vestergaard, E. K.; Bera, P.; Campbell, C. T. Heat of Adsorption of Naphthalene on Pt(111) Measured by Adsorption Calorimetry. *J. Phys. Chem. B* **2006,** *110*, 17539-17545.
3. Hill, T. L. *An Introduction to Statistical Thermodynamics*. Addison-Wesley Publishing Company, Inc.: Reading, MA, **1960**.
4. Redondo, A.; Zeiri, Y.; Low, J. J.; Goddard, W. A. Application of Transition State Theory to Desorption from Solid Surfaces: Ammonia on Ni(111). *J. Chem. Phys.* **1983,** *79*, 6410-6415.
5. Goubet, M.; Pirali, O. The Far-Infrared Spectrum of Azulene and Isoquinoline and Supporting Anharmonic Density Functional Theory Calculations to High Resolution Spectroscopy of Polycyclic Aromatic Hydrocarbons and Derivatives. *J. Chem. Phys.* **2014,** *140*, 044322.
6. Pirali, O.; Goubet, M.; Huet, T. R.; Georges, R.; Soulard, P.; Asselin, P.; Courbe, J.; Roy, P.; Vervloet, M. The Far Infrared Spectrum of Naphthalene Characterized by High Resolution Synchrotron FTIR Spectroscopy and Anharmonic DFT Calculations. *Phys. Chem. Chem. Phys.* **2013,** *15*, 10141-50.
7. Campbell, C. T.; Sellers, J. R. V. The Entropies of Adsorbed Molecules. *J. Am. Chem. Soc.* **2012,** *134*, 18109-18115.
8. Thrower, J. D.; Friis, E. E.; Skov, A. L.; Nilsson, L.; Andersen, M.; Ferrighi, L.; Jørgensen, B.; Baouche, S.; Balog, R.; Hammer, B., et al. Interaction between Coronene and Graphite from Temperature-Programmed Desorption and DFT-vdW Calculations: Importance of Entropic Effects and Insights into Graphite Interlayer Binding. *J. Phys. Chem. C* **2013,** *117*, 13520-13529.
9. McQuarrie, D. A. *Statistical Mechanics*. University Science Books: Sausalito, CA, **2000**.
10. Alberty, R. A.; Reif, A. K. Standard Chemical Thermodynamic Properties of Polycyclic Aromatic Hydrocarbons and Their Isomer Groups I. Benzene Series. *J. Phys. Chem. Ref. Data* **1988,** *17*, 241-253.
11. Oja, V.; Suuberg, E. M. Vapor Pressures and Enthalpies of Sublimation of Polycyclic Aromatic Hydrocarbons and Their Derivatives. *J. Chem. Eng. Data* **1998,** *43*, 486-492.
12. Zacharia, R.; Ulbricht, H.; Hertel, T. Interlayer Cohesive Energy of Graphite from Thermal Desorption of Polyaromatic Hydrocarbons. *Phys. Rev. B* **2004,** *69*, 155406.
13. Ulbricht, H.; Zacharia, R.; Cindir, N.; Hertel, T. Thermal Desorption of Gases and Solvents from Graphite and Carbon Nanotube Surfaces. *Carbon* **2006,** *44*, 2931-2942.
14. Käfer, D.; Wöll, C.; Witte, G. Thermally Activated Dewetting of Organic Thin Films: The case of pentacene on SiO_2 and gold. *Appl. Phys. A* **2009,** *95*, 273-284.
15. Antoine, C. Tensions Des Vapeurs: Nouvelle Relation Entre Les Tensions Et Les Temperatures. *C. R. Acad. Sci.* **1888**, 681-684, 778-780, 836-837.
16. Vapor Pressure Database, Version 2.2p, Thermodynamic Research Center. Texas A&M University: College Station, TX.

17. Meyer, E. F.; Gens, T. H. Vapor Pressure of Azulene between 114 and 261 °C. *J. Chem. Eng. Data* **1977,** *22*, 30-31.
18. Grimme, S.; Antony, J.; Ehrlich, S.; Krieg, H. A Consistent and Accurate Ab Initio Parametrization of Density Functional Dispersion Correction (DFT-D) for the 94 Elements H-Pu. *J. Chem. Phys.* **2010,** *132*, 154104.
19. Becke, A. D.; Johnson, E. R. Exchange-Hole Dipole Moment and the Dispersion Interaction. *J. Chem. Phys.* **2005,** *122*, 154104.
20. Grimme, S.; Ehrlich, S.; Goerigk, L. Effect of the Damping Function in Dispersion Corrected Density Functional Theory. *J. Comput. Chem.* **2011,** *32*, 1456-1465.
21. Kresse, G.; Hafner, J. Ab Initio Molecular Dynamics for Liquid Metals. *Phys. Rev. B* **1993,** *47*, 558-561.
22. Kresse, G.; Hafner, J. Ab Initio Molecular-Dynamics Simulation of the Liquid-Metal-Amorphous-Semiconductor Transition in Germanium. *Phys. Rev. B* **1994,** *49*, 14251-14269.
23. Kresse, G.; Furthmüller, J. Efficient Iterative Schemes for Ab Initio Total-Energy Calculations Using a Plane-Wave Basis Set. *Phys. Rev. B* **1996,** *54*, 11169-11186.
24. Kresse, G.; Furthmüller, J. Efficiency of Ab-Initio Total Energy Calculations for Metals and Semiconductors Using a Plane-Wave Basis Set. *Comput. Mater. Sci.* **1996,** *6*, 15-50.
25. Perdew, J. P.; Burke, K.; Ernzerhof, M. Generalized Gradient Approximation Made Simple. *Phys. Rev. Lett.* **1996,** *77*, 3865-3868.
26. Blöchl, P. E. Projector Augmented-Wave Method. *Phys. Rev. B* **1994,** *50*, 17953-17979.
27. Kresse, G.; Joubert, D. From Ultrasoft Pseudopotentials to the Projector Augmented-Wave Method. *Phys. Rev. B* **1999,** *59*, 1758-1775.
28. Ruiz, V. G.; Liu, W.; Zojer, E.; Scheffler, M.; Tkatchenko, A. Density-Functional Theory with Screened Van Der Waals Interactions for the Modeling of Hybrid Inorganic-Organic Systems. *Phys. Rev. Lett.* **2012,** *108*, 146103.
29. Ruiz, V. G.; Liu, W.; Tkatchenko, A. Density-Functional Theory with Screened Van Der Waals Interactions Applied to Atomic and Molecular Adsorbates on Close-Packed and Non-Close-Packed Surfaces. *Phys. Rev. B* **2016,** *93*, 035118.
30. Tkatchenko, A.; Scheffler, M. Accurate Molecular Van Der Waals Interactions from Ground-State Electron Density and Free-Atom Reference Data. *Phys. Rev. Lett.* **2009,** *102*, 073005.
31. Lifshitz, E. M. The Theory of Molecular Attractive Forces between Solids. *Soviet Physics JETP 2* **1956,** *2*, 73-83.
32. Zaremba, E.; Kohn, W. Van Der Waals Interaction between an Atom and a Solid Surface. *Phys. Rev. B* **1976,** *13*, 2270-2285.
33. Blum, V.; Gehrke, R.; Hanke, F.; Havu, P.; Havu, V.; Ren, X.; Reuter, K.; Scheffler, M. Ab Initio Molecular Simulations with Numeric Atom-Centered Orbitals. *Comput. Phys. Commun.* **2009,** *180*, 2175-2196.
34. Tkatchenko, A.; DiStasio, R. A.; Car, R.; Scheffler, M. Accurate and Efficient Method for Many-Body Van Der Waals Interactions. *Phys. Rev. Lett.* **2012,** *108*, 236402.
35. Ambrosetti, A.; Reilly, A. M.; DiStasio, R. A.; Tkatchenko, A. Long-Range Correlation Energy Calculated from Coupled Atomic Response Functions. *J. Chem. Phys.* **2014,** *140*, 18A508.

P2

36. Grimme, S. Semiempirical GGA-Type Density Functional Constructed with a Long-Range Dispersion Correction. *J. Comput. Chem.* **2006,** *27*, 1787-1799.
37. Giannozzi, P.; Baroni, S.; Bonini, N.; Calandra, M.; Car, R.; Cavazzoni, C.; Ceresoli, D.; Chiarotti, G. L.; Cococcioni, M.; Dabo, I., et al. Quantum Espresso: A Modular and Open-Source Software Project for Quantum Simulations of Materials. *J. Phys.: Condens. Matter* **2009,** *21*, 395502.
38. Vanderbilt, D. Soft Self-Consistent Pseudopotentials in a Generalized Eigenvalue Formalism. *Phys. Rev. B* **1990,** *41*, 7892-7895.
39. BAND 2017, SCM, Theoretical Chemistry, Vrije Universiteit, Amsterdam, the Netherlands, http://www.scm.com.
40. te Velde, G.; Baerends, E. J. Precise Density-Functional Method for Periodic Structure. *Phys. Rev. B* **1991,** *44*, 7888.
41. Philipsen, P. H. T.; Baerends, E. J. Relativistic Calculations to Assess the Ability of the Generalized Gradient Approximation to Reproduce Trends in Cohesive Properties of Solids. *Phys. Rev. B* **2000,** *61*, 1773-1778.
42. Franchini, M.; Philipsen, P. H. T.; Visscher, L. The Becke Fuzzy Cells Integration Scheme in the Amsterdam Density Functional Program Suite. *J. Comput. Chem.* **2013,** *34*, 1819-1827.
43. van Lenthe, E.; Baerends, E. J. Optimized Slater-Type Basis Sets for the Elements 1-118. *J. Comput. Chem.* **2003,** *24*, 1142-1156.
44. van Lenthe, E.; Baerends, E. J.; Snijders, J. G. Relativistic Regular Two-Component Hamiltonians. *J. Chem. Phys.* **1993,** *99*, 4597-4610.
45. Raupach, M.; Tonner, R. A Periodic Energy Decomposition Analysis Method for the Investigation of Chemical Bonding in Extended Systems. *J. Chem. Phys.* **2015,** *142*, 194105.

Enhanced Interaction of the Stone-Wales Defect at the Metal-Graphene Interface

Benedikt P. Klein[a], Alexander Ihle[b], Stefan R. Kachel[a], Lukas Ruppenthal[a], Samuel J. Hall[c,d], Lars E. Sattler[e], Sebastian M. Weber[e], Jan Herritsch[a], Andrea Jaegermann[a], Daniel Ebeling[b], Reinhard J. Maurer[d], Gerhard Hilt[e], Ralf Tonner[a], André Schirmeisen[b], J. Michael Gottfried[a*]

[a]*Fachbereich Chemie, Philipps-Universität Marburg, Hans-Meerwein-Straße. 4, 35032 Marburg, Germany*

[b]*Institut für Angewandte Physik, Justus-Liebig-Universität Gießen, Heinrich-Buff-Ring 16, 35392 Gießen, Germany*

[c]*MAS Centre for Doctoral Training, Senate House, and* [d]*Department of Chemistry and Centre for Scientific Computing, University of Warwick, Gibbet Hill Road, Coventry, CV4 7AL, United Kingdom*

[e]*Institut für Chemie, Carl von Ossietzky Universität Oldenburg, Carl-von-Ossietzky-Straße. 9-11, 26111 Oldenburg, Germany*

P3

Abstract

The performance of graphene-based (opto)electronic devices depends critically on the properties of the graphene/metal interface. One important method to tailor this interface is the employment of topological defects. Here, we focus on the prototypical Stone-Wales defect and combine theoretical studies of the defect/metal interface with experimental investigations of a molecular model system. Bonding analysis based on density functional theory reveals that the embedded defect engages in increased interaction with a Cu(111) surface, compared to regular graphene. This finding is experimentally corroborated by the molecular model, in which azupyrene mimics the Stone-Wales defect and its isomer pyrene represents the ideal graphene structure. Interaction energies determined with temperature programmed desorption, electronic-structure analysis by photoelectron spectroscopy and X-ray absorption spectroscopy, and apparent adsorption-height differences measured by atomic force microscopy confirm the enhanced bonding on a quantitative level. The methodology developed in this study can be expanded to other types of graphene defects.

Keywords: Graphene defects, Azupyrene, Pyrene, Adsorption, nc-AFM, TPD, NEXAFS, UPS, XPS, DFT, pEDA, Surface Chemical Bond, Metal-Organic Interfaces

Introduction

Graphene, a single atomic layer of graphite, is a versatile material with unique properties, such as high electrical and thermal conductivity, mechanical strength, optical transparency, and chemical inertness.[1] These physical and chemical properties of the ideal graphene lattice can be strongly modified by topological defects,[2] which occur as isolated defects [3-5] or collectively at grain boundaries.[6-9] These intrinsic defects influence the chemical reactivity,[10,11] mechanical strength,[9,12-14] electron transport,[6,15] and magnetism.[16] In addition, defects can be introduced artificially by topological design to tailor the properties of the graphene sheet.[17]

For application in (opto) electronic devices, the graphene-based active element must be contacted by metal electrodes.[18] The resulting graphene/metal interfaces crucially affect the performance of the devices.[19] It has been suspected that the defects play a decisive role in the graphene/metal interaction and therefore largely determine the interface properties.[20]

However, only rudimentary information is available regarding the interaction of the defects with metal surfaces. On the experimental side, these deficits are mainly due to methodological challenges. Interaction energies, vertical bond distances, or spectroscopic information about the electronic structure are usually obtained with laterally integrating techniques. Thus, contributions from the defects are obscured by background signals originating from the ideal graphene lattice.

To overcome these difficulties, it appears feasible to combine theoretical studies of the embedded defects with experiments using a model system that mimics the local chemical and physical environment at a defect site, but can be prepared in high and laterally uniform concentration. Following this idea, we approximate the isolated Stone-Wales defect by the azupyrene molecule, which has the same 5-7-5-7 topology of the carbon skeleton. The Stone-Wales defect was chosen because it is arguably one of the most important and ubiquitous intrinsic point defects of graphene and other 2D materials.[21,22] As a reference system, we use pyrene, which is an isomer of azupyrene and consists only of 6-membered rings, i.e., it has the topology of the regular graphene lattice. Both azupyrene and pyrene are polycyclic aromatic hydrocarbons and structural isomers with the sum formula $C_{16}H_{10}$. The nonalternant topology[23] of azupyrene is known to influence the electronic structure[24] and possibly the interfacial interactions.[25] No previous studies exist regarding the interaction of azupyrene with surfaces. Pyrene on Cu(111) was only studied by scanning tunneling microscopy (STM).[26]

We find that the embedded Stone-Wales defect engages in increased electronic interaction with the copper surface, compared to regular graphene, and observe transfer of electron density from the metal to the graphene sheet at the defect site. These results from density functional theory (DFT) calculations are corroborated by experimental studies of the molecular model system. Azupyrene as the molecular model defect forms a strong chemisorptive bond to the Cu(111) surface, whereas pyrene as a model for the regular graphene is only physisorbed. This conclusion is based on the following observations: (1) the much higher interaction energy of azupyrene, as derived from temperature-

programmed desorption (TPD), (2) the stronger electronic hybridization of the model defect, according to X-ray and ultra-violet photoelectron spectroscopy (XPS/UPS) and near edge X-ray absorption fine structure (NEXAFS), (3) the shorter bond between the model defect and the surface, as revealed by non-contact atomic force microscopy (nc-AFM).

P3

Results and Discussion

Surface interaction of embedded graphene defects. The interaction of embedded graphene defects with a metal surface was studied using dispersion-corrected periodic DFT calculations for two different defect topologies: the Stone-Wales defect and the 5-7 defect. Fig. 1a-c shows the free-standing, optimized structures of the ideal graphene lattice, the embedded Stone-Wales defect, and the embedded 5-7 defect. The Stone-Wales defect only slightly distorts the surrounding graphene lattice, whereas the 5-7 defects induces stronger deformations.

Next, the three different graphene unit cells were placed on a 4 layer Cu(111) slab. Geometry optimization yields the adsorbate structures of the embedded graphene defects, as shown in Fig. 1d-i. As a starting point, the adsorption structure of the ideal graphene lattice was chosen to be the (1×1) superstructure typically used in DFT investigations of the ideal graphene lattice on Cu(111).[27] The lattice mismatch between the optimized cell geometry of free-standing graphene and the forced (1×1) superstructure on the Cu(111) surface is only about 2 %.

The interaction of the embedded defects with the metal surface causes substantial charge redistribution, which is overlayed as charge density difference plots over the structures in Fig. 1d-i. For the ideal graphene lattice (Fig. 1d,g), some charge rearrangement occurs mostly by electron flow from the π-system of the graphene layer and from the first copper layer into the interface region between copper and graphene. For both defect structures, this charge flow is also present, but there is an additional strong localized charge transfer close to the defects. The charge transfer were quantified using different charge partitioning schemes (Supplementary Tab. 1). The absolute values obtained by these different schemes are prone to error, but is all methods show an appreciable, localized electron transfer from the surface to the defect regions of the graphene layer.

The geometry-optimized structures also reveal the influence of the defects on the height of the carbon atoms above the copper surface. As shown by the histogram in Fig. 1j, the Stone-Wales defect (blue) pulls the whole graphene lattice closer to the surface. Interestingly, the atoms in the actual defect are only slightly closer than the rest of the lattice (see heights below 3.09 Å in the blue histogram in Fig. 1j). In contrast, the 5-7 defect causes substantial corrugation of the graphene sheet, resulting in a much wider spread of the heights (green histogram on Fig. 1j). This structure has a larger average height than the ideal graphene lattice, because the distortion around the defect makes carbon atoms occupy unfavorable adsorption sites. This distortion is partly caused by the required periodicity of the overall structures. In the real graphene lattice, the 5-7 defect rarely occurs isolated or in periodic assemblies, but instead in chains forming rotational domain boundaries.[7] Related trends occur in the calculated adsorption energies. The incorporation of the Stone-Wales defect increases the adsorption energy of the whole unit cell by 6 kJ/mol, whereas the 5-7 defect lowers the adsorption energy by 35 kJ/mol.

The DFT calculations of the embedded graphene defects reveals an increased interaction of the defect structures with a contacting metal surface. Especially the Stone-Wales defect

shows a smaller adsorption height, a larger adsorption energy, and an enhanced electronic interaction with substantial charge transfer.

As pointed out above, these informations are difficult to obtain experimentally for the defects embedded in graphene. In the following, we will therefore use a molecular model system based on the interaction of azupyrene and pyrene with the Cu(111) surface. Various experimental and theoretical methods applied to this pair of isomers allow us to determine adsorbate-substrate interaction energies, details of the electronic structure, and the apparent difference of the adsorption heights.

P3

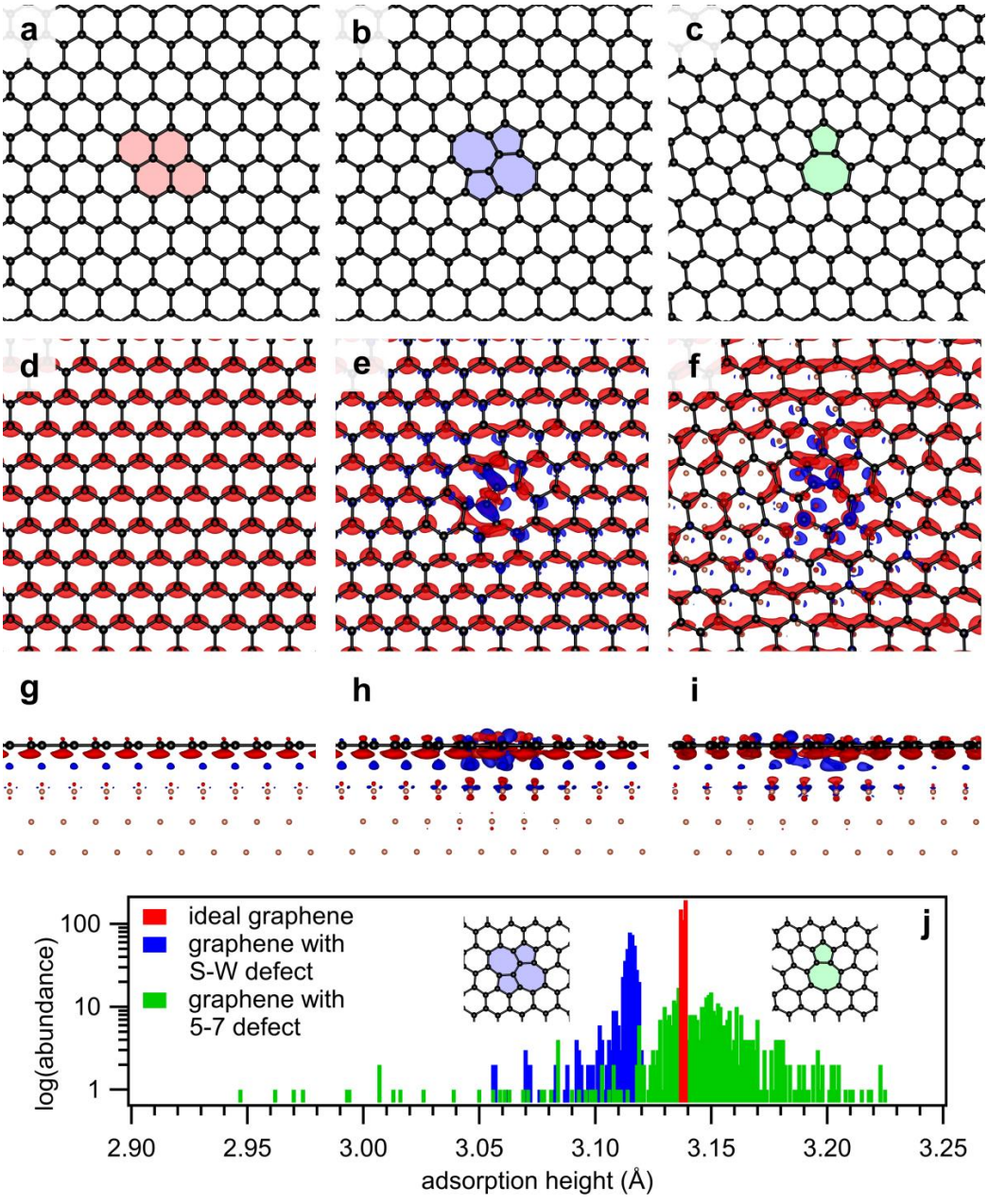

Fig. 1 | Interaction of graphene defects with the Cu(111) surface. Left: ideal graphene lattice, center: with embedded Stone-Wales defect, right: with embedded 5-7 defect. **a-c**, Optimized structure of the free standing graphene lattice. **d-f**, Top views and **g-i**, side views of the charge density difference plots for graphene adsorbed on Cu(111), isosurface value: 0.0005 $e^-/Å^3$, blue: electron accumulation, red: electron depletion. **j**, Abundance distribution for the adsorption heights of the carbon atoms above the Cu(111) substrate. Red, ideal graphene; blue, graphene with Stone-Wales defect; green, graphene with 5-7 defect. Large unit cells with 456 carbon atoms were chosen to reduce the lateral interaction between neighboring defects.

Adsorbate-substrate interaction energies. Quantitative information about the strength of adsorbate-substrate interactions can be experimentally obtained by TPD,[28,29] if (a) the adsorbate desorbs intact and (b) adsorption is nonactivated. Under these conditions, the desorption energy, E_{des}, is a good approximation for the negative differential adsorption energy.[30] Fig. 2a shows TPD traces for the desorption of azupyrene and pyrene from Cu(111). For both molecules the initial coverage for one trace was one monolayer (ML), while it was a low submonolayer coverage for pyrene and a about 0.6 ML for azupyrene. For pyrene, the low submonolayer coverage shows a first-order desorption peak centered at about 500 K. The monolayer spectrum spreads from 290 to 520 K, and represents complete desorption of the whole layer.

Desorption of azupyrene from the Cu(111) surface is only observed if the initial coverage exceeds approximately 0.5 ML. C1s XPS measurements performed after a TPD experiment with a full monolayer confirm that carbon corresponding to 0.53 ML azupyrene remains on the surface (Supplementary Fig. 3). As shown in Fig. 2a., the TPD peak for the lowest desorbing coverage of azupyrene, is centered at 630 K, which is considerably higher than in the case of pyrene (500 K) and thus qualitatively indicates stronger interaction of azupyrene with the metal surface. The TPD trace for initial monolayer coverage, which corresponds to the desorption of 0.47 ML, is broader than that of pyrene and ranges from 330 to 650 K.

The broadening of the monolayer TPD traces reveals substantial intermolecular repulsion, which is attributed to dipol-dipol interactions between vertical adsorption dipoles. These dipoles are mainly caused by rearrangement of electron density at the metal surface due to Pauli repulsion induced by the electrons of the molecule (Pauli pushback effect).[31] The more pronounced broadening in the case of azupyrene indicates stronger repulsion and thus larger adsorption dipoles, compared to pyrene case, providing additional evidence for the increased interaction of azupyrene with the copper surface. Note that the observed desorption above a certain coverage also results from intermolecular repulsion: While isolated azupyrene molecules bind too strongly to the surface to desorb, lateral repulsion weakens the adsorbate-substrate bond with increasing coverage until desorption becomes possible.

For quantitative analysis, we employed two complementary methods: the inverted Polanyi-Wigner equation (IPW) approach and an Arrhenius analysis, which is called LNR and

described in the Supplementary Methods and in the literature. [32] The desorption prefactors obtained by LNR were also used for the IPW analysis and, in the case of pyrene, confirmed by a prefactor of $2 \cdot 10^{15}$ s^{-1} obtained by heating rate variation (HRV) for a coverage of 0.1 ML (see Supplementary Fig. S2). The LNR and IPW analyses yield the coverage dependent desorption activation energies, which are plotted in Fig. 2b.

P3

For pyrene, the desorption energy in the zero-coverage limit is E_{des} = 159 kJ/mol. With increasing coverage, E_{des} decreases due to intermolecular repulsion and reaches 96 kJ/mol at monolayer coverage. Azupyrene has a higher desorption energy at monolayer coverage (122 kJ/mol) and the coverage dependence of E_{des} is much more pronounced than in the pyrene case. The highest desorption energy provided by the analysis is 198 kJ/mol at 0.53 ML. The desorption energy of pyrene at this coverage is only 130 kJ/mol.

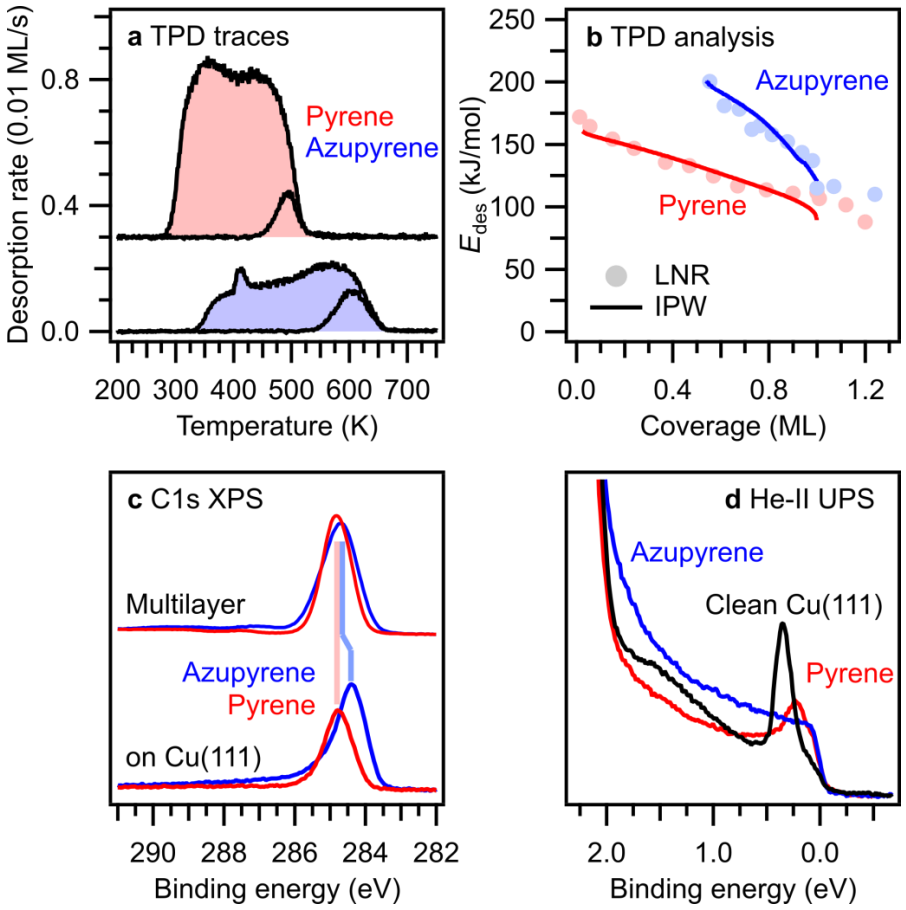

Fig. 2 | TPD and photoemission (XPS, UPS) data indicating that the azupyrene model defect binds stronger to the Cu(111) surface than its isomer pyrene. a. TPD traces of azupyrene and pyrene both for initial monolayer coverage and a lower initial coverage. **b** Coverage-dependent desorption energies obtained by analysis of the TPD data. **c** C1s XP monolayer spectra. Peak positions and shifts in relation to the multilayer peak positions are marked by dotted lines above the peaks. The asymmetry of the azupyrene peak indicates hybridization with the metal states of the surface. **d** He-II UP monolayer spectra of the

clean surface (black) and the monolayers of azupyrene and pyrene. The disappearance of the surface state (0.3 eV on the clean surface) shows a stronger interaction for azupyrene.

Occupied electronic states: Photoelectron spectroscopy. Photoemission spectroscopy (XPS, UPS) provides insight into the nature of the adsorbate-substrate interaction by probing the occupied electronic states. The adsorption-induced change of the electronic structure will enable us to discriminate between physisorptive and chemisorptive surface chemical bond. Physisorption is characterized by a weak interaction between molecule and surface, mainly caused by van der Waals forces, whereas chemisorption is associated with significant orbital contributions.[33]

To identify possible influences of the metal surface on the electronic structure, we compare C1s XP spectra of multilayers and monolayers of the two molecules (Fig. 2c). The multilayer spectra show a symmetric peak for pyrene and a broad peak with a shoulder at high binding energy (BE) for azupyrene, which can be explained by the topological difference between azupyrene and pyrene.[citation Azupyrene Paper 1] In the monolayer, pyrene still shows a symmetric peak positioned at the same BE as the multilayer peak. In the case of azupyrene, the monolayer peak shows a strongly asymmetric tailing and is shifted by -0.25 eV with respect to the multilayer signal. The asymmetric shape of the azupyrene peak can be explained by final state effects, which occur when density of states (DOS) close to the Fermi energy (E_F) is located at the corresponding atom, indicating a hybridization of molecular orbitals with metal states.[34]

Direct information about the valence electronic structure was obtained by UPS (Fig. 2d). For pyrene, the Cu(111) surface state is still visible, but shifted by 0.1 eV to lower BE, compared to the clean surface. This behavior is well known for flat-lying π-conjugated molecules physisorbed on metal surfaces. In the case of azupyrene, the surface state is not visible anymore. Instead, there is an increased intensity over the whole range between E_F and copper d-band, in agreement with hybridization causing the asymmetry of the C1s peak of azupyrene (Fig. 2c). The photoemission data thus indicate formation of a chemisorptive bond between azupyrene and the copper surface, the particular mechanism of which will be discussed it below in the context of DFT bonding analysis.

Work function changes. Interaction of the molecules with the copper surface influences the work function (WF), which was determined from the secondary electron cut-off of the UP spectra. While both molecules reduce the WF, the change is more negative for azupyrene (-1.18 eV) than for pyrene (-0.86 eV). The WF change is caused by the vertical adsorption dipoles, which are also responsible for the repulsion observed in TPD. Thus, the larger WF change for azupyrene corresponds to the stronger dipole-dipole repulsion in the desorption energy and overall confirms the stronger bonding of the model defect.

Unoccupied electronic states. NEXAFS provides information about the unoccupied valence electronic structure of the adsorbate systems. In Fig. 3, the carbon K-edge NEXAFS spectra of multilayers (Fig. 3a,b) and monolayers (Fig. 3c,d) of pyrene and azupyrene on Cu(111) are shown. The lower part of Fig. 3 shows the corresponding MO-

projected DFT NEXAFS calculations for both systems. In the multilayer spectra, the π* and σ* resonances can clearly be distinguished. The onset of the first π* resonance (which includes contributions of the C1s→LUMO and C1s→LUMO+1 transitions, according to our calculations) appears at a lower photon energy for azupyrene than for pyrene, indicating a lower lying LUMO of azupyrene. The dichroism of the monolayer spectra, especially the vanishing π* intensity at normal incidence angle, confirms that both molecules adsorb with the molecular plane parallel to the surface. In the case of pyrene, the monolayer spectrum taken with 25° incidence angle resembles the multilayer spectrum, with only a slight broadening of the prominent π* peaks and some peak shifts at higher lying transitions. For azupyrene, the situation changes distinctly: the interaction with the Cu surface induces a massive decrease of intensity and a completely different peak shape of the first π* resonance. As can be seen in the DFT calculations, this is mainly due to a strong decrease of the signal for the C1s→LUMO transition.

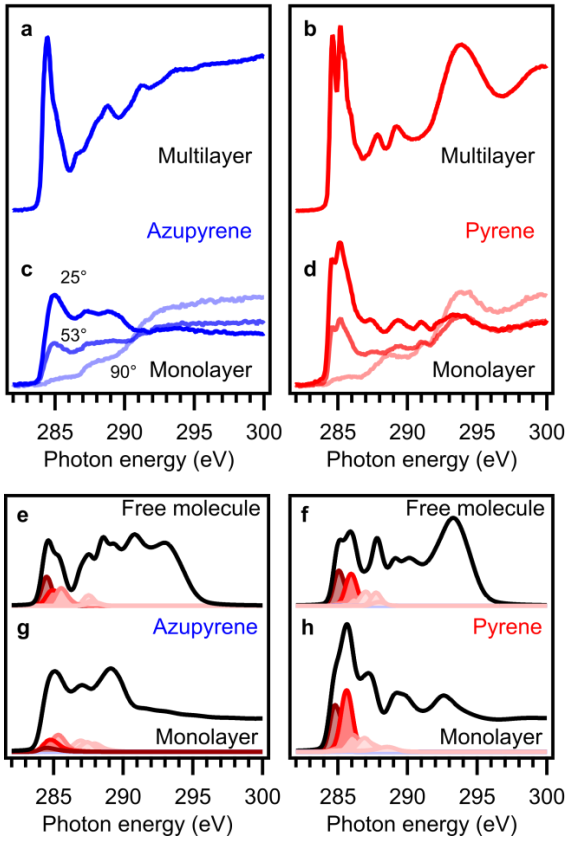

Fig. 3 | Carbon K-edge NEXAFS data for azupyrene and pyrene reveal interaction-induced changes in the unoccupied orbitals of azupyrene. Experimental spectra: **a**,**b**, multilayers; **c**,**d**, monolayers. The multilayer spectra were taken with the electric field vector oriented 53° relative to the surface normal, the monolayer spectra with the angles indicated by the color scheme (25°, bold color; 53°, intermediate color; 90°, faint color). MO-projection analysis of the DFT-calculated NEXAFS spectra of the free molecules **e**,**f** and the monolayers **g**,**h**. Contributions of the LUMO in dark red and of the higher orbitals

in incrementally lighter colors, total spectrum in black. The calculated spectra were rigidly shifted by -6 eV to match the experimental energy scale.

Structural data – nc-AFM.

The constant-height AFM images of azupyrene (Fig. 4a) and pyrene (Fig. 4b) confirm the different topologies of the ring systems: 5-7-5-7 for azupyrene and 6-6-6-6 for pyrene. Some features images can be attributed to the different adsorption conformations of the two molecules: The rightmost ring of the pyrene molecule appears slightly elongated in the horizontal direction and contains a bright vertical feature (marked by red arrow in Fig. 4b). These features are presumably caused by tip-induced movements of the molecule between two different adsorption positions that occur during scanning. In the constant-height AFM image of azupyrene (Fig. 4a), the C and H atoms at the periphery appear brighter than atoms in the center of the molecule. This is caused by the bowl-shaped adsorption conformation of azupyrene on Cu(111) (see DFT results below). Therefore, the outer atoms are closer to the CO tip, which leads to their brighter appearance in the constant-height AFM images.[35,36]

The adsorption topography of the molecules was obtained by three-dimensional frequency shift mapping (Supplementary Fig. 4 for details).[37,38] The reconstructed topographical information for the two molecules is shown in Fig. 4c,d. Corresponding topography scanlines indicating the apparent adsorption heights of the molecules with regard to the Cu(111) surface plane are depicted in Fig. 4e. The scanlines have been taken along the short and long molecular axes, respectively (see arrows in Fig. 4c,d). Note that the topography values correspond to apparent adsorption heights, since these values are deduced from the interactions between the CO tip and the sample, which may be different for the different molecules (Supplementary Fig. 5). The general suitability of AFM to determine differences in the vertical adsorbate-substrate distances (adsorption-heights) was demonstrated previously by direct comparison with absolute adsorption heights measured by the normal-incidence X-ray standing wave (NIXSW) technique.[25]

The topography scanlines for pyrene (red and orange lines in Fig. 4e) reveal a rather flat conformation. The molecule is not curved or bent, but only slightly tiled along the long molecular axis (red line in Fig. 4e), which may be explained by tip-induced movements of the molecule (Supplementary Fig. 6). In contrast, azupyrene assumes a non-tilted but bowl-shaped adsorption conformation, where the central C atoms are approximately 15 pm closer to the Cu(111) surface than the atoms in the circumference of the molecule. The measured adsorption positions and conformations of the two model compounds are in reasonable agreement with our DFT calculations (Fig. 5 and Supplementary Fig. 4). According to these apparent average adsorption heights, azupyrene is closer to the surface than pyrene by about 0.9 Å (Fig. 4e). This result is another piece of evidence for the stronger interaction of azupyrene with the Cu(111) surface. The measured difference in adsorption height is somewhat larger than the DFT value of 0.52 Å (see below). The deviation between AFM and DFT heights is in line with previous work, in which height differences between azulene

(chemisorbed) and naphthalene (physisorbed) on Cu(111) were obtained using AFM, NIXSW, and DFT.[25] AFM there also provided the largest (0.92 Å) and DFT (0.63 Å) the smallest difference, while the NIXSW method yielded an intermediate value (0.74 Å).

P3

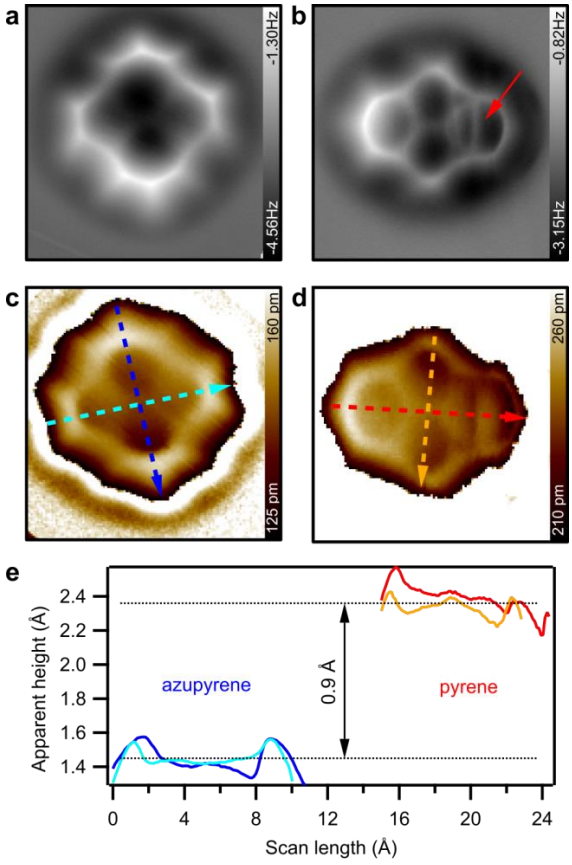

Fig. 4 | Low-temperature (LT) AFM measurements revealing the chemical structure and the apparent adsorption heights of azupyrene and pyrene on Cu(111). a,b Constant-height frequency shift AFM images of azupyrene and pyrene at z = -100 pm (a) and z = -50 pm (b) with respect to a tunneling set point of U = 100 mV and I = 20 pA. **c,d** Reconstructed topography images (i.e., adsorption distance) of pyrene and azupyrene obtained from a 3D grid measurement of $\Delta f(z)$-spectra (see Fig. S5 of the SI for details). **e** Topography scan lines of azupyrene (blue, cyan) and pyrene (red, yellow) showing a difference in the apparent adsorption height of the molecules. The scan lines are taken along the dashed arrows in c,d.

Density-functional theory (DFT) calculations. Dispersion-corrected periodic DFT calculations provide a deeper understanding of the effects governing the different interactions of the model defect and its isomer with the copper surface. The most favorable adsorption site as determined by DFT is shown together with structural information in Fig.

5. Both adsorption sites are in good agreement with the AFM results (see Supplementary Fig. 4).

The calculations yield adsorption heights of 2.43 Å for azupyrene and 2.96 Å for pyrene, confirming the experimental finding that azupyrene is much closer to the surface. Both the azupyrene molecule and the first surface layer undergo substantial out-of-plane deformation (Fig. 5c,g). In addition, the in-plane bond lengths of azupyrene change upon adsorption, resulting in an elongation of all perimeter bonds and especially of the central bond, as well as a shortening of the bonds connecting the central carbon atoms to the perimeter (Fig. 5e). In the case of pyrene, molecule and surface are structurally much less affected by the adsorption interaction (Fig. 5d,f,h).

The pattern of the surface-induced bond-length changes in azupyrene can be understood by electron donation into the LUMO (Fig. 6e), which has a nodal plane intersecting the elongated central bond and has bonding character with respect to the shortened bonds. In the context of aromaticity models, these changes can be described as a partial transition from a predominantly annulenoid conjugation along the perimeter in the free molecule to a more benzenoid conjugation in the adsorbed state. A detailed discussion on the basis of the *Harmonic Oscillator Model of Aromaticity* (HOMA) is presented in the Supplementary Discussion.

The calculated adsorption energies in the (4×4) superstructure are -243 kJ/mol for azupyrene and only -206 kJ/mol for pyrene. To compare these integral adsorption energies with the differential experimental desorption energies in a meaningful way, the latter must be integrated up to the coverage used in the calculations. The integrated desorption energies for the (4×4) structure are 209 kJ/mol for azupyrene and 132 kJ/mol for pyrene. This error of 34 and 74 kJ/mol is quite large, but the D3 dispersion correction used in the DFT calculation is well known for overestimating adsorption energies.[39,40] It is also not surprising that the overestimation is much worse for pyrene, as this problem is most pronounced for physisorbed systems.[25]

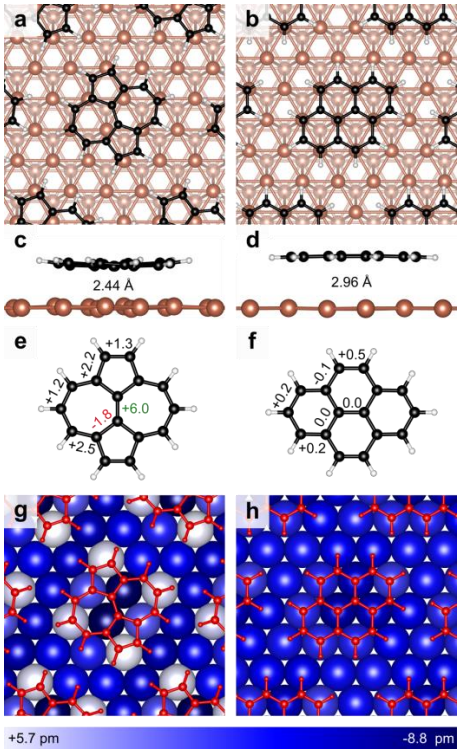

Fig. 5 | DFT calculations reveal substantial differences between the adsorption structures of azupyrene and pyrene on Cu(111). Top views **a**,**b** and side views **c**,**d** of the adsorbate structures. **e**,**f**, Changes of the bond lengths relative to the gas phase structure (in pm). **g**,**h**, vertical displacements (in pm) of the copper atoms in the topmost layer, compared to the relaxed surface without a molecule. Positive values (lighter shades of blue) indicate displacement towards the molecule.

Using the periodic energy decomposition analysis (pEDA) method with the natural orbitals for chemical valence (NOCV) extension allows us to gain profound insight into the surface chemical bond.[41-43] The pEDA method divides the interaction energy between two fragments (here: surface and molecule) into physically well-defined terms. The NOCV extension then pinpoints specific orbital interactions as constituents of the analyzed bond. This analysis shows that azupyrene forms a chemical bond to the surface, which is characterized by charge transfer from the surface to the LUMO (and, to lesser extent, the LUMO+1) of the molecule. In contrast, pyrene shows only physisorptive interaction. A more detailed discussion of the analysis results is provided in the Supplementary Discussion. The pEDA results agree with the overall charge density difference due to the adsorption, which is presented in the form of charge density difference plots (Fig. 6a-d). These shows electron accumulation in shape of the former LUMO for azupyrene (Fig. 6a,b), whereas for pyrene no substantial charge transfer is visible (Fig 6c,d).

To quantify the charge transfer between molecule and substrate, Hirshfeld's charge analysis,[44] iterative Hirshfeld,[45-47] Bader's atoms in molecules analysis,[48] and an integration of the molecular DOS up to the Fermi energy were performed. All show an

appreciable charge transfer for azupyrene and only a minor charge transfer for pyrene (see Supplementary Tab. 1).

Even as the net charge transfer is from the surface to the molecule, the rearrangement of electron density by the Pauli-pushback effect leads to a net dipole with the opposite direction. The orientation of the dipole agrees with the negative WF change experimentally observed by UPS. The magnitude of the DFT calculated dipole moment is 2.57 D for azupyrene and 2.25 D for pyrene, in line with the larger WF change and the stronger intermolecular repulsion observed in TPD.

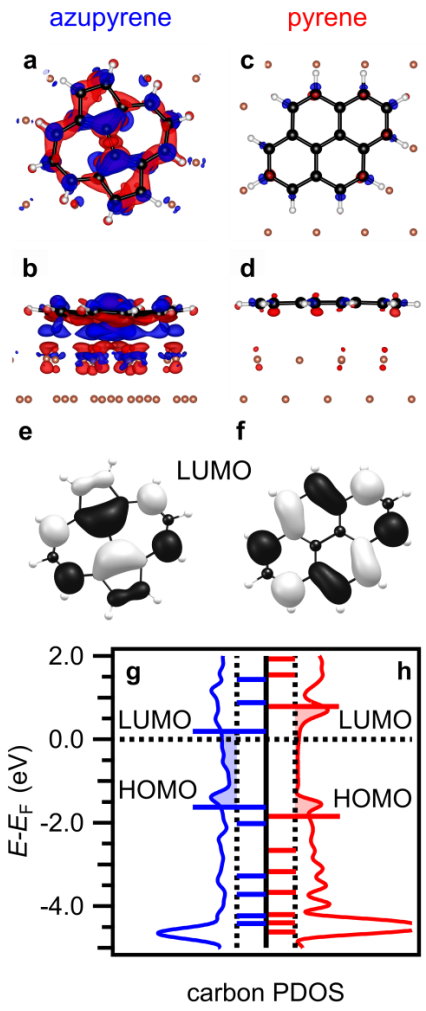

Fig. 6 | DFT-based bonding analysis shows electron transfer from the Cu(111) surface into the unoccupied LUMO of azupyrene and no charge transfer for pyrene. **a-d** Charge density difference plots for azupyrene and pyrene. The isosurface value is 0.002 $e^-/Å^3$ for all plots. Red, electron depletion; blue, electron accumulation. **e**,**f** Depiction of the LUMOs of the molecules, isosurface value 0.03. **g**,**h** Carbon-projected density of states of the azupyrene **g** and pyrene **h**, horizontal lines indicate the gas phase orbital energies, shifted to account for the work function.

P3

Conclusion

Topological graphene defects lead to an increased interaction strength of the lattice with a Cu(111) surface, as shown in adsorption heights, energies and charge transfer calculated by DFT. The experimental investigation of the corresponding molecular model systems reveals that azupyrene. the model molecule for the Stone-Wales defect forms a stronger chemical bond with the Cu(111) surface than its isomer pyrene, which is only physisorbed. In fact, azupyrene is so strongly bonded to the surface that no molecules desorb at coverages of 0.53 ML and less. At this coverages the desorption energy determined by TPD is 198 kJ/mol, compared to 130 kJ/mol for pyrene. Extensive spectroscopic studies show that the larger desorption energy is accompanied by a pronounced change in the electronic structure. The molecular orbitals of azupyrene hybridize with the states of the metal surface, as seen in XPS and UPS measurements, is and the LUMO and LUMO+1 orbitals are now partly occupied as seen in NEXAFS. The stronger bond is also expressed with a smaller adsorption height, nc-AFM results yield a difference of 0.9 Å in apparent adsorption height between the molecules. The experimental results are in agreement with an extensive bonding analysis performed on basis of the DFT calculations, which shows that this stronger bond of azupyrene is caused by the transfer of electron density from the surface into the molecular LUMO orbital.

Thus the model molecule representing the Stone-Wales defect in graphene indeed shows a stronger interaction with a metal surface in experiment, including increased adsorption energy, enhanced charge transfer and reduced adsorption height. This in agreement with the theoretically studied influence of the embedded graphene defect onto the properties of an extended graphene/metal interface.

We therefore could prove that the performance engineering of (opto)electronic devices with graphene-metal contacts might be improved if advantage is taken of topological defects.

Methods

Experimental Methods. The adsorption of azupyrene and pyrene on Cu(111) was studied under ultra-high vacuum (UHV) conditions at base pressures below 2×10^{-10} mbar.

The detailed synthesis procedure of azupyrene (dicyclopenta[ef,kl]heptalene) is described in detail in the Supplementary Information. Azupyrene and pyrene (Sigma-Aldrich, purity >99 %) were deposited onto the substrate with a home-build line-of-sight evaporator after initial pump-freeze-thaw cycles of the reservoirs. The polished Cu(111) single-crystal surface (purity >99.999 %, roughness < 0.01 µm, orientation accuracy < 0.4°, from MaTecK/Germany) was prepared by iterated cycles of sputtering with Ar^+ ions (1 keV, 15 µA, 30 min) and annealing (800-830 K, 15 min). Surface cleanliness and structure were confirmed by XPS, LEED and STM. Sample temperatures were measured with a type K thermocouple directly mounted to the single crystal. Coverages are given in the unit monolayer (ML) according one complete layer of molecules on the surface. For pyrene on

Cu(111) the complete monolayer is formed by a (4×4) structure corresponding to 0.063 molecules per first layer Cu atom, for azupyrene the monolayer is formed by a more dense (√13×√13) structure (0.077 molecules per Cu atom).

TPD measurements were performed with a HIDEN EPIC 1000 mass spectrometer mounted inside a differentially pumped cryoshroud for line-of-sight mass spectrometry.

The LT-AFM measurements were performed with a commercial low temperature atomic force microscope (ScientaOmicron, Germany). The temperature during the AFM measurements was about 5.2 K, the base pressure in the chamber is below $1 \cdot 10^{-10}$ mbar. All images and measurements were obtained with a CO-terminated tip.[49] The q-plus tuning fork sensor[50] has a resonance frequency of $f_{res} \approx 25.6$ kHz, a quality factor of $Q \approx 30000$ and an oscillation amplitude of $A \approx 70$ pm. During the AFM constant-height measurements a small gap voltage of -0.54 mV was applied to the sample to compensate the voltage offset of the tunneling amplifier.

XPS and UPS were performed with a PHOIBOS 150 electron energy analyzer equipped with an MCD-9 multi channeltron detector. For XPS, monochromatic Al-K_α radiation from a SPECS XR 50 M X-ray anode with a FOCUS 500 monochromator was employed. He-II UP spectra and work functions were measured with a UVS 10/35 gas discharge lamp and the same analyzer set up.

NEXAFS spectroscopy was performed at the synchrotron radiation facility BESSY II (Helmholtz-Zentrum Berlin) using the HE-SGM dipole beamline, the partial electron-yield (PEY) mode was used with a retarding field of -150 V and a channeltron detector voltage of 2.3 keV. The thus obtained NEXAFS data was treated as described previously.[25]

Density Functional Theory Calculations. Periodic density-functional-theory calculations were performed using the generalized gradient approximation (GGA) proposed by Perdew, Burke, and Ernzerhof (PBE)[51] for the exchange-correlation functional in combination with the D3 van-der-Waals correction scheme with Becke-Johnson damping,[52,53]. Further technical details of the calculations can be found in the Supplementary Methods.

Acknowledgments

Funded by the Deutsche Forschungsgemeinschaft (DFG,German Research Foundation)-Projektnummer 223848855-SFB 1083, the DFG Project EB 535/1-1 and the GRK (Research Training Group) 2204 "Substitute Materials for sustainable Energy Technologies". We thank the synchrotron radiation facility BESSY-II of the Helmholtz-Zentrum für Materialien und Energie, Berlin, for allocation of beam time at the HE-SGM beamline and for financial support. We further acknowledge computational resources from HRZ Marburg, Goethe-CSC Frankfurt and HLR Stuttgart. S.J.H and R.J.M acknowledge funding for a PhD studentship through the EPSRC Centre for Doctoral Training in Molecular Analytical Science (EP/L015307/1) and computing resources via the EPSRC-funded HPC Midlands+ computing centre (EP/P020232/1) and the EPSRC-funded Materials Chemistry Consortium for the ARCHER UK National Supercomputing Service

(EP/R029431/1). R.J.M acknowledges support via a UKRI Future Leaders Fellowship (MR/S016023/1).

Author contributions

P3

J.M.G. conceived the idea and supervised the project. B.P.K. performed the XPS, UPS, and NEXAFS experiments as well as most of the DFT calculations, analyzed the corresponding data and wrote the manuscript with contributions from all authors. A.I. conducted the nc-AFM experiments and analyzed the data, supervised by D.E and A.S. S.R.K. performed and analyzed the TPD measurements. L.R., J.H and A.J. supported the XPS, UPS and NEXAFS measurements. L.M.W. and S.M.W. synthesized azupyrene, supervised by G.H. S.J.H. and R.J.M. performed the MO-projections and NEXAFS simulations. R.T. supervised the DFT calculations and contributed to their discussion.

Competing interest

The authors declare no competing financial interest.

Additional Information

Supplementary information for this paper is available at https://doi.org/XXXXXX.

Reprints and permissions information is available at www.nature.com/reprints.

Correspondence and requests for materials should be addressed to J. M. G.

Publishers'note: Springer Nature remains neutral with regard to jurisdictional claims in published maps and institutional affiliations.

Graphical Abstract Version 1

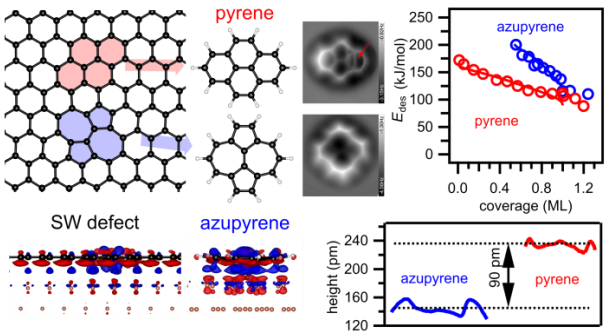

Graphical Abstract Version 2

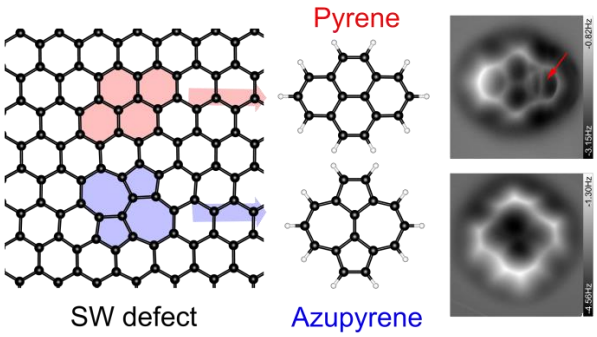

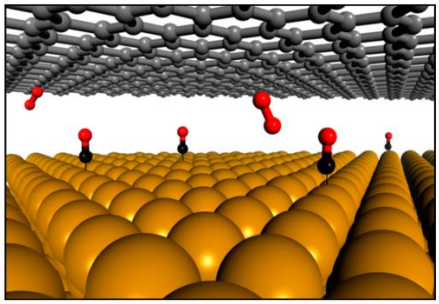

Graphical Abstract Version 3

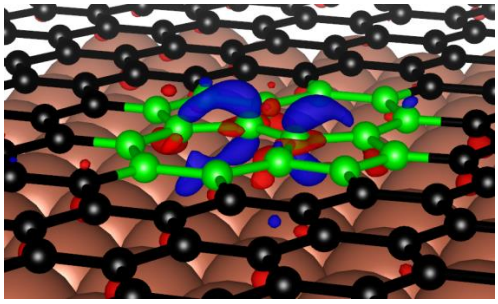

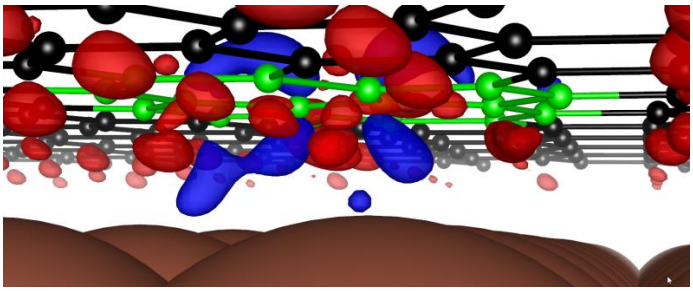

References

1 Geim, A. K. & Novoselov, K. S. The rise of graphene. *Nat. Mater.* **6**, 183-191 (2007).
2 Kim, P. Across the border. *Nat. Mater.* **9**, 792-793 (2010).
3 Hashimoto, A., Suenaga, K., Gloter, A., Urita, K. & Iijima, S. Direct evidence for atomic defects in graphene layers. *Nature* **430**, 870-873 (2004).
4 Kotakoski, J., Krasheninnikov, A. V., Kaiser, U. & Meyer, J. C. From Point Defects in Graphene to Two-Dimensional Amorphous Carbon. *Phys. Rev. Lett.* **106**, 105505, doi:10.1103/PhysRevLett.106.105505 (2011).
5 Meyer, J. C. *et al.* Direct Imaging of Lattice Atoms and Topological Defects in Graphene Membranes. *Nano Lett.* **8**, 3582-3586 (2008).
6 Tsen, A. W. *et al.* Tailoring Electrical Transport Across Grain Boundaries in Polycrystalline Graphene. *Science* **336**, 1143-1146, doi:10.1126/science.1218948 (2012).
7 Huang, P. Y. *et al.* Grains and grain boundaries in single-layer graphene atomic patchwork quilts. *Nature* **469**, 389-393 (2011).
8 Kim, K. *et al.* Grain Boundary Mapping in Polycrystalline Graphene. *ACS Nano* **5**, 2142-2146, doi:10.1021/nn1033423 (2011).
9 Rasool, H. I., Ophus, C., Klug, W. S., Zettl, A. & Gimzewski, J. K. Measurement of the intrinsic strength of crystalline and polycrystalline graphene. *Nat. Commun.* **4**, 2811, doi:10.1038/ncomms3811 (2013).
10 Ito, Y. *et al.* Correlation between Chemical Dopants and Topological Defects in Catalytically Active Nanoporous Graphene. *Adv. Mater.* **28**, 10644-10651, doi:10.1002/adma.201604318 (2016).
11 Malola, S., Häkkinen, H. & Koskinen, P. Structural, chemical, and dynamical trends in graphene grain boundaries. *Phys. Rev. B* **81**, 165447 (2010).
12 Grantab, R., Shenoy, V. B. & Ruoff, R. S. Anomalous Strength Characteristics of Tilt Grain Boundaries in Graphene. *Science* **330**, 946-948 (2010).
13 Wei, Y. *et al.* The nature of strength enhancement and weakening by pentagon-heptagon defects in graphene. *Nat. Mater.* **11**, 759-763 (2012).
14 Shekhawat, A. & Ritchie, R. O. Toughness and strength of nanocrystalline graphene. *Nat. Commun.* **7**, 10546, doi:10.1038/ncomms10546 (2016).
15 Yazyev, O. V. & Louie, S. G. Electronic transport in polycrystalline graphene. *Nat. Mater.* **9**, 806-809 (2010).
16 Cervenka, J., Katsnelson, M. I. & Flipse, C. F. J. Room-temperature ferromagnetism in graphite driven by two-dimensional networks of point defects. *Nat. Phys.* **5**, 840-844 (2009).
17 Ni, B., Zhang, T., Li, J., Li, X. & Gao, H. in *Handbook of Graphene* (eds E. Celasco *et al.*) (Wiley, 2019).
18 Sun, Y., Sun, M. & Xie, D. in *Graphene* (eds Hongwei Zhu, Zhiping Xu, Dan Xie, & Ying Fang) 103-155 (Academic Press, 2018).
19 Wang, R. *et al.* Graphene based functional devices: A short review. *Front. Phys.* **14**, 13603, doi:10.1007/s11467-018-0859-y (2019).
20 Cusati, T. *et al.* Electrical properties of graphene-metal contacts. *Sci. Rep.* **7**, 5109, doi:10.1038/s41598-017-05069-7 (2017).
21 Banhart, F., Kotakoski, J. & Krasheninnikov, A. V. Structural Defects in Graphene. *ACS Nano* **5**, 26-41 (2011).
22 Zhuang, D. C. a. Y. Z. a. L. L. a. G. Z. a. M. C. a. Y. J. a. H. Stone-Wales Defects Preserve Hyperuniformity in Amorphous Two-Dimensional Materials. *arXiv*, 2006.03765 (2020).
23 Mallion, R. B. & Rouvray, D. H. The Golden Jubilee of the Coulson-Rushbrooke Pairing Theorem. *J. Math. Chem.* **5**, 1-21 (1990).
24 Xin, H. & Gao, X. Application of Azulene in Constructing Organic Optoelectronic Materials: New Tricks for an Old Dog. *ChemPlusChem* **82**, 945-956 (2017).

25 Klein, B. P. *et al.* Molecular Topology and the Surface Chemical Bond: Alternant Versus Nonalternant Aromatic Systems as Functional Structural Elements. *Phys. Rev. X* **9**, 011030, doi:10.1103/PhysRevX.9.011030 (2019).

26 Wang, D., Wan, L.-J., Xu, Q.-M., Wang, C. & Bai, C.-L. Adlayer structures of pyrene and perylene on Cu(111): an in situ STM study. *Surf. Sci.* **478**, L320-L326, doi:10.1016/S0039-6028(01)00965-7 (2001).

27 Chanier, T. & Henrard, L. From carbon atom to graphene on Cu(111): an ab-initio study. *Eur. Phys. J. B* **88**, 5, doi:10.1140/epjb/e2014-50587-0 (2015).

28 de Jong, A. M. & Niemantsverdriet, J. W. Thermal desorption analysis: Comparative test of ten commonly applied procedures. *Surf. Sci.* **233**, 355-365 (1990).

29 Nieskens, D. L. S., van Bavel, A. P. & Niemantsverdriet, J. W. The analysis of temperature programmed desorption experiments of systems with lateral interactions; implications of the compensation effect. *Surf. Sci.* **546**, 159-169 (2003).

30 King, D. A. Thermal desorption from metal surfaces: A review. *Surf. Sci.* **47**, 384-402 (1975).

31 Witte, G., Lukas, S., Bagus, P. S. & Wöll, C. Vacuum level alignment at organic/metal junctions: “Cushion” effect and the interface dipole. *Appl. Phys. Lett.* **87**, 263502 (2005).

32 Kachel, S. R. *et al.* Chemisorption and Physisorption at the Metal/Organic Interface: Bond Energies of Naphthalene and Azulene on Coinage Metal Surfaces. *J. Phys. Chem. C* **124**, 8257-8268, doi:10.1021/acs.jpcc.0c00915 (2020).

33 Pecher, J. & Tonner, R. Precursor states of organic adsorbates on semiconductor surfaces are chemisorbed and immobile. *Chem. Phys. Chem.* **18**, 34-38 (2017).

34 Doniach, S. & Sunjic, M. Many-electron singularity in X-ray photoemission and X-ray line spectra from metals. *J. Phys. C: Solid State Phys.* **3**, 285-291 (1970).

35 Ebeling, D. *et al.* London Dispersion Directs On-Surface Self-Assembly of [121]Tetramantane Molecules. *ACS Nano* **11**, 9459-9466, doi:10.1021/acsnano.7b05204 (2017).

36 Ebeling, D. *et al.* Assigning the absolute configuration of single aliphatic molecules by visual inspection. *Nat. Commun.* **9**, 2420, doi:10.1038/s41467-018-04843-z (2018).

37 Hölscher, H., Langkat, S. M., Schwarz, A. & Wiesendanger, R. Measurement of three-dimensional force fields with atomic resolution using dynamic force spectroscopy. *Appl. Phys. Lett.* **81**, 4428-4430, doi:10.1063/1.1525056 (2002).

38 Schirmeisen, A., Weiner, D. & Fuchs, H. Single-Atom Contact Mechanics: From Atomic Scale Energy Barrier to Mechanical Relaxation Hysteresis. *Phys. Rev. Lett.* **97**, 136101, doi:10.1103/PhysRevLett.97.136101 (2006).

39 Maurer, R. J., Ruiz, V. G. & Tkatchenko, A. Many-body dispersion effects in the binding of adsorbates on metal surfaces. *J. Chem. Phys.* **143**, 102808 (2015).

40 Maurer, R. J. *et al.* Adsorption structures and energetics of molecules on metal surfaces: Bridging experiment and theory. *Prog. Surf. Sci.* **91**, 72-100, doi:10.1016/j.progsurf.2016.05.001 (2016).

41 Raupach, M. & Tonner, R. A periodic energy decomposition analysis method for the investigation of chemical bonding in extended systems. *J. Chem. Phys.* **142**, 194105 (2015).

42 Mitoraj, M. P., Michalak, A. & Ziegler, T. A Combined Charge and Energy Decomposition Scheme for Bond Analysis. *J. Chem. Theory Comput.* **5**, 962-975, doi:10.1021/ct800503d (2009).

43 Pecher, L. & Tonner, R. Deriving bonding concepts for molecules, surfaces, and solids with energy decomposition analysis for extended systems. *WIREs Comput Mol Sci.* **9**, e1401, doi:10.1002/wcms.1401 (2019).

44 Hirshfeld, F. L. Bonded-Atom Fragments for Describing Molecular Charge Densities. *Theor. Chim. Acta* **44**, 129-138 (1977).

45 Bultinck, P., Van Alsenoy, C., Ayers, P. W. & Carbó-Dorca, R. Critical analysis and extension of the Hirshfeld atoms in molecules. *J. Chem. Phys.* **126**, 144111, doi:10.1063/1.2715563 (2007).
46 Vanpoucke, D. E. P., Bultinck, P. & Van Driessche, I. Extending Hirshfeld-I to bulk and periodic materials. *J. Comput. Chem.* **34**, 405-417, doi:10.1002/jcc.23088 (2013).
47 Vanpoucke, D. E. P., Van Driessche, I. & Bultinck, P. Reply to 'comment on "extending Hirshfeld-I to bulk and periodic materials". *J. Comput. Chem.* **34**, 422-427, doi:10.1002/jcc.23088 (2013).
48 Bader, R. F. W. *Atoms in Molecules - A Quantum Theory*. (Oxford University Press, 1990).
49 Bartels, L., Meyer, G. & Rieder, K. H. Controlled vertical manipulation of single CO molecules with the scanning tunneling microscope: A route to chemical contrast. *Appl. Phys. Lett.* **71**, 213-215, doi:10.1063/1.119503 (1997).
50 Giessibl, F. J. High-speed force sensor for force microscopy and profilometry utilizing a quartz tuning fork. *Appl. Phys. Lett.* **73**, 3956-3958, doi:10.1063/1.122948 (1998).
51 Perdew, J. P., Burke, K. & Ernzerhof, M. Generalized Gradient Approximation Made Simple. *Phys. Rev. Lett.* **77**, 3865-3868 (1996).
52 Grimme, S., Antony, J., Ehrlich, S. & Krieg, H. A consistent and accurate ab initio parametrization of density functional dispersion correction (DFT-D) for the 94 elements H-Pu. *J. Chem. Phys.* **132**, 154104 (2010).
53 Becke, A. D. & Johnson, E. R. A density-functional model of the dispersion interaction. *J. Chem. Phys.* **123**, 154101, doi:10.1063/1.2065267 (2005).

SUPPLEMENTARY INFORMATION

Enhanced Interaction of the Stone-Wales Defect at the Metal-Graphene Interface

Benedikt P. Klein[a], Alexander Ihle[b], Stefan R. Kachel[a], Lukas Ruppenthal[a], Samuel J. Hall[c,d], Lars E. Sattler[e], Sebastian M. Weber[e], Jan Herritsch[a], Andrea Jaegermann[a], Daniel Ebeling[b], Reinhard J. Maurer[d], Gerhard Hilt[e], Ralf Tonner[a], André Schirmeisen[b], J. Michael Gottfried[a*]

[a]*Fachbereich Chemie, Philipps-Universität Marburg, Hans-Meerwein-Straße. 4, 35032 Marburg, Germany*

[b]*Institut für Angewandte Physik, Justus-Liebig-Universität Gießen, Heinrich-Buff-Ring 16, 35392 Gießen, Germany*

[c]*MAS Centre for Doctoral Training, Senate House, and* [d]*Department of Chemistry and Centre for Scientific Computing, University of Warwick, Gibbet Hill Road, Coventry, CV4 7AL, United Kingdom*

[e]*Institut für Chemie, Carl von Ossietzky Universität Oldenburg, Carl-von-Ossietzky-Straße. 9-11, 26111 Oldenburg, Germany*

P3

1. Supplementary Methods

1.1 Density Functional Theory Calculations.

The basic calculations for the adsorbed molecules were were performed using the Vienna Ab Initio Simulation Package (VASP)[1-4] with the generalized gradient approximation (GGA) proposed by Perdew, Burke, and Ernzerhof (PBE)[5] for the exchange-correlation functional in combination with the D3 van-der-Waals correction scheme with Becke-Johnson damping,[6,7] and the projector-augmented wave (PAW) ansatz[8,9] for the atomic cores. A plane-wave cutoff energy of 350 eV, a vacuum layer of 30 Å and a 6×6×1 Monkhorst Pack k-point grid were chosen.

X-ray absorption spectra were calculated using the pseudopotential plane-wave code CASTEP-18.1,[10] using the PBE functional with a plane-wave cutoff of 450 eV and an 8×8×1 k-point grid. For the XPS shifts the delta self-consistent field (ΔSCF) method of constraining electronic occupations to resemble full core-hole excitations was used. NEXAFS spectra were simulated using on-the-fly generated USPPs and the CASTEP module ELNES[11] and the transition-potential approach.[12,13] This method constrains the occupation of the initial state orbital, of the C 1s, to 0.5 and the corresponding Kohn-Sham eigenenergies are taken to reflect the NEXAFS spectrum. Individual XAS calculations for each carbon atom allow for an atom-wise projected NEXAFS spectrum to be generated. MO projections and core-level spectra were processed using a self-written post-processing tool for CASTEP.[14]

The pEDA method[15] allows to decompose the bond energy into several physically well-defined terms, thus permitting a more detailed interpretation of the character of the chemical bond between two fragments.[16] In our case the fragments are chosen to be the molecule and the surface in their respective singlet electronic states (see SI for analysis and more details).

The calculations for the free graphene defect structures were also performed in VASP on the level PBE-D3(BJ)/PAW with a plane-wave cutoff energy of 350 eV and 30 Å vacuum, the k-grid consisted only of the Γ-point. The unit cell with 456 carbon atoms was chosen large enough to contain one Stone-wales defect or two 5-7 defects isolated by a sufficiently large distance. The adsorbed graphene structures were generated with a 4-layer Cu slab containing 912 copper atoms and 456 carbon atoms (with a 10 Å vacuum layer) and optimized in a multistep procedure. As a starting point the simple (1×1) adsorption structure of the ideal graphene on Cu(111) often found in the literature[17] was used.

1.2 Synthesis of Azupyrene

1.2.1 General Information

All reactions with water- and/or air-sensitive starting materials were carried out in pre-dried glass wares under Argon atmosphere utilizing standard Schlenk techniques. All used solvents were dried over molecular sieves (3 Å) and were degassed prior to use. Thin layer chromatography (TLC) was carried out on prefabricated plates (silica gel 60, F254 with fluorescence indicator) by *Macherey Nagel*. Column Chromatography was carried out on silica gel 60 (40-63 µm, 230-400 mesh) by *Macherey Nagel*. Commercially available chemicals were used without further purification. Non-commercial reagents were synthesized by literature-known procedures.

^{1}H and ^{13}C NMR were either recorded on a *Bruker Fourier 300HD* or a *Bruker Avance III 500HD* spectrometer at room temperature utilizing preset pulse programs. The chemical shifts are given in parts per million (ppm). The residual solvent signal ($CDCl_3$: ^{1}H NMR: δ = 7.26 ppm, ^{13}C NMR: δ = 77.16 ppm, DMSO-d_6: ^{1}H NMR: δ = 2.50 ppm, ^{13}C NMR: δ = 39.52 ppm, CD_3CN: ^{1}H NMR: δ = 1.94 ppm, ^{13}C NMR: δ = 118.26 ppm) was used for calibration referred to tetramethylsilane. Infrared spectra were recorded on a *Shimadzu IRSpirit* FT-IR spectrometer. The absorption bands are given in wave numbers (cm^{-1}). High resolution mass spectra by electron spray ionization (ESI) were recorded on a *Waters Q-Top Premier* spectrometer. The ionization was accomplished with an energy of 3 kV. High resolution mass spectra by electron impact ionization (EI) were recorded on a *Thermo Scientific DFS* spectrometer with an ionization energy of 70 eV. GC/MS spectra were recorded on a *Shimadzu GC 2010 Plus* gas chromatograph coupled with a *Shimadzu QP2020* mass detector, using electron impact ionization (EI) at an energy of 70 eV.

P3

1.2.2 Reaction Sequence

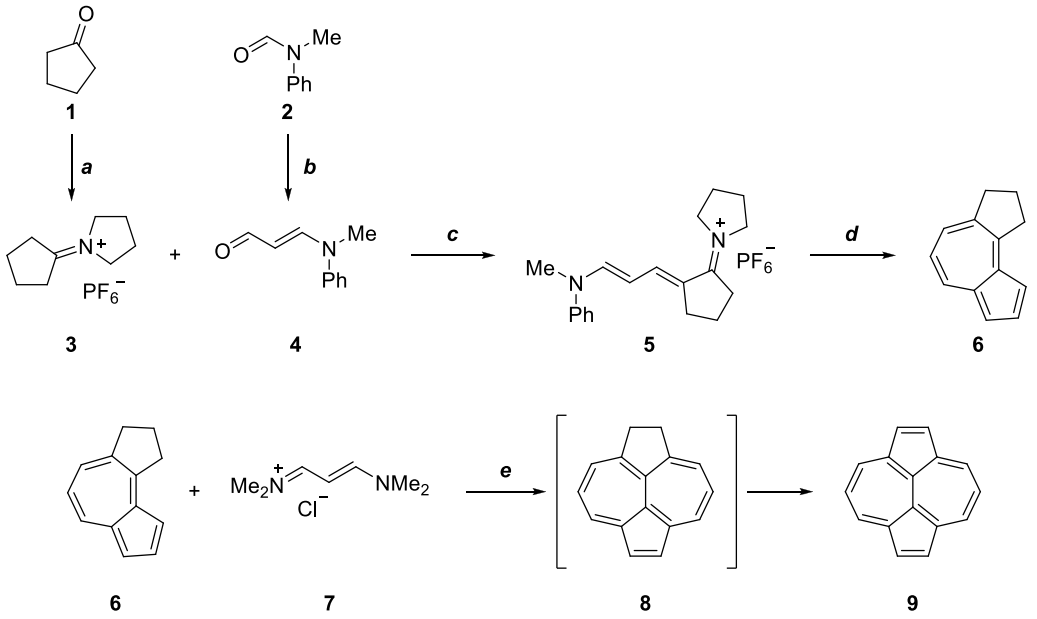

Supplementary Scheme 1: Schematic overview of the azupyrene synthesis reaction sequence - a) cyclopentanone (1.0 equiv.), pyrrolidine (1.2 equiv.), ammonium hexafluorophosphate (1.0 equiv.) in toluene, 135 °C, Dean-Stark trap; b) N-methylformanilid (1.0 equiv.), butyl vinyl ether (1.1 equiv.), oxalyl chloride (1.1 equiv.) in acetonitrile, -10 °C; c) 1-cyclopentylidenepyrrolidinium hexafluorophosphate (1.0 equiv.), (E)-3-(methyl(phenyl)amino)acrylaldehyde (1.0 equiv.), acetic anhydride (1.3 equiv.), pyridine (0.4 equiv.) in CH_2Cl_2, ambient temperature; d) 1-((E)-2-((E)-3-(methyl(phenyl)amino)allylidene)cyclopentylidene)pyrrolidinium hexafluorophosphate (1.0 equiv.), sodium cyclopentadienylide (1.0 equiv.) in pyridine, sealed tube, 40 °C for 12 h, then 120 °C for 24 h; e) azulene (1.0 equiv.), (E)-N-(3-(dimethylamino)allylidene)-N-methylmethanaminium chloride (1.5 equiv.), sodium methanolate (10 equiv.) in propylene carbonate, first ambient temperature for 5 h, then 90 °C / 12 h, 150 °C / 2 h and finally 200 °C over 3 d.

1.2.3 Experimental Section

1-Cyclopentylidenepyrrolidinium hexafluorophosphate

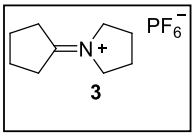

According to a literature-known procedure by Saba,[18] cyclopentanone (2.3 mL, 29.0 mmol, 1.45 equiv.), pyrrolidine (2.2 mL, 35.3 mmol, 1.76 equiv.) and ammonium hexafluorophosphate (3.26 g, 20 mmol, 1.0 equiv.) were suspended in toluene (40 mL). The reaction mixture was heated utilizing a Dean-Stark trap to 135 °C for 2 h. After that the mixture was cooled to 0 °C whereby the product crystallized. The solid was filtered and washed with Et_2O (20 mL) twice. The product **3** (5.36 g, 18.9 mmol, 95%) was obtained as a beige solid and it could be used without further purifications.

^{1}H NMR (500 MHz, DMSO-d_6) δ = 3.83 (ddq, *J* = 7.1, 4.7, 2.3 Hz, 2H), 2.79 (qt, *J* = 4.7, 2.2 Hz, 2H), 2.09 – 2.00 (m, 2H), 1.97 – 1.86 (m, 2H) ppm.

The analytical data are in accordance with the literature.[18]

3-(Methyl(phenyl)amino)acrylaldehyde

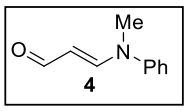

According to a literature-known procedure by Hayashi,[19] oxalyl chloride (4.7 mL, 55.1 mmol, 1.1 equiv.) was dissolved in acetonitrile (10 mL) and the mixture was cooled to -10 °C. Then a mixture consisting of *N*-methylformanilide (6.2 mL, 50.1 mmol, 1.0 equiv.) and butyl vinyl ether (6.9 mL, 53.6 mmol, 1.07 equiv.) in 10 mL acetonitrile was added dropwise to the solution over a period of 30 min. The reaction mixture may not warm up over -5 °C during the addition. After the addition, the reaction mixture was allowed to warm to ambient temperature, and it was stirred for an additional hour. After that, the mixture was cooled to 0 °C and saturated sodium carbonate (30 mL) was slowly added. Toluene was added and the aqueous phase was extracted with toluene three times. The organic phase was washed with brine, dried over $MgSO_4$, filtered and the solvent was removed under reduced pressure. The crude product was crystallized from isopropanol/*n*-pentane at 0 °C. The product **4** (4.93g, 30.5 mmol, 61%) was isolated as a beige solid.

^{1}H NMR (300 MHz, $CDCl_3$) δ = 9.26 (d, *J* = 8.1 Hz, 1H), 7.52 (d, *J* = 13.1 Hz, 1H), 7.39 (dd, *J* = 8.5, 7.3 Hz, 2H),
7.25 – 7.12 (m, 3H), 5.44 (dd, *J* = 13.1, 8.1 Hz, 1H), 3.31 (s, 3H) ppm. ^{13}C NMR (126 MHz, $CDCl_3$) δ = 190.3, 146.2, 129.8 (2C), 125.5, 120.7, 105.8, 31.0 ppm.

The analytical data are in accordance with the literature.{Zacharia, 2010 #514

1-(-2-(3-(Methyl(phenyl)amino)allylidene)cyclopentylidene)pyrrolidinium hexafluorophosphate

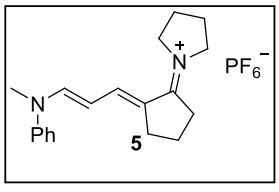

In accordance to a literature-known procedure by Jutz,{Jutz, 1974 #515} 1-cyclopentylidenepyrrolidinium hexafluorophosphate (2.54 g, 8.97 mmol, 1.00 equiv.) was dissolved in 6.0 mL CH_2Cl_2 giving a red solution. Afterwards, 3-(methyl(phenyl)amino)acrylaldehyde (1.47 g, 9.12 mmol, 1.02 equiv.), acetic anhydride (1.1 mL, 11.6 mmol, 1.29 equiv.) and pyridine (0.3 mL, 3.72 mmol, 0.41 equiv.) were added to the solution resulting in a

dark red mixture and stirred overnight. The product was precipitated by the addition of Et_2O. The resulting suspension was filtered, and the obtained crude product was purified by dissolving in CH_2Cl_2 again followed by precipitation with Et_2O. This procedure was repeated twice. The product **5** was obtained after drying *in vacuo* (3.02 g, 7.08 mmol, 79%) as a brown solid.

P3

^{1}H NMR (300 MHz, CD_3CN) δ = 7.79 (d, *J* = 12.3 Hz, 1H), 7.67 (d, *J* = 11.8 Hz, 1H), 7.50 – 7.38 (m, 2H), 7.37 – 7.22 (m, 3H), 5.63 (t, *J* = 12.0 Hz, 1H), 3.84 (t, *J* = 6.6 Hz, 2H), 3.81 – 3.70 (m, 4H), 3.43 (s, 3H), 2.83 (t, *J* = 7.6 Hz, 2H), 2.76 – 2.66 (m, 4H), 2.18 – 2.06 (m, 5H), 2.04 – 1.90 (m, 8H) ppm. ^{13}C NMR (75 MHz, CD_3CN) δ = 175.6, 150.2, 130.6, 126.7, 121.6, 104.1, 56.1, 55.8, 54.8, 38.3, 36.8, 31.9, 26.5, 25.3, 25.3, 24.7, 21.7 ppm. HRMS (ESI$^+$): *m/z* $[M]^+$ calcd for $C_{19}H_{25}N_2^+$: 281.2012, found: 281.2013, HRMS (ESI$^-$): *m/z* $[A]^-$ calcd. for PF_6^-: 144.9647, found 144.9639. IR (ATR) $\tilde{\nu}$ = 2986, 2890, 1709, 1622, 1583, 1579, 1533, 1530, 1493, 1457, 1449, 1436, 1401, 1360, 1340, 1326, 1300, 1276, 1250, 1209, 1193, 1164, 1124, 1102, 1031, 974, 961, 879, 830, 791, 776, 761, 741, 693, 643, 556, 526, 501 cm^{-1}.

Note: The ^{1}H NMR spectra shows impurities due to 1-cyclopentylidenepyrrolidinium hexafluorophosphate, which results in inconsistent integral ratios in the range from 4 to 1.5 ppm.

2,3-Dihydro-1H-cyclopenta[e]azulene

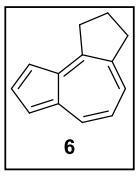
6

In accordance to a literature-known procedure by Jutz,[20] 1-((*E*)-2-((*E*)-3-(methyl(phenyl)amino)allylidene)cyclopentylidene)pyrrolidinium hexafluorophosphate (1.28 g, 3.00 mmol, 1.00 equiv.) was dissolved in 6.0 mL pyridine in a sealed tube. Afterwards, 1.55 mL (3.10 mmol, 1.03 equiv.) of sodium cyclopentadiene solution (2.0 M in tetrahydrofuran) was added dropwise. The resulting mixture was stirred at 40 °C for 12 h and heated up to 120 °C for additional 24 h. The solvent was removed *in vacuo*. The residue was dissolved in CH_2Cl_2 and filtered through a short pad of silica. The filtrate was washed with 60 mL of 1 M hydrochloric acid. The organic layer was dried over $MgSO_4$, filtered and the solvent was removed under reduced pressure. The product **6** was obtained after column chromatography (eluent: *n*-pentane) as a blue oil (65 mg, 0.386 mmol, 13%).

^{1}H NMR (300 MHz, $CDCl_3$) δ = 8.29 (d, *J* = 9.5 Hz, 1H), 7.85 (t, *J* = 3.8 Hz, 1H), 7.65 (d, *J* = 10.0 Hz, 1H), 7.30 (d, *J* = 3.0 Hz, 1H), 7.24 (d, *J* = 3.7 Hz, 1H), 7.10 (t, *J* = 9.8 Hz, 1H), 3.56 (t, *J* = 7.6 Hz, 2H), 3.28 (t, *J* = 7.4 Hz, 2H), 2.22 (pent, *J* = 7.5 Hz, 2H) ppm. GC/MS (EI+): *m/z* = 169 (13), 168 ([M]$^+$, 100), 167 (68), 166 (13), 165 (40), 164 (6), 154 (2), 153 (21), 152 (36), 139 (7), 83 (11), 82 (11), 63 (5).

The analytical data are in accordance with the literature.[21]

N-(3-(Dimethylamino)allylidene)-N-methylmethanaminium chloride

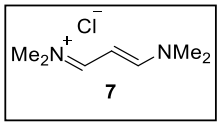

7

According to a modified procedure described by Anderson,[21] dimethylamine hydrochloride (1.63 g, 20.0 mmol, 1.0 equiv.) was suspended in ethanol (14 mL). Then dimethylaminoacroleine (2.0 mL, 20.0 mmol, 1.0 equiv.) was added

and the suspension was stirred at 80 °C for 2 days. After that, the reaction mixture was cooled to ambient temperature and the solvent was removed *in vacuo*. The residue was washed twice with cold Et_2O. The obtained crude product was recrystallized from acetone. The product **7** (2.26 g, 13.9 mmol; 69%) was isolated as a beige solid.

^{1}H NMR (300 MHz, $CDCl_3$) δ = 8.52 (d, *J* = 11.5 Hz, 2H), 5.10 (t, *J* = 11.5 Hz, 1H), 3.27 (s, 6H), 3.01 (s, 6H) ppm.
^{13}C NMR (126 MHz, $CDCl_3$) δ = 164.6 (2C), 90.0, 46.3, 38.3 ppm.

The analytical data is in accordance with the literature.[21] The product is moisture sensitive and decomposes under non-inert gas conditions.

Dicyclopenta[ef,kl]heptalene (Azupyrene)

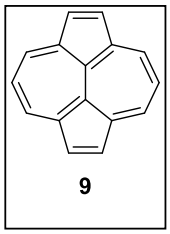

9

Following a modified procedure by Anderson,[21] azulene **6** (168 mg, 1.00 mmol, 1.0 equiv.) was dissolved in propylene carbonate (15 mL) and imine **7** (244 mg, 1.50 mmol, 1.5 equiv.) were added to the solution. Then sodium methanolate (540 mg, 10.0 mmol, 10 equiv.), dissolved in 5 mL methanol (2.5 M) were added. The mixture was stirred at room temperature for 5 h. After that, the reaction mixture was slowly heated to 90 °C for 12 h. Then the reaction mixture was heated to 150 °C for 2 h and at least it was heated to 200 °C and stirred for 3 d. The solvent was removed *in vacuo* and residue was dissolved in CH_2Cl_2 and filtered over Al_2O_3. The filtrate was washed with 1 M hydrochloric acid and distilled H_2O. The organic layer was dried over $MgSO_4$, filtered and the solvent was removed under reduced pressure. The product **9** was obtained after column chromatography (eluent: *n*-pentane/toluene 4:1) as a light brown solid (45.0 mg, 0.22 mmol, 22%).

^{1}H NMR (500 MHz, $CDCl_3$) δ = 8.71 (d, *J* = 9.6 Hz, 4H), 8.43 (s, 4H), 7.37 (t, *J* = 9.6 Hz, 2H) ppm. ^{13}C NMR (126 MHz, $CDCl_3$) δ = 141.0 (2C), 133.9 (4C), 133.8 (4C), 128.9 (4C), 116.8 (2C) ppm. HRMS(EI+): *m/z* $[M]^+$ calcd for $C_{16}H_{10}$: 202.0777, found: 202.07776.

P3

1.2.4 NMR Spectra

1-Cyclopentylidenepyrrolidinium hexafluorophosphate

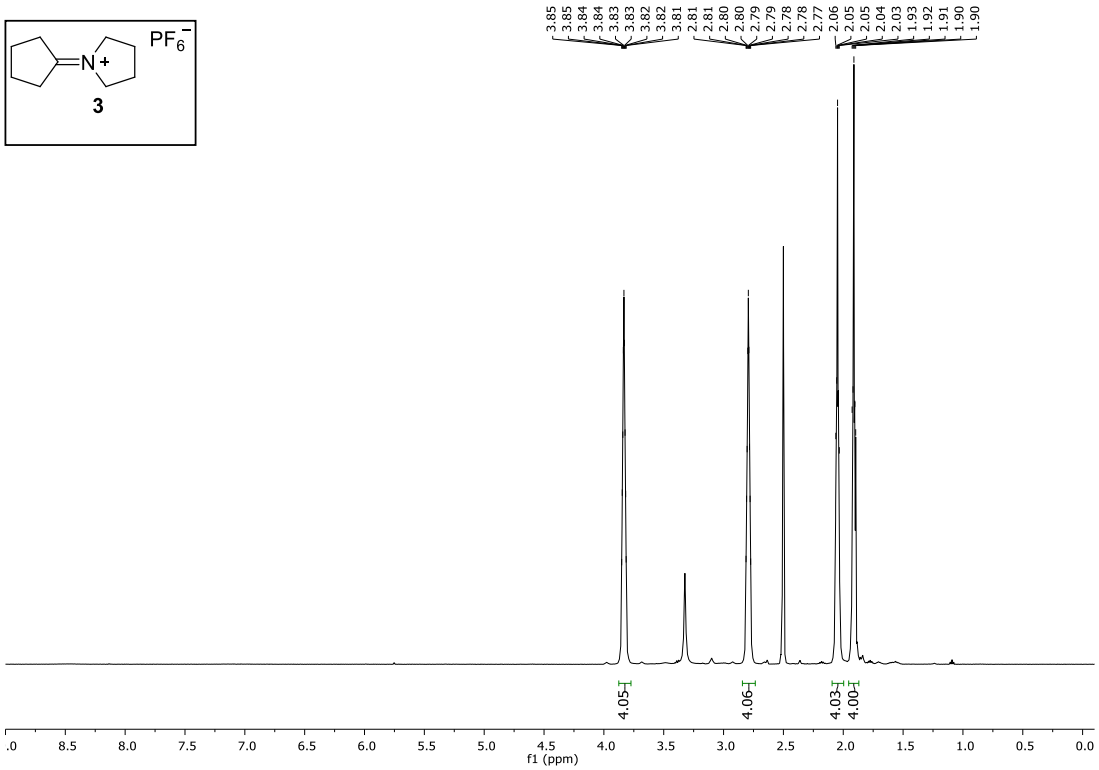

3-(Methyl(phenyl)amino)acrylaldehyde

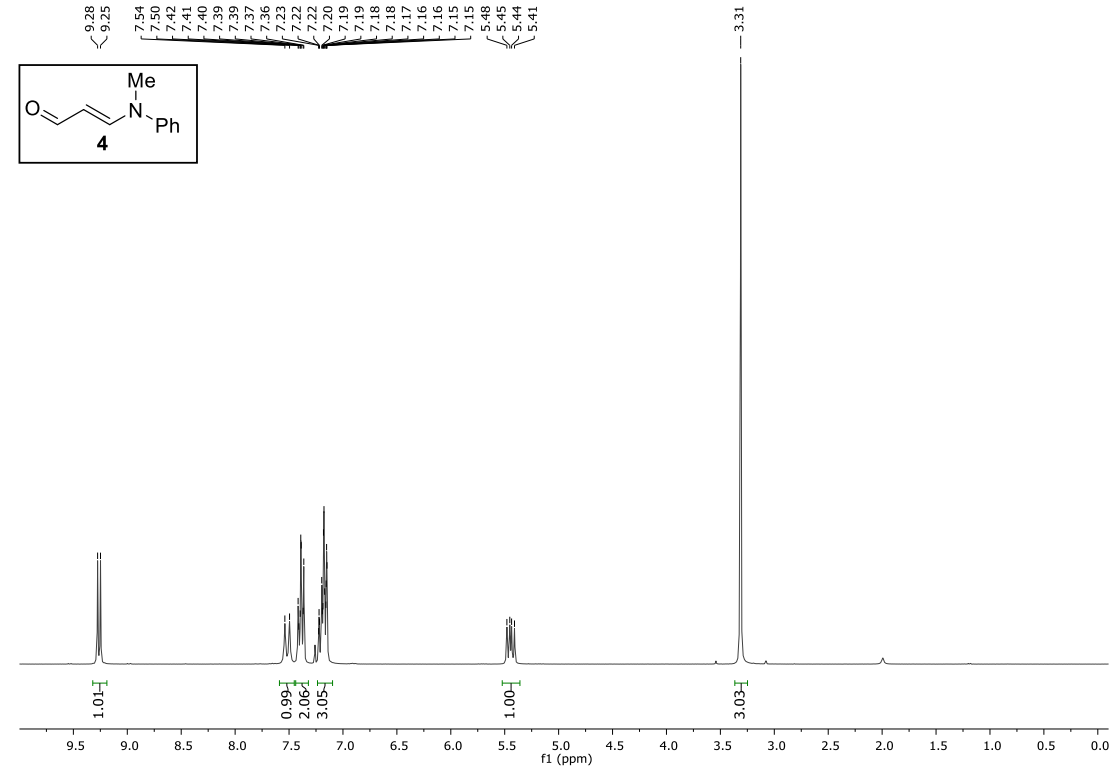

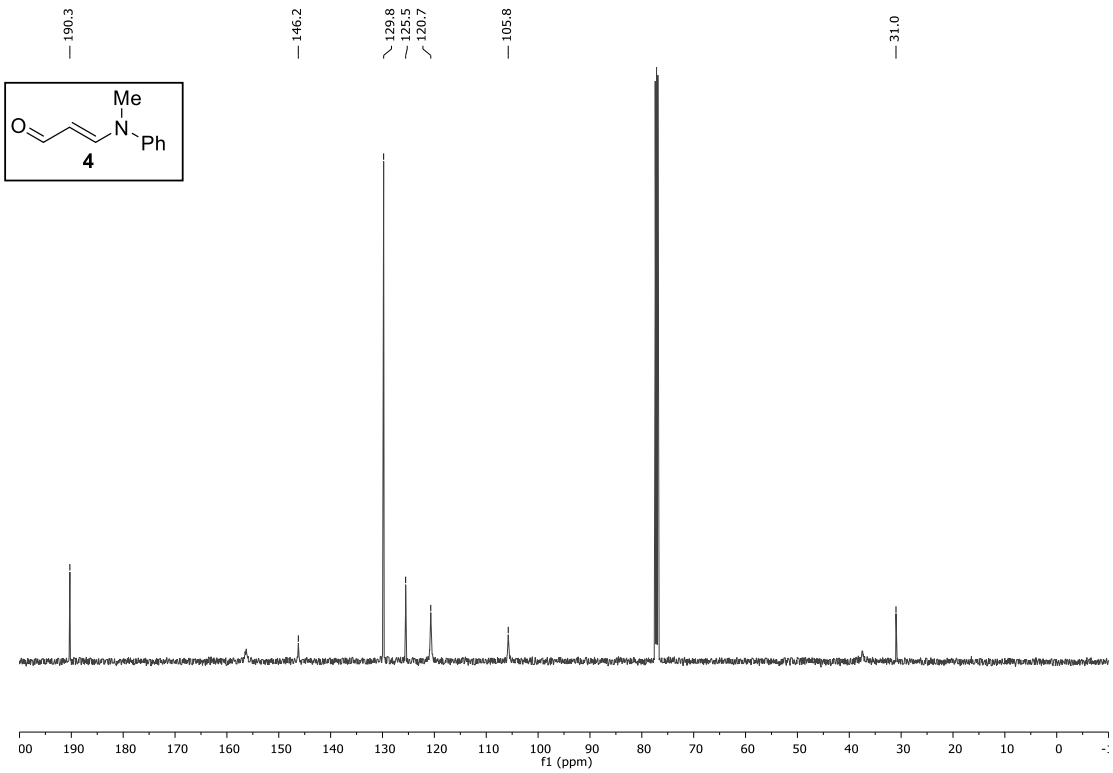

P3

1-(2-(3-(Methyl(phenyl)amino)allylidene)cyclopentylidene)pyrrolidinium hexafluorophosphate

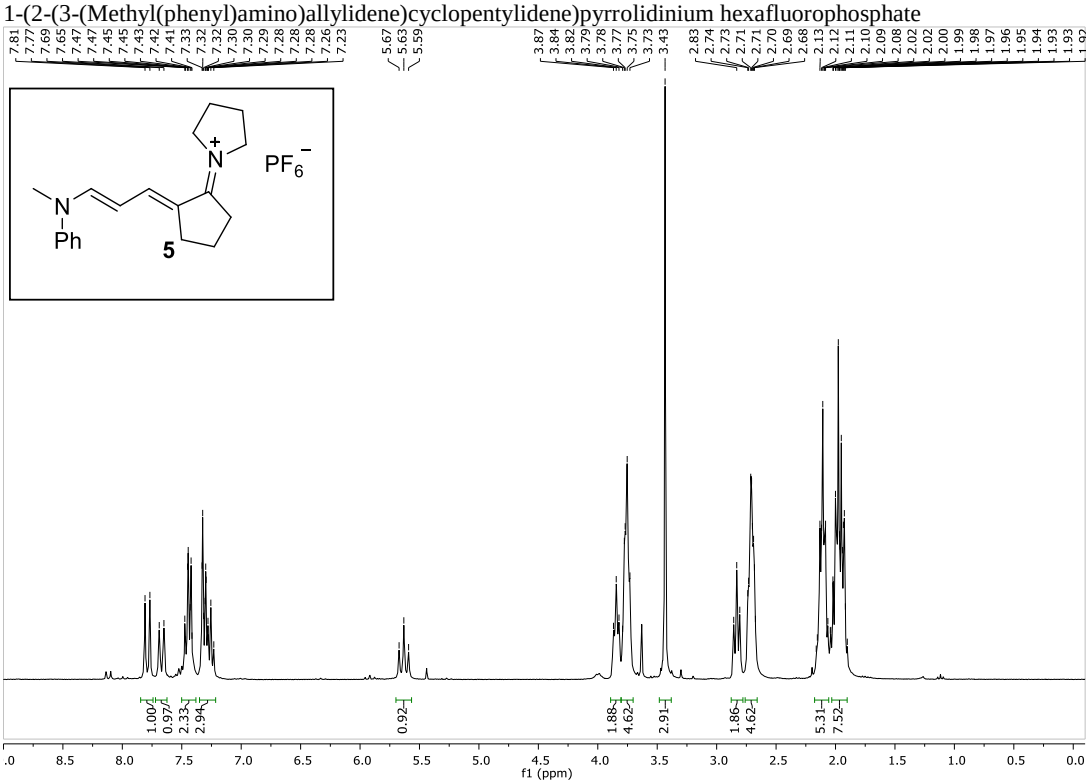

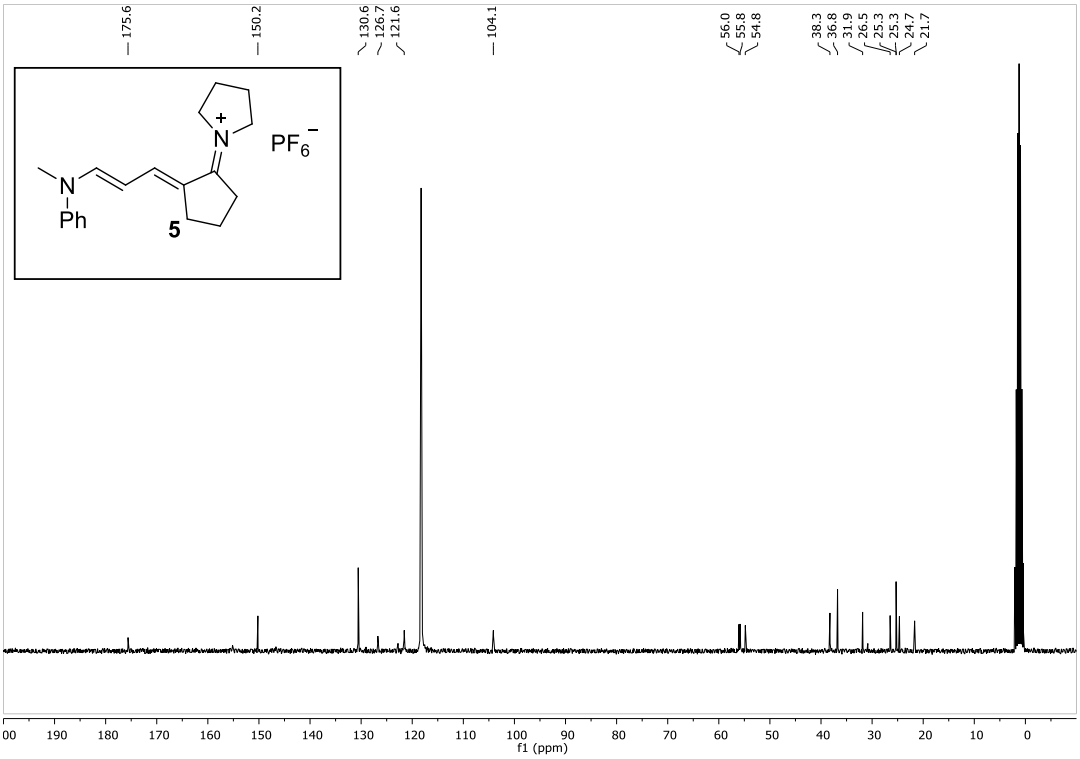

2,3-Dihydro-1H-cyclopenta[*e*]azulene

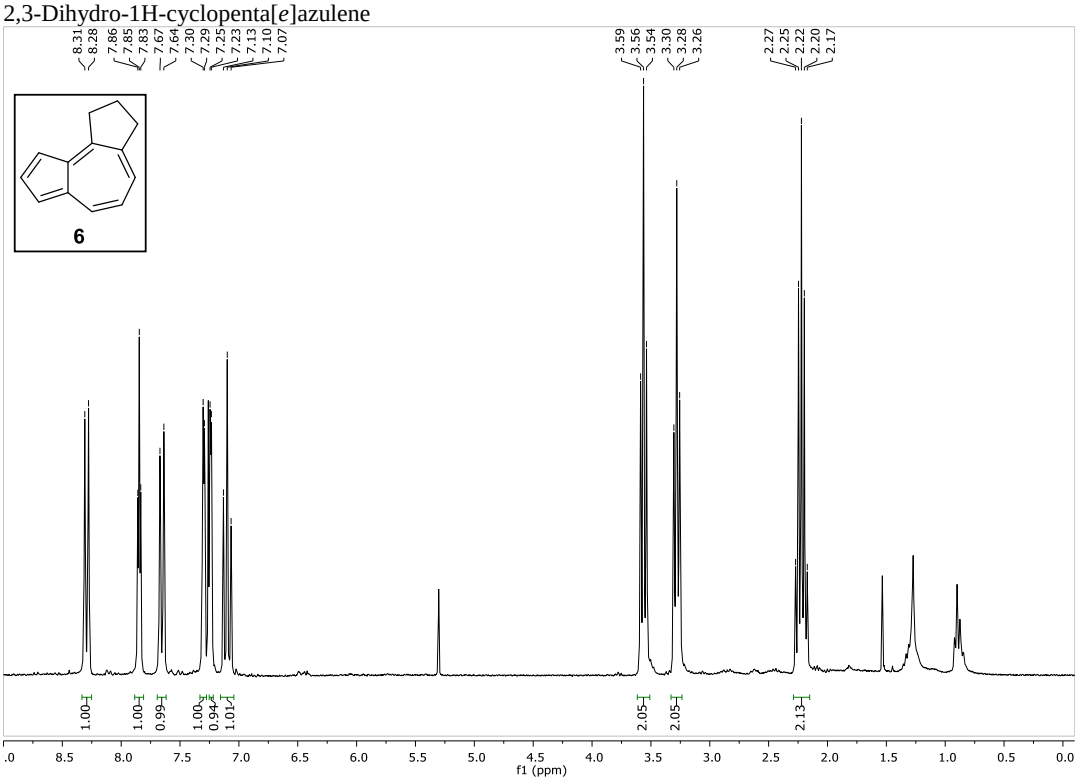

P3

N-(3-(Dimethylamino)allylidene)-*N*-methylmethanaminium chloride

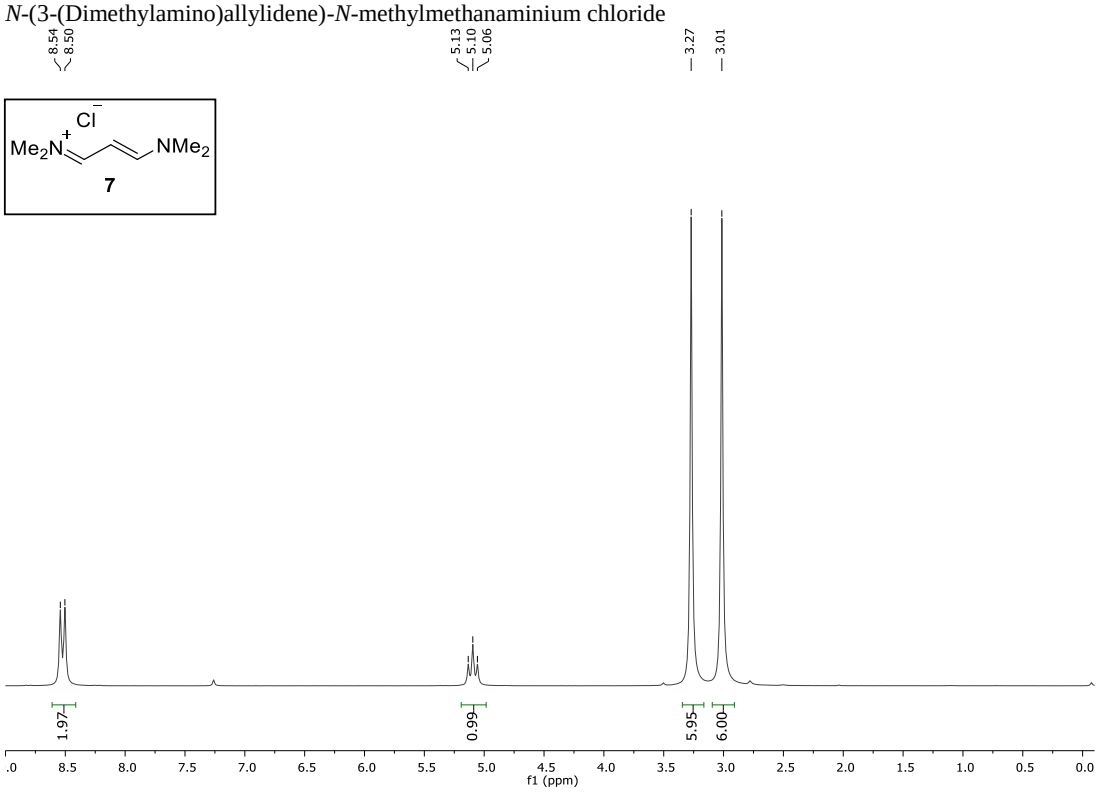

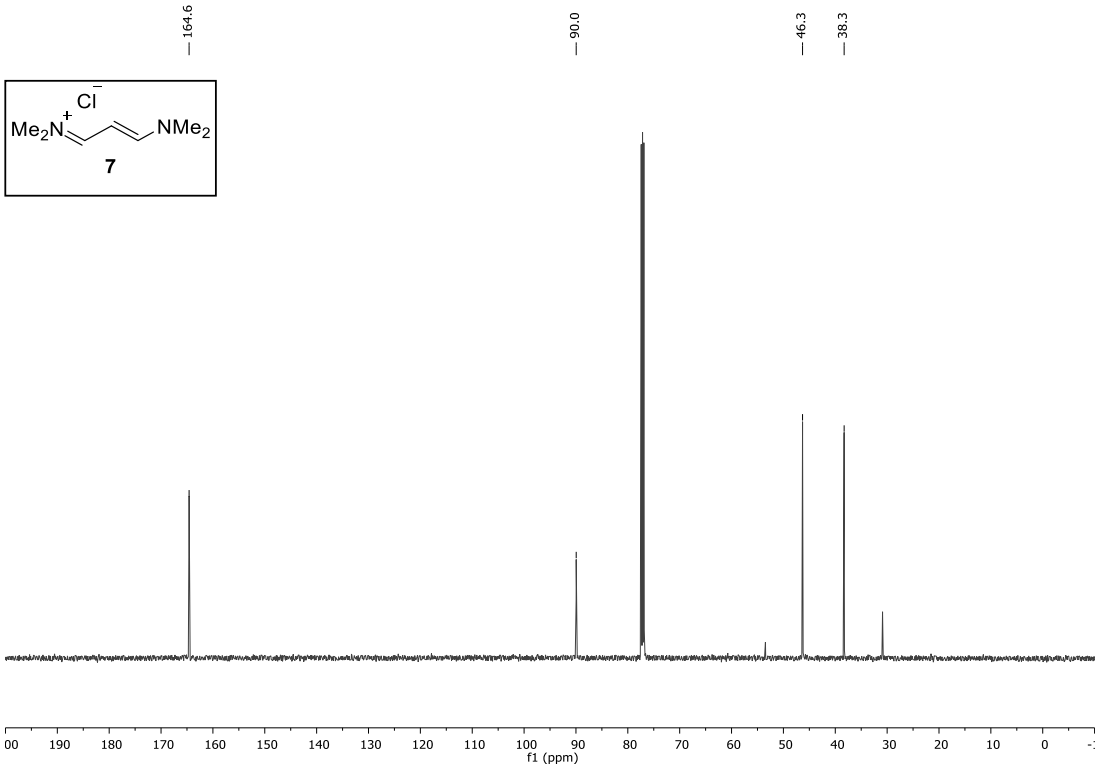

Dicyclopenta[*ef*,*kl*]heptalene (Azupyrene)

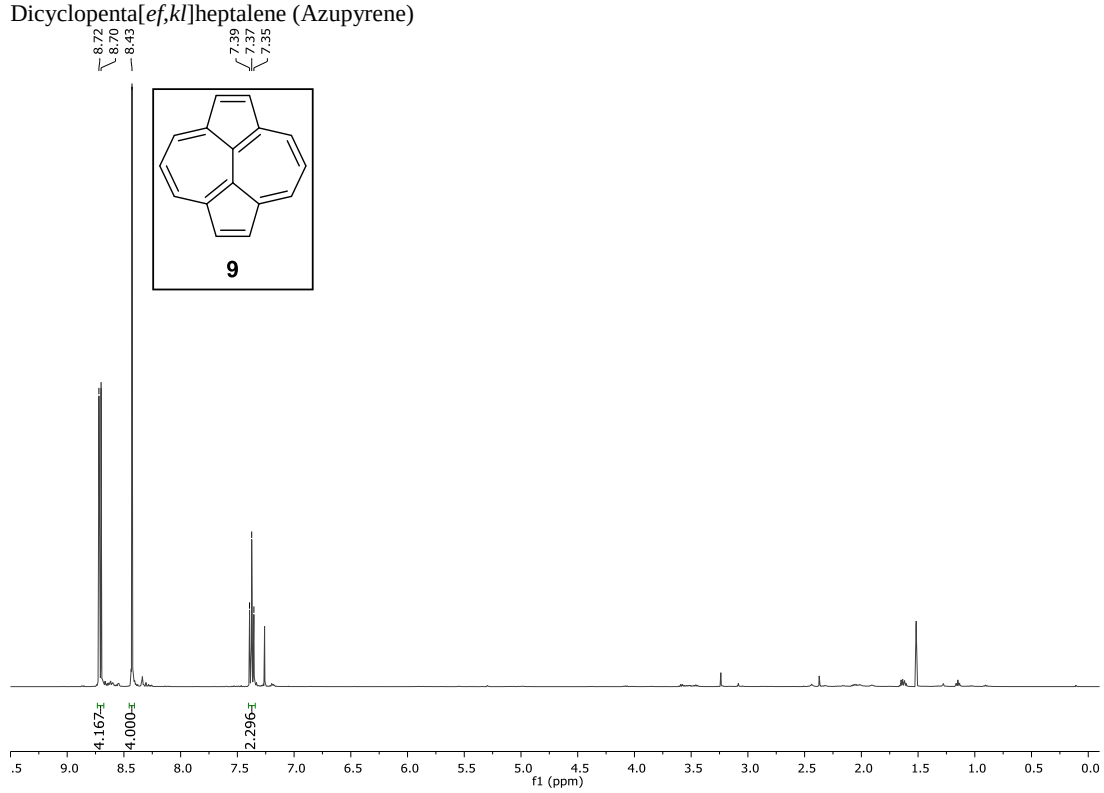

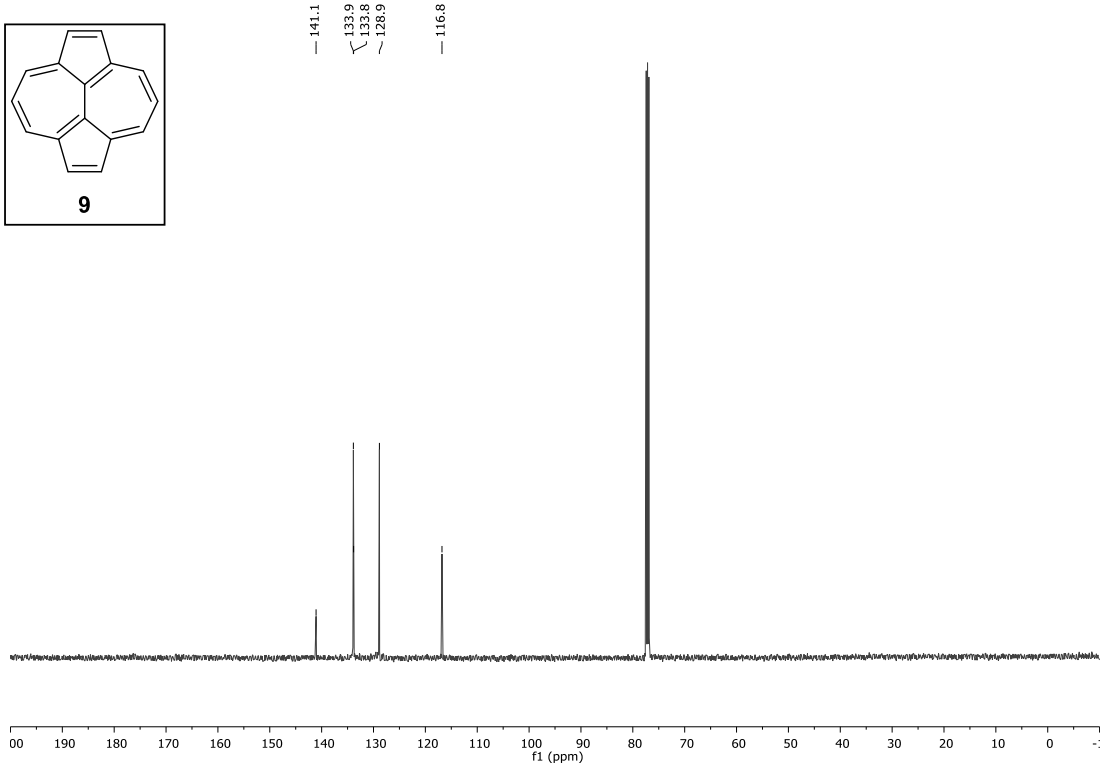

P3

2. Supplementary Discussion

2.1 Supplementary TPD Discussion

The strength of an adsorbate substrate interaction can be experimentally measured by temperature programmed desorption (TPD)[22-24], if the adsorbate desorbs intact from a surface. To determine the adsorption energy, TPD coverage series were taken for azupyrene (Fig. S1a,b) and pyrene (Fig. S1c,d). Pyrene shows the typical behavior observed for similar systems: For low submonolayer coverages there is a peak following first order desorption kinetics centered at about 500 K. With increasing initial coverage the TPD traces extend to lower temperatures, the monolayer spectrum (bold in Fig. S1c) is spread out from 520 a 290 K. At still higher coverages the peak for the second layer is visible at 270 K and finally the multilayer peak appears at 260 K.

For azupyrene the situation is quite different as small coverages do not desorb intact from the surface. Only if a coverage of more than about half a ML is deposited on the surface, a TPD peak appears and molecules start to desorb from the surface. TPD cannot give us information about the species remaining on the surface, so other methods are necessary to analyze this further. Below we will use XPS data to show that 0.53 ML of the azupyrene monolayer remains on the surface as it is too strongly bonded to the surface to desorb.

At the lowest coverage - where desorption is still possible - the azupyrene TPD peak is centered at 630 K with its tail reaching 650 K. The high temperature tail of this lowest coverage peak is decreasing faster than for the first order desorption peak, indicating a different kinetic behavior. If the initial coverage is increased the desorption peak extends to lower temperature. For the deposition of a full monolayer (bold in Fig. 2a), the peak stretches over a wide range from 330 K to 650 K with a small peak attributed to a compressed phase visible at 410 K. With even higher initial coverage the bilayer peak at 340 K and the multilayer peak at 280 K appear.

The massive broadening of the desorption peaks for both molecules are caused by the intermolecular lateral repulsion, which originates from dipol-dipol repulsion between the vertical adsorption dipoles. These adsorption dipoles are caused by the so-called Pauli-Pushback effect,[25-27] which describes the rearrangement of electron density in the surface region due to Pauli repulsion with the electrons of the molecule. The azupyrene spectrum is much wider than that of pyrene, even as it only includes the desorption of half of the monolayer. Apparently the azupyrene molecules show a stronger repulsion than the pyrene molecules, caused by a larger adsorption dipole. For azupyrene the repulsion is especially important: An isolated azupyrene molecule binds too strong to the surface to desorb, only the lateral repulsion at coverages of more than 0.53 ML decrease the desorption energy sufficiently to allow the intact desorption of the molecule.

The heating rate variation (HRV) analysis (Fig. S2) yields a desorption energy of 153.5 kJ/mol and a prefactor of $2.0 \cdot 10^{15}$ s^{-1}, which is in good agreement with the results of the LNR analysis and the IPW equation (Fig. 2b).

Supplementary XPS Discussion

If the monolayers of both molecules are annealed to temperatures higher than 300 K the resulting XPS spectra provide complementary information to the TPD results (Fig. 3e). The C 1s intensity of pyrene drops quickly between 300 and 500 K and only a very small residual intensity remains on the surface. TPD shows in this case a broad monolayer desorption peak between 300 and 500 K. The residual C 1s intensity is most likely caused by beam damage as the remaining fraction gets higher, if the sample is exposed to the X-ray radiation over a longer time. For azupyrene the C 1s intensity decreases more slowly from a temperature of 300 K to 600 K, after which the intensity stays constant at a coverage of 0.53 monolayers. This finding is also in agreement with the TPD results, which show desorption only up to 600 K and with an irregular high temperature tail of the desorption peak (Fig. S1a).

2.2 Supplementary UPS Discussion

According to a model potential used in the literature, the surface state shift for pyrene of 0.1 eV (visible in the UP spectra in Figure 2) corresponds to an adsorption height of about 3.1 Å. [28] For azupyrene, the surface state is not visible, its shift is therefore greater than 0.4 eV, for which the model potential would imply an adsorption height of less than 2.9 Å. But as this model potential is not applicable for strongly bonded systems, the value of its prediction is limited.

The WF changes measured by UPS are in agreement with the values calculated by DFT, where azupyrene also possesses a larger value (-1.07 eV) than pyrene (-0.95 eV). For both molecules the work function change is caused by the Pauli-pushback effect,[25,26,29,30] which is known to dominate the work function change for similar molecules both if they are physisorbed or chemisorbed.[31,32] The Pauli-pushback effect is strongly dependent on the adsorption height, thus azupyrene showing a larger WF change is in line with the smaller adsorption height determined by nc-AFM and calculated by DFT.

2.3 Supplementary Discussion nc-AFM

To reveal adsorption positions of the molecules with regard to the Cu(111) lattice the adjacent Cu surface has been scanned with atomic resolution (Figure S3a,b). [33] Figure S3c and S3d show corresponding AFM images with fitted molecular structures (red and black structures) and substrate lattices (blue dots indicate Cu(111) top sites). While pyrene is adsorbed with its long axis parallel to a <1-21> symmetrical crystallographic direction (see white arrows in Fig. S4c,d) azupyrene is rotated by about 19° with respect to this direction. The pyrene molecule can be fitted by two molecular structures that either match with the left part of the molecule (red structure in Fig. S4c,e) or with the rightmost ring (black structure in Fig. 3c,e). The red and black structures are shifted by approximately 140 pm along the [1-21] direction and correspond to adsorption of the carbon rings above hcp and fcc hollow sites, respectively (see Fig. S4). Our DFT calculations reveal that these are the

two most favorable adsorption positions of pyrene on Cu(111), which differ by about 10 meV (~1 kJ/mol) in adsorption energy. From this analysis, we can rationalize that the pyrene molecule is manipulated by the CO tip during scanning, which indicates a relatively weak molecule-substrate interaction. We have recently uncovered similar non-stationary adsorption structures for 4,4″-diamino-p-terphenyl and 4-bromo-3″-iodo-p-terphenyl on Cu(111) [34 35].

P3

2.4 Supplementary HOMA Discussion

The change in the electronic structure of azupyrene due to the adsorption can also be discussed within the concept of aromaticity. One of the most widely used models to quantify aromaticity is the harmonic oscillator model of aromaticity (HOMA)[36]. This model is based on the molecular geometry and the deviation of each bond from the ideal aromatic bond. The model parameters R_{opt} (the ideal aromatic bond length) and α are chosen such that the benzene molecule (with six equally long bonds) has a HOMA value of 1, whereas the hypothetical Kekulé-like benzene (with three single and three double bonds) has a HOMA value of 0. For the HOMA values discussed below we used the bond lengths obtained from the DFT-optimized structures of our molecules both free and adsorbed on the surface. The model parameters (R_{opt} = 1.398 Å and α = 362.1 Å^{-2}) used to calculate the HOMA values were determined employing the the free benzene molecule optimized with the same method as reference.

For each molecule with more than one aromatic ring, it is possible to calculate different HOMA values, depending on which π-bonds and are taken into account. One possibility is to use all π-bonds in the molecule, this will be denoted as overall HOMA value O. If only the perimeter π-bonds of the molecule are used, this is called the perimeter HOMA value P. In addition, the HOMA value R for each ring can be calculated separately. Fig. S8a shows all these HOMA values for azupyrene, pyrene and the reference molecule benzene in their gas phase structure as well as adsorbed on Cu(111). Furthermore we introduced the Excess Perimeter Conjugation (EPC). This parameter is calculated as EPC = P-O and provides a convenient way to determine if the molecule shows annulenoid character, i.e. the aromatic conjugation is predominantly on the perimeter of the molecule, or if the conjugation is distributed over the whole molecule equally (benzenoid character). A higher the EPC value therefore shows a more annulene-like conjugation in the molecule. It should be noted that both molecules have the formula of $C_{16}H_{10}$, form a 16 π-electron system and should according to Hückel's 4*n* rule therefore be anti-aromatic. However, this is not the case and both molecules are aromatic, which was proven by NMR.[37] In the following we will discuss how the two molecules find a different way to avoid Hückel's rule and form stable aromatic systems.

The free pyrene molecule shows a small EPC value of 0.04 which shows that no annulenoid conjugation is present. It can be noted however, that the conjugation is not located equally over the whole molecule. The two apical rings possess higher HOMA values than the two

other rings and these rings with the smaller HOMA value have one especially short bond. Both facts indicate that the most fitting description of the pyrene molecule is a biphenyl doubly bridged by ethenediyl units (Fig. S8b). The two apical rings form Clar sextets (2 x 6 π-electrons) and the ethylene bridges form isolated double bonds (2 x 2 π-electrons), thus no 16 π-electron system is formed. Because of the weak interaction with the surface this situation stays the same when pyrene is adsorbed on Cu(111).

The free azupyrene molecule shows a large EPC value of 0.37 and also a short central bond with elongated bonds connecting the central two carbon atoms to the perimeter. Here, both facts are in agreement with the description as a [14]annulene with a inserted C_2 bridge (Fig S7b). This way the 16 π-electrons are divided in the 14 π-electrons on the perimeter and 2 π-electrons in the isolated central double bond, forming two Hückel compliant systems. The strong bond formed between azupyrene and the Cu(111) surface influences the conjugation pattern of the molecule as can be seen in the HOMA values and bond length pattern. The EPC values decreases from 0.37 to 0.17, the bond in the central ethenetetrayl (C_2) unit is elongated and the four connecting bonds are shortened, giving rise to higher HOMA values for each ring. In a way, the interaction with the surface introduces a new way to bypass Hückel's rule and the 16 π-electron overall conjugation is now at least partially realized.

2.5 Supplementary pEDA Discussion

Even as it is weaker bound than azupyrene, pyrene still shows (in theory and experiment) a quite large adsorption energy. But the magnitude of the adsorption energy is no clear proof of a covalent chemisorptive bond to the surface. Obviously, big molecules often have large desorption energies, as the individually small dispersive interactions between all parts of the molecule and the surface add up, even leading to non-reversible adsorption (e.g. tetrapyrroles on metal surfaces[38]). However, in the following we will show that the bond between pyrene and the surface is still physisorptive, whereas azupyrene in fact forms a chemisorptive bond to the surface.

The application of the periodic energy decomposition analysis (pEDA) yields insight in the adsorbate-substrate bond by dividing the adsorption energy in various physically meaningful contributions. For this analysis the system is divided into two fragments, one containing the molecule and the other the surface. The constituent terms of the adsorption energy are then generated from the wave functions of the relaxed fragments, the fragments in the adsorbate state and the relaxed adsorbate structure.[15]

The pEDA analysis was performed on the PBE-D3 level of theory, using the (4×4) structure for both molecules on the Cu(111) surface. The calculations were tested for convergence regarding the k-space and for consistency against the results from the plane wave calculations above (with adjusted parameters for better comparability) in terms of the total bond energies ΔE_{bond}. The values for the bond energy (Table 1) from both approaches agree within a quite large error of around 29 and 27 kJ/mol (11 and 12 %), also the k-space

convergence is rather slow for these systems (see SI). Nevertheless, the bonding interpretation based on the pEDA results is not affected since the differences between the systems are very large and show a qualitatively different bonding situation.

The pEDA energy terms compiled in Table S1 show striking differences in the surface chemical bond of azupyrene and pyrene.

P3

The dispersion part of the interaction energy, ΔE_{int} (disp) = -275 (AzPyr) and -232 kJ/mol (Pyr), is the major stabilizing contribution for both molecules to the total interaction energy, ΔE_{int} = -302 (AzPyr) and -223 kJ/mol (Pyr). The electronic part of the interaction energy is much smaller than the dispersive part for azupyrene and even repulsive for pyrene, ΔE_{int} (elec) = -27 (AzPyr) and +9 kJ/mol (Pyr). The small magnitude of the electronic interaction energy is the result of the compensation of its constituent terms. In these terms the vastly different bonding situation of each molecule is apparent, with large differences in the electrostatic interaction, ΔE_{elstat} = -1270 (AzPyr) and -312 kJ/mol (Pyr), the orbital interaction, ΔE_{orb}= -998 (AzPyr) vs. -234 kJ/mol (Pyr), as well as in the Pauli repulsion, ΔE_{Pauli} = +2241 (AzPyr) vs. +555 kJ/mol (Pyr). For azupyrene all of these terms are by a factor of four larger than for pyrene, strongly indicating a strong chemical interaction. The slightly larger contribution of the orbital attraction term to the total electronic attraction, 44 (AzPyr) vs. 43 % (Pyr), also is an indication of more covalent bond for azupyrene.

Only because the dispersion term is responsible for a large portion of the total interaction energy, the resulting bond is not necessarily dispersive in nature. A better way to describe the situation is in saying that the molecule gains energy during the adsorption both by attractive dispersive and electronic interactions. At some distance to the surface the Pauli repulsion can overcompensate both attractive forces and establish an equilibrium. The electronic interaction energy then includes both attraction and repulsion whereas the dispersive interaction energy only includes the (necessarily) attractive contribution of the semi-empirical van-der-Waals correction.

In addition to the magnitude of the sub-terms of the electronic interaction energy, the presence of a strong chemical bond in the case of azupyrene is also visible in the large positive preparation energies ΔE_{Prep} of molecule and surface, which are caused by the considerable distortion of both molecule and surface in the adsorbate structure.

The preparation energies for pyrene are smaller and in case of the molecule even negative, which should be impossible regarding the definition of the preparation energy.[15] This unexpected behavior is observed if the preparation energies are calculated by comparing the deformed molecule layer with the free molecule in the ground state. In this case the mutual attraction of molecules in neighboring cells leads to an decrease in energy of the deformed fragment and a negative preparation energy (ΔE_{prep}(mol,in cell)). By using the isolated deformed molecule as a reference point instead of the deformed molecule layer, this attraction can be avoided, yielding the correct positive preparation energy (ΔE_{prep}(mol,free)).

2.6 Discussion of the NOCV extension of the pEDA analysis

The pEDA method enables us to look even deeper into the chemical bond when the NOCV (natural orbitals for chemical valence) scheme is employed to further decompose the orbital interaction term ΔE_{orb}.[16,39] In this scheme the electron density difference $\Delta\rho$ between the intermediate and final state in the pEDA analysis can be expressed by a set of NOCVs that diagonalize the resulting density matrix. These NOCVs come in pairs with matching eigenvalues of $\pm\nu_i$. They can be discussed very instructively in the form of deformation densities $\Delta\rho_i$. Each deformation density shows the electron flow caused by the formation of the interaction between the corresponding pair of NOCVs and can be connected to the energy gained and the eigenvalue ν_i (which is an indicator of the amount of charge being transferred).

As one fragment is a metal surface the situation is more complex than for molecular systems, with a large number of NOCV terms contributing to the orbital interaction. However, the principal interactions determining the bonding situation can be identified by few dominant contributions. The parameters of the six most important deformation densities are compiled for both molecules in Table S4. Also the magnitude of the eigenvalues (indicative of charge transfer) and the corresponding energies are much smaller. This weaker interaction is obvious when the deformation densities are directly compared to those of azupyrene, as done in Fig. S7. The deformation densities of pyrene can only be visualized using a much smaller isosurface value. This is in agreement with a purely physisorptive bond where all deformation densities should only show slight charge rearrangement in the fragments.

Azupyrene possesses substantially larger eigenvalues and energies for the all deformation densities than pyrene, already showing the qualitative difference in interaction. The shape of the first two deformation densities of azupyrene (Fig. S7) clearly shows the outlines of the molecular LUMO and LUMO+1 orbitals as space of electron accumulation. For pyrene, no deformation density with clear assignment to molecular orbital shapes could be found.

P3

3. Supplementary Figures

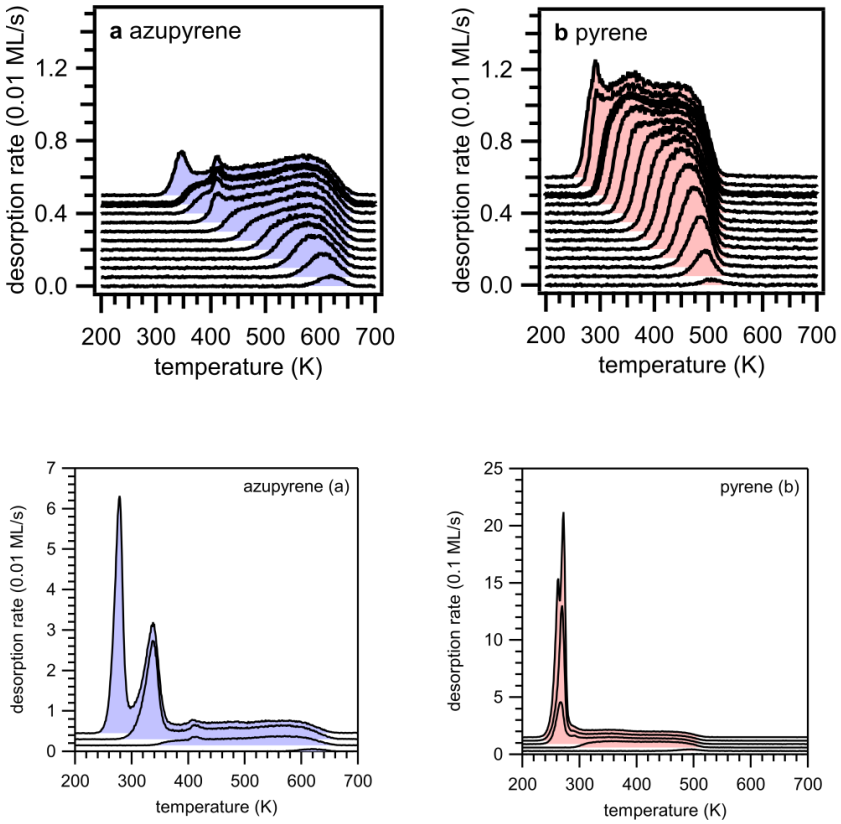

Supplementary Figure 1 | a,**b** TPD coverage series for pyrene (red) and azupyrene (blue), heating rate: 1 K/s, traces with a different initial coverage are shifted along the vertical axis. **c**,**d** extended coverage series showing the desorption of the bilayer and the beginning multilayer desorption.

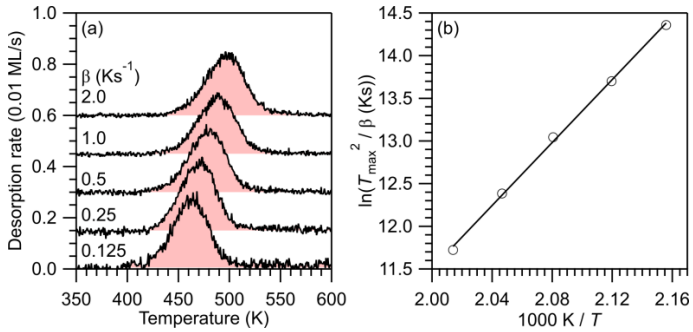

Supplementary Figure 2 | a,**b** HRV analysis for 0.1 ML pyrene on Cu(111). The fit yields a desorption energy of 153.5 kJ/mol and a prefactor of $2.0 \cdot 10^{15}$ s^{-1}.

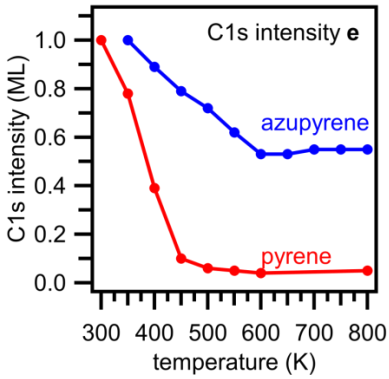

Supplementary Figure 3 | C 1s intensities of azupyrene (blue) and pyrene (red) in dependence of the temperature.

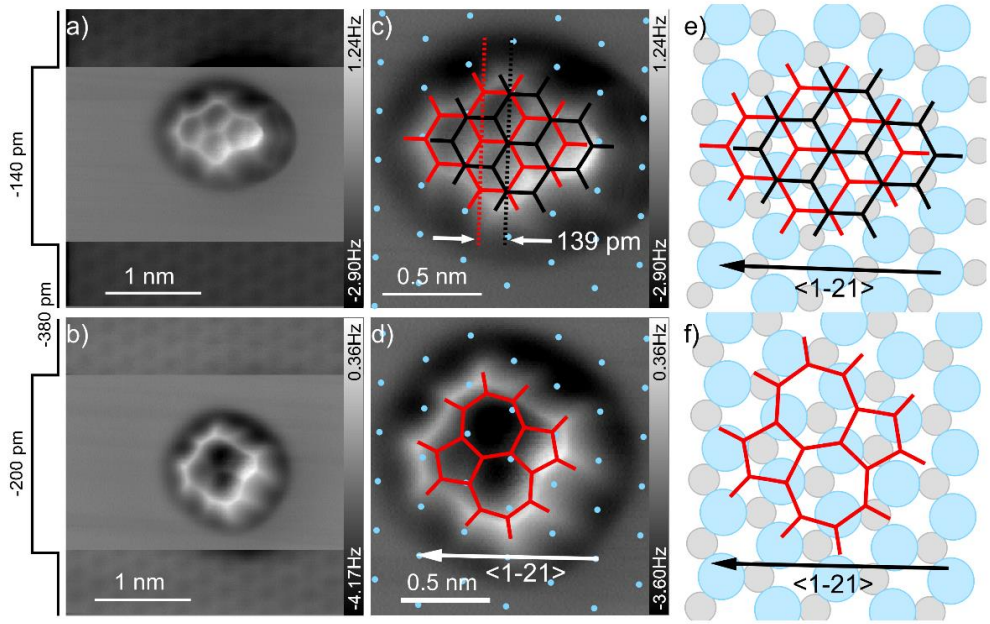

Supplementary Figure 4 | Determination of the adsorption positions of pyrene and azupyrene on Cu(111) a,b Constant-height frequency shift images at z = -140 pm (pyrene), z = -200 pm (azupyrene) and z = -380 pm (Cu surface) with respect to a tunneling set point of U = 100 mV and I = 5 pA. **c,d** Zoom-ins of a,b showing fitted positions of Cu(111) top sites (light blue) and fitted molecular structures (red and black). For pyrene two structures have been fitted, one to the left part of the molecule (red structure) and one to the rightmost ring that appears elongated in horizontal direction (black structure). **e,f** Sketches that indicate the measured adsorption positions with regard to the Cu(111) subsurface layer. The red and black molecular structures and the light blue circles (top sites) are identical to c,d. The gray circles indicate the on-top positions of the Cu(111) subsurface atoms. These

positions have been determined by an atomic resolution scan across a monoatomic step edge of the Cu(111) single crystal. The black arrows denote the crystallographic <1-21> directions.

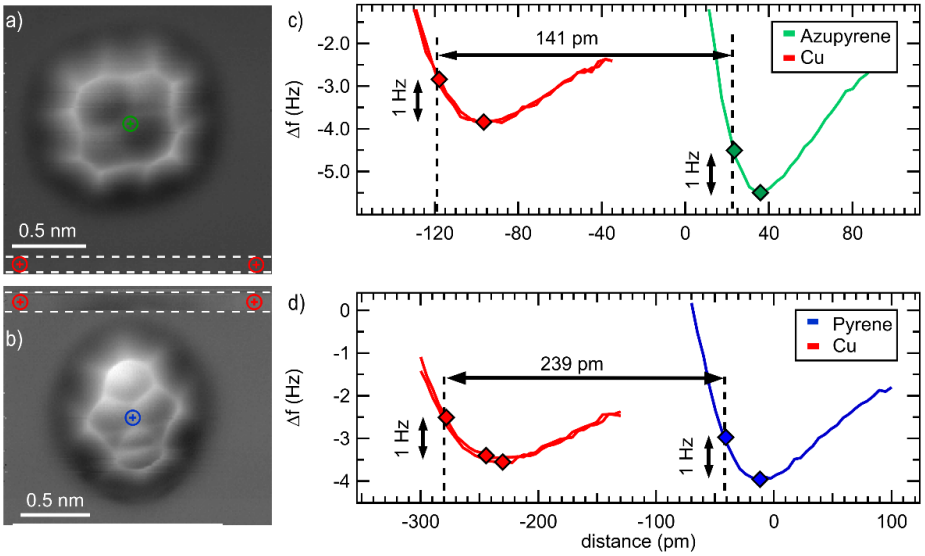

Supplementary Figure 5 | Determining the adsorption conformations and apparent adsorption heights of pyrene and azupyrene using 3D frequency shift mapping. a,b Slices of constant *z* taken from a 3D grid spectroscopy measurement of azupyrene and pyrene. Therefore, the frequency shift $\Delta f(z)$ has been measured in a box of 1.6 x 1.6 x 0.195 nm^3 at 160 x 160 x 30 positions (azupyrene) and 1.9 x 1.9 x 0.17 nm^3 at 180 x 180 x 35 positions (pyrene). The dashed white lines in a,b indicate regions where the starting point of the $\Delta f(z)$ curves was lowered to measure the interaction with the Cu surface. **c,d** Exemplary $\Delta f(z)$ spectroscopy curves that were measured over the centers of azupyrene (green line), pyrene (blue line), and the Cu(111) substrate (red lines). The positions of the curves are indicated in a,b by red, green, and blue markers. The "z = 0 pm" position in the two graphs corresponds to a tunneling setpoint of 100 mV and 100 pA for azupyrene (c) and 100 mV and 20 pA for pyrene (d). For determining the apparent adsorption distance of the molecules, first, for each curve the minimum of the $\Delta f(z)$ curve is determined (indicated by colored markers). The apparent adsorption distances are measured in the steep parts of the curves where the frequency shift has increased to a value of 1 Hz above the respective minima. As shown in the two graphs in c,d this results in an apparent adsorption distance of approx. 140 pm and 240 pm for the central parts of azupyrene and pyrene, respectively. This procedure was repeated at each pixel of the two images in a,b revealing the topography images that are presented in the manuscript in Figure 2e,f.

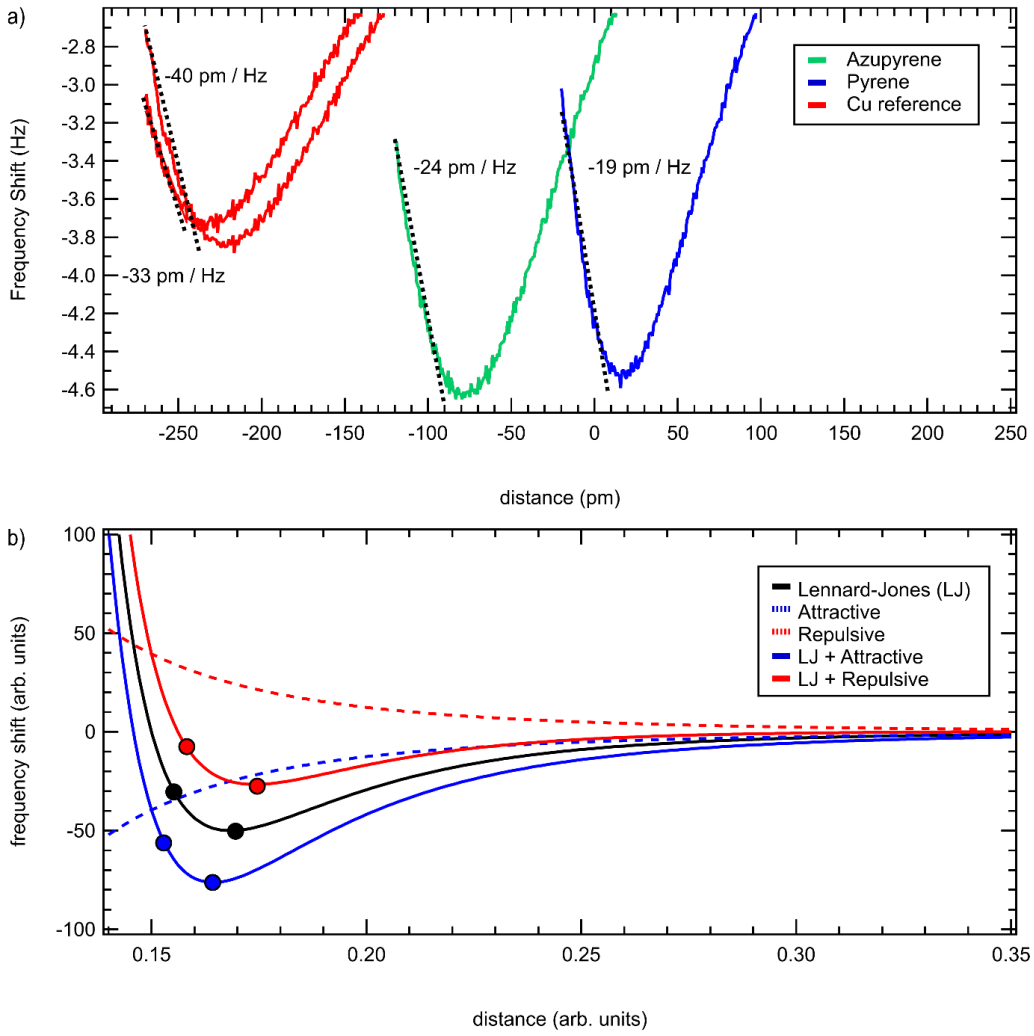

Supplementary Figure 6 | Apparent adsorption heights. a $\Delta f(z)$ curves measured over azupyrene (green), pyrene (blue), and Cu(111) (red). For each type of curve a different effective slope is observed in the part where the frequency increases (see dashed black lines). These different slopes lead to differences in the apparent adsorption distances. **b** Sketch that illustrates the effect of different tip-sample interaction contributions to the interaction potential. The black solid line represents a Lennard Jones potential between two atoms that is calculated by adding a relatively long range attractive potential ($\sim 1/z^6$) and a short range repulsive contribution ($\sim 1/z^{12}$). The red and blue dashed lines represent additional long range repulsive and attractive interaction contributions that could, for example, arise from different electrostatic interactions between the CO tip and the two molecules. These additional force contributions will obviously influence the measured apparent adsorption distances since it leads to a shift of the effective interaction curves in z-direction (see solid red and blue lines).

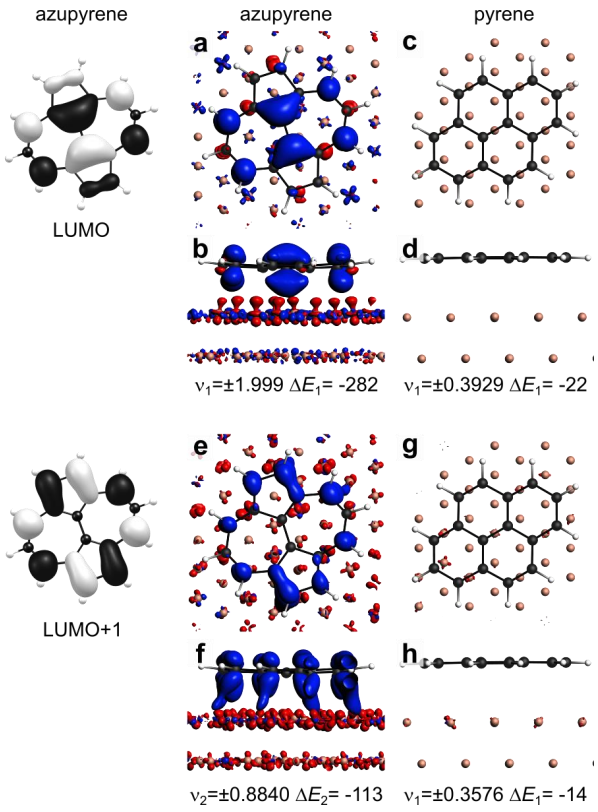

Supplementary Figure 7 | The pEDA analysis shows electron transfer from the on Cu(111) surface into the unoccupied LUMO and LUMO+1 orbitals of azupyrene and no charge transfer for pyrene. Left, molecular LUMO and LUMO+1 orbitals of azupyrene. **a-h**, Principal NOCV deformation densities (Δρ) for azupyrene in comparison to pyrene, red denotes electron depletion, blue denotes electron accumulation. **a-d**, $\Delta\rho_1$, isosurface value: 0.005 $e^-/Å^3$. For azupyrene $\Delta\rho_1$ shows the electron transfer from the surface in the LUMO of the molecule, for pyrene it contains only minor rearrangement not visible at this isosurface value. **e-h**, $\Delta\rho_2$, isosurface value: 0.001 $e^-/Å^3$. For azupyrene $\Delta\rho_2$ shows electron transfer from the surface to the LUMO+1 of the molecule, for pyrene it again contains only minor rearrangement. All eigenvalues in e and all energies in kJ/mol.

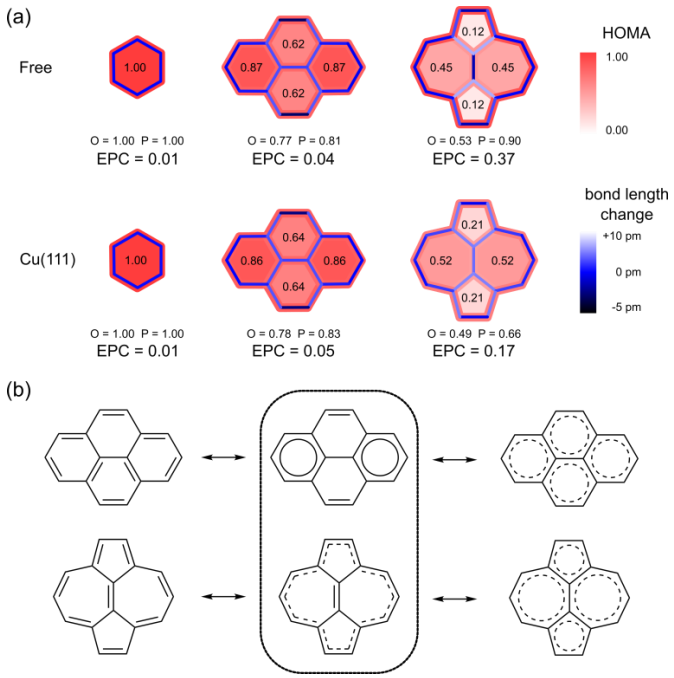

Supplementary Figure 8 | (a) HOMA analysis for the azupyrene and pyrene molecules, each in its gas phase structure and the adsorbate structure on Cu(111). The red color scheme shows the HOMA value. The filling of each ring is colored in its respective HOMA value (R), the peripheral bonds are colored according to the peripheral HOMA value (P) and the bridging bonds are colored according to the overall HOMA value (O). All bonds are additionally colored with a blue color scheme according to the bond length change in respect to the ideal aromatic bond. (b) Comparison of different conjugation possibilities for azupyrene and pyrene. For pyrene the structure of the doubly ethenediyl bridged biphenyl with two Clar sextets is supported by the HOMA values, EPCs and bond lengths. The free azupyrene is best described with annulene-like conjugation, when adsorbed on Cu(111) the conjugation is more delocalized over the whole molecule. The structures at the right describe how overall (benzenoid) conjugation would be expressed.

4. Supplementary Tables

Supplementary Table 1 | Graphene defects induce charge transfer at the metal interface, similar to the molecules modelling the defects. The charge transfer was calculated by integrating the molecular projected DOS up to E_F, by Bader's atoms in molecules method, by Hirshfeld's charge analysis, and by an iterated Hirshfeld charge analysis scheme, A negative sign means charge is transferred from the substrate to the graphene layer or molecule.

	ideal graphene	SW defect	5-7 defect	pyrene	azupyrene	azulene
q_{DOS}	-	-	-	-0.08	-1.40	-1.39
q_{AIM}	-	-	-	+0.02	-0.67	-0.49
q_H	+0.88	+0.18	-0.12/2	-0.04	-0.31	-0.25
q_{H-I}	+0.66	-0.19	-0.37/2	-0.19	-0.66	-0.60

Supplementary Table 2 | pEDA results for azupyrene and pyrene on Cu(111), all energy values in kJ/mol.

	azupyrene	pyrene
ΔE_{int}	-302	-223
ΔE_{int} (disp)	-275	-232
ΔE_{int} (elec)	-27	+9
ΔE_{Pauli}	+2241	+555
ΔE_{elstat} [a]	-1270 (56 %)	-312 (57 %)
ΔE_{orb} [a]	-998 (44 %)	-232 (43 %)
ΔE_{orb} (surf→LUMO)	-282	-
ΔE_{orb} (surf→LUMO+1)	-113	-
ΔE_{prep}(mol,in cell)[b]	+18	-11
ΔE_{prep}(mol,free)[c]	+31	+1
ΔE_{prep}(surf)	+12	+2
ΔE_{bond}	-271	-232
ΔE_{bond} (PAW)	-242	-205

[a] Percentage values give the relative contributions to the sum of the attractive pEDA terms ΔE_{elstat} and ΔE_{orb}
[b] referenced to the molecular fragment in the unit cell of the adsorbate structure
[c] referenced to the isolated molecular fragment

Supplementary Table 3 | NOCV eigenvalues and corresponding orbital energy contributions for the most important deformation densities ($\Delta\rho_i$) resulting from an pEDA analysis of azupyrene and pyrene on Cu(111).

	azupyrene		**pyrene**	
$\Delta\rho_i$	ν_i / e	$\Delta E_{orb,i}$ / kJ/mol	ν_i / e	$\Delta E_{orb,i}$ / kJ/mol
1	±1.999	-282	±0.3929	-22
2	±0.8840	-113	±0.3576	-14
3	±0.6051	-58	±0.3031	-20
4	±0.5493	-39	±0.2463	-12
5	±0.5055	-37	±0.2286	-11
6	±0.4702	-36	±0.2146	-13
	$\Delta E_{orb,rest}$	-393	$\Delta E_{orb,rest}$	-110

The results of the periodic energy decomposition analysis were carefully checked for k-space convergence. Table S2 shows the k-space convergence from k-grid 1×1 to 7×7 for both systems. As one can see the convergence is not especially good, but as the differences between the two systems are much greater, our discussion is still valid.

Supplementary Table 4 | k-space convergence for the pEDA calculations, basis set = TZ2P. Shown are the energies in kJ/mol and the deviation to the 7×7 value in percent.

ΔE_{int}	k-grid = 1×1		k-grid = 3×3		k-grid = 5×5		k-grid = 7×7
AzPyr/Cu	-284	-6%	-301	0%	-318	5%	-302
Pyr/Cu	-202	-10%	-213	-5%	-234	5%	-223

ΔE_{Pauli}	k-grid = 1×1		k-grid = 3×3		k-grid = 5×5		k-grid = 7×7
AzPyr/Cu	+2297	3%	+2257	1%	+2266	1%	+2241
Pyr/Cu	+572	3%	+555	0%	+565	2%	+555

ΔE_{elstat}	k-grid = 1×1		k-grid = 3×3		k-grid = 5×5		k-grid = 7×7
AzPyr/Cu	-1344	6%	-1308	3%	-1243	-2%	-1270
Pyr/Cu	-339	9%	-325	4%	-302	-3%	-312

ΔE_{orb}	k-grid = 1×1		k-grid = 3×3		k-grid = 5×5		k-grid = 7×7
AzPyr/Cu	-963	-4%	-975	-2%	-1066	7%	-998
Pyr/Cu	-203	-13%	-211	-10%	-266	13%	-234

Table S3 directly compares the pEDA terms of the calculations performed with the 7×7 k-space grid to the values obtained by the NOCV calculation. All energy contributions show a good agreement with deviations of less than 6 % for azupyrene and less than 14 % for pyrene. The NOCV analysis, which can only performed in the 1×1 grid, is therefore expected to give reasonable results and the energetic contributions ΔE_{orb}(surf→LUMO) and ΔE_{orb}(surf→LUMO+1) assigned from the deformation densities of azupyrene are included in Table S1.

Supplementary Table 5 | Comparison of the pEDA contributions for k=7×7 calculations of the regular pEDA analysis and the k=1×1 (Γ-only) calculations performed for the NOCV extension.

	AzPyr/Cu		**Pyr/Cu**	
	k = 7×7	k=1×1	k=7×7	k=1×1
ΔE_{int}	-302	-284	-223	-202
ΔE_{int} (disp)	-275	-275	-232	-232
ΔE_{int} (elec)	-27	-9	+9	+30
ΔE_{Pauli}	+2241	+2297	+555	+572
ΔE_{elstat}	-1270	-1344	-312	-339
ΔE_{orb}	-998	-963	-234	-203

5 Supplementary References

1 Kresse, G. & Hafner, J. Ab initio molecular dynamics for liquid metals. *Phys. Rev. B* **47**, 558-561 (1993).

2 Kresse, G. & Hafner, J. Ab initio molecular-dynamics simulation of the liquid-metal-amorphous-semiconductor transition in germanium. *Phys. Rev. B* **49**, 14251-14269 (1994).

3 Kresse, G. & Furthmüller, J. Efficient iterative schemes for ab initio total-energy calculations using a plane-wave basis set. *Phys. Rev. B* **54**, 11169-11186 (1996).

4 Kresse, G. & Furthmüller, J. Efficiency of ab-initio total energy calculations for metals and semiconductors using a plane-wave basis set. *Comput. Mater. Sci.* **6**, 15-50 (1996).

5 Perdew, J. P., Burke, K. & Ernzerhof, M. Generalized Gradient Approximation Made Simple. *Phys. Rev. Lett.* **77**, 3865-3868 (1996).

6 Grimme, S., Antony, J., Ehrlich, S. & Krieg, H. A consistent and accurate ab initio parametrization of density functional dispersion correction (DFT-D) for the 94 elements H-Pu. *J. Chem. Phys.* **132**, 154104 (2010).

7 Becke, A. D. & Johnson, E. R. A density-functional model of the dispersion interaction. *J. Chem. Phys.* **123**, 154101, doi:10.1063/1.2065267 (2005).

8 Blöchl, P. E. Projector augmented-wave method. *Phys. Rev. B* **50**, 17953-17979 (1994).

9 Kresse, G. & Joubert, D. From ultrasoft pseudopotentials to the projector augmented-wave method. *Phys. Rev. B* **59**, 1758-1775 (1999).

10 Clark, S. J. *et al.* First principles methods using CASTEP. *Z. Kristallogr. Cryst. Mater.* **220**, 567–570, doi:10.1524/zkri.220.5.567.65075 (2005).

11 Mizoguchi, T., Tanaka, I., Gao, S.-P. & Pickard, C. J. First-principles calculation of spectral features, chemical shift and absolute threshold of ELNES and XANES using a plane wave pseudopotential method. *J. Phys.: Condens. Matter* **21**, 104204 (2009).

12 Triguero, L., Pettersson, L. G. M. & Ågren, H. Calculations of near-edge x-ray-absorption spectra of gas-phase and chemisorbed molecules by means of density-functional and transition-potential theory. *Phys. Rev. B* **58**, 8097-8110 (1998).

13 Klues, M., Hermann, K. & Witte, G. Analysis of the near-edge X-ray-absorption fine-structure of anthracene: A combined theoretical and experimental study. *J. Chem. Phys.* **140**, 014302 (2014).

14 Maurer, R. J. & Reuter, K. Excited-state potential-energy surfaces of metal-adsorbed organic molecules from linear expansion Δ-self-consistent field density-functional theory (ΔSCF-DFT). *J. Chem. Phys.* **139**, 014708 (2013).

15 Raupach, M. & Tonner, R. A periodic energy decomposition analysis method for the investigation of chemical bonding in extended systems. *J. Chem. Phys.* **142**, 194105 (2015).

16 Pecher, L. & Tonner, R. Deriving bonding concepts for molecules, surfaces, and solids with energy decomposition analysis for extended systems. *WIREs Comput Mol Sci.* **9**, e1401, doi:10.1002/wcms.1401 (2019).

17 Chanier, T. & Henrard, L. From carbon atom to graphene on Cu(111): an ab-initio study. *Eur. Phys. J. B* **88**, 5, doi:10.1140/epjb/e2014-50587-0 (2015).

18 Saba, S. *et al.* One-Pot Preparation of Ternary and Quaternary Iminium Salts from Aldehydes and Ketones. *J. Chem. Res.* **2008**, 301-304, doi:10.3184/030823408X338387 (2008).

19 Zacharia, J. T., Tanaka, T. & Hayashi, M. Facile and Highly Enantioselective Synthesis of (+)- and (−)-Fluvastatin and Their Analogues. *J. Org. Chem.* **75**, 7514-7518, doi:10.1021/jo101542y (2010).

20 Jutz, C. & Schweiger, E. Über eine verbesserte Synthese des Dicyclopenta[ef,kl]heptalens. *Synthesis* **3**, 193-196, doi:DOI: 10.1055/s-1974-23277 (1974).

P3

21 Anderson, A. G., Daugs, E. D., Kao, L. G. & Wang, J. F. Dicyclopenta[ef,kl]heptalene (azupyrene) chemistry. Jutz synthesis byproducts. Synthesis and thermal isomerization of 1-methylazupyrene. *J. Org. Chem.* **51**, 2961-2965, doi:10.1021/jo00365a020 (1986).

22 Christmann, K. *Introduction to Surface Physical Chemistry*. (Steinkopff Verlag, Springer-Verlag, 1991).

23 de Jong, A. M. & Niemantsverdriet, J. W. Thermal desorption analysis: Comparative test of ten commonly applied procedures. *Surf. Sci.* **233**, 355-365 (1990).

24 Nieskens, D. L. S., van Bavel, A. P. & Niemantsverdriet, J. W. The analysis of temperature programmed desorption experiments of systems with lateral interactions; implications of the compensation effect. *Surf. Sci.* **546**, 159-169 (2003).

25 Witte, G., Lukas, S., Bagus, P. S. & Wöll, C. Vacuum level alignment at organic/metal junctions: "Cushion" effect and the interface dipole. *Appl. Phys. Lett.* **87**, 263502 (2005).

26 Tomba, G., Stengel, M., Schneider, W. D., Baldereschi, A. & De Vita, A. Supramolecular self-assembly driven by electrostatic repulsion: The 1D aggregation of rubrene pentagons on Au111. *ACS Nano* **4**, 7545-7551 (2010).

27 Vázquez, H., J. Dappe, Y. J., Ortega, J. & Flores, F. Energy level alignment at metal/organic semiconductor interfaces: "Pillow" effect, induced density of interface states, and charge neutrality level. *J. Chem. Phys.* **126**, 144703, doi:10.1063/1.2717165 (2007).

28 Armbrust, N., Schiller, F., Güdde, J. & Höfer, U. Model potential for the description of metal/organic interface states. *Scientific Reports* **7**, 46561, doi:10.1038/srep46561 (2017).

29 Fernandez-Torrente, I. *et al.* Long-range repulsive interaction between molecules on a metal surface induced by charge transfer. *Phys. Rev. Lett.* **99**, 176103 (2007).

30 Lukas, S., Vollmer, S., Witte, G. & Wöll, C. Adsorption of acenes on flat and vicinal Cu(111) surfaces: Step induced formation of lateral order. *J. Chem. Phys.* **114**, 10123-10130 (2001).

31 Klein, B. P. *et al.* Molecular Topology and the Surface Chemical Bond: Alternant Versus Nonalternant Aromatic Systems as Functional Structural Elements. *Phys. Rev. X* **9**, 011030, doi:10.1103/PhysRevX.9.011030 (2019).

32 Klein, B. P. *et al.* Molecule-Metal Bond of Alternant versus Nonalternant Aromatic Systems on Coinage Metal Surfaces: Naphthalene versus Azulene on Ag(111) and Cu(111). *J. Phys. Chem. C* **123**, 29219-29230, doi:10.1021/acs.jpcc.9b08824 (2019).

33 Schuler, B. *et al.* Adsorption Geometry Determination of Single Molecules by Atomic Force Microscopy. *Phys. Rev. Lett.* **111**, 106103 (2013).

34 Zhong, Q. *et al.* Symmetry breakdown of 4,4"-diamino-p-terphenyl on a Cu(111) surface by lattice mismatch. *Nat. Commun.* **9**, 3277, doi:10.1038/s41467-018-05719-y (2018).

35 Ebeling, D. *et al.* Adsorption Structure of Mono- and Diradicals on a Cu(111) Surface: Chemoselective Dehalogenation of 4-Bromo-3"-iodo-p-terphenyl. *ACS Nano* **13**, 324-336, doi:10.1021/acsnano.8b06283 (2019).

36 Kruszewski, J. & Krygowski, T. M. Definition of aromaticity basing on the harmonic oscillator model. *Tetrahedron Lett.* **13**, 3839-3842, doi:https://doi.org/10.1016/S0040-4039(01)94175-9 (1972).

37 Anderson, A. G., MacDonald, A. A. & Montana, A. F. Dicyclopenta[ef,kl]heptalene (azupyrene). *J. Am. Chem. Soc.* **90**, 2993-2994, doi:10.1021/ja01013a065 (1968).

38 Chen, M. *et al.* Coordination Reactions and Layer Exchange Processes at a Buried Metal–Organic Interface. *J. Phys. Chem. C* **118**, 8501-8507, doi:10.1021/jp5019235 (2014).

39 Mitoraj, M. P., Michalak, A. & Ziegler, T. A Combined Charge and Energy Decomposition Scheme for Bond Analysis. *J. Chem. Theory Comput.* **5**, 962-975, doi:10.1021/ct800503d (2009).

Engineering of TMDC-OSC Hybrid Interfaces: The Thermodynamics of Unitary and Mixed Acene Monolayers on MoS_2

Stefan R. Kachel [1,†], Pierre-Martin Dombrowski [2,†], Tobias Breuer [2], J. Michael Gottfried [1], and Gregor Witte [*,2]

[1] Fachbereich Chemie, Philipps-Universität Marburg, Hans-Meerwein-Straße 4, 35032 Marburg, Germany

[2] Fachbereich Physik, Philipps-Universität Marburg, Renthof 7, 35032 Marburg, Germany

Thermal stability, Temperature programmed desorption, Interaction energies, Aromatic compounds, Two-dimensional materials

ABSTRACT: Hybrid systems of two-dimensional (2D) materials such as transition metal dichalcogenides (TMDCs) and organic semiconductors (OSCs) have become subject of great interest for future device architectures. Although OSC-TMDC hybrid systems have been used in first device demonstrations, the precise preparation of ultra-thin OSC films on TMDCs has not been addressed. Due to the weak van der Waals interaction between TMDCs and OSCs, this requires precise knowledge of the thermodynamics at hand. Here, we use temperature-programmed desorption (TPD) and Monte-Carlo (MC) simulations of TPD traces to characterize the desorption kinetics of pentacene (PEN) and perfluoropentacene (PFP) on MoS_2 as a model system for OSCs on TMDCs. We show that the monolayers of PEN and PFP are thermally stabilized compared to their multilayers, which allows to prepare nominal monolayers by selective desorption of multilayers. This stabilization is, however, caused by entropy due to a high molecular mobility rather than an enhanced molecule-substrate bond. Consequently, the nominal monolayers are not densely packed films. Molecular mobility can be suppressed in mixed monolayers of PEN and PFP that, due to intermolecular attraction, form highly ordered films as shown by scanning tunneling microscopy. Although this reduces the entropic stabilization, the intermolecular attraction further stabilizes mixed films.

1. INTRODUCTION

Since the first successful isolation of graphene, interest in the field of two-dimensional materials has been continuously growing [1, 2]. Offering a wide range of charge transport properties ranging from insulators such as hexagonal boron nitride to semiconductors like transition metal dichalcogenides (TMDCs) to semi-metallic materials such as graphene, van der Waals (vdW) bound hetero systems of 2D materials (2DMs) provide unprecedented prospects for device miniaturization in next-generation electronics [3-8]. Besides the aspect of device miniaturization, the single-layer structure of these materials offers versatile possibilities for the development of flexible nanostructures with atomically sharp interfaces [9, 10].

A promising extension of the number of possible vdW hetero systems that retains the desired 2D structure and flexibility is provided by the combination of 2DMs with thin layers of organic semiconductors (OSCs) [11, 12] in organic-2DM hybrid systems. Since properties of OSCs are more easily tunable through synthesis than those of 2DMs, such hybrid heterostructures can greatly facilitate device engineering. Moreover, OSCs can complement 2DMs: While 2DMs generally have a higher charge carrier mobility, OSCs offer a high optical absorption efficiency, which renders the combination of OSCs with 2DMs particularly beneficial for optoelectronic applications such as photovoltaics [13]. In fact, OSC-2DM hybrid systems have already been realized in photovoltaic devices [14-17] and p-n junctions [16, 18-23]. However, while theoretical concept studies focus on highly ordered OSC monolayers or single molecules on 2DMs [24, 25], real hybrid heterosystems are usually restricted to OSC multilayers. This is because, unlike monolayers of 2DMs that are commercially available, the fabrication of true single-layer hybrid systems remains challenging as it requires highly precise dosing in molecular beam epitaxy.

A more scalable approach to the fabrication of molecular monolayers is that of selective desorption of multilayers that is commonly applied on metallic surfaces, where the first molecular layer is often chemisorbed and thereby thermally stabilized against dewetting and 3D growth [26, 27]. This approach eliminates the requirement of precise thickness-control of the molecular film since any film thickness can be annealed until only the stabilized first molecular layer remains on the inorganic substrate. However, such a thermal stabilization is to date not reported for any TMDC and it is uncertain whether the relatively weak vdW interaction at the OSC-TMDC interface is capable of stabilizing the first molecular layer. Consequently, an in-depth study of the thermal stability of OSCs on TMDCs is of paramount importance, as it serves as a model system for the emerging field of engineering molecular nanostructures [28, 29] and could also enable a scalable fabrication of 2D OSC-TMDC hybrid heterostructures.

In this work, we present a detailed analysis of the desorption characteristics of ultra-thin pentacene ($C_{22}H_{14}$, PEN) and perfluoropentacene ($C_{22}F_{14}$, PFP) films on molybdenum disulfide (MoS_2). Hybrid systems of PEN and MoS_2, in particular, have already been used in various photovoltaic devices and p-n junctions with remarkable properties [16, 17, 19, 21]. Additional theoretical studies have provided first insight into electronic interactions at the PEN / MoS_2 interface [24, 25]. In contrast to PEN, PFP is an n-type OSC [30]. Although its carbon backbone is structurally identical to that of PEN, it exhibits a distinctly modified charge distribution due to its electronegative fluorine atoms that lead to an inverted quadrupole moment. Not only does the comparison of these two OSCs enable us to study influences of electronic configuration on the thermal stability of molecular monolayers, but it also provides an interesting prospect for mixed films of PEN and PFP that are additionally stabilized by intermolecular attraction as reported for their multilayer mixtures in a previous work [31]. To minimize the influence of defects at the MoS_2 surface on the OSC-TMDC interface, we use pristine exfoliated MoS_2 single crystals on which we found epitaxial growth of PEN and PFP in a previous study [32].

To study molecular desorption kinetics, we use temperature-programmed desorption (TPD) as a versatile technique for investigating the thermal evolution and interfacial bond strength of organic/inorganic hybrid systems. In recent years, TPD has been increasingly employed to study interfaces between large aromatic molecules and metals [33-48] or graphite [49-52]. On metals, the activation energy of desorption (often referred to as desorption energy) is commonly used as a measure for the adsorption energy, i.e. the OSC/metal binding energy. On weakly interacting substrates, however, the relation between desorption energy and interface binding energy can be more complex due to an increasing importance of entropy as a result of a larger mobility of the molecular adsorbates. Entropic effects can lead to a thermal stabilization of the first molecular layer in spite of a smaller desorption energy compared to the multilayer, as entropy can reduce the prefactor of desorption, which increases desorption temperatures [50]. Since prefactors depend on a system's entropy and the partition function, they do not only depend on the molecular species [53], but also on the particular interface that can influence molecular mobility. Therefore, prefactors are generally not precisely known, which complicates the determination of reliable desorption energies from TPD as common approximations such as Redhead's method [54] are not applicable. Moreover, intermolecular interactions can also noticeably influence desorption energies, especially in weakly interacting hybrid systems. While such effects are often mentioned [36, 38, 45, 47, 52], they are rarely discussed quantitatively and even then, the analysis is restricted to simple linear approximations of coverage-dependent interactions [38, 52].

To study intermolecular interaction energies more accurately, and to understand the complex interplay of intermolecular and OSC-TMDC interactions in unitary and mixed monolayers of PEN and PFP, we combine our experimental TPD data with Monte Carlo (MC) simulations that take structural configurations and interactions of molecules into account to compute TPD traces. In addition to TPD, we use near-edge X-ray absorption fine structure (NEXAFS) spectroscopy and work function measurements by means of the Kelvin probe technique to analyze the electronic coupling of the OSCs to MoS_2 as well as scanning tunneling microscopy (STM) for a characterization of the geometrical arrangement of the OSC films.

Analysis of our TPD data shows that both PEN and PFP form thermally stabilized monolayers on MoS_2 that desorb at significantly higher temperatures than the respective multilayers, although the desorption energies are smaller in the monolayer regime than in the multilayer regime. While this, in principle, allows for a preparation of nominal molecular monolayers by means of selective desorption of multilayers, we also find evidence for a significant intermolecular repulsion in unitary PEN and PFP films, which is attributed to their electrostatic interaction. This repulsion, coupled with a relatively weak OSC-2DM interface bond, leads to the formation of a highly mobile, gas-like phase in the unitary molecular (sub-) monolayers that prevents the formation of densely packed monolayers at room temperature. However, mutual (electrostatic) attraction of PEN and PFP can be used to increase the packing density in intermixed monolayers, as it favors the formation of ordered co-structures, which is corroborated by STM data.

2. METHODS

Experimental Details. PEN (Sigma Aldrich, purity ≥ 99.9%) and PFP (Kanto Denka Kogyo, purity ≥ 99%) films were grown by means of organic molecular beam deposition under ultrahigh vacuum (UHV) conditions from resistively heated Knudsen cells. If not stated differently, molecular films were grown at a substrate temperature of 270 K at typical deposition rates of 2 Å/min as monitored by quartz crystal microbalances.

Similar to a previously described growth protocol [55], MoS_2 crystals (2H-MoS_2) were grown by means of chemical vapor transport, starting from stoichiometric amounts of Mo, S and Br_2, the latter being the source for the transport agent $MoBr_4$ that is formed in-situ. The reaction was performed in an evacuated quartz glass ampoule that was subjected to a temperature gradient from 1300 K to 1220 K for 20 days. This procedure yields crystals of almost centimeter size as shown in reference [32]. The crystals were exfoliated under ambient conditions before being evacuated. Prior to the deposition of molecules, the crystals were annealed at a temperature of 650 K for 15 min.

TPD measurements were carried out in a dedicated UHV apparatus with a base pressure in the low 10^{-10} mbar regime, as described elsewhere [46, 48]. Briefly, the apparatus hosts a HIDEN EPIC 1000 quadrupole mass spectrometer (QMS) with a mass range up to 1000 amu that enables detection of the intact molecular ions PEN^+ (m/z = 278 amu) and PFP^+ (m/z = 530 amu). If not stated differently, TPD traces were recorded with heating rates of 1 K/s. Sample temperatures were precisely measured using a calibrated type K thermocouple mounted on top of the MoS_2 crystal.

The microstructural order of molecular thin films was characterized in UHV (base pressure < 10^{-10} mbar) by means of STM (Omicron VT STM) in constant current mode using etched tungsten tips at sample temperatures of 110 K. The same UHV system hosts a Kelvin Probe (Besocke Delta Phi

GmbH, Kelvin Probe S) that is used for work function measurements.
NEXAFS measurements in partial electron yield mode (retarding field: 150 V) were performed at the HE-SGM dipole beam line of the synchrotron storage ring BESSY II in Berlin (Germany). Details on the experimental setup and the data analysis can be found in reference [56].

Computational Details. MC simulations of TPD traces were performed using a modified version of the algorithm described in reference [57]. Molecules are modeled as two-dimensional circular discs to describe an averaged intermolecular interaction and to account for all possible relative rotational orientation that can be expected at elevated temperatures. These discs can diffuse freely on a jellium-like substrate. Intermolecular interactions are modeled by vdW and Coulomb interactions, the latter leading to a repulsive contribution in unitary films and an attractive contribution in mixed films of PEN and PFP. Structural configurations of the adlayer after molecular diffusion are used as input to compute coverage-dependent desorption energies. Details on the model and the algorithm can be found in the Supporting Information. The simulated TPD traces that are shown in this work are averaged from at least 50 randomized ensembles. For unitary and mixed PEN and PFP films, we use 64 and 100 molecules, respectively, per calculated TPD trace.

3. RESULTS AND DISCUSSION

Electronic Coupling and Molecular Orientation. At first, we performed temperature-dependent NEXAFS measurements of PEN and PFP thin films grown on exfoliated MoS_2 single crystals to find out whether the molecular monolayers are thermally stabilized and to obtain information on the molecular orientation at elevated temperatures. Therefore, we deposited 0.5 nm of the molecules on MoS_2 and slowly heated the sample to incrementally increasing temperatures [58]. The resulting series of spectra are shown in Figures 1 (a) and (b) for PEN and PFP, respectively. Upon annealing of the molecular films, we observe a decrease of the intensity due to desorption of molecules, with residual intensity even after annealing to 410 K. At this temperature, molecular multilayers were found to be completely desorbed on SiO_2 and gold [31, 41], showing that the first molecular layer of PEN and PFP on MoS_2 is thermally stabilized relative to the bulk substance.
Comparing the monolayer spectra to NEXAFS spectra of multilayers of PEN and PFP on SiO_2, where no coupling of the molecules to the substrate occurs (green curves), we identify a modified NEXAFS signature for the PEN monolayer on MoS_2 in the sharp π*-resonances at excitation energies below the C 1s absorption edge (dashed lines). This is also found for PEN on Ag(111) and Au(111) and suggests a small chemical interaction [39, 41]. In contrast, no difference is found for PFP, in line with findings for Ag(111) [59]. Complementary measurements of the work function show, however, no changes upon deposition of monolayers and thin films of both molecular species (see Supporting Information). Since, in contrast to metals, there is no push-back effect on MoS_2 that could compensate work function changes caused by a charge transfer between the molecular

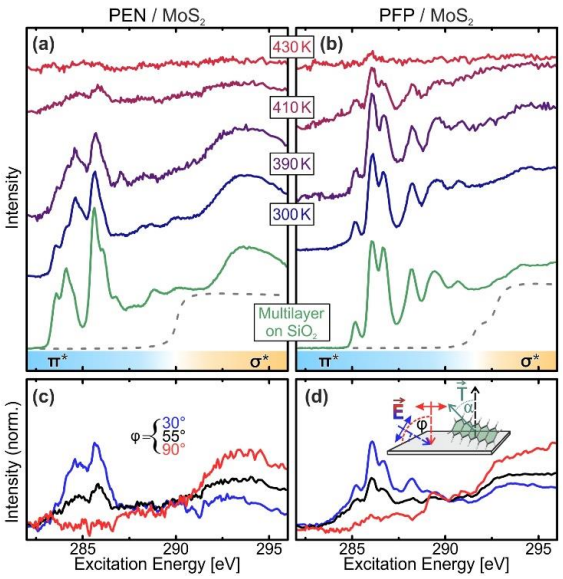

Figure 1: Temperature-dependent C 1s-NEXAFS spectra (θ = 55°) of (a) PEN and (b) PFP films on MoS_2 (initial film thickness 0.5 nm; green spectra: multilayers on SiO_2 with nominal thickness of 30 nm recorded at 300 K). The dashed lines mark the C 1s absorption edges. Panels (c) and (d) show C 1s-NEXAFS dichroism measurements of the PEN and PFP films, respectively, after annealing to 410 K.

film and MoS_2, we can conclude that no notable charge transfer between the molecular films and MoS_2 takes place. This agrees with a density functional theory study of PEN on MoS_2 [24] and indicates that the electronic coupling of both molecular entities to MoS_2 is relatively weak, in spite of the observed modification of the monolayer NEXAFS signature of PEN.
In addition to the thermal stability, we can also use NEXAFS to determine the molecular orientation on the substrate surface by quantitative analysis of the dichroism of NEXAFS spectra recorded at different angles of incidence of the synchrotron radiation as described in detail in reference [56]. In short, since the transition dipole moments (TDMs) corresponding to excitations into unoccupied π*-orbitals are oriented normal to the molecular backbone (see inset in Figure 1 (d)), the absorption of X-rays with the related photon energies depends on the relative orientation of the molecules and the polarization of the X-ray beam. Thus, one can determine the average orientation of molecules in the film by acquiring NEXAFS spectra at different sample orientations, i.e. at different angles of incidence φ. Figures 1 (c) and (d) show such measurements for acene films that were heated to 410 K. The quantitative analysis of the dichroism of the leading π*-resonances yields molecular tilt angles of $\alpha < 10°$, showing that in the (sub-) monolayer regime, PEN and PFP are lying flat on the MoS_2 surface even at elevated temperatures.

Thermal Stability of Unitary Monolayers. To further investigate the nature of the thermally stabilized first layer, TPD

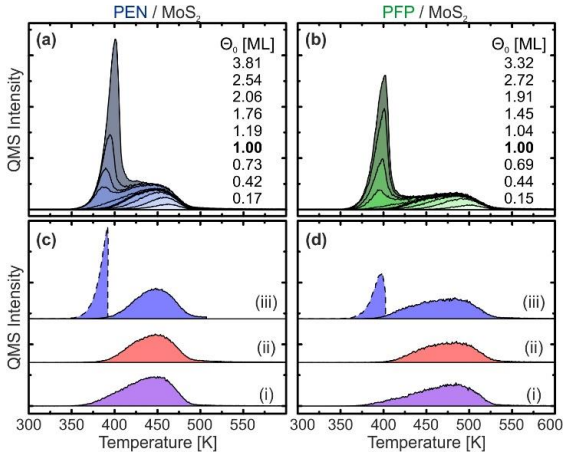

Figure 2: Series of TPD traces for different film thicknesses of (a) PEN and (b) PFP on MoS_2. The nominal monolayers are marked with bold lines. Panels (c) and (d) depict monolayer traces of PEN and PFP, respectively, prepared with three different methods: (i) deposition of 3 Å (nominal monolayer) at 270 K, (ii) deposition of 8 Å at elevated temperature (PEN: 390 K; PFP: 400 K) and (iii) deposition of 8 Å at 270 K and subsequent annealing for 1 min (PEN: 390 K; PFP: 400 K), dashed lines indicate the desorbing multilayers upon annealing. Afterwards, the sample is cooled down and heated again to record the TPD trace (solid line).

measurements with different film thicknesses ranging from 0.5 Å to 12 Å were conducted that are shown in Figures 2 (a) and (b) for PEN and PFP, respectively. For both molecules, two clearly separated peaks are observed. The high-temperature peak occurs at all coverages, but increases in intensity and width only up to nominal film thicknesses of 3 Å. From this coverage on, a low-temperature peak begins to form that increases in height with the film thickness but exhibits the same ascending peak flank. As this behavior is characteristic for multilayer desorption, which can be well described by zeroth-order desorption kinetics [61], we ascribe the low-temperature peak to multilayer desorption and the high-temperature peak to monolayer desorption.

In the monolayer regime, we find substantial differences in the desorption traces of the two molecules that range from 380 K to 490 K for PEN and from 390 K to 530 K for PFP. The higher desorption temperatures of PFP indicate a stronger interaction with MoS_2 in comparison to PEN. Since for both acenes, notable multilayer desorption starts at approximately 350 K, the molecular monolayers are sufficiently stabilized to allow for a preparation of nominal monolayers by means of selective desorption of multilayers. This is shown in Figures 2 (c) and (d) for PEN and PFP, respectively, where TPD traces of nominal monolayers prepared by (i) direct deposition of 3 Å of the respective molecule (corresponding to a nominal coverage of 1 ML) at a substrate temperature of 270 K, (ii) deposition of 8 Å on a crystal at an elevated temperature (390 K for PEN and 400 K for PFP) and (iii) deposition of 8 Å at 270 K and subsequent annealing at 390 K (PEN) or 400 K (PFP) for 1 min are presented. Both annealing methods yield monolayer TPD traces with no multilayer peak, showing that nominal monolayers of PEN and PFP on MoS_2 can be prepared by selective desorption of multilayers. In contrast, method (i) shows a weak low-temperature tail below 400 K that suggests an onset of multilayer formation, possibly prior to the completion of a densely packed monolayer. Therefore, we use the TPD traces obtained by method (ii), i.e. deposition of 8 Å on a hot MoS_2, to define the nominal coverage of 1 ML.

The quantitative analysis of TPD traces is based on the Polanyi-Wigner equation [60]:

$$r = \nu\, \theta^n e^{-E_d/RT} \quad . \qquad (1)$$

Here, r is the desorption rate that is measured in dependence of the substrate temperature T, θ is the surface coverage, n is the order of desorption kinetics and R is the universal gas constant. The parameters to be determined from the experimental TPD traces are the so-called kinetic parameters, i.e. the activation energy for desorption, or short desorption energy E_d, and the pre-exponential factor, or prefactor, ν.

For the quantitative analysis of E_d and ν in the multilayer regime, we have performed a leading-edge analysis [61]. This analysis (for details, see Supporting Information) yields desorption energies of (141±3) kJ/mol and (149±3) kJ/mol and prefactors of $10^{17.7\pm0.4}$ s^{-1} and $10^{18.5\pm0.4}$ s^{-1} for PEN and PFP, respectively. These values are in reasonable agreement with the PEN sublimation enthalpy of (157 ± 14) kJ/mol [62], considering the large margins of error of the literature value. Larger sublimation enthalpies of fluorinated species compared to their non-fluorinated siblings are also reported for naphthalene and octafluoronaphthalene [63]. This finding can be attributed to a slightly higher polarizability and quadrupole moment as calculated for the case of PEN and PFP [64], which enable stronger vdW interactions. A comparison of the crystalline phases of PEN and PFP revealed further a somewhat larger Kitaigorodskii packing coefficient for PFP [64], which is indicative of stronger dispersion interactions.

In the monolayer regime, the TPD traces do not exhibit the same leading-edge for different initial coverages, which can be seen more clearly in Figures 3 (a) and (b) that depict only the (sub-) monolayer TPD traces of PEN and PFP, respectively. To extract the kinetic parameters from this data, we have used a modified leading-edge analysis (mLEA) that is described in detail in a previous publication [48]. This method uses only small temperature intervals (approximately 20 K) at the leading-edge of a TPD trace (corresponding to a coverage change of approx. 1%, details in the Supporting Information) to determine E_d and ν and can therefore provide coverage-specific values.

The results of the mLEA are presented as circles in Figures 3 (d) and (e) for PEN and PFP, respectively. In the sub-monolayer regime (coverage < 0.8 ML), we find desorption energies in the range between 105 kJ/mol and 110 kJ/mol with prefactors of the order of magnitude of 10^{11} s^{-1} for PEN. Upon saturation of the monolayer, E_d increases to 127 kJ/mol and ν increases to 10^{14} s^{-1}. For PFP, we find larger desorption energies in the range between 121 kJ/mol and 132 kJ/mol and prefactors of the order of magnitude of 10^{12} s^{-1} in the submonolayer regime. These values slightly change to 129 kJ/mol and 10^{14} s^{-1}, respectively, upon saturation of the monolayer.

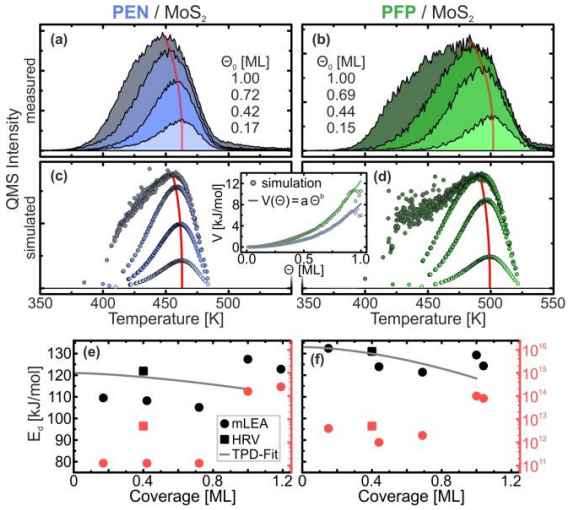

Figure 3: (a) and (b) TPD traces of PEN and PFP, respectively, on MoS_2 for different initial (sub-) monolayer coverages Θ_0. (c) and (d) MC simulations of TPD traces for PEN, respectively, for the same initial coverages as in (a) and (b). The inset shows the intermolecular interaction energy V as a function of the coverage Θ for PEN (blue) and PFP (green) obtained from the MC TPD simulations (circles) with exponential fits (lines). (e) and (f) Coverage-dependent desorption energies E_d (black) and pre-exponential factors ν (red) of PEN and PFP, respectively, on MoS_2.

The finding of larger desorption energies for the PFP monolayer compared to the PEN monolayer is in line with the observation of an onset of monolayer desorption at higher temperatures. However, all of these kinetic parameters are significantly smaller than the respective results for multilayer desorption. In particular, desorption energies are significantly smaller in the monolayer than in the multilayer. Since notable multilayer desorption starts at lower temperatures than monolayer desorption, this result is, at first glance, rather surprising and counterintuitive. Notably, the prefactors of both PEN and PFP are smaller than k_BT/h ($\sim 10^{13}$ s^{-1} at T = 400 K), which, according to transition state theory (TST), is the theoretical lowest limit for the prefactor [64]. This raises the questions whether these results are robust or erroneous, possibly due to the rather low signal-to-noise ratio of the leading edge that is used in the mLEA.

To test the results of the mLEA, we have also performed heating-rate variation (HRV) experiments. Therefore, TPD traces were recorded for a selected coverage at varying heating rates. The heating rate-dependent peak temperature can then be used to derive E_d and ν independently of each other, as described in detail in reference [48]. Because this method requires multiple measurements per initial coverage, only one submonolayer coverage was used per molecule (0.4 ML for PEN and PFP). For precise control of the initial coverages, these submonolayers were prepared by deposition of 8 Å of the respective molecule and subsequent annealing to desorb multilayers and parts of the monolayer. Analysis of the initial coverages from the TPD traces shows that this method yields highly reproducible initial coverages. The HRV data and the corresponding analysis are presented in the Supporting Information. From the HRV analysis, we obtain E_d = (122±4) kJ/mol and $\nu = 10^{12.7\pm0.5}$ s^{-1} for PEN and E_d = (131±4) kJ/mol and $\nu = 10^{12.7\pm0.4}$ s^{-1} for PFP (squares in Figure 3).

Considering the uncertainty of the mLEA (desorption energy error 4 kJ/mol and 9 kJ/mol and prefactor error 0.5 and 1.1 orders of magnitude for PEN and PFP, respectively), these HRV results are in fair agreement with those of the mLEA and thus confirm the general trend. Although the HRV desorption energies are slightly larger than those obtained from the mLEA, they are still significantly smaller than those of the multilayers. The HRV prefactors are an order of magnitude larger than those obtained from the mLEA and thus in agreement with the lower limit from TST, but still orders of magnitude smaller than typical prefactors obtained in TPD experiments with large molecules [34, 49, 50, 53, 65-70].

This effect, i.e. a small desorption energy in the monolayer compared to the multilayer in combination with an increase of the prefactor upon saturation of the monolayer by several orders of magnitude, has already been observed and described in detail for 2,4'-bis(terpyridine) on highly oriented pyrolytic graphite (HOPG) [50]. An explanation for this phenomenon is provided by TST: The reaction rate constant k_{TST} for the transition from the adsorbed initial state (IS) to the transition state (TS), that is the rate of desorption, can be related to the standard Gibbs free energy of activation, $\Delta G^{\ddagger}$ [71] (for a more detailed derivation, see Supporting Information):

$$k_{TST} = \frac{k_B T}{h} e^{-\Delta G^{\ddagger}/RT} \quad . \qquad (2)$$

Using equation 2 and the relation $\Delta G^{\ddagger} = \Delta H^{\ddagger} - T\Delta S^{\ddagger}$, where $\Delta H^{\ddagger}$ is the standard enthalpy of activation and $\Delta S^{\ddagger}$ is the standard entropy of activation, one can identify the desorption energy as [71]

$$E_d = \Delta H^{\ddagger} + RT \quad . \qquad (3)$$

With equation 3, equation 2 can be brought into the form $k_{TST} = \nu e^{-E_d/RT}$, which allows to identify the prefactor as

$$\nu = \frac{k_B T}{h} e^{(\Delta S^{\ddagger}/R)+1} \quad . \qquad (4)$$

On this basis, the exceptionally small prefactors can be interpreted. Equation 4 shows that the prefactor scales with the entropy gain upon transition from the adsorbed IS to the TS. When a chemisorbed molecule reaches the TS for desorption, it typically gains additional degrees of freedom (DOFs) compared to the IS, because bonds to the surface break and formerly frustrated translations and rotations turn into (nearly) free translations and rotations. Therefore, the partition function in the transition state is frequently larger than in the adsorbed state, giving rise to a desorption prefactor larger than k_BT/h [72].

If the prefactor is in the range of k_BT/h or even smaller, as is the case here, then the situation must be reversed, i.e. the TS must have a reduced number of DOFs, compared to the IS. This is the case when the adsorbed molecules are very mobile, while certain geometry restrictions apply to the TS. According to STM (see below), the adsorbed PEN molecules are indeed very mobile, resulting in large partition functions for two translation DOFs and one rotational DOF (around the axis perpendicular to the surface). In addition, due to the weak interaction with the surface, the two remaining frustrated rotations and one remaining frustrated

translation (vibration perpendicular to the surface) are expected to contribute substantially to the total partition function. Especially the latter contributes only to the IS and can therefore substantially reduce the desorption prefactor.
Regarding the geometry of the TS, it is obvious that the potential energy of a large planar molecule above a surface depends not only on the distance between its center-of-mass and the surface, but also on its orientation relative to the surface. This implies that the lowest-energy path of the desorption process is closely related to geometric parameters. Hence, of the many adsorption configurations available for the mobile adsorbed molecule, not all are equally suitable for the TS. The reduced number of configurations in the TS means that the partition function is reduced compared to the IS. In addition, a large planar molecule such as pentacene needs to be rather far away from the surface before it can freely rotate around all three axes. Geometry considerations for the case of pentacene show that its center-of-mass must be at least ~7 Å above the surface, which far exceeds the vdW distance of <3 Å between the molecular plane and the substrate [73]. It is therefore possible that the rotational partition function in the TS is still reduced compared to that of the gas phase. In contrast to the mobile molecules in the (sub-) monolayers, multilayers of PEN and PFP form crystalline films, as shown in a previous study [32]. In these films, the molecules are immobile, resulting in a larger entropy gain upon desorption and therefore a larger prefactor for desorption.
An energetic argument for the stabilization of the mobile molecular monolayer can be made on the basis of equation 2, which illustrates that the relevant thermodynamic potential for desorption is the standard Gibbs free energy of activation, not the standard enthalpy of activation that is closely related to the desorption energy. Consequently, the energy barrier for desorption does not only depend on the desorption energy, but also on the entropy change and thus on the prefactor. Using equations 3 and 4, one can calculate $\Delta G^{\ddagger}_{\text{mono}} - \Delta G^{\ddagger}_{\text{multi}}$, i.e. the difference in the standard Gibbs free energies of activation for desorption from mono- and multilayer (for details, see the Supporting Information):

$$\Delta G^{\ddagger}_{\text{mono}} - \Delta G^{\ddagger}_{\text{multi}} = E_{d,\,\text{mono}} - E_{d,\,\text{multi}} + RT \ln\left(\frac{\nu_{\text{multi}}}{\nu_{\text{mono}}}\right). \quad (5)$$

At 400 K, equation 5 yields a difference of the mono- and multilayer standard Gibbs free energy of activation of 19 kJ/mol for PEN and 26 kJ/mol for PFP, using the results of the HRV for the monolayer parameters. This shows that for both molecules, the barrier for desorption, given by the standard Gibbs free energy of activation, is larger in the monolayer than in the multilayer, which explains the stabilization of the molecular monolayers. The stabilization of the PEN and PFP monolayers is thus caused by entropy due to the formation of a highly mobile gas phase rather than a strong interface bond.
Upon saturation of the monolayer, the results of the mLEA (squares in Figures 3 (e) and (f)) show that the prefactors of PEN and PFP increase to about 10^{14} s^{-1}, indicating a reduction of the molecular mobility. Comparing the prefactors for monolayer desorption to those for the multilayers, they are, however, still several orders of magnitude smaller. This indicates that only multilayer growth can reduce molecular mobility, which allows to conclude that no close-packed and therefore well-ordered monolayers of PEN and PFP are formed on MoS_2 at room temperature, as observed for PFP on Ag(111) in a previous study [59]. Hence, the nominal monolayer that can be prepared by selective desorption of multilayers does not correspond to a densely and therefore complete monolayer.

Intermolecular Repulsion. A microscopic explanation for the formation of a highly mobile gas phase in the molecular monolayers can be found upon closer inspection of the (sub-) monolayer TPD traces. Figures 3 (a) and (b) show only the monolayer TPD traces of PEN and PFP, respectively, that exhibit a distinct peak shift to lower temperatures for increasing coverages as indicated by red lines. Such a peak shift is already reported for other systems including PEN on Au(111) [36, 38, 45, 47, 52] and commonly attributed to (sometimes substrate-mediated) intermolecular repulsion. This causes a reduction of the desorption energy for increasing coverages as the repulsion increases with decreasing average nearest-neighbor distances. Such a reduction of the desorption energy at increasing coverage can also be found in Figures 3 (e) and (f) in the mLEA results for both molecules.
Using MC TPD simulations with electrostatic intermolecular interactions that are based on the molecular quadrupole moments calculated by density functional theory [64], we can find an estimate for the intermolecular interaction energies. Starting with the charge distribution of isolated molecules that exhibit a distinct quadrupole moment, the molecular charge distributions were represented by discrete point charges, which mediate the lateral electrostatic coupling. Slight adjustment of the effective charges in our disc shaped molecules allows to reproduce the experimentally observed coverage-dependence of the TPD traces. The resulting simulated TPD traces are presented in Figures 3 (c) and (d) for PEN and PFP, respectively. With kinetic parameters that are close to those derived from the HRV experiments (PEN: E_d = 121 kJ/mol, ν = $10^{12.5}$ s^{-1}; PFP: E_d = 133 kJ/mol, ν = $10^{12.7}$$s^{-1}$), the lowest coverage TPD traces can be reproduced accurately with Coulomb charges of q = 0.07e for PEN and q = 0.105e for PFP (for details on the modeled charge distribution, see the Supporting Information). The Coulombic intermolecular repulsion leads, as expected, to a peak shift towards lower temperatures for increasing coverages as well as a significant broadening of the TPD traces of the saturated monolayers, in particular in the case of PFP. Only at intermediate coverages, the simulated coverage-dependent peak shift is less pronounced than the experimentally observed shift. This suggests that the real interaction potential has a somewhat longer range, i.e. decreases less strongly with distance, than the one used for the simulation.
Our simulation further allows to derive an effective potential V for intermolecular interactions as a function of the surface coverage Θ that is inversely related to the average intermolecular nearest-neighbor distance. The effective lateral interaction potentials of PEN and PFP obtained from our MD simulations are shown as circles in the inset of Figures 3 (c) and (d). Both curves can be modeled accurately by a simple exponential function of the form $V(\theta) = a\theta^b$. Fitting of this function to the simulated potential yields similar exponents b for PEN and PFP with (2.6±0.1) and

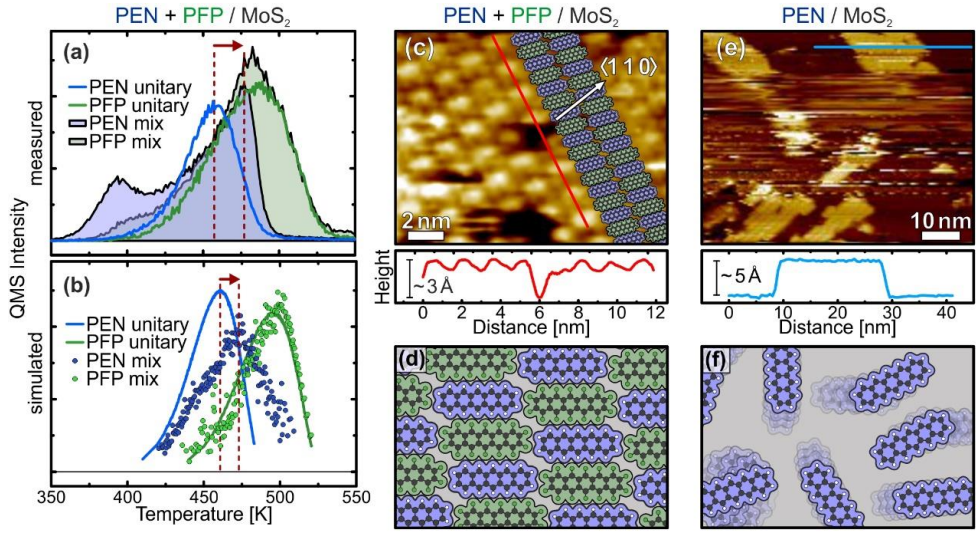

Figure 4: (a) Quasi-simultaneously recorded TPD traces of 0.6 ML PEN and 0.8 ML PFP in a mixed film (filled traces) and unitary films of 0.4 ML PEN (blue line) and 0.7 ML PFP (green line) on MoS_2. (b) Simulated TPD traces of a randomized mixture of 0.5 ML PEN and 0.5 ML PFP (dots), 0.5 ML PEN (blue line) and 0.5 ML PFP (green line). (c) STM micrograph (-2.5 V, 250 pA, 110 K) of an intermixed monolayer of PEN and PFP on MoS_2 with a linescan. The inset illustrates the alternating molecular structure. The substrate azimuth was determined from low-energy electron diffraction. (d) Illustration of the intermixed monolayer. (e) STM micrograph (-3.76 V, 120 pA, 110 K) of 8 Å PEN on MoS_2 after annealing to 390 K for 1 min. (f) Illustration of a highly mobile (sub-) monolayer of PEN.

(2.5±0.1), respectively. For the maximum interaction energy that is given by the factor a, we find (8.2±0.1) kJ/mol and (12.5±0.2) kJ/mol for PEN and PFP, respectively. This corresponds to ~7% and ~9% of the desorption energy in the zero-coverage limit, respectively, in line with a result of ~7% reported for *para*-hexaphenyl on Au(111) [38].

The coverage-dependence of the interaction potential obtained from our MC TPD simulation can be plugged into the Polanyi-Wigner equation (equation 1) to determine the interaction energies directly from the experimental data. Therefore, we have used the prefactors that were also used for the MC TPD simulations, which are in agreement with the HRV results, and fitted the Polanyi-Wigner equation with a coverage-dependent desorption energy $E_d(\theta) = E_0 - a\theta^b$ to the sets of TPD traces shown in Figures 3 (a) and (b). The resulting fits (see Supporting Information) are in excellent agreement with the experimental TPD traces for all coverages. For the desorption energies (lines in Figures 3 (e) and (f)), we find $E_d(\theta)$ =(121 - 7.5 $\theta^{1.5}$) kJ/mol for PEN and $E_d(\theta)$ =(133 - 14.5 $\theta^{1.7}$) kJ/mol for PFP. In comparison to the simulation, the exponents are significantly smaller, reflecting the finding that our model somewhat underestimates the range of the intermolecular interactions. Nonetheless, the maximum interaction energies are of the same order of magnitude as those of the simulation with 7.5 kJ/mol for PEN and 14.5 kJ/mol for PFP and therefore still of the order of magnitude of only 10% of the zero-coverage desorption energy.

Intermixed Monolayers. The above discussed TPD data shows that the unitary submonolayer phases of PEN and PFP are mainly entropically stabilized, i.e. by an entropy gain through the high mobility of the adsorbed molecules. These are unfavorable conditions for the formation of stable, densely packed monolayers, in which the mobility of the molecules and thus the entropic stabilization of the layer would be reduced. Therefore, it is desirable to achieve enthalpic stabilization of the monolayer by introducing attractive intermolecular interactions, which result in the formation of ordered, close-packed molecular monolayers.

In a previous study on intermixed thin multilayer films of PEN and PFP, we found evidence for intermolecular attraction [31]. To test whether these attractive forces also occur laterally in monolayer films with a flat-lying molecular orientation, we have conducted further TPD measurements on mixed monolayers of PEN and PFP. Figure 4 (a) shows the quasi-simultaneously recorded TPD traces of PEN (filled blue curve) and PFP (filled green curve) from an equimolar intermixture with a coverage slightly exceeding 1 ML, resulting in small multilayer desorption peaks. In comparison to the unitary PEN monolayer (blue line), the ascending flank of the PEN monolayer signal of the mixed film (filled blue curve) is less steep and the peak maximum shifts by approximately 20 K to higher temperatures, followed by a rather sharp high-temperature tail. In contrast, the TPD trace of PFP (filled green curve) is almost identical to the unitary phase (green line). Above 500 K, the TPD traces of unitary and intermixed PFP are equal because PEN has completely desorbed, leaving a nearly pristine PFP film on the surface.

Due to a continuous variation of the stoichiometric ratio of PEN:PFP during the desorption experiment, the desorption

parameters are continuously changing. This is equivalent to a superposition of many partially overlapping desorption peaks that are slightly shifted on the temperature axis with respect to each other. This results in a distorted leading edge that yields unreasonable results using the mLEA. A HRV analysis is difficult since precise reproducibility of two coverages (for PEN and PFP) is needed to achieve identical samples for the several required experiments with different heating rates. Hence, the TPD traces of the mixed film were only analyzed qualitatively. The modified desorption behaviors compared to the unitary phases of PEN and PFP can be explained by an interplay of intermolecular and molecule-substrate interactions. From our TPD traces of unitary PEN and PFP monolayers, we know that PFP desorbs at higher temperatures than PEN. Due to an electrostatic attraction between the opposing quadrupole moments of PEN and PFP [64], PFP acts as an anchor for PEN by increasing its desorption energy. However, since PFP binds stronger to MoS_2 than PEN, PEN still desorbs at a higher rate than PFP until finally, only PFP remains on the substrate surface. At this point, the desorption rate of PEN rapidly drops to zero and the descending flanks of the unitary and intermixed phase PFP monolayer TPD traces are equal.

This behavior is well reproduced by our MC TPD simulations, as shown in Figure 4 (b). Note that the same interaction parameters were used for the simulation of TPD traces of unitary and mixed films of PEN and PFP. As in the experiment, we find a shift of the PEN desorption peak of the mixed film (blue dots) to higher temperatures, i.e. closer to the PFP peak, in comparison to the unitary PEN film (blue line). Although the simulated peak shift is somewhat smaller with only approximately 15 K in comparison to the experiment, the slope of the ascending flank of PEN in the mixed film is reduced in comparison to the unitary film, as in the experiment. For PFP, the simulation shows no significant difference between unitary (green line) and mixed phase (green dots), which agrees well with the experiment. Only a slight shift of the PFP peak of the mixed film to higher temperatures can be seen that indicates a stabilization of PFP beyond the stabilization of the unitary PFP monolayer due to the mutual attraction of PEN and PFP.

The above discussed TPD data illustrates the importance of intermolecular interactions for the kinetic parameters, showing that molecular monolayers can be stabilized by electrostatic attraction in mixed films. However, since a quantitative analysis of the TPD data is not possible at the current state for mixed films of PEN and PFP as the mixing ratio of PEN and PFP changes dynamically, no conclusion can be drawn on the molecular mobility in the mixed film. To find out whether the mutual attraction of PEN and PFP can reduce molecular mobility and lead to the formation of an ordered, densely packed molecular layer, we have performed STM measurements on unitary and mixed films at temperatures of 110 K. Figure 4 (c) shows an STM micrograph of a mixed monolayer of PEN and PFP that clearly shows an ordered molecular structure. A contrast between neighboring molecules is visible that is caused by different electronic properties of PEN and PFP, showing that a well-ordered stoichiometric 1:1 intermixture is formed as illustrated in the inset of the figure. The linescan along a molecular row (bottom panel) shows the alternating structure of the mixed film more clearly. A vacancy in the molecular adlayer reveals a layer height of approximately 3 Å, corresponding to a flat-lying molecular orientation. A more detailed analysis of the molecular geometry can be found in the Supporting Information. The molecular arrangement is illustrated in Figure 4 (d).

In addition to the mixed phase, we have also conducted STM measurements on unitary monolayers on MoS_2. Imaging of these films has proven to be rather challenging, which can be directly attributed to the high lateral mobility of the molecules. Figure 4 (e) shows an STM micrograph of 4 Å PEN on MoS_2, corresponding to a coverage slightly above one monolayer. While no molecular structure could be resolved in the first layer and the image shows areas of instable contact caused by frequent tip changes, it is possible to image molecular islands in the second layer. A linescan across a bilayer island (bottom panel) reveals a step height of about 5 Å, which is larger than the typical height of 3 Å observed for flat-lying acenes. These findings are perfectly in line with our NEXAFS and TPD data: In the (sub-) monolayer regime, PEN lies flat on the MoS_2 surface. Due to their mobility, it is not possible to image molecules in the first layer at a temperature of 110 K, as illustrated in Figure 4 (f). Upon multilayer growth, however, PEN tilts and forms a herringbone structure, leading to condensation of the highly mobile phase and formation of islands that can be imaged by STM. The molecular tilt in the multilayer phase causes an increased step height between the flat-lying first and tilted second on tilted first layer, as reported for PEN on HOPG in a previous study [43].

The combination of STM with TPD reveals that the mutual electrostatic attraction of PEN and PFP is indeed capable of inducing the formation of well-ordered, close-packed molecular monolayers on MoS_2, at least at a temperature of 110 K, at which PEN is still mobile in its unitary phase. In the mixed film, the attractive forces between PEN and PFP add an enthalpic stabilization, which compensates for a potential loss of entropic stabilization.

4. CONCLUSIONS

In this study, we show that PEN and PFP on MoS_2 form (sub-) monolayers that are stabilized with respect to their multilayer phases, preventing dewetting and 3D growth of the nominal monolayer. In contrast to, for instance, adsorption on metallic surfaces, the origin of this stabilization lies in the entropy of the mobile molecular film rather than the strength of the interfacial bond. This entropic stabilization effect has previously been reported for 2,4'-bis(terpyridine) on HOPG [50], another planar polycyclic aromatic hydrocarbon on a weakly interacting substrate and can be expected to be a general phenomenon occurring for planar polycyclic aromatic molecules adsorbed on weakly interacting substrates (with a small corrugation of the molecule-substrate interaction potential).

The high mobility of the molecules in the unitary monolayers can be ascribed to a combination of a relatively weak interface bond and intermolecular repulsion. Consequently, the entropic stabilization is an interface effect that can only occur in the (sub-) monolayer regime, as is illustrated in Figure 5: In multilayer films, molecules adopt packing motifs that lead to stabilizing attractive contributions to the intermolecular interactions, for instance a herringbone packing

motif (Figure 5 (a)), whereas in (sub-) monolayers, molecules are forced into a flat-lying orientation by the substrate that results in a repulsive intermolecular interactions in unitary films (Figure 5 (b)) and attractive interactions between PEN and PFP (Figure 5 (c)).

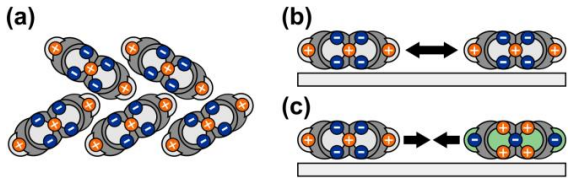

Figure 5: Illustration of electrostatic intermolecular interactions of PEN in a multilayer film with a herringbone packing motif (a), in a (sub-) monolayer film of PEN (b) and a mixed (sub-) monolayer film of PEN and PFP (c), shown in a side view along the long molecular axis. The molecular quadrupole moments are indicated by negative (blue) and positive (orange) point charges.

These findings show that, in spite of a relatively weak interface bond, nominal molecular monolayers can be prepared on TMDCs and other weakly interacting substrates by means of selective desorption of multilayers, which is a more scalable process than the direct deposition of monolayers. The stabilization comes, however, at the price of reduced structural order and packing density: a mobile monolayer cannot be a highly ordered nanostructure. Nonetheless, such monolayers can find technical applications, for instance as spacer layers between layers of 2DMs.
Finally, we have shown that attractive intermolecular interactions can further stabilize molecular monolayers even though attraction is likely to reduce the entropic stabilization of unitary films, thus paving the way for the preparation of highly ordered molecular films on weakly interacting substrates. Attractive intermolecular interactions in monolayers are often found in heterostructures of fluorinated and non-fluorinated OSCs [74-78], so the concept of stabilization by intermolecular attraction should be applicable beyond our model system of PEN and PFP. Molecules that are only partially fluorinated, such as the unilaterally fluorinated 1,2,10,11,12,14-hexafluoropentacene [79], could extend this concept to homomolecular films.

ASSOCIATED CONTENT

Supporting Information. Detailed description of the MC TPD simulation, Kelvin probe measurements of MoS_2 and molecular films on MoS_2, analysis of TPD traces, derivation of equations from transition state theory, structural analysis of STM data. This material is available free of charge via the Internet at http://pubs.acs.org.

AUTHOR INFORMATION

Corresponding Author

* E-mail: gregor.witte@physik.uni-marburg.de

ORCID

Stefan R. Kachel: 0000-0003-0323-2440
Pierre-Martin Dombrowski: 0000-0001-5203-4163
Tobias Breuer: 0000-0002-9962-9444
J. Michael Gottfried: 0000-0001-5579-2568
Gregor Witte: 0000-0003-2237-0953

Author Contributions

† S.R.K. and P.-M.D. contributed equally to this work.

G.W. and T.B. initiated the project. T.B. and P.-M.D. performed the NEXAFS measurements. P.-M.D. performed the STM and Kelvin Probe measurements and developed and ran the MC TPD simulation. S.R.K., P.-M.D. and T.B. performed the TPD measurements. S.R.K. analyzed the experimental TPD data. P.-M.D., G.W., S.R.K. and J.M.G. wrote the manuscript.

Notes

The authors declare no competing financial interest.

ACKNOWLEDGMENT

We gratefully acknowledge financial support from the German Research Foundation (DFG) in the framework of the Collaborative Research Center 'Structure and Dynamics of Internal Interfaces' (223848855-SFB 1083, TP A2 and TP A4) and the Helmholtz-Zentrum Berlin (electron storage ring BESSY II) for provision of synchrotron radiation at the HE-SGM beamline. We further thank Steffen Zörb (Fachbereich Chemie, Philipps-Universität Marburg) for providing MoS_2 crystals.

ABBREVIATIONS

2D, two-dimensional; 2DM, two-dimensional material; DOF, degree of freedom; HOPG, highly oriented pyrolytic graphite; HRV, heating rate variation; IS, initial state; MC, Monte Carlo; mLEA, modified leading-edge analysis; NEXAFS, near-edge X-ray absorption fine-structure; OSC, organic semiconductor; PEN, pentacene; PFP, perfluoropentacene; QMS, quadrupole mass spectrometer; STM, scanning tunneling microscopy; TDM, transition dipole moment; TMDC, transition metal dichalcogenide; TPD, temperature-programmed desorption; TS, transition state; TST, transition state theory; UHV, ultrahigh vacuum; vdW, van der Waals.

REFERENCES

[1] Novoselov, K. S.; Geim, A. K.; Morozov, S. V.; Jiang, D.; Zhang, Y.; Dubonos, S. V.; Grigorieva, I. V.; Firsov, A. A. Electric Field Effect in Atomically Thin Carbon Films. *Science* **2004**, 306, 666-669.

[2] Novoselov, K. S.; Mishchenko, A.; Carvalho, A.; Castro Neto, A. H. 2D materials and van der Waals heterostructures. *Science* **2016**, 353, aac9439.

[3] Wang, Q. H.; Kalantar-Zadeh, K.; Kis, Andras; Coleman, J. N.; Strano, M. S. Electronics and optoelectronics of two-dimensional transition metal dichalcogenides. *Nat. Nanotechnol.* **2012**, 7, 699-712.

[4] Britnell, L.; Gorbachev, R. V.; Jalil, R.; Belle, B. D.; Schedin, F.; Mishchenko, A.; Georgiou, T.; Katsnelson, M. I; Eaves, L.; Morozov, S. V.; Peres, N. M. R.; Leist, J.; Geim, A. K.; Novoselov, K. S.; Ponomarenko, L. A. Field-Effect Tunneling Transistor Based on Vertical Graphene Heterostructures. *Science* **2012**, 335, 947-950.

[5] Britnell, L.; Ribeiro, R. M.; Eckmann, A.; Jalil, R.; Belle, B. D.; Mishchenko, A.; Kim, Y.-J.; Gorbachev, R. V.; Gorgeiou, T.; Morozov, S. V.; Grigorenko, A. N.; Geim, A. K.; Caisraghi, C.;

Castro Neto, A. H.; Novoselov, K. S. Strong Light-Matter Interactions in Heterostructures of Atomically Thin Films. *Science* **2013**, 340, 1311-1314.

[6] Geim, A. K.; Grigorieva, I. V. Van der Waals heterostructures. *Nature* **2013**, 499, 419-425.

[7] Withers, F.; Del Pozo-Zamudio, O.; Schwarz, S.; Dufferwiel, S.; Walker, P. M.; Godde, T.; Rooney, A. P.; Gholinia, A.; Woods, C. R., Blake, P.; Haigh, S. J.; Watanabe, K.; Taniguchi, T.; Aleiner, I. L.; Geim, A. K.; Fal'ko, V. I.; Tartakovskii, A. I.; Novoselov, K. S. WSe_2 Light-Emitting Tunneling Transistors with Enhanced Brightness at Room Temperature. *ACS Nano Lett.* **2015**, 15, 8223-8228.

[8] Zeng, M.Q.; Xiao, Y.; Liu, J.X.; Yang, K., Fu, L. The organic—2D transition metal dichalcogenide interface. Exploring Two Dimensional Materials towards the Next-Generation Circuits: From Monolayer Design to Assembly Control. *Chem. Rev.* **2018**, 118, 6236-6296.

[9] Akinwande, D.; Petrone, N.; Hone, J. Two-dimensional flexible nanoelectronics. *Nat. Commun.* **2014**, 5, 5678.

[10] Zhu, W.; Park, S.; Yogeesh, M. N.; Akinwande, D. Advancements in 2D flexible nanoelectronics: from material perspectives to RF applications. *Flex. Print. Electron.* **2017**, 2, 043001.

[11] Gobbi, M.; Orgiu, E.; Samori, P. When 2D Materials Meet Molecules: Opportunities and Challenges of Hybrid Organic/Inorganic van der Waals Heterostructures. *Adv. Mater.* **2018**, 30, 1706103.

[12] Huang, Y. L.; Zheng, Y. J.; Song, Z.; Chi, D.; Wee, A. T. S.; Quek, S. Y. The organic—2D transition metal dichalcogenide interface. *Chem. Soc. Rev.* **2018**, 47, 3241-3264.

[13] Huang, Y.; Zheng, W.; Qiu, Y.; Hu, P. Effects of Organic Molecules with Different Structures and Absorption Bandwidth on Modulating Photoresponse of MoS2 Photodetector. *ACS Appl. Mater. Interfaces* **2016**, 8, 23362-23370.

[14] Gan, L-Y.; Zhang, Q.; Cheng, Y.; Schwingenschlögl, U. Photovoltaic Heterojunctions of Fullerenes with MoS_2 and WS_2 Monolayers. *J. Phys. Chem. Lett.* **2014**, 5, 1445-1449.

[15] Vélez, S.; Ciudad, D.; Island, J.; Buscema, M.; Txoperena, O.; Parui, S.; Steele, G. A.; Casanova, F.; van der Zant, H. S. J.; Castellanos-Gomez, A.; Hueso, L. E. Gate-tunable diode and photovoltaic effect in an organic-2D layered material p-n heterojunction. *Nanoscale* **2015**, 7, 15442-15449.

[16] Jariwala, D.; Howell, S. L.; Chen, K.-S.; Kang, J.; Sangwan, V. K.; Filippone, S. A.; Turrisi, R.; Marks, T. J.; Lauhon, L. J.; Hersam, M. C. Hybrid, Gate-Tunable van der Waals p—n Heterojunctions from Pentacene and MoS_2. *ACS Nano Lett.* **2016**, 16, 497-503.

[17] Homan, S. B.; Sangwan, V. K.; Balla, I.; Bergeron, H.; Weiss, E. A.; Hersam, M. C. Ultrafast Exciton Dissociation and Long-Lived Charge Separation in a Photovoltaic Pentacene—MoS_2 van der Waals heterojunction. *ACS Nano Lett.* **2017**, 17, 164-169.

[18] Chen, R.; Lin, C.; Yu, H.; Tang, Y.; Song, C.; Yuwen, L.; Li, H.; Xie, X.; Wang, L.; Huang, W. Templating C_{60} on MoS_2 Nanosheets for 2D Hybrid van der Waals p-n Nanoheterojunctions. *Chem. Mater.* **2016**, 28, 4300-4306.

[19] Kim, J.-K.; Cho, K.; Kim, T.-Y.; Pak, J.; Jang, J.; Song, Y.; Kim, Y.; Choi, B. Y.; Chung, S.; Hong, W.-K.; Lee, T. Trap-mediated electronic transport properties of gate-tunable pentacene/MoS_2 p-n heterojunction diodes. *Sci. Rep.* **2016**, 6, 36775.

[20] Petoukhoff, C. E.; Krishna, M. B. M.; Vori, D.; Bozkurt, I.; Deckoff-Jones, S.; Chhowalla, M.; O'Carroll, D. M.; Dani, K. M. Ultrafast Charge Transfer and Enhanced Absorption in MoS_2-Organic van der Waals Heterojunctions Using Plasmonic Metasurfaces. *Phys. Rev. Lett.* **2002**, 89. 196103.

[21] Dong, J.; Liu, F.; Wang, F.; Wang, J.; Li, M.; Wen, Y.; Wang, L.; Wang, G.; He, J.; Jiang, C. Configuration-dependent anti-ambipolar van der Waals p-n heterostructures based on pentacene single crystal and MoS_2. *Nanoscale* **2017**, 9, 7519-7525.

[22] Park, H. J.; Park, C.-J.; Kim, J. Y.; Kim, M. S.; Kim, J.; Joo, J. Hybrid Characteristics of MoS_2 Monolayer with Organic Semiconducting Tetracene and Application to Anti-Ambipolar Field Effect Transistor. *ACS Appl. Mater. Interfaces* **2018**, 10, 32556-32566.

[23] Zhang, L.; Sharma, A.; Zhu, Y.; Zhang, Y.; Wang, B.; Dong, M.; Nguyen, H. T.; Wang, Z.; Wen, B.; Cao, Y.; Liu, B.; Sun, X.; Yang, J.; Li, Z.; Kar, A.; Shi, Y.; Macdonald, D.; Yu, Z.; Wang, X.; Lu, Y. Efficient and Layer-Dependent Exciton Pumping across Atomically Thin Organic-Inorganic Type-I Heterostructures. *Adv. Mater.* **2018**, 30. 1803986.

[24] Shen, N.; Tao, G. Charge Transfer and Interface Engineering of the Pentacene and MoS_2 Monolayer Complex. *Adv. Mater. Interfaces* **2017**, 4, 1601083.

[25] Xie, X.-Y.; Liu, X.-Y.; Fang, Q.; Fang, W.-H.; Cui, G. Photoinduced Carrier Dynamics at the Interface of Pentacene and Molybdenum Disulfide. *J. Phys. Chem. A* **2019**, 123, 7693-7703.

[26] Söhnchen, S.; Lukas, S.; Witte, G. Epitaxial growth of pentacene films on Cu(110). *J. Chem. Phys.* **2004**, 121, 525-534.

[27] Widdascheck, F.; Hauke, A. A.; Witte, G. A Solvent-Free Solution: Vacuum-Deposited Organic Monolayers Modify Work Functions of Noble Metal Electrodes. *Adv. Funct. Mater.* **2019**, 1808385.

[28] Barth, J. V.; Costantini, G.; Kern, K. Engineering atomic and molecular nanostructures at surfaces. *Nature* **2005**, 437, 671-679.

[29] Liu, H.; Xu, J.; Li, Y.; Li, Y. Aggregate Nanostructures of Organic Molecular Materials. *Acc. Chem. Res.* **2010**, 43, 1496-1508.

[30] Sakamoto, Y.; Suzuki, T.; Kobayashi, M.; Gao, Y.; Fukai, Y.; Inoue, Y.; Fumio, S.; Tokito, S. Perfluoropentacene: High-Performance p-n Junctions and Complementary Circuits with Pentacene. *J. Am. Chem. Soc.* **2004**, 126, 8138-8140.

[31] Breuer, T; Witte, G. Thermally activated intermixture in pentacene-perfluoropentacene heterostructures. *J. Chem. Phys.* **2013**, 138, 114901.

[32] Breuer, T.; Maßmeyer, T.; Mänz, A.; Zoerb, S.; Harbrecht, B.; Witte, G. Structure of van der Waals bound hybrids of organic semiconductors and transition metal dichalcogenides: the case of acene films on MoS_2. *Phys. Status Solidi RRL* **2016**, 10, 905-910.

[33] Lukas, S.; Vollmer, S.; Witte, G.; Wöll, C. Adsorption of acenes on flat and vicinal Cu(111) surfaces: Step induced formation of lateral order. *J. Chem. Phys.* **2001**, 114, 10123-10130.

[34] Fichthorn, K. A.; Miron, R. A. Thermal Desorption of Large Molecules from Solid Surfaces. *Phys. Rev. Lett.* **2002**, 89. 196103.

P4

[35] Müllegger, S.; Salzmann, I.; Resel, R.; Hlawacek, G.; Teichert, C.; Winkler, A. Growth kinetics, structure and morphology of para-quaterphenyl thin films on gold(111). *J. Chem. Phys.* **2004**, 121, 2272-2277.

[36] Müllegger, S.; Stranik, O.; Zojer, E.; Winkler, A. Adsorption, initial growth and desorption kinetics of p-quaterphenyl on polycrystalline gold surfaces. *Appl. Surf. Sci.* **2004**, 221, 184-196.

[37] Mülleger, S.; Winkler, A. The influence of carbon on the adsorption/desorption kinetics and monolayer formation of p-quaterphenyl on Au(111).

[38] Müllegger, S.; Winkler, A. Hexaphenyl thin films on clean and carbon covered Au(111) studied with TDS and LEED. *Surf. Sci.* **2006**, 600, 1290-1299.

[39] Käfer, D.; Witte, G. Evolution of pentacene films on Ag(111): Growth beyond the first monolayer. *Chem. Phys. Lett.* **2007**, 442, 376-383.

[40] Frank, P.; Koch, N.; Koini, M.; Rieger, R.; Müllen, K.; Resel, R.; Winkler, A. Layer growth and desorption kinetics of a discoid molecular acceptor on Au(111). *Chem. Phys. Lett.* **2009**, 473, 321-325.

[41] Käfer, D.; Wöll, C.; Witte, G. Thermally activated dewetting of organic thin films: the case of pentacene on SiO_2 and gold. *Appl. Phys. A* **2009**, 95, 273-284.

[42] Frank, P.; Djuric, T.; Koini, M.; Salzmann, I.; Rieger, R.; Müllen, K.; Resel, R.; Koch, N.; Winkler, A. Layer growth, Thermal Stability, an Desorption Behavior of Hexaaza-triphenylene-hexacarbonnitrile on Ag(111). *J. Phys. Chem. C* **2010**, 114, 6650-6657.

[43] Götzen, J.; Käfer, D.; Wöll, C.; Witte, G. Growth and structure of pentacene films on graphite: Weak adhesion as a key for epitaxial film growth. *Phys. Rev. B* **2010**, 114, 6650-6657.

[44] Winkler, A. Initial stages of organic film growth characterized by thermal desorption spectroscopy. *Surf. Sci.* **2016**, 643, 124-137.

[45] Maaß, F.; Jiang, Y.; Liu, W.; Tkatchenko, A.; Tegeder, P. Binding energies of benzene on coinage metal surfaces: Equal stability on different metals. *J. Chem. Phys.* **2018**, 148, 214703.

[46] Klein, B. P.; van der Heijden, N.; Kachel, S. R.; Franke, M.; Krug, C. K.; Greulich, K. K.; Ruppenthal, L.; Müller, P.; Rosenow, P.; Parhizkar, S.; Bocquet, F. C.; Schmid, M.; Hieringer, W.; Maurer, R. J.; Tonner, R.; Kumpf, C.; Swart, I.; Gottfried, J. M. Molecular Topology and the Surface Chemical Bond: Alternant Versus Nonalternant Aromatic Systems as Functional Structural Elements. *Phys. Rev. X.* **2019**, 9, 011030.

[47] Maaß, F.; Ajdari, M.; Kabeer, F. C.; Vogtland, M.; Tkatchenko, A.; Tegeder, P. Nonadditivity of the Adsorption Energies of Linear Acenes on Au(111): Molecular Anisotropy and Many-Body Effects. *J. Phys. Chem. Lett.* **2019**, 10, 1000-1004.

[48] Kachel, S. R.; Klein, B. P.; Morbec, J. M.; Schöninger, M.; Hutter, M.; Schmid, M.; Kratzer, P.; Meyer, B.; Tonner, R.; Gottfried, J. M. Chemisorption and Physisorption at the Metal/Organic Interface: Bond Energies of Naphthalene and Azulene on Coinage Metal Surfaces. *J. Phys. Chem. C* **2020**, 124, 8257-8268.

[49] Zacharia, R.; Ulbricht, H.; Hertel, T. Interlayer cohesive energy of graphite from thermal desorption of polyaromatic hydrocarbons. *Phys. Rev. B.* **2004**, 69, 155406.

[50] Roos, M.; Breitruck, A.; Hoster, H. E.; Behm, R. J. Entropic stabilization of large adsorbates on weakly binding substrates—a thermal desorption and scanning tunneling microscopy study. *Phys. Chem. Chem. Phys.* **2010**, 12, 818-822.

[51] Weippert, J.; Hauns, J.; Bachmann, J.; Böttcher, A.; Yao, X.; Yang, B.; Narita, A.; Müllen, K.; Kappes, M. M. A TPD-based determination of the graphite interlayer cohesion energy. *J. Chem. Phys.* **2018**, 149, 194701.

[52] Weippert, J.; Huber, P.; Schulz, A.; Amsharov, K. Y.; Böttcher, A.; Kappes, M. M. Influence of Dispersion Interactions on the Thermal Desorption of Nonplanar Polycyclic Aromatic Hydrocarbons on HOPG. *Phys. Status Solidi RRL* **2019**, 1900348.

[53] Tait, S. L.; Dohnálek, Z.; Campbell, C. T.; Kay, B. D. n-alkanes on MgO(100). II. Chain length dependence of kinetic desorption parameters for small n-alkanes. *J. Chem. Phys.* **2005**, 122, 164708.

[54] Redhead, P. A. Thermal Desorption of Gases. *Vacuum* **1962**, 12, 203-211.

[55] Piña, C.; Bosch, P.; Acosta, D.; Barreto, J.; Vazquez, A.; Camarillo, E. Growth of MoS_2 and MoS_2: Co crystals using I_2 as transport material. *J. Cryst. Growth* **1989**, 96, 685-690.

[56] Breuer, T.; Klues, M.; Witte, G. Characterization of orientational order in π-conjugated molecular thin films by NEXAFS. *J. Electron Spectrosc. Relat. Phenomena* **2015**, 204, 102-115.

[57] Meng, B.; Weinberg, W. H. Monte Carlo simulations of temperature programmed desorption spectra. *J. Chem. Phys.* **1994**, 100, 5280-5289.

[58] Individual heating steps took approximately 5 min. Heating was stopped for the NEXAFS measurements, but sample temperatures decreased rather slowly due to the thermal capacity of the sample mount.

[59] Marks, M.; Schmidt, C.; Schwalb, C. H.; Breuer, T.; Witte, G.; Höfer, U. Temperature Dependent Structural Phase Transition at the Perfluoropentacene/Ag(111) Interface. *J. Phys. Chem. C* **2012**, 116, 1904-1911.

[60] Polanyi, M.; Wigner, E. Über die Interferenz von Eigenschwingungen als Ursache von Energieschwankungen und chemischer Umsetzungen. *Z. Phys. Chem.* **1928**, 139A, 439-452.

[61] Habenschaden, E.; Küppers, J. Evaluation of Flash Desorption Spectra. *Surf. Sci.* **1984**, 138k L147-L150.

[62] Oja, V.; Suuberg, E. M. Vapor Pressures and Enthalpies of Sublimation of Polycyclic Aromatic Hydrocarbons and Their Derivatives. *J. Chem. Eng. Data* **1998**, 43, 486-492.

[63] Radchenko, L. G.; Kitaigorodskii, A. I. The Vapor Pressures and Heats of Sublimation of Naphthalene, Biphenyl, Octafluoronaphthalene, Decafluorobiphenyl, Acenaphthene and α-Nitronaphthalene. *Russ. J. Phys. Chem.* **1974**, 48, 1595-1596.

[64] Klues, M.; Witte, G. Crystalline packing in pentacene-like organic semiconductors. *CrystEngComm* **2018**, 20, 63-74.

[65] Gottfried, J. M.; Vestergaard, E. K.; Bera, P.; Campbell, C. T. Heat of Adsorption of Naphthalene on Pt(111) Measured by Adsorption Calorimetry. *J. Phys. Chem. B* **2006**, 110, 17539-17545.

[66] Tait, S. L.; Bohnálek, Z.; Campbell, C. T.; Kay, B. D. n-alkanes on MgO(100). I. Coverage-dependent desorption kinetics of n-butane. *J. Chem. Phys.* **2005**, 122, 164707.

[67] Ulbricht, H.; Zacharia, R.; Cindir, N.; Hertel, T. Thermal desorption of gases and solvents from graphite and carbon nanotube surfaces. *Carbon* **2006**, 44, 2931-2942.

[68] Thrower, J. D.; Friis, E. E.; Skov, A. L.; Nilsson, L.; Andersen, M.; Ferrighi, L.; Jørgensen, B.; Baouche, S.; Balog, R.; Hammer, B.; Hornekær, L. Interaction between Coronene and Graphite from Temperature-Programmed Desorption and DFT-vdW Calculations: Importance of Entropic Effects and Insights into Graphite Interlayer Binding. *J. Phys. Chem. C* **2013**, 117, 13520-13529.

[69] Schwerwitzl, B.; Resel, R.; Winkler, A. Film growth, adsorption and desorption kinetics of indigo on SiO_2. *J. Chem. Phys.* **2014**, 140, 184705.

[70] Scherwitzl, B.; Lassnig, R.; Truger, M.; Resel, R.; Leising, G.; Winkler, A. Adsorption, desorption, and film formation of quinacridone and its thermal cracking product indigo on clean and carbon-covered silicon dioxide surfaces. *J. Chem. Phys.* **2016**, 145, 094702.

[71] Chorkendorff, I.; Niemantsverdriet, J. W. *Concepts of Modern Catalysis and Kinetics*; Wiley-VCH Verlag GmbH & Co. KGaA: Weinheim, Germany, 2003.

[72] Redondo, A.; Zeiri, Y.; Low, J. J.; Goddard, W. A. Application of transition state theory to desorption from solid surfaces: Ammonia on Ni(111). *J. Chem. Phys.* **1983**, 79, 6410-6415.

[73] Franco-Cañellas, A.; Duhm, S.; Gerla, A.; Schreiber, F. Binding and electronic level alignment of π-conjugated systems on metals. *Rep. Prog. Phys.* **2020**, 83, 066501.

[74] de Oteyza, D. G.; Silanes, I.; Ruiz-Osés, M.; Barrena, E.; Doyle, Bryan P.; Arnau, A.; Dosch, H.; Wakayama, Y.; Ortega, J. E. Balancing Intermolecular and Molecule-Substrate Interactions in Supramolecular Assemblies. *Adv. Funct. Mater.* **2009**, 19, 259-264.

[75] Huang, Y. L.; Li, H.; Ma, J.; Huang, H.; Chen, W.; Wee, A. T. S. Scanning Tunneling Microscopy Investigation of Self-Assembled CuPc/F_{16}CuPc Binary Superstructures on Graphite. *Langmuir* **2010**, 26, 3329-3334.

[76] Wakayama, Y.; de Oteyza, D. G.; Garcia-Lastra, J. M.; Mowbray, D. J. Solid-State Reactions in Binary Molecular Assemblies of F_{16}CuPc and Pentacene. *ACS Nano* **2011**, 5, 581-589.

[77] Goiri, E.; Matena, M.; El-Sayed, A.; Lobo-Checa, J.; Borghetti, P.; Rogero, C.; Detlefs, B.; Duvernay, J.; Ortega, J. E.; de Oteyza, D. G. Self-Assembly of Bicomponent Molecular Monolayers: Adsorption Height Changes and Their Consequences. *Phys. Rev. Lett.* **2014**, 112, 117602.

[78] de Oteyza, D. G.; Garcia-Lastra, J. M.; Goiri, E.; El-Sayed, A.; Wakayama, Y.; Ortega, J. E. Asymmetric Response toward Molecular Fluorination in Binary Copper-Phthalocyanine/Pentacene Assemblies. *J. Phys. Chem. C* **2014**, 118, 18626-18630.

[79] Hofmann, P. E.; Tripp, M. W.; Bischof, D.; Grell, Y.; Schiller, A. L. C.; Breuer, T.; Ivlev, S. I.; Witte, G.; Koert, U. Unilaterally Fluorinated Acenes: Synthesis and Solid-State Properties. *Angew. Chem. Int. E.* **2020**, 59, 1-6.

P4

Insert Table of Contents artwork here

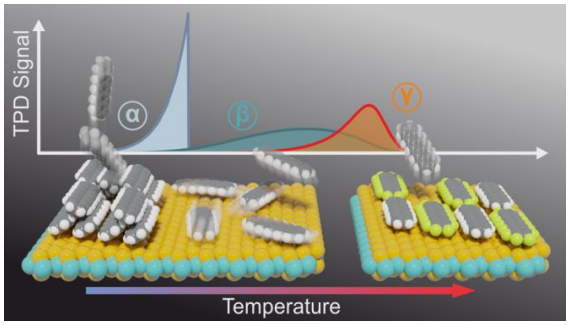

13

Supporting Information

Engineering of TMDC-OSC Hybrid Interfaces: The Thermodynamics of Unitary and Mixed Acene Monolayers on MoS_2

Stefan R. Kachel [1,†], *Pierre-Martin Dombrowski* [2,†], *Tobias Breuer* [2], *J. Michael Gottfried* [1], *Gregor Witte* [2,*]

[1] Fachbereich Chemie, Philipps-Universität Marburg, Hans-Meerwein-Straße 4, 35032 Marburg, Germany

[2] Fachbereich Physik, Philipps-Universität Marburg, Renthof 7, 35032 Marburg, Germany

**E-Mail: gregor.witte@physik.uni-marburg.de*

†S.R.K. and P.-M.D. contributed equally to this work.

P4

Contents

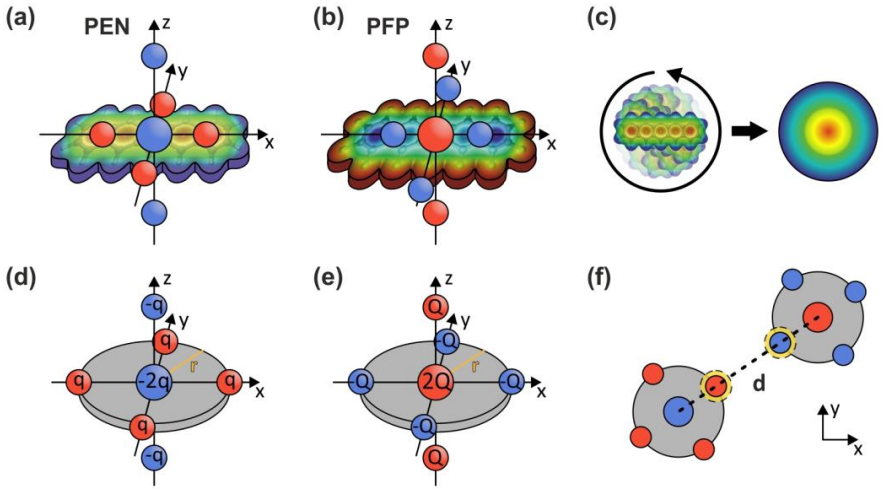

1. Details on the Monte Carlo simulations of TPD traces

Figure S1: (a) and (b) Visualization of the quadrupole moments of PEN and PFP, respectively, as point charges (negative charges are blue, positive ones red) together with the molecular electrostatic potentials (MEPs). (c) Superposition of differently oriented PEN molecules with their MEPs. The average charge distribution is modeled as a circular disc with positive charges at the outer rim of the molecule and a negative charge at the center. (d) and (e) Illustration of the disc shaped models of PEN and PFP, respectively, with location of the point charges. (f) Illustration of the geometry for pair-wise intermolecular interactions. The yellow circles indicate the positions of H or F atoms for van der Waals interactions.

The Monte Carlo simulations of TPD traces presented in this work are based on a modified version of the algorithm described by Meng and Weinberg in Reference [S1]. Structural configurations of molecules within a unit surface (with periodic boundary conditions) are used to calculate interaction energies V_i for individual molecules. These interaction energies then effect desorption probabilities through the microscopic rate equation

$$r_i = \nu \exp\left(\frac{E_0 - V_i}{R\,T}\right). \qquad \text{(S1)}$$

Here, r_i is the rate of desorption of the molecule with index i, ν and E_0 are the prefactor and activation energy, respectively, for thermal desorption of a given molecular species in the limit of zero coverage, R is the gas constant and T is the surface temperature.

For intermolecular interactions, we consider only van der Waals (vdW) and electrostatic interactions. Due to the absence of Pauli repulsion and any significant interface dipole formed upon adsorption of the molecule on the MoS_2(0001) surface [S2, S3] we can neglect any substrate-mediated intermolecular interactions that would, for instance, be present on metallic surface. We have verified the absence of any notable interface dipole by measurements of the work functions of different molecular films of PEN and PFP on a MoS_2 crystal as well as the clean crystal surface, finding no significant differences (cf. Table S1).

P4

The electrostatic interactions in our model are based on the molecular quadrupole moments of PEN and PFP that are the first non-zero terms in the multipole expansion of the electrostatic intermolecular interactions of PEN and PFP [S4]. In the far-field approximation, these quadrupole moments can be represented by seven point charges per molecule as illustrated in Figures S1 (a) and (b) for PEN and PFP, respectively. Since PEN and PFP are highly mobile on MoS_2 at (sub-) monolayer coverages, as evidenced by our experimental TPD data, molecules are not restricted to specific adsorption sites and relative orientations to the substrate, but can move freely across (and rotate freely on) the MoS_2 surface. Consequently, there is a multitude of relative orientations of molecules for pair-wise intermolecular interactions as illustrated in Figure S1 (c). We simplify our model by modeling molecules as two-dimensional circular discs, thus effectively averaging over all possible rotational orientations. The restriction to two dimensions is valid due to the flat-lying orientation of the molecules at (sub-) monolayer coverages that is retained even at elevated temperatures as evidenced by NEXAFS dichroism measurements (see Figure 1). Figures S1 (d) and (e) show the disc shaped models of PEN and PFP, respectively. We chose a disc radius of 5 Å that roughly reflects the molecular dimensions. This radius is equal for PEN and PFP to simplify heteromolecular structures.

The electrostatic potentials of PEN and PFP are modeled by seven point charges per molecule as illustrated in Figures S1 (d) and (e), so that the total charge adds to zero. Although the point charges only describe the molecular quadrupole moments accurately in the far-field approximation, we use this rather simple charge distribution to keep the model simple. Four equal charges are placed at the outer rim of the disc-shaped molecules. Using the quadrupole moments that were calculated in Reference [S4], one can calculate the average quadrupole moment in the molecular plane, $\theta_{\text{in plane}} = \frac{1}{2}(\theta_{xx} + \theta_{yy})$ (PEN: $4.45 \cdot 10^{-34}$ C cm^2;

PFP: $-4.6 \cdot 10^{-34}$ C cm^2). Using the identity $\theta_{xx} = q_x\, x^2$ where x denotes the distance of the charge q_x from the center of the molecule, one can calculate an effective charge q in the molecular plane. Since the two charges outside of the molecular plane on the z-axis have the same absolute value as those in the molecular plane, one can use q and θ_{zz} to calculate the distance of those charges from the molecular plane that is 7.1 Å for both PEN and PFP for a disc radius of 5 Å.

Because we want to neglect molecular orientation, interacting pairs of molecules are assumed to always have the same relative orientation with two charges of the outer rim of each molecule lying on the line connecting the centers of the two molecules, as illustrated in Figure S1 (f). This allows for a parameterization of the pair-wise interaction potential that only depends on the center-to-center distance d:

$$V(d) = \frac{q_1 q_2}{4\pi\varepsilon_0}\left(\frac{10}{d} - \frac{4}{d-r} - \frac{4}{d+r} + \frac{1}{d-2r} + \frac{1}{d+2r} - \frac{8}{\sqrt{d^2+r^2}} + \frac{8}{\sqrt{d^2+z^2}} + \frac{4}{\sqrt{(d-r)^2+r^2}} - \frac{4}{\sqrt{(d-r)^2+z^2}} + \frac{4}{\sqrt{(d+r)^2+r^2}} - \frac{4}{\sqrt{(d+r)^2+z^2}} - \frac{8}{\sqrt{d^2+r^2+z^2}} + \frac{2}{\sqrt{d^2+4r^2}} + \frac{2}{\sqrt{d^2+4z^2}}\right) + V_{\mathrm{vdW}}(d)$$

Here $r = 5$ Å is the disc radius and $z = 7.1$ Å is the distance of the two charges outside of the disc to the disc plane and V_{vdW} is the vdW potential. q_i denotes the charge at the outer rim of molecule i that is positive in the case of PEN and negative in the case of PFP

The vdW potential is added to emulate the vdW box of a molecule. Therefore, we add a single hydrogen or fluorine atom to PEN or PFP, respectively, per molecule at the position of the charge that is closest to the interaction partner as illustrated by the orange circles in Figure S1 (f). We use the MM3 force field vdW potential [S5]

$$V_{\mathrm{vdW}}(d) = \sqrt{\varepsilon_1 \varepsilon_2}\left[184000 \exp\left(\frac{r_1 + r_2}{d}\right) - 2.25\left(\frac{d}{r_1 + r_2}\right)^6\right]$$

where r_i are the vdW radii of the interacting species (hydrogen: 1.62 Å; fluorine: 1.71 Å) and ε_i are the respective energy parameters (hydrogen: 0.082 kJ mol^{-1}; fluorine: 0.31 kJ mol^{-1}) [S6].

Due to the relatively large size of the two molecular species studied in this work, PEN and PFP, discrete adsorption sites are not as clearly defined as in the case of small adsorbates such as CO. Moreover, at the elevated temperatures that occur in our TPD experiments, molecules can be assumed to be able to move freely on a chemically inert substrate such as MoS_2 , which is corroborated by our experimental TPD data and our STM data. Therefore, we model the MoS_2 surface as a Jellium-like system with a uniform binding energy that does not favor specific adsorption sites. Between desorption events, molecules are allowed to diffuse freely until the mean square displacement of all molecules, $\langle \Delta x^2 \rangle$, reaches $\langle \Delta x^2 \rangle = (a\,\overline{D})^2$ where $\overline{D}$ is the nearest-neighbor distance in a uniformly spaced layer at the current surface coverage and a is a scaling factor. Thus, the mean diffusion length scales with surface coverage. We chose $a = 6$ as no notable changes to the simulated TPD traces were observed for larger values of a.

P4

The procedure of the algorithm can be summarized as follows:

(1) Populate a rectangular unit surface with N molecules in a uniformly spaced structure for the given initial surface coverage. Assign Maxwell-Boltzmann distributed random velocities according to the initial surface temperature.
(2) Calculate molecular diffusion while monitoring the mean square displacement $\langle \Delta x^2 \rangle$ of all molecules. Stop diffusion when $\langle \Delta x^2 \rangle = (a\,\overline{D})^2$.
(3) Use equation S1 to calculate the individual desorption rates r_i for all molecules for the given spatial distribution of molecules.
(4) Randomly chose a molecule of index k that is allowed to desorb with a probability $p_k = {}^{r_k}/_{r_{\max}}$ where $r_{\max}$ is the current largest desorption rate of all molecules. Repeat until one molecule desorbs successfully.
(5) Remove the desorbed molecule and increase time by $\tau = (\sum_i r_i)^{-1}$, temperature by $\beta\tau$ and kinetic energy by $k_B\beta\tau$.
(6) Repeat steps (2) – (5) until all molecules have desorbed.

For the initial velocity distribution, we chose a 2D Maxwell-Boltzmann distribution. To account for the coverage-dependent mean free path of the molecules, we chose a first-order approximation and scale the Maxwell-Boltzmann velocities with $(1 - \theta)$ where θ is the surface coverage. Thus, we assign no velocity at maximum coverage and the Maxwell-Boltzmann distribution in the zero-coverage limit.

Periodic boundary conditions are implemented by replicating the rectangular unit surface to create eight identical surrounding unit surfaces. Intermolecular forces and interaction energies are calculated under consideration of these identical neighboring unit surfaces. Inclusion of more neighboring unit surfaces does not change the simulated TPD traces due to the limited range of the intermolecular interactions.

As activation energies and prefactors, we chose the experimental results for the smallest initial coverages. These values are then fine-tuned manually to fit low-coverage simulated TPD traces to the experimental ones. Then, the interaction parameters, i.e., the charges of PEN and PFP, are adjusted so that the larger-coverage TPD traces match the experimentally recorded coverage series.

For heterostructures of PEN and PFP, we assume no structural order with regard to the intermixture. Instead, the species is randomly assigned to each individual molecule with equal probabilities for PEN and PFP, creating a randomized intermixture with an average stoichiometric ratio of 1:1 PEN:PFP. Due to the attraction between PEN and PFP, these randomized distributions tend to form ordered structures of alternating species once the coverage is sufficiently small to allow for structural reconfigurations.

The TPD traces presented in this work are averaged from at least 50 individual computations with randomized starting conditions. For homomolecular films, 64 molecules are used per run. Since in heteromolecular films, two TPD traces are simultaneously created from a single ensemble of molecules, we use 100 molecules for mixed films. Since time / temperature steps vary between these individual runs, TPD traces were averaged over temperature bins of equal size. For homomolecular films, we chose a bin size of 0.1 K. For heteromolecular films, we chose a larger bin size of 0.5 K due to a larger run-to-run variation of the TPD traces caused by the randomization of the stoichiometric ratio and spatial distribution of PEN and PFP in mixed films.

2. Work functions of molecular films on MoS_2

Table S1: Work functions of clean MoS_2, monolayers (nominal thickness: 3 Å) of PEN and PFP on MoS_2, multilayers of PEN and PFP on MoS_2 and a multilayer heterostack of PEN and PFP on MoS_2.

Sample	Work Function [eV]
MoS_2	4.62
MoS_2 + 3 Å PFP	4.59
MoS_2 + 3 Å PEN	4.63
MoS_2 + 20 Å PFP	4.59
MoS_2 + 20 Å PEN	4.58
MoS_2 + 20 Å PFP + 20 Å PEN	4.58

P4

To verify that no interface dipole is formed upon adsorption of PEN and PFP on MoS_2, we have measured the work functions of clean MoS_2, monolayers (nominal thickness: 3 Å) of PEN and PFP on MoS_2, multilayers of PEN and PFP on MoS_2 and a multilayer heterostack of PEN and PFP on MoS_2 by means of the Kelvin probe technique at room temperature. The results are shown in Table S1. As a standard reference, we have used clean Au(111) surfaces with a work function of 5.35 eV [S7]. Repeated measurements on the same sample yield a relative accuracy of 0.02 eV. The absolute values are subject to additional uncertainties due to the referencing process via Au(111).

Considering the relative accuracy of the Kelvin probe measurements, no significant change of the work function of MoS_2 upon deposition of molecular films is found. The absolute value of the work function of bulk MoS_2 lies within the range of reported results from ultraviolet photoelectron spectroscopy of 4.542 eV to 4.75 eV [S8-S10].

3. Leading-edge analysis of multilayer TPD traces

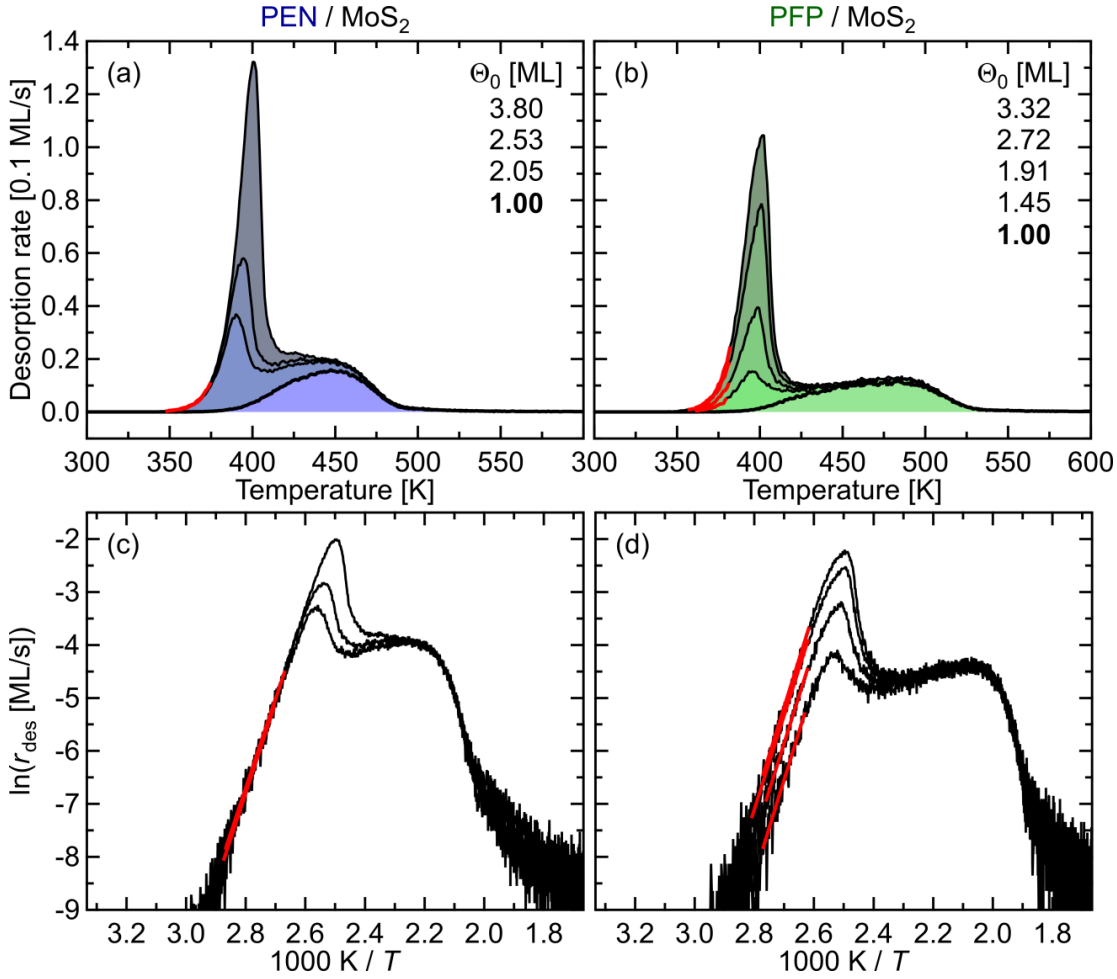

Figure S2: (a) and (b) Series of multilayer TPD traces for different film thicknesses of PEN and PFP, respectively, on MoS_2. Four point-reduction (four measured data points are averaged) for better visualization. Film thicknesses range from 3 Å to 12 Å. The nominal monolayers are marked with bold lines. The section of the leading edge that was used for the leading-edge analysis is indicated by bold, red traces. All measurements were performed with heating rates of 1 K/s by mass spectrometric detection of m/z = 278 amu for PEN and m/z = 530 amu for PFP. (c) and (d) Leading-edge analysis for PEN and PFP on MoS_2, respectively. TPD traces without point-reduction used for the analysis. The linear fit is marked as a bold, red line. The fitting results are given in Table S2.

Leading-edge analysis (LEA), according to:

$$\ln(r) = -\frac{E_d}{RT} + \ln(\nu) \quad \text{(S2)}$$

Table S2: Fitting results ($y = a + bx$) as well as desorption energies and prefactors for the LEA of PEN and PFP on MoS_2 as shown in Figure S2.

P4

Coverage [ML]	a	b [K]	E_d [kJ/mol]	ν [s^{-1}]
		PEN		
2.05	40.9±1.2	-17030±424	141.6±3.5	$10^{17.8\pm0.5}$
2.53	40.6±1.0	-16883±373	140.4±3.1	$10^{17.6\pm0.5}$
3.80	40.6±0.7	-16899±261	140.5±2.2	$10^{17.6\pm0.3}$
		PFP		
1.45	42.3±1.8	-18095±673	150.4±5.6	$10^{18.4\pm0.8}$
1.91	42.3±1.0	-17836±364	148.3±3.0	$10^{18.4\pm0.4}$
2.72	42.6±0.6	-17757±231	147.6±1.9	$10^{18.5\pm0.3}$
3.32	43.3±0.5	-17950±192	149.2±1.6	$10^{18.8\pm0.2}$

4. Modified leading-edge analysis of monolayer

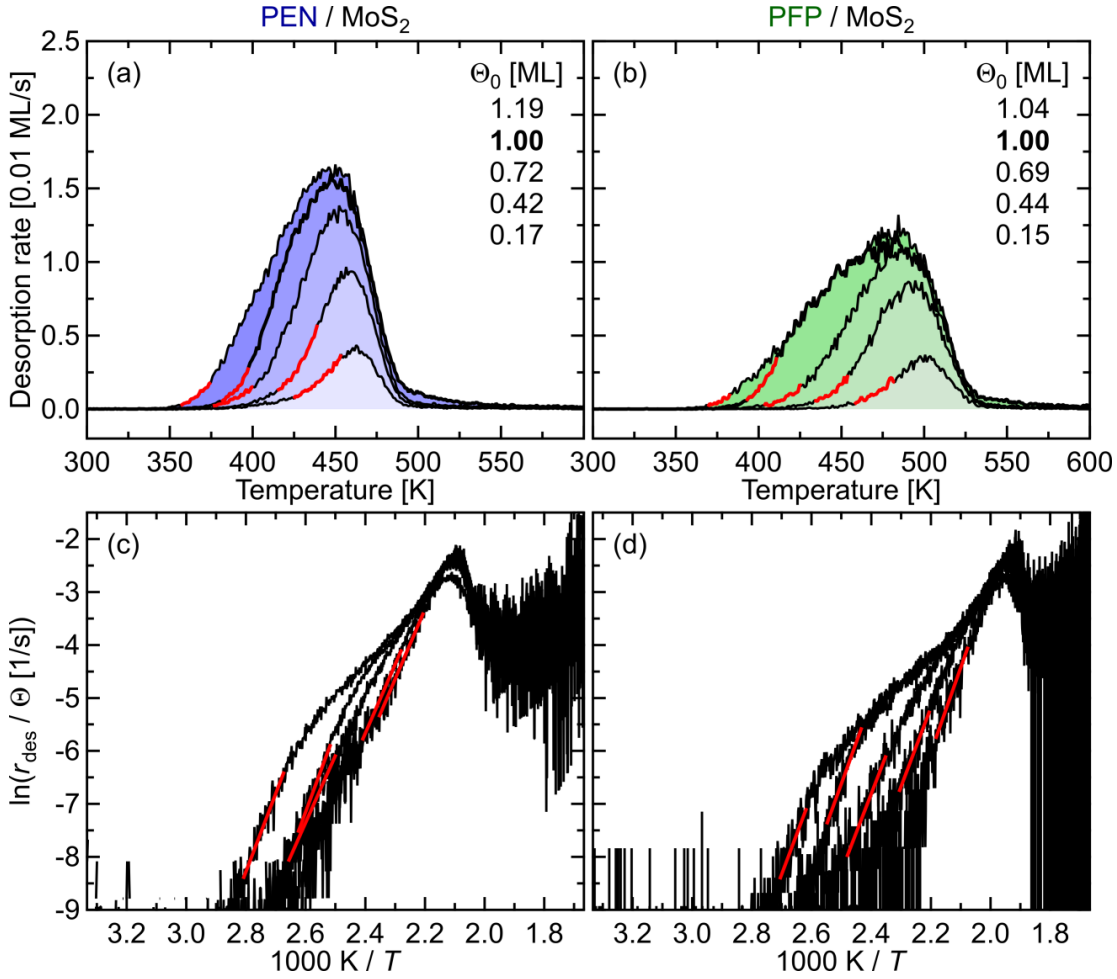

Figure S3: (a) and (b) Series of (sub-) monolayer TPD traces for different film thicknesses of PEN and PFP, respectively, on MoS_2. Four point-reduction (four measured data points are averaged) for better visualization. Film thicknesses range from 0.5 Å to 3 Å. The nominal monolayers are marked with bold lines. The section of the leading edge that was used for the modified leading-edge analysis is indicated by bold, red traces. All measurements were performed with heating rates of 1 K/s by mass spectrometric detection of m/z = 278 amu for PEN and m/z = 530 amu for PFP. (c) and (d) Modified leading-edge analysis for PEN and PFP on MoS_2, respectively. TPD traces without point-reduction used for the analysis. The linear fit is marked as a bold, red line. The fitting results are given in Table S3.

Modified leading-edge analysis (mLEA), according to:

$$\ln\left(\frac{r}{\theta}\right) = -\frac{E_\mathrm{d}}{RT} + \ln(\nu) \tag{S3}$$

Table S3: Fitting results ($y = a + bx$) as well as desorption energies and prefactors for the mLEA of PEN and PFP on MoS_2 as shown in Figure S3.

P4

Coverage [ML]	a	b [K]	E_d [kJ/mol]	ν [s^{-1}]
		PEN		
0.17	25.6±0.7	-13172±304	109.5±2.5	$10^{11.1\pm0.3}$
0.42	25.6±0.6	-13015±261	108.2±2.2	$10^{11.1\pm0.3}$
0.72	25.5±1.2	-12638±478	105.1±4.0	$10^{11.1\pm0.5}$
1.00	32.7±1.9	-15319±747	127.4±6.2	$10^{14.2\pm0.8}$
1.19	33.1±1.7	-14767±611	122.8±5.1	$10^{14.4\pm0.7}$
		PFP		
0.15	28.9±1.7	-15921±801	132.4±6.7	$10^{12.6\pm0.7}$
0.44	27.6±2.1	-14905±916	123.9±7.6	$10^{12.0\pm0.9}$
0.69	28.2±2.4	-14604±1000	121.4±8.3	$10^{12.3\pm1.0}$
1.00	32.3±1.8	-15553±717	129.3±6.0	$10^{14.0\pm0.8}$
1.04	32.0±5.1	-14947±1900	124.3±15.8	$10^{13.9\pm2.2}$

5. Heating rate variation data and analysis

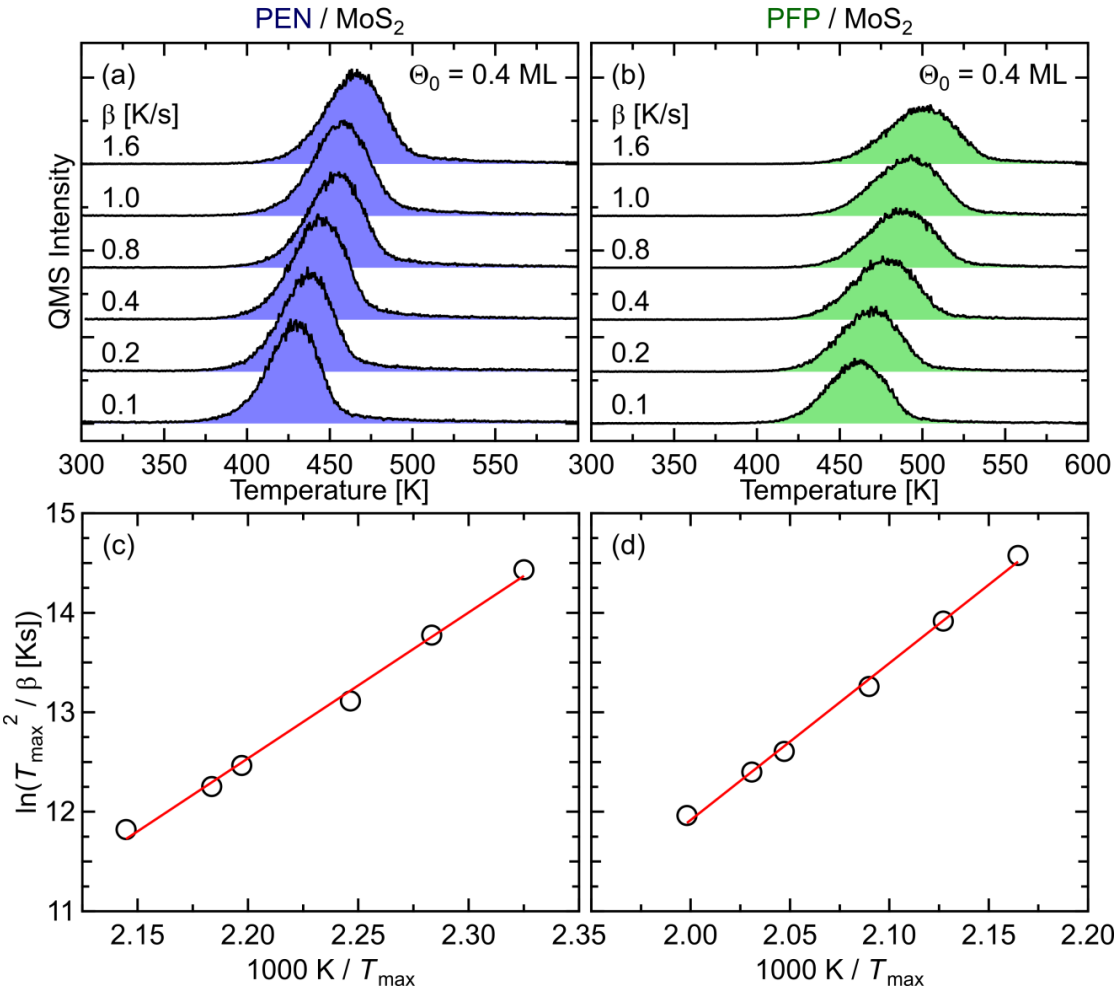

Figure S4: (a) and (b) Heating-rate variation (HRV) series for PEN and PFP, respectively, on MoS_2 for heating rates from 0.1 to 1.6 K/s. Initial coverages were prepared by depositing 8 Å of the molecules and annealing the sample to 430 K and 455 K for 10 s for PEN and PFP, respectively, yielding coverages of 0.4 ML for both molecules. (c) and (d) Linear fit (red line) of $\ln(T_{max}^2/\beta)$ vs. $1/T_{max}$. The fitting results are given in Table S4.

Heating-rate variation (mLEA) analysis, according to:

$$\ln\left(\frac{T_{\mathrm{max}}^2}{\beta}\right) = \frac{E_{\mathrm{d}}}{RT_{\mathrm{max}}} + \ln\left(\frac{E_{\mathrm{d}}}{R\nu}\right) \tag{S4}$$

Table S4: Fitting results of ($y = a + bx$) as well as desorption energies and prefactors for the HRV analysis of PEN and PFP on MoS_2 as shown in Figure S4.

P4

Coverage [ML]	***a***	***b* [K]**	**E_d [kJ/mol]**	**ν [s^{-1}]**
		PEN		
0.4	-19.7±1.2	14665±538	121.9±4.5	$10^{12.7\pm0.5}$
		PFP		
0.4	-19.6±1.0	15760±471	131.0±3.9	$10^{12.7\pm0.4}$

6. Derivation of the Gibbs free energy difference upon desorption of molecular mono- and multilayers

In transition state theory (TST), the rate constant, k_{TST}, can be expressed as a function of the standard Gibbs free energy of activation, $\Delta G^{\ddagger}$:

$$k_{\mathrm{TST}} = \frac{k_{\mathrm{B}}T}{h} \exp\left(-\frac{\Delta G^{\ddagger}}{RT}\right), \tag{S5}$$

where k_{B} is Boltzmann's constant, T is the temperature, h is Planck's constant, and R is the universal gas constant. In the here considered case of thermal desorption, $\Delta G^{\ddagger}$ describes the change of the standard Gibbs free energy upon transition from the adsorbed state to the transition state of desorption. $\Delta G^{\ddagger}$ is related to the standard enthalpy of activation, $\Delta H^{\ddagger}$, and the standard entropy of activation, $\Delta S^{\ddagger}$, of the desorption process by equation S6:

$$\Delta G^{\ddagger} = \Delta H^{\ddagger} - T\Delta S^{\ddagger} \tag{S6}$$

Inserting equation S6 into equation S5 leads to equation S7, which shows the entropic and enthalpic contributions to k_{TST} as separate terms:

$$k_{\mathrm{TST}} = \frac{k_{\mathrm{B}}T}{h} \exp\left(\frac{\Delta S^{\ddagger}}{R}\right) \exp\left(-\frac{\Delta H^{\ddagger}}{RT}\right). \tag{S7}$$

The activation energy of desorption, or desorption energy E_{d}, is defined by the empirical Arrhenius equation for the rate constant k_{A}:

$$k_{\mathrm{A}} = \nu \exp\left(-\frac{E_{\mathrm{d}}}{RT}\right). \tag{S8}$$

After taking the logarithm, equation S8 can be re-written in differential form:

$$E_{\mathrm{d}} = -R\frac{\mathrm{d}\ln k_{\mathrm{A}}}{\mathrm{d}\left(\frac{1}{T}\right)}. \tag{S9}$$

Likewise, equation S7 can be logarithmized and re-written in differential form:

$$\Delta H^{\ddagger} = -R\frac{\mathrm{d}\ln\left(\frac{k_{\mathrm{TST}}}{T}\right)}{\mathrm{d}\left(\frac{1}{T}\right)}. \tag{S10}$$

Here, we have assumed that $\Delta H^{\ddagger}$ and $\Delta S^{\ddagger}$ are independent of the temperature. To establish a relationship between E_{d} with $\Delta H^{\ddagger}$, we subtract equation S10 from equation S9:

$$E_{\mathrm{d}} - \Delta H^{\ddagger} = -R\left[\frac{\mathrm{d}\ln k_{\mathrm{A}}}{\mathrm{d}\left(\frac{1}{T}\right)} - \frac{\mathrm{d}\ln\left(\frac{k_{\mathrm{TST}}}{T}\right)}{\mathrm{d}\left(\frac{1}{T}\right)}\right]$$

$$= -R \frac{(\mathrm{d} \ln k_\mathrm{A} - \mathrm{d} \ln k_\mathrm{TST}) - \mathrm{d} \ln \left(\frac{1}{T}\right)}{\mathrm{d} \left(\frac{1}{T}\right)}. \qquad \text{(S11)}$$

Assuming that $k_\mathrm{TST} = k_\mathrm{A}$, we obtain:

$$E_\mathrm{d} - \Delta H^\ddagger = R \frac{\mathrm{d} \ln \left(\frac{1}{T}\right)}{\mathrm{d} \left(\frac{1}{T}\right)} = RT. \qquad \text{(S12)}$$

P4

Replacing $\Delta H^\ddagger$ in equation S7 with equation S12 leads to:

$$k_\mathrm{TST} = \frac{k_\mathrm{B} T}{h} \exp\left(\frac{\Delta S^\ddagger}{R} + 1\right) \exp\left(-\frac{E_d}{RT}\right). \qquad \text{(S13)}$$

Comparing equation S13 to the Arrhenius equation (equation S8) and again assuming that $k_\mathrm{TST} = k_\mathrm{A}$, we can express the prefactor ν in the Arrhenius equation in terms of TST:

$$\nu = \frac{k_\mathrm{B} T}{h} \exp\left(\frac{\Delta S^\ddagger}{R} + 1\right). \qquad \text{(S14)}$$

Now, using equation S14, differences in the entropy gain upon desorption from different adsorbed phases, e.g., mono- and multilayers, can be calculated from the respective prefactors:

$$\Delta S^\ddagger{}_\mathrm{multi} - \Delta S^\ddagger{}_\mathrm{mono} = R \ln\left(\frac{\nu_\mathrm{multi}}{\nu_\mathrm{mono}}\right). \qquad \text{(S15)}$$

Inserting equations S12 and S15 into equation S6, we obtain equation (5) in the main text.

7. Fits of the Polanyi-Wigner equation to the monolayer TPD traces

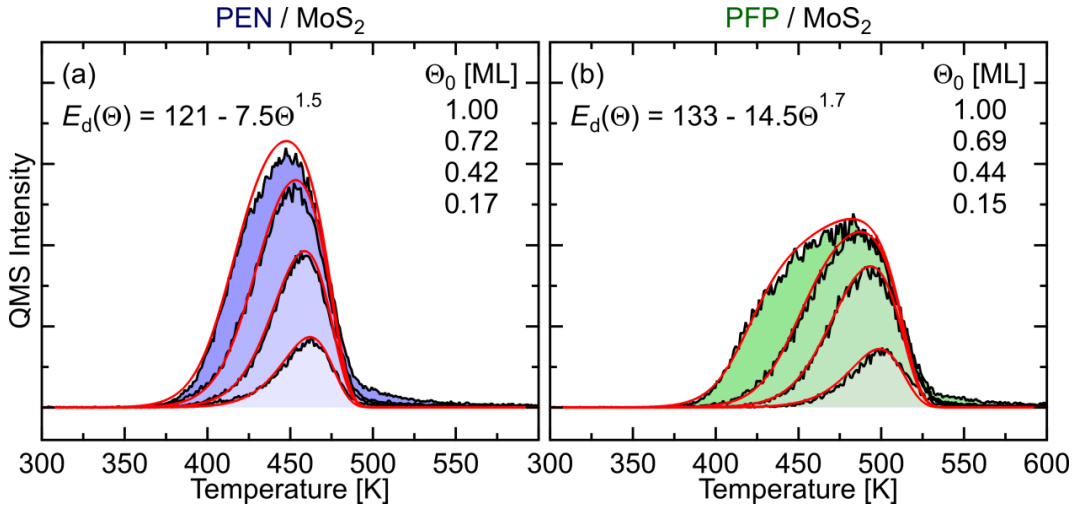

Figure S5: (a) and (b) TPD coverage series of PEN and PFP on MoS2 (black lines) and simulated TPD traces (red lines) using an exponential function for the desorption energy (shown in graphs, in kJ/mol). Constant prefactors, as obtained by the MC simulations, were used (PEN: $10^{12.5}$ s^{-1}, PFP: $10^{12.7}$ s^{-1}).

The simulations of TPD traces were performed according to equation S13:

$$r = \nu\, \Theta \exp\left(-\frac{E_d - a\Theta^b}{RT}\right) \qquad \text{(S13)}$$

8. Analysis of the STM data of the mixed PEN + PFP film on MoS_2

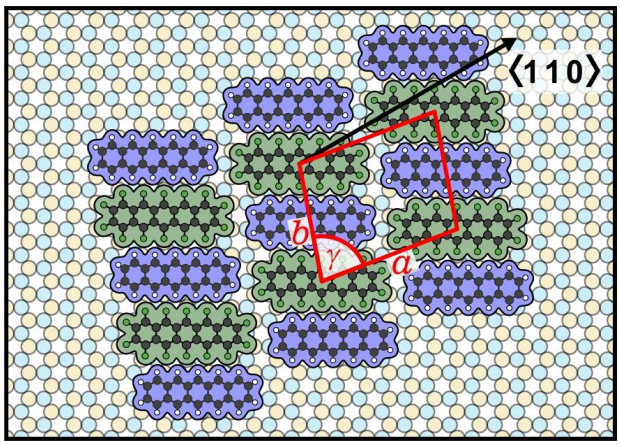

Figure S6: Illustration of the structural model for the stoichiometric 1:1 intermixture of PEN and PFP on MoS_2 based on STM results.

From the STM micrograph in Figure 4, we find an oblique unit cell with a = (16.2 ± 1.0) Å, b = (14.6 ± 1.0) Å and γ = (83 ± 5)°. The angle between the long side of the unit cell and the $\langle 110 \rangle_{MoS_2}$ azimuth (determined from LEED data of the MoS_2 crystal) is (3 ± 5)°. The angle between the long molecular axes and the $\langle 110 \rangle_{MoS_2}$ azimuth is (35 ± 5)°.

The experimentally determined unit cell parameters are in good agreement with a $\begin{pmatrix} 5 & 1 \\ -4 & 5 \end{pmatrix}$ commensurate superstructure that is illustrated in Figure S6. The corresponding unit cell parameters are a = 17.4 Å, b = 14.5 Å and γ = 80°. The angle between long side of the unit cell and the $\langle 110 \rangle_{MoS_2}$ azimuth is 9°. The angle between the long molecular axes and the $\langle 110 \rangle_{MoS_2}$ azimuth is 30°.

9. References

[S1] Meng, B.; Weinberg, W. H. Monte Carlo Simulations of temperature programmed desorption spectra. *J. Chem. Phys.* **1994**, 100, 5280-5289.

[S2] Jin, C.; Rasmussen, F. A.; Thygesen, K. S. Tuning the Schottky Barrier at the Graphene/MoS_2 Interface by Electron Doping: Density Functional Theory and Many-Body Calculations. *J. Phys. Chem. C* **2015**, 119, 19928-19933.

[S3] Shen, N.; Tao, G. Charge Transfer and Interface Engineering of the Pentacene and MoS_2 Monolayer Complex. *Adv. Mater. Interfaces* **2017**, 4, 1601083.

[S4] Klues, M.; Witte, G. Crystalline packing in pentacene-like organic semiconductors. *CrystEngComm* **2018**, 20, 63-74.

[S5] Allinger, N. L.; Yuh, Y. H.; Lii, J.-H. Molecular Mechanics. The MM3 Force Field for Hydrocarbons. 1. *J. Am. Chem. Soc.* **1989**, 111, 8551-8561.

[S6] Allinger, N. L.; Zhou, X.; Bergsma, J. Molecular mechanics parameters. *J. Mol. Struc.* **1994**, 312, 69-83.

[S7] Widdascheck, F.; Hauke, A. A.; Witte, G. A Solvent-Free Solution: Vacuum-Deposited Organic Monolayers Modify Work Functions of Noble Metal Electrodes. *Adv. Funct. Mater.* **2019**, 1808385.

[S8] Lin, J.; Zhong, J.; Zhong, S.; Li, H.; Zhang, H.; Chen, W. Modulating electronic transport properties of MoS_2 field effect transistors by surface overlayers. *Appl. Phys. Lett.* **2013**, 103, 063109.

[S9] Ning-Tong, C.; Lei, Z.; Lu, L.; Hai-Peng, X.; Han, H.; Dong-Mei, N.; Yong-Li, G. The van der Waals heterostructures of CuPc/MoS_2(0001). *Acta Phys. Sin.* **2014**, 63, 167903.

[S10] Lee, S. Y.; Kim, U. J.; Chung, J.; Nam, H.; Jeong, H. Y.; Han, G. H.; Kim, H.; Oh, H. M.; Lee, H.; Kim, H.; Roh, Y.-G.; Kim, J.; Hwang, S. W., Park, Y.; Lee, Y. H. Large Work Function Modulation of Monolayer MoS_2 by Ambient Gases. *ACS Nano* **2016**, 10, 6100-6107.

Journal of Physics: Condensed Matter

PAPER

Reactive metal-organic interfaces studied with hard x-ray photoelectron spectroscopy: controlled formation of metalloporphyrin interphase layers during metal vapor deposition onto porphyrin films

To cite this article: Martin Schmid *et al* 2019 *J. Phys.: Condens. Matter* **31** 094002

IOP Publishing Journal of Physics: Condensed Matter
J. Phys.: Condens. Matter **31** (2019) 094002 (10pp) https://doi.org/10.1088/1361-648X/aafa2b

Reactive metal-organic interfaces studied with hard x-ray photoelectron spectroscopy: controlled formation of metalloporphyrin interphase layers during metal vapor deposition onto porphyrin films

Martin Schmid[1], Stefan R Kachel, Benedikt P Klein, Nicolas Bock, Philipp Müller, René Riedel, Norbert Hampp and J Michael Gottfried

Philipps-Universität Marburg, Fachbereich Chemie, Hans-Meerwein-Str. 4, 35032 Marburg, Germany

E-mail: schmidm5@staff.uni-marburg.de

Received 24 September 2018, revised 9 December 2018
Accepted for publication 20 December 2018
Published 18 January 2019

Abstract

Interfaces between organic semiconductors and metallic layers are ubiquitous in organic (opto-) electronic devices and can significantly influence their functionality. Here, we studied *in situ* prepared metal-organic interfaces, which were obtained by vapor deposition of metals (Co, Fe) onto organic semiconductor films (2H-tetraphenylporphyrin), with hard x-ray photoelectron spectroscopy. In these systems, the inter*phase* zones, which are formed by diffusion and reaction of the metal in the organic material, can be clearly distinguished spectroscopically from the unreacted organic bulk, since they comprise the corresponding metalloporphyrins, CoTPP and FeTPP. In order to gain control over the thickness of the interphase layers, we varied process parameters such as sample temperature and metal-atom flux during interface preparation. We found that the temperature of the organic film during metal deposition was the only parameter that significantly influenced the formation of the interphase layers: their thicknesses were typically ~0.5 nm for deposition at 90 K, compared to ~1 nm at 300 K, irrespective of metal atom flux and chemical nature of the metal atom (Fe versus Co). Notably, these values are significantly smaller than the thicknesses of other metal/organics interphase regions reported in the literature.

Keywords: metal-organic interphase, HAXPES, internal interface, metalation reaction of porphyrins

(Some figures may appear in colour only in the online journal)

1. Introduction

In organic electronic devices, interfaces between organic (semiconducting) materials and metal electrodes play a decisive role [1, 2], because the transport of charge carriers across these interfaces often limits the performance of a device [3–5]. The charge injection efficiency at the interface can be influenced by an interlayer between the metal and the organic semiconductor. For example, it has been demonstrated that an ultrathin vanadium oxide (VO_x) interlayer at the Cu/pentacene interface leads to a reduced contact resistance and an enhanced performance in organic field-effect transistors. Similar findings were reported for Au/VO_x/pentacene and Au/VO_x/BOPAnt systems [6]. Such performance-modifying interlayers can also be formed spontaneously when interdiffusion and reaction between the metal and the organic material occurs at the interface, in particular, when a metal is vapor-deposited onto an organic material [7]. Due to the importance

[1] Author to whom any correspondence should be addressed.

J. Phys.: Condens. Matter **31** (2019) 094002 M Schmid *et al*

of related effects in microelectronics and organic electronics, the diffusion and reaction of metal atoms in polymer films, as well as the dynamics of the metal film formation on top of polymers, have been studied in the past [8–16]. However, in organic electronic applications, the organic semiconductor is not necessarily a polymer, but can also be a (reactive) molecular solid [17].

Here, we consider especially the processes that occur when the metal electrodes are vapor-deposited onto the molecular organic materials under ultrahigh-vacuum conditions. Using a suitable model system that allows monitoring the diffusion depth of the metal, we study the extent of interlayer (interphase) formation. During the initial stages of metal deposition, single metal atoms impinge directly on the organic layer, where they can engage in the following processes: (a) desorption back into the gas phase [18, 19], (b) diffusion on the surface and (possibly) reaction with an organic molecule, (c) diffusion on the surface and attachment to a metal cluster, and (d) diffusion into the bulk and (possibly) reaction with a subsurface molecule or formation of (or attachment to) a subsurface metal cluster. Figure 1 illustrates these reaction pathways. Due to the low vapor pressure of most metals at room temperature, the supply of metal atoms into the subsurface region of the organic material is expected to stop as soon as there is a complete, closed metallic layer on top of the organic material [9]. Hence, the thickness of the interphase layer depends on the rate by which a complete metal film on the surface forms, relative to the rates of the competing processes, as long as the mobility of the molecules in the organic film is negligible and no molecular scrambling between reacted and unreacted molecules takes place. It should be emphasized that the formation of the closed metal film is the only limiting factor for the diffusion of the metal in the organic layer (unless there is a reaction and the reaction products create a barrier for diffusion). Without this self-limiting effect, the diffusion (and reaction) of the metal would likely continue indefinitely, creating a metalation reaction front that would propagate into the organic bulk material [20], creating a conceptually well understood instance of a reaction-diffusion system [20–26].

In this study, we attempt to influence the rate of formation of a closed metal film—relative to the rates of the competing processes—by changing various parameters: (a) temperature, (b) flux of metal atoms, and (c) chemical nature of the metal. These parameters should affect the interface formation as follows: (a) A lower temperature of the organic film during the metal deposition is expected to result in a lower diffusion rate of (thermalized) metal atoms on and in the film. Therefore, more metal atoms are expected to end up close to, or at, the surface. (b) Low metal-atom fluxes should be detrimental to the aggregation of the metal, because they reduce the probability of metal–metal encounters in favor of reactive encounters between metal atoms and molecules. It was previously shown by Faupel *et al* that flash deposition of metals onto polymers effectively reduces diffusion of the metals into the organic material [9]. (c) Chemical nature of the metal atom: A low reaction barrier facilitates the reaction between metal and molecules and thus the formation of the interphase. Conversely, the growth of a metal film as a competing process is impeded.

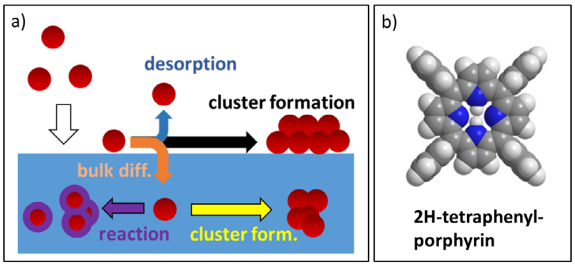

Figure 1. (a) Possible pathways for metal atoms upon vapor deposition onto a bulk phase of organic molecules. Metal atoms impinging on the surface can either desorb back into the gas phase, form cluster on the surface, or diffuse into the bulk, where they can again form (or attach to) clusters or react with the organic molecules. (b) The molecule used in this study: 2H-tetraphenylporphyrin (2HTPP).

We want to clarify how process parameters such as metal deposition rate, sample temperature, and chemical nature of the metal influence the interphase formation between an *in situ* deposited metallic layer and a bulk phase of organic molecules. For this aim, we use a bulk film of 2H-tetraphenylporphyrin (2HTPP) and study its reaction with vapor-deposited metallic Co and Fe. The interaction of 2HTPP with these metals is known to result in the formation of the respective M(II)tetraphenylporphyrins (MTPP, M = Co, Fe), according to the equation: $M + 2HTPP \rightarrow MTPP + H_2$ [27–29]. The MTPP interphase layer between the metal and the pristine 2HTPP is then investigated by chemical depth profiling with hard x-ray photoelectron spectroscopy (HAXPES). The porphyrin metalation represents a suitable model system for monitoring interfacial metal/organic reactions for several reasons. First, the reaction is well defined and typically does not have side reactions. Second, the pristine and the reacted organic material can easily be discriminated by x-ray photoelectron spectroscopy. Third, the metalation reaction works for a wide range of different metals [27, 28, 30]. According to previous work, the energy barrier for the metalation reaction of 2HTPP varies with the reactant metal. According to previous density functional theory (DFT) calculations, the reaction is barrierless in the case of Fe, while a small barrier of approximately 10 kJ mol^{-1} was predicted for Co [29]. This could lead to reactivity differences at the interface, particularly at low sample temperatures.

2. Experimental details

The samples were prepared *in situ* under ultrahigh voltage (UHV) conditions at the HIKE endstation of the KMC-1 beamline at BESSY II, Helmholtz-Zentrum Berlin [31, 32]. 2HTPP (98%, Porphyrin Systems) was evaporated at 660 K from a Knudsen cell and deposited onto a Si(0 0 1) surface and commercial Al foil. The deposition of 2HTPP, with typical fluxes of 2 nm min^{-1}, was monitored by a quartz crystal microbalance (QCM). Typical film thicknesses L were in the range of 40–60 nm.

Rods of cobalt (99.995%, Alfa Aesar) and iron (99.99+%, Hauner Metallische Werkstoffe) were used for metal vapor deposition using a commercial e-beam evaporator

J. Phys.: Condens. Matter **31** (2019) 094002 M Schmid *et al*

Table 1. Material parameters and coefficients for 2HTPP, CoTPP, and FeTPP that are used for the calculation of the IMFP with equation (2).

Compound	Stoichiometry	H/C	Density ρ (g cm^{-3})	k_1	k_2	V_a (cm^3 mol^{-1})	Z^*
2HTPP	$C_{44}H_{30}N_4$	0.682	1.270	0.00145	1	6.214	1.902
CoTPP	$CoC_{44}H_{28}N_4$	0.636	1.404	0.00141	1	6.221	1.968
FeTPP	$FeC_{44}H_{28}N_4$	0.636	1.398	0.00141	1	6.219	1.967

(FOCUS EFM-4). The metal deposition rates were either 0.7 nm min^{-1} or 0.035 nm min^{-1}, depending on the details of the experiment. During the deposition, a permanently mounted cold-cathode gauge indicated a pressure below 5×10^{-9} mbar. In subsequent x-ray photoelectron spectroscopy (XPS) experiments, no oxygen or other unwanted impurities were detected on the metallic films.

Photoelectron spectra were recorded close to normal emission (14° relative to the surface normal) with a VG Scienta R4000 electron spectrometer. A piece of gold foil, which was mounted in the analysis chamber of the HIKE endstation, was used to calibrate the binding energy scale with the Au $4f_{7/2}$ line at 84.0 eV. All HAXPES measurements were performed with the samples at room temperature, including those samples that had been cooled to 90 K during the metal deposition. In order to avoid beam damage during the measurements, the samples were systematically moved relative to the x-ray beam. The effectively irradiated area on the sample has dimensions of 0.2 mm × 4 mm (as measured in a calibration experiment); the elongated shape results from grazing incidence of the x-ray beam when the sample is in measurement position. The photon energy was varied between 3 keV and 5 keV; hereby, the Si(1 1 1) monochromator crystal was used for 3 keV and the Si(3 1 1) crystal for 5 keV photon energy. Changing the monochromator crystals allowed measuring the spectra with similar resolutions, irrespective of the photon energies [31, 32]. Although photon energies of up to 10 keV are available at this beamline, higher photon energies than 5 keV were not used because of the low cross sections, which lead to an increasingly unfavorable balance between signal-to-noise ratio on the one hand and radiation damage on the other hand. Moreover, photon energies below 2 keV, as available from, e.g. conventional AlKα or MgKα sources, are not suitable. With the resulting low information depths, the interphase region does not contribute sufficiently to the total XPS signal.

The acquired photoelectron spectra have been fitted with the following Pseudo-Voigt function [33, 34]:

$$\mathrm{PV} = (1-m)\sqrt{\frac{4\ln(2)}{\pi\ (\omega_{(x)})^2}}\exp\left(-\frac{4\ln(2)}{(\omega_{(x)})^2}x^2\right) + m\frac{1}{2\pi}\frac{\omega_{(x)}}{(\omega_{(x)}/2)^2+x^2}$$
$$\omega_{(x)} = \frac{2\ \omega_0}{1+\exp(-a(x-b))} \quad \text{where} \quad x = (E-E_0) \tag{1}$$

with the following parameters:

$\omega_{(x)}$	Full width at half maximum function	ω_0	Full width at half maximum parameter
a	asymmetry parameter, 0: symmetric peak	b	asymmetry shift parameter
E	binding energy	E_0	peak position

For background subtraction, a combination of Shirley background and second order polynomial has been used. The peaks and the background are displayed in the corresponding spectra.

The morphologies of the pristine 2HTPP layers were analyzed with atomic force microscopy (AFM, Nanoscope V, Bruker, USA). Topological imaging was conducted in tapping mode in air, using a sharp silicon nitride cantilever (SNL, tip radius 2 nm, spring constant $k = 0.24$ N m^{-1}, oscillation frequency $f = 56$–75 kHz).

3. Data analysis

In accordance with the results by Seah and Spencer [35], we will use the Gries G-1 equation [36, 37] to calculate the IMFPs in the investigated 2HTPP and MTPP/2HTPP layer systems (M = Co or Fe). In the G-1 equation, the inelastic mean free path (IMFP) λ is expressed as:

$$\lambda_{(E_{\mathrm{kin}})} = k_1\left(\frac{V_a}{Z^*}\right)\frac{E_{\mathrm{kin}}}{\log(E_{\mathrm{kin}}) - k_2}. \tag{2}$$

In this equation, the kinetic energy E_{kin} is given in eV and the IMFP λ in nanometers. For a certain compound, the parameter V_a is determined by the stoichiometry and density ρ of the material, while Z^* depends only on the stoichiometry [36]. The parameters k_1 and k_2 also depend on the material; for organic compounds, k_2 is unity and k_1 depends on the H/C ratio of the material: $k_1 = 0.0017$ at H/C = 1 and $k_2 = 0.0023$ at H/C = 2 [35, 36]. Seah and Spencer [35] found that a linear relation interpolation of k_1 for materials with H/C ratios different from either 1 or 2 leads to excellent results. Table 1 summarizes the parameters for 2HTPP, CoTPP, and FeTPP. V_a and Z^* are calculated according to Gries [36]. The density of the *in situ* prepared FeTPP was calculated under the assumption that its molar volume is identical to the air-stable and well characterized CoTPP.

The interphase formation was monitored by recording N 1s core level spectra at photon energies of 3 keV and 5 keV; the corresponding kinetic energies were 2.6 keV and 4.6 keV. These values result in the IMFPs given in table 2.

The N 1s signal intensity of the MTPP layer will be denoted as I_r (r for reacted) and the N 1s signal intensity of 2HTPP as I_{ur} (ur for unreacted). The intensities I_r and I_{ur} depend on the distribution of the reacted species within the near-surface region of the sample. For the mathematical treatment, it is helpful to think of the sample as a sequence of infinitesimally thin layers that are oriented parallel to the sample's surface at a distance z to the metal/MTPP interface. Each of these layers

J. Phys.: Condens. Matter **31** (2019) 094002 M Schmid *et al*

Table 2. IMFPs for 2HTPP, CoTPP, and FeTPP for 3 and 5 keV photon energy obtained by application of equation (2).

Compound	$h\nu = 3$ keV (nm)	$h\nu = 5$ keV (nm)
2HTPP	5.10	8.18
CoTPP	4.80	7.70
FeTPP	4.80	7.70

consists of a fraction of metalated ($c_{r(z)}$) and unmetalated ($1 - c_{r(z)}$) molecules. Layers at a distance z to the interface contribute with a weight of $\exp(-z/(\text{IMFP}\cos\theta))$ to the total signal (Beer–Lambert law, emission angle θ relative to the surface normal, IMFP: inelastic mean free path). Accordingly, the intensity ratio $I_r{:}I_{ur}$ can be expressed with the following equation:

$$\left(\frac{I_r}{I_{ur}}\right)_{(E_{kin})} = \frac{\int_0^L c_{r(z)}\ \exp(-z/(\Lambda_{(E_{kin},\,z)}\cos\theta))\mathrm{d}z}{\int_0^L (1 - c_{r(z)})\ \exp(-z/(\Lambda_{(E_{kin},\,z)}\cos\theta))\mathrm{d}z}. \tag{3}$$

Here, L stands for the total thickness of the organic layer, i.e. the initial thickness of the 2HTPP layer before metal deposition; θ is the photoelectron detection angle, in this study $\theta = 14°$. (Specifically in our experiments, L was chosen to be approximately 50 nm.) The effective IMFP, Λ, which is experienced by photoelectrons that emerge from a certain depth z, is given by the composition of the layers above; here, we estimate it as an average value of all IMFPs of the layers at depths between 0 and z:

$$\Lambda_{(E_{kin},\,z)} = \frac{1}{z}\int_0^z c_{r(z')}\,\lambda_{r(E_{kin})} + \left(1 - c_{r(z')}\right)\lambda_{ur(E_{kin})}\,\mathrm{d}z'. \tag{4}$$

The concentration profiles that are expected in our experiments are described with a *complementary error function* ('erfc'), a type of function that is frequently encountered in the analysis of concentration profiles in reaction-diffusion systems [20–26, 38–40] and theoretically predicted for this class of system [20]. Accordingly, the following equation was used to parameterize the curves (see figure 2(a)):

$$c_{r(z)} = 0.5 \cdot \mathrm{erfc}\left(\frac{z-d}{b}\right). \tag{5}$$

An individual concentration profile is described by two parameters: the 'width parameter' b and the 'reaction depth' d, see figure 2(a). (The width parameter is directly related to the width of the Gaussian function from which the error function is calculated.) It is of great importance in the discussion below that the integral of equation (5) is independent of the parameter b, as long as the reaction depth d is kept constant. For b close to zero, the curves approach the shape of a Heaviside step function. If one assumes such a strict layer-by-layer sequence of MTPP and 2HTPP, that is, an abrupt transition between a pure MTPP layer with a certain thickness d and a 2HTPP layer below, one can extract the value of d from the intensity ratio between the N 1s signals of MTPP and 2HTPP analytically. In this case, equations (3) and (4) lead to the following expression for $I_r{:}I_{ur}$, which is a transcendental equation for the reaction depth d:

$$\left(\frac{I_r}{I_{ur}}\right)_{(E_{kin})} = \frac{\lambda_{r(E_{kin})}}{\lambda_{ur(E_{kin})}} \times \frac{1 - \exp(-d/(\lambda_{r(E_{kin})}\cos\theta))}{\exp(-d/(\lambda_{ur(E_{kin})}\cos\theta)) - \exp(-L/(\lambda_{ur(E_{kin})}\cos\theta))}. \tag{6}$$

3.1. Limitations of the experimental approach

Before we proceed with the presentation and discussion of our results, an important question has to be addressed: is it possible to extract the shape of the concentration profile, and, in particular, the parameter b with arbitrary precision from HAXPES data? The samples in our study necessitate the use of hard x-rays to obtain sufficiently large values for the IMFP. Only in this way, signals originating from the buried metal/organic interface region contribute enough to the total signal. What are the consequences of the large IMFPs for our analysis?

In the limit of $\Lambda \to \infty$, the Beer–Lambert factor $\exp(-z/(\Lambda\cos\theta))$ in equation (3) is unity for all z, and, as a consequence, all concentration profiles with the same reaction depth d have the same intensity ratio $I_r{:}I_{ur}$, regardless of b. (This is due to the fundamental fact that the integral of the complementary error function is independent of the width parameter b.) A similar argument holds true for $\Lambda \gg b$: then, the Beer–Lambert factor $\exp(-z/(\Lambda\cos\theta))$ is practically constant in the region of interest $z = d \pm b$ where the erfc function changes from unity to zero. In this range for z, $\Lambda \gg b$ leads to:

$$\int \mathrm{erfc}\left(\frac{z-d}{b}\right)\exp\left(-\frac{z}{\Lambda\cos\theta}\right)\mathrm{d}z \approx \text{const.}\int \mathrm{erfc}\left(\frac{z-d}{b}\right)\mathrm{d}z \tag{7}$$

where the last integral is independent of b. In other words, for $\Lambda \gg b$ the ratio $I_r{:}I_{ur}$ is only controlled by the reaction thickness d and not by the width parameter b.

We will demonstrate this numerical phenomenon with the data reported in a previous article by Chen *et al* [41] (see figure 2(b)). There, I_r and I_{ur} correspond, like in the present study, to the intensity ratios of metalated and unmetalated porphyrins. The authors use an equation equivalent to equation (6) (without distinguishing between different IMFPs for reacted and unreacted species), a fit by a genetic algorithm, and a SESSA simulation to show that the investigated system comprises a sharp layer-by-layer structure. Reproducing the procedures of Chen *et al* [41] (with additionally distinguishing between IMFPs for reacted and unreacted species, as well as using the complementary error function) we reach essentially the same result as these authors. However, we obtain further insight if we analyze the ensemble of concentration profiles that corresponds to an estimated confidence interval of the fit $I_r{:}I_{ur}$ (theory) versus $I_r{:}I_{ur}$ (experiment); this interval is highlighted as gray shaded region in figure 2(b). For the estimation, the width of the confidence band is calculated as two times the average deviation of the experimental data points from the best fit (black curve in figure 2(b)). We find that these concentration profiles cluster around a reaction depth of 1.55 nm, but show a wide variety of width parameters b, ranging from 0

J. Phys.: Condens. Matter **31** (2019) 094002 M Schmid *et al*

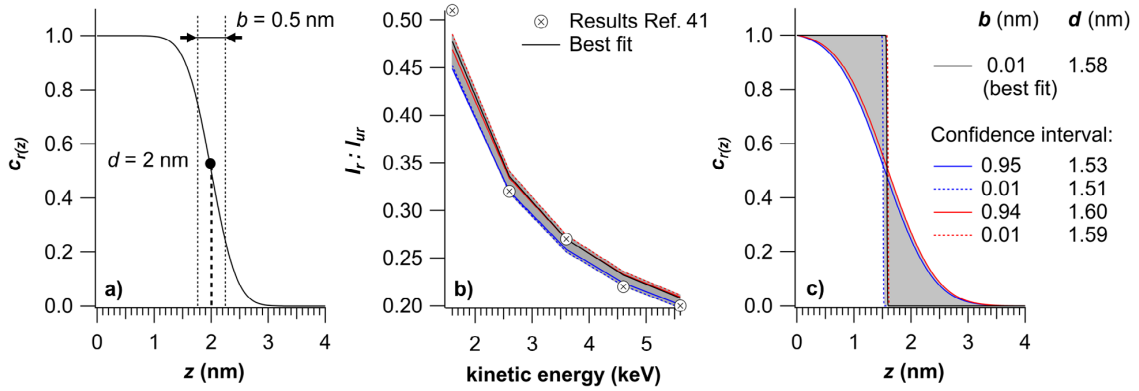

Figure 2. (a) A complementary error function for $b = 0.5$ nm and $d = 2$ nm. (b) Experimental I_r:I_{ur} values by Chen *et al* [41], along with the best fit to these data (black solid curve) and the estimated confidence region of the fit (gray shaded band). The width of the gray shaded band is two times the average deviation of the experimental data points from the best fit (black solid curve). It should be pointed out that the best fit, which gives an abrupt interface (black curve in frames (b) and (c)), has nearly exactly the same predicted I_r:I_{ur} values as a profile with high b (0.94 nm) and high d (1.6 nm) (solid red curve). (c) Range of different concentration profiles corresponding to the estimated confidence interval of the fit. The curves that define the 'envelope' of the ensemble are specifically highlighted in red and blue, and the associated I_r:I_{ur} values are highlighted in a similar way in (b).

P5

to 0.95 nm. The gray shaded region in figure 2(c) contains all concentration profiles that are associated with the confidence interval in figure 2(b). In addition, the concentration profiles that define the 'envelope' of the ensemble in figure 2(c) are highlighted with red and blue color. Because the ensemble of possible concentration profiles includes (i) the abrupt layer-by-layer configuration ($b = 0$) and (ii) comprises concentration profiles with virtually identical reaction depths d, one can directly use equation (6) as a shortcut for calculating the reaction depth of this ensemble in a simple way.

We reach the following conclusion: the reaction depth d is a measure of the total amount of reacted molecules and can be extracted with high accuracy. However, an equally accurate extraction of the width parameter b (in the range of only a few Angstroms) would require an information depth Λ in the same order of magnitude as b, a condition that cannot be fulfilled because the examination of buried interfaces requires high IMFPs. As a consequence, we will only use the reaction depth d in the further discussion of our results, and stress the point that the actual shape of the concentration profile (i.e. the width parameter b) is not a reliable quantity under the specific experimental conditions in our experiments (i.e. large IMFPs in combination with typically small values for b).

4. Results and discussion

4.1. Morphology of the 2HTPP film

The morphology of the organic layer is an important factor that can potentially influence the metalation behavior and the morphology of the reaction zone (and of the resulting interphase layer) between the metal and the pristine 2HTPP. In a previous study [41], cobalt has been evaporated onto an 18 nm thick 2HTPP film supported on commercial aluminium foil; however, it was not clarified if this particular choice of film thickness and (relatively rough) carrier material is associated with (unwanted) morphological features of the 2HTPP layer.

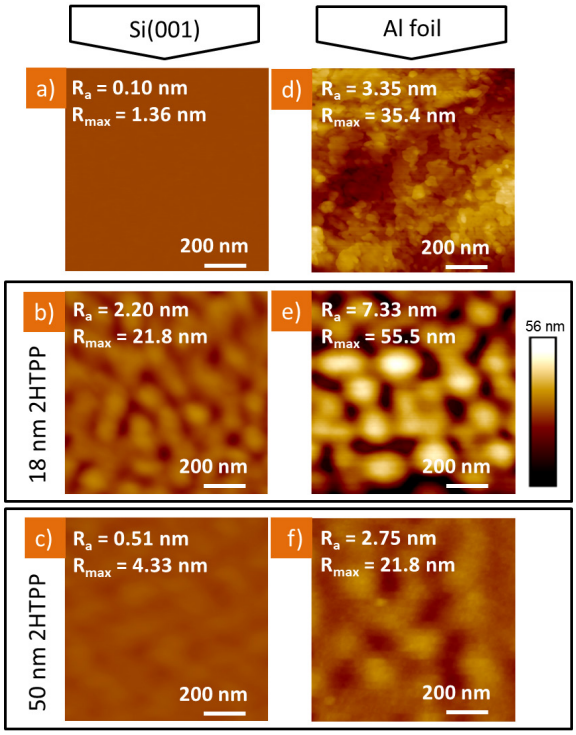

Figure 3. AFM images of the clean substrates (a) Si(0 0 1) and (d) Al foil, of 18 nm thick 2HTPP films on both substrates (b) and (e), and of 50 nm thick 2HTPP films on both substrates (c) and (f). The contrast in all images is normalized to the contrast in frame (e) to make all frames directly comparable; on this contrast scale, frame (a) does not show any features because of the very small roughness of the pristine Si(0 0 1) surface. R_a and R_{max} are the average and maximum roughness, respectively.

In order to determine the morphology of 2HTPP layers in the thickness regime $\leqslant$60 nm on a smooth substrate material, the molecules were vapor deposited onto a flat Si(0 0 1)

J. Phys.: Condens. Matter **31** (2019) 094002 M Schmid *et al*

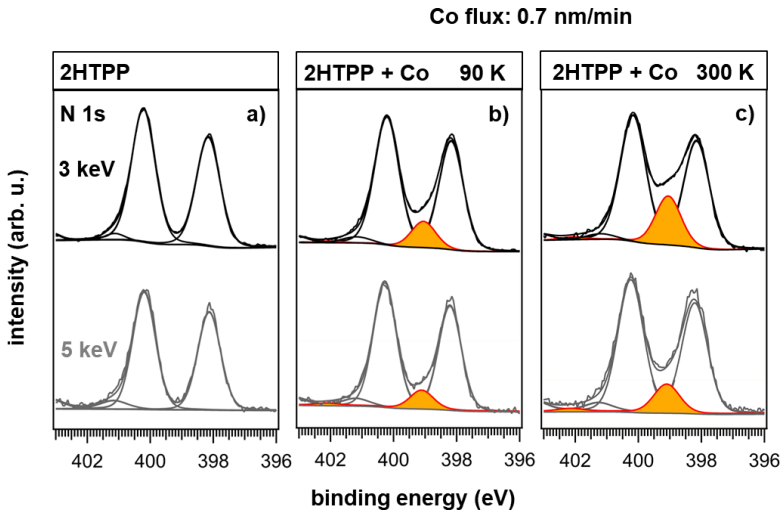

Figure 4. (a) N 1s XP spectra of a pristine 2HTPP layer (60 nm) on Si(0 0 1) taken at 3 and 5 keV photon energy. The two distinct peaks at 398.2 and 400.2 eV are attributed to iminic nitrogen (=N−) and pyrrolic nitrogen (−NH−), respectively. Additional peaks in the fit are satellites. (b), (c) After deposition of Co at 90 K (b) and 300 K (c), an additional peak emerges at 399.1 eV, which is attributed to the formation of CoTPP at the interface. Looking deeper into the material by increasing the photon energy from 3 to 5 keV reduces the relative contribution of this signal, indicating the formation of a CoTPP layer (as opposed to a homogeneous mixture of CoTPP and 2HTPP). When the 2HTPP film was held at 90 K during the deposition of Co, significantly less CoTPP is formed, compared to deposition at 300 K.

substrate with a very low average roughness R_a of 0.1 nm and maximum roughness R_{max} of 1.36 nm. (During deposition, the substrate was kept at room temperature.) The average roughness is defined as the variance of the height distribution on a given sample and is smaller than the maximum roughness, which can be observed by AFM. Large, smooth islands show a small average roughness but a high maximum roughness. After deposition of 18 nm 2HTPP, an increase in the roughness ($R_a = 2.20$ nm, $R_{max} = 21.8$ nm) was observed. The fact that the maximum height is larger than the nominal thickness is due to 3D island growth. Subsequent deposition of more material led to a reduction of the film roughness. At a 2HTPP film thickness of 50 nm, an average roughness of 0.51 nm and a maximum roughness of 4.33 nm were found.

In a reference experiment, Al-foil with an R_a value of 3.35 nm and R_{max} of 35.4 nm was used as a substrate to reproduce the conditions described in a previous publication [41]. As a result of the much higher roughness of the Al-foil, the deposited 2HTPP film were rougher on the Al-foil than on Si(0 0 1): After deposition of 18 nm 2HTPP onto Al-foil at 300 K, the sample showed a maximum roughness of 55.5 nm, compared to 21.8 nm for a 2HTPP film with the same thickness on Si(0 0 1). The nominally 18 nm thick 2HTPP film on Al foil (figure 3(e)) is not flat, but comprises large islands with heights in the range of 50 nm, at mutual distances of 100–200 nm. In this context, it is instructive to note that a spherical segment with a base diameter of 200 nm and a height of 45 nm contains the same volume as a flat, quadratic slab of material with 200 nm side length and 18 nm height. After deposition of further material, the roughness is reduced, reaching $R_a = 2.75$ nm and $R_{max} = 21.8$ nm at a film thickness of 50 nm. These values are significantly larger than those obtained with the Si substrate.

It appears that on both substrates, Al-foil and Si(0 0 1), thin multilayers (18 nm) consist of 3D islands, which merge together upon deposition of additional material, resulting in smoother films at higher thicknesses (50 nm). Because the 2HTPP films are more well defined on Si(0 0 1), this type of substrate was chosen for the HAXPES experiments that will be described in the following section.

4.2. Measurement of the reaction depths in M/MTPP/2HTPP systems

In order to examine the influence of different experimental parameters on the extension of the MTPP interphase layer between metals and 2HTPP, HAXPES measurements with photon energies of 3 and 5 keV were performed. These measurements were then used to calculate the reaction depths according to equation (6). The parameters of interest were: (i) the temperature of the organic film (90 and 300 K), (ii) metal flux (0.035 and 0.7 nm min^{-1}), and (iii) the chemical nature of the deposited metal (Fe and Co).

4.2.1. Temperature variation. In the first experiment, a cobalt film with a thickness of 4 nm (as measured by QCM) was deposited at a rate of 0.7 nm min^{-1} onto a 2HTPP film with a thickness of approximately 60 nm kept at 90 K during the deposition. The low temperature of the organic film during metal deposition was expected to reduce the rate of diffusion of metal atoms into the bulk. Likewise, the diffusion of CoTPP out of the reaction zone into the 2HTPP bulk should also be reduced. The related N 1s XP spectra, which were recorded at 3 and 5 keV photon energy, are shown in figure 4. For the pristine 2HTPP layer (figure 4(a)), two peaks at 398.2 eV (iminic nitrogen, =N−) and 400.2 eV (pyrrolic nitrogen, −NH−)

Table 3. Summary of the measured I_r:I_{ur} ratios and the resulting reaction depths. The values in brackets indicate the ±10% error interval of the ratio I_r:I_{ur}; the values in brackets, additionally highlighted in bold face, represent the associated values of d. For each experiment (that is, each column), 3 and 5 keV results for d are not significantly different from each other.

	Co, 90 K, 0.7 nm min^{-1}	Co, 300 K, 0.7 nm min^{-1}	Co, 90 K, 0.035 nm min^{-1}	Co, 300 K, 0.035 nm min^{-1}	Fe, 90 K, 0.7 nm min^{-1}	Fe, 300 K, 0.7 nm min^{-1}
3 keV	I_r:I_{ur} = 0.111 [0.099; 0.122]	I_r:I_{ur} = 0.210 [0.189; 0.231]	I_r:I_{ur} = 0.093 [0.084; 0.102]	I_r:I_{ur} = 0.211 [0.190; 0.232]	I_r:I_{ur} = 0.123 [0.111; 0.135]	I_r:I_{ur} = 0.211 [0.190; 0.232]
	d = 0.52 nm [0.47; 0.57]	**d = 0.95 [0.86; 1.03]**	**d = 0.44 [0.40; 0.48]**	**d = 0.95 [0.86; 1.04]**	**d = 0.58 [0.52; 0.63]**	**d = 0.95 [0.86; 1.04]**
5 keV	I_r:I_{ur} = 0.079 [0.071; 0.087]	I_r:I_{ur} = 0.118 [0.106; 0.130]	I_r:I_{ur} = 0.066 [0.059; 0.073]	I_r:I_{ur} = 0.138 [0.124; 0.152]	I_r:I_{ur} = 0.076 [0.068; 0.084]	I_r:I_{ur} = 0.125 [0.113; 0.138]
	d = 0.60 nm [0.54; 0.66]	**d = 0.88 [0.80; 0.97]**	**d = 0.51 [0.46; 0.55]**	**d = 1.02 [0.93; 1.12]**	**d = 0.58 [0.52; 0.63]**	**d = 0.93 [0.85; 1.02]**

are observed. After deposition of Co, an additional contribution appears at a binding energy of 399.1 eV (red line, yellow shading). This new contribution is associated with a metalloporphyrin complex, indicating that the central cavity of the porphyrin macrocycle incorporated a cobalt atom and released the −NH − hydrogen atoms as H_2, in line with previous work [28, 29, 42]. The relative intensities of the N 1s peaks associated with CoTPP (I_r) and 2HTPP (I_{ur}) (figure 4(b)) allow to estimate the width of the CoTPP layer. Increasing the photon energy from 3 keV to 5 keV, and consequently enhancing the IMFP for 2HTPP and CoTPP by a factor of approx. 1.6 (see table 2), leads to a smaller relative contribution of the N 1s signal from CoTPP: the ratio I_r:I_{ur} changes from 0.111 at 3 keV to 0.079 at 5 keV. This result is in agreement with the assumption of a layered system. (In contrast, in a homogeneous mixture of 2HTPP and CoTPP, the relative signal contributions would be independent of the degree of surface sensitivity of the individual measurements, i.e. they would be independent of the photon energy. This is apparently not the case here.) Using equation (6) with the above values for I_r:I_{ur}, we obtain reaction depths d of 0.52 nm and 0.60 nm for 3 keV and 5 keV, respectively. These thickness values are not significantly different from each other: If we assume a 10% experimental error of the ratio I_r:I_{ur} (estimated from the uncertainty in the actual shape of the signal background), we find that the corresponding error intervals for the thicknesses overlap. At 3 keV, the interval is 0.47 to 0.57 nm, and at 5 keV it is 0.54 to 0.66 nm. These intervals, plus the equivalent values for all following experiments, are compiled in table 3.

When the experiments were repeated with the 2HTPP film held at 300 K during metal deposition, a larger contribution of the reacted species (red line, yellow shading) was observed in the N 1s spectra (figure 4(c)), corresponding to a larger reaction depths d (i.e. a thicker CoTPP interphase layer). The related intensity ratios were I_r:I_{ur} = 0.210 and 0.118 at 3 and 5 keV, respectively. Again, this reduction of the I_r:I_{ur} ratio with increasing photon energy is a direct, but qualitative, indication for the presence of a distinct CoTPP layer. Application of equation (6) (with a 2HTPP layer thickness of 40 nm for this specific experiment) results in thicknesses of 0.95 nm (3 keV) and 0.88 nm (5 keV). Notably, the increase in temperature from 90 K to 300 K led to an increase in the width of the CoTPP layer by a factor of 1.6. Apparently, the mobility of 2HTPP and CoTPP is still low at 300 K—otherwise CoTPP and 2HTPP molecules would start to interdiffuse, which would lead to a transition away from a layered to a homogeneously mixed configuration. Hence, the increase in CoTPP layer thickness must be attributed to an increased mobility of the Co atoms after their adsorption on the surface.

4.2.2. Variation of the metal flux during deposition. In order to elucidate the influence of the metal flux on the extension of the CoTPP interphase, a further set of experiments with a reduced flux of 0.035 nm min^{-1} was conducted at sample temperatures of 90 K and 300 K. A lower flux of metal atoms reduces their transient concentration on the surface of the organic material. The thereby reduced probability for the encounter of the metal atoms is detrimental for the initial metal nucleation and cluster formation. The competing processes, i.e. the diffusion of the metal atoms into the organic film and the reaction with the molecules, should therefore be favored. This expectation is also in agreement with literature [8, 9].

Figure 5 shows the result for the deposition of Co at a reduced flux of 0.035 nm min^{-1} at 2HTPP film temperatures of 90 and 300 K. At 90 K (figure 5(a)), the differences to the experiments with a twenty-fold higher deposition rate are marginal. At 3 keV photon energy, the intensity ration I_r:I_{ur} is 0.093 and at 5 keV it is 0.066. With equation (6), this leads to thicknesses d of 0.44 nm (3 keV) and 0.51 nm (5 keV). The result is not significantly different from the corresponding low-temperature experiment with a Co flux of 0.7 nm min^{-1}. This unexpected result can be explained with the low temperature and the resulting small diffusion rate of Co, which confines the reaction to the topmost layer of the organic film, regardless of the flux.

Figure 5(b) shows the corresponding data for the low-flux Co deposition at 300 K. Here, the 3 keV measurement shows a ratio between reacted and unreacted signals of 0.211, while the measurement at 5 keV yields a ratio of 0.138. Application of equation (6) to these values results in reaction depths of 0.95 nm (3 keV) and 1.02 nm (5 keV). Again, this result is in contrast to the expectation: the flux reduction does not result in a significant increase of the reaction depth. Apparently,

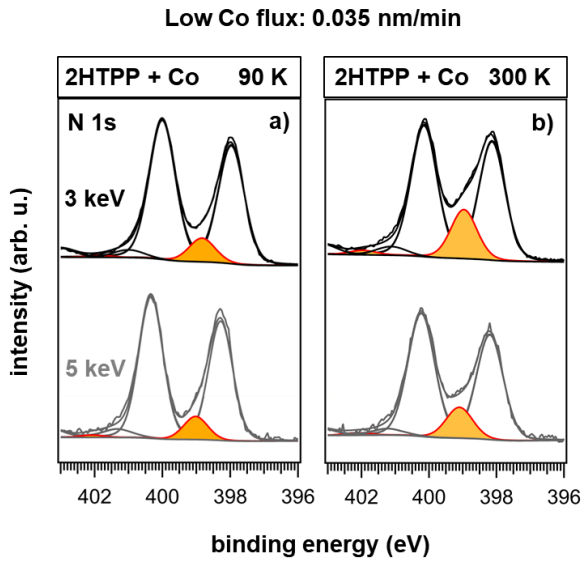

Figure 5. N 1s XP spectra of the Co/2HTPP reactive interface recorded with $h\nu = 3$ keV and 5 keV after cobalt deposition at a lower flux of 0.035 nm min^{-1}. Keeping the sample temperature at (a) 90 K results in a significantly thinner CoTPP layer than Co deposition at (b) 300 K.

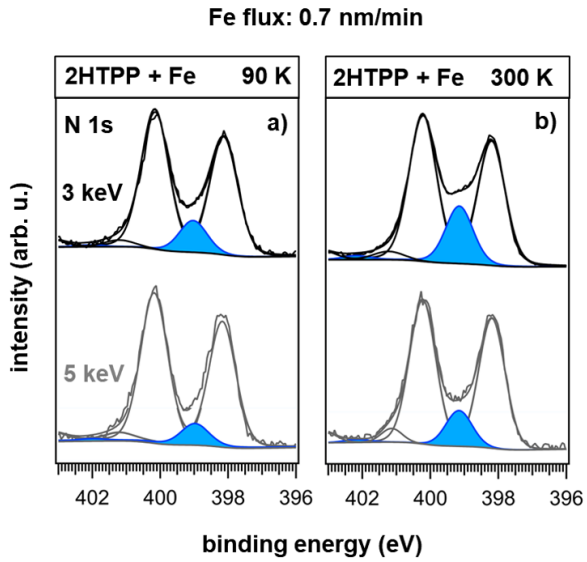

Figure 6. N 1s XP spectra recorded after iron deposition onto 2HTPP films with a flux of 0.7 nm min^{-1}. The photon energies were $h\nu = 3$ keV and 5 keV. At 90 K (a), the fraction of FeTPP (blue) is significantly smaller than at 300 K (b).

the variation of the flux by a factor of twenty is not enough to observe the anticipated effects. This result can possibly be attributed to attractive interactions between Co atoms and CoTPP molecules. These interactions could immobilize free cobalt atoms in the near-surface region even at room temperature and thus induce the initial formation of clusters on the organic film even at very low surface concentrations of metal atoms, i.e. at very low fluxes. (Note that only the initial metal nucleation and cluster formation are relevant here, because they depend on the surface concentration of the metal atoms. Once metal clusters are present on the surface, the relative probabilities for the attachment of a metal atom to a cluster versus its diffusion/reaction in the bulk becomes independent of the surface concentration of the metal atoms and, thus, independent of the flux of metal atoms. This follows from basic considerations of the reaction kinetics and the facts that both the cluster growth and the metalation reaction of the porphyrin are irreversible under the experimental conditions.) The formation of such a M—MTPP bond is not purely speculative, but is supported by DFT calculations from literature. For example, the bond between a Ag atom and a CoTPP molecule was found to have a dissociation energy of 92 kJ mol^{-1} [43]. That a bond of this strength can easily lead to the postulated trapping effect is shown by a simple estimation of the corresponding rate constant for bond dissociation: Assuming a pre-exponential factor of 1×10^{13} s^{-1}, the rate constant for the bond dissociation at 300 K is only 10^{-3} s^{-1}. This means that the average lifetime of a trapped metal atom is ~15 min. One way to test this hypothesis would be to extend the experiments to temperatures well above 300 K. However, this is not possible, because the elevated temperatures would lead to recrystallization of the organic films and thus make the (laterally integrating) HAXPES studies meaningless [44, 45]. The alternative approach, much lower metal fluxes, can also not be realized because of problems with sample contamination during the resulting extremely long deposition times.

4.2.3. Variation of the type of metal atoms. In a final set of experiments, iron was used instead of cobalt to clarify whether the surprisingly thin interphase layers observed in the Co/CoTPP/2HTPP system are specific for cobalt or also occur with other metals. It is known from (gas phase) DFT calculations that the reaction of 2HTPP with Co atoms has a small energy barrier of approximately 10 kJ mol^{-1}, while the porphyrin metalation reaction with iron proceeds without a barrier [29]. Thus, an increased amount of interface reaction may occur in the case of Fe deposition. In the first experiment, iron was deposited with a flux of 0.7 nm min^{-1} onto a 44 nm thick 2HTPP film, held at 90 K. Figure 6(a) shows the related N 1s HAXPES spectra. Measuring the intensity ratio I_r:I_{ur} results in values of 0.123 and 0.076 at 3 and 5 keV, respectively. These values are virtually identical to those observed for the deposition of Co under similar conditions (0.111 and 0.079). Hence, the calculated film thicknesses are 0.58 nm for both photon energies. Finally, when Fe was deposited with a rate of 0.7 nm min^{-1} onto a 42 nm thick 2HTPP film kept at 300 K (figure 6(b)), we found ratios of 0.211 (3 keV) and 0.125 (5 keV), leading to a thickness of 0.95 and 0.93 nm, respectively. It is not surprising that this experiment does not show significant deviation to the analogue Co experiment, because the differences between the metalation barriers for the different metals should not matter at room temperature. Table 3 summarizes the obtained ratios between reacted and unreacted species for the different systems.

The generally low reaction depths at low *and* ambient temperatures are even more surprising if one considers that metal atoms can usually easily diffuse through organic layers, unless special precautions are taken to prevent this movement [46]. For example, when gold was deposited onto a film of TMC-polycarbonate at 230 K with a rate of 0.1 nm min^{-1}, the metal was found to diffuse several tens of nanometers into the polymer [9]. In contrast, we find that Co and Fe atoms are exclusively present close to the surface of the porphyrin film. Apparently, there is a mechanism that traps the metal atoms efficiently in the near-surface region and allows only a few metal atoms to penetrate into the organic film before the metal film on top closes and disconnects the organic film irreversibly from further supply with single Co or Fe atoms. One candidate for such a mechanism is the M—MTPP interaction, which was theoretically predicted for related systems [43, 47]. It appears likely that the M—MTPP complexes, if they exist, would act as seeds for the growth of metal clusters, favoring a fast closure of the metallic film on top of the porphyrin layer. Similar effects are expected to occur in other reactive metal/organic interfaces when the reaction at the interface leads to the formation of metal complexes that can act as nucleation sites for the formation of metal clusters. The comparison of the investigated systems to the diffusion of gold atoms in polymers offers also another interesting aspect, regarding the different sizes of the metal atoms. Due to the fact that gold atoms are significantly larger than Co or Fe atoms, one would expect that the diffusion of gold atoms in organic materials is slower by several orders of magnitude—an effect that has indeed been observed in previous studies in inorganic samples [48, 49]. The fact that Fe and Co, despite their smaller atomic radii, show here much less diffusion than gold in an organic polymer further corroborates our conclusion that the free diffusion of Fe and Co is blocked by chemical interactions.

5. Summary

The formation of interlayers (interphases) at reactive metal-organic interfaces was studied with HAXPES. Specifically, it was shown that vapor deposition (under UHV conditions) of the transition metals iron and cobalt onto tetraphenylporphyrin (2HTPP) films leads to the formation of interlayers of the corresponding metalloporphyrins (CoTPP and FeTPP) between the metal and the pristine organic material. Variation of the deposition conditions revealed that the temperature of the organic material during the metal deposition is the single most important parameter that controls the thickness the MTPP interlayers. Deposition at 90 K resulted in FeTPP and CoTPP interphase layers that are roughly only half as thick as those obtained by room temperature deposition: typically ~0.5 nm at 90 K versus ~1 nm at 300 K. In contrast, variation of the metal flux within experimentally feasible boundaries (by a factor 20) had a negligible influence on the thickness of the formed MTPP interlayer. Likewise, very similar results were obtained for Fe and Co, despite differences in the reaction barriers for the formation of the respective metalloporphyrin complexes. The low values for the reaction depth generally indicate that metal diffusion into the 2HTPP film seems to be heavily restricted. Our results point towards the existence of a mechanism that traps the Co and Fe atoms close the 2HTPP film surface. In addition, we demonstrate that HAXPES readily provides the overall thickness of the formed interlayer, while the shape of the concentration profile at the MTPP/2HTPP interface cannot be reliably determined.

Acknowledgments

Financial support by the Deutsche Forschungsgemeinschaft (DFG) through the SFB 1083 'Structure and Dynamics of Internal Interfaces' is gratefully acknowledged. We thank the Helmholtz-Zentrum Berlin for allocation of synchrotron radiation beamtime at BESSY II and financial support. Furthermore we want to express our gratitude to Dr Roberto Felix Duarte for assistance at the HIKE endstation. MS thanks the Stiftung Stipendien-Fonds des Verbandes der Chemischen Industrie for funding.

ORCID iDs

Martin Schmid https://orcid.org/0000-0002-1686-241X
Benedikt P Klein https://orcid.org/0000-0002-6205-8879
Nicolas Bock https://orcid.org/0000-0002-4990-8533

References

[1] Knupfer M and Peisert H 2005 Electronic properties of interfaces between model organic semiconductors and metals *Physics of Organic Semiconductors* ed W Brütting (New York: Wiley) p 41
[2] Koch N, Ueno N and Wee A T S (ed) 2013 *The Molecule-Metal Interface* (New York: Wiley)
[3] Scott J C 2003 *J. Vac. Sci. Technol.* A **21** 521
[4] Kumatani A, Li Y, Darmawan P, Minari T and Tsukagoshi K 2013 *Sci. Rep.* **3** 1026
[5] Tajima H, Yoshida K, Sato S, Kadoya T and Yamada J 2017 *J. Phys. Chem.* C **121** 14725
[6] Gao Y H, Shao Y D, Yan L J, Li H, Su Y T, Meng H and Wang X W 2016 *Adv. Funct. Mater.* **26** 4456
[7] Gottfried J M 2016 *New J. Phys.* **18** 111002
[8] Strunskus T, Kiene M, Willecke R, Thran A, von Bechtolsheim C and Faupel F 1998 *Mater. Corros.* **49** 180
[9] Strunskus T, Zaporojtchenko V, Behnke K, von Bechtolsheim C and Faupel F 2000 *Adv. Eng. Mater.* **2** 489
[10] Zaporojtchenko V, Strunskus T, Behnke K, Von Bechtolsheim C, Thran A and Faupel F 2000 *Microelectron. Eng.* **50** 465
[11] Leidheiser H and Deck P D 1988 *Science* **241** 1176
[12] Salaneck W R and Bredas J L 1996 *Adv. Mater.* **8** 48
[13] Ozawa K, Kakubo T, Shimizu K, Amino N, Mase K, Ikenaga E, Nakamura T, Kinoshita T and Oji H 2014 *Appl. Surf. Sci.* **320** 177
[14] Karim A and Kumar S (ed) 2000 *Polymer Surfaces, Interfaces and Thin Films* (Singapore: World Scientific)
[15] Sacher E, Pireaux J-J and Kowalczyk S P 1990 *Metallization of Polymers* (*ACS Symposium Series* vol 440) (Washington, DC: American Chemical Society)
[16] Sacher E (ed) 2002 *Metallization of Polymers* vol 2 (Dordrecht: Kluwer)

[17] Zhu X Y 2004 *Surf. Sci. Rep.* **56** 1
[18] Diaz S F, Zhu J F, Harris J J W, Goetsch P, Merte L R and Campbell C T 2005 *Surf. Sci.* **598** 22
[19] Zhu J F, Goetsch P, Ruzycki N and Campbell C T 2007 *J. Am. Chem. Soc.* **129** 6432
[20] Larralde H, Araujo M, Havlin S and Stanley H E 1992 *Phys. Rev.* A **46** R6121
[21] Fife P C and Ling H 1988 *Nonlinear Anal.* **12** 19
[22] Galfi L and Racz Z 1988 *Phys. Rev.* A **38** 3151
[23] Hilhorst D, vanderHout R and Peletier L A 1996 *J. Math. Anal. Appl.* **199** 349
[24] Langhoff T A and Schnack E 2008 *Chem. Eng. Sci.* **63** 3948
[25] Muntean A, Böhm M and Kropp J 2011 *Chem. Eng. Sci.* **66** 538
[26] Permikin D V and Zverev V S 2013 *Int. J. Heat Mass Transfer* **57** 215
[27] Diller K, Papageorgiou A C, Klappenberger F, Allegretti F, Barth J V and Auwärter W 2016 *Chem. Soc. Rev.* **45** 1629
[28] Marbach H 2015 *Acc. Chem. Res.* **48** 2649
[29] Shubina T E, Marbach H, Flechtner K, Kretschmann A, Jux N, Buchner F, Steinrück H P, Clark T and Gottfried J M 2007 *J. Am. Chem. Soc.* **129** 9476
[30] Gottfried J M 2015 *Surf. Sci. Rep.* **70** 259
[31] Gorgoi M *et al* 2009 *Nucl. Instrum. Methods Phys. Res.* A **601** 48
[32] Schäfers F, Mertin M and Gorgoi M 2007 *Rev. Sci. Instrum.* **78** 123102
[33] Schmid M, Steinrück H P and Gottfried J M 2015 *Surf. Interface Anal.* **47** 1080
[34] Schmid M, Steinrück H P and Gottfried J M 2014 *Surf. Interface Anal.* **46** 505
[35] Seah M P and Spencer S J 2011 *Surf. Interface Anal.* **43** 744
[36] Gries W H 1996 *Surf. Interface Anal.* **24** 38
[37] Werner W S M, Gries W H and Stori H 1991 *Surf. Interface Anal.* **17** 693
[38] Hagberg A and Meron E 1994 *Nonlinearity* **7** 805
[39] Batens N and Van Keer R 2003 *Chem. Eng. Sci.* **58** 4815
[40] Chopard B and Droz M 1991 *Europhys. Lett.* **15** 459
[41] Chen M, Zhou H, Klein B P, Zugermeier M, Krug C K, Drescher H J, Gorgoi M, Schmid M and Gottfried J M 2016 *Phys. Chem. Chem. Phys.* **18** 30643
[42] Gottfried J M and Marbach H 2009 *Z. Phys. Chem.* **223** 53
[43] Hieringer W, Flechtner K, Kretschmann A, Seufert K, Auwärter W, Barth J V, Görling A, Steinrück H P and Gottfried J M 2011 *J. Am. Chem. Soc.* **133** 6206
[44] Stöhr M, Gabriel M and Möller R 2002 *Europhys. Lett.* **59** 423
[45] Käfer D, Wöll C and Witte G 2009 *Appl. Phys. A: Mater. Sci. Process.* **95** 273
[46] Tai Y, Shaporenko A, Noda H, Grunze M and Zharnikov M 2005 *Adv. Mater.* **17** 1745
[47] Hötger D *et al* 2018 *Nanoscale* **10** 21116
[48] Dyson B F 1966 *J. Appl. Phys.* **37** 2375
[49] Hahn H and Averback R S 1988 *Phys. Rev.* B **37** 6533

ChemComm

COMMUNICATION

View Article Online
View Journal | View Issue

Cite this: *Chem. Commun.*, 2019, **55**, 13665

Received 13th September 2019,
Accepted 15th October 2019

DOI: 10.1039/c9cc07170a

rsc.li/chemcomm

Direct synthesis of dilithium tetraphenylporphyrin: facile reaction of a free-base porphyrin with vapor-deposited lithium†

Maik Schöniger, ‡ Stefan R. Kachel,‡ Jan Herritsch, Philipp Schröder, Mark Hutter and J. Michael Gottfried *

A solvent-free dilithium porphyrin was synthesized by direct reaction of free-base *meso*-tetraphenylporphyrin with elemental lithium in ultra-high vacuum. The reaction product dilithium tetraphenylporphyrin was studied by temperature-programmed desorption mass spectrometry (TPD-MS) and hard X-ray photoelectron spectroscopy (HAXPES). The solid-state reaction is thermodynamically favored, according to density functional theory (DFT) calculations.

Porphyrins, the 'colors of life',[1] are widespread in nature and find numerous technological applications.[2–4] While transition-metal porphyrins can be very stable with respect to metal exchange, alkali metal porphyrins (AMPs) with electron-rich ligands such as *meso*-tetraphenylporphyrin (TPP) are considered as labile and water-sensitive complexes.[5] Although AMPs were observed as early as 1938,[6] they were mainly characterized in solution or as solvates. The lability of AMPs in solution has been used for the synthesis of other metalloporphyrins by metal exchange.[7–10] The first X-ray structure of an AMP solvate was obtained for the tetrahydrofuran (THF) adduct of dilithium octaethylporphyrin, $Li_2OEP(THF)_4$, formed by reaction of octaethylporphyrin (H_2OEP) with $LiN(SiMe_3)_2$.[11] The solid consists of a $[Li(THF)_4]^+$ cation and a $[Li(OEP)]^-$ anion with a square-planar coordination of Li in the center of the porphyrin ring.[11] In other AMP solvates such as $Li_2TPP(OEt_2)_2$, both Li ions are bound to opposite sides of the porphyrin ring in a square-bipyramidal fashion and carry an additional diethyl ether (OEt_2) ligand.[12] This bipyramidal structure has also been reported for dilithium porphyrins in solution and for solid Na and K porphyrins.[13] Besides these structurally well-characterized solvates, the two solvent-free AMPs Li_2TPP and Li_2OEP have been obtained from solution, but have not been studied in detail.[14]

Here, we report that solvent-free dilithium tetraphenylporphyrin (Li_2TPP) can be prepared by vapor deposition of lithium onto free-base *meso*-tetraphenylporphyrin (H_2TPP) in ultra-high vacuum (UHV), by the reaction shown in Fig. 1. Unlike the very limited reaction depths of transition metals in bulk porphyrins,[15,16] or the metalation of monolayers,[4,17–19] we find that Li diffuses readily into the solid porphyrin film, which makes the reaction useful for synthetic purposes. The bulk reaction between metallic Li and organic molecules is also relevant for the field of organic electronics, where metals with low work functions are vapor-deposited onto organic semiconductors as electron-injecting electrodes and intermixing or reaction of the layers is usually not desirable.[20–22] The reaction of Li with organic materials also plays a role in Li-based electrochemical energy storage, in which the formation of the solid–electrolyte interphase (SEI) and the diffusion of lithium in the SEI is crucial for device performance.[23,24] Porphyrin-based electrodes have also proven to be efficient electrode materials in lithium batteries.[25]

The Li_2TPP layers obtained by the reaction shown in Fig. 1 were investigated by temperature-programmed desorption mass

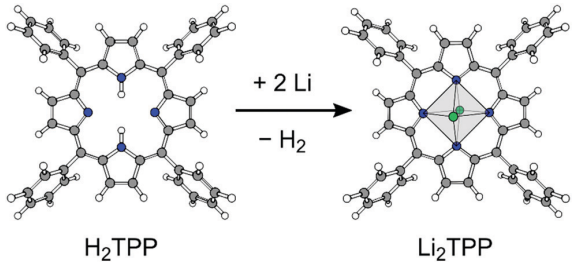

Fig. 1 Direct metalation of *meso*-tetraphenylporphyrin (H_2TPP) with two equivalents of elemental Li, resulting in the formation of dilithium tetraphenylporphyrin (Li_2TPP) and H_2. The figure shows the geometry-optimized gas-phase structures calculated by DFT. The distorted square-bipyramidal polyhedron formed by the lithium and nitrogen atoms in Li_2TPP is highlighted.

Department of Chemistry, Philipps University Marburg, Hans-Meerwein-Straße 4, 35032 Marburg, Germany. E-mail: michael.gottfried@chemie.uni-marburg.de

† Electronic supplementary information (ESI) available: Experimental and computational details, additional TPD-MS and XPS data, XPS information depths, Born–Haber cycle, additional DFT results. See DOI: 10.1039/c9cc07170a

‡ These authors contributed equally to this study and share first authorship.

View Article Online
Communication ChemComm

spectrometry (TPD-MS) and hard X-ray photoelectron spectroscopy (HAXPES). Complementary density functional theory (DFT) calculations provide insight into the energetics of the reaction.

Before the reaction between H_2TPP and Li was studied, reference TPD-MS measurements were performed with pristine H_2TPP. For this purpose, a film of H_2TPP with a thickness of 20 nm was vapor-deposited onto a clean Au(111) surface. Subsequently, a TPD-MS experiment was performed by heating the sample with a constant rate of 0.1 K s^{-1} between 300 and 700 K while rapidly recording mass spectra, as described in the ESI.† The resulting temperature-resolved mass spectra are shown as TPD-MS maps in Fig. 2a and Fig. S1a in the ESI.† Around 485 K a dominant peak is observed in a mass range that indicates desorption of intact H_2TPP (614 amu). Arrhenius plot analysis of the zeroth-order desorption trace (Fig. 2e) yields a desorption activation energy of 200 kJ mol^{-1}, which is in the range of literature values for the sublimation enthalpy (between 111 and 240 kJ mol^{-1}).[26]

To study the reaction between H_2TPP and Li, a fresh 20 nm thick film of H_2TPP was deposited onto the clean Au(111) surface, followed by the deposition of 1 nm Li at 300 K. This thickness of Li is close (within 5%) to the stoichiometric amount required for complete conversion of the H_2TPP film to Li_2TPP. After this preparation, a TPD-MS experiment was performed. The results in Fig. 2b show a dominant signal around the mass of Li_2TPP (626 amu), indicating the formation of the dilithium complex in high yield. The peak temperature of 565 K, which exceeds that of H_2TPP by 80 K, and the higher desorption energy of 234 kJ mol^{-1} (Fig. 2d) reveal increased intermolecular interactions, compared to H_2TPP. The H_2TPP signal has completely disappeared, which shows that the free-base porphyrin reacts completely. Weak additional features appear at 619 and 637 amu. These masses correspond to LiTPP and LiTPP·H_2O, respectively. The LiTPP is most likely formed by fragmentation of Li_2TPP in the mass spectrometer, because the desorption traces of Li_2TPP and LiTPP have the same temperature dependence (see Fig. S2 in the ESI†) and their intensities have a constant ratio of ≈12 : 1. The LiTPP·H_2O adduct (≈5% of the Li_2TPP signal) is attributed to reaction with residual water. The small Li_2TPP-related signal around 500 K is due to the formation of small crystallites with lower desorption energy (see Arrhenius analysis in Fig. S3 in the ESI†), in agreement with previous work.[27] It is worth mentioning that the LiTPP·H_2O adduct is only observed at temperatures where the crystallites desorb.

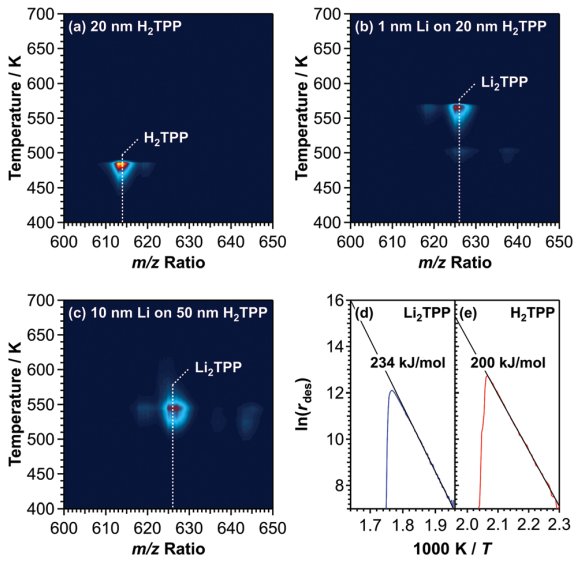

Fig. 2 TPD-MS maps for (a) 20 nm H_2TPP, (b) 1 nm Li on 20 nm H_2TPP, and (c) 10 nm Li on 50 nm H_2TPP, each on Au(111), in the relevant mass region from 600 to 650 amu. Data for other mass ranges are shown in the ESI.† The spectra were normalized to the maximum intensity of the H_2TPP signal (a). The heating rate was 0.1 K s^{-1} and one mass range cycle took 8 seconds (see the ESI† for further experimental details). Arrhenius plot analysis for (d) Li_2TPP and (e) H_2TPP, with the desorption rates r_{des} divided by the mass spectrometer unit (counts per second, for further details see the ESI†), yields desorption energies of 234 and 200 kJ mol^{-1}, respectively.

To investigate whether even thicker H_2TPP films can be fully converted, 10 nm Li were deposited onto a 50 nm H_2TPP film. An over-stoichiometric amount of Li was chosen to ensure complete reaction. The TPD-MS map in Fig. 2c shows that the main product is again Li_2TPP, with the water adduct Li_2TPP·H_2O (644 amu) as a side product (≈13%). Analysis of the individual TPD traces (see Fig. S2b in the ESI†) indicates that the film substantially recrystallizes during the heating,[27] which leads to the observed broadening of the Li_2TPP peak. Again, no traces of residual H_2TPP were found, indicating complete reaction.

The mass spectra presented above show that free-base H_2TPP reacts completely with Li forming Li_2TPP. However, it remains unclear whether the reaction occurs already at room temperature or is induced by the elevated temperatures during the TPD-MS experiment. To clarify this question, additional experiments with X-ray photoelectron spectroscopy (XPS) were performed.

The XPS measurements were carried out with synchrotron radiation in the hard X-ray regime between 2 and 7 keV, to take advantage of the increased information depth of photoelectrons with high kinetic energies.[16,28] In this way, the composition of the film can be probed over the entire thickness and not only at the surface, as is the case for conventional XPS. At the highest photon energy (E_{ph}) of 7 keV, the information depth of N 1s photoelectrons is 33.6 nm for H_2TPP and 32.7 nm for Li_2TPP, as was calculated by the Gries approach.[16,29] The details of the calculation and the information depths for the other photon energies are given in the ESI.† The XPS measurements were performed with a H_2TPP film of 24 nm thickness, which is substantially smaller than the maximum information depth. By variation of E_{ph} (and thus, the information depth), the depth homogeneity of the reacted film can additionally be examined. This film was prepared on a Si(001) surface, as is described in detail in the ESI.†

The resulting N 1s XP spectra are shown in Fig. 3. The spectrum of the pristine H_2TPP film (Fig. 3a) consists of two peaks, which are attributed to the pyrrolic (–N(H)–, 400.2 eV) and iminic (–N═, 398.1 eV) nitrogen species,[4,30] see Fig. 1. After deposition of Li at room temperature (Fig. 3b–e), a new peak appears at a

View Article Online
ChemComm Communication

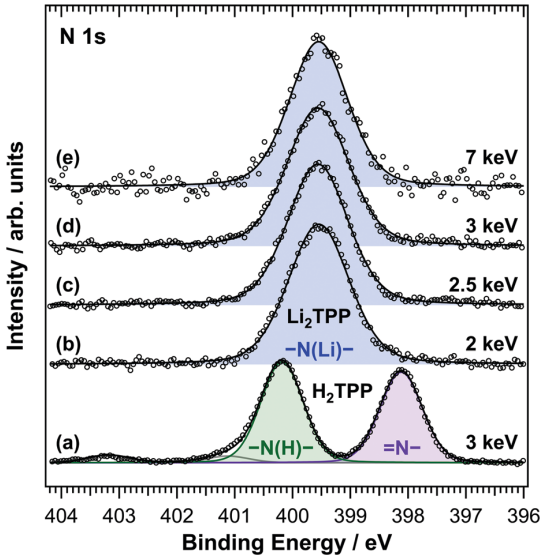

Fig. 3 N 1s X-ray photoelectron spectra of (a) H_2TPP and (b)–(e) Li_2TPP formed by deposition of Li onto a 24 nm thick H_2TPP layer, taken with the indicated photon energies.

binding energy (BE) of 399.6 eV, while the two H_2TPP-related peaks disappear. The presence of a single N 1s peak indicates that all four nitrogen atoms are chemically equivalent, which is the case in the metal complex.[4,18,19] The information depth of the experiment exceeds the film thickness also after deposition of Li, as can be seen from the Si 1s signal related to the Si(001) substrate in Fig. S4 in the ESI.† The formation of Li_2TPP is also supported by the related Li 1s XPS data in Fig. S5 in the ESI,† which show a chemical shift to higher BE in line with the oxidation of metallic Li to Li^+ ions.

The absence of any H_2TPP-related signals at a photon energy of 7 keV, where the information depth exceeds the film thickness, proves that the H_2TPP film reacts over its entire thickness at room temperature. For the photon energies of 2, 2.5 and 3 keV (Fig. 3b–d), the information depths in Li_2TPP are 10.1, 12.6 and 15.0 nm (see Table S3 in the ESI†), respectively, *i.e.*, they are smaller than the film thickness. Still, position and general shape of the N 1s peaks are the same as for the 7 keV spectrum, indicating that the reaction is homogeneous over the entire depth of the film.

The fact that the H_2TPP film reacts over its entire thickness of 24 nm (or even 50 nm in the TPD-MS experiment) is exceptional when compared to related reactions with transition metals. For example, when Fe or Co are deposited onto H_2TPP films at room temperature, formation of the related FeTPP and CoTPP complexes is limited to a depth of approximately 1 nm.[16] Additionally deposited metal forms a layer of metallic Fe or Co on-top of the organic film. It can be concluded that the room-temperature mobility of Li atoms in the solid porphyrin is much higher than that of typical transition metals.

To evaluate whether the direct formation of Li_2TPP is thermodynamically feasible, gas-phase DFT calculations were performed. For the reaction shown in Fig. 1, a total energy of ΔE_{DFT} = −499.8 kJ mol^{-1} was obtained, indicating that the gas-phase process is strongly exothermic. In the following, we use this gas-phase value to estimate the energy for the corresponding solid-state reaction by means of a Born–Haber (BH) cycle (see Fig. S6 in the ESI†), which includes the sublimation enthalpy of Li metal and the desorption energies of H_2TPP and Li_2TPP as obtained from TPD-MS above. The BH cycle yields an approximate reaction energy of −215 kJ mol^{-1}, which is still strongly exothermic. Another driving force of the solid-state reaction is the entropy gain from the release of gaseous H_2 $\left(S^\circ_{\text{gas,1 bar}} = 130.68 \text{ J mol}^{-1} \text{ K}^{-1} \text{ at } 298.15 \text{ K}\right)$.[31] Energetic and entropic contributions add up to a standard Gibbs energy of approximately −254 kJ mol^{-1}, indicating that the formation of Li_2TPP is thermodynamically favored even in the solid state. Vapor deposition should therefore not be necessary to induce the reaction, except to overcome kinetic barriers. The calculated minimum energy structure of the Li_2TPP complex is shown in Fig. S7 in the ESI.† The Li ions are located on both sides of the porphyrin ring, but not above (or below) the center of the porphyrin ring, in agreement with previous theory work.[32] The frontier orbitals HOMO−1, HOMO, LUMO and LUMO+1 are exclusively localized at the porphyrin ring; the Li ions do not contribute (see Fig. S8 in the ESI†).

In conclusion, we have demonstrated that dilithium tetraphenylporphyrin (Li_2TPP) can be prepared in solvent-free form by direct reaction of *meso*-tetraphenylporphyrin (H_2TPP) with vapor-deposited metallic Li at room temperature. DFT calculations show that the reaction is strongly exothermic in the gas phase. A negative standard Gibbs energy for the solid-state reaction confirms that the reaction is thermodynamically favored also in the condensed phase. Our results may pave the way to simple solid-state syntheses of alkali metal porphyrins and thus increase the availability of these compounds as reactants for organic and inorganic synthesis. The exceptionally high mobility of Li in the organic material is relevant for the deposition of metal electrodes in organic electronic devices and the transport of Li in electrochemical energy storage.

Financial support by the Deutsche Forschungsgemeinschaft (DFG, German Research Foundation) through project number 223848855 – SFB 1083 is gratefully acknowledged. We thank the Helmholtz-Zentrum Berlin for allocation of synchrotron radiation beamtime at BESSY II and financial support. We thank M. Albus, C. Zülch and F. Fillsack for assistance during the measurements. We thank the HRZ Marburg for computational resources.

Conflicts of interest

There are no conflicts to declare.

Notes and references

1 L. R. Milgrom, *The Colors of Life*, Oxford University Press, 1997.
2 *Handbook of Porphyrin Science*, ed. K. M. Kadish, K. M. Smith and R. Guilard, Singapore, 2010.
3 W. Auwärter, D. Ecija, F. Klappenberger and J. V. Barth, *Nat. Chem.*, 2015, 7, 105.

4 J. M. Gottfried, *Surf. Sci. Rep.*, 2015, **70**, 259.
5 J. Arnold, in *The Porphyrin Handbook*, ed. K. M. Kadish, K. M. Smith and R. Guilard, Inorganic, Organometallic and Coordination Chemistry, Academic Press, 2000, vol. 3, ch. 17, p. 113.
6 H. Fischer and K. Herrle, *Hoppe-Seyler's Z. Physiol. Chem.*, 1938, **251**, 85.
7 J. W. Barnes and G. D. Dorough, *J. Am. Chem. Soc.*, 1950, **72**, 4045.
8 J. W. Buchler, J. Hüttermann and J. Löffler, *Bull. Chem. Soc. Jpn.*, 1988, **61**, 71.
9 J. A. Cissell, T. P. Vaid and G. P. A. Yap, *J. Am. Chem. Soc.*, 2007, **129**, 7841.
10 A. Weiss, M. C. Hodgson, P. D. W. Boyd, W. Siebert and P. J. Brothers, *Chem. – Eur. J.*, 2007, **13**, 5982.
11 J. Arnold, *J. Chem. Soc., Chem. Commun.*, 1990, 976.
12 D. Y. Dawson and J. Arnold, *J. Porphyrins Phthalocyanines*, 1997, **1**, 121.
13 J. Arnold, D. Y. Dawson and C. G. Hoffman, *J. Am. Chem. Soc.*, 1993, **115**, 2707.
14 H. Brand, J. A. Capriotti and J. Arnold, *Inorg. Chem.*, 1994, **33**, 4334.
15 M. Chen, H. Zhou, B. P. Klein, M. Zugermeier, C. K. Krug, H. J. Drescher, M. Gorgoi, M. Schmid and J. M. Gottfried, *Phys. Chem. Chem. Phys.*, 2016, **18**, 30643.
16 M. Schmid, S. R. Kachel, B. P. Klein, N. Bock, P. Müller, R. Riedel, N. Hampp and J. M. Gottfried, *J. Phys.: Condens. Matter*, 2019, **31**, 094002.
17 T. E. Shubina, H. Marbach, K. Flechtner, A. Kretschmann, N. Jux, F. Buchner, H. P. Steinrück, T. Clark and J. M. Gottfried, *J. Am. Chem. Soc.*, 2007, **129**, 9476.
18 K. Diller, A. C. Papageorgiou, F. Klappenberger, F. Allegretti, J. V. Barth and W. Auwärter, *Chem. Soc. Rev.*, 2016, **45**, 1629.
19 H. Marbach, *Acc. Chem. Res.*, 2015, **48**, 2649.
20 F. Bebensee, M. Schmid, H. P. Steinrück, C. T. Campbell and J. M. Gottfried, *J. Am. Chem. Soc.*, 2010, **132**, 12163.
21 F. Bebensee, J. F. Zhu, J. H. Baricuatro, J. A. Farmer, Y. Bai, H. P. Steinrück, C. T. Campbell and J. M. Gottfried, *Langmuir*, 2010, **26**, 9632.
22 J. Zhu, F. Bebensee, W. Hieringer, W. Zhao, J. H. Baricuatro, J. A. Farmer, Y. Bai, H.-P. Steinrück, J. M. Gottfried and C. T. Campbell, *J. Am. Chem. Soc.*, 2009, **131**, 13498.
23 A. Ramasubramanian, V. Yurkiv, T. Foroozan, M. Ragone, R. Shahbazian-Yassar and F. Mashayek, *J. Phys. Chem. C*, 2019, **123**, 10237.
24 X.-B. Cheng, R. Zhang, C.-Z. Zhao, F. Wei, J.-G. Zhang and Q. Zhang, *Adv. Sci.*, 2016, **3**, 1500213.
25 P. Gao, Z. Chen, Z. Zhao-Karger, J. E. Mueller, C. Jung, S. Klyatskaya, T. Diemant, O. Fuhr, T. Jacob, R. J. Behm, M. Ruben and M. Fichtner, *Angew. Chem., Int. Ed.*, 2017, **56**, 10341.
26 A. Stefanov, A. Stibor, A. Dominguez-Clarimon and M. Arndt, *J. Chem. Phys.*, 2004, **121**, 6935.
27 P. Jakob and D. Menzel, *J. Chem. Phys.*, 1996, **105**, 3838.
28 C. Weiland, A. K. Rumaiz, P. Pianetta and J. C. Woicik, *J. Vac. Sci. Technol., A*, 2016, **34**, 030801.
29 W. H. Gries, *Surf. Interface Anal.*, 1996, **24**, 38–50.
30 F. Buchner, K. Flechtner, Y. Bai, E. Zillner, I. Kellner, H. P. Steinrück, H. Marbach and J. M. Gottfried, *J. Phys. Chem. C*, 2008, **112**, 15458.
31 M. W. Chase, Jr., *J. Phys. Chem. Ref. Data, Monogr.*, 1998, **9**, 1.
32 D.-M. Chen, X. Liu, T.-J. He and F.-C. Liu, *Chem. Phys. Lett.*, 2002, **361**, 106.

P6

Electronic Supplementary Information (ESI) for

Direct Synthesis of Dilithium Tetraphenylporpyhrin: Facile Reaction of a Free-Base Porphyrin with Vapor-Deposited Lithium

Maik Schöniger‡, Stefan R. Kachel‡, Jan Herritsch, Philipp Schröder, Mark Hutter, J. Michael Gottfried*

Department of Chemistry, Philipps University Marburg, Hans-Meerwein-Straße 4, 35032 Marburg, Germany. E-mail: michael.gottfried@chemie.uni-marburg.de

‡ These authors contributed equally to this study and share first authorship.

1. Experimental and computational methods

TPD-MS was carried out in a dedicated UHV apparatus with a base pressure in the low 10^{-10} mbar regime. The apparatus hosts a HIDEN EPIC 1000 quadrupole mass spectrometer (QMS) mounted inside a pumped cryoshroud cooled to 80 K with l-N_2. This version of a line-of-sight mass spectrometer was described elsewhere.[1] Temperatures were measured directly at the sample using a calibrated Type K thermocouple. A polished Au(111) single-crystal surface (diameter 10 mm, purity > 99.999%, roughness < 0.01 µm, orientation accuracy < 0.1°, from MaTecK/Germany) was prepared by iterated sputtering with Ar^+ ions (1.0 keV, 3-5 µA, 30 min) and annealing (850 K, 3 min). H_2TPP (purity > 98%, PorphyChem) was evaporated from a home-built Knudsen cell (glass crucible) at fluxes of 0.1 to 1.0 nm min^{-1}. The molecular flux was measured using a quartz crystal microbalance (QCM). Unless otherwise noted, the Au(111) sample was held at 100 K during deposition of H_2TPP. Li (purity > 99.9%, Sigma-Aldrich) was evaporated from a home-built Knudsen cell (boron nitride crucible) at fluxes of 0.1 to 1.0 nm min^{-1}. The prepared sample was placed directly in front of the orifice (8 mm diameter) of the cryoshroud. The crystal was heated resistively via tungsten wires with a constant heating rate of 0.1 K s^{-1}. During heating, survey mass spectra from 4 to 10 amu (0.2 amu step width) and from 600 to 650 amu (0.5 amu step width) were recorded together with the temperature. Acquisition of one cycle took around 8 s, leading to a temperature rise of 0.8 K per cycle. With this procedure, the possible products of the reaction of Li with H_2TPP can be detected, including side products or contaminations with higher masses. The results are presented in the form of TPD-MS maps.

P6

Hard X-ray photoelectron spectroscopy (HAXPES) was performed at the HIKE endstation of the KMC-I beamline at BESSY II, Helmholtz-Zentrum Berlin.[2] The spectra were recorded at 300 K in almost grazing incidence and near normal-emission geometry (incidence angle 77°, detection angle 13°, both relative to the surface normal). Binding energies were referenced to Au $4f_{7/2}$ (84.00 eV). Photon energies of 2 to 3 keV and 7 keV were obtained from Si(111) and Si(422) monochromator crystals, respectively. The samples were prepared under UHV conditions at a base pressure better than $1 \cdot 10^{-9}$ mbar. H_2TPP was vapor-deposited onto clean Si(001) with a rate of ≈1.2 nm min^{-1}, as measured with a QCM. This led to a smooth film (average roughness ≈2.20 nm)[3] with a thickness of 24 nm. After the measurement of the pristine H_2TPP sample, an excess of Li (≈19 nm, purity > 99.9%, Sigma-Aldrich) was deposited at a rate of ≈0.3 nm min^{-1}.

Density functional theory (DFT) calculations were performed with Gaussian09, C.01.[4] A full geometry optimization was carried out using the PBE[5] functional and the def2-TZVPP[6] basis set.

2. Additional TPD-MS data

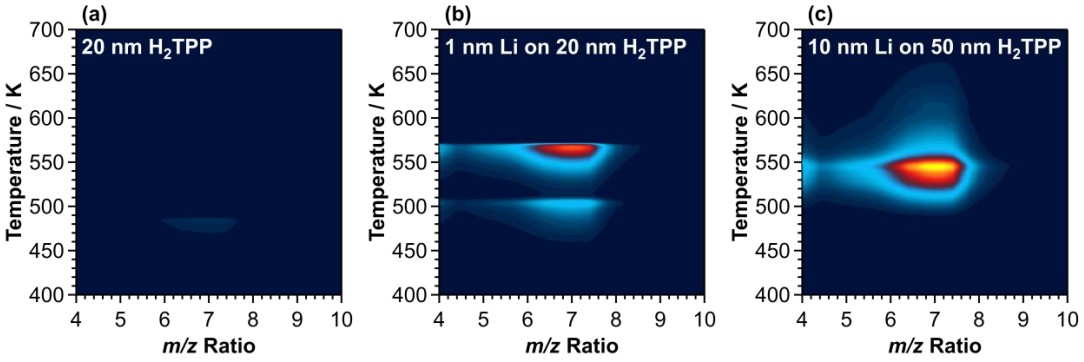

Figure S1. TPD-MS maps for (a) 20 nm H_2TPP, (b) 1 nm Li on 20 nm H_2TPP and (c) 10 nm Li on 50 nm H_2TPP, each on Au(111), in the mass region 4 to 10 amu to probe for Li desorption. The heating rate was 0.1 K s^{-1} and one mass range cycle took 8 s. The spectra were normalized to the maximum intensity of the Li signal (Figure S1c).

P6

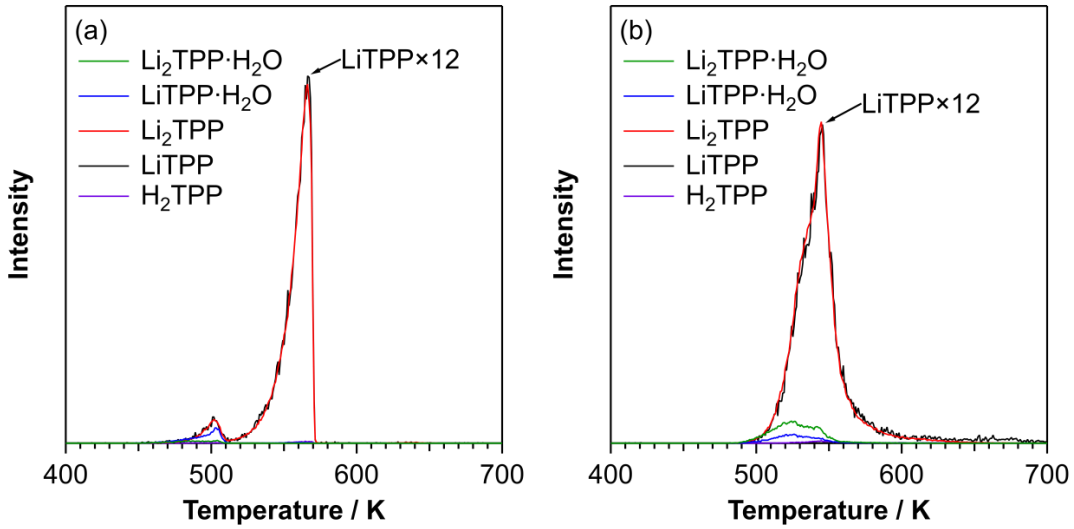

Figure S2. Common TPD traces for the relevant species for (a) 1 nm Li on 20 nm H_2TPP and (b) 10 nm Li on 50 nm H_2TPP, both on Au(111). The TPD signal of LiTPP (black) was multiplied by a factor of 12 to show that it exactly reflects the TPD signal of Li_2TPP (red), and hence, is the consequence of fragmentation of Li_2TPP in the mass spectrometer. Furthermore, for (b) recrystallization of the Li_2TPP film is observed as indicated by the peak broadening on the low temperature side. Intensities are in arbitrary units.

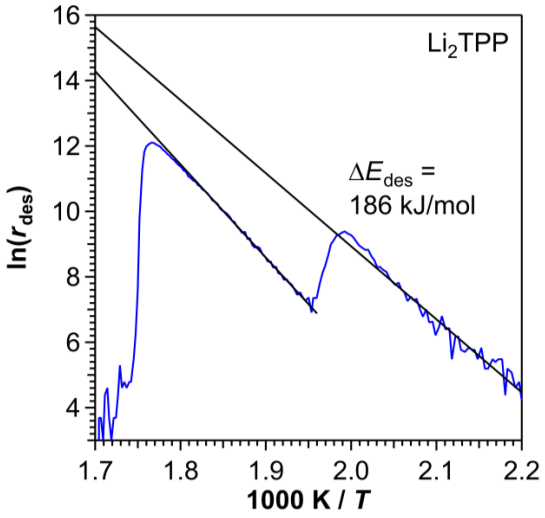

Figure S3. Arrhenius plot analysis for the first small peak (see Figure 2b) compared to the multilayer peak for 1 nm Li on 20 nm H_2TPP on Au(111). The desorption rate r_{des} was divided by the mass spectrometer unit (counts per second).

P6

The Arrhenius plot analysis (Figures 2d, 2e and S3) was performed using the Polanyi-Wigner Equation (S1)

$$r_{des} = -\frac{d\Theta}{dt} = \nu \cdot \exp\left(-\frac{\Delta E_{des}}{RT}\right) \cdot \Theta^n \qquad \text{(S1)}$$

with the desorption rate r_{des}, the coverage Θ, the time t, the pre-exponential factor ν, the activation energy of desorption ΔE_{des}, the gas constant R, the sample temperature T, and the desorption order n. In case of multilayer desorption, n is zero, hence, the desorption rate becomes coverage-independent. Taking the natural logarithm yields a simple Arrhenius Equation (S2) in the form of $y = mx + b$. Note that mathematically this is only allowed if the quantities are divided by their units.

$$\ln\left(r_{des}\right) = -\frac{\Delta E_{des}}{RT} + \ln\left(\nu\right) \qquad \text{(S2)}$$

ΔE_{des} is derived from the slope m of a plot of $\ln(r_{des})$ *vs.* $1/T$. The resulting values are shown in Table S1.

Table S1. Fit results of the Arrhenius plot analysis for the spectra in Figures 2d, 2e and S3. The pre-exponential factors ν were not calculated because multilayer experiments have been performed.

Spectra	**Species**	**Slope (*m*) / K**	**ΔE_{des} / kJ/mol**
Figure 2d	Li_2TPP	-28131	234
Figure 2e	H_2TPP	-24095	200
Figure S3	Li_2TPP (cryst.)	-22343	186

3. Additional XPS data

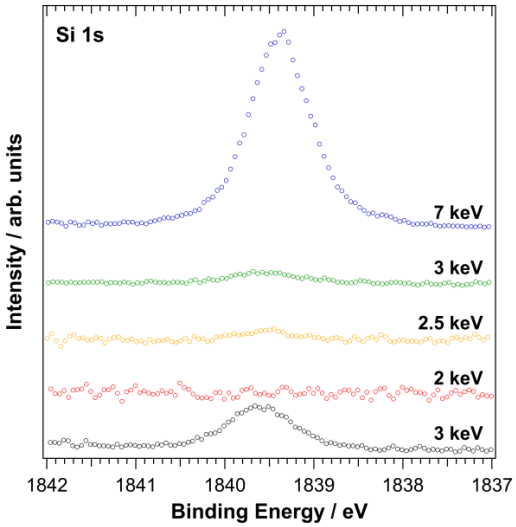

Figure S4. Si 1s XP spectra of H_2TPP (bottom) and Li_2TPP formed by deposition of Li onto a 24 nm thick H_2TPP layer (other spectra). The spectra were taken with the indicated photon energies.

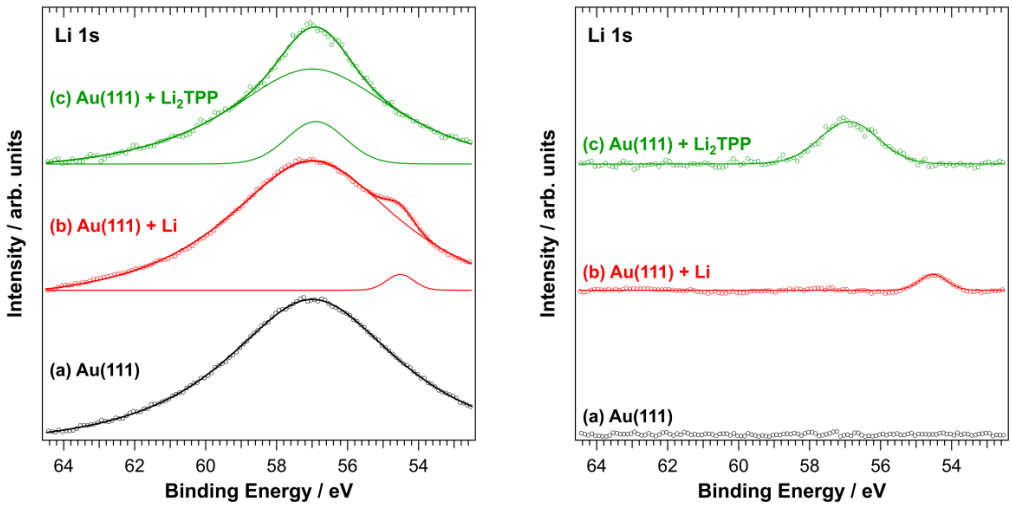

Figure S5. XP spectra of the Li 1s region of (a) a clean Au(111) crystal, (b) Li deposited onto Au(111) and (c) Li_2TPP on Au(111). Subtraction of the Au $5p_{3/2}$ signal at 57.1 eV (a) from the spectra (b) and (c) led to the Li 1s peaks in the graph on the right-hand side. Al Kα (1486.71 eV) was used as X-ray source. It can clearly be seen, that the Li 1s peak of (c) Li_2TPP (56.9 eV) is shifted to higher binding energies compared to that one of (b) metallic Li (54.6 eV). The value for the metallic Li 1s peak is in agreement with the literature (54.8 eV).[7]

4. Information depth of the XPS experiments

The probability that a photoelectron, created at a depth *z* below the solid/vacuum interface, actually reaches this interface without energy loss decreases exponentially with increasing *z*. The ratio between the initial flux of photoelectrons at a depth *z*(I_0) and the flux measured at the solid/vacuum interface *I* is given by:

$$\frac{I}{I_0} = \exp\left(-\frac{z}{\lambda\cos\theta}\right) \tag{S3}$$

Equation (S1), in which θ is the angle between the electron trajectory and the surface normal, also provides the precise definition of the inelastic mean free path (IMFP) λ.[8] Because of the exponential dampening of the signal with increasing *z*, approximately 95% of the total signal of a given photoelectron line emerge from a near-surface layer with a thickness of 3λ·cosθ. This value is typically referred to as *information depth*. For most materials, λ increases monotonically with the kinetic energy for energies above 100 eV.[8] As a consequence, the relative contribution of the electrons originating from deeper layers to the total signal increases for larger photon energies.

P6

In accordance with the results by Seah and Spencer,[9] we will use the Gries G1 equation[10,11] to calculate the IMFPs and information depths for H_2TPP and Li_2TPP. In the G1 equation, the energy-dependent inelastic mean free path (IMFP) λ is expressed as:

$$\lambda\left(E_{\mathrm{kin}}\right) = k_1\left(\frac{V_{\mathrm{a}}}{Z^*}\right)\frac{E_{\mathrm{kin}}}{\log_{10}\left(E_{\mathrm{kin}}\right) - k_2} \tag{S4}$$

The kinetic energy E_{kin} in Equation (S4) is given in eV and the IMFP λ in nm. For a certain compound, the parameter V_{a} is determined by the stoichiometry and density ρ of the material, while *Z** depends only on the stoichiometry.[10] The parameters k_1 and k_2 also depend on the material; for organic compounds, k_2 is unity and k_1 depends on the H/C ratio of the material: k_1 = 0.0017 at H/C = 1 and k_1 = 0.0023 at H/C = 2.[9,10] Seah and Spencer found that a linear interpolation of k_1 for materials with H/C ratios different from either 1 or 2 leads to excellent results for the calculated IMFPs.[9] Table S2 summarizes the parameters for H_2TPP and Li_2TPP. V_{a} and *Z** are calculated according to Gries.[10] Due to the lack of actual data, the density of the *in-situ* prepared Li_2TPP was calculated under the simplifying assumption that its molar volume is identical to that of H_2TPP.

Table S2. Material parameters and coefficients for H_2TPP and Li_2TPP that are used for the calculation of the IMFP with Equation (S4).

	Formula	**H/C**	**Density ρ / g cm^{-3}**	**k_1 / nm mol / eV cm^3**	**k_2**	**V_{a} / cm^3 mol^{-1}**	***Z****
H_2TPP	$C_{44}H_{30}N_4$	0.682	1.274	0.00151	1	6.1863	1.902
Li_2TPP	$Li_2C_{44}H_{28}N_4$	0.636	1.2986	0.00148	1	6.1863	1.921

The Li_2TPP formation was monitored by recording N 1s core level spectra at photon energies E_{ph} between 2 and 7 keV; the corresponding kinetic energies E_{kin} were ≈0.4 keV lower due to the N 1s binding energy. These values result in the following information depths $3\lambda \cdot \cos\theta$ (θ_{exp} = 13°) in nm (Table S3):

Table S3. Calculated information depths $3\lambda \cdot \cos\theta$ (θ_{exp} = 13°) obtained by application of Equation (S4), for the different photon energies applied for the acquisition of the N 1s XP spectra of H_2TPP and Li_2TPP.

E_{ph} / keV	E_{kin} / keV	Information depth / nm	
		H_2TPP	Li_2TPP
2	1.6	10.4	10.1
2.5	2.1	13.0	12.6
3	2.6	15.4	15.0
7	6.6	33.6	32.7

P6

5. Estimation of the reaction energy in the solid state

Gas-phase DFT calculations of the metalation reaction yield a total energy of $\Delta E_{DFT} = -499.8$ kJ mol^{-1}. This gas-phase value is used to estimate the energy for the corresponding solid-state reaction by means of a Born-Haber (BH) cycle (Figure S6), which includes the sublimation enthalpy ΔH_{sub} of metallic Li and the desorption activation energies ΔE_{des} of H_2TPP and Li_2TPP as obtained from TPD-MS. The BH cycle yields an approximate reaction energy of $\Delta E_{R,s} = -215$ kJ mol^{-1}, which means that the solid-state reaction is strongly exothermic.

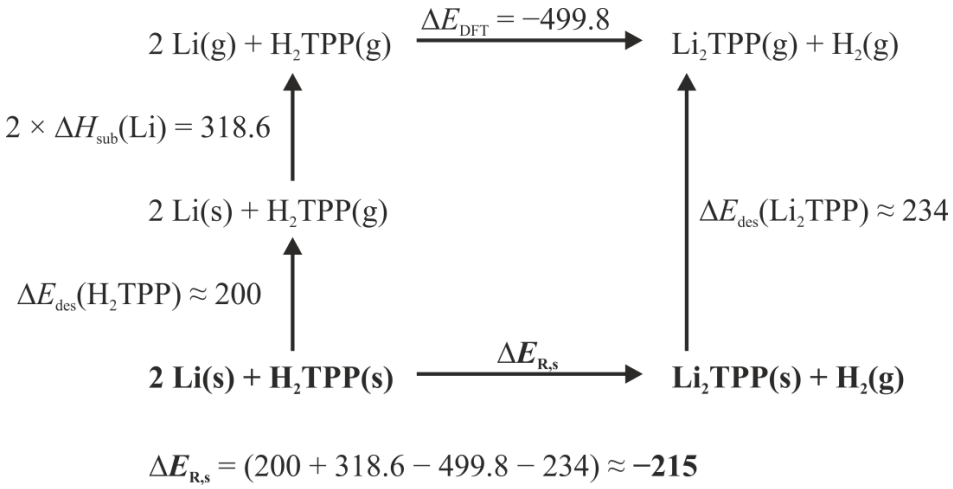

Figure S6. Born-Haber cycle for the estimation of the solid-state reaction energy $\Delta E_{R,s}$ from the reaction energy of the gas-phase reaction obtained by DFT calculations. All energies are given in kJ mol^{-1}. This estimation neglects small numerical differences between the measured desorption activation energies and sublimation enthalpies, as well as the temperature dependence of these quantities. This simplification is justified considering the large uncertainties of related literature values. For example, for the sublimation enthalpy of H_2TPP, values between 111 and 240 kJ mol^{-1} have been reported.[12]

6. Additional results of the DFT calculations

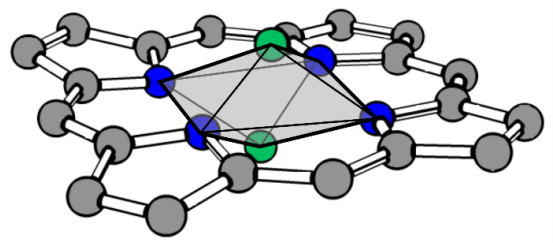

Figure S7. Geometry-optimized ground state structure of Li_2TPP. The phenyl groups and hydrogen atoms attached to carbon atoms are omitted for the sake of clarity, but were included in the calculations. The Li ions are displaced from the central positions above or below the porphyrin plane and the porphyrin ring shows a slight saddle-shape distortion.

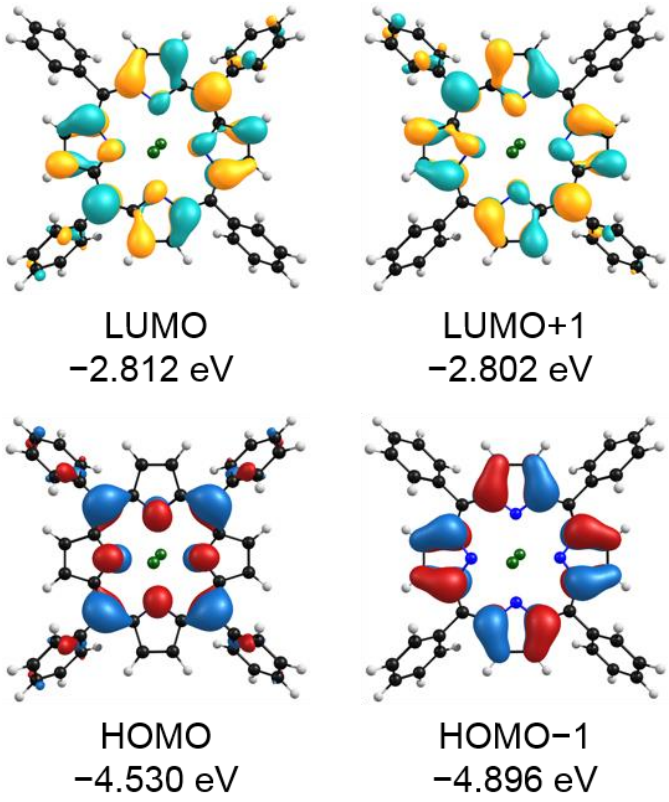

Figure S8. Selected frontier orbitals of Li_2TPP and related energies referenced to the vacuum level.

References

1. B. P. Klein, N. J. van der Heijden, S. R. Kachel, M. Franke, C. K. Krug, K. K. Greulich, L. Ruppenthal, P. Müller, P. Rosenow, S. Parhizkar, F. C. Bocquet, M. Schmid, W. Hieringer, R. J. Maurer, R. Tonner, C. Kumpf, I. Swart and J. M. Gottfried, *Phys. Rev. X*, 2019, **9**, 011030.
2. M. Gorgoi, S. Svensson, F. Schäfers, G. Öhrwall, M. Mertin, P. Bressler, O. Karis, H. Siegbahn, A. Sandell, H. Rensmo, W. Doherty, C. Jung, W. Braun and W. Eberhardt, *Nucl. Methods Phys. Res. A*, 2009, **601**, 48.
3. M. Schmid, S. R. Kachel, B. P. Klein, N. Bock, P. Müller, R. Riedel, N. Hampp and J. M. Gottfried, *J. Phys. Condens. Matter*, 2019, **31**, 094002.
4. M. J. Frisch, G. W. Trucks, H. B. Schlegel, G. E. Scuseria, M. A. Robb, J. R. Cheeseman, G. Scalmani, V. Barone, B. Mennucci, G. A. Petersson, H. Nakatsuji, M. Caricato, X. Li, H. P. Hratchian, A. F. Izmaylov, J. Bloino, G. Zheng, J. L. Sonnenberg, M. Hada, M. Ehara, K. Toyota, R. Fukuda, J. Hasegawa, M. Ishida, T. Nakajima, Y. Honda, O. Kitao, H. Nakai, T. Vreven, J. J. A. Montgomery, J. E. Peralta, F. Ogliaro, M. Bearpark, J. J. Heyd, E. Brothers, K. N. Kudin, V. N. Staroverov, R. Kobayashi, J. Normand, K. Raghavachari, A. Rendell, J. C. Burant, S. S. Iyengar, J. Tomasi, M. Cossi, N. Rega, J. M. Millam, M. Klene, J. E. Knox, J. B. Cross, V. Bakken, C. Adamo, J. Jaramillo, R. Gomperts, R. E. Stratmann, O. Yazyev, A. J. Austin, R. Cammi, C. Pomelli, J. W. Ochterski, R. L. Martin, K. Morokuma, V. G. Zakrzewski, G. A. Voth, P. Salvador, J. J. Dannenberg, S. Dapprich, A. D. Daniels, Ö. Farkas, J. B. Foresman, J. V. Ortiz, J. Cioslowski and D. J. Fox, 2009.
5. J. P. Perdew, K. Burke and M. Ernzerhof, *Phys. Rev. Lett.*, 1996, **77**, 3865.
6. F. Weigend and R. Ahlrichs, *Phys. Chem. Chem. Phys.*, 2005, **7**, 3297.
7. S. P. Kowalczyk, L. Ley, F. R. McFeely, R. A. Pollak and D. A. Shirley, *Phys. Rev. B*, 1973, **8**, 3583.
8. M. P. Seah and W. A. Dench, *Surf. Interface Anal.*, 1979, **1**, 2.
9. M. P. Seah and S. J. Spencer, *Surf. Interface Anal.*, 2011, **43**, 744.
10. W. H. Gries, *Surf. Interface Anal.*, 1996, **24**, 38.
11. W. S. M. Werner, W. H. Gries and H. Störi, *Surf. Interface Anal.*, 1991, **17**, 693.
12. A. Stefanov, A. Stibor, A. Dominguez-Clarimon and M. Arndt, *J. Chem. Phys.*, 2004, **121**, 6935.

Synthesis of Partially Metalated Lithium Tetraphenylporphyrin: Characterization of LiHTPP

Stefan R. Kachel*, Maik Schöniger*, Jan Herritsch, Philipp Schröder, J. Michael Gottfried

Philipps-Universität Marburg, Fachbereich Chemie, Hans-Meerwein-Str. 4, 35032 Marburg, Germany

** These two authors contributed equally and share first authorship*

Used techniques/Keywords: Porphyrins, Alkali, Lithium, organic electronic devices, OLEDs, batteries, XPS, TPD, IVD, DFT.

Introduction

In a recent paper we have shown that the solid state synthesis of a bulk alkali tetraphenylporpyhrin, Li_2TPP, in-vacuum is possible (up to a thickness of ~50 nm) when the stoichiometry between metallic Li and *meso*-tetraphenylporpyhrin (H_2TPP) of 2:1 (Li:H_2TPP) is met or exceeded. The question arises if this product is obtained directly, i.e. simultaneous reaction of 2 Li atoms with H2TPP, or if it is the result of a consecutive reaction, where the mono-metallic LiHTPP species would be observed.

A metalloporphyrin with an abandoned H (where only 1 H is exchanged by the metal) has not been observed to date. By correct choice of the stoichiometry between Li and H_2TPP we indeed find that LiHTPP can be formed with high yield. Furthermore, this product is exceptionally thermally stable and can be purified/separated by the remaining products using a new technique we call in-vacuo distillation (IVD).

Li doped organic compounds have been shown to have very useful properties when used in organic electronic devices. Researchers reported (for instance that) doping electron transporting layers with Li lowers (which is favorable) the driving voltages of OLEDs dramatically (and the external quantum efficiency was increased from 3.4 to 12.9%).[1-2] demonstrate efficient electron injection in Li doped films from transparent conducting oxides such as ITO. Several other examples show the high Li storage capability of organic molecules,[3-8] which makes these molecules attractive for battery applications. Wu et al. report tetrakis(4-carboxyphenyl)porphyrin used as high performance organic anode material with high capacities and cycling performance.[6]

P7

Experimental Part

Clean Au(111) and Ag(111) single-crystal surfaces were prepared by iterated Ar^+ ion bombardment (sputtering) and annealing cycles. Cleanliness was verified by XPS or AES prior to the experiments. H_2TPP (purity > 98%, PorphyChem) was vapor-deposited onto the clean metal surfaces from a home-built Knudsen cell (stainless steel or glass crucible) at fluxes of 0.1 to 1.0 nm min^{-1}. The molecular flux was measured using a quartz crystal microbalance (QCM). Resulting films had a thickness of 7.5 – 20 nm dependent on the experimental requirements. Li (purity > 99.9%, Sigma-Aldrich) was evaporated from a home-built Knudsen cell (boron nitride crucible) at fluxes of 0.1 to 1.0 nm min^{-1}.

X-ray photoelectron spectroscopy (XPS) and temperature-programmed desorption mass spectrometry (TPD-MS) experiments were carried out under ultra-high vacuum (UHV) conditions with a base pressure better than $2 \cdot 10^{-10}$ mbar. For XPS experiments, monochromatic Al K_α radiation (1486.7 eV) and a SPECS Phoibos 150 electron energy analyzer equipped with an MCD-9 multichannel detector were used. Sample preparation and measurements were performed at room temperature. Measured spectra were referenced to Au $4f_{7/2}$ (84.0 eV) and Ag $3d_{5/2}$ (368.3 eV) substrate signals, respectively. Experimental data were analyzed with XPS Tools[9], assuming pseudo-Voigt functions[10] with a Gaussian-Lorentzian ratio of 0.3 (which equals 70% Gaussian contribution to the line shape). For the N 1s spectra, relevant parameters (such as the ratio and the separation of the 2 distinct nitrogen species in H_2TPP (pyrollic: -N(H)- and iminic: =N-) obtained for the pristine, i.e., unmetalated films, were used for the subsequent analysis of the metalated films. The Li 1s signals overlap with the Au

$5p_{3/2}$ signal. Hence, the signal of the unmetalated Li 1s region was subtracted from for metalated spectra (with a self-written program).

The TPD-MS apparatus hosts a HIDEN EPIC 1000 quadrupole mass spectrometer (QMS) mounted inside a pumped cryoshroud cooled to 80 K with liquid N_2. This version of a line-of-sight mass spectrometer was described elsewhere.[11-12] Temperatures were measured directly at the sample using a calibrated type K thermocouple. Unless otherwise noted, the Au(111) sample was held at 100 K during deposition of H_2TPP and Li. The prepared sample was placed directly in front of the orifice (8 mm diameter) of the cryoshroud. The crystal was heated resistively via tungsten wires with a constant heating rate of 0.1 K s^{-1}. During heating, survey mass spectra from 4 to 10 amu (0.2 amu step width) and from 600 to 650 amu (0.5 amu step width) were recorded together with the temperature. Acquisition of one cycle took around 8 s, leading to a temperature rise of 0.8 K per cycle. With this procedure, the possible products of the reaction of Li with H_2TPP can be detected, including side products or contaminations with higher masses. The results are presented in the form of TPD-MS maps.

Density functional theory (DFT) calculations were performed with Gaussian09, C.01. A full geometry optimization was carried out using the PBE functional and the def2-TZVPP basis set.

P7

Results and Discussion

XPS Metalation Series. We prepared a smooth 10 nm thick H_2TPP film on a clean Au(111) single-crystal. The N 1s XP spectrum of the pristine film (Fig. 1 a) shows the typical almost 1:1 ratio between the pyrrolic (–N(H)–, 400.1 eV) and iminic (=N–, 398.0 eV) nitrogen species.
We stepwise deposited Li onto the H_2TPP film (Fig. 1 b-g). Due to the reaction of Li with the NH of the porphyrin macrocycle, the pyrrolic signal at higher binding energy (BE) decreases in intensity until finally only 1 peak is observed (Fig. 1 g). The Latter indicates that all 4 N atoms are chemically equivalent which is a typical feature of metal porphyrins[12-18] and non-metal porphyrins,[18] and verifies the formation of Li_2TPP.[12] Furthermore, we observe a shift in both the N 1s and C 1s signal to higher BE. The ongoing deposition of Li (b→g) onto the sample can also be observed/identified in the Li 1s region (right in Fig. 1). Here, the intensity of a broad feature steadily increases in intensity with further deposition of Li. In the C 1s region (Fig. 1 middle) we observe neither additional signals nor changes in the signal shape. We can hence exclude a reaction of Li with the C atoms of the porphyrin, e.g., with the phenyl rings. The experimental data were fitted with (for simplicity) two different C species. The signal at higher BE corresponds to the 8 C atoms which are directly connected to nitrogen. The signal at lower BE corresponds to the remaining 36 sp^2 C atoms. For fitting, the ratio and separation between both species was kept constant.

While the N1s spectra of pristine H_2TPP (Fig. 1 a) and fully metalated Li_2TPP (Fig. 1 g) can easily be described with a single species, describing the intermediate (Fig. 1 b-f) region exclusively with these species is impossible in a consistent way. However, adding a (hypothetical) third species, which assumes a N:N ratio of 1:3 (pyrrolic:iminic) leads to a consistent fitting model

which excellently describes the measured data. For small amounts of Li we observe, that H_2TPP initially reacts to the mono-metalated LiHTPP (Fig. 1 b). For higher metal dosages both H_2TPP and LiHTPP continuously decrease in intensity under the steady formation of more Li_2TPP (illustrated in Fig. S1 left). The small decrease in the overall intensity (black line) might be due to desorption of some molecules from the sample into the UHV, which is in line with the observed decrease of the C 1s signals.

The broad feature in the Li 1s region (Fig. 1 right) cannot be described with a single signal/peak. However, using a fitting procedure which assumes two different Li species describes the experimental data excellently. The nature/origin of the different species cannot unambiguously be clarified. None of the peaks might be attributed to metallic Li because this species would rather be expected at a binding energy of 54.5 eV.[12] In our case, one species is centered at a BE of 55.6 – 56.0 eV and the other one at 56.9 – 57.1 eV. The signal at higher BE might be attributed to Li bound to N (because of a smaller electron density at the Li). It might be speculated that the signal at lower BE was due to additional Li intercalated in the organic material. During the whole course of experiments there were no indications for oxygen contaminations.

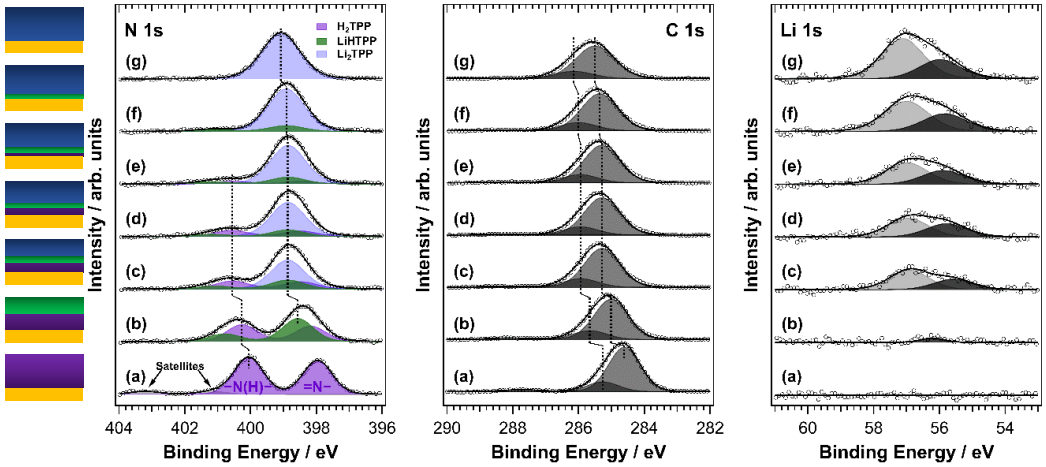

Fig. 1: X-ray photoelectron spectra of the stepwise metalation (b-g) of a 10 nm thick H_2TPP film (a) on Au(111). For the pristine/unmetalated H_2TPP (a) 2 disctinct N species (pyrrolic –N(H)–: 400.1 eV, iminic =N–: 398.0 eV) with a N:N ratio of 1.1:1 are observed in the N 1s region (left). Due to the deposition of Li (b-g) the pyrrolic signal decreases and finally vanishes. 3 distinct N species are observed: pristine/unmetalated H_2TPP (violet, N:N = 1.1:1), mono-metalated LiHTPP (green, N:N = 1:3) and fully metalated Li_2TPP (blue). The increasing amount of Li is clearly visible in the Li 1s spectra (right). Li 1s spectra show no indication for metallic Li which would be expected at 54.5 eV.[12] The C 1s spectra (middle) show neither additional peaks nor a change in the peak shape which excludes a reaction of C with Li. C 1s spectra were fitted with 2 species: C atoms directly connected to N (higher BE) and remaining sp^2 C atoms with a ratio of 8:36. Spectra were recorded with Al K_α radiation and are referenced to the binding energy of the Au $4f_{7/2}$ substrate signal (84.0 eV).

DFT. We performed DFT calculations and calculated energies of optimized gas-phase structures of H_2TPP, the mono-metalated porphyrin and the fully converted/metalated Li_2TPP (Fig. 2). We considered three different mono-metalated porphyrin species (Fig. 2, middle): the porphyrin without loss of hydrogen (LiH_2TPP), the porphyrin which lost 1 H (LiHTPP), and the porphyrin which lost both H ($LiTPP^+$). As can be seen in Fig. 2, the latter is the least stable while LiHTPP might be expected as the product of a single metalation step. From this structure a N:N ratio of 1:3 might be expected as is also found for the XPS data analysis. A detailed gas-phase structure is shown in Figure S2. Furthermore, it might be concluded that there is an energy barrier that needs to be overcome for the second metalation step.

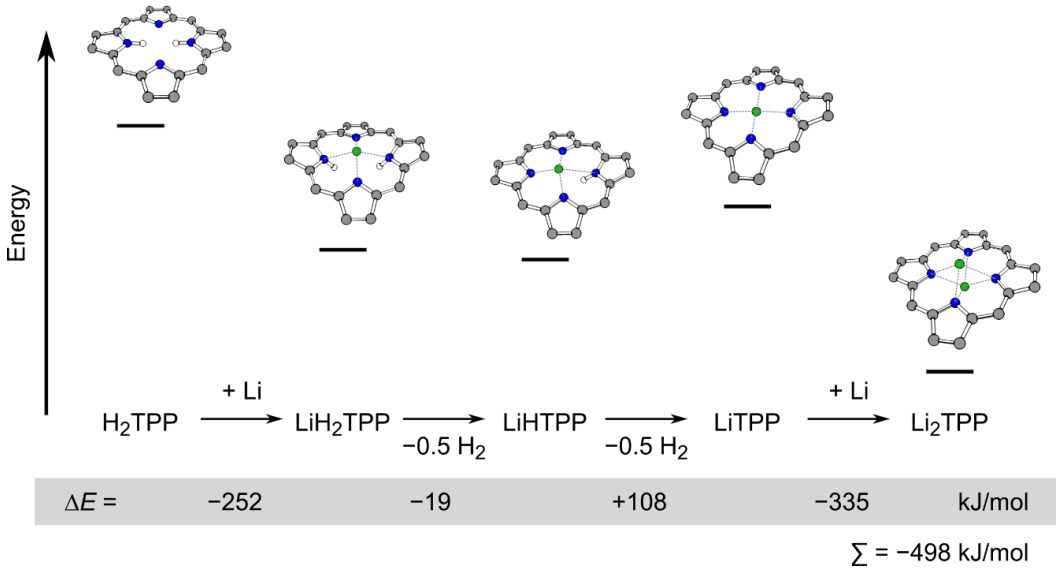

Fig. 2: Calculated gas-phase structures and corresponding energy levels for H_2TPP, LiH_2TPP, LiHTPP, $LiTPP^+$ and Li_2TPP by DFT.

In Fig. 3 the calculated N 1s core level orbital energies are shown. From this we rather expect a ratio of 1:2:1 (–N(H)– : =N– : –N(Li)–), however, the difference between the latter both is quite small. We furthermore see that the N 1s signal of Li_2TPP is expected at the same position as the major species in LiHTPP, and that this species is at slightly higher BE compared to the iminic N in the unmetalated H_2TPP. Lastly, the separation of the N species is expected to be larger in LiHTPP than in H_2TPP by approximately 0.2 eV. All these findings are also observed in our fitted data when a 1:3 ratio in LiHTPP was assumed, i.e., we assumed no distinction between the N atoms bound to Li. Our fits show qualitatively the same picture. Although the absolute values for the NN separation in our fits was higher (H_2TPP: 2.1 eV, LiHTPP: 2.3 eV) the difference is in excellent agreement with the theoretical prediction. This might be expected because in the gas-phase calculations no interactions between adjacent molecules are included, which occur in the solid phase. The difference between the –N(Li)– of LiHTPP and Li_2TPP and the =N– of H_2TPP was found to be 0.37 eV, which is somewhat higher than predicted.

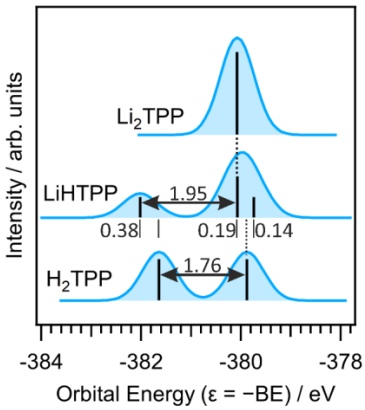

Fig. 3: Calculated orbital energies for H_2TPP, LiHTPP and Li_2TPP by DFT.

TPD-MS. In order to corroborate our theoretical and photoemission results and to proof the existence of the mono-metalated LiHTPP species we performed temperature-programmed desorption mass spectrometry (TPD-MS) experiments for different amounts of deposited Li. Experimental details can be found elsewhere.[12] Briefly, in order to obtain TPD-MS maps a sample is heated with a constant rate, in our case 0.1 K s^{-1}. Simultaneously, mass spectra of the relevant regions (which have been identified in prior experiments) are continuously recorded in the temperature range between 300 and 700 K. At certain temperatures molecules start desorbing from the sample and are detected by a quadrupole mass spectrometer. The resulting TPD-MS maps illustrate the measured intensity (color code, *z*) as a function of sample temperature in K (*y*-axis) and mass-to-charge ratio in atomic units (*x*-axis). The brighter the color the more intense is the signal.

P7

Essentially, TPD-MS delivers the same results as XPS. For small/sub-stoichiometric amounts of Li (Fig. 4a and b) only H_2TPP (614 amu) and LiHTPP (620 amu) are observed while no Li_2TPP (626 amu) is detected. Here, a stoichiometry of 100% means/equals 1 Li atom per H_2TPP molecule. For the sub-stoichiometric amounts of Li, the intensity of H_2TPP is significantly higher than that of LiHTPP. H_2TPP decreases and LiHTPP increases in intensity when the amount of Li is increased from 20% to 38% (Fig. 4a and b). Both species exhibit two desorption peaks. The first one ranges from 420 to 440 K and can be attributed to crystallites that were already observed elsewhere.[12, 19] Subsequently, the main multilayer desorption peak evolves and ends abruptly at 490 K following zeroth order kinetics. The multilayer spectrum for the pristine H_2TPP (614 u) is in agreement with previous results.[12]

Increasing the Li:H_2TPP ratio to approximately 1:1 (Figure 4c), a coexistence regime is found, where all three species are formed. There, H_2TPP desorbs between 440 and 465 K, LiHTPP between 440 and 480 K, and Li_2TPP between 500 to 550 K. Note that the desorption trace of LiTPP (619 u) from 510 to 550 K is a fragment of the Li_2TPP species, observed previously, and not LiHTPP.[12]

For a stoichiometric amount of 2:1 (200%) Li_2TPP is formed exclusively, as we have shown before. [12] Our DFT results suggest that the formation of $LiTPP^+$, i.e., the mono-metalated species which lost both hydrogens (see also Fig. 2), is energetically unfavored, which we can also prove with a high-resolution TPD-MS experiment (Fig. 4d). We clearly observe that LiHTPP (620 amu) is formed while LiTPP (619 amu) is not observed.

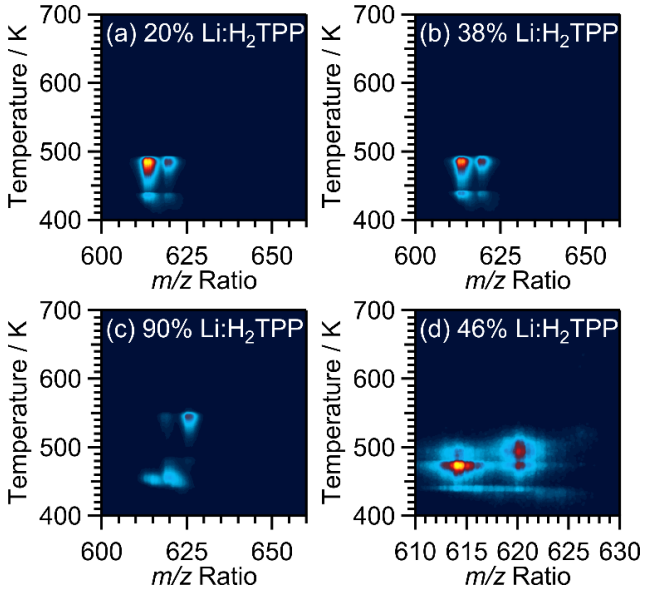

Fig. 4: TPD-MS maps for (a) 20%, (b) 38% Li on a 20 nm and (c) 90% Li on a 10 nm H_2TPP film on Au(111), in the relevant mass region 600 to 650 amu. The spectra were normalized to the maximum intensity of the H_2TPP signal (a). (d) High resolution TPD-MS map for 46% Li on 20 nm H_2TPP on Au(111) in the range of 610 to 630 u with a step width of 0.1 u. The heating rate was 0.1 K s^{-1} and one mass range cycle took about 8 s. 100% Li refers to a stoichiometry of 1 Li atom per H_2TPP molecule.

Clearly, XPS and TPD-MS are qualitatively in very good agreement. However, while the TPD experiments suggest the exclusive formation of Li_2TPP for a stoichiometric amount of 2 Li atoms per H_2TPP molecule, this condition is not met in XPS experiments. As mentioned before, when Li is deposited onto the H_2TPP sample at room temperature, over-stoichiometric amounts of Li are required in order to achieve full conversion to Li_2TPP. One possibility might be that additional Li is intercalated in the organic film before the second reaction step takes place and that thermal activation is required to trigger deintercalation followed by the second metalation step.

In order to test if we have additional (yet unreacted) Li on our sample, we performed another experiment. As can be seen in Fig. 4c there is a quite high difference in the desorption temperature between LiHTPP and Li_2TPP of ~90-100 K (with respect to its maximum intensity). Hence, it might be possible to further react additional Li by thermal activation and separate both reaction products LiHTPP and Li_2TPP from each other via an in-vacuo distillation (IVD) experiment.

In-Vacuo Distillation (IVD) Experiment. We prepared a 7.5 nm thick H_2TPP film on Au(111) and deposited Li on top. According to the N 1s and Li 1s XP spectra (we used exactly the same fitting routine described before) this yielded a sample in the coexistence regime (Fig. IVD a). Subsequently, we heated the sample at a rate of 1 Ks^{-1} to a final temperature of 484 K. The sample was held at this temperature for 15 min while a clean Ag(111) crystal was positioned (upside down) above the prepared sample to "collect" the species that desorb from the heated sample (see Fig. S3). Afterwards, the residuals on Au(111) and the distilled species on Ag(111) were measured with XPS (Fig. 5b). A photograph of the experimental setup during the experiment is shown in Fig. S3.

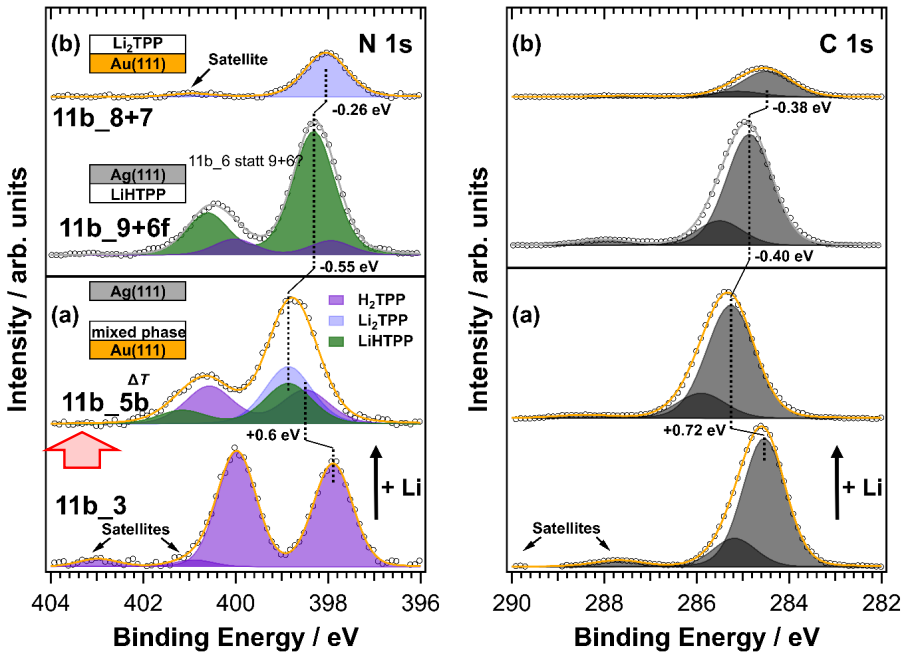

Fig. 5: N 1s (left) and C 1s (right) XP spectra (a) before and (b) after the in-vacuo distillation (IVD) experiment. After deposition of metallic Li onto the clean H_2TPP film, a mixed phase of 3 different species is obtained (a). The shifts to higher BE might be due to additional Li in the film. Heating the Au(111) sample to 484 K and "collecting" the desorbing species on Ag(111) yields enhanced LiHTPP and some residual H_2TPP on Ag(111), while Li_2TPP remains on the Au(111) sample. The C 1s spectra (right) qualitatively show the same shifts although the absolute values slightly deviate. All spectra were normalized to the Au $4f_{7/2}$ and Ag $3d_{5/2}$ substrate signal, respectively.

As expected, the amount of LiHTPP increases strongly while the amount of H_2TPP decreases when the sample is heated (Fig. 5b). The residual amount of Li_2TPP on Au(111) remains unchanged. The signals on both Au(111) and Ag(111) shift back towards lower BE. This might indicate that the original shift to higher BE was doping/intercalation induced, as was reported for similar systems as well.[1-2, 5, 20-21] We can also easily prove the shift is due to Li by conversion of the LiHTPP/Ag(111) to Li_2TPP (Fig. 6a). After subsequent IVD at 10 min at 600 K the peaks on Au(111) are again shifted back to lower BE (Fig. 6b).

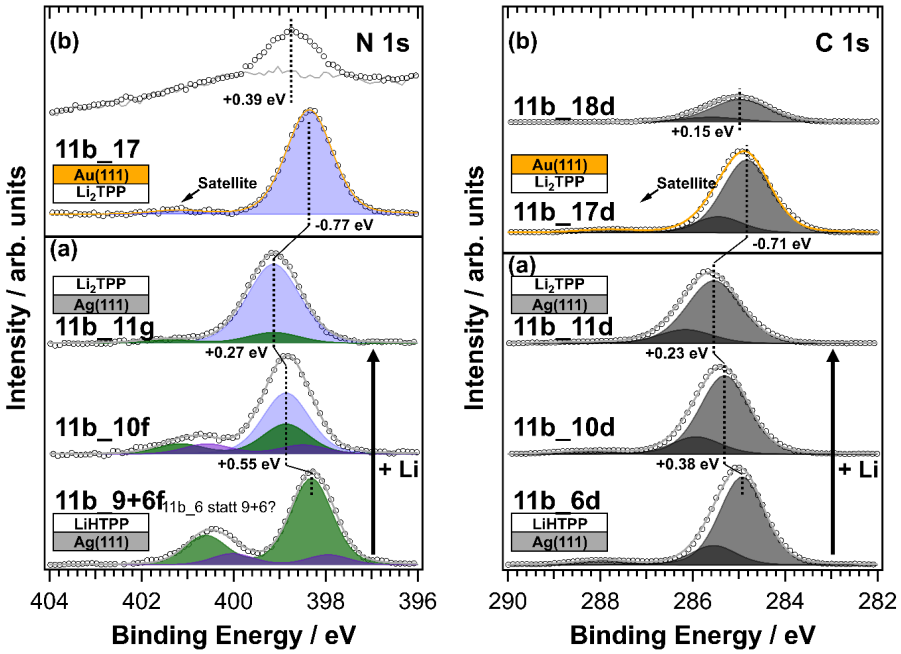

Fig. 6: N 1s (left) and C 1s (right) XP spectra of IVD experiment on Ag(111). Onto the previously prepared LiHTPP sample metallic Li was deposited. Again, all peaks shift to higher BE due to Li intercalation/deposition of Li (a). Heating the Ag(111) sample for 10 min at 600 K and "collecting" the desorbing species on Au(111) a clean Li_2TPP sample is obtained with high yield (b). The C 1s spectra (right) qualitatively show the same shifts although the absolute values slightly deviate. All spectra were normalized to the Au $4f_{7/2}$ or Ag $3d_{5/2}$ substrate signal, respectively.

P7

Conclusion

We have shown that the substoichiometric Li metalation of H_2TPP yields mono-metalated LiHTPP by XPS, TPD-MS and DFT calculations. It can be synthesized with high yield and is thermally exceptionally stable. Due to the different desorption temperatures of LiHTPP and Li_2TPP, it is possible to isolate LiHTPP in a in-vacuo distillation (IVD) experiment. IVD might be a new experimental approach to fabricate smooth partially metalated organic films onto different substrates, e.g., to the best of our knowledge a bulk mono-lithiated porphyrin species cannot be prepared in any other way with high purity. Within the reaction of H_2TPP to Li_2TPP additional Li can be stored, which has been found for other organic materials as well. Such Li doped materials have been shown to improve performances of organic electronic devices dramatically, e.g., for Li battery applications.[6]

References

1. *Mechanistic Understanding of Improved Performance of Graphene Cathode Inverted Organic Light-Emitting Diodes by Photoemission and Impedance Spectroscopy*; Moon, J.; Cho, H.; Maeng, M.-J.; Choi, K.; Nguyen, D. T.; Han, J.-H.; Shin, J.-W.; Kwon, B.-H.; Lee, J.; Cho, S.; Lee, J.-I.; Park, Y.; Lee, J.-S.; Cho, N. S.; ACS Applied Materials & Interfaces 10, 26456 (2018).
2. *Suitability of lithium doped electron injection layers for organic semiconductor lasers*; Rabe, T.; Hamwi, S.; Meyer, J.; Görrn, P.; Riedl, T.; Johannes, H.-H.; Kowalsky, W.; Applied Physics Letters 90, 151103 (2007).
3. *High levels of alkali-metal storage in thin films of hexa-peri- hexabenzocoronene*; Keil, M.; Samori, P.; dos Santos, D. A.; Birgerson, J.; Friedlein, R.; Dkhissi, A.; Watson, M.; Müllen, K.; Brèdas, J. L.; Rabe, J. P.; Salaneck, W. R.; The Journal of Chemical Physics 116, 10854 (2002).
4. *High Conductive Two-Dimensional Covalent Organic Framework for Lithium Storage with Large Capacity*; Yang, H.; Zhang, S.; Han, L.; Zhang, Z.; Xue, Z.; Gao, J.; Li, Y.; Huang, C.; Yi, Y.; Liu, H.; Li, Y.; ACS Applied Materials & Interfaces 8, 5366 (2016).
5. *Alkali metal storage mechanism in organic semiconductor of perylene-3,4,9,10-tetracarboxylicdianhydride*; Lian, X.; Ma, Z.; Zhang, Z.; Yang, J.; Liu, Y.; Gu, C.; Guo, R.; Wang, Y.; Ye, X.; Sun, S.; Zheng, Y.; Ding, H.; Hu, J.; Cao, X.; Mao, H.; Zhu, J.; Li, S.; Chen, W.; Applied Surface Science 524, 146396 (2020).
6. *A large π-conjugated tetrakis (4-carboxyphenyl) porphyrin anode enables high specific capacity and superior cycling stability in lithium-ion batteries*; Wu, H.; Zhang, J.; Du, X.; Zhang, M.; Yang, J.; Zhang, J.; Luo, T.; Liu, H.; Xu, H.; Cui, G.; Chemical Communications 55, 11370 (2019).
7. *A Porphyrin Complex as a Self-Conditioned Electrode Material for High-Performance Energy Storage*; Gao, P.; Chen, Z.; Zhao-Karger, Z.; Mueller, J. E.; Jung, C.; Klyatskaya, S.; Diemant, T.; Fuhr, O.; Jacob, T.; Behm, R. J.; Ruben, M.; Fichtner, M.; Angewandte Chemie International Edition 56, 10341 (2017).
8. *Favorable Lithium Nucleation on Lithiophilic Framework Porphyrin for Dendrite-Free Lithium Metal Anodes*; Li, B.-Q.; Chen, X.-R.; Chen, X.; Zhao, C.-X.; Zhang, R.; Cheng, X.-B.; Zhang, Q.; Research 2019, 1 (2019).
9. *XPST - X-ray Photoelectron Spectroscopy Tools*; Schmid, M.; www.igorexchange.com/project/XPStools (2015).
10. *A new asymmetric Pseudo-Voigt function for more efficient fitting of XPS lines*; Schmid, M.; Steinrück, H.-P.; Gottfried, J. M.; Surface and Interface Analysis 46, 505 (2014).
11. *Molecular Topology and the Surface Chemical Bond: Alternant Versus Nonalternant Aromatic Systems as Functional Structural Elements*; Klein, B. P.; van der Heijden, N. J.; Kachel, S. R.; Franke, M.; Krug, C. K.; Greulich, K. K.; Ruppenthal, L.; Müller, P.; Rosenow, P.; Parhizkar, S.; Bocquet, F. C.; Schmid, M.; Hieringer, W.; Maurer, R. J.; Tonner, R.; Kumpf, C.; Swart, I.; Gottfried, J. M.; Physical Review X 9, (2019).
12. *Direct synthesis of dilithium tetraphenylporphyrin: facile reaction of a free-base porphyrin with vapor-deposited lithium*; Schöniger, M.; Kachel, S. R.; Herritsch, J.; Schröder, P.; Hutter, M.; Gottfried, J. M.; Chemical Communications 55, 13665 (2019).
13. *Direct Synthesis of Nickel(II) Tetraphenylporphyrin and Its Interaction with a Au(111) Surface: A Comprehensive Study*; Chen, M.; Feng, X.; Zhang, L.; Ju, H.; Xu, Q.; Zhu, J.; Gottfried, J. M.; Ibrahim, K.; Qian, H.; Wang, J.; The Journal of Physical Chemistry C 114, 9908 (2010).
14. *Formation of an interphase layer during deposition of cobalt onto tetraphenylporphyrin: a hard X-ray photoelectron spectroscopy (HAXPES) study*; Chen, M.; Zhou, H.; Klein, B. P.; Zugermeier, M.; Krug, C. K.; Drescher, H.-J.; Gorgoi, M.; Schmid, M.; Gottfried, J. M.; Physical Chemistry Chemical Physics 18, 30643 (2016).
15. *Reactive metal-organic interfaces studied with hard x-ray photoelectron spectroscopy: controlled formation of metalloporphyrin interphase layers during metal vapor deposition onto porphyrin films*; Schmid, M.; Kachel, S. R.; Klein, B. P.; Bock, N.; Müller, P.; Riedel, R.; Hampp, N.; Gottfried, J. M.; Journal of Physics: Condensed Matter 31, 094002 (2019).

P7

16. *Ordering aspects and intramolecular conformation of tetraphenylporphyrins on Ag(111)*; Buchner, F.; Kellner, I.; Hieringer, W.; Görling, A.; Steinrück, H.-P.; Marbach, H.; Physical Chemistry Chemical Physics 12, 13082 (2010).
17. *Surface chemistry of porphyrins and phthalocyanines*; Gottfried, J. M.; Surface Science Reports 70, 259 (2015).
18. *On-Surface Synthesis of Nonmetal Porphyrins*; Baklanov, A.; Garnica, M.; Robert, A.; Bocquet, M.-L.; Seufert, K.; Küchle, J. T.; Ryan, P. T. P.; Haag, F.; Kakavandi, R.; Allegretti, F.; Auwärter, W.; Journal of the American Chemical Society 142, 1871 (2020).
19. *Initial stages of multilayer growth and structural phase transitions of physisorbed benzene on Ru(001)*; Jakob, P.; Menzel, D.; The Journal of Chemical Physics 105, 3838 (1996).
20. *Lithium doping of semiconducting organic charge transport materials*; Parthasarathy, G.; Shen, C.; Kahn, A.; Forrest, S. R.; Journal of Applied Physics 89, 4986 (2001).
21. *Synthesis and XPS investigation of superdense lithium-graphite intercalation compound, LiC_2*; Mordkovich, V. Z.; Synthetic Metals 80, 243 (1996).

Supporting Information

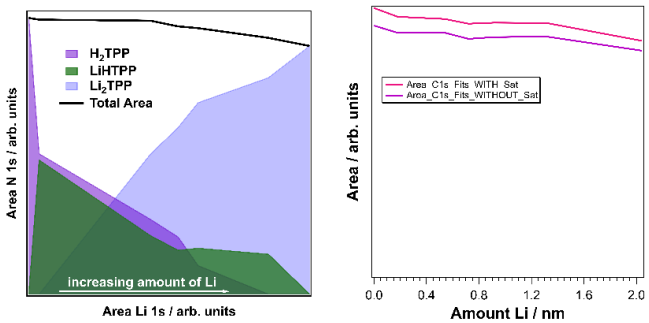

Fig. S1: Areas of the H2TPP (violet), LiHTPP (green) and Li2TPP (blue) related N 1s signals (left) as a function of increasing amount of deposited Li. The small decrease in the total area might be attributed to some desorbing molecules and is also observed in the C 1s spectra (right).

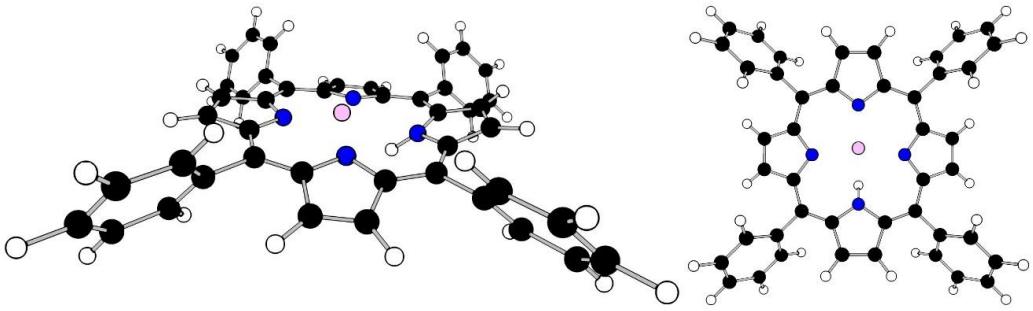

Fig. S2: Gas-phase structure of LiHTPP calculated by DFT for different views.

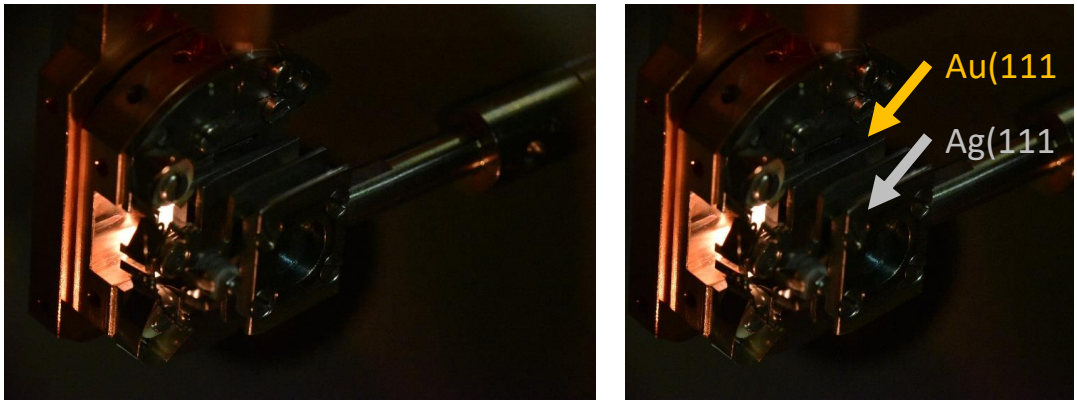

Fig. S3: Photograph of the experimental setup during the IVD experiment. The Au(111) sample (in the back) was heated radiatively from its backside, the temperature was measured directly at the Au(111) single-crystal with a type K thermocouple. The Ag(111) single-crystal was positioned as close as possible to the Au sample without touching it. After cool-down to 300 K both crystals were measured again with XPS.

Examination of the Reaction Zone in a Metal–Organic Semiconductor Interface by Multi-Technique Approach: Characterization and Control of the Ca/6T Interphase

Stefan R. Kachel[a], Maik Schöniger[a], Han Zhou[a], Hans-Jörg Drescher[a], Claudio K. Krug[a], Lukas Ruppenthal[a], Benedikt P. Klein[a], Malte Sachs[a], Katharina Gries[b], Janika Hochstraßer[a], Florian Fillsacka, Rene Riedel[a], N. Hampp[a], Martin Schmid[a], J. Michael Gottfried[a]

[a]*Philipps-Universität Marburg, Fachbereich Chemie, Hans-Meerwein-Str. 4, 35032 Marburg, Germany.*

[b]*Faculty of Physics and Materials Science Center (WZMW), Philipps-Universität Marburg, Hans-Meerwein-Straße, 35032 Marburg, Germany.*

Abstract

The formation of a reaction layer between metallic calcium and α-sexithiophene (6T) was studied in a multi-technique approach including, energy dispersive X-ray spectroscopy (EDX), atomic force microsopy (AFM), X-ray photoelectron spectroscopy (XPS), hard X-ray photoelectron spectroscopy (HAXPES), nano-joule adsorption calorimetry (NAC) and temperature-programmed desorption mass spectrometry (TPD-MS). EDX results show that Ca vapor deposited onto 6T diffuses to a depth of approximately 30 nm into the organic material at room temperature. The chemical changes associated with this diffusion were quantified with XPS and HAXPES, where the interaction between the molecular units and Ca was predominantly associated with strong chemical modifications of the sulfur within the thiophene units. Furthermore, indications for significant chemical changes of the carbon atoms were found that point towards a metallacycle formation within the reaction layer. A detailed chemical depth profile derived from HAXPES data shows that there is a coexistence of reacted and unreacted thiophene subunits within the reaction zone. The fact that no complete conversion of all sulfur atoms from the 6T molecules was achieved at room temperature is likely due to kinetic reasons, i.e., steric barriers due to the chemical modification and geometric distortion of the carbon backbone of the 6T molecules. The complex structure of the carbon backbone is indicated by the fact that no desorbing species are detected in TPD-MS experiments. In order to control the geometric extension of the reaction zone, it was established by HAXPES and NAC that calcium deposition at ~150 K leads to the formation of a permanently thinner reaction zone between Ca and 6T, i.e., a better defined interface.

Introduction

The design and fabrication of organic electronic devices such as organic light emitting diodes[1], photodiodes[2], or field effect transistors[3] require detailed knowledge about the properties of the involved materials and, in particular, the desired and undesired interactions at the internal interfaces of the devices. Organic polymers which are used within this context are, for example, polythiophenes, polyfluorene, and poly(p-phenylene vinylene); molecular systems involve for instance α-sexithiophene, triphenyl-diamin- and 1,2,4 triazole-derivates.[4-5] The interfaces between these materials and inorganic semiconductors or metals are particularly important as they control important properties such as charge injection rates[6] which are decisive for a device performance. This is nicely illustrated by the fact that the charge transport between a SiO_2 substrate and an α-sexithiophene layer is only determined by the first two layers of 6T molecules next to the SiO_2 material.[7]

To facilitate the charge transfer across the materials, a low work-function metal can be combined with a stable π-conjugated organic semiconductor/polymer.[8-11] A good example for this approach is the combination of metallic Ca (work function: 2.9 eV)[12] and rr-P3HT, which was characterized in detail in several previous studies.[13-15] It was shown that vapor deposited calcium initially diffuses into the organic rr-P3HT matrix before eventually forming a closed metallic layer on top of the organic film. The diffused Ca reacts with the rr-P3HT units, and in particular with the sulfur atoms from individual thiophene units. Accordingly, the metallic layer and the organic semiconductor are separated from each other by a reaction zone or *interphase* layer, a phenomenon which is potentially lowering device performance.[16-18] It was shown that the extension of the reaction zone can be permanently minimized by lowering the temperature during Calcium deposition to ~ 130 K.[13] It is, however, not clear if those results can be readily transferred from a polymeric to a molecular organic semiconductor.

To address this question, the present study examines the combination of calcium and α-sexithiophene (6T). 6T was selected as it is (i) in a first approximation the direct molecular counterpart to the rr-p3HT and (ii) by itself a widely studied and interesting system in the context of organic electronics[19-21]. Furthermore, the literature about the interfacial phenomena at metal/6T interfaces is still surprisingly sparse, showing only a few examples, e.g., about gold/6T interfaces[20]. It is the main objective of the present study, to characterize the reaction zone which forms between metallic calcium and a thick α-sexithiophene film. The reaction zone was examined with energy dispersive X-ray spectroscopy (EDX), atomic force microscopy (AFM), X-ray photoelectron spectroscopy (XPS), hard X-ray photoelectron spectroscopy (HAXPES), temperature-programmed desorption mass spectrometry (TPD-MS) and nanojoule adsorption calorimetry (NAC). The results will be compared with the deposition of calcium onto the polymeric organic semiconductor rr-P3HT.

Experimental and computational details

To analyze the Ca/6T layer structure with EDX a sample consisting of 100 nm 6T covered by 82.5 nm Ca and 320 nm gold was fabricated on Al foil. A thin slice (thickness approximately 0.1 µm – as observed from scanning electron microscopy) was cut from the sample by a focused ion beam (FIB) and then analyzed by EDX under ultra-high vacuum (UHV) conditions.

The morphologies of the pristine 6T layers were analyzed with atomic force microscopy (AFM, Nanoscope V, Bruker, USA). Topological imaging was conducted in tapping mode in air, using a sharp silicon nitride cantilever (SNL, tip radius 2 nm, spring constant k = 0.24 N m−1, oscillation frequency f = 56–75 kHz).

Laboratory photoelectron spectra were acquired with monochromatized Al K_α radiation (1486.6 eV) using a Phoibos 150 electron analyzer from SPECS under 0° and 70° emission angle. The samples were prepared in-situ: 11.4 ML of Ca were evaporated onto 21.6 nm 6T. The flux of Ca and 6T were both monitored with a quartz-crystal microbalance (QCM). The base pressure of the UHV setup in which the experiments have been performed was approximately $1 \cdot 10^{-10}$ mbar, avoiding a rapid reaction of the Ca atoms with residual gases, in particular H_2O.

Further photoemission measurements were carried out at the synchrotron radiation facility BESSY II (Helmholtz-Zentrum Berlin) using the HIKE endstation located at the KMC-1 beamline.[22-23] The HIKE system is designed for hard X-ray high kinetic energy photoelectron spectroscopy (HAXPES) experiments. A Scienta R4000 hemispherical electron analyzer, which is suitable for electron kinetic energies of up to 10 keV, is installed in the experimental setup. Photoelectron spectra were recorded at room temperature and in the direction of the surface normal (the initial photon flux hit the surface under approximately 78° relative to the surface normal). The photon energy was varied between 2.7 keV and 3.6 keV with 0.1 keV steps and between 3.6 keV and 5 keV in 0.2 keV steps. For these energies the Si(111) monochromator crystal was used. In addition, experiments with photon energies of 5 keV and 5.5 keV were conducted, using the Si(311) crystal. The acquired photoelectron spectra have been fitted with a Pseudo-Voigt function.[24] Reduced photon flux of the beam line at high photon energies was partially compensated by an increased measurement time. In order to minimize potential beam damage, the position of the incident beam on the sample was shifted for each recorded spectrum. The reported binding energies were referenced to the Au 4f peak of a clean Au surface, which was mounted in close vicinity of the sample. The base pressure of the preparation chamber was better than 5×10^{-9} mbar and the pressure of the analysis chamber was 1×10^{-8} mbar. 6T (no purity stated, Sigma Aldrich) was evaporated at 550 K from a Knudsen cell and deposited onto a Si(001) surface. The deposition of 6T, with typical fluxes of 1 nm min^{-1}, was monitored by a quartz crystal microbalance (QCM). Typical film thicknesses *L* were in the range of 20–30 nm. Metallic calcium was evaporated at 770 K from another Knudsen cell. The metal deposition rates were either 1.0 nm min^{-1} or 15 nm min^{-1}, depending on the details of the experiment. During the deposition, a permanently mounted hot filament ionization gauge indicated a pressure below $1 \cdot 10^{-7}$ mbar. In subsequent x-ray photoelectron spectroscopy (XPS) experiments, no unwanted impurities were detected on the metallic films except from oxygen. For background subtraction, a combination of Shirley background and linear slope has been used.

The NAC measurements were performed in a UHV setup with a base pressure below 10^{-10} mbar. At first, the reflectivity of the unaltered sample is measured using laser pulses. Afterwards, the laser power itself is measured. The detector surface is sputtered by Ar^+ ions (10^{-6} mbar, 3keV, 10 min) subsequently. The molecular beam of 6T and Ca is chopped producing small dosages. Furthermore, the zero-sticking coefficient is determined using a

QMS. During deposition, the heat increase of the detector is measured by an pyroelectrical material. The obtained data is referenced to the sticking coefficient and the reflectivity. The experiments were conducted at room temperature and at l-N_2 temperature.

TPD-MS was carried out in a dedicated UHV apparatus with a base pressure in the low 10^{-10} mbar regime. The apparatus hosts a HIDEN EPIC 1000 quadrupole mass spectrometer (QMS) mounted inside a differentially pumped cryo shroud cooled to 90 K with l-N_2 enabling detection of the molecule ions of 6T (494 amu) and potential reaction products and dimers. This version of a line-of-sight mass spectrometer was described elsewhere.[25-27] Temperatures were measured directly at the sample using a calibrated Type K thermocouple. A polished Au(111) single-crystal surface (diameter 10 mm, purity > 99.999%, roughness < 0.03 μm, orientation accuracy < 0.1°, from MaTecK/Germany) as substrate was prepared by sputtering with Ar+ ions (0.5 keV, 2 μA, 60 min) and subsequent annealing (850 K, 10 min). 6T (no purity stated, Sigma Aldrich) was evaporated from a home-built Knudsen cell at fluxes of about 0.1 nm min^{-1} measured using a QCM. The Au(111) sample was held at 100 K during deposition of 6T. Sample temperatures during Ca deposition were varied and are given for each experiment. The prepared sample was placed directly in front of the orifice (8 mm diameter) of the cryo shroud. The crystal was heated resistively via tungsten wires with a constant heating rate of 0.1 K s^{-1}. During heating, survey mass spectra from 1 to 1000 amu (1 amu step width) were recorded together with the temperature. Acquisition of one cycle took around 40 s, leading to a temperature rise of 4 K per cycle. With this procedure, the possible products of the reaction of Ca with 6T can be detected, including side products or contaminations with higher masses. The results are presented in the form of TPD-MS maps.

Results and Discussion

EDX: Investigations of interphase systems by means of X-ray photoelectron spectroscopy (XPS) require well-defined surfaces. Issues may arise from rough features and crystallites on the surface. A quantitative depth analysis by XPS is only possible for a layered system. To gain insight into the interphase energy-dispersive X-ray spectroscopy (EDX) as well as atomic force microscopy (AFM) was applied. For EDX and AFM different samples were prepared. For further information see the Experimental Section. The EDX analysis shows clearly that sulfur and calcium coexist in an approximately 30 nm thick interphase layer, if Ca is deposited onto the 6T film at room temperature (marked region in Fig. 1). It is well known that Ca atoms interact with thiophene based materials/polymers, resulting in the formation of CaS.[13-15] A detailed inspection of Figure 1 shows that the interphase between Ca and 6T is rather diffuse. It remains unclear at this point if the preparation by a focused ion beam (FIB) caused this. Therefore, AFM is used to investigate surface roughness of thick and thin layers of pristine 6T with high and low deposition rates.

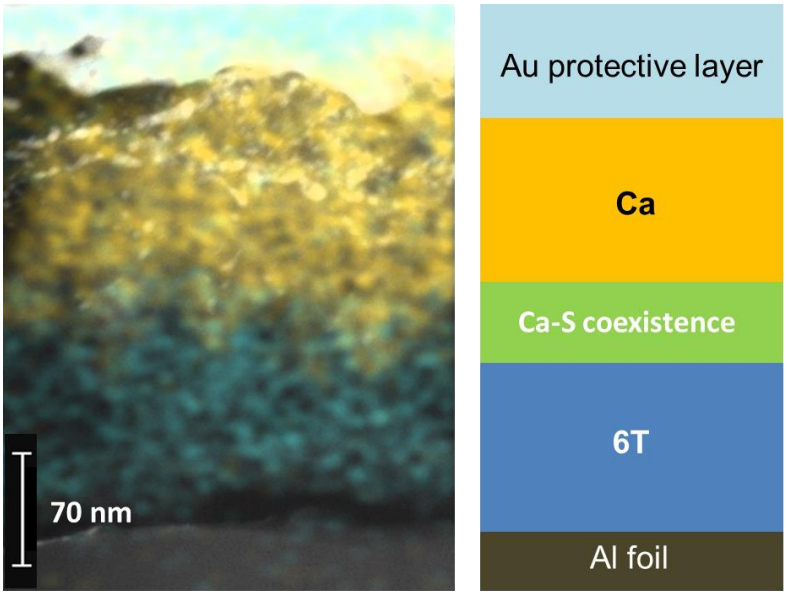

Figure 1. EDX map showing the chemical composition of Au/Ca/6T sample (The Au acts as a protective layer against oxidation under ambient conditions). Ca and 6T are separated by a 30-40 nm wide coexistence region of Ca and S.

P8

Figure 2 shows an AFM image of a 20 nm thick 6T layer deposited with a deposition rate of 0.35 nm/min on a Si(001) wafer together with a line scan. The 6T layer exhibits several islands resulting in a rather rough structure. Determination of the layer heights by a line scan reveals that the steps are 1.6 to 2.2 nm high. This is in good agreement with upright standing 6T molecules if compared to the unit cell of crystalline 6T (2.2 – 2.5 nm).[28-29] The smaller steps can be attributed to bent molecules. Similar findings were obtained for three additional samples with different thicknesses and deposition rates. Comparing all samples two trends were noticed: i) higher deposition fluxes result in a higher roughness of the surface and ii) higher thicknesses result in smoother surfaces. However, the former is much more important as a high flux drastically increase crystallite growth. The latter can be explained by the fact that 6T tends to form crystallites even at small coverages at room temperature. Hence, the first multilayers exhibit Volmer-Weber-like growth which turns into Stranski-Krastanov growth for higher coverages. The lowest roughness was found for the sample shown in Figure 2, thus preparing the samples for photoelectron spectroscopy measurements in a similar way.

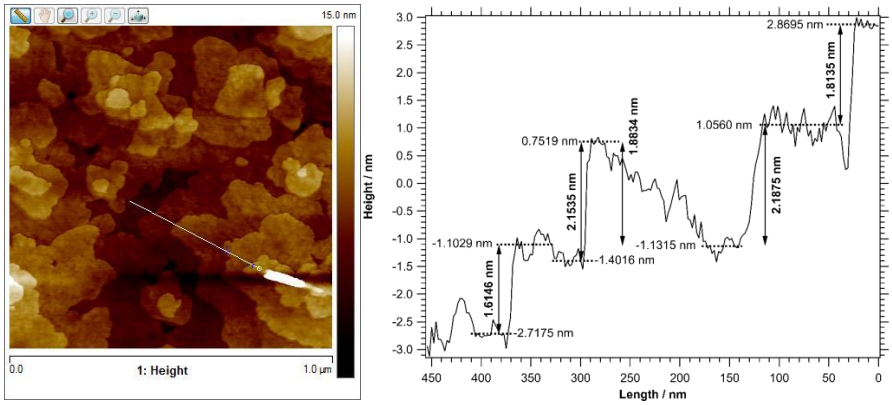

Figure 2. a) AFM image of a 20 nm thick 6T layer deposited with a rate of 0.35 nm/min on a Si(001) wafer. b) Line scan of the white line in a). Step heights are shown in the graph corresponding to bent (1.6 nm) and up-right standing (2.1 nm) molecules.

Lab-XPS: As EDX is not sensitive towards the chemical states of the sulfur atoms, it is not clear whether every sulfur atom within the Ca-S interphase layer has actually reacted with Ca or whether there is a coexistence between reacted and unreacted sulfur. To address this question and obtain the depth of the reaction, we examined the Ca/6T system with photoelectron spectroscopy with a regular laboratory X-ray Al K_α (1486.6 eV) source. In a first experiment, we deposited increasing amounts of calcium on a 21.6 nm thick 6T film and observed specific changes in the S 2p and C 1s core levels. To obtain depth resolved information, spectra were collected under normal emission (0°) and grazing emission (70°) with an information depth (3x inelastic mean free path) of ~12 and ~4.1 nm, respectively.[30]

P8

The most distinct changes upon Ca deposition arise in the S 2p core level region between 160 and 170 eV. While the pristine sample shows only a doublet comprising of the S $2p_{3/2}$ and S $2p_{1/2}$ lines at 164 and 165.1 eV, respectively, the reaction with calcium atoms leads to the evolution of another, strongly shifted multiplet at a 2.9 eV lower binding energy. Apparently, the calcium leads to a strong modification of the sulfur atoms. This finding is in accordance with previous investigations of other combinations of Ca and thiophene based materials.[13-15] A comparison of surface and bulk sensitive spectra (recorded at 0° and 70° respectively) reveals, however, an unexpected trend. Up to a calcium coverage of about 2.6 ML, the surface sensitive spectra show the expected enrichment of reacted sulfur in the near surface region. The doublet associated with the reacted sulfur at 161.1 and 162.2 eV is there significantly higher if recorded under 70° instead of 0°. If the amount of calcium is further increased (up to 19.3 ML), the expected increase in the signal associated with reacted sulfur–but also an unexpected independence of the spectra to bulk or surface sensitive conditions–is observed. In a simple picture, the surface sensitive spectra recorded under 70° should nearly exclusively comprise of the signal associated with reacted sulfur as most of the sulfur close to the Ca/6T interface should be reacted. However, such a behavior was not observed, rather it appears that, despite the continued deposition of Ca, a situation arises where the sample shows a homogeneous mixture between reacted and unreacted sulfur within a depth of ~12 nm (XPS information depth).

Noteworthy, even prolonged deposition of Ca does not lead to a full conversion of the sulfur into the reacted species. Even after the deposition of nominal 19.4 ML of Ca ~25% of the sulfur atoms still appear to be in their pristine state.

In addition to the changes in the relative intensity between the signal components of reacted and unreacted sulfur, an increasing Ca coverage is associated with a distinct shift of the sulfur signals to higher binding energies. The sulfur spectra after the deposition of 19.4 ML of Ca are shifted by 0.6 eV compared to the pristine 6T film. Such a behavior is, if observed in transition regions between metals and (organic) semiconductors, usually attributed to band bending effects.[31]

Further insights into the formation of the reaction zone are obtained by an analysis of the evolution of the C 1s signal at 284 eV with increasing Ca deposition at 300 K. The pristine signal comprises two distinct components at 284.4 eV and 285 eV, associated with carbon with and without contact to the sulfur atoms, respectively. An increasing amount of Ca leads to slight shift in particular of the C 1s levels of carbon atoms close to the surface (recorded under 70°). For calcium dosages beyond 1.3 ML a distinct shoulder appears at lower binding energy, however, no clear substructure is visible. The intensity of this shoulder increases with subsequent calcium deposition. Similar to the situation observed in the S 2p spectra, surface and bulk sensitive measurements are virtually identical – again indicating a homogeneous chemical composition of the reacted layer within the information depth of the C 1s line of ~12 nm (for hν = 1486.6 eV and 0° emission)[30].

P8

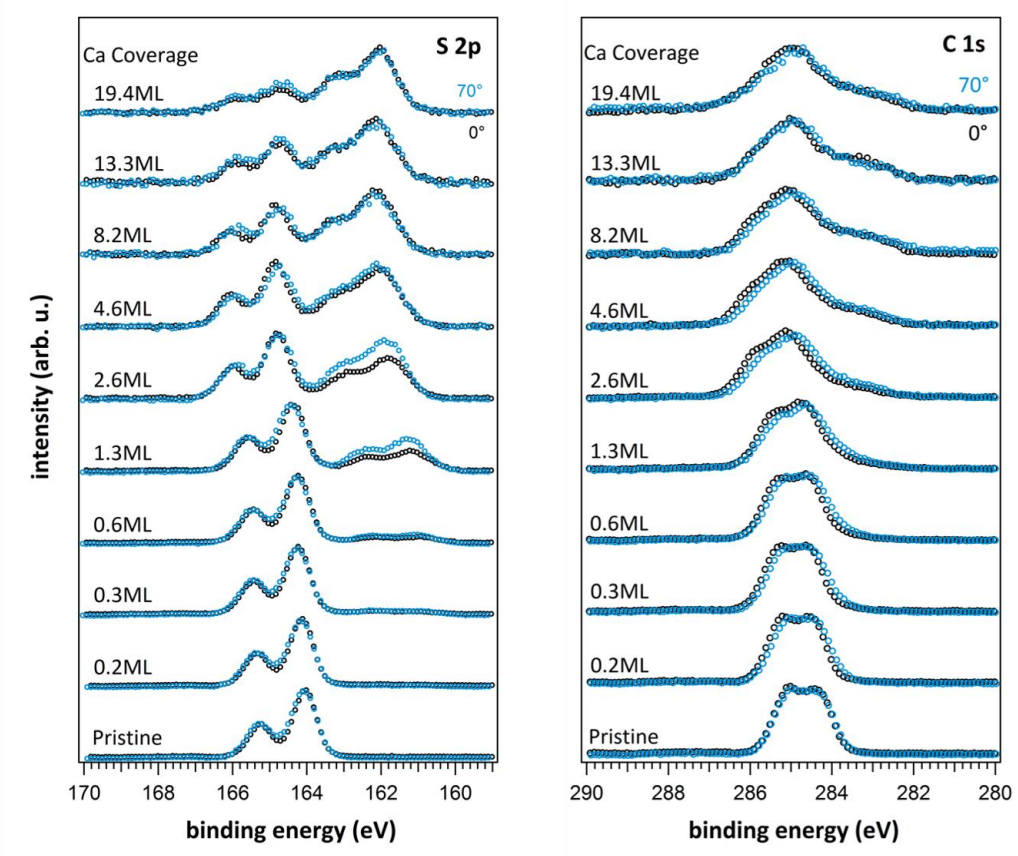

Figure 3. S2p and C1s core level spectra of a 6T film recorded under 0° and 70° with Al K_α radiation depending on the amount of deposited Ca.

HAXPES: The progress of the reaction of Ca with 6T can be easily followed with photoelectron spectroscopy by recording the S 1s, S 2s and S 2p regions, because the sulfur species of the 6T has a distinct chemical shift than the sulfur in CaS. Measuring these regions at different photon energies in a hard X-ray photoelectron spectroscopy (HAXPES) experiment, the reaction depth can be obtained.

In Figure 4 the S 1s and S 2s XP spectra of a sample prepared under standard conditions (300 K, Ca flux of 1 nm/min) is presented. The S 1s region of pristine 6T (Figure 4, top left) exhibits one sharp peak corresponding to the sulfur in the thiophene units. Upon deposition of Ca, two new peaks appear at lower binding energy (Figure 4, bottom left). The shift to lower binding energies suggests an electron richer sulfur species attributed to CaS. The larger peak resembles the main product (CaS) whereas the smaller one may be due to side products or CaS in a different chemical environment than the main CaS. Increasing the photon energy results in a higher inelastic mean free path (IMFP) and thus a higher information depth. Unreacted 6T underneath the reacted phase gets more pronounced, hence changing the ratio of reacted to unreacted peak intensity (Fig. 4, right).

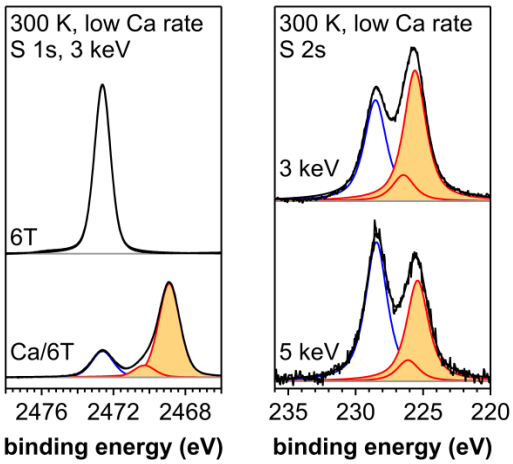

Figure 4. XP spectra of Ca on 6T for the sample at standard conditions (300 K, Ca flux of 1 nm/min). Left: S 1s XP spectra of pristine 6T (top) and Ca on 6T (bottom). The yellow-shaded peaks correspond to reacted CaS species. Right: S 2s XP spectra recorded at 3 and 5 keV showing different ratios of reacted to unreacted species.

For each spectrum the ratio of reacted to unreacted peak intensities is calculated. This was done for a large number of different energies between 2003 and 5500 eV (Fig. 5, left). The exponential decrease due to the higher IMFP is nicely reproduced. Furthermore, there is only low scattering and the three different sulfur orbitals are in good agreement with each other. With equation (1) the reaction depth can be calculated for three different samples: i) 300 K, low

Ca flux (standard conditions), ii) 90 K, low Ca flux and iii) 300 K, high Ca flux (15 nm/min). For each sample different reaction depths are obtained (Fig 5, right). The reduced preparation temperature decreases the reaction thickness again by a factor of 2 what was observed for Co on 2HTPP.[32] However, increasing the metal atom flux shrinks the interlayer depth by 25%. This shows that the metal atom flux has an impact on the interphase formation, in contrast to the previous results of Co and Fe on 2HTPP.[32]

$$d = \lambda \ln\left(\frac{\frac{I_r}{I_{ur}}+1}{\frac{I_r}{I_{ur}}\exp\left(-\frac{L}{\lambda}\right)+1}\right) \quad (1)$$

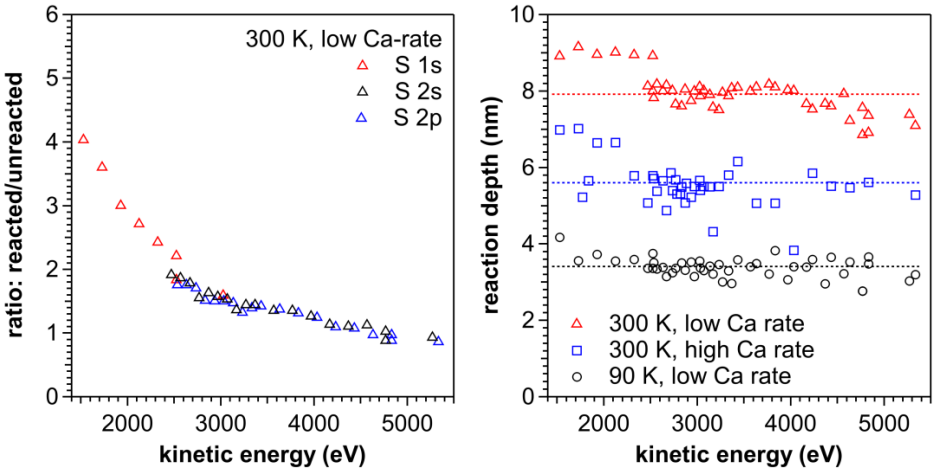

Figure 5. Left: Calculated ratios of reacted to unreacted sulfur species for the S 1s, S 2s and S 2p regions of the sample at standard conditions. Right: Obtained reaction depth for the three different samples showing the influence of temperature and metal atom flux.

NAC: Ca atoms were deposited on 20 nm thick 6T layers and the head of adsorption is measured in a NAC experiment (Figure 6). At small Ca coverages, the head of adsorption is very high attributed to the reaction of Ca with thiophene units and the formation of CaS. The head of adsorption quickly decreases for additional Ca atoms because the Ca atoms do not diffuse deep into the 6T bulk. This observation is in line with the previous methods. After deposition of 2 ML Ca at room temperature and below 0.5 ML Ca at 80 K, the heat of adsorption approaches the sublimation enthalpy of Ca, indicated by the dashed line in Figure 6, since at this point Ca is only deposited on a Ca layer. The reaction depth can be calculated from the behavior of the heat of adsorption, yielding 3.4 and 1.7 nm at room temperature and 80 K, respectively. Again, the extend of the reaction zone is halved by cooling the sample during metal atom deposition, although the absolute values differ in comparison with the HAXPES analysis. Since the reaction products besides CaS are not known, the measured reaction enthalpy is difficult to interpret. In literature, the formation of cyclooctatetraene is suggested,

however, this does not fit with the obtained heat of adsorption. Unless the reaction products are clarified, quantitative analysis of the data is not possible.

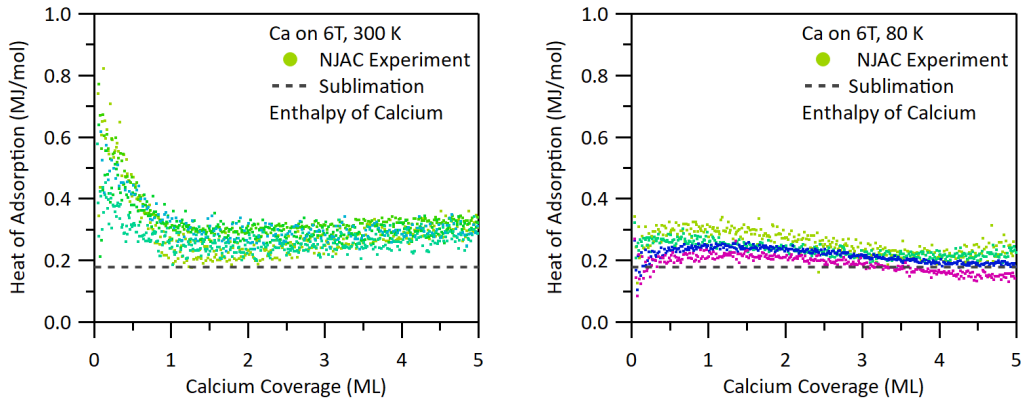

Figure 6. Heats of adsorption obtained by NAC for calcium deposition on 20 nm thick 6T layers. Different colors indicate specific experiments. The dashed line corresponds to the sublimation enthalpy of Ca. Left: at room temperature, right at low temperature (80 K).

TPD-MS: Temperature-programmed desorption mass spectrometry (TPD-MS) is used to investigate possible desorbing reaction products as a multilayer of cyclooctatetraene should be able to desorb. The TPD-MS map of pristine 6T as a reference is found in the Supporting Information. Figure 7 shows the TPD-MS maps of different stoichiometries of Ca on 2 nm 6T. With increasing Ca amounts the peak intensity of 6T is decreasing. However, no reaction products are detected neither at higher masses nor at lower masses. Note that a possible 6T dimer without two sulfurs atoms of 924 amu could still be detected. This suggests that the remaining carbon species form a variety of possible clusters and polymers. No decomposition into lower fragments like cyclobutadiene or cyclooctatetraene is observed. Hence, interpretations of the reaction enthalpy are meaningless as well as a calculation of the size of CaS clusters.[13-15]

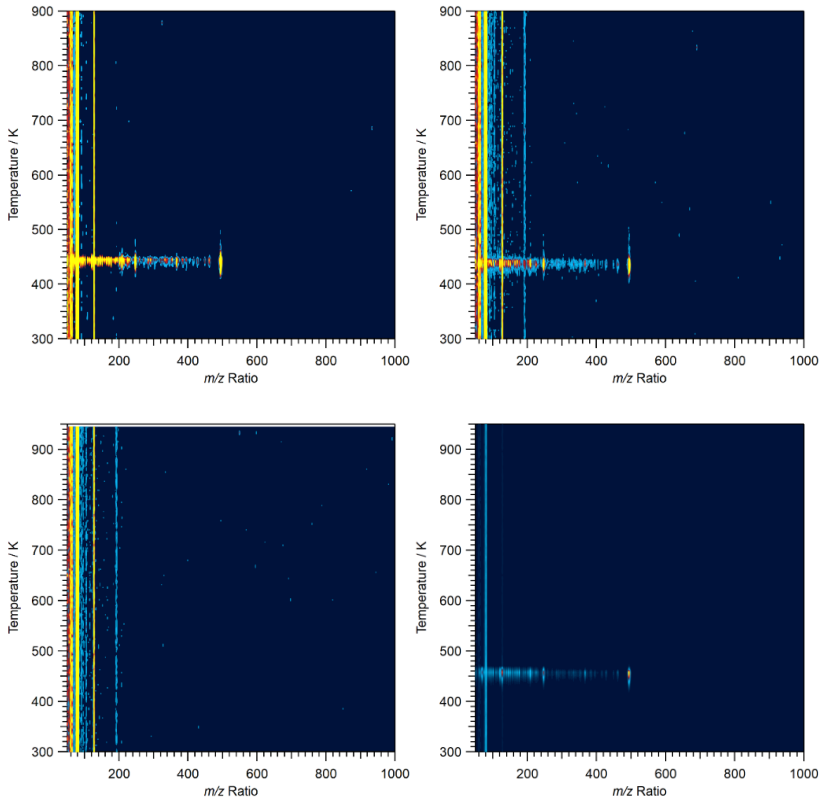

Figure 7[. TPD-MS maps of Ca on 6T for different Ca:S stoichiometries a) 1:3, b) 1:1, c) 2:1 and d) 2.5:1. d) HAXPES analog, 4 nm Ca on 20 nm 6T. Recorded masses 1 to 1000 amu in 1 amu steps. The heating rates were 0.1 Ks^{-1} in all experiments. Ca was deposited at 300 K.

P8

Conclusion: An examination of the interface between metallic Calcium and α-sexithiophene revealed the temperature dependent formation of an extended interphase layer, in which Ca reacts with the sulfur atoms from the 6T molecules. At 300 K, EDX shows that the reaction zone extends between 30 and 40 nm into the organic matrix, the transition to the pristine 6T being rather abrupt within a few nm. This abrupt transition indicates that Ca atoms may only migrate over very short distances within the pristine 6T layer before undergoing a reaction with the sulfur atoms in their vicinity. An advanced analysis based on hard X-ray photoelectron spectroscopy reproduces the dimension of the reaction zone and additionally shows that at RT only ~2/3 of the Sulfur atoms participate in the reaction. While each 6T molecule within the reaction zone is altered by the calcium atoms, ~1/3 of the sulfur atoms remain chemically uninfluenced. Strong changes in the C1s spectra upon Ca deposition point towards a significant distortion of the carbon backbone, possibly giving rise to metallacylce compounds. It appears likely that the strong distortions of the carbon backbone lead to a situation where a reaction of all sulfur atoms is sterically hindered. In complementary experiments at 150 K, a fundamentally different situation was observed in HAXPES measurements: The reaction zone is substantially thinner and shows a pronounced tail into the pristine 6T bulk material. Such a behavior is only

possible if individual Ca atoms may migrate through the organic matrix without immediately reacting with the surrounding 6T molecules. Apparently, the reduction in temperature not only reduced the mobility of the Ca atoms in the organic material, but also significantly quenched the reaction rate between sulfur and calcium, favoring the formation of a metallic Ca film on top of the sample. The observed situation persists even after warming up the sample to room temperature.

References

1. Friend, R. H.; Gymer, R. W.; Holmes, A. B.; Burroughes, J. H.; Marks, R. N.; Taliani, C.; Bradley, D. D. C.; Santos, D. A. D.; Bredas, J. L.; Lögdlund, M.; Salaneck, W. R., Electroluminescence in conjugated polymers. Nature 1999, 397 (6715), 121-128.

2. Tedde, S. F.; Kern, J.; Sterzl, T.; Fürst, J.; Lugli, P.; Hayden, O., Fully Spray Coated Organic Photodiodes. Nano Letters 2009, 9 (3), 980-983.

3. Garnier, F.; Hajlaoui, R.; Yassar, A.; Srivastava, P., All-Polymer Field-Effect Transistor Realized by Printing Techniques. Science 1994, 265 (5179), 1684-1686.

4. Mori, T., Molecular materials for organic field-effect transistors. Journal of Physics: Condensed Matter 2008, 20 (18), 184010.

5. Kido, J.; Kimura, M.; Nagai, K., Multilayer White Light-Emitting Organic Electroluminescent Device. Science 1995, 267 (5202), 1332-1334.

6. Wang, L.; Chen, W.; Wee, A. T. S., Charge transfer across the molecule/metal interface using the core hole clock technique. Surface Science Reports 2008, 63 (11), 465-486.

7. Dinelli, F.; Murgia, M.; Levy, P.; Cavallini, M.; Biscarini, F.; de Leeuw, D. M., Spatially Correlated Charge Transport in Organic Thin Film Transistors. Physical Review Letters 2004, 92 (11).

8. Janssen, F. J. J.; van IJzendoorn, L. J.; van der Gon, A. W. D.; de Voigt, M. J. A.; Brongersma, H. H., Interface formation between metal and poly-dialkoxy-p-phenylene vinylene. Physical Review B 2004, 70 (16).

9. Lee, D. W.; Kim, K.; Jin, J.-I.; Park, Y., Interface formation between Ca and poly(p-phenylene vinylene) derivatives having electron-withdrawing 1,3,4-oxadiazole or electron-donating alkoxy pendants. Synthetic Metals 2004, 143 (2), 181-185.

10. Liao, L. S.; Cheng, L. F.; Fung, M. K.; Lee, C. S.; Lee, S. T.; Inbasekaran, M.; Woo, E. P.; Wu, W. W., Interface formation between poly(9,9-dioctylfluorene) and Ca electrode investigated using photoelectron spectroscopy. Chemical Physics Letters 2000, 325 (4), 405-410.

11. van Gennip, W. J. H.; van Duren, J. K. J.; Thüne, P. C.; Janssen, R. A. J.; Niemantsverdriet, J. W., The interfaces of poly(p-phenylene vinylene) and fullerene derivatives with Al, LiF, and Al/LiF studied by secondary ion mass spectroscopy and x-ray photoelectron

spectroscopy: Formation of AlF3 disproved. The Journal of Chemical Physics 2002, 117 (10), 5031-5035.

12. Tipler, P.; Llewellyn, R., Modern physics. W.H. Freeman: New York, 1999.

13. Bebensee, F.; Zhu, J.; Baricuatro, J. H.; Farmer, J. A.; Bai, Y.; Steinrück, H.-P.; Campbell, C. T.; Gottfried, J. M., Interface Formation between Calcium and Electron-Irradiated Poly(3-hexylthiophene). Langmuir 2010, 26 (12), 9632-9639.

14. Bebensee, F.; Schmid, M.; Steinrück, H.-P.; Campbell, C. T.; Gottfried, J. M., Toward Well-Defined Metal-Polymer Interfaces: Temperature-Controlled Suppression of Subsurface Diffusion and Reaction at the Calcium/Poly(3-Hexylthiophene) Interface. Journal of the American Chemical Society 2010, 132 (35), 12163-12165.

15. Zhu, J.; Bebensee, F.; Hieringer, W.; Zhao, W.; Baricuatro, J. H.; Farmer, J. A.; Bai, Y.; Steinrück, H.-P.; Gottfried, J. M.; Campbell, C. T., Formation of the Calcium/Poly(3-Hexylthiophene) Interface: Structure and Energetics. Journal of the American Chemical Society 2009, 131 (37), 13498-13507.

16. Jo, S. J.; Kim, C. S.; Kim, J. B.; Ryu, S. Y.; Noh, J. H.; Baik, H. K.; Kim, Y. S.; Lee, S.-J., Increase in indium diffusion by tetrafluoromethane plasma treatment and its effects on the device performance of polymer light-emitting diodes. Journal of Applied Physics 2008, 103 (11), 114502.

17. Lee, S. T.; Gao, Z. Q.; Hung, L. S., Metal diffusion from electrodes in organic light-emitting diodes. Applied Physics Letters 1999, 75 (10), 1404-1406.

P8

18. Zhang, Y.; Ren, J.; Lei, J.; Xie, S., Effect of Co permeation on spin polarized transport in a Co/organic semiconductor (OSC) structure. Organic Electronics 2009, 10 (4), 568-572.

19. Horowitz, G.; Delannoy, P.; Bouchriha, H.; Deloffre, F. o.; Fave, J.-L.; Garnier, F.; Hajlaoui, R.; Heyman, M.; Kouki, F. a.; Valat, P.; Wintgens, V. R.; Yassar, A., Two-layer light-emitting diodes based on sexithiophene and derivatives. Advanced Materials 1994, 6 (10), 752-755.

20. Kelley, T. W.; Frisbie, C. D., Gate Voltage Dependent Resistance of a Single Organic Semiconductor Grain Boundary. The Journal of Physical Chemistry B 2001, 105 (20), 4538-4540.

21. Fichou, D.; Nunzi, J.-M.; Charra, F.; Pfeffer, N., ?-Sexithiopene$$ A new photochromic material for a prototype ultrafast incoherent-to-coherent optical converter. Advanced Materials 1994, 6 (1), 64-67.

22. Gorgoi, M.; Svensson, S.; Schäfers, F.; Öhrwall, G.; Mertin, M.; Bressler, P.; Karis, O.; Siegbahn, H.; Sandell, A.; Rensmo, H.; Doherty, W.; Jung, C.; Braun, W.; Eberhardt, W., The high kinetic energy photoelectron spectroscopy facility at BESSY progress and first results. Nuclear Instruments and Methods in Physics Research Section A: Accelerators, Spectrometers, Detectors and Associated Equipment 2009, 601 (1-2), 48-53.

23. Schaefers, F.; Mertin, M.; Gorgoi, M., KMC-1: A high resolution and high flux soft x-ray beamline at BESSY. Review of Scientific Instruments 2007, 78 (12), 123102.

24. Schmid, M.; Steinrück, H.-P.; Gottfried, J. M., A new asymmetric Pseudo-Voigt function for more efficient fitting of XPS lines. Surface and Interface Analysis 2014, 46 (8), 505-511.

25. Klein, B. P.; van der Heijden, N. J.; Kachel, S. R.; Franke, M.; Krug, C. K.; Greulich, K. K.; Ruppenthal, L.; Müller, P.; Rosenow, P.; Parhizkar, S.; Bocquet, F. c., ,ois C.; Schmid, M.; Hieringer, W.; Maurer, R. J.; Tonner, R.; Kumpf, C.; Swart, I.; Gottfried, J. M., Molecular Topology and the Surface Chemical Bond: Alternant Versus Nonalternant Aromatic Systems as Functional Structural Elements. Physical Review X 2019, 9 (1).

26. Schöniger, M.; Kachel, S. R.; Herritsch, J.; Schröder, P.; Hutter, M.; Gottfried, J. M., Direct synthesis of dilithium tetraphenylporphyrin: facile reaction of a free-base porphyrin with vapor-deposited lithium. Chemical Communications 2019, 55 (91), 13665-13668.

27. Kachel, S. R.; Klein, B. P.; Morbec, J. M.; Schöniger, M.; Hutter, M.; Schmid, M.; Kratzer, P.; Meyer, B.; Tonner, R.; Gottfried, J. M., Chemisorption and Physisorption at the Metal/Organic Interface: Bond Energies of Naphthalene and Azulene on Coinage Metal Surfaces. The Journal of Physical Chemistry C 2020, 124 (15), 8257-8268.

28. Servet, B.; Ries, S.; Trotel, M.; Alnot, P.; Horowitz, G.; Garnier, F., X-ray determination of the crystal structure and orientation of vacuum evaporated sexithiophene films. Advanced Materials 1993, 5 (6), 461-464.

29. Horowitz, G.; Bachet, B.; Yassar, A.; Lang, P.; Demanze, F.; Fave, J.-L.; Garnier, F., Growth and Characterization of Sexithiophene Single Crystals. Chemistry of Materials 1995, 7 (7), 1337-1341.

30. Lesiak, B.; Kosinski, A.; Jablonski, A.; Köv\'e, r, L.; T\'o, th, J.; Varga, D.; Cserny, I.; Zagorska, M.; Kulszewicz-Bajer, I.; Gergely, G., Determination of the inelastic mean free path of electrons in polythiophenes using elastic peak electron spectroscopy method. Applied Surface Science 2001, 174 (1), 70-85.

31. Ettedgui, E.; Hsieh, B. R.; Gao, Y., Interface formation of metals and poly(p-phenylene vinylene): surface species and band bending. Polymers for Advanced Technologies 1997, 8 (7), 408-416.

32. Schmid, M.; Kachel, S. R.; Klein, B. P.; Bock, N.; Müller, P.; Riedel, R. e., ,; Hampp, N.; Gottfried, J. M., Reactive metal-organic interfaces studied with hard x-ray photoelectron spectroscopy: controlled formation of metalloporphyrin interphase layers during metal vapor deposition onto porphyrin films. Journal of Physics: Condensed Matter 2019, 31 (9), 094002.

Acknowledgments

Philipp Müller for conducting HIKE experiments and the HZB for the opportunity to conduct measurements at the HIKE Beamtime.

TOC

Supporting Information

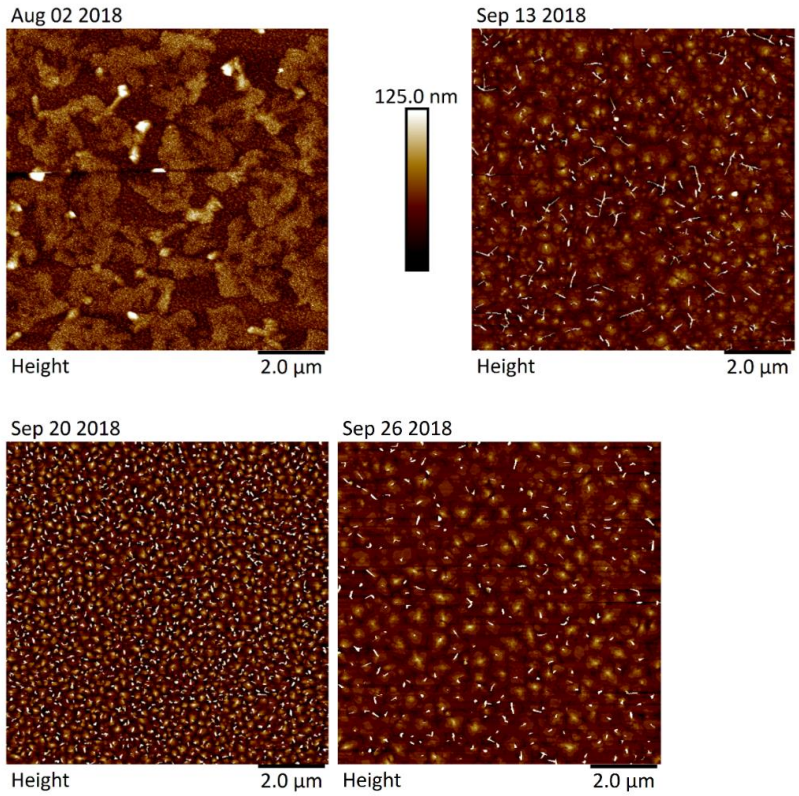

Figure S1. AFM images of different thicknesses 6T on Si(001) wafers deposited by different rates. a) 63 nm @ 72 nm/min (top left), b) 20 nm @ 0.35 nm/min (top right), c) 21.3 nm @ 3 nm/min (bottom left) and d) 12.2 nm @ 0.33 nm/min (bottom right).

Table S1. Preparation parameters and resulting roughnesses for four differently prepared 6T on Si(001) samples.

6T thickness	**63.3**	**21.3 nm**	**19.9 nm**	**12.2 nm**
Flux	**~72 nm/min**	**~3 nm/min**	**~0.35 nm/min**	**~0.33 nm/min**
Roughness 10x10 µm, flattening: 2nd order				
Rq	**18.7 nm**	**6.80 nm**	**4.60 nm**	**~5.18 nm**
Ra	**13.9 nm**	**4.18 nm**	**2.29 nm**	**~2.27 nm**

Rz	**16.8 nm**	**49.3 nm**	**14.2 nm**	**~22.3 nm**
Rz Count	**15546**	**338**	**1016**	**~697**
Roughness 1x1 µm, flattening: 1st order				
Rq	**-**	**7.85 nm**	**2.14 nm**	**~5.48 nm**
Ra	**-**	**4.62 nm**	**1.60 nm**	**~2.05 nm**
Rz	**-**	**4.17 nm**	**0.39 nm**	**~0.62 nm**
Rz Count	**-**	**142**	**738**	**~569**

TPD-MS

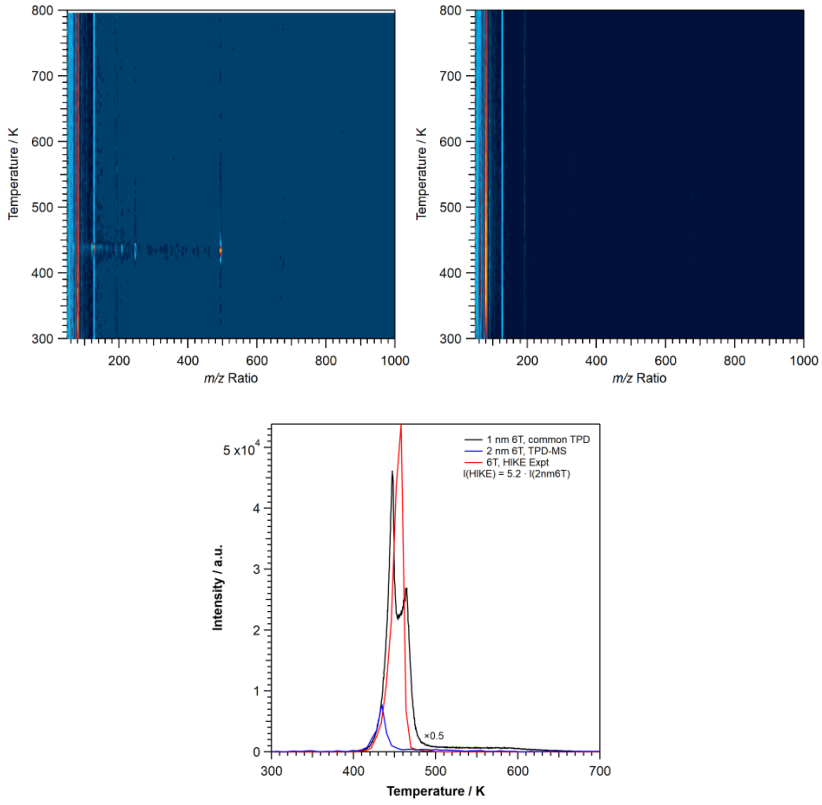

Figure S2. Top left: TPD-MS map of pristine 6T on Au(111). Top right: blank measurement. Mass ranges from 1-1000 amu with 1 amu step width. Heating rates were 1 Ks^{-1}. Bottom: QMS intensity of mass 494 amu for pristine 6T and the HIKE analog.

Tracking the Pb−Cu Exchange of PbTPP on Cu(111) by Multi-Method Approach

Jan Herritsch, Stefan Renato Kachel, Qitang Fan, Mark Hutter, Lukas Heuplick, Florian Münster, J. Michael Gottfried

Fachbereich Chemie, Philipps-Universität Marburg,
Hans-Meerwein-Straße, 35032 Marburg, Germany

Abstract

The on-surface transmetalation of a monolayer of lead(II) 5,10,15,20-tetraphenylporphyrin with the underlying Cu(111) substrate is studied by multiple surface-sensitive techniques under ultra-high vacuum (UHV) conditions. By temperature dependent X-ray photoelectron spectroscopy (XPS) of the Pb 4f region the reaction is traced by the reduction of the central atom. The metal-exchange starts already at 350 K and is almost completed at 550 K. A partial desorption of the monolayer enables the detection of the product CuTPP by mass spectrometry in a temperature-programmed reaction (TPR) experiment. Scanning tunneling microscopy (STM) reveals a highly chemisorbed adsorbate structure at 300 K and uncovers structural changes, which accompany the transmetalation as well as side-reactions of the phenyl substituents. Moreover, individual free lead atoms are visible as a product of the metal-exchange.

Introduction

Tetrapyrrole ligands such as porphyrins and phthalocyanines provide a defined coordination environment for metal cations and are used in catalysis[1-3], in sensor technology[4] but also as components in molecular electronics[5-6]. Typically, the optoelectronic and chemical properties of the complexes are largely determined by the incorporated cation. Hence, their reactivity is given by the electronic structure of the central atom, i.e., by the number of occupied and unoccupied metal states and their energy level as well as their spatial distribution. By varying the central atom or its redox state, the valence structure and thus the reactivity can be specifically altered.

In the domain of interfaces or especially of single molecular layers on a substrate, the molecule-substrate interactions are of major importance.[7-8] These include, e.g., interfacial charge transfer, detachment of the central atom[9-11] or even metal-exchange reactions[12-15]. The latter were described for an exchange of the central atom of tetrapyrrole complexes on metal substrates with a surface adatom[12-13] or with another metal atom[14-15], which was subsequently vapor-deposited on the monolayer film. Such on-surface transmetalations has been described especially for transition metal complexes of porphyrins[12, 15] and phthalocyanines[13] on metal substrates. In these studies, the transmetalation was tracked by the reduction of the leaving central atom M(II) → M(0). The change of the electronic state was proven experimentally by X-ray photoelectron spectroscopy (XPS), near-edge X-ray absorption fine-structure (NEXAFS) spectroscopy and scanning tunneling microscopy (STM). The described transmetalation reactions provide access to mixed-metal layers with unique properties. However, a clear evidence that the in-place atom actually leaves the macrocycle and is exchanged by the entering atom was not provided so far.

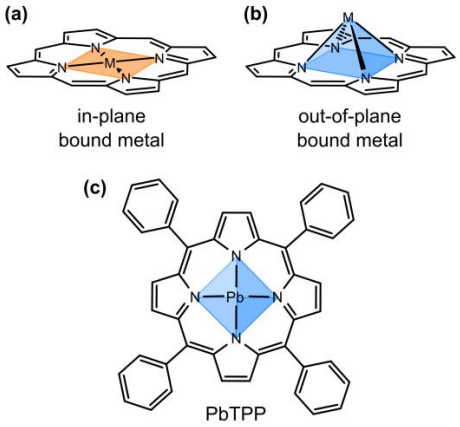

Figure 1. Porphyrin complexes with (a) an in-plane bound and (b) an out-of-plane bound metal center are shown with the central atom's coordination environment colored in orange and blue, respectively. (c) Molecular structure of lead(II) 5,10,15,20-tetraphenylporphyrin (PbTPP), which exhibits an out-of-plane bound central lead atom.

In contrast to the extensively studied transition metal complexes, post-transition metal tetrapyrroles received little attention in the field of surface science. Thus there are only very few studies of corresponding lead(II) complexes[9-11, 16] despite their interesting molecular properties. Due to the large ionic radius of lead(II) these complexes adopt a non-planar structure with an out-of-plane bound metal center.[17] According to crystal structures the central atom is located about 1.2 Å above the center of the N_4 plane

forming a square pyramid.[17-19] As a result lead tetrapyrroles differ considerably from their transition metal analogues with an N_4 in-plane coordination of the central atom (Figure 1a,b). The combination of the large ionic radius and the highly undercoordinated lead atom enables a diverse coordination chemistry of lead(II) tetrapyrroles.[20-21] Furthermore, the complexes are known to be prone to metal-exchange reactions in solution chemistry[20, 22-23] as a consequence of the non-planar structure. On a surface, the out-of-plane bound metal center leads to the formation of two different conformers during a flat-lying adsorption of the macrocycle. In the so-called metal-down conformer the central atom is located between the substrate and the ligand while in the metal-up conformer it is located above the ligand. For lead(II) phthalocyanine (PbPc) on Ag(111) both conformers could be clearly distinguished by STM.[16] Moreover, it was reported that PbPc undergoes a detachment of the central atom by interactions with Pt(111)[9] and Ag(111)[11] metal substrates as well as InSb(100) and InAs(100) III-V semiconductors[10]. This reaction was tracked by the reduction of lead(II), but the product remained unidentified.

In the present paper, we have investigated the reactivity of an adsorbed monolayer of lead(II) 5,10,15,20-tetraphenylporphyrin (PbTPP, Figure 1c) towards a metal-exchange reaction with the underlying Cu(111) substrate. Thus, the concept of an on-surface transmetalation is applied to a period 6 post-transition metal porphyrin complex. An exchange of the central atom, i.e., a transmetalation of type PbTPP + Cu → CuTPP + Pb is accompanied by a change in the oxidation state of the leaving lead atom. Therefore, we start our investigation with temperature-dependent XP spectra of the Pb 4f region providing information on the electronic state of the central atom of PbTPP. A partial desorption of the investigated monolayer at higher temperatures caused by an on-surface side-reaction of the peripheral phenyl substituents enables the identification of CuTPP by mass spectrometry. In addition to this direct evidence of CuTPP by the temperature-programmed reaction (TPR) experiment, we are providing further details on the adsorption of PbTPP on Cu(111) by STM.

Experimental Methods

All experiments were performed in ultra-high vacuum (UHV) with a base pressure in the range of 10^{-10} mbar. PbTPP (purity XX, supplier XX) was purchased from commercial sources. The Cu(111) single crystals (purity > 99.9999%, roughness < 0.03 µm, orientation accuracy < 0.1°, MaTecK/Germany) used as substrate were cleaned by repeated cycles of Ar^+ ion bombardments (0.5 keV) followed by annealing (> 800 K). Surface cleanliness was confirmed by XPS prior to the XPS and STM experiments. XPS and STM was performed in a two-chamber UHV setup using a monochromatized Al Kα X-ray source (1486.7 eV) and a SPECS Phoibos 150 electron energy analyzer equipped with an MCD-9 multi channeltron detector as well as a SPECS Aarhus 150 STM. Sample preparation was carried out in another chamber connected to this UHV setup. Here, the samples were prepared by vapor deposition of PbTPP (610 K) on a clean Cu(111) single crystal. The flux was monitored at the sample position using a quartz crystal microbalance. During preparation the substrate was kept at room temperature. For STM the sample was cooled to about 100 K with l-N_2 and images were obtained in constant current mode. For a background correction of the N 1s and Pb 4f regions, spectra of the pristine Cu(111) surface were used. Therefore, the background spectra were interpolated by a smoothing spline and afterwards the spline function was subtracted from the measured spectra. TPR experiments were carried out using a HIDEN EPIC 1000 quadrupole mass spectrometer mounted inside a differentially pumped cryo shroud cooled to 90 K with l-N_2. The used setup[24-25] with a line-of-sight mass spectrometer enables the direct detection of the molecule ions of CuTPP (*m/z* 675) and PbTPP (*m/z* 820). After cleaning of the Cu crystal, a monolayer coverage of PbTPP was annealed to 650 K (see discussion). The Cu(111) sample was held at 100 K during deposition of PbTPP. The prepared sample was placed directly in front of the orifice (8 mm diameter) of the cryo shroud. The crystal was heated resistively via tungsten wires with a constant heating rate of 1 K/s. Temperatures were measured directly at the sample using a calibrated Type K thermocouple.

Results and Discussion

Figure 2 shows the corresponding spectrum of (a) a vapor deposited monolayer of PbTPP on Cu(111) at 300 K and after heating the sample to 450 K and 550 K. Furthermore, the spectra can be compared with (b) a PbTPP multilayer of 4.0 nm thickness. In the multilayer the probed molecules are decoupled from the interactions with the Cu(111) surface. The spin-orbit components are well separated at binding energies (BE) of 138.5 eV and 143.4 eV for the Pb $4f_{7/2}$ and Pb $4f_{5/2}$ signal, respectively. Thus the spectrum represents the typical shape of similar Pb(II) tetrapyrrole complexes.[9, 11, 26-27] Moreover, the multilayer also provides information about the purity of the deposited films. Therefore, a contamination with the unmetalated free ligand H_2TPP can be excluded according to additional C 1s and N 1s spectra as described in the supporting information (SI). A comparison with the monolayer at 300 K reveals that the BE of the Pb 4f signals at 138.3 eV and 143.2 eV remains mostly unchanged by the direct influence of the Cu(111) surface. Thus, the molecules stay intact in the monolayer at 300 K. However, after annealing to higher temperatures a second set of signals appears at 136.6 eV and 141.5 eV at lower BE relative to the Pb(II) signal of the intact molecule. These signals can be assigned to a reduced Pb(0) species, which emerge as the product of the transmetalation. The progress of the reaction can be traced by a thorough fitting of the Pb $4f_{7/2}$ region. By comparing the areas of the Pb(II) signal of the intact molecule (blue fit function) with those of the Pb(0) signal (grey fit function), about 55% of lead atoms have already been reduced after annealing to 450 K. Further heating to 550 K leads to almost full conversion. XP spectra of the Pb 4f region of additional heating steps between 350 K and 600 K are provided in the SI. Figure 2c shows the area of the Pb(II) and the Pb(0) components of this more detailed temperature series. The reaction starts already at temperatures higher than 350 K and is almost completed at 550 K.

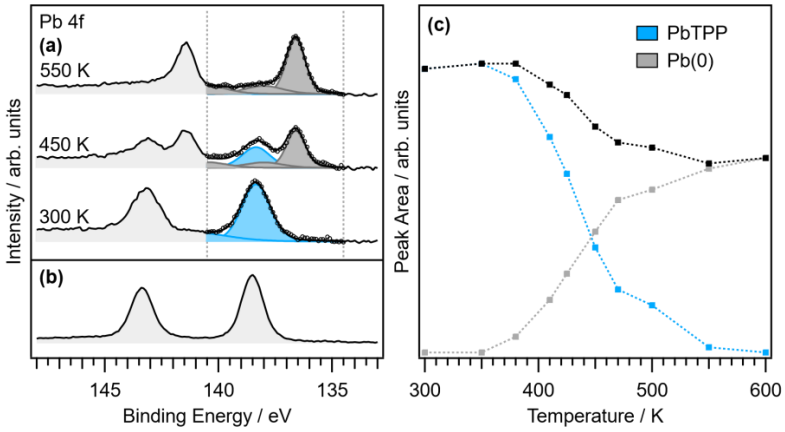

Figure 2. Pb 4f XP spectra of (a) a PbTPP monolayer on Cu(111) deposited at room temperature and after annealing to the given temperatures (450 K, 550 K) for 3 min. The Pb $4f_{7/2}$ region between 134.5 eV and 140.5 eV is described by a fit of the Pb(II) (colored in blue) and the Pb(0) (colored in gray) moieties. Here, the black line is the sum of both components while open circles represent the experimental data. The monolayer spectra can be compared with (b) a PbTPP multilayer. (c) In a more detailed temperature series, areas as well as the sum of both components area given for different temperatures. Corresponding spectra can be found in the SI.

Moreover, a decrease in the overall intensity above 425 K of the Pb 4f signals is observed. The corresponding C 1s signals show a decrease in intensity, which is even more pronounced and which is accompanied by a change of the peak shape (see details in the SI). This behavior can be explained by a partial desorption of the monolayer caused by a reaction of the peripheral phenyl substituents at higher temperatures. This side-reaction is a common behavior of the used TPP ligand and is known for the unmetalated H_2TPP molecule[28-29] as well as for several metal complexes[30-31]. In the course of dehydrogenation and coupling of the phenyl rings to the porphyrin ring, the molecule adopts a completely planar structure. In this way it is no longer possible for attractive π-stacking interactions between the phenyl rings to keep the individual molecules densely-packed together. Because of the increased lateral repulsion, the monolayer partially desorbs above 425 K.

Based on the analysis of the Pb 4f XP spectra, we can safely conclude that a monolayer of PbTPP is exposed to an on-surface reaction with the underlying Cu(111) surface. In the course of this reaction at temperatures higher than 350 K the Pb(II) central atom is reduced and Pb(0) is formed. In the following, we show that the observed reaction corresponds to our description of a Pb → Cu metal-exchange and the formation of CuTPP. Since partial desorption of the monolayer occurs above 425 K, part of the CuTPP product should also leave the surface and can be measured by mass spectrometry. Hence, with a specifically designed temperature-programmed reaction (TPR) experiment it is possible to prove the outcome of the observed reaction. Prior to the experiment, a monolayer coverage of PbTPP was deposited on the pristine Cu(111) surface and annealed to 650 K to precover the surface with the dehydrogenation products of PbTPP/CuTPP. Afterwards, in successive TPR cycles layers of PbTPP were deposited on the sample and the sample was annealed with a constant heating rate (1 K/s) to 650 K. During annealing the desorption of PbTPP (*m*/*z* = 820) and CuTPP (*m*/*z* = 675) were tracked and recorded by mass spectrometry. Assuming a constant residual coverage after each cycle, additional deposited molecules will desorb completely enabling the detection of the molecule ion without loss of hydrogen atoms.

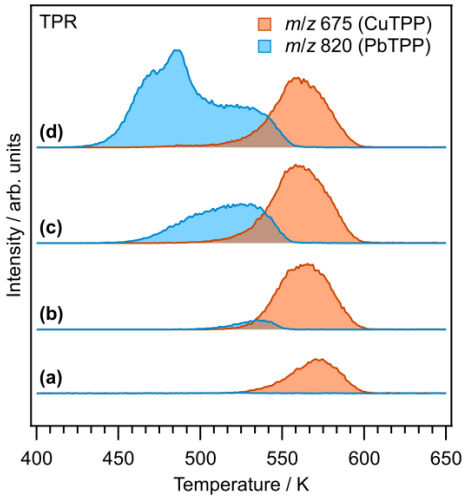

Figure 3. Traces of sequential TPR experiments of the recorded mass-to-charge ratio *m*/*z* 675 (CuTPP) and *m*/*z* 820 (PbTPP) of PbTPP deposited on pre-covered Cu(111) with increasing dosages of PbTPP from (a) to (d). The heating rate was 1 K/s for each spectrum.

Figure 3 shows TPR traces for different amounts of PbTPP deposited on the pre-covered Cu(111) surface. For the lowest coverage (Figure 3a), only the desorption of CuTPP in the range from 510 K to 605 K is observed, which shows a complete transmetalation of PbTPP. After increasing the amount of deposited PbTPP (Figure 3b), the transmetalation saturates and the desorption of PbTPP starts from 490 K to 555 K. The CuTPP peak exhibits slight broadening and the peak maximum shifts to lower temperatures caused by stronger intermolecular repulsion at higher coverages. Since the transmetalation is only possible in the monolayer, the PbTPP peak can either be attributed to desorption from the monolayer (no full transmetalation) or the bilayer (full transmetalation). For even higher initial dosages (Figure 3c), only the PbTPP desorption peak increases and gets broadened, while the desorption of CuTPP remains constant. Once saturation of CuTPP is reached, no change in peak form and maximum is observed anymore (Figure 3c,d). For the highest coverage (Figure 3d) the closed mono- and bilayer peak (485 K) as well as a small multilayer shoulder at lower temperatures (470 K) are observed. No transmetalation reaction is found in the multilayer.

An STM investigation of submonolayers provides additional insight into the adsorbate structure of PbTPP on the Cu(111) surface and gives more details on structural changes of the individual molecules upon the on-surface transmetalation and the side-reaction of the peripheral phenyl substituents. For this purpose, submonolayers with two different coverages (0.25 ML and 0.40 ML) were investigated. ML refers here to the number of adsorbed molecules relative to a closely packed monolayer determined by the C 1s XPS intensities.

In a submonolayer with low coverage (0.25 ML) the molecules are well separated and do not aggregate into islands. The individual PbTPP molecules appear all in the same rectangular shape and in the center a characteristic elevation emerges (Figure 4a). Porphyrin complexes with an out-of-plane bound metal usually adsorb in two distinguishable conformers, in which the central atom is located between the porphyrin and the underlying metal substrate (metal-down conformer) or above the ring (metal-up conformer).[sperl2011] Thus, the observed adsorbate structure differs clearly from that and since neither a metal-up nor a metal-down conformer is present in case of PbTPP, it can be assumed that there are substantial changes in the molecular structure of the complex upon adsorption on the Cu(111) surface. The highly distorted shape suggests that the molecule interacts strongly with the surface and is clearly chemisorbed. The adsorbate structure can be explained by the shown molecular formula (Figure 4a, right). Here, the molecule including the peripheral phenyl substituents adsorbs flat on the surface except for two upright-standing pyrrole units. A similar adsorbate structure, which is referred to the inverted conformer in the literature[32-33], is also formed by the unmetalated free ligand H_2TPP on Cu(111). Bending of the two upright-standing pyrrole units provides additional space for the incorporated lead atom and explains the absence of a metal-down and metal-up conformer. Due to the increased Pb−N distance, it can be assumed that the metal-ligand bond is already weakened in this adsorbate structure. This structure also explains why the molecules do not tend to form islands at low coverage of 0.25 ML. Because the peripheral substituents lie flat on the surface, no attractive π stacking interactions can hold the molecules together and they are separated by lateral repulsion. However, increasing the coverage (0.40 ML) the molecules also form islands and adopt a second island conformer (see details in the SI). In this conformer the phenyl rings do not lie flat on the surface and enable the formation of attractive T-shaped π stacking interactions. Note that the island conformer is not stable at high temperatures as the islands disappear after annealing the sample. Annealing the submonolayer to 450 K sample (0.25 ML) causes the molecule to take different shapes. This change in the overall appearance is due to the step-wise cyclodehydrogenation of the peripheral phenyl substituents. In the course of this side-reaction, which was extensively described in literature for the free ligand H_2TPP[29, 31, 34-35] or various TPP metal complexes[30-31], parts of the molecules are flattened. Apart from these changes, the center of the molecules

additionally has different heights, which indicates that some of the molecules undergo the metal-exchange reaction and some of the lead atoms are still incorporated inside the porphyrin macrocycle. For selected molecules STM images including a proposed molecular structure are shown in Figure 4b,c. In (b) a molecule is shown with partial cyclodehydrogenated phenyl rings. In the course of this reaction one of the two upright standing pyrrole units become flat. Moreover, the bright protrusion in the center indicates that Pb(II) is still embedded inside the macrocycle. In contrast to this (c) shows a molecule where the substituents have reacted like in (b), but without the elevation in the center of the ring. Thus, this molecule has already lost the Pb(II) atom. Whether there is already a Cu(II) atom incorporated cannot be definitely concluded. However, the center of the macrocycle does not appear as a dark pore and it can be assumed that there is already Cu(II) inside. Further annealing to 550 K leads again to a change in the appearance of the individual molecules (Figure 4d). Most of the molecules are completely flat-lying on the surface without any bright features. This can be explained by the completion of the dehydrogenative side-reaction as well as the release of the bulky lead atom from the porphyrin macrocycle.

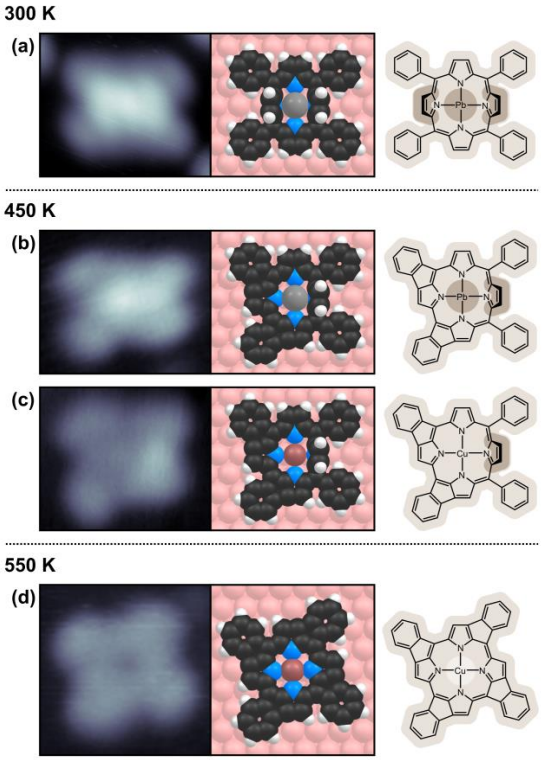

Figure 4. (left) STM images of single molecules of a PbTPP submonolayer (0.25 ML) on Cu(111) and (center) proposed adsorbate structures as well as (right) the corresponding molecular structure with shadings highlighting protruding parts. (a) PbTPP after deposition at 300 K, (b-c) selected partially reacted molecules after annealing to 450 K and (c) product of the completed transmetalation and dehydrogenation after annealing to 550 K. Tunneling parameters: (a) $U = -2.75$ V, $I = -0.21$ nA; (b) U = -0.69 V, $I = -0.16$ nA; (c) $U = -0.69$ V, $I = -0.14$ nA; (d) $U = -0.99$ V, $I = -0.15$ nA.

Figure 5 directly compares the electronic structure of the central atom by Pb $4f_{7/2}$ spectra with the adsorbate structure according to STM images of the same submonolayer sample (0.25 ML) for different temperatures. In Figure 5a, according to the XP spectra the reaction has the same progress after annealing to 450 K and 550 K than in the monolayer discussed above (see more details in the SI). While in the STM images at (b) 300 K PbTPP exclusively occurs in the inverted adsorbate structure, annealing to (c) results in a distribution of a large number of partially reacted molecules. About half of the observed molecules have no bright center and therefore no incorporated Pb(II). In addition, small objects can be seen located between the individual molecules. Those only weakly protruding dots can be assigned to Pb(0) atoms formed as a side product of the transmetalation. While at (c) 450K only a few of these are observed, further annealing to (d) 550 K leads to a significant increase of the number of Pb(0) atoms. This is in a good agreement with the fact that most of the molecules are completely flat-lying on the surface without any bright features. Only a few protruding structures can be recognized, which imply that a very small minority of macrocycles might still contain a lead atom or upright-standing substituents. Thus, at 550 K the dehydrogenative side-reactions as well as the release of the bulky lead atom from the porphyrin macrocycle are about to be completed. The yield of the Pb → Cu exchange can be derived by counting the molecules and the individual lead(0) atoms in the STM images for each temperature step (see details in the SI). Therefore, after annealing to 450 K about 53% of the molecules have already reacted and increasing the temperature to 550 K leads to a corresponding value of 95%. This is in a good agreement with 47% and 94% obtained by XPS, respectively.

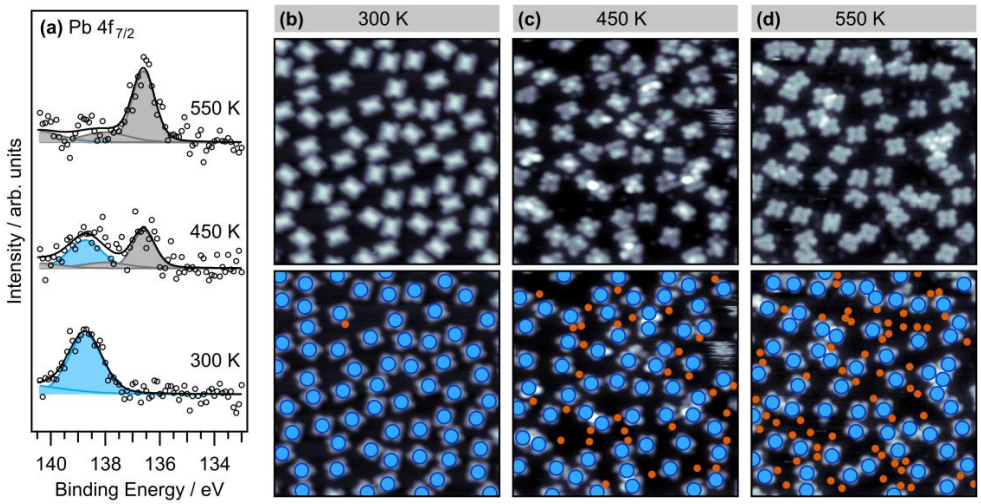

Figure 5. (a) Pb 4f spectra of a PbTPP submonolayer (0.25 ML) on Cu(111) at 300 K and after annealing to 450 K and 550 K as indicated and (b-c) STM images of the same sample. Each of the upper STM images show an area of 20.0x20.0 nm^2. The bottom STM images are the same as those above but with overlaid blue circles representing the molecules and orange circles representing visible lead(0) atoms. Tunneling parameters: (b) $U = -2.75$ V, $I = -0.13$ nA; (c) $U = -0.69$ V, $I = -0.16$ nA; (d) $U = -0.97$ V, $I = -0.23$ nA. Metal-exchange reaction yield: (b) 300 K, XPS = 0%, STM = 2%; (c) 450 K, XPS = 47%, STM = 53%; (d) 550 K, XPS = 94%, STM = 95%.

Conclusion

A monolayer of PbTPP adsorbs intact on Cu(111) after deposition at 300 K according to the Pb 4f spectra as the electronic structure of the central atom remains unchanged by the direct influence of the substrate. However, a temperature-dependent XPS series reveals an on-surface reaction that can be tracked by the reduction of the Pb(II) central atom. The reaction starts at temperatures above 350 K and is completed at 550 K with a total conversion of Pb(II) to Pb(0). The reaction can be explained by an on-surface transmetalation, in which Pb is exchanged by a Cu atom of the underlying substrate. Moreover, a partial desorption of the monolayer enables the detection of the product. Hence, desorbing CuTPP is detected by the *m*/*z* in a TPR experiment and, thus, a metal-exchange is proven. The experiment was conducted on a Cu(111) surface, which was pre-covered with TPP dehydrogenation products. At low coverages only CuTPP desorbs in a range from 510 K to 605 K. Increasing the dosage also leads to desorption of PbTPP from 490 K to 555 K, which is attributed to either the bilayer or unreacted molecules from the monolayer. The adsorbate structure of a submonolayer (0.25 ML) was investigated in detail. STM images revealed a highly distorted and chemisorbed PbTPP molecule which adopts an adsorbate structure with flat-lying phenyl substituents and two pyrrole units, which are upright standing with respect to the substrate. With this structure the distorted ligands provides additional space inside the cavity for the large Pb(II) central atom. Thus, in this structure neither a metal-up nor a metal-down conformer could be found. Annealing the submonolayer sample shows a change of the molecules' shape caused by the transmetalation as well as the dehydrogenation reaction of the peripheral phenyl substituents. At 450 K, this side reaction leads to a large number of different partially dehydrogenated product. In addition, the release of the Pb(II) center of individual molecules can be observed by the loss of the bright protrusion in the porphyrin center. Further annealing to 550 K leads to entirely flat-lying molecules without any protrusions. Thus, the transmetalation as well as the dehydrogenation is completed. The metal-exchange can be also traced by Pb(0) atoms, which are visible in STM images as small dots between the individual molecules. By counting their number, the temperature-dependent yield of the transmetalation can be estimated with 53% and 95% after annealing to 450 K and 550 K, respectively. Therefore, the resulting values are in good agreement with the yield of 47% and 94% derived from XPS measurements.

Acknowledgements

Financial support by the Deutsche Forschungsgemeinschaft (DFG) through the SFB 1083 "Structure and Dynamics of Internal Interfaces" is gratefully acknowledged.

Supporting Informations

Additional multilayer XP spectra, a detailed monolayer temperature-dependent XP series as well as description of the island conformer and the temperature-dependent yield of the transmetalation.

References

1. Zhang, W.; Lai, W.; Cao, R., Energy-Related Small Molecule Activation Reactions: Oxygen Reduction and Hydrogen and Oxygen Evolution Reactions Catalyzed by Porphyrin- and Corrole-Based Systems. *Chem. Rev.* **2016,** *117*, 3717-3797.
2. Barona-Castano, J. C.; Carmona-Vargas, C. C.; Brocksom, T. J.; Oliveira, K. T. d., Porphyrins as Catalysts in Scalable Organic Reactions. *Molecules* **2016,** *21*, 1-27.
3. Pereira, M. M.; Dias, L. D.; Calvete, M. J. F., Metalloporphyrins: Bioinspired Oxidation Catalysts. *ACS Catal.* **2018,** *8*, 10784-10808.
4. Paolesse, R.; Nardis, S.; Monti, D.; Stefanelli, M.; Natale, C. D., Porphyrinoids for Chemical Sensor Application. *Chem. Rev.* **2017,** *117*, 2517-2583.
5. Jurow, M.; Schuckman, A. E.; Batteas, J. D.; Drain, C. M., Porphyrins as molecular electronic components of functional devices. *Coord. Chem. Rev.* **2010,** *254*, 2297-2310.
6. Martynov, A. G.; Safonova, E. A.; Tsivadze, A. Y., Functional molecular switches involving tetrapyrrolic macrocycles. *Coord. Chem. Rev.* **2019,** *387*, 325-347.
7. Auwärter, W.; Écija, D.; Klappenberger, F.; Barth, J. V., Porphyrins at interfaces. *Nature Chemistry* **2015,** *7*, 105-120.
8. Gottfried, J. M., Surface chemistry of porphyrins and phthalocyanines. *Surf. Sci. Rep.* **2015,** *70*, 259-379.
9. Papageorgiou, N.; Mossoyan, J. C.; Mossoyan-Deneux, M.; Terzian, G.; Janin, E.; Göthelid, M.; Giovanelli, L.; Layet, J. M.; Lay, G. L., High resolution synchrotron radiation PES study of PbPc deposited on Pt(111). *Appl. Surf. Sci.* **2000,** *162-163*, 178-183.
10. Giovanelli, L.; Papageorgiou, N.; Terzian, G.; Layet, J. M.; Mossoyan, J. C.; Mossoyan-Deneux, M.; Göthelid, M.; Lay, G. L., Electronic structure of self-assembled organic/inorganic semiconductor interfaces: lead phthalocyanine on InSb and InAs(100)-4x2/c(8x2). *J. Electron. Spect. Rel. Phen.* **2001,** *114-116*, 375-381.
11. Baran, J. D.; Larsson, J. A.; Woodley, R. A. J.; Cong, Y.; Moriarty, P. J.; Cafolla, A. A.; Schulte, K.; Dhanak, V. R., Theoretical and experimental comparison of SnPc, PbPc and CoPc adsorption on Ag(111). *Pys. Rev. B* **2010,** *81*, 075413.
12. Doyle, C. M.; Cunnife, J. P.; Krasnikov, S. A.; Preobrajenski, A. B.; Li, Z.; Sergeeva, N. N.; Cafolla, M. O. S. A., Ni-Cu ion exchange observed for Ni(II)-Porphyrins on Cu(111). *Chem. Commun.* **2014,** *50*, 3447-3449.
13. Shen, K.; Narsu, B.; Ji, G.; Sun, H.; Hu, J.; Liang, Z.; Gao, X.; Li, H.; Li, Z.; Song, B.; Jiang, Z.; Huang, H.; Wells, J. W.; Song, F., On-surface manipulation of atom substitution between cobalt phthalocyanine and the Cu(111) substrate. *RSC Adv.* **2017,** *7*, 13827-13835.
14. Rieger, A.; Schnidrig, S.; Probst, B.; Ernst, K.-H.; Wächerlin, C., Ranking the Stability of Transition-Metal Complexes by On-Surface Atom Exchange. *J. Phys. Chem. Lett.* **2017,** *8*, 6193-6198.
15. Hötger, D.; Abufager, P.; Morchutt, C.; Alexa, P.; Grumelli, D.; Dreiser, J.; Stepanow, S.; Gambardella, P.; Busnengo, H. F.; Etzkorn, M.; Gutzler, R.; Kern, K., On-surface transmetalation of metalloporphyrins. *Nanoscale* **2018,** *10*, 21116.
16. Sperl, A.; Kröger, J.; Berndt, R., Electronic Superstructure of Lead Phthalocyanine on Lead Islands. *J. Phys. Chem. A.* **2011,** *115*, 6973-6978.
17. T. Yamaki; Nobusada, K., Theoretical Study of Metal-Ligand Bonds in Pb(II) Porphyrins. *J. Phys. Chem. A.* **2003,** *107*, 2351-2355.
18. Barkigia, K. M.; Fajer, J.; Adler, A. D.; Williams, G. J. B., Crystal and Molecular Structure of (5,10,15,20-Tetra-n-propylporphinato)lead(II): A "Roof" Porphyrin. *Inorg. Chem.* **1980,** *19*, 2057-2061.
19. Plater, M. J.; Aiken, S.; Gelbrich, T.; Hursthouse, M. B.; Bourhill, G., Structures of Pb(II) porphyrins: [5,10,15,20-tetrakis-triisopropylsilylethynylporphinato]lead(II) and [5,15-bis-(3,5-bis-tert-butylphenyl)-10,20-bis-triisopropylsilylethynylporphinato]lead(II). *Polyhedron* **2001,** *20*, 3219-3224.
20. Gac, S. L.; Boitrel, B., Structurally characterized bimetallic porphyrin complexes of Pb, Bi, Hg and Tl based on unusual coordination modes. *J. Porphyrins Phthalocyanines* **2016,** *20*, 1-17.
21. Lemon, C. M.; Brothers, P. J.; Boitrel, B., Porphyrin complexes of the period 6 main group and late transition metals. *Dalton Trans.* **2011,** *40*, 6591-6609.

P9

22. Sayer, P.; Gouterman, M.; Connell, C. R., Metalloid Porphyrins and Phthalocyanines. *Acc. Chem. Res.* **1982,** *15*, 73-79.
23. Kawai, T.; Fujiyoshi, R.; Sawamura, S., Solvent extraction of zinc(II) and manganese(II) with 5,10,15,20-tetraphenyl-21H,23H-porphine (TPP) through the metal exchange reaction of lead(II)-TPP. *Solvent Extr. Res. Dev.* **2000,** *7*, 36-43.
24. Klein, B. P.; Heijden, N. J. v. d.; Kachel, S. R.; Franke, M.; Krug, C. K.; Greulich, K. K.; Ruppenthal, L.; Müller, P.; Rosenow, P.; Parhizkar, S.; Bocquet, F. C.; Schmid, M.; Hieringer, W.; Maurer, R. J.; Tonner, R.; Kumpf, C.; Swart, I.; Gottfried, J. M., Molecular Topology and the Surface Chemical Bond: Alternant Versus Nonalternant Aromatic Systems as Functional Structural Elements. *Phys. Rev. X* **2019,** *9*, 011030.
25. Kachel, S. R.; Klein, B. P.; Morbec, J. M.; Schöniger, M.; Hutter, M.; Schmid, M.; Kratzer, P.; Meyer, B.; Tonner, R.; Gottfried, J. M., Chemisorption and Physisorption at the Metal/Organic Interface: Bond Energies of Naphthalene and Azulene on Coinage Metal Surfaces. *J. Phys. Chem. C.* **2020,** *124* (15), 8257-8268.
26. Rager, A.; Gompf, B.; Dürselen, L.; Mockert, H.; Schmeisser, D.; Göpel, W., Stability of Organic Thin Films on Inorganic Substrates: Prototype Studies Using Metal Phthalocyanines. *J. Mol. Electron.* **1989,** *5*, 227-238.
27. Ottaviano, L.; Lozzi, L.; Santucci, S.; Nardo, S. D.; Passacantando, M., PbPc growth on Si surfaces studied with XPS and various SPM techniques. *Surf. Sci.* **1997,** *392*, 52-61.
28. Xiao, Y.; Ditze, S.; Chen, M.; Buchner, F.; Stark, M.; Drost, M.; Steinrück, H.-P.; Gottfried, J. M.; Marbach, H., Temperature-Dependent Chemical and Structural Transformations from 2H-tetraphenylporphyrin to Copper(II)-Tetraphenylporphyrin on Cu(111). *J. Phys. Chem. C.* **2012,** *116*, 12275-12282.
29. Röckert, M.; Franke, M.; Tariq, Q.; Ditze, S.; Stark, M.; Uffinger, P.; Wechsler, D.; Singh, U.; Xiao, J.; Marbach, H.; Steinrück, H.-P.; Lytken, O., Coverage- and Temperature Dependent Metalation and Dehydrogenation of Tetraphenylporphyrin on Cu(111). *Chem. Eur. J.* **2014,** *20*, 8948-8953.
30. Wiengarten, A.; Lloyd, J. A.; Seufert, K.; Reichert, J.; Auwärter, W.; Duncan, D. A.; Allegretti, F.; Fischer, S.; Oh, S. C.; Saglam, Ö.; Jiang, L.; Vijayaraghavan, S.; Écija, D.; Papageorgiou, A. C.; Barth, J. V., Cyclodehydrogenation; Break the Symmetry, Enhance the Selectivity. *Chem. Eur. J.* **2015,** *21*, 12285-12290.
31. Ruggieri, C.; Rangan, S.; Bartynski, R. A.; Galoppini, E., Zinc(II) Tetraphenylporphyrin on Ag(110) and Ag(111): Multilayer Desorption and Dehydrogenation. *J. Phys. Chem. C.* **2016,** *120* (14), 7575-7585.
32. Albrecht, F.; Bischoff, F.; Auwärter, W.; Barth, J. V.; Repp, J., Direct Identification and Determination of Conformational Response in Adsorbed Individual Nonplaar Molecular Species Using Noncontact Atomic Force Microscopy. *Nano Lett.* **2016,** *16* (12), 7703-7709.
33. Lepper, M.; Köbl, J.; Schmitt, T.; Gurrath, M.; Siervo, A. d.; Schneider, M. A.; Steinrück, H.-P.; Meyer, B.; Marbach, H.; Hieringer, W., "Inverted" porphyrins: a distorted adsorption geometry of free-base porphyrins on Cu(111). *Chem. Commun.* **2017,** *53*, 8207-8210.
34. Röckert, M.; Franke, M.; Tariq, Q.; Lungerich, D.; Jux, N.; Stark, M.; Kaftan, A.; Ditze, S.; Marbach, H.; Laurin, M.; Libuda, J.; Steinrück, H.-P.; Lytken, O., Insights in Reaction Mechanistics: Isotopic Exchange during the Metalation of Deuterated Tetraphenyl-21,23D-porphyrin on Cu(111). *J. Phys. Chem. C.* **2014,** *118*, 26729-26736.
35. Röckert, M.; Ditze, S.; Stark, M.; Xiao, J.; Steinrück, H.-P.; Marbach, H.; Lytken, O., Abrupt Coverage-Induced Enhancement of the Self-Metalation of Tetraphenylporphyrin with Cu(111). *J. Phys. Chem. C.* **2014,** *118*, 1661-1667.

Supporting Information for

Tracking the Pb−Cu Exchange of PbTPP on Cu(111) by Multi-Method Approach

Jan Herritsch, Stefan Renato Kachel, Qitang Fan, Mark Hutter,
Lukas Heuplick, Florian Münster, J. Michael Gottfried

Fachbereich Chemie, Philipps-Universität Marburg,
Hans-Meerwein-Straße, 35032 Marburg, Germany

Table of Contents

1 PbTPP Multilayer Spectra and Purity of the Deposited Films

In addition to the information about the electronic structure of the surface-decoupled PbTPP molecules, multilayer spectra can be used to evaluate the purity of the deposited films. In particular, a contamination by the free ligand H_2TPP is critical. The unmetalated porphyrin H_2TPP does react with the Cu(111) in an on-surface self-metalation at 420−450 K forming CuTPP.[1-5] Therefore, if such an H_2TPP impurity is present in the studied PbTPP films, the detection of CuTPP in the TPR experiment can no longer be attributed solely to the transmetalation of type PbTPP + Cu → CuTPP + Pb. The unmetalated porphyrin H_2TPP could be easily identified by XPS because it exhibits two pyrrolic (−NH−) and two iminic (−N=) nitrogen atoms and consequently there is a splitting of the N 1s signal. In contrast to this, the measured N 1s consists only of a single narrow peak indicating that all nitrogen atoms are equivalent (N−Pb). Thus, it can be concluded that there are no significant contaminations by H_2TPP. Moreover, the Pb 4f signal corresponds to the typical shape of lead(II) tetrapyrroles.[6-9]

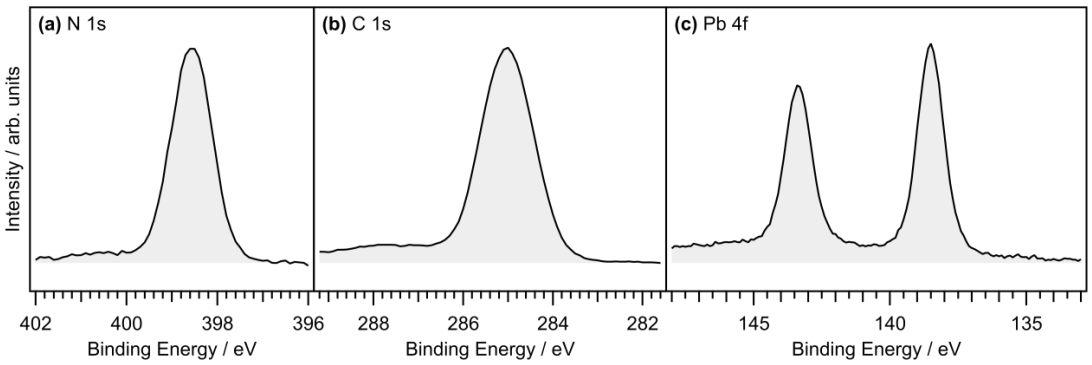

Figure S1. XP spectra of the PbTPP multilayer of 4.0 nm thickness deposited on the Cu(111) substrate for (a) the N 1s, (b) C1s and (c) Pb 4f region. For a simple representation the intensity was scaled differently for the individual regions.

P9

2 Detailed Temperature Series of a PbTPP Monolayer on Cu(111)

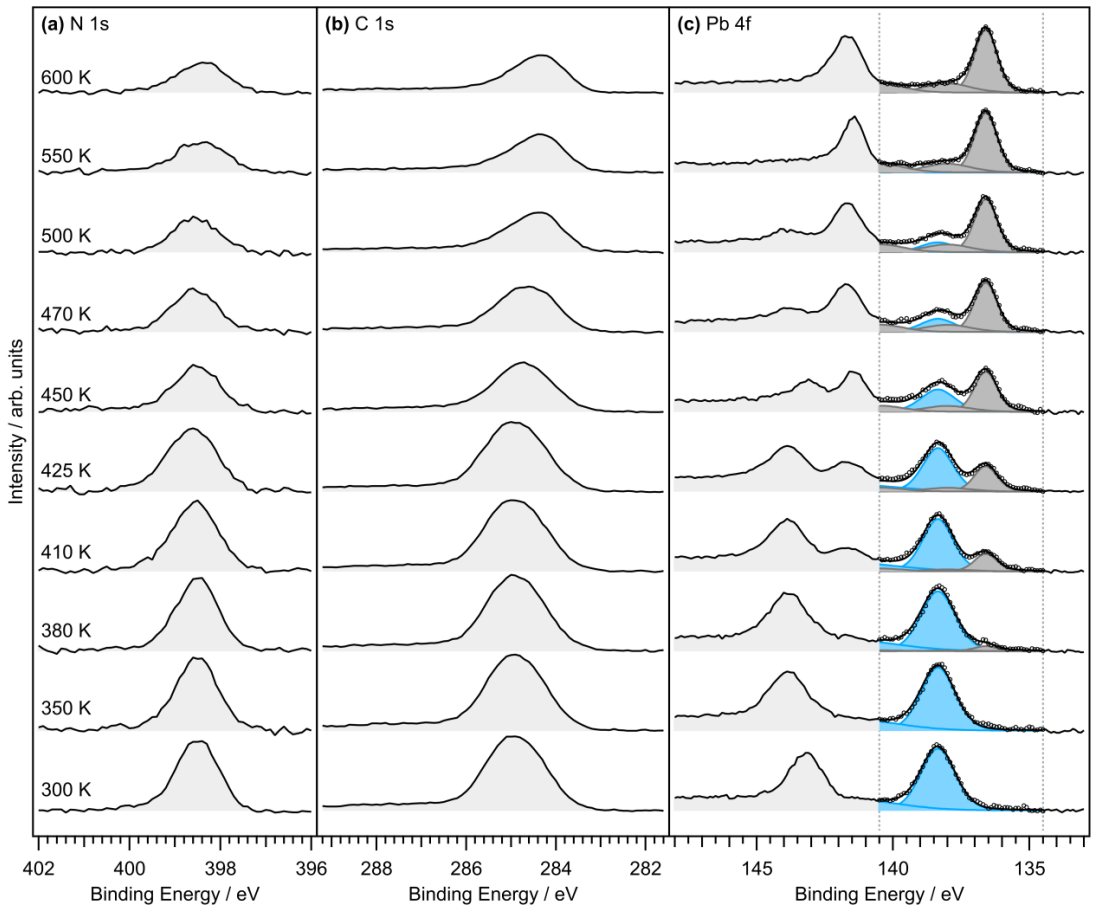

Figure S2. XPS series of a monolayer PbTPP on Cu(111) for (a) the N 1s, (b) the C 1s and (c) the Pb 4f region. Spectra were measured at 300K after annealing the sample for 3 min at temperatures as indicated. The Pb $4f_{7/2}$ region between 134.5 eV and 140.5 eV is described by a fit of the Pb(II) (colored in blue) and the Pb(0) (colored in gray) moieties. Here, the black line is the sum of both components while open circles represent the experimental data. For a simple representation the intensity was scaled differently for the individual regions.

3 Island Conformer at Higher Coverages (>0.25 ML)

At low submonolayer coverages (0.25 ML), the molecules are separated and do not aggregate. They appear rectangular shape (see discussion in the manuscript). However, increasing the coverage (0.40 ML) the molecules start to form islands, which are shown in Figure S3a,b. In this islands PbTPP is densely packed and adopts a square shape. Moreover, the peripheral substituents are protruding which can be explained by a rotation of the phenyl rings. Thus, the upright standing substituents enable the formation of T-shaped π stacking interaction because the phenyl rings point towards the center of the neighboring molecule's phenyl ring. Figure S3c shows the proposed molecular structure of the island conformer in comparison with the single molecule conformer. The islands are not stable at higher temperatures and are disappearing completely after annealing the sample. This process might be associated with the partial desorption of the monolayer.

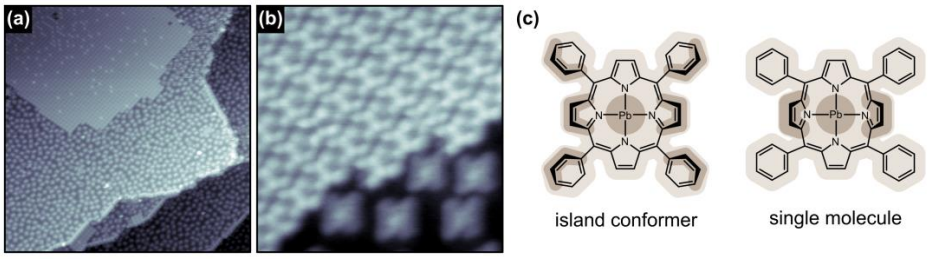

Figure S3. STM images of (a,b) a PbTPP submonolayer (0.40 ML) on Cu(111); (c) proposed molecular structures for the island conformer compared to the single molecule or inverted conformer, which is discussed in the manuscript in detail. The shading highlights protruding parts. Tunneling parameters: (a) $U = -0.27$ V, $I = -0.02$ nA, 100.0x100.0 nm^2; (b) $U = -0.27$ V, $I = -0.03$ nA, 10.0x10.0 nm^2.

P9

4 Temperature-Dependent Yield of Transmetalation (Monolayer vs Submonolayer)

The temperature-dependent yield for the transmetalation can be derived from the XPS heating series with the fitted Pb 4f region. The yield is obtained directly from the ratio of the Pb(II) and the Pb(0) signal intensities *I*.

$$\text{yield(XPS)} = \frac{I_{\text{Pb(0)}}}{I_{\text{Pb(0)}} + I_{\text{Pb(II)}}} \times 100$$

Alternatively, it can be estimated using STM images by counting the number of molecules $n_{\text{molecules}}$ and visible Pb(0) atoms $n_{\text{Pb(0)}}$. Thereby it is assumed that the difference between $n_{\text{molecules}}$ and $n_{\text{Pb(0)}}$ is equal to the number of molecules containing Pb(II) $n_{\text{Pb(II)}}$.

$$\text{yield(STM)} = \frac{n_{\text{Pb(0)}}}{n_{\text{Pb(0)}} + n_{\text{Pb(II)}}} \times 100 = \frac{n_{\text{Pb(0)}}}{n_{\text{Pb(0)}} + (n_{\text{molecules}} - n_{\text{Pb(0)}})} \times 100 = \frac{n_{\text{Pb(0)}}}{n_{\text{molecules}}} \times 100$$

In Table S1, the resulting values for the submonolayer sample (0.25 ML) are compared. There is a good agreement of the yield obtained by XPS with STM. Moreover, a comparison with the monolayer heating series in Figure S4 reveal very similar results.

Table S1. Result obtained from Figure 6.

temperature / K	$n_{\text{molecules}}$	$n_{\text{Pb(0)}}$	yield (STM)	yield (XPS)
300	65	1	2%	0%
450	60	32	53%	47%
550	62	59	95%	94%

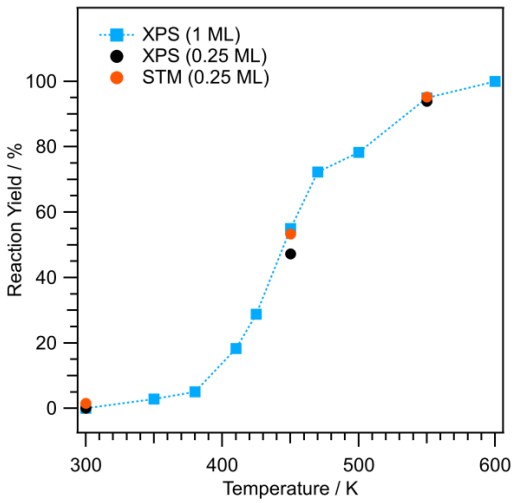

Figure S4. Temperature-dependent yield for the on-surface transmetalation derived from the detailed XPS series of a PbTPP monolayer (1 ML) compared to the corresponding values of a submonolayer (0.25) obtained by XPS and STM images.

5 References

1. Y. Xiao, S. Ditze, M. Chen, F. Buchner, M. Stark, M. Drost, H.-P. Steinrück, J. M. Gottfried and H. Marbach, *J. Phys. Chem. C.*, **116**, 12275 (2012).
2. K. Diller, F. Klappenberger, M. Marschall, K. Hermann, A. Nefedov, C. Wöll and J. V. Barth, *J. Chem. Phys.*, **136**, 014705 (2012).
3. M. Röckert, M. Franke, Q. Tariq, D. Lungerich, N. Jux, M. Stark, A. Kaftan, S. Ditze, H. Marbach, M. Laurin, J. Libuda, H.-P. Steinrück and O. Lytken, *J. Phys. Chem. C.*, **118**, 26729 (2014).
4. M. Röckert, M. Franke, Q. Tariq, S. Ditze, M. Stark, P. Uffinger, D. Wechsler, U. Singh, J. Xiao, H. Marbach, H.-P. Steinrück and O. Lytken, *Chem. Eur. J.*, **20**, 8948 (2014).
5. M. Röckert, S. Ditze, M. Stark, J. Xiao, H.-P. Steinrück, H. Marbach and O. Lytken, *J. Phys. Chem. C.*, **118**, 1661 (2014).
6. A. Rager, B. Gompf, L. Dürselen, H. Mockert, D. Schmeisser and W. Göpel, *J. Mol. Electron.*, **5**, 227 (1989).
7. L. Ottaviano, L. Lozzi, S. Santucci, S. D. Nardo and M. Passacantando, *Surf. Sci.*, **392**, 52 (1997).
8. N. Papageorgiou, J. C. Mossoyan, M. Mossoyan-Deneux, G. Terzian, E. Janin, M. Göthelid, L. Giovanelli, J. M. Layet and G. L. Lay, *Appl. Surf. Sci.*, **162-163**, 178 (2000).
9. J. D. Baran, J. A. Larsson, R. A. J. Woodley, Y. Cong, P. J. Moriarty, A. A. Cafolla, K. Schulte and V. R. Dhanak, *Pys. Rev. B*, **81**, 075413 (2010).

ChemPubSoc Europe
DOI: 10.1002/chem.201903954
CHEMISTRY A European Journal Full Paper

Inorganic Chemistry |Hot Paper|

Binary Lead Fluoride Pb_3F_8

H. Lars Deubner[+],[a] Malte Sachs[+],[a] Jascha Bandemehr,[a] Sergei I. Ivlev,[a] Antti J. Karttunen,[b] Stefan R. Kachel,[a] Benedikt P. Klein,[a] Lukas Ruppenthal,[a] Maik Schöniger,[a] Claudio K. Krug,[a] Jan Herritsch,[a] J. Michael Gottfried,[a] Jamal N. M. Aman,[c] Jörn Schmedt auf der Günne,[c] and Florian Kraus*[a]

Abstract: The binary lead fluoride Pb_3F_8 was synthesized by the reaction of anhydrous HF with Pb_3O_4 or by the reaction of BrF_3 with PbF_2. The compound was characterized by single-crystal and powder X-ray diffraction, IR, Raman, and solid-state MAS ^{19}F NMR spectroscopy, as well as thermogravimetric analysis, XP and near-edge X-ray absorption fine structure (NEXAFS) spectroscopy. Solid-state quantum-chemical calculations are provided for the vibrational analyses and band assignments. The electronic band structure offers an inside view of the mixed valence compound.

Introduction

The binary lead fluorides PbF_2 and PbF_4 are well established compounds.[1,2] Their first lab synthesis dates back to the first half of the 19th century and the determination of their crystal structures to 1944 and 1962, respectively.[1–4] In addition, PbF_3, which is better described as Pb_2F_6 containing Pb^{II} and Pb^{IV} atoms, was reported.[5] While for Sn and Ge also the mixed valence compounds M_3F_8 (M = Sn, Ge), and even Ge_5F_{12} and Ge_7F_{16} are known, only the three binary lead fluorides mentioned above are unambiguously known.[6–9] Therefore, the existence of a mixed valence compound of the composition Pb_3F_8 appears to be likely. For lead, mixed valence compounds are nothing special and the well-characterized compound Pb_3O_4 (*latin*: Minium), which was used as a pigment in ancient Rome and in anti-corrosion coatings, or which is even today in usage for charlatanism, comes to the mind.[10–13] A compound of the average chemical composition {Pb_3F_8} was mentioned only twice in the literature. Nothing besides this average composition has been reported. Pb_3F_8 was first mentioned in 1972 by Banner and co-workers as a result of the reaction of Pb_3O_4 with gaseous HF on a thermogravimetric scale.[14] In their search for Pb_2F_6, Charpin and co-workers described reactions leading to Pb_3F_8 as a product or side product. Again, no details on Pb_3F_8 were given, even not how the compound was identified as Pb_3F_8.[15] Herein, we present the synthesis and characterization of the binary lead(II/IV) fluoride Pb_3F_8.

Results and Discussion

The formation of the title compound can be envisaged by the following stoichiometric Equation (1).

$$Pb_3O_4 + 8\,HF \rightarrow Pb_3F_8 + 4\,H_2O \quad (1)$$

Pb_3O_4 is reacted with an excess of anhydrous HF (aHF) at room temperature, so that the equilibrium of the reaction is shifted to the product side. After a few minutes of reaction time the deep-orange color of Pb_3O_4 is already gone and the reaction is complete within one hour at room temperature. After the removal of the volatiles (HF and H_2O), the product is obtained as a slightly beige powder (Figure S1, Supporting Information) that is easily ground. The dry powder of Pb_3F_8 is stable for several hours in air. The compound prepared in this way always contains small amounts of PbF_2 (typically 5–8%), as evidenced by Rietveld analysis (Table S1, Figure S2, Supporting Information) on powder X-ray diffraction patterns. The obtained lattice parameters are a = 8.8434(1), b = 7.5427(1), c = 10.2339(1) Å, β = 98.810(1)°, V = 672.3(3) Å^3 at T = 298 K. They agree well with those obtained from single-crystal X-ray diffraction, see below. To suppress the back reaction by hydrolysis, a large excess of circa 100 equivalents of aHF is needed. If the reaction mixture is allowed to stand for three days at room temperature, or, if an excess of aHF is used that is too small, a

[a] *Dipl.-Chem. H. L. Deubner,[+] M. Sachs,[+] J. Bandemehr, Dr. S. I. Ivlev, S. R. Kachel, B. P. Klein, L. Ruppenthal, M. Schöniger, C. K. Krug, J. Herritsch, Prof. Dr. J. M. Gottfried, Prof. Dr. F. Kraus*
Fachbereich Chemie, Philipps-Universität Marburg
Hans-Meerwein-Str. 4, 35032 Marburg (Germany)
E-mail: florian.kraus@chemie.uni-marburg.de

[b] *Prof. Dr. A. J. Karttunen*
Department of Chemistry and Materials Science
Aalto University, 00076 Aalto (Finland)

[c] *J. N. M. Aman, Prof. Dr. J. Schmedt auf der Günne*
Inorganic Materials Chemistry, University of Siegen
Adolf-Reichwein-Str. 2, 57076 Siegen (Germany)

[+] *These authors contributed equally.*

Supporting information and the ORCID identification number(s) for the author(s) of this article can be found under: https://doi.org/10.1002/chem.201903954.

P10

product is obtained that always contains larger amounts of PbF_2 than mentioned above. To obtain phase pure Pb_3F_8 we attempted to oxidize PbF_2 using an excess of BrF_3 under warming up to 130 °C. However, after evaporation of the residual BrF_3, the remaining colorless powder consists of Pb_3F_8 and small amounts of Pb_2F_6 (circa 3%). Thermogravimetric investigations (Figures S3, S4, Supporting Information, and for further details see the Supporting Information) indicate that the thermal decomposition of Pb_3F_8 is complex. The decomposition under loss of fluorine gas starts roughly around 80 °C. After thermal decomposition, pure PbF_2 is obtained as evidenced by powder XRD (Figure S5, Supporting Information). The overall mass loss during this procedure has been determined twice, once to 5.2 and once to 4.7%. Both values are in reasonably good agreement with the theoretically expected mass loss of 4.9%. Thus, Pb_3F_8 decomposes thermally to three equivalents of PbF_2 and one equivalent of F_2. Further details will be reported elsewhere. Helium pycnometric density determination (see the Supporting Information) yields a density of circa 7.68 g cm^{-3} for the used sample of Pb_3F_8. Due to the presence of circa 15% PbF_2 ($\rho = 8.44$ g cm^{-3}) in the sample used for density determination, a value of 7.74 g cm^{-3} is to be expected from the measurements. Thus, the experimentally determined density is in very good agreement with the measurement and with the crystallographic density of Pb_3F_8 of circa 7.61 g cm^{-3}.

Single-crystal X-ray diffraction shows Pb_3F_8 to crystallize in the monoclinic space group *I*2/*a* (No. 15, *mS*44, 15*ef*[5]) with the lattice parameters $a = 8.7800(18)$, $b = 7.4927(15)$, $c = 10.196(5)$ Å; $\beta = 98.78(3)°$; $V = 662.9(4)$ Å^3; $Z = 4$, at $T = 100$ K, while at room temperature lattice parameters of $a = 8.8400(5)$, $b = 7.5398(5)$, $c = 10.2297(7)$ Å, $\beta = 98.82(2)°$, $V = 673.77(8)$ Å^3 are obtained. The latter agree well with the values determined from powder X-ray diffraction at room temperature. No phase change was observed upon cooling from room temperature to 100 K and Table S2, Supporting Information, holds details of the single crystal structure determination. Surprisingly, Pb_3F_8 is not isotypic to the compounds M_3F_8 (M = Ge, Sn) but, to the best of our knowledge, represents a novel structure type.[6,7] As the crystal structure of Pb_3F_8 is complicated we will start with the local structure description before we describe it globally. There are two types of Pb atoms, Pb(1) and Pb(2). The Pb(1) atoms (Wyckoff position 4*e*) are coordinated by F atoms (8*f*) in the shape of an irregular octahedron, while the coordination polyhedron around the Pb(2) atom (8*f*) reminds of a pentagonal pyramid (Figure 1).

All F atoms around the Pb(1) atom are μ_2-bridging to Pb(2) atoms. The Pb(1)–F atomic distances are observed in the range from 2.048(3) to 2.063(3) Å. They agree well with reported ones for hexafluoridoplumbates(IV) in compounds such as $M^{II}PbF_6$ (M^{II} = Mg (1.99 Å), Ni (1.99 Å), Zn (1.97 Å), Sr (2.042–2.060 Å), Ba (2.04 Å), Pb (1.991–2.011 Å)) or $M^{I}_2PbF_6$ (M^{I} = Ag (2.021–2.100 Å), Li (1.997 Å)), which however all contain spatially separated $[PbF_6]^{2-}$ octahedra.[16–20] Therefore, we assign oxidation state +IV to these octahedron-like coordinated Pb(1) atoms. As stated above, the Pb(2) atoms are coordinated by six fluorine atoms in a shape similar to a pentagonal pyramid (Figure 1) and the Pb(2)–F distances span a rather broad range

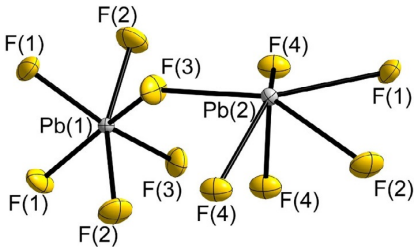

Figure 1. The coordination spheres of the two lead atoms of Pb_3F_8. The Pb(1) atom is coordinated octahedron-like, the Pb(2) atom like a pentagonal pyramid. Pb atoms are shown in grey, F atoms in yellow. Displacement ellipsoids at 70% probability at 100 K.

from 2.330(3) to 2.651(3) Å. As they are clearly longer than the Pb(1)–F distances, we assign oxidation state +II to the Pb(2) atoms. Charge distribution (CHARDI) calculations[21] (Table S3, Supporting Information) agree with the description of Pb_3F_8 as a mixed valence compound as charges of +4.12 and +1.94 are calculated for the Pb(1) and Pb(2) atoms, respectively. Thus, the assignment of the oxidation states is supported.

One Pb(2)–F(4) distance within the pentagonal pyramid is shortest with 2.330(3) Å, and represents the "tip" of the pyramid pointing to the bottom in Figure 1. The other two Pb(2)–F(4) distances are longer and equal within the standard uncertainty (2.446(3) and 2.449(3) Å). The other Pb(2)–F distances are significantly longer and range from 2.505(3) to 2.651(3) Å. As can be seen in Figure 1, the Pb(2) atom is not located in the center of the coordination polyhedron but resides close to the pentagonal face. Such a coordination polyhedron is reminiscent of the text-book anion $[XeOF_5]^-$,[22–24] and the peculiar location and coordination sphere of the Pb(2) atom is attributed to an accumulation of electron density in real space as shown in the quantum chemical calculations below. Due to the chemical hardness of the fluoride anion and its extremely low polarizability, its electron density leads to repulsion and deformation of the electron density at the Pb atom. Some call this effect the "sterically active lone-pair" and its influence on local as well as crystal structure is known for example from α- and β-PbO, or from the black and pigeon blood red modifications of SnO.[25–27] However, above the "lone-pair" of the Pb^{II} atom there are three additional F atoms with Pb–F distances of 2.851(4), 2.874(3), and 3.051(3) Å. According to the distance histogram one could count those three F atoms to the coordination sphere of Pb(2) leading to coordination number 6+3. The coordination polyhedron around Pb(2) is then irregular with ten triangles and one tetragon as the faces. Also, the calculated effective coordination number (ECoN) of 6.9 hints to a small contribution of the three next-nearest fluorine atoms to its coordination sphere, whereas the calculated ECoN for Pb(1) agrees well with C. N. = 6 as assigned by our structure analysis.

We will now come to the global structure description by explaining how the coordination polyhedra are interconnected. The F(4) atoms are μ_3-bridging between Pb(2) atoms and that leads to the formation of a 1D infinite zigzag ladder shown in Figure 2a. The two longer Pb(2)–F(4) distances form the stringers of the ladder, while the short Pb(2)–F(4) distances represent

P10

the rungs of the ladder (Figure 2a). Thus, the "lone-pairs" on the Pb(2) atoms point to the left and right in Figure 2a.

The topside and underside of the infinite ladder are coordinated by $[Pb(1)F_6]^{2-}$ octahedra as shown in Figure 2b. The ladders are sandwiched between the octahedra and vice versa, leading to a 2D infinite layer of ladders interconnected by octahedra. A section is shown in Figure 3a.

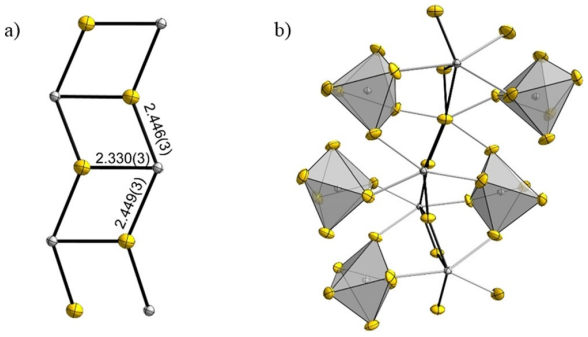

Figure 2. a) Ladder-like connection of the Pb(2) atoms (grey) via μ_3-bridging F(4) atoms (yellow). b) Connection of the Pb(2) containing ladder to the Pb(1) containing octahedra. Displacement ellipsoids shown with 70% probability at 100 K.

Thus, the "sterically active lone-pairs" of the Pb(2) atoms point out of the topside and underside of these layers (Figure 3b) separating them from each other. Figure 3b shows a section of the crystal structure of Pb_3F_8 with the 2D infinite layers parallel to the *ab* plane stacked along the *c* axis. The *Niggli* formula indicates the coordination number and environment of the Pb atoms nicely. For the Pb^{II} atom $[PbF_{3/2}F_{3/3}]$ and for the Pb^{IV} atom $[PbF_{6/2}]$ is obtained. Thus, Pb_3F_8 can be described by the *Niggli* formula $^2_\infty[PbF_{3/2}F_{3/3}]_2[PbF_{6/2}]$. The Pb atoms are hexagonally packed and each is anticuboctahedrally surrounded by twelve Pb atoms. Thus, the arrangement of the Pb atoms of Pb_3F_8 corresponds to the simple Mg structure type. However, the F atoms neither fill the octahedral nor the tetrahedral voids of the sphere packing.

Raman spectroscopic investigations have been carried out on Pb_3F_8 and on PbF_2 for comparison. For experimental details see the Supporting Information. The experimentally obtained spectra were then compared with ones obtained from DFT-PBE0/TZVP calculations based on the crystal structures of Pb_3F_8 and PbF_2. The most striking difference between the Raman spectrum of Pb_3F_8 and the spectrum of PbF_2 (see Figures S6 and S7, Supporting Information) is the strong vibrational band at 531 cm^{-1} that is only present in the Raman spectrum of Pb_3F_8. This band is well reproduced by our theoretical findings and can be attributed to a symmetric stretching of the Pb^{IV}–F bonds, which explains the absence of this band in PbF_2. Pb_3F_8 is also clearly identified by the lattice vibrational bands around 100 cm^{-1} as this frequency region corresponds to a minimum in Raman intensity in the spectrum of PbF_2. The two peaks at around 250 cm^{-1} and the two peaks at around 200 cm^{-1} belong to a symmetric stretching of the Pb^{II}–F bonds and bending modes of the Pb^{IV}–F bonds, respectively. In summary, the Raman spectrum supports our classification of Pb_3F_8 as a mixed valence compound. Full band assignments are available from Tables S4 to S6, Supporting Information.

An IR spectroscopic investigation of Pb_3F_8 powder in the range from 4000 to 450 cm^{-1} (Figure S8) shows only a single broader band at 466 cm^{-1}, which is comprised of intense Pb^{IV}–F stretch and weaker Pb^{II}–F scissoring and rocking modes. For Li_2PbF_6, which contains $[PbF_6]^{2-}$ octahedra, a band at 475 cm^{-1} has been observed.[16] This agrees well considering the different connectivity of the $[PbF_6]^{2-}$ octahedra in the two compounds. The experimentally determined band position of Pb_3F_8 agrees well with the quantum chemically calculated bands at 493, 470, and 456 cm^{-1}. The complete assignment of IR bands is given in Table S5, Supporting Information. The obtained Pb_3F_8 is essentially free of impurities such as H_2O, OH^-, or HF, as no bands in the range from 4000 to circa 450 cm^{-1} are present.

Solid-state ^{19}F MAS NMR experiments (Figure 4 and Table 1) of Pb_3F_8 were performed to further corroborate the crystal structure model. The ^{19}F DEPTH MAS NMR spectrum shows four resonances, one occurring at $\delta = -18.2$ ppm and a group of three overlapping signals at $\delta = -40$, -48.5, and -56 ppm. All four resonances have peak areas including spinning sidebands of 1:0.84:1.03:0.90. The spectrum also contains a fifth peak at $\delta = -24.2$ ppm with a lower intensity which is likely to originate from the PbF_2 impurity.[28] These observations are expected for F atoms which do not have fast ion-dynamics on

P10

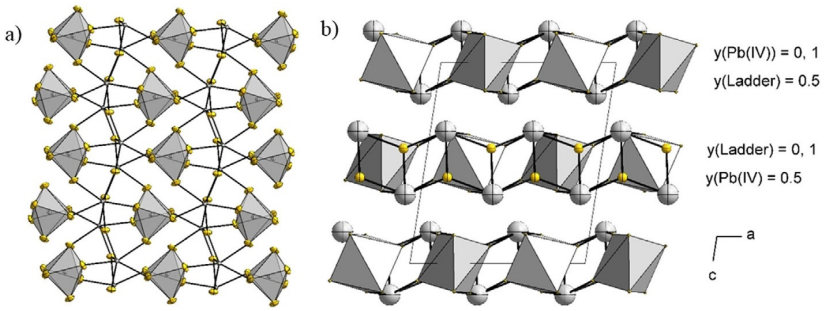

Figure 3. a) A part of the 2D infinite layer formed by the sandwiching of $[Pb(1)F_6]^{2-}$ octahedra by Pb(2) containing ladders. Displacement ellipsoids at 70% probability at 100 K. b) A section of the crystal structure of Pb_3F_8. Atoms are shown isotropic with arbitrary radii. Pb atoms grey, F atoms yellow. The 2D infinite layers run parallel to the ab plane. The height along the b axis is shown with the approximate *y* coordinate of the gravimetric center of the building units.

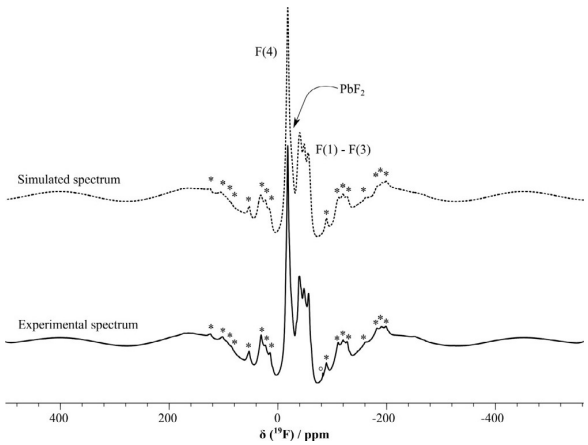

Figure 4. ^{19}F DEPTH MAS NMR spectrum (experimental: solid line, simulated: dashed line) of Pb_3F_8 at 20 kHz spinning frequency. The spinning side bands are marked with asterisks. The simulation includes a version of the DEPTH[32,33] sequence with four π-pulses: $\pi/2$-π-π-π-π-$\tau_{deadtime}$-FID. The DEPTH experiment results in MAS NMR spectra free of probe head background. The simulation includes the effect of the deadtime delay and excitation profile of the DEPTH sequences which causes the baseline rolling. Zeroth and first order phase correction are included as variable parameters in the least-square fit.

Table 1. Estimates for the ^{19}F solid-state NMR chemical shift parameters for Pb_3F_8 obtained by a least-square fit of the experimentally obtained spectrum (Figure 4) with SIMPSON version 3.1.2[29] simulations of the used version of the DEPTH[30,31] experiment.

Site	δ_{iso} [ppm]	δ_{aniso} [ppm]	η	δ_{11} [ppm]	δ_{22} [ppm]	δ_{33} [ppm]
F(4)	−18.2	66.1	0.60	47.9	−31.5	−71.2
F(1)–F(3)	−40.0	−111.8	0.61	50.5	−18.5	−151.7
F(1)–F(3)	−48.5	−121.0	0.65	51.5	−27.4	−169.5
F(1)–F(3)	−56.0	−119.2	0.47	31.6	−24.5	−175.2

the NMR timescale, as four symmetry-inequivalent F atoms (F(1) to F(4)) with the same site multiplicity are present in the crystal structure.

A tentative peak assignment of the ^{19}F resonances follows the idea that neighboring cations contribute to the ^{19}F chemical shift according to their coordination number and distance to F atoms in ionic fluorides.[32] Consequently, F atoms with a similar bonding situation should feature similar isotropic and anisotropic chemical shift values. In the present case (Table 1) the group of three resonances has an anisotropic chemical shift which is larger by about a factor of two compared to the peak which appears at the highest ppm values. In the structure three F atoms are coordinated to two Pb atoms, one F atom is coordinated to three. Therefore, the resonance at −18.2 ppm is assigned to the three-fold coordinated fluorine site (F(4)) and the three signals at −40, −48.5, and −56 ppm are assigned to the fluorine atoms F(1), F(2), and F(3) coordinated by the two lead Pb(1) and Pb(2) atoms.

We have performed X-ray photoelectron spectroscopy (XPS) as well as near-edge X-ray absorption fine structure (NEXAFS) measurements to get information about the electronic structure of Pb_3F_8. The survey XP spectrum of Pb_3F_8 on carbon tape is presented in Figure 5a. The spectrum only shows contributions from Pb and F atoms, besides minor C 1s and O 1s peaks from the carbon tape.

Another sample that was studied with hard X-ray photoelectron spectroscopy (HAXPES, Figure S9 in the Supporting Information) shows the same features and even less contributions from the carbon tape. During the XPS and HAXPES measurements, the sample exhibits substantial photoemission-induced charging, which results in peak shifts and broadening. For this reason, a refined analysis of the XPS peak shapes with a discrimination between Pb^{II} and Pb^{IV} contributions is not possible. Instead, we performed NEXAFS spectroscopy measurements on the Pb M_5-edge to gain further insight into the electronic structure of Pb_3F_8 (Figure 5c). As a reference, we also studied PbF_2 and Pb_3O_4. Between 2490 and 2495 eV, a pre-edge feature is observed, which is followed by the M_5-edge for all three species. PbF_2 shows a sharp peak at 2490 eV with a minimum at 2495 eV. In contrast, there is only a broad feature between 2490 and 2495 eV for Pb_3O_4. The Pb_3F_8 spectrum resembles a mixture of both reference samples. A peak at 2490 eV is observed, whereas there is no minimum at 2495 eV like for PbF_2.

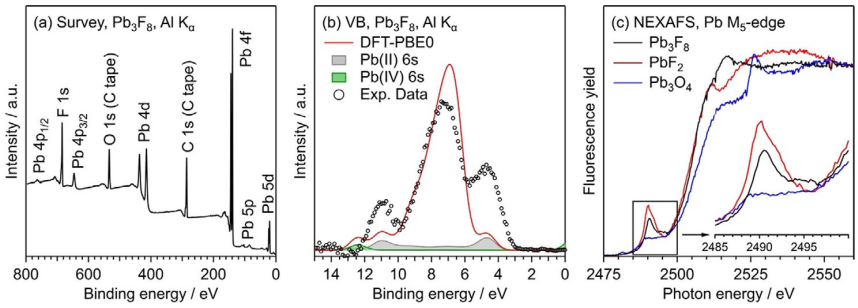

Figure 5. (a) Survey XP spectrum of Pb_3F_8 on carbon tape, taken with monochromatic Al K_α radiation. (b) Valence band spectrum of Pb_3F_8 measured with Al K_α radiation in comparison to DFT calculations (PBE0/NCPW). A Shirley background was subtracted from the experimental data to compare it to the theoretical results. The contribution of the Pb 6s orbitals to the total calculated DOS is highlighted. Further details concerning the data treatment are given in the Supporting Information. (c) Pb M_5-edge NEXAFS spectra of Pb_3F_8, PbF_2 and Pb_3O_4 measured by the X-ray fluorescence yield. Inset: Zoom-in of the pre-edge feature.

Instead, there is a broad feature similar to the case of Pb_3O_4. This is in line with the presence of both Pb^{II} and Pb^{IV} species in the Pb_3F_8 sample and with a small contamination of PbF_2, as stated above. The differences in the M_5-edge itself are more complicated as there are nearly no similarities between the three compounds. In the range from 2500 to 2510 eV, PbF_2 and Pb_3F_8 show similar spectral features, but above that range PbF_2 exhibits a local minimum, whereas Pb_3F_8 shows a peak. A similar peak is observed in the Pb_3O_4 spectrum but shifted by nearly 10 eV to higher energies.

We have calculated the electronic structure of Pb_3F_8 by DFT methods using the hybrid functional PBE0 and fully relativistic pseudopotentials.[33,34] To estimate the accuracy of our calculations we compared the experimentally determined valence band XP spectrum with the calculated partial density of states (pDOS) that is corrected by background and cross-section effects (see the Supporting Information). The results are shown in Figure 5b. The valence band width as well as its three-peaked shape are well reproduced by the DFT calculations.

In the following, we investigate the electronic structure of Pb_3F_8 in more detail by calculating its band structure and charge distribution. The band structure as well as the total DOS are given in Figure 6.

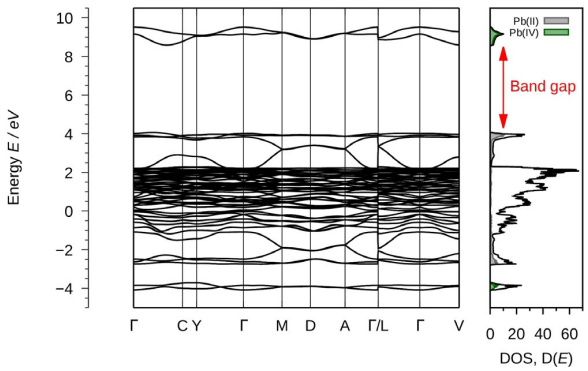

Figure 6. Left: Electronic band structure of Pb_3F_8. Right: Total Density of States (DOS) and the projected DOS of the 6s orbitals of Pb^{II} and Pb^{IV}. The position of the band gap (4.5 eV) is highlighted (DFT-PBE0/NCPP with SOC).

The band structure calculations show Pb_3F_8 to be an insulator with a band gap of approximately 4.5 eV in line with its off-white color. The DOS of the valence band is dominated by F 2p states that range from −1 eV to 2 eV. At about 4 eV the top of the valence band consists of four bands with only a small amount of dispersion that can be attributed to the filled Pb^{II} 6s bands. The conduction band is located at about 9 eV and consists of two bands. Both show nearly exclusive Pb^{IV} 6s character as illustrated by the pDOS in the right of Figure 6. A small amount of the Pb^{IV} 6s states is located at the bottom of the valence band at about −4 eV due to some covalent Pb^{IV}–F bond character. For the same reason Pb^{II} 6s states are present at about −2 eV. The band structure of the mixed valence compound Pb_3O_4 shows similar characteristics.[11] We thus conclude that like Pb_3O_4 also Pb_3F_8 is a mixed valence compound with the lead atoms in the oxidation states +II and +IV.

The crystal structure of Pb_3F_8 indicates that the Pb^{II} atoms feature "sterically active lone-pairs". We calculated electron-density difference maps of Pb_3F_8 which display the difference of the electron density of the compound compared to a superposition of the electron density of free atoms, yielding information where electron density is accumulated or depleted. The electron-density difference map of Pb_3F_8 is shown in Figure 7. It is drawn in a view perpendicular to the ladder-like connection of the Pb(2) atoms and the F(4) atoms, compare Figure 2a.

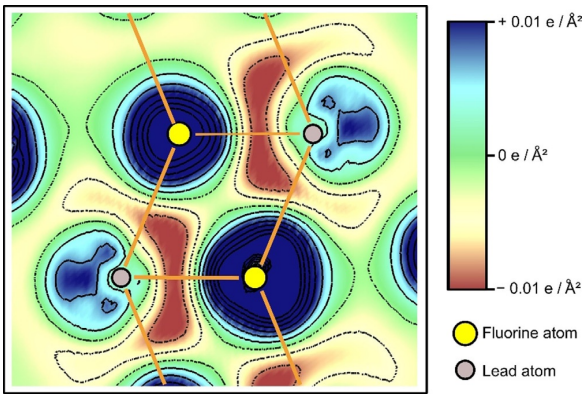

Figure 7. Electron-density difference map (DFT-PBE0/NCPP + SOC) of Pb_3F_8 along the ladder-like connection (sketched) of the Pb(2) atoms (grey color) via μ_3-bridging F(4) atoms (yellow color). An increase in electron density is shown in blue color and solid black lines, while a decrease in electron density is shown in brown color and dashed black lines.

The map displays a strong polarization of the electron density around the Pb^{II} atoms. The electron density along the Pb–F bonds is minimized (brownish colors) in line with the expected high amount of ionic bonding character. Moreover, there is an accumulation of electron density (in blue colors) besides the Pb^{II} atoms, pointing to the left and right side of the depicted ladder. Therefore, the electron density at the Pb^{II} atoms is "pushed" away from the fluorine atoms inside the ladder. This effect is often referred to "sterically active lone-pairs" of the Pb^{II} atoms. The electron density around the fluorine atoms (in yellow color) is strongly and nearly spherically increased as is expected for F^- anions due to the high electronegativity of the F atom.

Conclusions

The binary lead(II/IV) fluoride Pb_3F_8 was synthesized from Pb_3O_4 in anhydrous HF at room temperature. The bulk phase appears off-white while single crystals are colorless. It is thermally stable up to circa 80 °C and then decomposes to PbF_2 under loss of F_2. The compound crystallizes in the monoclinic space group $I2/a$ (No. 15) with the lattice parameters a = 8.7800(18), b = 7.4927(15), c = 10.196(5) Å; β = 98.78(3)°; V =

P10

662.9(4) Å^3; $Z=4$ at $T=100$ K, as evidenced by single-crystal X-ray analysis. The description of Pb_3F_8 as a mixed valence Pb^{II}/Pb^{IV} compound is evidenced by the thermal decomposition products, the crystal structure, the ^{19}F solid-state NMR, valence and core level photoelectron, as well as near-edge X-ray absorption fine structure (NEXAFS) spectroscopic investigations and further supported by IR and Raman spectra. Additionally, quantum chemical calculations were carried out to elucidate the electronic structure of Pb_3F_8. The calculated band gap is in line with the color of the compound. An accumulation of electron density next to the Pb^{II} atoms that some call "sterically active lone-pairs" seems to be responsible for the formation of the peculiar layer structure of Pb_3F_8.

Acknowledgements

We thank the Deutsche Forschungsgemeinschaft for several types of funding (also through 223848855-SFB 1083 and INST 221/117-1 FUGG), Solvay for the generous donation of F_2 and B. Scheibe for the Raman measurement. We thank the analytical service department of Dr. Uwe Linne, Marburg, the Helmholtz-Zentrum Berlin (HZB) for the allocation of synchrotron radiation beamtime at BESSY-II, and Florian Fillsack and Mark Hutter for technical support. We thank Prof. Dr. Michael Ruck, Dresden, for a helpful discussion on "sterically active lone-pairs".

Conflict of interest

The authors declare no conflict of interest.

Keywords: IR and Raman spectroscopy · lead fluoride · NEXAFS · NMR spectroscopy · quantum chemical calculations

[1] J. J. Berzelius, *Ann. Phys.* **1824**, *77*, 1 – 48.
[2] B. Brauner, *J. Chem. Soc. Trans.* **1894**, *65*, 393 – 402.
[3] U. Croatto, *Gazz. Chim. Ital.* **1944**, *74*/75, 20 – 22.
[4] R. Hoppe, W. Dähne, *Naturwissenschaften* **1962**, *49*, 254 – 255.
[5] P. Charpin, H. Marquet-Ellis, H. Nguyen-Nghi, P. Plurien, *C. R. Seances Acad. Sci., Ser. C* **1972**, *275*, 1503 – 1506.
[6] M. F. A. Dove, R. King, T. J. King, *J. Chem. Soc. Chem. Commun.* **1973**, 944.
[7] A. L. Hector, A. Jolleys, W. Levason, D. Pugh, G. Reid, *Dalton Trans.* **2014**, *43*, 14514 – 14516.
[8] J. C. Taylor, P. W. Wilson, *J. Am. Chem. Soc.* **1973**, *95*, 1834 – 1838.
[9] P. Köhler, J.-H. Chang, *Z. Anorg. Allg. Chem.* **1997**, *623*, 596 – 602.
[10] A. Levol, *Ann. Chim. Phys.* **1840**, *75*, 108 – 111.
[11] H. J. Terpstra, R. A. De Groot, C. Haas, *J. Phys. Chem. Solids* **1997**, *58*, 561 – 566.
[12] E. Van Elslande, V. Guérineau, V. Thirioux, G. Richard, P. Richardin, O. Laprévote, G. Hussler, P. Walter, *Anal. Bioanal. Chem.* **2008**, *390*, 1873 – 1879.
[13] A. Bose, K. Vashistha, B. J. O'Loughlin, *Pediatrics* **1983**, *72*, 106 – 108.
[14] M. Bannert, G. Blumenthal, H. Sattler, M. Schönherr, H. Wittrich, *Z. Chem.* **2010**, *12*, 191 – 192.
[15] P. Charpin, H. Marquet-Ellis, Nguyen-Nghi, P. Plurien, F. Perrin, *C. R. Seances Acad. Sci., Ser. C* **1972**, *275*, 1503 – 1506.
[16] J. Bandemehr, H. L. Deubner, M. Sachs, F. Kraus, *Z. Anorg. Allg. Chem.* **2018**, *644*, 1721 – 1726.
[17] R. Homann, R. Hoppe, *Z. Anorg. Allg. Chem.* **1969**, *368*, 271 – 278.
[18] H. Hoppe, K. Blinne, *Z. Anorg. Allg. Chem.* **1958**, *293*, 251 – 263.
[19] F. Schrötter, B. G. Müller, *Z. Kristallogr.* **1991**, *196*, 261 – 268.
[20] R. Fischer, B. G. Müller, *Z. Anorg. Allg. Chem.* **2001**, *627*, 445 – 452.
[21] M. Nespolo, B. Guillot, *J. Appl. Crystallogr.* **2016**, *49*, 317 – 321.
[22] K. O. Christe, D. A. Dixon, J. C. P. Sanders, G. J. Schrobilgen, S. S. Tsai, W. W. Wilson, *Inorg. Chem.* **1995**, *34*, 1868 – 1874.
[23] A. Ellern, K. Seppelt, *Angew. Chem. Int. Ed. Engl.* **1995**, *34*, 1586 – 1587; *Angew. Chem.* **1995**, *107*, 1772 – 1773.
[24] E. J. Baran, *J. Fluorine Chem.* **2000**, *101*, 61 – 63.
[25] R. Seshadri, *J. Chem. Sci.* **2001**, *113*, 487 – 496.
[26] A. Walsh, G. W. Watson, *J. Solid State Chem.* **2005**, *178*, 1422 – 1428.
[27] J. Köhler, J. Tong, R. Dinnebier, A. Simon, *Z. Anorg. Allg. Chem.* **2012**, *638*, 1970 – 1975.
[28] F. Wang, C. P. Grey, *J. Am. Chem. Soc.* **1998**, *120*, 970 – 980.
[29] M. Bak, J. T. Rasmussen, N. C. Nielsen, *J. Magn. Reson.* **2000**, *147*, 296 – 330.
[30] M. Robin Bendall, R. E. Gordon, *J. Magn. Reson. (1969-1992)* **1983**, *53*, 365 – 385.
[31] Y. S. Avadhut, J. Weber, E. Hammarberg, C. Feldmann, I. Schellenberg, R. Pöttgen, J. Schmedt auf der Günne, *Chem. Mater.* **2011**, *23*, 1526 – 1538.
[32] B. Bureau, G. Silly, J. Y. Buzaré, J. Emery, *Chem. Phys.* **1999**, *249*, 89 – 104.
[33] C. Adamo, V. Barone, *J. Chem. Phys.* **1999**, *110*, 6158 – 6170.
[34] M. Schlipf, F. Gygi, *Comput. Phys. Commun.* **2015**, *196*, 36 – 44.

Manuscript received: August 29, 2019
Accepted manuscript online: September 23, 2019
Version of record online: November 4, 2019

P10

CHEMISTRY
A European Journal

Supporting Information

Binary Lead Fluoride Pb_3F_8

H. Lars Deubner+,[a] Malte Sachs+,[a] Jascha Bandemehr,[a] Sergei I. Ivlev,[a] Antti J. Karttunen,[b] Stefan R. Kachel,[a] Benedikt P. Klein,[a] Lukas Ruppenthal,[a] Maik Schöniger,[a] Claudio K. Krug,[a] Jan Herritsch,[a] J. Michael Gottfried,[a] Jamal N. M. Aman,[c] Jörn Schmedt auf der Günne,[c] and Florian Kraus*[a]

chem_201903954_sm_miscellaneous_information.pdf

P10

Contents

P10

Experimental Procedures

General: All operations were carried out in an atmosphere of dry and purified argon (5.0 Praxair, Germany), so that possible contact of the substances with moisture and air was minimized. Anhydrous HF was additionally dried by mixing it with K_2NiF_6, which reacts with traces of moisture, and separated by vacuum distillation in a Monel Schlenk line. Pb_3O_4 (Merck, ≥ 99 %) was used without further purification.

Synthesis of Pb_3F_8

A FEP tube with a stainless-steel valve was charged with Pb_3O_4 (250 mg, 0.365 mmol). A large excess of anhydrous HF (ca. 100 eq. compared to Pb_3O_4) was condensed on the Pb_3O_4 powder at −196 °C. The reaction vessel was slowly warmed to room temperature and kept for 1 h under sporadic shaking after the orange color had disappeared. Then, the volatiles (HF and H_2O) were carefully removed *in vacuo* at room temperature. The isolated product, which was used for further characterization, weighed 281 mg (0.363 mmol, 99.4 % of theory). Some small single crystals were always obtained among the powder.

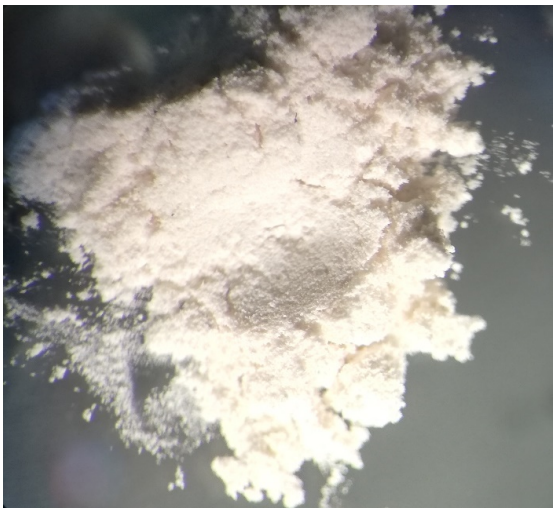

Figure S 1. Pb_3F_8 powder after removal of the volatiles (HF and H_2O).

Powder X-Ray Diffraction

The powder X-ray pattern was recorded with a StadiMP diffractometer (Stoe & Cie) in transmission geometry using a flat foil sample holder. The diffractometer was operated with Cu $K_{\alpha 1}$ radiation (1.5406 Å, germanium monochromator) and equipped with a MYTHEN 1K detector. The diffraction pattern was indexed using the WinXPOW suite.[1] Rietveld refinement was done with Topas-Academic V6.[2] The powder diffraction pattern with the Rietveld refinement is shown in Figure S 2.

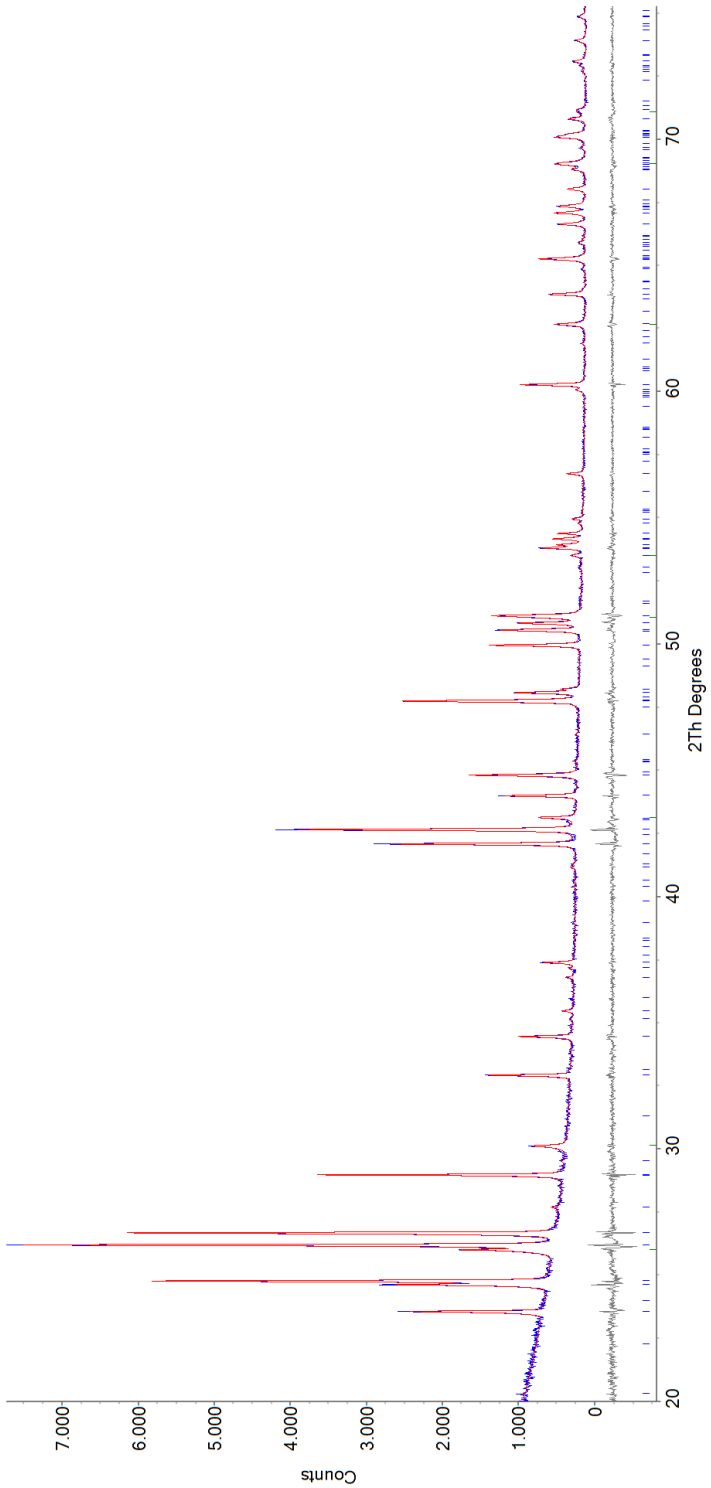

Figure S 2. Powder diffraction pattern of a Pb_3F_8 flat sample. The measured powder pattern is shown in blue, the fitted pattern (Rietveld refinement) is shown in red, the grey curve on the bottom shows the difference curve. The refined lattice parameters for Pb_3F_8 are a = 8.84344(8), b = 7.54266(8), c = 10.23393(11) Å, β = 98.8124(6)°, V = 674.580(12) Å^3. GOF 1.187, R_p = 0.0467, R_{wp} = 0.0611.

P10

Table S 1. Technical data of the Rietveld refinement of Pb_3F_8.

Measurement conditions	
Sample	Pb_3F_8
Diffractometer, generator	Stoe STADI MP; 40 kV, 40 mA
Diffractometer geometry	Transmission (flat foil)
Radiation, monochromator	Cu $K_{\alpha1}$, Ge(111)
Measurement range, step size (2θ / °)	20−75, 1.00
Measurement time per step / s	15.0
Data acquisition	step scan
Temperature *T* / K	298
Global parameters	
Software	TOPAS-Academic v6
Number of phases	2
Relative phase amounts in mass / %	Pb_3F_8 93.49(8), PbF_2 6.51(8)
Number of parameters	58
Zero shift (2θ / °)	0 (within 3σ)
Profile function	TCHZ Pseudo-Voigt
Asymmetry	TOPAS Simple axial model
Background treatment	Chebyshev polynomial of 9th order
Structural data	
Space group (No.)	*I*2/*a* (15)
Pearson symbol	*mS*44
a / Å	8.84344(8)
b / Å	7.54266(8)
c / Å	10.23393(11)
β / °	98.8124(6)
V / Å^3	674.580(12)
Crystallographic density / g cm^{-1}	7.61707(13)
Profile parameters	
Peak.shape parameter *V*	0.05689(16)
Peak.shape parameter *W*	0.05931(19)
Peak.shape parameter *Z*	0.070(2)
Peak.shape parameter *X*	0.1024(12)
Asymmetry parameter	8.86(6)
Global residual values	
R_p	0.0467
R_{wp}	0.0611
R_{Bragg}	0.0137
GOF	1.186

P10

Density determination

The density of Pb_3F_8 was measured using the automated gas displacement pycnometry system AccuPyc II 1340 (Micromeritics) with a calibrated 1 cm^3 sample holder and helium as the displacement gas. The number of preliminary purges was set to 30, while the subsequent density measurements were performed 100 times with measurement averaging. The density of the sample was determined to be 7.682(16) g·cm^{-3}, the sample contained 84.5(9) % Pb_3F_8 and 15.5(9) % PbF_2. A total sample mass of 855.6 mg was used.

Single crystal X-ray diffraction

A crystal of Pb_3F_8 was selected under pre-dried perfluorinated oil and mounted using a MiTeGen loop. Intensity data of a suitable crystal were recorded with an IPDS 2T diffractometer (Stoe & Cie) at an offset of 30°. The diffractometer was operated with Mo K_α radiation (0.71073 Å, graphite monochromator) and equipped with an image plate detector. Evaluation, integration and reduction of the diffraction data was carried out using the X-Area software suite.[3] A numerical absorption correction was applied with the modules X-Shape and X-Red32 of the X-Area software suite. The structure was solved with dual-space methods (SHELXT-2014/5) and refined against F^2 (SHELXL-2014/7).[4,5] All atoms were refined with anisotropic displacement parameters. The highest residual electron density of 1.380 e·Å^{-3} after the final refinement was 1.2 Å distant from atom Pb(1). The cif file was deposited with the CCDC (https://www.ccdc.cam.ac.uk/), depository number: 1945512.

Table S 2. Selected crystallographic data and details of the structure determination of Pb_3F_8.

	Pb_3F_8
Colour and appearance	colorless
Molecular mass /g·mol^{-1}	773.56
Crystal system	monoclinic
Space group (No.)	*I*2/*a* (15)
Pearson code	*mS*44
Wyckoff sequence	15*ef*^{5}
a /Å	8.7800(18)
b /Å	7.4927(15)
c /Å	10.196(5)
α /°	90
β /°	98.78(3)
γ /°	90
V /Å^3	662.9(4)
Z	4
λ /Å	0.71073
T /K	100(2)
μ(Mo K_α) /mm^{-1}	76.100
R_{int}, R_σ	0.0594, 0.0252
$R(F)$ ($I \geq 2\sigma(I)$, all)	0.0195, 0.0279
$wR(F^2)$ ($I \geq 2\sigma(I)$, all)	0.0358, 0.0382
S (all data)	1.133
Data, parameters, restrains, constraints	1021, 52, 0, 0
$\Delta\rho_{max}$, $\Delta\rho_{min}$ /e·Å^{-3}	1.380, −1.599

P10

Thermal analysis

Thermal measurements were performed with a DSC-TGA 3 (Mettler Toledo) with a heating rate of 1 and 0.1 K·min^{-1} in a stream of nitrogen (20 sccm). The diagram was plotted with OriginPro 2017.[6]

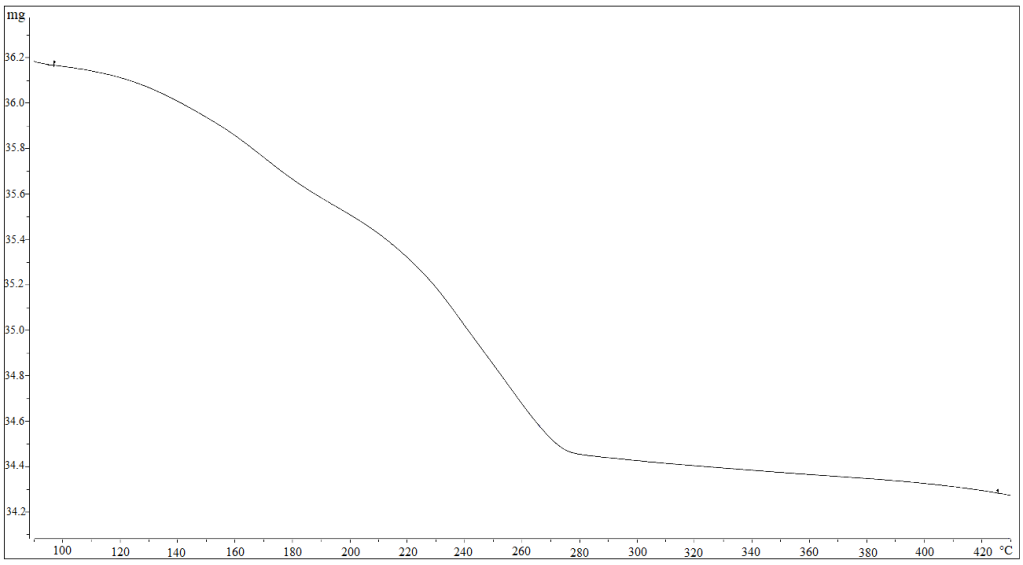

Figure S 3. Thermogravimetric measurement from 80 to 430 °C under a stream of nitrogen with a heating rate of 0.1 K·min^{-1}.

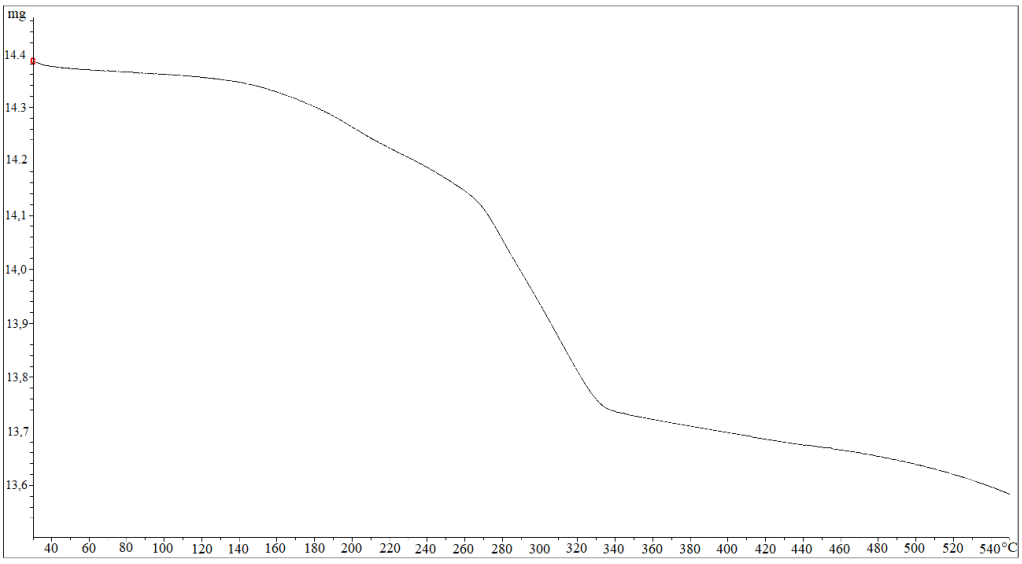

Figure S 4. Thermogravimetric measurement from 30 to 550 °C under a stream of nitrogen with a heating rate of 1 K·min^{-1}.

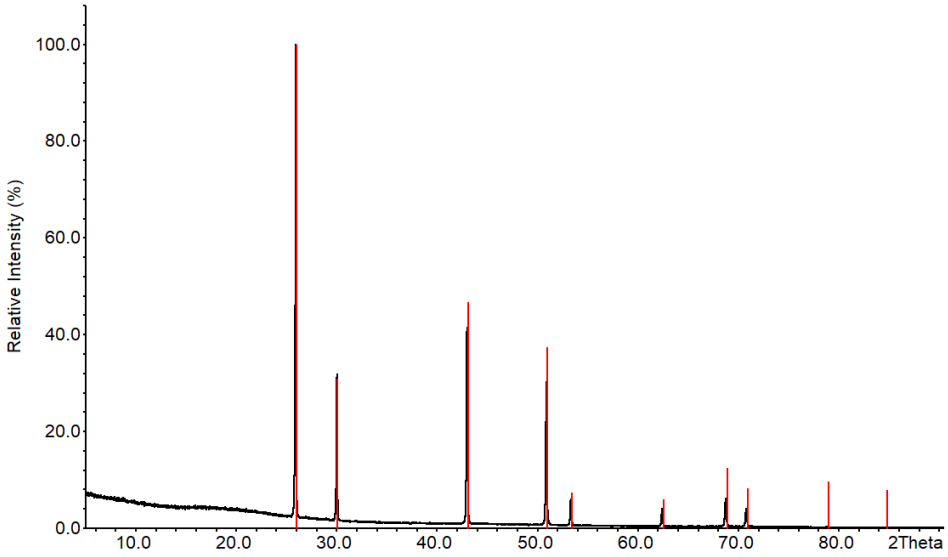

Figure S 5. Powder X-ray diffraction pattern of the product of the thermal decomposition of Pb_3F_8 powder after heating to 470 °C for 12h and subsequent cooling to room temperature. The sample was flame sealed under vacuum into a borosilicate glass ampoule which was heated inside a tube furnace.

P10

CHARDI Calculations

We applied the charge distribution method (CHARDI) introduced by Hoppe and coworkers as implemented in the program CHARDI2015[7] to validate the assignment of the coordination numbers as well as the oxidation states of the lead atoms. We used the crystal structure data determined in this paper as input parameters. The results are summarized in Table S 3.

Table S 3. Results of CHARDI calculations of Pb_3F_8 (*I*2/*a*, *mS*44). Coordination number (C.N.) as discussed above, effective coordination number (ECoN), mean fictive ionic radius (MEFIR), assigned oxidation state based on structure-chemical reasoning, and calculated charge distribution (CHARDI).

Atom	C.N.	ECoN	MEFIR / Å	Oxidation state	CHARDI
Pb(1)	6	6.0	0.886	+IV	+4.12
Pb(2)	6 [+3]	6.9	1.344	+II	+1.94
F(1)	2	1.2	1.209	−I	−1.01
F(2)	2	1.1	1.211	−I	−1.10
F(3)	2	1.4	1.191	−I	−0.97
F(4)	3	2.9	1.113	−I	−0.93

The CHARDI calculation supports the description of Pb_3F_8 as a mixed valence compound. The calculated mean fictive ionic radii (MEFIR) of Pb(1) (0.886 Å) and Pb(2) (1.344 Å) are in line with the Shannon ionic radii of Pb(IV) (0.775 Å) and Pb(II) (1.19 Å) for coordination number six. Therefore, the CHARDI calculations demonstrate that a valid, valence-balanced description of Pb_3F_8 is possible stating Pb_3F_8 as a mixed valence compound.

Raman Spectroscopy

We have performed Raman spectroscopy on Pb_3F_8 and PbF_2. Raman spectra were recorded with a Confocal Raman Microscope S+I MonoVista CRS+, using the 532 nm excitation line of an integrated diode laser (resolution < 1 cm^{-1}; range 50 to 9000 cm^{-1}). A sample of Pb_3F_8 was sealed inside a 0.3 mm borosilicate glass capillary, which was several times flame dried under vacuum before use.

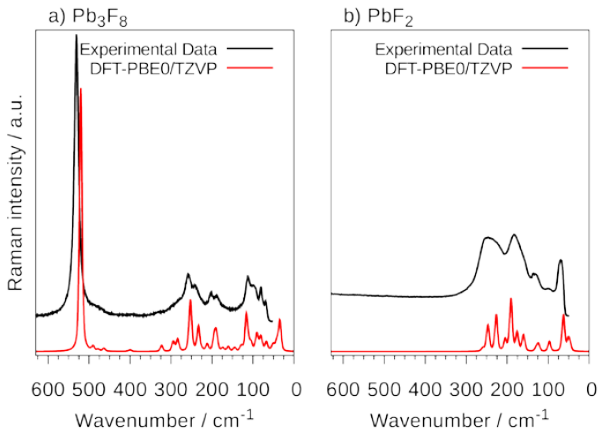

Figure S 6. **a)** Raman spectrum of Pb_3F_8 in comparison with **b)** the Raman spectrum of PbF_2. The calculated Raman intensities are shown in red (DFT-PBE0/TZVP).

The experimental results are compared with theoretical spectra from DFT calculations in Figure S 6. The observed peaks from the measured spectra are listed in Table S 4. The peak assignment of the calculated spectra of Pb_3F_8 and PbF_2 are given in Table S 5 and Table S 6, respectively. The most striking difference between the Raman spectrum of Pb_3F_8 compared to the spectrum of PbF_2 is the strong vibrational band at 531 cm^{-1} that is only present in the Raman spectrum of Pb_3F_8. This band is well reproduced by our theoretical findings and can be attributed to a symmetric stretching of the Pb(IV)−F bonds, which explains the absence of this band in PbF_2. The Raman spectrum of Pb_3F_8 thus supports our findings of Pb_3F_8 being a mixed valence compound.

P10

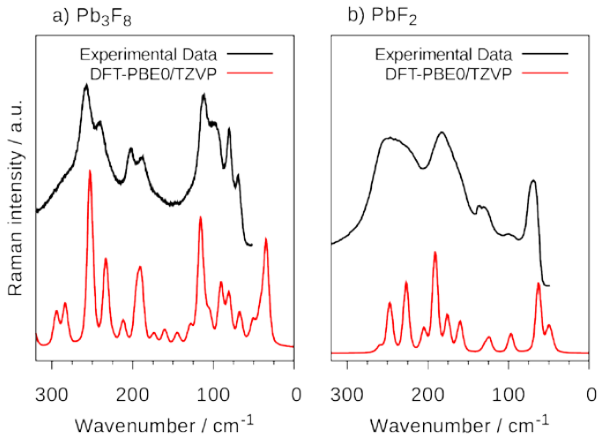

Figure S 7. Low wavenumber section of the Raman spectrum of Pb_3F_8 in comparison with **b)** the Raman spectrum of PbF_2. The calculated Raman intensities are shown in red (DFT-PBE0/TZVP).

The low frequency section of the Raman spectra of Pb_3F_8 and PbF_2 are given in Figure S 7. The Raman bands of both compounds display a similar shape and are distinctly broadened in this frequency range. It is thus difficult to estimate the phase purity of Pb_3F_8 from Raman data as the broad background of the Pb_3F_8 Raman spectrum could result from PbF_2 that is also present as evidenced by powder X-ray diffraction data (see Section Powder X-Ray Diffraction). Pb_3F_8 is best identified by the lattice vibrational bands around 100 cm^{-1} as this frequency region corresponds to a minimum in Raman intensity in the spectrum of PbF_2. Despite the broad background, the maxima of the Pb_3F_8 are well reproduced by our DFT calculations: This allows us to assign the two peaks at around 250 cm^{-1} and the two peaks at around 200 cm^{-1} to a symmetric stretching of the Pb(II)−F bonds and a bending of the Pb(IV)−F bonds, respectively.

Table S 4. Observed bands in the measured Raman spectra of Pb_3F_8 in comparison to PbF_2.

Pb_3F_8		PbF_2	
Raman active mode / cm^{-1}	Assignment	Raman active mode / cm^{-1}	Assignment
531	Pb(IV)−F symmetric stretching	244	Stretching/Bending of the whole lattice
258	Pb(II)−F symmetric stretching + Pb(IV) bending	183	Pb−F asymmetric stretching
241	Pb(II)−F symmetric stretching + Pb(IV) bending	133	Bending of the whole lattice
209	Pb(IV) bending	99	Pb−F wagging/scratching
189	Pb(IV) bending	69	Pb−F scissoring
112	Pb−F bending of the whole lattice		
98	Pb−F bending of the whole lattice		
80	Pb−F bending of the whole lattice		
69	Pb−F bending of the whole lattice		

Table S 5. Band assignment for the calculated Raman spectrum of Pb_3F_8 (DFT-PBE0/TZVP). The calculations were performed in the space group *I*2/*a* (15) with the point group symmetry C_{2h} at the Γ-point.

Frequency / cm^{-1}	IR intensity (arb. units)	Raman intensity (arb. units)	Assignment	Irreducible rep. (C_{2h})
520	0.0	1000.0	Pb(IV)−F symmetric stretching + Pb(II)−F scissoring	*Ag*
517	12.3	0.0	Pb(IV)−F symmetric stretching + Pb(II)−F scissoring	*Au*
493	580.8	0.0	Pb(IV)−F asymmetric stretching + Pb(II)−F scissoring	*Bu*
490	0.0	15.8	Pb(IV)−F asymmetric stretching + Pb(II)−F scissoring	*Bg*
478	0.0	6.7	Pb(IV)−F asymmetric stretching + Pb(II)−F rocking	*Bg*
470	546.0	0.0	Pb(IV)−F asymmetric stretching + Pb(II)−F rocking	*Bu*
464	0.0	11.2	Pb(IV)−F asymmetric stretching + Pb(II)−F rocking	*Ag*
456	554.3	0.0	Pb(IV)−F asymmetric stretching + Pb(II)−F rocking	*Au*
456	290.3	0.0	Pb(IV)−F asymmetric stretching + Pb(II)−F scissoring	*Au*
406	0.0	1.7	Pb(IV)−F asymmetric stretching + Pb(II)−F rocking/wagging	*Bg*
399	0.0	5.9	Pb(IV)−F asymmetric stretching + Pb(II)−F wagging	*Ag*
385	0.5	0.0	Pb(IV)−F asymmetric stretching + Pb(II)−F twisting	*Bu*
329	35.0	0.0	Pb(II)−F symmetric stretching	*Au*
323	0.0	22.5	Pb(II)−F symmetric stretching + Pb(IV)−F scissoring	*Bg*
320	132.3	0.0	Pb(II)−F wagging + Pb(IV)−F scissoring	*Bu*
295	0.0	37.4	Pb(II)−F asymmetric stretching	*Ag*
284	0.0	46.0	Pb(II)−F wagging	*Ag*
253	0.0	82.9	Pb(II)−F symmetric stretching + Pb(IV)−F wagging	*Bg*
253	0.0	111.6	Pb(II)−F symmetric stretching + Pb(IV)−F scissoring	*Ag*
250	17.9	0.0	Pb(II)−F asymmetric stretching + Pb(IV)−F scissoring	*Au*
247	0.0	0.2	Pb(II)−F scissoring + Pb(IV)−F scissoring	*Bg*
242	340.9	0.0	Pb(II)−F symmetric stretching + Pb(IV)−F scissoring	*Bu*
237	3.8	0.0	Pb(II)−F scissoring + Pb(IV)−F scissoring	*Au*
233	0.0	94.6	Pb(II)−F symmetric stretching + Pb(IV)−F scissoring	*Ag*
225	0.0	7.8	Pb(II)−F asymmetric stretching + Pb(IV)−F wagging	*Bg*
215	78.8	0.0	Pb(II)−F asymmetric stretching + Pb(IV)−F scissoring	*Au*
213	231.5	0.0	Pb(IV)−F wagging + Pb(II)−F asymmetric stretching	*Bu*
212	0.0	26.1	Pb−F bending/stretching of the whole lattice	*Bg*
198	9.7	0.0	Pb(II)−F symmetric stretching + Pb(IV)−F scissoring	*Au*
196	354.5	0.0	Pb(II)−F asymmetric stretching + Pb(IV)−F scissoring	*Bu*
195	0.0	54.0	Pb(IV)−F scissoring	*Ag*
189	0.0	69.3	Pb(IV)−F twisting	*Ag*
186	0.1	0.0	Pb(IV)−F scissoring	*Au*
174	0.0	12.4	Pb(IV)−F rocking	*Bg*
160	0.0	160.4	Pb(IV)−F twisting	*Ag*
154	179.6	0.0	Pb−F bending of the whole lattice	*Bu*
150	1050.0	0.0	Pb−F bending of the whole lattice	*Bu*
145	0.0	13.7	Pb−F bending of the whole lattice	*Bg*
129	0.0	19.4	Pb−F bending of the whole lattice	*Bg*
129	351.2	0.0	Pb(II)−F scissoring	*Au*
121	1.2	0.0	Pb−F bending of the whole lattice	*Bu*
116	0.0	137.9	Pb−F bending of the whole lattice	*Ag*
115	379.7	0.0	Pb(IV)−F rocking/scissoring + Pb(II)−F wagging	*Au*
111	0.0	15.44	Pb−F bending of the whole lattice	*Bg*
108	32.9	0.0	Pb−F bending of the whole lattice	*Bu*
105	0.0	29.4	Pb−F bending of the whole lattice	*Ag*
104	36.1	0.0	Pb−F bending of the whole lattice	*Au*
91	0.0	26.8	Pb−F bending of the whole lattice	*Bg*
91	0.0	39.4	Pb−F bending of the whole lattice	*Ag*
90	0.9	0.0	Pb(IV)−F twisting	*Au*
86	51.2	0.0	Pb(IV)−F rocking	*Bu*
82	0.0	25.6	Pb−F bending of the whole lattice	*Ag*
80	0.0	30.3	Pb−F bending/stretching of the whole lattice	*Bg*
76	185.3	0.0	Pb−F bending of the whole lattice	*Au*
74	184.8	0.0	Pb−F bending of the whole lattice	*Bu*
67	0.0	35.0	Pb−F bending of the whole lattice	*Bg*
62	147.1	0.0	Pb−F bending of the whole lattice	*Bu*
59	0.0	2.3	Pb−F bending/stretching of the whole lattice	*Ag*
51	95.3	0.0	Pb−F bending of the whole lattice	*Bu*
51	0.0	25.0	Pb−F bending of the whole lattice	*Bg*
49	0.1	0.0	Pb(II)−F scissoring	*Au*
42	0.0	33.3	Pb−F bending of the whole lattice	*Bg*
35	0.0	115.0	Pb−F bending of the whole lattice	*Ag*
0	0.0	0.0	lattice vibrations (low frequency modes spanning the whole lattice)	*Bu*
0	0.0	0.0	lattice vibrations (low frequency modes spanning the whole lattice)	*Bu*
0	0.0	0.0	lattice vibrations (low frequency modes spanning the whole lattice)	*Au*

Table S 6. Band assignment for the calculated Raman spectrum of PbF_2 (DFT-PBE0/TZVP). The calculations were performed in the space group *Pnma* (62) with the point group symmetry D_{2h} at the Γ-point.

Frequency / cm^{-1}	IR intensity (arb. units)	Raman intensity (arb. Units)	Assignment	Irreducible rep. (D_{2h})
362	3.9	0.0	Stretching/Bending of the whole lattice	*B1u*
326	105.2	0.0	Stretching/Bending of the whole lattice	*B2u*
294	0.0	0.2	Stretching/Bending of the whole lattice	*B3g*
260	0.0	59.5	Pb−F asymmetric stretching	*B3g*
248	0.0	337.8	Pb−F symmetric stretching / scissoring	*Ag*
246	0.0	182.4	Pb−F scissoring	*B2g*
228	140.1	0.0	Pb−F rocking	*B3u*
227	0.0	204.3	Pb−F scissoring	*B1g*
227	0.0	491.9	Pb−F asymmetric stretching	*Ag*
221	57.2	0.0	Pb−F asymmetric stretching	*B1u*
205	0.0	215.6	Pb−F asymmetric stretching + scissoring	*B3g*
204	91.6	0.0	Pb−F asymmetric stretching + rocking	*B2u*
196	0.0	0.0	Pb−F asymmetric stretching + wagging	*Au*
191	0.0	1000.0	Pb−F asymmetric stretching	*Ag*
176	0.0	352.0	Pb−F scissoring	*B2g*
174	143.0	0.0	Pb−F asymmetric stretching + rocking	*B2u*
164	832.1	0.0	Bending of the whole lattice	*B1u*
162	0.0	56.8	Bending of the whole lattice	*B3g*
160	0.0	257.4	Bending of the whole lattice	*B1g*
130	0.0	59.3	Bending of the whole lattice	*Au*
130	0.0	0.0	Pb−F twisting/stretching	*Ag*
124	0.0	141.2	Stretching/Bending of the whole lattice	*B3g*
117	0.0	0.5	Stretching/Bending of the whole lattice	*B3g*
115	100.8	0.0	Stretching/Bending of the whole lattice	*B1u*
113	727.5	0.0	Pb−F scissoring	*B2u*
97	0.0	189.4	Pb−F wagging/stretching	*Ag*
89	1158.8	0.0	Pb−F scissoring	*B3u*
63	0.0	699.5	Pb−F scissoring	*Ag*
61	314.1	0.0	Stretching/Bending of the whole lattice	*B2u*
51	0.0	204.6	Rocking of the Pb atoms	*B1g*
50	19.1	0.0	Bending of the whole lattice	*B1u*
47	0.0	97.2	Rocking of the Pb atoms	*B2g*
27	0.0	0.0	Scissoring of the Pb atoms	*Au*
0	0.0	0.0	lattice vibrations (low frequency modes spanning the whole lattice)	*B3u*
0	0.0	0.0	lattice vibrations (low frequency modes spanning the whole lattice)	*B1u*
0	0.0	0.0	lattice vibrations (low frequency modes spanning the whole lattice)	*B2u*

IR spectroscopy

The IR spectrum was recorded inside a glovebox (MBraun) under argon atmosphere on a Bruker alpha FT-IR spectrometer using the ATR Diamond module with a resolution of 4 cm^{-1}. The spectra were processed with the OPUS software package.[8]

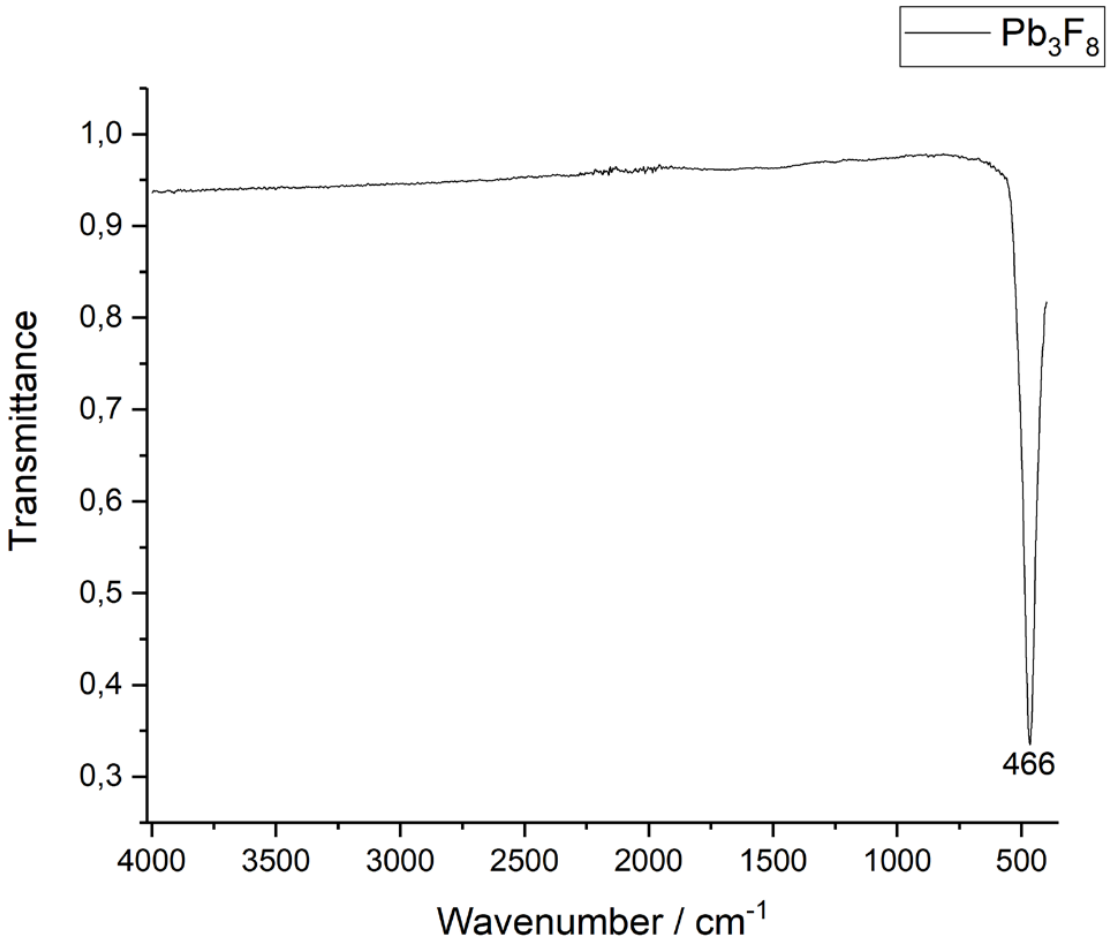

Figure S 8. ATR-IR spectrum of Pb_3F_8.

P10

Solid-state NMR spectroscopy

^{19}F solid-state MAS NMR measurements were performed at 7.05 T on a Bruker Avance II NMR spectrometer at a ^{19}F frequency of 282.406 MHz equipped with a 2.5 mm MAS Bruker double-resonance probe head. The chemical shift of ^{19}F is reported relative to $CFCl_3$. The ^{1}H resonance of 1% TMS in $CDCl_3$ served as an external secondary reference using the Ξ values for ^{19}F as reported by IUPAC.[9,10] ^{19}F MAS NMR spectra were acquired at 20 and 17 kHz spinning rate width a 90° pulse of 2.5 µs and a recycle delay of 4 s. The ^{19}F DEPTH[11,12] NMR spectrum was acquired at 20 kHz spinning rate with 90° and 180° pulses of 2.5 and 5 µs, respectively, and a recycle delay of 4 s. The ^{19}F NMR simulation was performed using SIMPSON-3.1.2.[13]

XPS, HAXPES and NEXAFS

X-ray photoelectron spectroscopy (XPS) was performed with monochromatic Al K_α radiation using a SPECS XR 50 M X-ray anode, a SPECS FOCUS 500 monochromator, and a SPECS PHOIBOS 150 electron energy analyzer equipped with an MCD-9 multi channeltron detector. The spectrometer is housed in a UHV system with a base pressure of $2 \cdot 10^{-10}$ mbar. The sample was prepared in a glove box by evenly distributing a small amount of powder on carbon tape, which was attached to a sample plate. The sample was then transferred into the UHV chamber using a glove bag filled with nitrogen gas to avoid any contact with air. The valence band and the survey spectrum were shifted with the Pb $4f_{7/2}$ peak as reference[14] located at a binding energy of 139.2 eV to correct for charging. For better comparison of the valence region with the DFT calculations, a Shirley background was subtracted.

The near-edge X-ray absorption fine structure (NEXAFS) and hard X-ray photoelectron spectroscopy (HAXPES) measurements were performed at the KMC-1 beamline of the synchrotron radiation facility BESSY II (Helmholtz-Zentrum für Materialien und Energie, Berlin, Germany) using the HIKE end-station with a Scienta R4000 hemispherical electron energy analyzer for HAXPES and a Bruker XFlash 4010 fluorescence detector for NEXAFS. The general properties of this setup are described elsewhere.[15,16] The spot size of the photon beam was approximately 0.3×0.4 mm^2. Typical photon fluxes were in the order of 10^{11} to 10^{12} photons/s over the entire energy range. For sample preparation, a small amount of the pulverulent compounds were distributed on carbon tape (sticking to the sample holder) in such a way that a thin film of the compound was visible to the naked eye. After preparation under ambient conditions, the samples were rapidly transferred to the vacuum to minimize reaction with and contamination by air. The cleanliness of the samples was checked by HAXPES survey spectra. The HAXPES data were referenced to the Au 4f signal of a gold foil located near the sample. The data points of each original spectrum were reduced by a factor of five by averaging five successive points to one point. NEXAFS measurements were performed on the M_5-edge of Pb in the range of 2460 to 2560 eV with a step width of 0.25 eV. For each sample two NEXAFS spectra were recorded, normalized to the ionization current and afterwards averaged. The background was normalized to the same starting and end points.

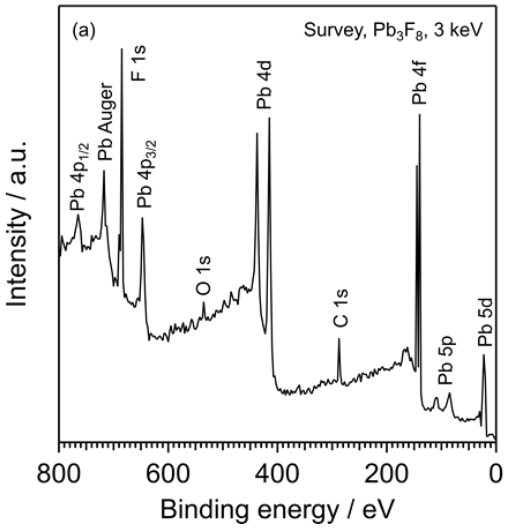

Figure S 9. HAXPES survey spectrum of the Pb_3F_8 sample using a photon energy of 3000 eV. The spectrum shows signs of photoemission-induced charging, as manifested by peak shifts and broadening. The spectrum shows the core levels of Pb and F atoms, besides small C 1s and O 1s contributions from the carbon tape used for mounting the sample. The spectrum confirms that the sample used in the subsequent NEXAFS experiment (see Figure 5c in the main text) is well-defined and unaffected by reaction with ambient air or water vapor.

Table S 7. Assignment of XPS peaks of the Pb_3F_8 survey spectrum in Figure S 9.

Energy / eV	Element	Assignment
21 – 24	Pb 5d	Pb_3F_8
84 – 109	Pb 5p	Pb_3F_8
139 – 145	Pb 4f	Pb_3F_8
286	C 1s	Carbon Tape
415 – 438	Pb 4d	Pb_3F_8
534	O 1s	Carbon Tape
646	Pb $4p_{3/2}$	Pb_3F_8
685	F 1s	Pb_3F_8
718	Pb Auger ($M_4N_{6,7}N_{6,7}$ Transition)	Pb_3F_8
763	Pb $4p_{1/2}$	Pb_3F_8
819	Pb Auger ($M_5N_{6,7}N_{6,7}$ Transition)	Pb_3F_8

Quantum chemical calculations

The vibrational spectra were calculated with the program CRYSTAL17 that uses Gaussian-type atom-centered basis functions[17]. We applied the density functional theory (DFT) PBE0 hybrid functional[18] and triple-zeta-valence + polarization (TZVP) level basis sets for the lead and fluorine atoms. The basis sets were derived from the molecular Karlsruhe basis sets, full basis set details are given below.[19] We applied a 4×4×4 Monkhorst-Pack-type grid of *k*-points for the reciprocal space integration of the electronic structure of Pb_3F_8 and PbF_2. For the evaluation of the Coulomb and exchange integrals (TOLINTEG) we used tightened tolerance factors of 8, 8, 8, 8, and 16. We performed the structural optimizations of the atomic positions and lattice parameters within the constraints imposed by the respective space group symmetry and the default optimization convergence thresholds. The vibrational frequencies were calculated in the harmonic approximation using the data from the structural optimizations.[20,21] The Raman intensities were calculated for a polycrystalline powder sample with total isotropic intensities in arbitrary units adjusting the temperature and laser wavelength to the experimental setup (T = 298.15 K, λ = 533 nm).[22,23] The Raman spectrum was broadened applying a pseudo-Voigt peak profile (50:50 Lorenzian:Gaussian) and a FWHM of 8 cm^{-1}. The peak assignment was carried out by visual inspection of the normal modes (Jmol program package).[24]

We calculated the electronic structure of Pb_3F_8 via DFT using the software package *Quantum Espresso* version 6.3 that is based on plane waves and pseudopotentials.[25] We used scalar as well as full-relativistic norm-conserving pseudopotentials of the SG15 Optimized Norm-Conserving Vanderbilt Pseudopotential Database.[26] We chose the GGA functional PBE and the hybrid functional PBE0 for our calculations.[18,27] The DFT calculations were carried out at the geometry of the experimentally determined single crystal structure. The calculations were performed with an 80 Ry kinetic-energy cutoff, a 320 Ry charge-density cutoff and a centered 4×4×3 Monkhorst-Pack-type grid of *k*-points. In case of the hybrid PBE0 functional, the Fock operator was sampled *via* a Γ-centered grid at each *k*-point. The divergence of the Coulomb potential was treated with the Gygi-Baldereschi approach.[28] We analyzed the electronic structure constructing a set of maximally localized Wannier functions (MLWFs) from the converged ground state electronic density of the plane-wave calculations. We used the program *Wannier90* for this purpose.[29] We defined a target dimension consisting of a set of three *p* orbitals for each fluorine atom and a set of one *s* orbital for each lead atom. The MLWFs were constructed using a 4×4×3 grid of *k*-points. The MLWF basis received can reproduce the F 2*p*/Pb 6*s* valence band as well as the Pb 6*s* conduction band of the plane-wave

electronic structure calculations as shown in Figure S 10. We used the WF basis to calculate Wannier-interpolated band structures as well as densities of states (DOS) with a fine *k*-point sampling of 20×20×20.

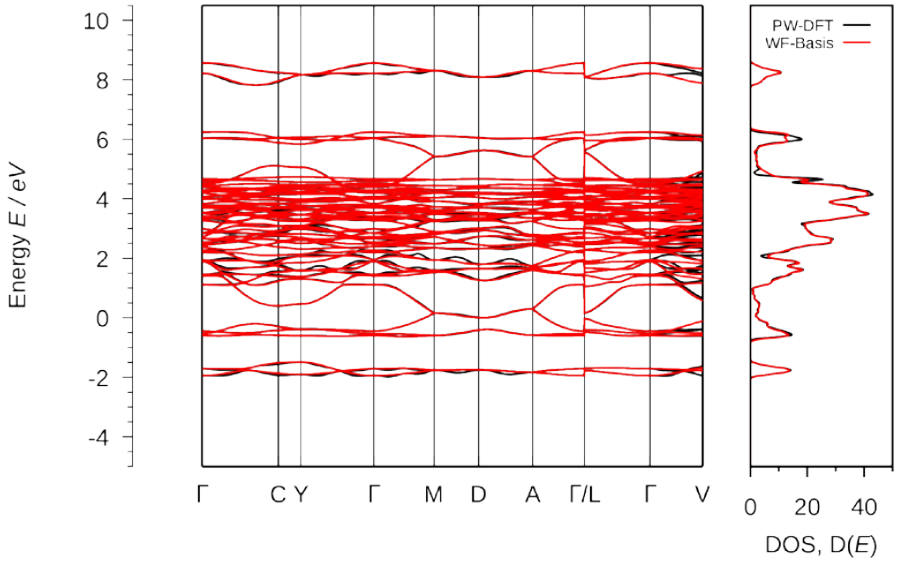

Figure S 10. Left: Electronic band structure of Pb_3F_8. Right: Total Density of States (DOS). Solid red lines: Wannier-interpolated bands. Solid black lines: bands from DFT calculation (DFT-PBE/NCPP).

The obtained projected densities of states were compared to experimentally determined valence band X-ray photoelectron (XP) spectra. The intensities of the calculated pDOSs were adjusted to the experimental data by weighting their intensities with the photoelectron cross sections[30] of the corresponding F 2p and Pb 6s orbitals at the photon energy of 1486.6 eV of the Al K_α radiation and subtracting a Shirley background from the experimental data.

Basis set details for the CRYSTAL17 calculations

F: The TZVP level basis set was taken from a previous study.[31]

Pb: The def2-TZVP basis set with a 60-electron effective core potential was used as a starting point.[19] We fixed the exponents of the outermost s and p functions to 0.09 and reoptimized the exponents of the other s and p functions in the valence space for the lead atom in its ground state. Finally, the outermost s and p functions were combined into one sp-type function. The resulting energy loss with respect to the original molecular basis set is 4.4 mH. The exponent of the outermost d-function was increased from 0.115 to 0.141. The energy cost of this change was only 0.03 mH. The steep f-type polarization function with an exponent of 1.0 was removed. The final basis set in CRYSTAL input format is as follows:

```
282 13
INPUT
22. 0 2 4 4 2 2
12.296303 281.285499 0
8.632634   62.520217 0
10.241790  72.276897 0
8.924176  144.591083 0
6.581342    4.758693 0
6.255403    9.940621 0
7.754336   35.848507 0
7.720281   53.724342 0
4.970264   10.115256 0
4.563789   14.833731 0
3.887512   12.209892 0
3.811963   16.190291 0
5.691577   -9.096665 0
5.715567  -11.531996 0
0 0 4 2.0 1.0
  591.61124370      0.22126521076E-03
  46.757232559      0.56961959130E-02
  20.746462696     -0.21374063831
  14.610796419      0.40502620616
0 0 2 2.0 1.0
  20.181581827     -0.83541883299E-01
  6.4652701641      0.97910892388
0 0 1 0.0 1.0
 1.6683946428       1.0000000000
0 0 1 0.0 1.0
 0.80992082883      1.0000000000
0 0 1 0.0 1.0
 0.23931594794      1.0000000000
0 1 1 0.0 1.0
 0.09             1.0 1.0
0 2 3 6.0 1.0
  15.189102118      0.61952303583
  14.693144415     -0.72498497086
  6.8705890048      0.37680007984
0 2 3 2.0 1.0
  2.2028784073      0.40196284806
  1.2204723142      0.46058131862
 0.63442046718      0.19367655397
0 2 1 0.0 1.0
  0.28121361746     1.0000000000
0 3 6 10.0 1.0
  61.315369628      0.33870800787E-03
  12.372195840      0.13788683942E-01
  6.9254944983     -0.75979608103E-01
  2.3319539939      0.28113784298
  1.2108730003      0.44474512269
 0.60090478506      0.35326874351
0 3 1 0.0 1.0
 0.28135869813      1.0000000000
0 3 1 0.0 1.0
 0.140679349065     1.0000000000
0 4 1 0.0 1.0
 0.28962          1.0000000000
```

P10

Structural Optimization

We have optimized the crystal structure of Pb_3F_8 and PbF_2 with DFT using the hybrid functional PBE0. The results of the optimization are collected in Table S 8 to Table S 11. Overall, the structural data agrees well with the experimental results. The lattice parameters and the volume of the unit cell are overestimated by DFT by 1 % to 2 %. This is probably due to the negligence of relativistic effects in the calculations that should result in a contraction of the Pb 6s orbitals. This also effects the atomic distances that are overestimated by approximately 2 pm by theory. In case of Pb_3F_8 the calculated Pb(IV)−F distances range from 2.080 Å to 2.088 Å compared to experimental distances ranging from 2.048(3) to 2.063(3) Å. In case of Pb(II) DFT yield Pb(IV)−F distances of 2.359 Å to 2.632 Å compared to 2.330(3) to 2.651(3) Å from experiment.

Table S 8. Comparison of experimental cell parameters of Pb_3F_8 (*I*2/*a*, *mS*44) at 100 K with the results of DFT structure optimization (DFT-PBE0/TZVP) at 0 K

	Experiment	DFT	Difference Δ / %
a / Å	8.782(2)	8.89	+1.2
b / Å	7.495(2)	7.56	+0.9
c / Å	10.192(5)	10.33	+1.0
ß / °	98.76(3)	98.40	−0.4
V / Å^3	673.77(8)	686.82	+1.9

Table S 9. Comparison of experimental atomic positions in fractional coordinates of Pb_3F_8 (*I*2/*a*, *mS*44) at 100 K with the results of DFT structure optimization (DFT-PBE0/TZVP) at 0 K.

Atom	Wyckoff	Site sym.		*x*	*y*	*z*
Pb(1)	4*e*	2	Exp.	1/4	0.58692(4)	1/2
			DFT	1/4	0.587	1/2
Pb(2)	8*f*	1	Exp.	0.41214(2)	0.07912(2)	0.65692(2)
			DFT	0.410	0.078	0.656
F(1)	8*f*	1	Exp.	0.2241(4)	0.3868(4)	0.3601(3)
			DFT	0.223	0.385	0.361
F(2)	8*f*	1	Exp.	0.3622(3)	0.0394(4)	0.4277(3)
			DFT	0.362	0.035	0.428
F(3)	8*f*	1	Exp.	0.0579(4)	0.6351(4)	0.5859(3)
			DFT	0.059	0.634	0.590
F(4)	8*f*	1	Exp.	0.3669(4)	0.7490(4)	0.6452(3)
			DFT	0.369	0.748	0.644

Table S 10. Comparison of experimental cell parameters of PbF_2 (*Pnma*, *oP*12) at 293 K with the results of DFT structure optimization (DFT-PBE0/TZVP) at 0 K.

	Experiment	DFT	Difference Δ / %
a / Å	6.4567(1)	6.484	+0.4
b / Å	3.9071(5)	3.909	+0.1
c / Å	7.666(1)	7.743	+1.0
V / Å^3	193.39	196.24	+1.5

Table S 11. Comparison of experimental atomic positions in fractional coordinates of PbF_2 (*Pnma*, *oP*12) at 298 K with the results of DFT structure optimization (DFT-PBE0/TZVP) at 0 K.

Atom	Wyckoff	Site sym.		*x*	*y*	*z*
Pb	4*c*	.*m*.	Exp.	0.246(3)	1/4	0.3933(5)
			DFT	0.243	1/4	0.400
F(1)	4*c*	.*m*.	Exp.	0.109(7)	1/4	0.051(7)
			DFT	0.141	1/4	0.067
F(2)	4*c*	.*m*.	Exp.	0.011(8)	1/4	0.650(6)
			DFT	0.021	1/4	0.648

Optimized geometries in CRYSTAL input format

The optimized geometries of Pb_3F_8 in CRYSTAL input format:

```
Pb3F8 P21/c
CRYSTAL
0 0 0
14
5.43382754 5.45042112 13.49734191 110.601641
6
282 3.544324421267E-01  3.552484713783E-02  3.371459639870E-01
282 0.0000 0.0000 0.0000
9   -2.192906516313E-03 -4.814423038974E-01  3.449861753130E-01
9    2.255261635756E-01 -3.166917143964E-01  3.938616342148E-02
9    4.127833958637E-01  3.901304742516E-01  2.579705030519E-01
9    3.376138871129E-01  2.062908644521E-01  3.119245407245E-02
```

The optimized geometries of PbF_2 in CRYSTAL input format:

```
PbF2 Pnma
CRYSTAL
0 0 0
62
6.48416408 3.90862526 7.74313041
3
282 2.438503876734E-01  2.500000000000E-01  4.001980726789E-01
9   2.083538578373E-02  2.500000000000E-01 -3.519218410496E-01
9   1.410241797137E-01  2.500000000000E-01  6.733279160078E-02
```

P10

Literature

[1] *WinXPOW*, STOE & Cie GmbH, Hilpertstrasse 10, 64295 Darmstadt, Germany, **2015**.

[2] A. A. Coelho, *J. Appl. Crystallogr.* **2018**, *51*, 210–218.

[3] *X-Area*, STOE & Cie GmbH, Darmstadt, Germany, **2018**.

[4] G. M. Sheldrick, *Acta Crystallogr., Sect. A: Found. Adv.* **2015**, *71*, 3–8.

[5] G. M. Sheldrick, *Acta Crystallogr., Sect. C: Struct. Chem.* **2015**, *71*, 3–8.

[6] *OriginPro 2017*, OriginLAb Corporation, **2017**.

[7] M. Nespolo, B. Guillot, *J. Appl. Crystallogr.* **2016**, *49*, 317–321.

[8] *OPUS V7.2*, Bruker Optik GmbH, Ettlingen, Germany, **2012**.

[9] R. K. Harris, E. D. Becker, *Journal of Magnetic Resonance* **2002**, *156*, 323–326.

[10] R. K. Harris, E. D. Becker, *Journal of Magnetic Resonance* **2002**, *156*, 323–326.

[11] M. Robin Bendall, R. E. Gordon, *Journal of Magnetic Resonance (1969)* **1983**, *53*, 365–385.

[12] Y. S. Avadhut, J. Weber, E. Hammarberg, C. Feldmann, I. Schellenberg, R. Pöttgen, J. Schmedt auf der Günne, *Chemistry of Materials* **2011**, 110222062928031.

[13] M. Bak, J. T. Rasmussen, N. C. Nielsen, *J. Magn. Reson.* **2000**, *147*, 296–330.

[14] W. E. Morgan, J. R. Van Wazer, *J. Phys. Chem.* **1973**, *77*, 964–969.

[15] F. Schaefers, M. Mertin, M. Gorgoi, *Rev. Sci. Instrum.* **2007**, *78*, 123102.

[16] M. Gorgoi, S. Svensson, F. Schäfers, G. Öhrwall, M. Mertin, P. Bressler, O. Karis, H. Siegbahn, A. Sandell, H. Rensmo, et al., *Nucl. Instruments Methods Phys. Res. Sect. A Accel. Spectrometers, Detect. Assoc. Equip.* **2009**, *601*, 48–53.

[17] R. Dovesi, A. Erba, R. Orlando, C. M. Zicovich-Wilson, B. Civalleri, L. Maschio, M. Rérat, S. Casassa, J. Baima, S. Salustro, et al., *WIREs Comput. Mol. Sci.* **2018**, *8*, 1–36.

[18] C. Adamo, V. Barone, *J. Chem. Phys.* **1999**, *110*, 6158–6170.

[19] F. Weigend, R. Ahlrichs, *Phys. Chem. Chem. Phys.* **2005**, *7*, 3297–3305.

[20] F. Pascale, C. M. Zicovich-Wilson, F. López Gejo, B. Civalleri, R. Orlando, R. Dovesi, *J. Comput. Chem.* **2004**, *25*, 888–897.

[21] C. M. Zicovich-Wilson, F. Pascale, C. Roetti, V. R. Saunders, R. Orlando, R. Dovesi, *J. Comput. Chem.* **2004**, *25*, 1873–1881.

[22] L. Maschio, B. Kirtman, M. Rérat, R. Orlando, R. Dovesi, *J. Chem. Phys.* **2013**, *139*, 164101.

[23] L. Maschio, B. Kirtman, M. Rérat, R. Orlando, R. Dovesi, *J. Chem. Phys.* **2013**, *139*, 164102.

[24] *Jmol: An Open-Source Java Viewer for Chemical Structures in 3D. Http://Www.Jmol.Org/*, Jmol Team, **2017**.

[25] P. Giannozzi et al, *Journal of Physics: Condensed Matter* **2009**, *21*, 1–19.

[26] M. Schlipf, F. Gygi, *Computer Physics Communications* **2015**, *196*, 36–44.

[27] J. P. Perdew, K. Burke, M. Ernzerhof, *Phys. Rev. Lett.* **1996**, *77*, 3865–3868.

[28] F. Gygi, A. Baldereschi, *Phys. Rev. B* **1986**, *34*, 4405–4408.

P10

[29] A. A. Mostofi, J. R. Yates, G. Pizzi, Y.-S. Lee, I. Souza, D. Vanderbilt, N. Marzari, *Computer Physics Communications* **2014**, *185*, 2309–2310.

[30] J. J. Yeh, I. Lindau, *Atomic Data and Nuclear Data Tables* **1985**, *32*, 1–155.

[31] A. J. Karttunen, T. Tynell, M. Karppinen, *J. Phys. Chem. C* **2015**, *119*, 13105–13114.

B Permissions of Use for the Included Publications

In the following list, the copyright status of used figures and all articles that are part of this thesis is given. For those publications, where it applies, the permission of use is appended on the following pages.

Fig. 1.2 Adapted with permission from ref. [61]. Copyright 2015 John Wiley & Sons, Inc.

Fig. 2.4 Reprinted with permission from ref. [104]. Copyright 2007 John Wiley & Sons, Inc.

P1 Published by the American Physical Society under the terms of the Creative Commons Attribution 4.0 International license. This copyright allows the use of this article, as long as it is properly cited [221].

P2 Reprinted with permission from ref. [197]. Copyright 2020 American Chemical Society.

P3 Not yet published, therefore no permission is necessary [222].

P4 Not yet accepted, therefore no permission is necessary [223].

P5 Copyright IOP Publishing. Reproduced with permission. All rights reserved [224].

P6 Republished with permission of the Royal Society of Chemistry, from [225], Copyright 2019; permission conveyed through Copyright Clearance Center, Inc.

P7 Not yet published, therefore no permission is necessary [226].

P8 Not yet published, therefore no permission is necessary [227].

P9 Not yet published, therefore no permission is necessary [228].

P10 Available under the terms of the Creative Commons Attribution License (CC BY). Use, distribution, and reproduction is permitted, provided that the article is properly cited [229].

JOHN WILEY AND SONS LICENSE
TERMS AND CONDITIONS

Aug 13, 2020

This Agreement between Philipps-Universität Marburg -- Stefan Renato Kachel ("You") and John Wiley and Sons ("John Wiley and Sons") consists of your license details and the terms and conditions provided by John Wiley and Sons and Copyright Clearance Center.

License Number	4887081111047
License date	Aug 13, 2020
Licensed Content Publisher	John Wiley and Sons
Licensed Content Publication	Chemistry - A European Journal
Licensed Content Title	Efficient Syntheses of Novel Fluoro-Substituted Pentacenes and Azapentacenes: Molecular and Solid-State Properties
Licensed Content Author	Ulrich Koert, Gregor Witte, Klaus Harms, et al
Licensed Content Date	Aug 6, 2015
Licensed Content Volume	21
Licensed Content Issue	39
Licensed Content Pages	14
Type of use	Dissertation/Thesis
Requestor type	University/Academic

Format	Print and electronic
Portion	Figure/table
Number of figures/tables	1
Will you be translating?	No
Title	Investigation of Metal/Organic Interfaces and Metalation Reactions of Organic Semiconductors
Institution name	Philipps-Universität Marburg
Expected presentation date	Oct 2020
Portions	Figure 2
Requestor Location	Philipps-Universität Marburg Hans-Meerweinstraße 4 Fachbereich Chemie AG Gottfried Marburg, Hesse 35032 Germany Attn: Stefan Renato Kachel
Publisher Tax ID	EU826007151
Total	0.00 EUR

Terms and Conditions

TERMS AND CONDITIONS

This copyrighted material is owned by or exclusively licensed to John Wiley & Sons, Inc. or one of its group companies (each a"Wiley Company") or handled on behalf of a society with which a Wiley Company has exclusive publishing rights in relation to a particular work (collectively "WILEY"). By clicking "accept" in connection with completing this licensing transaction, you agree that the following terms and conditions apply to this transaction (along with the billing and payment terms and conditions established by the Copyright Clearance Center Inc., ("CCC's Billing and Payment terms and conditions"), at the time that you opened your RightsLink account (these are available at any time at

http://myaccount.copyright.com).

Terms and Conditions

- The materials you have requested permission to reproduce or reuse (the "Wiley Materials") are protected by copyright.
- You are hereby granted a personal, non-exclusive, non-sub licensable (on a stand-alone basis), non-transferable, worldwide, limited license to reproduce the Wiley Materials for the purpose specified in the licensing process. This license, **and any CONTENT (PDF or image file) purchased as part of your order,** is for a one-time use only and limited to any maximum distribution number specified in the license. The first instance of republication or reuse granted by this license must be completed within two years of the date of the grant of this license (although copies prepared before the end date may be distributed thereafter). The Wiley Materials shall not be used in any other manner or for any other purpose, beyond what is granted in the license. Permission is granted subject to an appropriate acknowledgement given to the author, title of the material/book/journal and the publisher. You shall also duplicate the copyright notice that appears in the Wiley publication in your use of the Wiley Material. Permission is also granted on the understanding that nowhere in the text is a previously published source acknowledged for all or part of this Wiley Material. Any third party content is expressly excluded from this permission.
- With respect to the Wiley Materials, all rights are reserved. Except as expressly granted by the terms of the license, no part of the Wiley Materials may be copied, modified, adapted (except for minor reformatting required by the new Publication), translated, reproduced, transferred or distributed, in any form or by any means, and no derivative works may be made based on the Wiley Materials without the prior permission of the respective copyright owner.**For STM Signatory Publishers clearing permission under the terms of the STM Permissions Guidelines only, the terms of the license are extended to include subsequent editions and for editions in other languages, provided such editions are for the work as a whole in situ and does not involve the separate exploitation of the permitted figures or extracts,** You may not alter, remove or suppress in any manner any copyright, trademark or other notices displayed by the Wiley Materials. You may not license, rent, sell, loan, lease, pledge, offer as security, transfer or assign the Wiley Materials on a stand-alone basis, or any of the rights granted to you hereunder to any other person.
- The Wiley Materials and all of the intellectual property rights therein shall at all times remain the exclusive property of John Wiley & Sons Inc, the Wiley Companies, or their respective licensors, and your interest therein is only that of having possession of and the right to reproduce the Wiley Materials pursuant to Section 2 herein during the continuance of this Agreement. You agree that you own no right, title or interest in or to the Wiley Materials or any of the intellectual property rights therein. You shall have no rights hereunder other than the license as provided for above in Section 2. No right, license or interest to any trademark, trade name, service mark or other branding ("Marks") of WILEY or its licensors is granted hereunder, and you agree that you shall not assert any such right, license or interest with respect thereto
- NEITHER WILEY NOR ITS LICENSORS MAKES ANY WARRANTY OR REPRESENTATION OF ANY KIND TO YOU OR ANY THIRD PARTY, EXPRESS, IMPLIED OR STATUTORY, WITH RESPECT TO THE MATERIALS OR THE ACCURACY OF ANY INFORMATION CONTAINED IN THE MATERIALS, INCLUDING, WITHOUT LIMITATION, ANY IMPLIED

WARRANTY OF MERCHANTABILITY, ACCURACY, SATISFACTORY QUALITY, FITNESS FOR A PARTICULAR PURPOSE, USABILITY, INTEGRATION OR NON-INFRINGEMENT AND ALL SUCH WARRANTIES ARE HEREBY EXCLUDED BY WILEY AND ITS LICENSORS AND WAIVED BY YOU.

- WILEY shall have the right to terminate this Agreement immediately upon breach of this Agreement by you.
- You shall indemnify, defend and hold harmless WILEY, its Licensors and their respective directors, officers, agents and employees, from and against any actual or threatened claims, demands, causes of action or proceedings arising from any breach of this Agreement by you.
- IN NO EVENT SHALL WILEY OR ITS LICENSORS BE LIABLE TO YOU OR ANY OTHER PARTY OR ANY OTHER PERSON OR ENTITY FOR ANY SPECIAL, CONSEQUENTIAL, INCIDENTAL, INDIRECT, EXEMPLARY OR PUNITIVE DAMAGES, HOWEVER CAUSED, ARISING OUT OF OR IN CONNECTION WITH THE DOWNLOADING, PROVISIONING, VIEWING OR USE OF THE MATERIALS REGARDLESS OF THE FORM OF ACTION, WHETHER FOR BREACH OF CONTRACT, BREACH OF WARRANTY, TORT, NEGLIGENCE, INFRINGEMENT OR OTHERWISE (INCLUDING, WITHOUT LIMITATION, DAMAGES BASED ON LOSS OF PROFITS, DATA, FILES, USE, BUSINESS OPPORTUNITY OR CLAIMS OF THIRD PARTIES), AND WHETHER OR NOT THE PARTY HAS BEEN ADVISED OF THE POSSIBILITY OF SUCH DAMAGES. THIS LIMITATION SHALL APPLY NOTWITHSTANDING ANY FAILURE OF ESSENTIAL PURPOSE OF ANY LIMITED REMEDY PROVIDED HEREIN.
- Should any provision of this Agreement be held by a court of competent jurisdiction to be illegal, invalid, or unenforceable, that provision shall be deemed amended to achieve as nearly as possible the same economic effect as the original provision, and the legality, validity and enforceability of the remaining provisions of this Agreement shall not be affected or impaired thereby.
- The failure of either party to enforce any term or condition of this Agreement shall not constitute a waiver of either party's right to enforce each and every term and condition of this Agreement. No breach under this agreement shall be deemed waived or excused by either party unless such waiver or consent is in writing signed by the party granting such waiver or consent. The waiver by or consent of a party to a breach of any provision of this Agreement shall not operate or be construed as a waiver of or consent to any other or subsequent breach by such other party.
- This Agreement may not be assigned (including by operation of law or otherwise) by you without WILEY's prior written consent.
- Any fee required for this permission shall be non-refundable after thirty (30) days from receipt by the CCC.
- These terms and conditions together with CCC's Billing and Payment terms and conditions (which are incorporated herein) form the entire agreement between you and WILEY concerning this licensing transaction and (in the absence of fraud) supersedes all prior agreements and representations of the parties, oral or written. This Agreement may not be amended except in writing signed by both parties. This Agreement shall be binding upon and inure to the benefit of the parties' successors, legal representatives,

and authorized assigns.

- In the event of any conflict between your obligations established by these terms and conditions and those established by CCC's Billing and Payment terms and conditions, these terms and conditions shall prevail.
- WILEY expressly reserves all rights not specifically granted in the combination of (i) the license details provided by you and accepted in the course of this licensing transaction, (ii) these terms and conditions and (iii) CCC's Billing and Payment terms and conditions.
- This Agreement will be void if the Type of Use, Format, Circulation, or Requestor Type was misrepresented during the licensing process.
- This Agreement shall be governed by and construed in accordance with the laws of the State of New York, USA, without regards to such state's conflict of law rules. Any legal action, suit or proceeding arising out of or relating to these Terms and Conditions or the breach thereof shall be instituted in a court of competent jurisdiction in New York County in the State of New York in the United States of America and each party hereby consents and submits to the personal jurisdiction of such court, waives any objection to venue in such court and consents to service of process by registered or certified mail, return receipt requested, at the last known address of such party.

WILEY OPEN ACCESS TERMS AND CONDITIONS

Wiley Publishes Open Access Articles in fully Open Access Journals and in Subscription journals offering Online Open. Although most of the fully Open Access journals publish open access articles under the terms of the Creative Commons Attribution (CC BY) License only, the subscription journals and a few of the Open Access Journals offer a choice of Creative Commons Licenses. The license type is clearly identified on the article.

The Creative Commons Attribution License

The Creative Commons Attribution License (CC-BY) allows users to copy, distribute and transmit an article, adapt the article and make commercial use of the article. The CC-BY license permits commercial and non-

Creative Commons Attribution Non-Commercial License

The Creative Commons Attribution Non-Commercial (CC-BY-NC)License permits use, distribution and reproduction in any medium, provided the original work is properly cited and is not used for commercial purposes.(see below)

Creative Commons Attribution-Non-Commercial-NoDerivs License

The Creative Commons Attribution Non-Commercial-NoDerivs License (CC-BY-NC-ND) permits use, distribution and reproduction in any medium, provided the original work is properly cited, is not used for commercial purposes and no modifications or adaptations are made. (see below)

Use by commercial "for-profit" organizations

Use of Wiley Open Access articles for commercial, promotional, or marketing purposes requires further explicit permission from Wiley and will be subject to a fee.

Further details can be found on Wiley Online Library http://olabout.wiley.com/WileyCDA/Section/id-410895.html

Other Terms and Conditions:

v1.10 Last updated September 2015

Questions? customercare@copyright.com or +1-855-239-3415 (toll free in the US) or +1-978-646-2777.

Copyright Clearance Center Marketplace™

Order Number: 1056147
Order Date: 17 Aug 2020

Payment Information

Stefan Renato Kachel
kachel@students.uni-marburg.de
Payment method: Invoice

Billing Address:
Mr. Stefan Renato Kachel
Philipps-Universität Marburg
Hans-Meerweinstraße 4
Fachbereich Chemie
AG Gottfried
Marburg, Hesse 35032
Germany

+49 64212822548
kachel@students.uni-marburg.de

Customer Location:
Mr. Stefan Renato Kachel
Philipps-Universität Marburg
Hans-Meerweinstraße 4
Fachbereich Chemie
AG Gottfried
Marburg, Hesse 35032
Germany

Order Details

1. Spectroscopy in catalysis : an introduction

Billing Status: Open

Order license ID	1056147-1
Order detail status	Completed
ISBN-13	9783527316519
Type of use	Republish in other published product
Publisher	Wiley-VCH,John Wiley, distributor]
Portion	Chart/graph/table/figure

0,00 EUR
Republication Permission

LICENSED CONTENT

Publication Title	Spectroscopy in catalysis : an introduction	**Country**	Germany
		Rightsholder	John Wiley & Sons - Books
Author/Editor	Niemantsverdriet, J. W.	**Publication Type**	Book
Date	01/01/2007		
Language	English		

REQUEST DETAILS

Portion Type	Chart/graph/table /figure	**Distribution**	Worldwide
		Translation	Original language of publication
Number of charts / graphs / tables / figures requested	1	**Copies for the disabled?**	No
Format (select all that apply)	Print,Electronic	**Minor editing privileges?**	No

Who will republish the content?	Not-for-profit entity	**Incidental promotional use?**	No
Duration of Use	Life of current edition	**Currency**	EUR
Lifetime Unit Quantity	Up to 499		
Rights Requested	Main product		

NEW WORK DETAILS

Title	Investigations of Metal/Organic Interfaces and Metalation Reactions of Organic Semiconductors	**Produced by**	Philipps-Universität Marburg
		Expected publication date	2020-10-01
Author	Stefan Renato Kachel		

ADDITIONAL DETAILS

The requesting person / organization to appear on the license	Stefan Renato Kachel		

REUSE CONTENT DETAILS

Title, description or numeric reference of the portion(s)	Fig. 2.10	**Title of the article/chapter the portion is from**	Temperature-Programmed Techniques
Editor of portion(s)	J. W. Niemantsverdriet	**Author of portion(s)**	Niemantsverdriet, J. W.
Volume of serial or monograph	Third Edition	**Publication date of portion**	2007-01-01
Page or page range of portion	27		

John Wiley & Sons - Books Terms and Conditions

No right, license or interest to any trademark, trade name, service mark or other branding ("Marks") of WILEY or its licensors is granted hereunder, and you agree that you shall not assert any such right, license or interest with respect thereto. You may not alter, remove or suppress in any manner any copyright, trademark or other notices displayed by the Wiley material. This Agreement will be void if the Type of Use, Format, Circulation, or Requestor Type was misrepresented during the licensing process. In no instance may the total amount of Wiley Materials used in any Main Product, Compilation or Collective work comprise more than 5% (if figures/tables) or 15% (if full articles/chapters) of the (entirety of the) Main Product, Compilation or Collective Work. Some titles may be available under an Open Access license. It is the Licensors' responsibility to identify the type of Open Access license on which the requested material was published, and comply fully with the terms of that license for the type of use specified Further details can be found on Wiley Online Library http://olabout.wiley.com/WileyCDA/Section/id-410895.html.

Total Items: 1

Subtotal: 0,00 EUR

Order Total: 0,00 EUR

Copyright Clearance Center RightsLink®

Home | Help | Email Support | Stefan Renato Kachel

ACS Publications
Most Trusted. Most Cited. Most Read.

Chemisorption and Physisorption at the Metal/Organic Interface: Bond Energies of Naphthalene and Azulene on Coinage Metal Surfaces

Author: Stefan R. Kachel, Benedikt P. Klein, Juliana M. Morbec, et al
Publication: The Journal of Physical Chemistry C
Publisher: American Chemical Society
Date: Apr 1, 2020

PERMISSION/LICENSE IS GRANTED FOR YOUR ORDER AT NO CHARGE

This type of permission/license, instead of the standard Terms & Conditions, is sent to you because no fee is being charged for your order. Please note the following:

- Permission is granted for your request in both print and electronic formats, and translations.
- If figures and/or tables were requested, they may be adapted or used in part.
- Please print this page for your records and send a copy of it to your publisher/graduate school.
- Appropriate credit for the requested material should be given as follows: "Reprinted (adapted) with permission from (COMPLETE REFERENCE CITATION). Copyright (YEAR) American Chemical Society." Insert appropriate information in place of the capitalized words.
- One-time permission is granted only for the use specified in your request. No additional uses are granted (such as derivative works or other editions). For any other uses, please submit a new request.

BACK CLOSE WINDOW

Copyright Clearance Center Marketplace™

Order Number: 1061814
Order Date: 09 Sep 2020

Payment Information

Stefan Renato Kachel
kachel@students.uni-marburg.de
Payment method: Invoice

Billing Address:
Mr. Stefan Renato Kachel
Philipps-Universität Marburg
Hans-Meerweinstraße 4
Fachbereich Chemie
AG Gottfried
Marburg, Hesse 35032
Germany

+49 64212822548
kachel@students.uni-marburg.de

Customer Location:
Mr. Stefan Renato Kachel
Philipps-Universität Marburg
Hans-Meerweinstraße 4
Fachbereich Chemie
AG Gottfried
Marburg, Hesse 35032
Germany

Order Details

1. Journal of Physics : Condensed Matter

Billing Status: Open

Article: Reactive metal-organic interfaces studied with hard x-ray photoelectron spectroscopy: controlled formation of metalloporphyrin interphase layers during metal vapor deposition onto porphyrin films.

Order license ID	1061814-1
Order detail status	Completed
ISSN	0953-8984
Type of use	Republish in a thesis/dissertation
Publisher	IOP Publishing
Portion	Chapter/article

0,00 EUR
Republication Permission

LICENSED CONTENT

Publication Title	Journal of Physics : Condensed Matter	**Rightsholder**	IOP Publishing, Ltd
Article Title	Reactive metal-organic interfaces studied with hard x-ray photoelectron spectroscopy: controlled formation of metalloporphyrin interphase layers during metal vapor deposition onto porphyrin films.	**Publication Type**	Journal
		Start Page	094002
		Issue	9
		Volume	31

Author/Editor	Institute of Physics (Great Britain)
Date	01/01/1989
Language	English
Country	United Kingdom of Great Britain and Northern Ireland

REQUEST DETAILS

Portion Type	Chapter/article	**Rights Requested**	Main product
Page range(s)	1-10	**Distribution**	Worldwide
Total number of pages	10	**Translation**	Original language of publication
Format (select all that apply)	Print,Electronic	**Copies for the disabled?**	No
Who will republish the content?	Author of requested content	**Minor editing privileges?**	No
Duration of Use	Life of current edition	**Incidental promotional use?**	No
Lifetime Unit Quantity	Up to 499	**Currency**	EUR

NEW WORK DETAILS

Title	Investigations of Metal/Organic Interfaces and Metalation Reactions of Organic Semiconductors	**Institution name**	Philipps-Universität Marburg
		Expected presentation date	2020-10-01
Instructor name	Stefan Renato Kachel		

ADDITIONAL DETAILS

The requesting person / organization to appear on the license	Stefan Renato Kachel

REUSE CONTENT DETAILS

Title, description or numeric reference of the portion(s)	whole article	**Title of the article/chapter the portion is from**	Reactive metal-organic interfaces studied with hard x-ray photoelectron spectroscopy: controlled formation of metalloporphyrin interphase layers during metal vapor deposition onto porphyrin films.
Editor of portion(s)	Gottfried, J Michael; Hampp, Norbert; Riedel, René; Müller, Philipp; Bock, Nicolas; Klein, Benedikt P; Kachel, Stefan R; Schmid, Martin		
Volume of serial or monograph	31	**Author of portion(s)**	Gottfried, J Michael; Hampp, Norbert; Riedel, René; Müller, Philipp; Bock, Nicolas; Klein, Benedikt P; Kachel, Stefan R; Schmid, Martin
Page or page range of portion	094002		

Issue, if republishing an article from a serial	9
Publication date of portion	2019-03-06

IOP Publishing, Ltd Terms and Conditions

These special terms and conditions are in addition to the standard terms and conditions for CCC's Republication Service and, together with those standard terms and conditions, govern the use of the Works. As the User you will make all reasonable efforts to contact the author(s) of the article which the Work is to be reused from, to seek consent for your intended use. Contacting one author who is acting expressly as authorised agent for their co-author(s) is acceptable. User will reproduce the following wording prominently alongside the Work: the source of the Work, including author, article title, title of journal, volume number, issue number (if relevant), page range (or first page if this is the only information available) and date of first publication. This information can be contained in a footnote or reference note; and a link back to the article (via DOI); and if practicable, and IN ALL CASES for new works published under any of the Creative Commons licences, the words "© IOP Publishing. Reproduced with permission. All rights reserved" Without the express permission of the author(s) and the Rightsholder of the article from which the Work is to be reused, User shall not use it in any way which, in the opinion of the Rightsholder, could: (i) distort or alter the author(s)' original intention(s) and meaning; (ii) be prejudicial to the honour or reputation of the author(s); and/or (iii) imply endorsement by the author(s) and/or the Rightsholder. This licence does not apply to any article which is credited to another source and which does not have the copyright line '© IOP Publishing Ltd'. User must check the copyright line of the article from which the Work is to be reused to check that IOP Publishing Ltd has all the necessary rights to be able to grant permission. User is solely responsible for identifying and obtaining separate licences and permissions from the copyright owner for reuse of any such third party material/figures which the Rightsholder is not the copyright owner of. The Rightsholder shall not reimburse any fees which User pays for a republication license for such third party content. This licence does not apply to any material/figure which is credited to another source in the Rightsholder's publication or has been obtained from a third party. User must check the Version of Record of the article from which the Work is to be reused, to check whether any of the material in the Work is third party material. Third party citations and/or copyright notices and/or permissions statements may not be included in any other version of the article from which the Work is to be reused and so cannot be relied upon by the User. User is solely responsible for identifying and obtaining separate licences and permissions from the copyright owner for reuse of any such third party material/figures where the Rightsholder is not the copyright owner. The Rightsholder shall not reimburse any fees which User pays for a republication license for such third party content. User and CCC acknowledge that the Rightsholder may, from time to time, make changes or additions to these special terms and conditions without express notification, provided that these shall not apply to permissions already secured and paid for by User prior to such change or addition. User acknowledges that the Rightsholder (which includes companies within its group and third parties for whom it publishes its titles) may make use of personal data collected through the service in the course of their business. If User is the author of the Work, User may automatically have the right to reuse it under the rights granted back when User transferred the copyright in the article to the Rightsholder. User should check the copyright form and the relevant author rights policy to check whether permission is required. If User is the author of the Work and does require permission for proposed reuse of the Work, User should select 'Author of requested content' as the Requestor Type. The Rightsholder shall not reimburse any fees which User pays for a republication license. If User is the author of the article which User wishes to reuse in User's thesis or dissertation, the republication licence covers the right to include the Accepted Manuscript version (not the Version of Record) of the article. User must include citation details and, for online use, a link to the Version of Record of the article on the Rightsholder's website. User may need to obtain separate permission for any third party content included within the article. User must check this with the copyright owner of such third party content. User may not include the article in a thesis or dissertation which is published by ProQuest. Any other commercial use of User's thesis or dissertation containing the article would also need to be expressly notified in writing to the Rightsholder at the time of request and would require separate written permission from the Rightsholder. User does not need to request permission for Work which has been published under a CC BY licence. User must check the Version of Record of the CC BY article from which the Work is to be reused, to check whether any of the material in the Work is third party material and so not published under the CC BY licence. User is solely responsible for identifying and obtaining separate licences and permissions from the copyright owner for reuse of any such third party material/figures. The Rightsholder shall not reimburse any fees which User pays for such licences and permissions. As well as CCC, the Rightsholder shall have the right to bring any legal action that it deems necessary to enforce its rights should it consider that the Work infringes those rights in any way. For STM Signatories ONLY (as agreed as part of the STM Guidelines) Any licence granted for a particular edition of a Work will apply also to subsequent editions of it and for editions in other languages, provided such editions are for the Work as a whole in situ and do not involve the separate exploitation of the permitted illustrations or excerpts.

IOP Publishing, Ltd Special Terms

When you transferred the copyright in your article to IOP, we granted back to you certain rights, including the right to include all or part of the Final Published Version of the article within any thesis or dissertation. Please note you may need to obtain separate permission for any third party content you included within your article. Please include citation details, "© IOP Publishing. Reproduced with permission. All rights reserved" and for online use, a link to the Version of Record. The only restriction is that if, at a later date, you wanted your thesis/dissertation to be published commercially, further permission would be required.

Total Items: 1

Subtotal: 0,00 EUR

Order Total: 0,00 EUR

Copyright Clearance Center Marketplace™

Royal Society of Chemistry - License Terms and Conditions

This is a License Agreement between Stefan Renato Kachel ("You") and Royal Society of Chemistry ("Publisher") provided by Copyright Clearance Center ("CCC"). The license consists of your order details, the terms and conditions provided by Royal Society of Chemistry, and the CCC terms and conditions.

All payments must be made in full to CCC.

Order Date	04-Sep-2020	Type of Use	Republish in a thesis/dissertation
Order license ID	1060665-1	Publisher	ROYAL SOCIETY OF CHEMISTRY
ISSN	1364-548X	Portion	Chapter/article

LICENSED CONTENT

Publication Title	Chemical communications	Rightsholder	Royal Society of Chemistry
Article Title	Direct synthesis of dilithium tetraphenylporphyrin: facile reaction of a free-base porphyrin with vapor-deposited lithium.	Publication Type	e-Journal
		Start Page	13665
		End Page	13668
		Issue	91
		Volume	55
Author/Editor	Royal Society of Chemistry (Great Britain)		
Date	01/01/1996		
Language	English		
Country	United Kingdom of Great Britain and Northern Ireland		

REQUEST DETAILS

Portion Type	Chapter/article	Rights Requested	Main product
Page range(s)	13665-13668	Distribution	Worldwide
Total number of pages	4	Translation	Original language of publication
Format (select all that apply)	Print, Electronic	Copies for the disabled?	No
Who will republish the content?	Academic institution	Minor editing privileges?	No
Duration of Use	Life of current edition	Incidental promotional use?	No
Lifetime Unit Quantity	Up to 499	Currency	EUR

NEW WORK DETAILS

Title	Investigations of Metal/Organic Interfaces and Metalation Reactions of Organic Semiconductors	Institution name	Philipps-Universität Marburg
		Expected presentation date	2020-10-01
Instructor name	Stefan Renato Kachel		

ADDITIONAL DETAILS

Order reference number	N/A	**The requesting person / organization to appear on the license**	Stefan Renato Kachel

REUSE CONTENT DETAILS

Title, description or numeric reference of the portion(s)	whole article	**Title of the article/chapter the portion is from**	Direct synthesis of dilithium tetraphenylporphyrin: facile reaction of a free-base porphyrin with vapor-deposited lithium.
Editor of portion(s)	Gottfried, Michael; Hutter, Mark; Schröder, Philipp; Herritsch, Jan; Kachel, Stefan Renato; Schöniger, Maik	**Author of portion(s)**	Gottfried, Michael; Hutter, Mark; Schröder, Philipp; Herritsch, Jan; Kachel, Stefan Renato; Schöniger, Maik
Volume of serial or monograph	55		
Page or page range of portion	13665-13668	**Issue, if republishing an article from a serial**	91
		Publication date of portion	2019-10-15

PUBLISHER SPECIAL TERMS AND CONDITIONS

Permission is granted as long as the article is fully acknowledged and a link is given back to the article on our Platform. Please go to rsc.li/permissions for details. Please note that if the material specified above or any part of it appears with credit or acknowledgement to a third party then you must also secure permission from that third party before reproducing that material.

CCC Republication Terms and Conditions

1. Description of Service; Defined Terms. This Republication License enables the User to obtain licenses for republication of one or more copyrighted works as described in detail on the relevant Order Confirmation (the "Work(s)"). Copyright Clearance Center, Inc. ("CCC") grants licenses through the Service on behalf of the rightsholder identified on the Order Confirmation (the "Rightsholder"). "Republication", as used herein, generally means the inclusion of a Work, in whole or in part, in a new work or works, also as described on the Order Confirmation. "User", as used herein, means the person or entity making such republication.

2. The terms set forth in the relevant Order Confirmation, and any terms set by the Rightsholder with respect to a particular Work, govern the terms of use of Works in connection with the Service. By using the Service, the person transacting for a republication license on behalf of the User represents and warrants that he/she/it (a) has been duly authorized by the User to accept, and hereby does accept, all such terms and conditions on behalf of User, and (b) shall inform User of all such terms and conditions. In the event such person is a "freelancer" or other third party independent of User and CCC, such party shall be deemed jointly a "User" for purposes of these terms and conditions. In any event, User shall be deemed to have accepted and agreed to all such terms and conditions if User republishes the Work in any fashion.

3. Scope of License; Limitations and Obligations.

   3.1. All Works and all rights therein, including copyright rights, remain the sole and exclusive property of the Rightsholder. The license created by the exchange of an Order Confirmation (and/or any invoice) and payment by User of the full amount set forth on that document includes only those rights expressly set forth in the Order Confirmation and in these terms and conditions, and conveys no other rights in the Work(s) to User. All rights not expressly granted are hereby reserved.

   3.2. General Payment Terms: You may pay by credit card or through an account with us payable at the end of the month. If you and we agree that you may establish a standing account with CCC, then the following terms apply: Remit Payment to: Copyright Clearance Center, 29118 Network Place, Chicago, IL 60673-1291. Payments Due: Invoices are payable upon their delivery to you (or upon our notice to you that they are available to you for downloading). After 30 days, outstanding amounts will be subject to a service charge of 1-1/2% per month or, if less, the maximum rate allowed by applicable law. Unless otherwise specifically set forth in the Order Confirmation or in a separate written agreement signed by CCC, invoices are due and

payable on "net 30" terms. While User may exercise the rights licensed immediately upon issuance of the Order Confirmation, the license is automatically revoked and is null and void, as if it had never been issued, if complete payment for the license is not received on a timely basis either from User directly or through a payment agent, such as a credit card company.

3.3. Unless otherwise provided in the Order Confirmation, any grant of rights to User (i) is "one-time" (including the editions and product family specified in the license), (ii) is non-exclusive and non-transferable and (iii) is subject to any and all limitations and restrictions (such as, but not limited to, limitations on duration of use or circulation) included in the Order Confirmation or invoice and/or in these terms and conditions. Upon completion of the licensed use, User shall either secure a new permission for further use of the Work(s) or immediately cease any new use of the Work(s) and shall render inaccessible (such as by deleting or by removing or severing links or other locators) any further copies of the Work (except for copies printed on paper in accordance with this license and still in User's stock at the end of such period).

3.4. In the event that the material for which a republication license is sought includes third party materials (such as photographs, illustrations, graphs, inserts and similar materials) which are identified in such material as having been used by permission, User is responsible for identifying, and seeking separate licenses (under this Service or otherwise) for, any of such third party materials; without a separate license, such third party materials may not be used.

3.5. Use of proper copyright notice for a Work is required as a condition of any license granted under the Service. Unless otherwise provided in the Order Confirmation, a proper copyright notice will read substantially as follows: "Republished with permission of [Rightsholder's name], from [Work's title, author, volume, edition number and year of copyright]; permission conveyed through Copyright Clearance Center, Inc. " Such notice must be provided in a reasonably legible font size and must be placed either immediately adjacent to the Work as used (for example, as part of a by-line or footnote but not as a separate electronic link) or in the place where substantially all other credits or notices for the new work containing the republished Work are located. Failure to include the required notice results in loss to the Rightsholder and CCC, and the User shall be liable to pay liquidated damages for each such failure equal to twice the use fee specified in the Order Confirmation, in addition to the use fee itself and any other fees and charges specified.

3.6. User may only make alterations to the Work if and as expressly set forth in the Order Confirmation. No Work may be used in any way that is defamatory, violates the rights of third parties (including such third parties' rights of copyright, privacy, publicity, or other tangible or intangible property), or is otherwise illegal, sexually explicit or obscene. In addition, User may not conjoin a Work with any other material that may result in damage to the reputation of the Rightsholder. User agrees to inform CCC if it becomes aware of any infringement of any rights in a Work and to cooperate with any reasonable request of CCC or the Rightsholder in connection therewith.

4. Indemnity. User hereby indemnifies and agrees to defend the Rightsholder and CCC, and their respective employees and directors, against all claims, liability, damages, costs and expenses, including legal fees and expenses, arising out of any use of a Work beyond the scope of the rights granted herein, or any use of a Work which has been altered in any unauthorized way by User, including claims of defamation or infringement of rights of copyright, publicity, privacy or other tangible or intangible property.

5. Limitation of Liability. UNDER NO CIRCUMSTANCES WILL CCC OR THE RIGHTSHOLDER BE LIABLE FOR ANY DIRECT, INDIRECT, CONSEQUENTIAL OR INCIDENTAL DAMAGES (INCLUDING WITHOUT LIMITATION DAMAGES FOR LOSS OF BUSINESS PROFITS OR INFORMATION, OR FOR BUSINESS INTERRUPTION) ARISING OUT OF THE USE OR INABILITY TO USE A WORK, EVEN IF ONE OF THEM HAS BEEN ADVISED OF THE POSSIBILITY OF SUCH DAMAGES. In any event, the total liability of the Rightsholder and CCC (including their respective employees and directors) shall not exceed the total amount actually paid by User for this license. User assumes full liability for the actions and omissions of its principals, employees, agents, affiliates, successors and assigns.

6. Limited Warranties. THE WORK(S) AND RIGHT(S) ARE PROVIDED "AS IS". CCC HAS THE RIGHT TO GRANT TO USER THE RIGHTS GRANTED IN THE ORDER CONFIRMATION DOCUMENT. CCC AND THE RIGHTSHOLDER DISCLAIM ALL OTHER WARRANTIES RELATING TO THE WORK(S) AND RIGHT(S), EITHER EXPRESS OR IMPLIED, INCLUDING WITHOUT LIMITATION IMPLIED WARRANTIES OF MERCHANTABILITY OR FITNESS FOR A PARTICULAR PURPOSE. ADDITIONAL RIGHTS MAY BE REQUIRED TO USE ILLUSTRATIONS, GRAPHS, PHOTOGRAPHS, ABSTRACTS, INSERTS OR OTHER PORTIONS OF THE WORK (AS OPPOSED TO THE ENTIRE WORK) IN A MANNER CONTEMPLATED BY USER; USER UNDERSTANDS AND AGREES THAT NEITHER CCC NOR THE RIGHTSHOLDER MAY HAVE SUCH ADDITIONAL RIGHTS TO GRANT.

7. Effect of Breach. Any failure by User to pay any amount when due, or any use by User of a Work beyond the scope of the license set forth in the Order Confirmation and/or these terms and conditions, shall be a material breach of the license created by the Order Confirmation and these terms and conditions. Any breach not cured within 30 days of written notice thereof shall result in immediate termination of such license without further notice. Any unauthorized (but licensable) use of a Work that is terminated immediately upon notice thereof may be liquidated by payment of the Rightsholder's ordinary license price therefor; any unauthorized (and unlicensable) use that is not terminated immediately for any reason (including, for example, because materials containing the Work cannot reasonably be recalled) will be subject to all remedies available at law or in equity, but in no event to a payment of less than three times the Rightsholder's ordinary license price for the most closely analogous licensable use plus Rightsholder's and/or CCC's costs and expenses incurred in collecting such payment.

8. Miscellaneous.

    8.1. User acknowledges that CCC may, from time to time, make changes or additions to the Service or to these terms and conditions, and CCC reserves the right to send notice to the User by electronic mail or otherwise for the purposes of notifying User of such changes or additions; provided that any such changes or additions shall not apply to permissions already secured and paid for.

    8.2. Use of User-related information collected through the Service is governed by CCC's privacy policy, available online here:https://marketplace.copyright.com/rs-ui-web/mp/privacy-policy

    8.3. The licensing transaction described in the Order Confirmation is personal to User. Therefore, User may not assign or transfer to any other person (whether a natural person or an organization of any kind) the license created by the Order Confirmation and these terms and conditions or any rights granted hereunder; provided, however, that User may assign such license in its entirety on written notice to CCC in the event of a transfer of all or substantially all of User's rights in the new material which includes the Work(s) licensed under this Service.

    8.4. No amendment or waiver of any terms is binding unless set forth in writing and signed by the parties. The Rightsholder and CCC hereby object to any terms contained in any writing prepared by the User or its principals, employees, agents or affiliates and purporting to govern or otherwise relate to the licensing transaction described in the Order Confirmation, which terms are in any way inconsistent with any terms set forth in the Order Confirmation and/or in these terms and conditions or CCC's standard operating procedures, whether such writing is prepared prior to, simultaneously with or subsequent to the Order Confirmation, and whether such writing appears on a copy of the Order Confirmation or in a separate instrument.

    8.5. The licensing transaction described in the Order Confirmation document shall be governed by and construed under the law of the State of New York, USA, without regard to the principles thereof of conflicts of law. Any case, controversy, suit, action, or proceeding arising out of, in connection with, or related to such licensing transaction shall be brought, at CCC's sole discretion, in any federal or state court located in the County of New York, State of New York, USA, or in any federal or state court whose geographical jurisdiction covers the location of the Rightsholder set forth in the Order Confirmation. The parties expressly submit to the personal jurisdiction and venue of each such federal or state court.If you have any comments or questions about the Service or Copyright Clearance Center, please contact us at 978-750-8400 or send an e-mail to support@copyright.com.

v 1.1

C Constructional Drawings

The constructional drawings used to manufacture the designed parts described in Section 3.1 are given below. The drawings were created with the CAD software *Inventor Professional 2017* by AUTODESK. Dimensions, necessary precisions and the building material are provided in the drawings, which were handed to the department's mechanical workshop or external companies. All quantities are given in [mm].

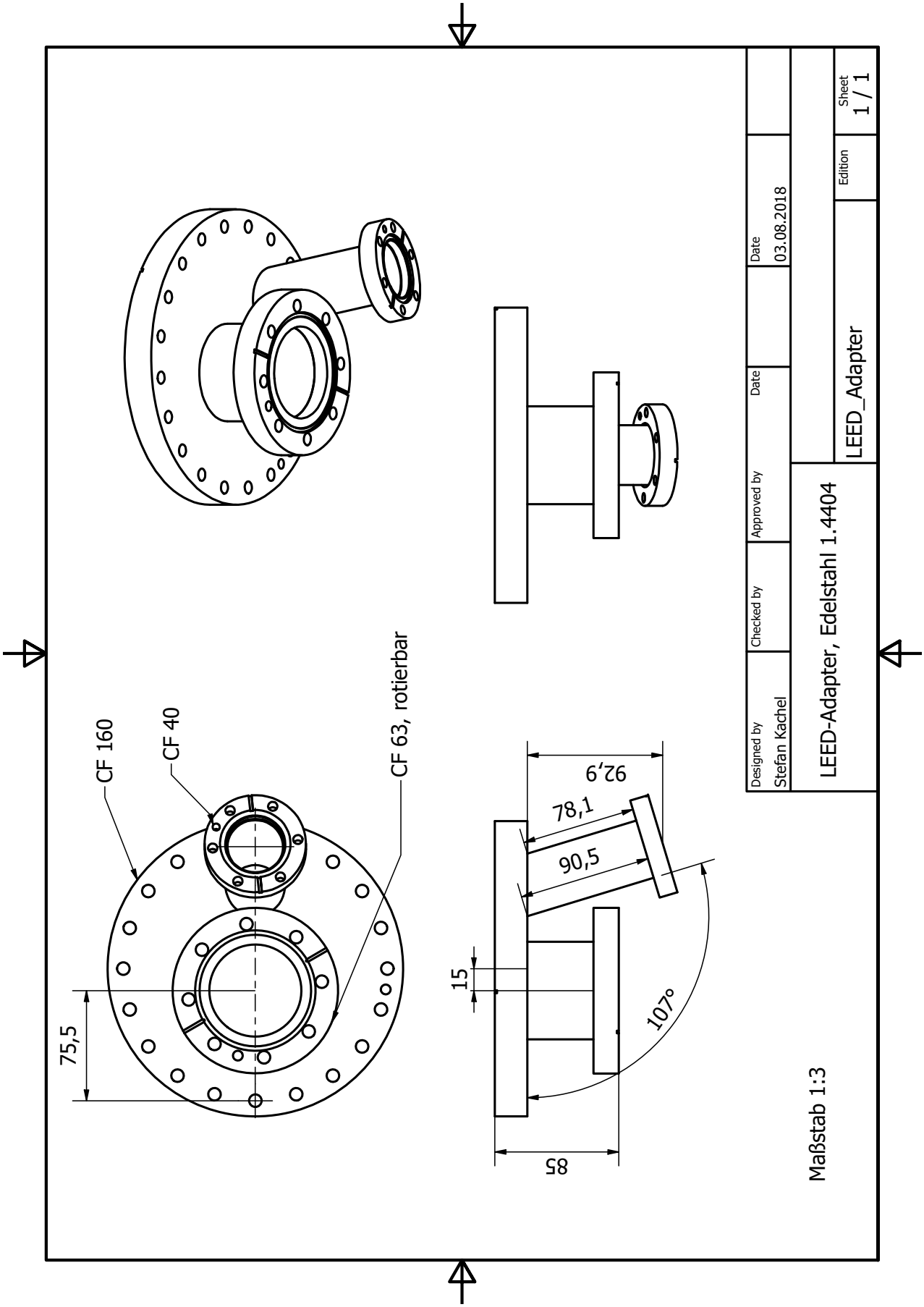
CF 160
CF 40
CF 63, rotierbar
75,5
92,9
78,1
90,5
15
107°
85
Maßstab 1:3
Designed by
Stefan Kachel
Checked by
Approved by
Date
Date
03.08.2018
LEED-Adapter, Edelstahl 1.4404
LEED_Adapter
Edition
Sheet
1 / 1

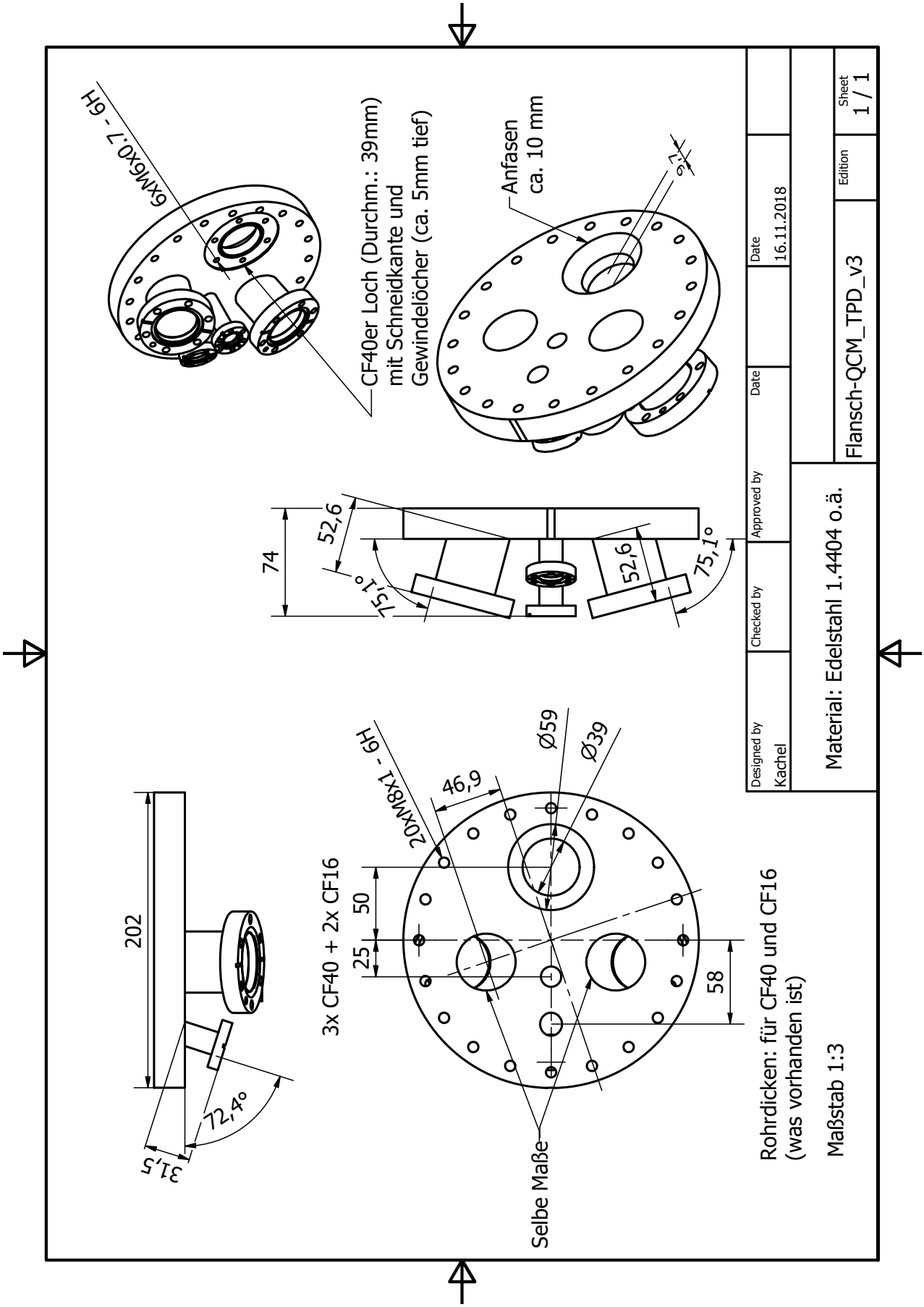
6xM6x0.7 - 6H
CF40er Loch (Durchm.: 39mm)
mit Schneidkante und
Gewindelöcher (ca. 5mm tief)
Anfasen
ca. 10 mm
2
74
52,6
75,1°
52,6
75,1°
20xM8x1 - 6H
46,9
Ø59
Ø39
3x CF40 + 2x CF16
50
25
58
Selbe Maße
202
72,4°
31,5
Rohrdicken: für CF40 und CF16
(was vorhanden ist)
Maßstab 1:3
Designed by
Kachel
Checked by
Approved by
Date
Date
16.11.2018
Material: Edelstahl 1.4404 o.ä.
Flansch-QCM_TPD_v3
Edition
Sheet
1 / 1

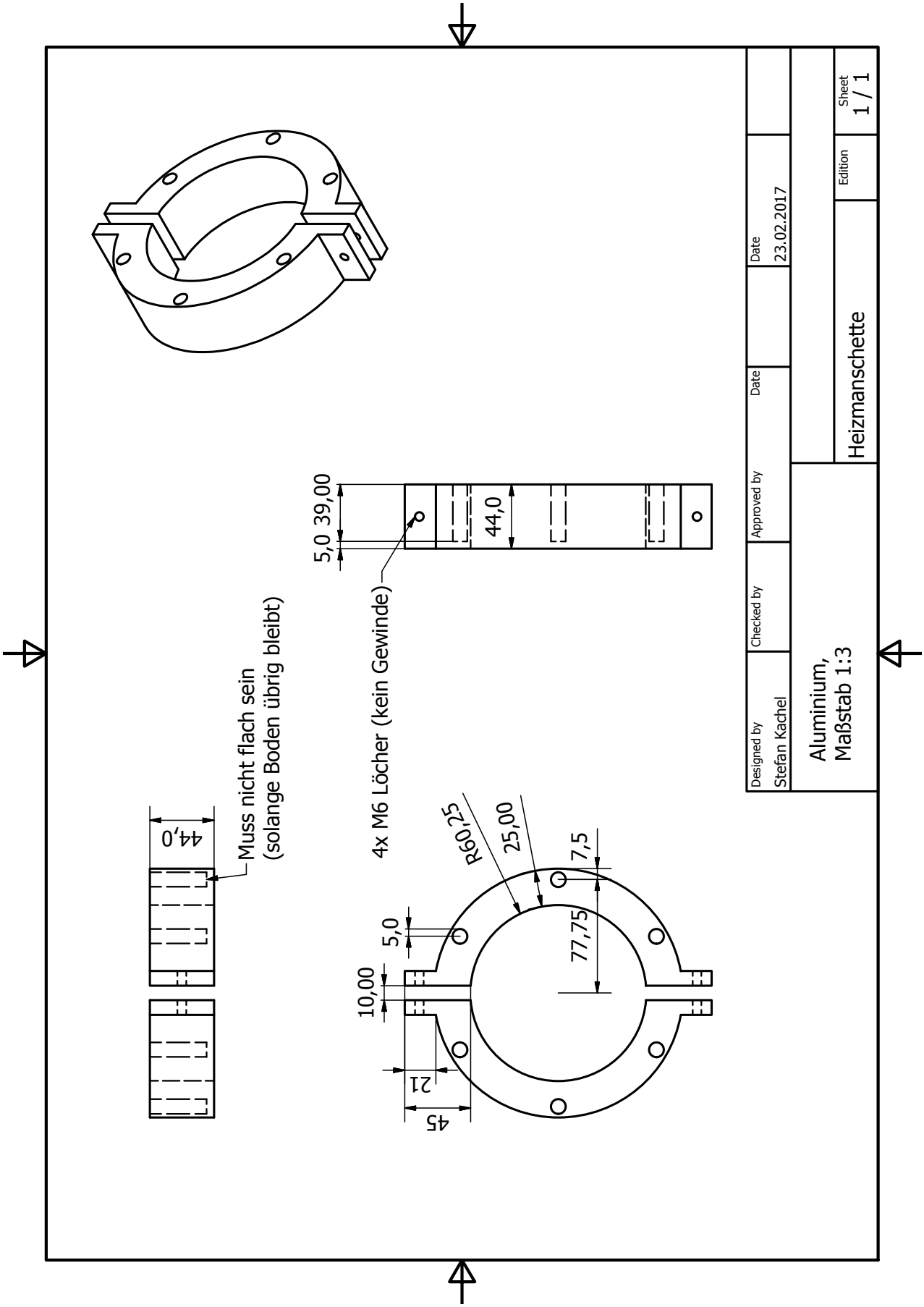
Heizmanschette
Aluminium,
Maßstab 1:3
Designed by
Stefan Kachel
Checked by
Approved by
Date
23.02.2017
Edition
Sheet
1 / 1
5,0
39,00
44,0
4x M6 Löcher (kein Gewinde)
Muss nicht flach sein
(solange Boden übrig bleibt)
44,0
R60,25
25,00
7,5
77,75
5,0
10,00
21
45

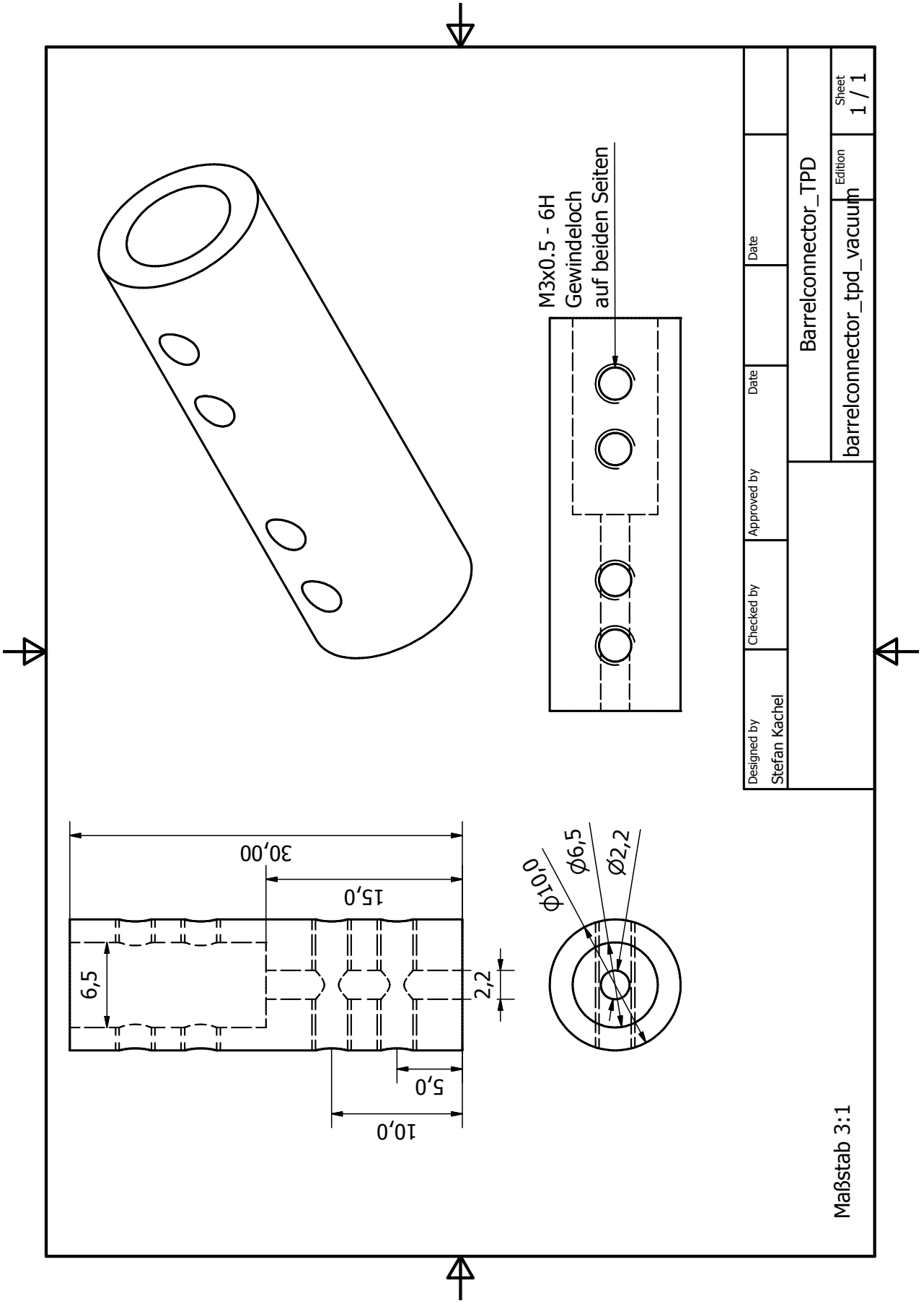
M3x0.5 - 6H
Gewindeloch
auf beiden Seiten
Barrelconnector_TPD
barrelconnector_tpd_vacuum
Edition
Sheet
1 / 1
Designed by
Stefan Kachel
Checked by
Approved by
Date
Date
30,00
15,0
6,5
2,2
5,0
10,0
ϕ10,0
ϕ6,5
ϕ2,2
Maßstab 3:1

D Program Code of Igor Modules

This chapter provides the manual for the *TPD-Analyzer* as well as the program code of the modules *TPD-Analyzer* and *Import-Procedures* as already mentioned in Section 3.2 and its subsections. In case functions are unclear or new functions are desired, please contact me via email (skachel@gmx.de).

D.1 Manual for the Module TPD-Analyzer

Manual – TPD-Analyzer

The TPD-Analyzer contains most of the classical TPD analysis methods, like the 'Redhead Analysis', the leading edge analysis and others. In addition there are new methods implemented like the Persson-Model and the inverted Polanyi-Wigner equation. The aim of this manual is to guide the reader (You) through all functions of the procedure and make him aware of small programming issues. Until now the TPD-Analyzer has no macros and can only be called via the command window. The procedure is devided into static functions for each analysis method. All methods can be accessed via a main menu. The main menu can be called typing "TPD#Main()" into the command line (not case sensitive, without ""). A specific function can be called with "TPD#*Function_Name*(*Variables, Strings*). The corresponding names and variables will be explained during the manual.

1. The Main Menu

The main menu can be called with the command "TPD#Main()" typed into the command window in Igor. The follow window will pop up:

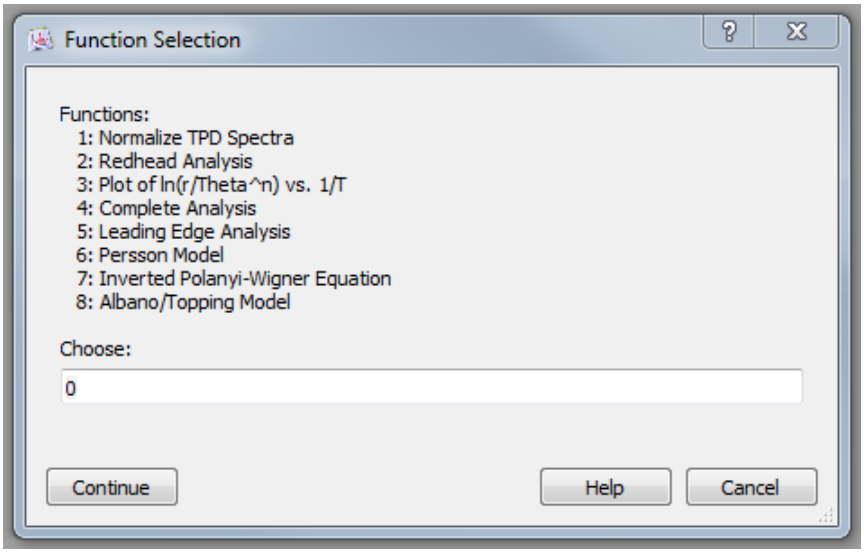

You see now an overview over all implemented functions. In the below "Choose:" you can type in the number of the corresponding function you want to use. Upon press >Enter< (on keyboard) or the <Continue> button the selected function will be started. If you type in a number that is not shown (<1 or >8) the program will close and in the command window will appear "Nothing selected. Now closing...". In Igor Pro 7 you are not able to type in anything different from numbers, hence this is fail-safe.

The >Help< button will display the general help information of Igor for "Parameter Input Dialogs". The >Cancel< and the X (top right) button closes the procedure without any further comments. The >?< button is currently without function. All possibilities on this window are discussed now. The manual continues with explaining each function in detail.

2. Normalize TPD Spectra

If 1 is selected in the main menu a new window will pop up and prompt you the parameters needed for the function. This is shown next:

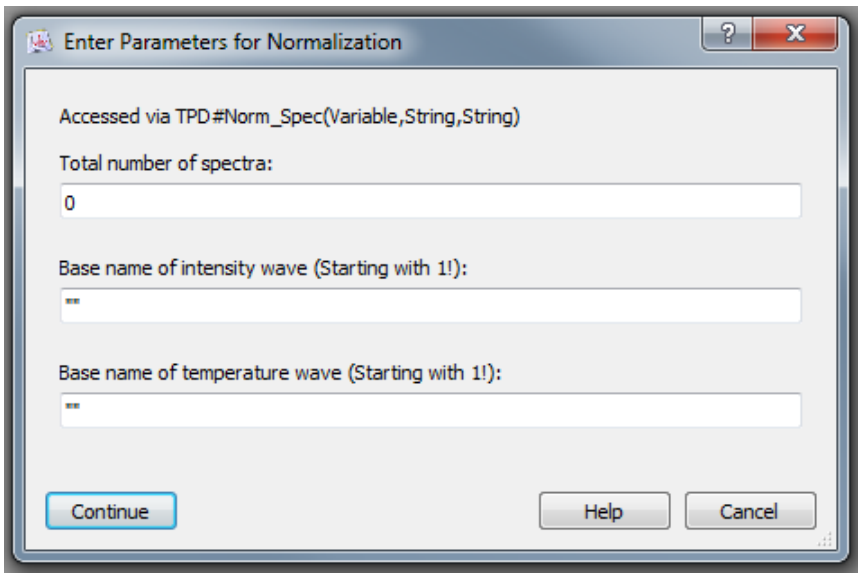

In the first line you see how the function can be directly accessed from the command window. The expressions in the brackets refer to the corresponding prompts below in the same order (the first string expressions refer to the name of the intensity wave and the second string expressions refers to the temperature wave). The first variable that is needed for the function is the total number of spectra. The procedure needs to know how many spectra are to be analyzed starting with spectrum 1. This value input is not fail-safe! Inputting wrong spectra numbers can cause error reports or leads to malfunction. In the second and third line you are prompted to give the name of your first spectrum as a string (“”). This name must contain the number 1, so that the program recognize where the control variable in the string is. The remaining structure does not matter as long as only the control variable is changing (int1, int2, int3, …), so the general structure can be: aaa1aaa, 1bbb, ccc1. The second line corresponds to the name of the intensity wave and the third line to the temperature wave. If all parameters are set the program will be running upon clicking on >Continue<.

If the function is running it prompts the user to enter the number of the monolayer spectrum. This means you have to insert the number which is defined as one complete monolayer (=1.0 ML). The step here is fail-safe as every number <1 and >*Number of Spectra* leads to canceling the function without doing anything. The procedure calculates the integral of the monolayer spectrum and then divides all other spectra by this monolayer integral. The original waves remain unchanged, but new waves with the suffix “_ML” will be created, which are the normalized spectra.

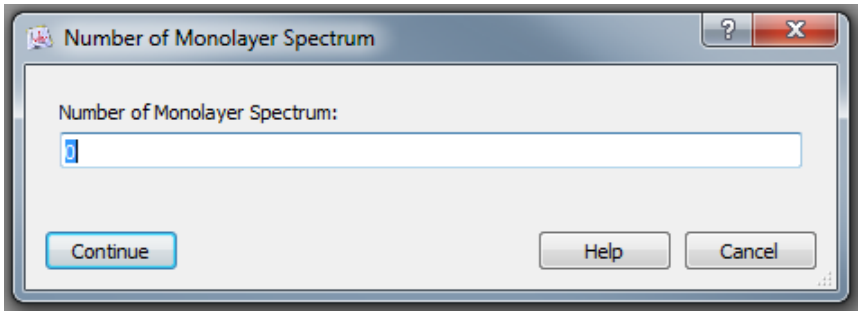

After the calculation and the function has finished another window pops up, which is connected to the main menu.

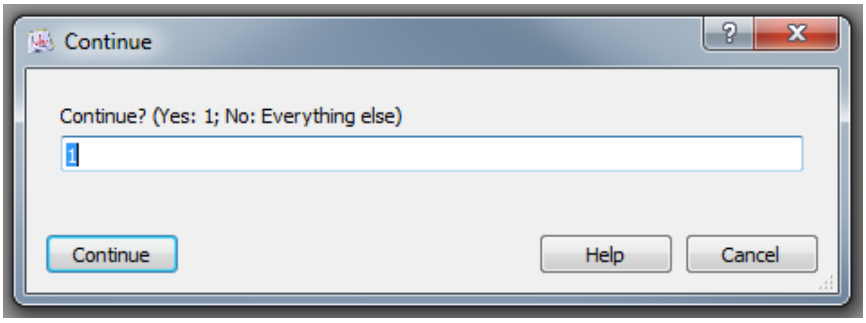

The windows function is relative obvious as the user can select to repeat the whole cycle again and start at the main menu (==1) or close the whole procedure. If selected to continue, the values entered in the functions (e.g. Norm_Spec) are remembered for faster fitting (e.g. Persson-Fit).

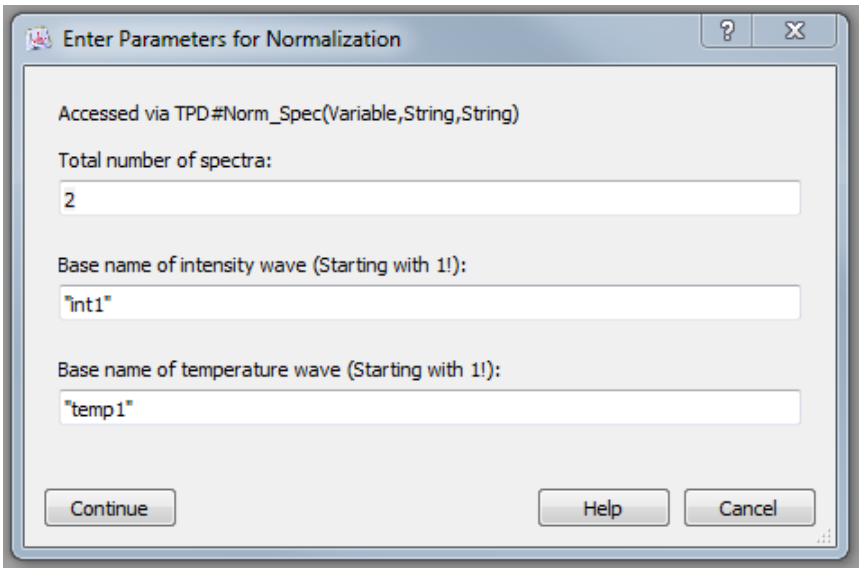

3. Redhead Analysis

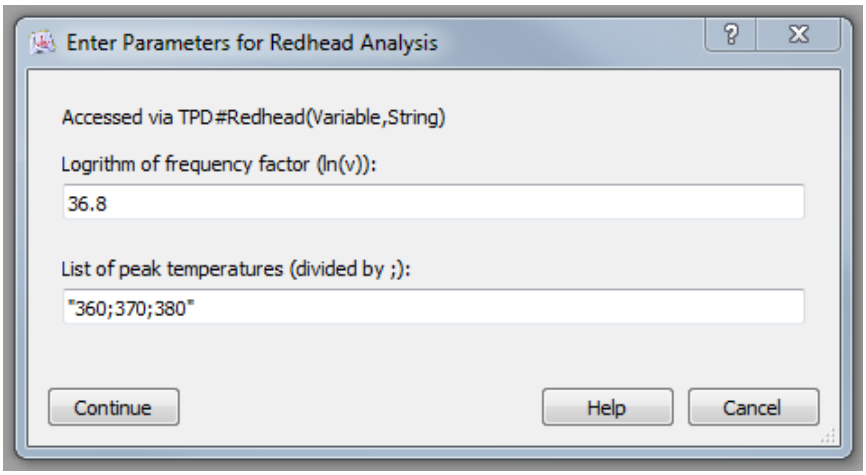

If 2 in the main menu is selected, then the Redhead analysis starts. Again, in the first line you can see how the procedure is called directly from the command window. The procedure needs the frequency factor and the maximum temperatures for calculating the desorption energy. For easier input you must give the logarithm of the frequency factor for example 36.8 for a factor of 1E16. The peak temperatures are given via a string of temperatures. An example would be “350;360;370”. The separation must be *;* so that Igor identifies the string as a list. Anything else will lead false results, like “abcd” or “350,360,370”. After the calculation two waves named “Edes” and “Tpeak” are created. The “Edes” wave contains the desorption energies and “Tpeak” contains the peak maximum temperatures.

4. Plot of ln(r/Theta^n) vs. 1/T

This function is rather simple as only two waves have to be provided in the current data folder. One intensity wave called “int” and one temperature wave called “temp” need to be in the data folder. The procedure calculates the inversion of the temperature (wave “inverseTemp”), the residual coverage (wave “ResidualCoverage”) and the term ln(r/theta^n) for n= 0, 0.5, 1, 1.5 and 2 (waves “ROverThetaZero”, “ROverThetaOneHalf”, “ROverTheta”, “ROverThetaThreeHalf” and “ROverThetaSquare”.). The function plots all ln(r/theta^n) plots against 1/T in one graph. An example is shown below. The function can be called via TPD#lnRTheta1().

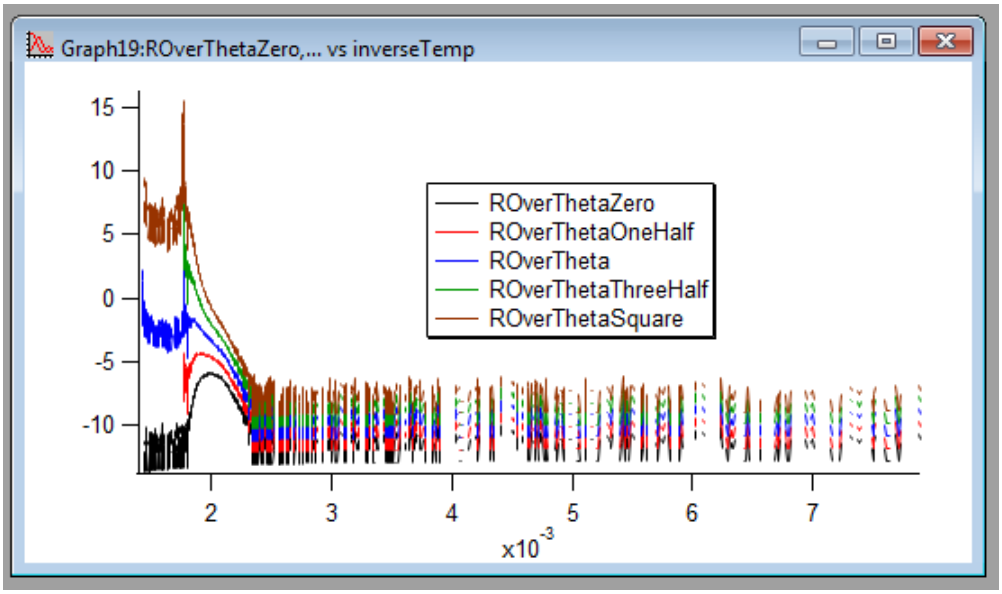

5. Complete Analysis

If selecting the Complete Analysis (CA) from the main menu (#4) then a window appears prompting 2 variables and 2 strings. The first variable is the coverage, for which the CA should be done in the unit [ML]. The remaining three parameters are the same as for the function Norm_Spec, because the CA function will normalize the spectra again, if they are not normalized beforehand. Below example parameter are shown. Upon continuing the procedure prompts the user to give the number of the monolayer spectra like in the Norm_Spec function. If the spectra are already normalized then just type “0” and continue, so that the function skips the normalization. The function outputs the logarithm of the specific rates and the inverse of the corresponding temperatures. In addition a graph will pop up where the logarithm is plotted against the inverse temperature (see below).

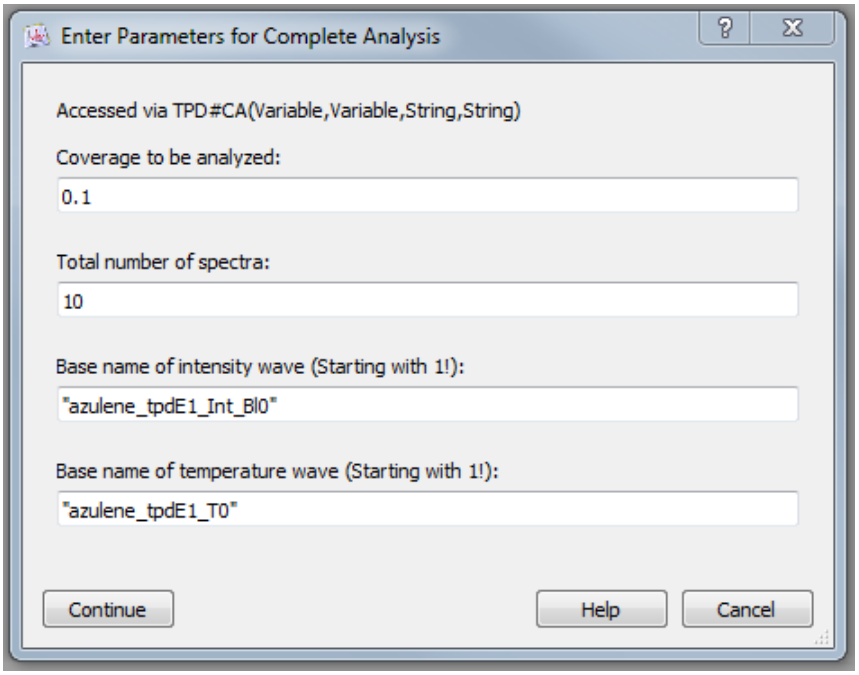

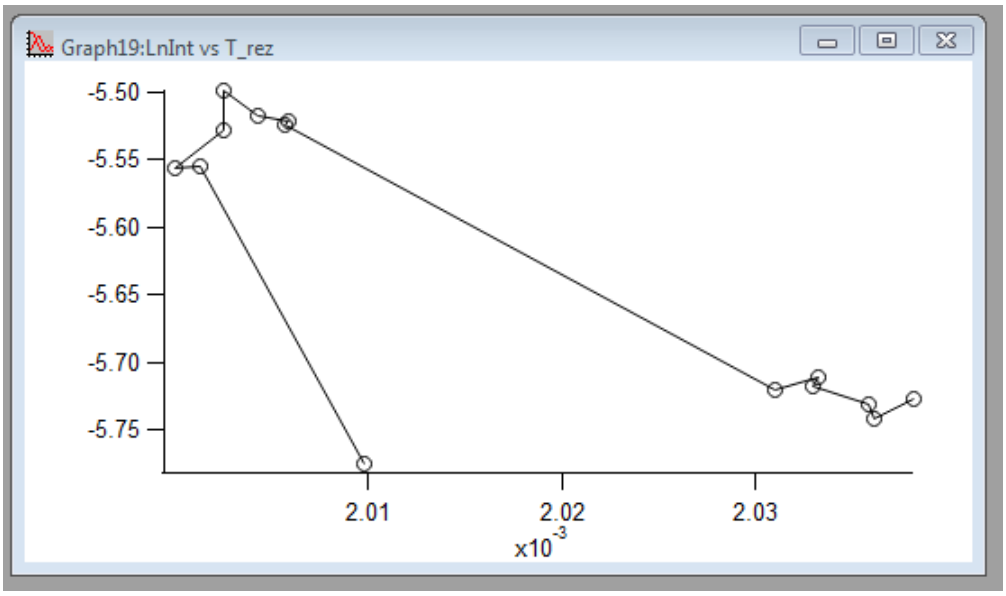

6. Leading Edge Analysis

The leading edge analysis (LEA) needs the same parameters as the Norm_Spec function as the spectra are normalized again, which can be skipped on demand (see 5. Complete Analysis). The function takes the logarithm of each spectrum and saves this in a separate wave called “ln(int)_1” for spectrum 1. The same will be done for inverse of the temperature (“1/T_1”). Furthermore all logarithms are plotted against the corresponding 1/T waves. For higher visibility each spectrum is plotted with an offset of 1. Hence, it is easier to fit the graphs. The starting window is shown below.

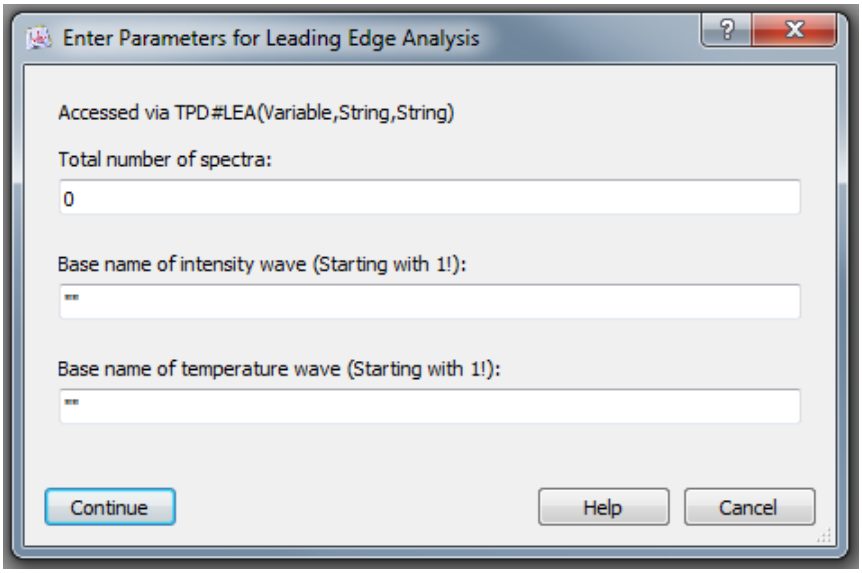

7. Persson Model

This fit is based on the Persson Model. Persson takes the relaxation of adsorbates from their favored adsorption site into account. The coverage dependent desorption energy is modeled by $E(\theta) = E(0) - Repulsion * \theta - Relaxation * \theta^2$. The repulsion and relaxation are no quantitative values and cannot be compared to other values. But depending on the fit parameters, repulsive systems like azulene on Cu(111) or Ag(111) can be fitted quite well. The procedure itself needs 5 mandatory parameters and one optional (see below).

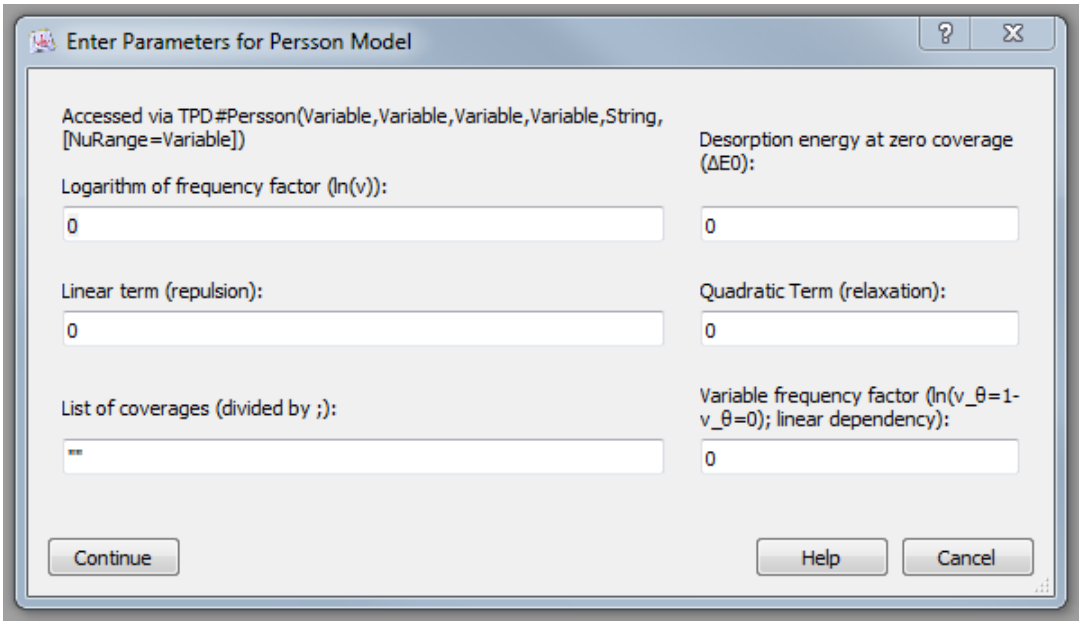

Again, in the first line you see how the function is called in the command line. Note, that you can call the function with only 5 parameters. To provide the optional parameter, for example “NuRange=5” has to be added to the parameters. The first parameter is the logarithm of the frequency factor like in previous functions. The second is the desorption energy at zero coverage, the third the repulsion term and the forth the relaxation term according to Persson. Furthermore a list of coverages has to be

provided. All coverages, for which the simulation should be done, has to be in this list. An example list could be "0.5;0.4;0.3;0.2;0.1". Once again all coverages need to be separated with an ";" and there should be no other than numbers in the list. The last parameter is optional and is called by "NuRange=". The default value is 0, which means that there is no coverage dependency. The number, that is given here, will vary the frequency factor with the coverage. The equation for the frequency factor is: $\nu(\theta) = (1-\theta) * \exp(a) + \theta * \exp(a + NuRange)$ with a being the logarithm of the frequency factor (first parameter of the function). At zero coverage this equals the normal frequency factor, which increases linearly with the coverage.

After clicking continue, in the current folder the function creates an intensity wave called "sample_*Coverage*" and a temperature wave called "sampleT_*Coverage*" for each coverage provided within the coverage list. Furthermore there is a wave with the residual coverage of the last coverage, for double checking whether the calculation was correct or not. The waves can be plotted inside a graph containing a coverage series of TPD spectra. For a faster fitting I recommend calling the function via the command line. It is way faster than cycling through the whole main menu for changing the parameters like the repulsion or relaxation term.

8. Inverted Polanyi-Wigner Equation

The second to last function is the inverted Polanyi-Wigner equation. This function rearranges the Polanyi-Wigner equation to the desorption energy. If the frequency factor is known one can input the desorption rate (=Intensity) to calculate the desorption energy for each temperature and coverage. This method is especially powerful, because no further assumptions are taken. But for a reliable calculation the frequency factor must be well known, what is often a problem. Furthermore the procedure gives a wave, which contains the difference between the desorption energy at zero coverage and the coverage dependent energy. This difference can be understood as the total repulsion for the corresponding coverage and is called φ. φ at full monolayer coverage can be divided by the number of nearest neighbors for a specific system to obtain the repulsion per nearest neighbor in kJ/mol. Note, that this repulsion cannot be compared to the repulsion from the Persson model, because no relaxation is taken into account for the IPW! Also it is not clear if it can be compared to other energies like the Coulomb repulsion (dipole-dipole repulsion). If the optional value for ΔG is given (see below), than not the desorption energy is calculated but the free Gibbs enthalpy ΔG according to the transition state theory (TST). Down below you find the menu window for the IPW.

The first and second parameter is the same as for the Persson model, namely the logarithm of the frequency factor and the desorption energy at zero coverage. The third parameter is an optional one and is given by "NuRange=**". It is the same linear dependency as in the Persson model. The default value is 0, which corresponds to no coverage dependency. The last parameter is optional, too. The default value is 0, leading to the calculation of the desorption energy. Only if entering 1 or adding DeltaG=1 to the command line, ΔG will be calculated. All other values will result in the desorption energy.

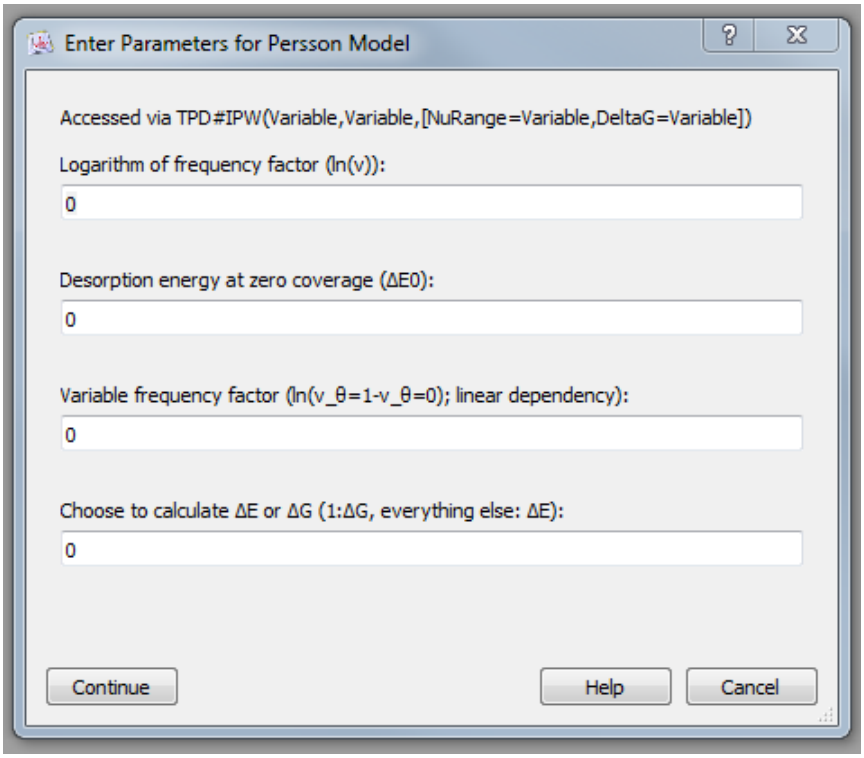

In the current folder there has to two waves called “int” and “temp”. Note that the intensity wave “int” has to be normalized for a meaningful result. The procedure calculates with the help of these two waves the desorption energy, φ and the residual coverage. After the calculation a plot of the intensity (red), desorption energy (black) and φ (blue) vs. temperature is shown. An example plot is shown below.

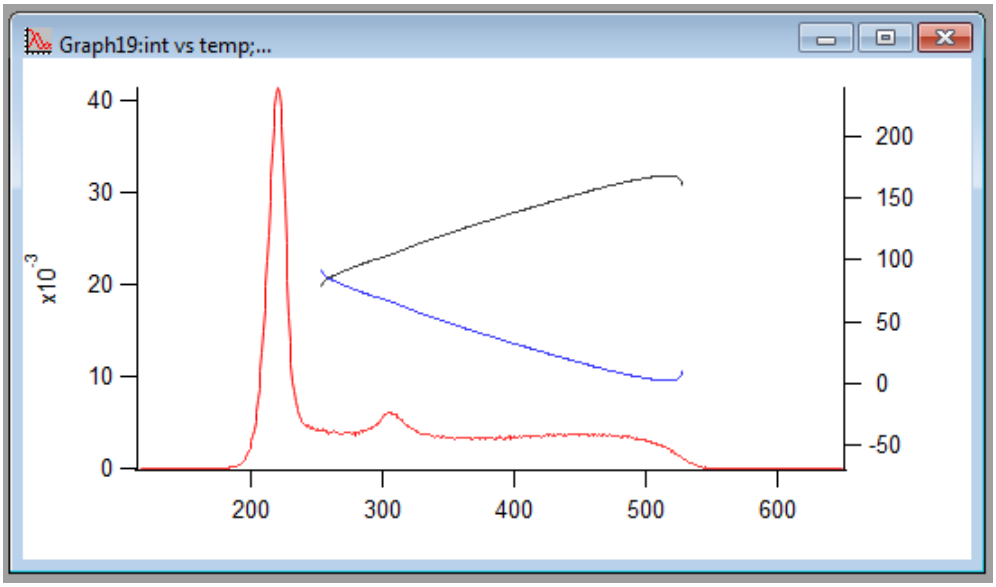

9. Albano/Topping Model

The last but not least method is the Albano or Topping model. Albano used the Topping model to give the coverage dependency for the desorption energy assuming dipoles perpendicular to the surface. For this model the properties of the dipole are of interest, namely the dipole moment μ and the polarizability α.

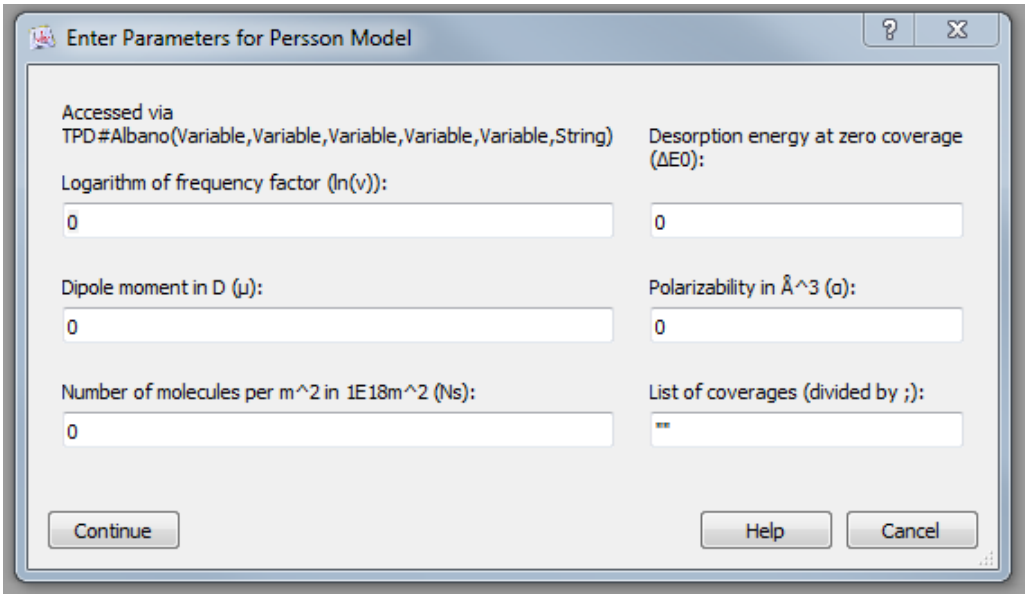

Again the first two parameters are the logarithm of the frequency factor und the desorption energy at zero coverage. Nothing new here. The next three parameters are new and exclusively for the Albano model. The third parameter is the dipole moment μ. The dipole moment has to be given in units of D (Debye). This is a cgs unit and the conversion into SI units will be done by the procedure. The same accounts for the forth parameter, the polarizability α, which will be given in units of Å³. The fifth variable is the number of molecules per m² for the full monolayer. This means how many molecules can be put onto the surface for the favorite adsorption superstructure. Common numbers are in the order of magnitude of 10^{18}. Hence, for an easier input the procedure multiplies the input value with 10^{18}. The last parameter is the coverage list that was described above. Note, that again the separation of the coverages has to be done with ";". Upon calculation the procedure creates intensity and temperature waves in the current order in the same way as in the Persson Model.

10. Troubleshooting

The biggest problem that can occur in the TPD_Analyzer is that prompted parameters do not have the correct type. So, if a number (integer, float, …) is prompted, than a number should be given and not a string or letters. If you are using the main menu (TPD#main()) than many of such mistakes are prohibited. But in the command line there is no such a protection. But if you input only meaningful values that are discussed above then everything should work fine. If you should find mistakes, have questions or other notes, please contact me (skachel@gmx.de) for improvement of the Analyzer and the manual.

D.2 TPD-Analyzer

```
#pragma TextEncoding = "UTF-8"
#pragma rtGlobals=3     // Use modern global access method and strict wave access.
#pragma modulename = TPD

static constant R = 0.008314 //kJ

static function Main()
    variable i, a, b, c, d, e
    string x, y, z
    variable ContinueTPD = 1
    do
        i=0
        string str_norm = ": Normalize TPD Spectra"
        string str_ra = ": Redhead Analysis"
        string str_lnrt = ": Plot of ln(r/Theta^n) vs. 1/T"
        string str_ca = ": Complete Analysis"
        string str_lea = ": Leading Edge Analysis"
        string str_persson = ": Persson Model"
        string str_ipw = ": Inverted Polanyi-Wigner Equation"
        string str_albano = ": Albano/Topping Model"
       prompt i, "Functions: \n   1" + str_norm + "\n   2" + str_ra + "\n   3" +
       str_lnrt + "\n   4" + str_ca + "\n   5" + str_lea + "\n   6" + str_persson +
       "\n   7" + str_ipw + "\n   8" + str_albano + "\n\nChoose:"
        DoPrompt "Function Selection", i

        if (V_Flag)
            return -1
        endif

        if (i==1)
            prompt a, "Accessed via TPD#NormSpec(Variable,String,String)\n\nTotal
            number of spectra: "
            prompt x, "Base name of intensity wave (Starting with 1!): "
            prompt y, "Base name of temperature wave (Starting with 1!): "
            DoPrompt "Enter Parameters for Normalization", a,x,y
            NormSpec(a,x,y)

            if (V_Flag)
                return -1
            endif

        elseif (i==2)
            prompt a, "Accessed via TPD#Redhead(Variable,String)\n\nLogrithm of
            frequency factor (ln(\u03BD)): "
            prompt x, "List of peak temperatures (divided by ;): "
            DoPrompt "Enter Parameters for Redhead Analysis", a,x
            Redhead(a,x)

            if (V_Flag)
                return -1
            endif

        elseif (i==3)
            prompt a, "Specific Reaction Order n: "
            DoPrompt "Enter Parameters for ln(R/Theta^n) vs. 1/T", a
            lnRTheta1(ROrder=a)

        elseif (i==4)
            prompt a, "Accessed via
            TPD#CA(Variable,Variable,String,String)\n\nCoverage to be analyzed: "
            prompt b, "Total number of spectra: "
            prompt x, "Base name of intensity wave (Starting with 1!): "
            prompt y, "Base name of temperature wave (Starting with 1!): "
            DoPrompt "Enter Parameters for Complete Analysis", a,b,x,y
            CA(a,b,x,y)

            if (V_Flag)
                return -1
            endif

        elseif (i==5)
            prompt a, "Accessed via TPD#LEA(Variable,String,String)\n\nTotal number
            of spectra: "
```

```
68              prompt x, "Base name of intensity wave (Starting with 1!): "
69              prompt y, "Base name of temperature wave (Starting with 1!): "
70              DoPrompt "Enter Parameters for Leading Edge Analysis", a, x ,y
71              LEA(a,x,y)
72
73              if (V_Flag)
74                  return -1
75              endif
76
77          elseif (i==6)
78              prompt a, "Accessed via
                TPD#Persson(Variable,Variable,Variable,Variable,String,[NuRange=Variable])
                \n\nLogarithm of frequency factor (ln(\u03BD)): "
79              prompt b, "Desorption energy at zero coverage (\u0394E0): "
80              prompt c, "Linear term (repulsion): "
81              prompt d, "Quadratic Term (relaxation): "
82              prompt x, "List of coverages (divided by ;): "
83              prompt e, "Variable frequency factor
                (ln(\u03BD_\u03B8=1-\u03BD_\u03B8=0); linear dependency): "
84              DoPrompt "Enter Parameters for Persson Model", a,b,c,d,x,e
85              Persson(a,b,c,d,x,NuRange=e)
86
87              if (V_Flag)
88                  return -1
89              endif
90
91          elseif (i==7)
92              prompt a, "Accessed via
                TPD#IPW(Variable,Variable,[NuRange=Variable,DeltaG=Variable])\n\nLogarithm
                 of frequency factor (ln(\u03BD)): "
93              prompt c, "Variable frequency factor
                (ln(\u03BD_\u03B8=1-\u03BD_\u03B8=0); linear dependency): "
94              prompt d, "Choose to calculate \u0394E or \u0394G (1:\u0394G, everything
                else: \u0394E): "
95              DoPrompt "Enter Parameters for Persson Model", a,c,d
96              IPW(a,NuRange=c,DeltaG=d)
97
98              if (V_Flag)
99                  return -1
100             endif
101
102         elseif (i==8)
103             prompt a, "Accessed via
                TPD#Albano(Variable,Variable,Variable,Variable,Variable,String)\n\nLogarit
                hm of frequency factor (ln(\u03BD)): "
104             prompt b, "Desorption energy at zero coverage (\u0394E0): "
105             prompt c, "Dipole moment in D (\u03BC): "
106             prompt d, "Polarizability in \u00C5^3 (\u03B1): "
107             prompt e, "Number of molecules per m^2 in 1E18m^2 (Ns): "
108             prompt x, "List of coverages (divided by ;): "
109             DoPrompt "Enter Parameters for Persson Model", a,b,c,d,e,x
110             Albano(a,b,c,d,e,x)
111
112             if (V_Flag)
113                 return -1
114             endif
115
116         else
117             print "Nothing selected. Now closing..."
118             return -1
119         endif
120
121         prompt ContinueTPD, "Continue? (Yes: 1; No: Everything else)"
122         DoPrompt "Continue", ContinueTPD
123     while (ContinueTPD==1)
124 end
125
126 //_____________________________________________________________________________
    _____________________________________
127
128 static function NormSpec(SpecNum, intbasis, tempbasis)
129     variable SpecNum
130     string intbasis, tempbasis
```

```
131
132       variable NumMono=0
133       variable MonoCov=1
134       prompt NumMono, "Select Spectrum to normalize to:"
135       prompt MonoCov, "Coverage of Selected Spectrum:"
136       DoPrompt "Number of Monolayer Spectrum", NumMono, Monocov
137
138       if (V_Flag || NumMono<1 || NumMono>SpecNum || MonoCov<=0)
139           return -1
140       endif
141
142       string intname, tempname, intname_old
143       variable i, Coverage
144       variable startposition_i = strsearch(intbasis, "1", 0)
145       variable startposition_t = strsearch(tempbasis, "1", 0)
146
147       make /d /o /n=(SpecNum) Coverage_List
148       wave Coverage_List = Coverage_List
149
150       intname = intbasis[0,startposition_i-1] + num2str(NumMono) +
          intbasis[startposition_i+1,strlen(intbasis)-1]
151       tempname = tempbasis[0,startposition_t-1] + num2str(NumMono) +
          tempbasis[startposition_t+1,strlen(tempbasis)-1]
152
153       wave intwave = $intname
154       wave tempwave = $tempname
155       Coverage = areaxy(tempwave, intwave)/MonoCov
156
157       for(i=1; i<=SpecNum; i+=1)
158           intname_old = intbasis[0,startposition_i-1] + num2str(i) +
              intbasis[startposition_i+1,strlen(intbasis)-1]
159           wave intwave_old = $intname_old
160           intname = intbasis[0,startposition_i-1] + num2str(i) +
              intbasis[startposition_i+1,strlen(intbasis)-1]+"_ML"
161           tempname = tempbasis[0,startposition_t-1] + num2str(i) +
              tempbasis[startposition_t+1,strlen(tempbasis)-1]
162           duplicate /d /o intwave_old $intname
163           wave intwave = $intname
164           wave tempwave = $tempname
165           intwave /= coverage
166           Coverage_List[i-1] = areaxy(tempwave, intwave)
167       endfor
168   end
169
170   //_____________________________________________________________________________________
      _____________________________________________
171
172   static function NormSpec_Multi(SpecNum, intbasis, tempbasis, masslist)
173       variable SpecNum
174       string intbasis, tempbasis, masslist
175
176       variable NumMono=0
177       variable MonoCov=1
178       prompt NumMono, "Select Spectrum to normalize to:"
179       prompt MonoCov, "Coverage of Selected Spectrum:"
180       DoPrompt "Number of Monolayer Spectrum", NumMono, Monocov
181
182       if (V_Flag || NumMono<1 || NumMono>SpecNum || MonoCov<=0)
183           return -1
184       endif
185
186       string intname, tempname, intname_old
187       variable i,j, Coverage
188       variable startposition_i = strsearch(intbasis, "1", 0)
189       variable startposition_t = strsearch(tempbasis, "1", 0)
190       variable startmass = strsearch(intbasis, StringFromList(0,masslist), 0)
191
192       make /d /o /n=(SpecNum) Coveragelist_total
193       wave Coveragelist_total = Coveragelist_total
194       duplicate /o Coveragelist_total Intensitylist_total
195       string auxwavename, auxwavename2, mass
196
197       for(i=0; i<ItemsInList(masslist); i+=1)
```

```
198         auxwavename = "Coveragelist_mass"+StringfromList(i, masslist)
199         duplicate /o Coveragelist_total $auxwavename
200         auxwavename = "Intensitylist_mass"+StringfromList(i, masslist)
201         duplicate /o Coveragelist_total $auxwavename
202     endfor
203
204     for(i=1; i<=SpecNum; i+=1)
205         for(j=0; j<ItemsInList(masslist); j+=1)
206             mass = Stringfromlist(j, masslist)
207             intname = intbasis[0,startposition_i-1] + num2str(i) +
                intbasis[startposition_i+1, startmass-1] + mass +
                intbasis[startmass+strlen(mass),strlen(intbasis)-1]
208             tempname = tempbasis[0,startposition_t-1] + num2str(i) +
                tempbasis[startposition_t+1,strlen(tempbasis)-1]
209             wave intwave = $intname
210             wave tempwave = $tempname
211             auxwavename = "Intensitylist_mass"+mass
212             wave auxwave = $auxwavename
213             auxwave[i-1] = areaxy(tempwave, intwave)
214             Intensitylist_total[i-1]+=auxwave[i-1]
215         endfor
216     endfor
217
218     Coveragelist_total=Intensitylist_total*Monocov/Intensitylist_total[NumMono-1]
219
220     for(i=1; i<=SpecNum; i+=1)
221         for(j=0; j<ItemsInList(masslist); j+=1)
222             mass = Stringfromlist(j, masslist)
223             intname_old = intbasis[0,startposition_i-1] + num2str(i) +
                intbasis[startposition_i+1, startmass-1] + mass +
                intbasis[startmass+strlen(mass),strlen(intbasis)-1]
224             wave intwave_old = $intname_old
225             intname = intname_old + "_ML"
226             tempname = tempbasis[0,startposition_t-1] + num2str(i) +
                tempbasis[startposition_t+1,strlen(tempbasis)-1]
227             duplicate /D /o intwave_old $intname
228             wave intwave = $intname
229             wave tempwave = $tempname
230             auxwavename = "Intensitylist_mass"+mass
231             wave auxwave = $auxwavename
232             auxwavename2 = "Coveragelist_mass"+mass
233             wave auxwave2 = $auxwavename2
234             auxwave2[i-1] =
                auxwave[i-1]*Coveragelist_total[i-1]/Intensitylist_total[i-1]
235             intwave = intwave*Coveragelist_total[i-1]/Intensitylist_total[i-1]
236         endfor
237     endfor
238 end
239
240 //_____________________________________________________________________________
    _____________________________________
241
242 static function Redhead(Prefac, templist)
243     variable Prefac
244     string templist
245
246     make /d /o /n=(ItemsInList(templist)) Tpeak
247     wave Tpeak = Tpeak
248     make /d /o /n=(ItemsInList(templist)) Edes
249     wave Edes = Edes
250
251     variable i, j, l
252     variable Tmax, aux, X, X_final, deviation, deviation_final
253     variable HeatingRate = 1 //K/s
254     variable accuracy, switcher, counter=0, threshold=1e-5
255
256     for(i=0; i<ItemsInList(templist); i+=1)
257         Tmax = str2num(StringFromList(i, templist))
258         aux = ln(exp(Prefac)*Tmax/HeatingRate)
259         accuracy = 0.1
260         switcher = 1
261         deviation_final=0
262         l = 1
```

```
263         do
264             for(j=l-5*accuracy; j<=l+5*accuracy;j+=accuracy)
265                 X = aux*j   //empirical: X is similar to ln(nu*T/beta) --> variing
                    ln(nu*T/beta) with term between 0.5 and 1.5
266                 deviation=abs(X-(aux-ln(X)))
267                 if (deviation<deviation_final || deviation_final==0)
268                     deviation_final=deviation
269                     X_final=X
270                     l=j
271                     counter+=1
272                 endif
273             endfor
274
275             if(counter<=1 || l==1.0+5*accuracy)
276                 print "Error in calculating of peak: ", i
277                 return -1
278             endif
279
280             if(deviation_final<=threshold)
281                 switcher=0
282             endif
283
284             accuracy/=10
285         while (switcher ==1)
286
287         Tpeak[i]=Tmax
288         Edes[i]=X_final*R*Tmax
289     endfor
290 end
291
292 //_____________________________________________________________________________
    _____________________________________________
293
294 static function lnRTheta1([ROrder])
295     variable ROrder
296     ROrder = paramIsDefault(ROrder) ? 0 : ROrder
297
298     wave xwave = temp
299     wave ywave = int
300
301     duplicate /o ywave ResidualCoverage
302     duplicate /o ywave ROverTheta
303     duplicate /o ywave ROverThetaSquare
304     duplicate /o ywave ROverThetaZero
305     duplicate /o ywave ROverThetaOneHalf
306     duplicate /o ywave ROverThetaThreeHalf
307     duplicate /o xwave inverseTemp
308
309     wave ResidualCoverage = ResidualCoverage
310     wave ROverTheta = ROverTheta
311     wave ROverThetaSquare = ROverThetaSquare
312     wave ROverThetaZero = ROverThetaZero
313     wave ROverThetaOneHalf = ROverThetaOneHalf
314     wave ROverThetaThreeHalf = ROverThetaThreeHalf
315     wave inverseTemp = inverseTemp
316
317     variable i
318
319     for (i = 0; i<numpnts(ResidualCoverage); i += 1)
320         ResidualCoverage[i] = areaxy(xwave, ywave,xwave[i],inf)
321     endfor
322
323     inverseTemp = 1/xwave
324
325
326
327     ROverTheta = ln(ywave/(ResidualCoverage))
328     ROverThetaSquare = ln(ywave/(ResidualCoverage)^2)
329     ROverThetaZero = ln(ywave)
330     ROverThetaOneHalf = ln(ywave/(ResidualCoverage)^0.5)
331     ROverThetaThreeHalf = ln(ywave/(ResidualCoverage)^1.5)
332
333     if (ROrder!=0)
```

```
334          duplicate /o ywave ROverThetaN
335          wave ROverThetaN = ROverThetaN
336          ROverThetaN = ln(ywave/(Residualcoverage)^ROrder)
337          Display ROverThetaZero, ROverThetaOneHalf, ROverTheta, ROverThetaThreeHalf,
             ROverThetaSquare, ROverThetaN vs inverseTemp
338      else
339          Display ROverThetaZero, ROverThetaOneHalf, ROverTheta, ROverThetaThreeHalf,
             ROverThetaSquare vs inverseTemp
340      endif
341
342
343  ModifyGraph rgb(ROverThetaZero)=(0,0,0), rgb(ROverTheta)=(0,0,65280);
344  ModifyGraph rgb(ROverThetaThreeHalf)=(0,39168,0);
345  ModifyGraph rgb(ROverThetaSquare)=(39168,13056,0)
346
347  Legend/C/N=text0/S=3/A=MC
348  end
349
350  //_____________________________________________________________________________
     _____________________________________________
351
352  static function lnRTheta2(ROrder, SpecNum, intbasis, tempbasis)
353      variable ROrder, SpecNum
354      string intbasis, tempbasis
355
356      variable i, j
357      variable startposition_i = strsearch(intbasis, "1", 0)
358      variable startposition_t = strsearch(tempbasis, "1", 0)
359
360      string WaveTag
361      string XWaveTag
362      string waveTag_old
363      string XwaveTag_old
364
365      for (i=1; i<=SpecNum; i+=1)
366          waveTag_old = intbasis[0,startposition_i-1] + num2str(i) +
             intbasis[startposition_i+1,strlen(intbasis)-1]
367          XwaveTag_old = tempbasis[0,startposition_t-1] + num2str(i) +
             tempbasis[startposition_t+1,strlen(tempbasis)-1]
368          wave intwave_old = $wavetag_old
369          wave tempwave_old = $xwavetag_old
370
371          WaveTag = "ln(r/Theta^n)_" + num2str(i)
372          XWaveTag = "1/T_" + num2str(i)
373
374          duplicate /d /o intwave_old $WaveTag
375          duplicate /d /o tempwave_old $XWaveTag
376          duplicate /d /o intwave_old ResidualCoverage
377
378          wave intwave = $WaveTag
379          wave tempwave = $XWaveTag
380          wave ResidualCoverage = ResidualCoverage
381
382          for (j=0; j<numpnts(ResidualCoverage); j+=1)
383              ResidualCoverage[j] = areaxy(tempwave_old,
                 intwave_old,tempwave_old[j],tempwave_old[numpnts(tempwave_old)-1])
384          endfor
385
386          intwave =ln(intwave/(Residualcoverage^ROrder))
387          tempwave=1/tempwave
388
389          if (i==1)
390              Display Intwave vs Tempwave
391          else
392              Appendtograph Intwave vs Tempwave
393              ModifyGraph offset($wavetag)={0,i*1.5}
394          endif
395      endfor
396      ModifyGraph margin(left)=85,margin(bottom)=70,margin(right)=28,margin(top)=28
397      ModifyGraph width=453.543,height=453.543
398      Label left "\\f01ln(\\f03r\\f01\\Bdes\\M/(\u0394E0^n) / ML/s)"
399      Label bottom "\\f011000 K/\\f03T"
400      ModifyGraph mirror=2,fSize=18,standoff=0
```

```
401         ModifyGraph minor=1
402     end
403
404     //_____________________________________________________________________________
        ____________________________________________
405
406     static function CA(Coverage, SpecNum, intbasis, tempbasis)
407         variable coverage, SpecNum
408         string intbasis, tempbasis
409
410         if (tpd#normspec(SpecNum, intbasis, tempbasis)!=-1)
411             intbasis += "_ML"
412         endif
413
414         make /d /o /n=(SpecNum) LnInt, T_rez
415
416         variable i, j
417         string intname, tempname
418         variable startposition_i = strsearch(intbasis, "1", 0)
419         variable startposition_t = strsearch(tempbasis, "1", 0)
420         variable currentcoverage
421         variable xstart, marker
422
423         for(i=1; i<=SpecNum; i+=1)
424             intname = intbasis[0,startposition_i-1] + num2str(i) +
                intbasis[startposition_i+1,strlen(intbasis)-1]
425             tempname = tempbasis[0,startposition_t-1] + num2str(i) +
                tempbasis[startposition_t+1,strlen(tempbasis)-1]
426             wave intwave = $intname
427             wave tempwave = $tempname
428             currentcoverage = areaxy(tempwave, intwave)
429             marker = 0
430             if (currentcoverage<1.05*coverage)  //spectrum should be at least 5% higher
                than the threshold
431                 LnInt[i-1]=NAN
432                 T_rez[i-1]=NAN
433             else
434                 j=-1
435                 do
436                     j += 1
437                     xStart = tempwave[j]
438                     currentcoverage = areaxy(tempwave, intwave,
                        xStart,tempwave[numpnts(tempwave)-1])
439                     if (currentcoverage < Coverage || xStart >= WaveMax(Tempwave))
440                         marker = 1
441                     endif
442                 while (marker == 0 )
443                 LnInt[i-1]=ln(1/3*(Intwave[j-1]+Intwave[j]+Intwave[j+1]))
444                 T_rez[i-1]=1/(1/3*(Tempwave[j-1]+Tempwave[j]+Tempwave[j+1]))
445             endif
446         endfor
447         display /K=1 lnInt vs T_rez
448         ModifyGraph mode=4,marker=8,rgb=(0,0,0)
449     end
450
451     //_____________________________________________________________________________
        ____________________________________________
452
453     static function CA_Cov(SpecNum, intbasis, tempbasis)
454         variable SpecNum
455         string intbasis, tempbasis
456
457         variable i, j
458         string intname, tempname, covname
459         variable startposition_i = strsearch(intbasis, "1", 0)
460         variable startposition_t = strsearch(tempbasis, "1", 0)
461         variable currentcoverage
462         variable xstart, marker
463
464         for(i=1; i<=SpecNum; i+=1)
465             intname = intbasis[0,startposition_i-1] + num2str(i) +
                intbasis[startposition_i+1,strlen(intbasis)-1]
466             tempname = tempbasis[0,startposition_t-1] + num2str(i) +
```

```
            tempbasis[startposition_t+1,strlen(tempbasis)-1]
467         covname = "coverage_" + num2str(i)
468         wave intwave = $intname
469         wave tempwave = $tempname
470         duplicate /d /o intwave $covname
471         wave covwave = $covname
472         currentcoverage = areaxy(tempwave, intwave)
473         marker = 0
474         j=-1
475         do
476             j += 1
477             xStart = tempwave[j]
478             currentcoverage = areaxy(tempwave, intwave,
                xStart,tempwave[numpnts(tempwave)-1])
479             covwave[j]=currentcoverage
480             if (xStart >= WaveMax(Tempwave))
481                 marker = 1
482             endif
483         while (marker == 0 )
484         if (i==1)
485             Display covwave vs tempwave
486         else
487             Appendtograph covwave vs Tempwave
488         endif
489     endfor
490     ModifyGraph rgb=(0,0,0)
491 end
492
493 //_____________________________________________________________________________
    _____________________________________
494
495 static function LEA(SpecNum, intbasis, tempbasis)
496     variable SpecNum
497     string intbasis, tempbasis
498
499     if (tpd#normspec(SpecNum, intbasis, tempbasis)!=-1)
500         intbasis += "_ML"
501     endif
502
503     variable i
504     variable startposition_i = strsearch(intbasis, "1", 0)
505     variable startposition_t = strsearch(tempbasis, "1", 0)
506
507     string WaveTag
508     string XWaveTag
509     string waveTag_old
510     string XwaveTag_old
511
512     for (i=1; i<=SpecNum; i+=1)
513         waveTag_old = intbasis[0,startposition_i-1] + num2str(i) +
            intbasis[startposition_i+1,strlen(intbasis)-1]
514         XwaveTag_old = tempbasis[0,startposition_t-1] + num2str(i) +
            tempbasis[startposition_t+1,strlen(tempbasis)-1]
515         wave intwave_old = $wavetag_old
516         wave tempwave_old = $xwavetag_old
517
518         WaveTag = "ln(int)_" + num2str(i)
519         XWaveTag = "1/T_" + num2str(i)
520
521         duplicate /d /o intwave_old $WaveTag
522         duplicate /d /o tempwave_old $XWaveTag
523
524         wave intwave = $WaveTag
525         wave tempwave = $XWaveTag
526         intwave =ln(intwave)
527         tempwave=1/tempwave
528
529         if (i==1)
530             Display Intwave vs Tempwave
531         else
532             Appendtograph Intwave vs Tempwave
533             ModifyGraph offset($wavetag)={0,i*1.5}
534         endif
```

```
535       endfor
536       ModifyGraph margin(left)=85,margin(bottom)=70,margin(right)=28,margin(top)=28
537       ModifyGraph width=453.543,height=453.543
538       Label left "\\f01ln(\\f03r\\f01\\Bdes\\M / ML/s)"
539       Label bottom "\\f011000 K/\\f03T"
540       ModifyGraph mirror=2,fSize=18,standoff=0
541       ModifyGraph minor=1
542   end
543
544   //_____________________________________________________________________________________
      _____________________________________________
545
546   static function Persson(Prefac, E0, Rep, Rel, coverageList, [NuRange])
547   //implement GA from HRV and loop for different Spectra
548   //implement Persson-Model in GA
549       variable Prefac, E0, Rep, Rel, NuRange
550       string coverageList
551
552       NuRange = paramIsDefault(NuRange) ? 0 : NuRange
553
554       variable TStart = 100
555       variable TStopp = 600
556
557       make /d /n=40000 /o ResidualCoverage
558       SetScale /I x, TStart, TStopp, ResidualCoverage
559
560       string waveTag
561       string XwaveTag
562
563       variable curveIndex
564       variable coverage
565       variable i
566       variable endIt = numpnts(ResidualCoverage)
567       variable dT = (TStopp-TStart)/endIt
568       variable dTheta
569       variable CurrentRate
570       variable order =1
571       variable heatingRate=1
572
573   //this is the calculation of the TPD curves
574       for (curveIndex = 0; curveIndex < ItemsInList(coveragelist); curveIndex += 1)
575           coverage = str2num(StringFromList(curveIndex,coverageList))
576           waveTag = "sample_" + num2str(coverage)
577           XwaveTag =  "sampleT_" + num2str(coverage)
578           duplicate /o ResidualCoverage $waveTag
579           duplicate /o ResidualCoverage $XwaveTag
580           wave Rate = $waveTag
581           wave Temp = $XwaveTag
582           Rate = 0
583           Temp = 0
584           ResidualCoverage[0] = coverage
585
586           for ( i = 0; i < endIt; i += 1 )
587               CurrentRate = 1/heatingRate*exp(Prefac+coverage*NuRange)*(coverage)^order\
588               *exp(-(E0-Rep*coverage-Rel*coverage^2)/(R*(TStart+i*dT)))
589               dTheta = CurrentRate * dT
590               coverage -= dTheta
591               if (dTheta < 0)
592                   break
593               endif
594               if ( i > 0 )
595                   ResidualCoverage[i] = coverage
596               endif
597               Rate[i] = CurrentRate
598               Temp[i] = TStart + i*dT
599           endfor
600       endfor
601   end
602
603   //_____________________________________________________________________________________
      _____________________________________________
604
605   static function ExpFit(Prefac, E0, A, B, C coverageList, [NuRange])
```

```
606 //implement GA from HRV and loop for different Spectra
607 //implement Persson-Model in GA
608     variable Prefac, E0, A, B, C, NuRange
609     string coverageList
610 
611     NuRange = paramIsDefault(NuRange) ? 0 : NuRange
612 
613     variable TStart = 100
614     variable TStopp = 600
615 
616     make /d /n=40000 /o ResidualCoverage
617     SetScale /I x, TStart, TStopp, ResidualCoverage
618 
619     string waveTag
620     string XwaveTag
621 
622     variable curveIndex
623     variable coverage
624     variable i
625     variable endIt = numpnts(ResidualCoverage)
626     variable dT = (TStopp-TStart)/endIt
627     variable dTheta
628     variable CurrentRate
629     variable order =1
630     variable heatingRate=1
631 
632 //this is the calculation of the TPD curves
633     for (curveIndex = 0; curveIndex < ItemsInList(coveragelist); curveIndex += 1)
634         coverage = str2num(StringFromList(curveIndex,coverageList))
635         waveTag = "sample_" + num2str(coverage)
636         XwaveTag =  "sampleT_" + num2str(coverage)
637         duplicate /o ResidualCoverage $waveTag
638         duplicate /o ResidualCoverage $XwaveTag
639         wave Rate = $waveTag
640         wave Temp = $XwaveTag
641         Rate = 0
642         Temp = 0
643         ResidualCoverage[0] = coverage
644 
645         for ( i = 0; i < endIt; i += 1 )
646             CurrentRate =
                1/heatingRate*((1-coverage)*exp(Prefac)+coverage*exp(prefac+NuRange))*(cov
                erage)^order\
647             *exp(-(E0-A*coverage-B*exp(coverage/C))/(R*(TStart+i*dT)))
648             dTheta = CurrentRate * dT
649             coverage -= dTheta
650             if (dTheta < 0)
651                 break
652             endif
653             if ( i > 0 )
654                 ResidualCoverage[i] = coverage
655             endif
656             Rate[i] = CurrentRate
657             Temp[i] = TStart + i*dT
658         endfor
659     endfor
660 end
661 
662 //_____________________________________________________________________________
663 
664 static function IPW(nu, [NuRange, DeltaG])
665     variable nu, NuRange, DeltaG
666 
667     NuRange = paramIsDefault(NuRange) ? 0 : NuRange
668     DeltaG = paramIsDefault(DeltaG) ? 0 : DeltaG
669 
670     wave Rate = 'int'
671     wave Temp = 'temp'
672 
673     duplicate /o Rate Residualcoverage
674     wave ResCov = Residualcoverage
675 
```

```
676       duplicate /o Rate DesorptionEnergy
677       wave Edes = Desorptionenergy
678
679       variable coverage = areaxy(Temp, Rate)
680       variable HeatingRate = 1
681       variable dT = 1/numpnts(Temp)
682       variable i
683       ResCov[0] = coverage
684
685       if(DeltaG!=1)
686           for (i=0; i<numpnts(Rate); i+=1)
687               Edes[i] =
                  -R*Temp[i]*ln(Rate[i]*HeatingRate/((1-ResCov[i])*(exp(nu+Rescov[i]*NuRange
                  )*ResCov[i])))
688               if (i<numpnts(Rate)-1)
689                   ResCov[i+1] = areaxy(Temp, Rate, Temp[i], inf)
690               endif
691           endfor
692       else
693           for (i=0; i<numpnts(Rate); i+=1)
694               Edes[i] =
                  -R*Temp[i]*ln(Rate[i]*HeatingRate/((1.381*10^(-23)*Temp[i]/(6.626*10^(-34)
                  ))*ResCov[i]))
695               if (i<numpnts(Rate)-1)
696                   ResCov[i+1] = areaxy(Temp, Rate, Temp[i], inf)
697               endif
698           endfor
699       endif
700
701       display Rate vs Temp
702       AppendToGraph/R Edes vs Temp
703       ModifyGraph rgb(DesorptionEnergy)=(0,0,0)
704   end
705
706   //_____________________________________________________________________________________
      _____________________________________________
707
708   static function IPW2(Edes)
709       variable Edes
710
711       wave Rate = 'int'
712       wave Temp = 'temp'
713
714       duplicate /o Rate Residualcoverage
715       wave ResCov = Residualcoverage
716
717       duplicate /o Rate Prefactor
718       wave prefac = Prefactor
719
720       variable coverage = areaxy(Temp, Rate)
721       variable HeatingRate = 1
722       variable dT = 1/numpnts(Temp)
723       variable i
724
725       ResCov[0] = coverage
726
727           for (i=0; i<numpnts(Rate); i+=1)
728               prefac[i] = Rate[i]*HeatingRate/(rescov[i]*exp(-Edes/(R*Temp[i])))
729               if (i<numpnts(Rate)-1)
730                   ResCov[i+1] = areaxy(Temp, Rate, Temp[i], inf)
731               endif
732           endfor
733
734       display Rate vs Temp
735       AppendToGraph/R prefac vs Temp
736       ModifyGraph rgb(Prefactor)=(0,0,0), log(right)=1
737   end
738
739   //_____________________________________________________________________________________
      ____________________________________________
740
741   static function Albano(Prefac, E0, Mu, Alpha, NsInput, coverageList)
742       variable Prefac, E0, Mu, Alpha, NsInput
```

```
743       string coverageList
744
745       variable TStart = 100
746       variable TStopp = 600
747
748       make /d /n=40000 /o ResidualCoverage
749       SetScale /I x, TStart, TStopp, ResidualCoverage
750
751       string waveTag
752       string XwaveTag
753
754       variable curveIndex
755       variable coverage
756       variable i
757       variable Edes
758       variable endIt = numpnts(ResidualCoverage)
759       variable dT = (TStopp-TStart)/endIt
760       variable dTheta
761       variable CurrentRate
762       variable order =1
763       variable heatingRate=1
764       variable epsilon = 8.854E-12
765       variable Na = 6.022E23
766       variable Ns = NsInput*1E18
767
768   //this is the calculation of the TPD curves
769       for (curveIndex = 0; curveIndex < ItemsInList(coveragelist); curveIndex += 1)
770           coverage = str2num(StringFromList(curveIndex,coverageList))
771           waveTag = "sample_" + num2str(coverage)
772           XwaveTag =  "sampleT_" + num2str(coverage)
773           duplicate /o ResidualCoverage $waveTag
774           duplicate /o ResidualCoverage $XwaveTag
775           wave Rate = $waveTag
776           wave Temp = $XwaveTag
777           Rate = 0
778           Temp = 0
779           ResidualCoverage[0] = coverage
780
781           for ( i = 0; i < endIt; i += 1 )
782               Edes = E0 -
                  Na*(8.89*(mu*3.34E-30)^2*(coverage*Ns)^1.5)/(1000*epsilon*(1+8.89*Alpha*1e
                  -30*(coverage*Ns)^1.5)^2)
783               CurrentRate =
                  1/heatingRate*exp(Prefac)*(coverage)^order*exp(-(Edes)/(R*(TStart+i*dT)))
784               dTheta = CurrentRate * dT
785               coverage -= dTheta
786               if (dTheta < 0)
787                   break
788               endif
789               if ( i > 0 )
790                   ResidualCoverage[i] = coverage
791               endif
792               Rate[i] = CurrentRate
793               Temp[i] = TStart + i*dT
794               endfor
795       endfor
796   end
797
798   //_____________________________________________________________________________
      ____________________________________
799
800   static function PeakPicking()   //no idea for this
801       print "PeakPicking currently not working."
802   end
803
804   //_____________________________________________________________________________
      ____________________________________________
805
806   static function TempCalib(a, b, SpecNum, Tempbasis, [Fit, Skip])
807       variable a, b, SpecNum, Fit, Skip
808       string tempbasis
809
810       Fit = paramIsDefault(Fit) ? 1 : Fit
```

```
811       Skip = paramIsDefault(Skip) ? 0 : Skip
812
813       string tempname, tempname_old
814       variable i, j
815       variable startposition, start_aux, stepwidth
816       start_aux=0
817
818       for(i=0; i<=Skip; i+=1)
819           startposition = strsearch(tempbasis, "1", start_aux)
820           start_aux=startposition+1
821       endfor
822
823       for(i=1; i<=SpecNum; i+=1)
824           tempname_old = tempbasis[0,startposition-1] + num2str(i) +
          tempbasis[startposition+1,strlen(tempbasis)-1]
825           wave tempwave_old = $tempname_old
826           tempname = tempname_old+"_calib"
827           duplicate /d /o tempwave_old $tempname
828           wave tempwave = $tempname
829           setscale x, 0, numpnts(tempwave)-1, tempwave
830
831           if(Fit==1)
832               CurveFit/W=2/Q=1 line, tempwave
833               wave coef = W_coef
834               stepwidth =
                  (tempwave[numpnts(tempwave)-1]-tempwave[0])/(numpnts(tempwave)-1)
835               for(j=0; j<numpnts(tempwave); j+=1)
836                   tempwave[j] = (j*coef[1]+coef[0])*b+a
837               endfor
838           else
839               tempwave = tempwave*b+a
840           endif
841       endfor
842   end
843
844   //_____________________________________________________________________________
      ____________________________________
845
846   static function PlotGraph(SpecNum, StartSpec, Offset, Intbasis, Tempbasis)
847       variable SpecNum, StartSpec, Offset
848       string intbasis, tempbasis
849
850       string intname, tempname
851       variable i
852       variable startposition_i = strsearch(intbasis, "1", 0)
853       variable startposition_t = strsearch(tempbasis, "1", 0)
854
855       for(i=Specnum; i>=StartSpec; i-=1)
856           intname = intbasis[0,startposition_i-1] + num2str(i) +
          intbasis[startposition_i+1,strlen(intbasis)-1]
857           tempname = tempbasis[0,startposition_t-1] + num2str(i) +
          tempbasis[startposition_t+1,strlen(tempbasis)-1]
858           wave intwave = $intname
859           wave tempwave = $tempname
860           AppendToGraph intwave vs tempwave
861           ModifyGraph offset($intname)={0,(i-Startspec)*Offset}
862       endfor
863   end
864
865   //_____________________________________________________________________________
      ____________________________________
866
867   static function RevertWave(WaveStr)
868       string Wavestr
869
870       wave originalwave=$wavestr
871       string wavetorevert = Wavestr+"_rev"
872       duplicate /d /o originalwave $wavetorevert
873       wave revert_wave = $wavetorevert
874
875       variable i
876       for(i=0; i<numpnts(originalwave); i+=1)
877           revert_wave[i] = originalwave[numpnts(originalwave)-1-i]
```

```
878         endfor
879     end
880
881     //_____________________________________________________________________________
        ____________________________________________
882
883     static function IntEnergy(Ywave, Xwave, [Invert])
884         string Ywave, Xwave
885         variable Invert
886
887         Invert = paramIsDefault(Invert) ? 0 : Invert
888
889         if (Invert!=0)
890             revertwave(Xwave)
891             xwave = xwave + "_rev"
892             revertwave(Ywave)
893             ywave = ywave + "_rev"
894         endif
895
896         Integrate/METH=1 $(Ywave)/X=$(Xwave)/D=$(Ywave+"_INT")
897
898         wave Temp = $(Ywave+"_INT")
899         duplicate /d /o Temp $"E_Int"
900         wave E_Int = $"E_Int"
901         wave Theta = $(Xwave)
902         E_Int /= Theta
903     end
904
905     //_____________________________________________________________________________
        ____________________________________________
906
907     static function SMP(Specnum, Intbasis, Tempbasis)
908         variable SpecNum
909         string intbasis, tempbasis
910
911         variable i
912         variable startposition_i = strsearch(intbasis, "1", 0)
913         variable startposition_t = strsearch(tempbasis, "1", 0)
914
915         string WaveTag
916         string XWaveTag
917         string waveTag_old
918         string XwaveTag_old
919
920         for (i=1; i<=SpecNum; i+=1)
921             waveTag_old = intbasis[0,startposition_i-1] + num2str(i) +
            intbasis[startposition_i+1,strlen(intbasis)-1]
922             XwaveTag_old = tempbasis[0,startposition_t-1] + num2str(i) +
            tempbasis[startposition_t+1,strlen(tempbasis)-1]
923             wave intwave_old = $wavetag_old
924             wave tempwave_old = $xwavetag_old
925
926             WaveTag = "log(int)_" + num2str(i)
927             XWaveTag = "1/T_" + num2str(i)
928
929             duplicate /d /o intwave_old $WaveTag
930             duplicate /d /o tempwave_old $XWaveTag
931
932             wave intwave = $WaveTag
933             wave tempwave = $XWaveTag
934             intwave =log(intwave)
935             tempwave=1/tempwave
936
937             if (i==1)
938                 Display/T Intwave_old vs Tempwave
939             else
940                 Appendtograph/T Intwave_old vs Tempwave
941             endif
942         endfor
943         make /N=50 /o invtemp
944         for(i=0;i<50;i+=1)
945             invtemp[i]=i*0.0005*2+0.0005
946         endfor
```

```
947         make /T /N=50 /o temptext
948         temptext = num2str(round(1/invtemp))
949         AppendToGraph invtemp vs invtemp
950         ModifyGraph hideTrace(invtemp)=2
951         ModifyGraph userticks(bottom)={invtemp,temptext}
952         ModifyGraph margin(left)=113,margin(bottom)=70,margin(right)=28,margin(top)=70
953         ModifyGraph width=453.543,height=453.543
954         ModifyGraph log(left)=1
955         Label left "\\f01\\f03r\\f01\\Bdes\\M / ML/s"
956         Label top "\\f011000 K/\\f03T"
957         Label bottom "\\f03T\\f01 / K"
958         SetAxis/A/R top
959         SetAxis/A/R bottom
960         SetAxis/A left
961         ModifyGraph mirror(left)=2,fSize=18,standoff=0
962         ModifyGraph minor=1
963     end
964     end
965
966     //_____________________________________________________________________________
        _____________________________________________
967
968     static function SimTPD(ROrder, Edes, Lin, Quad, Nu, Coverage, Hrate, Tstart, Tend,
        [Nuvar, Stepsize])
969         variable ROrder, Edes, Lin, Quad, Nu, Hrate, Tstart, Tend, Stepsize
970         string Coverage
971         variable Nuvar
972         Nuvar = paramIsDefault(NuVar) ? 0 : NuVar
973         Stepsize = paramIsDefault(Stepsize) ? 0.1 : Stepsize
974         make /d /n=((Tend-Tstart)*Hrate/Stepsize) /o rate //*10
975         make /d /n=((Tend-Tstart)*Hrate/Stepsize) /o temp //*10
976         string wave_rate, wave_temp
977
978         variable i, j
979         variable Tstep = (Tend-Tstart)/(numpnts(rate)-1)
980         variable T = Tstart
981         variable R=0.008314, rescoverage
982
983         for(j=1; j<=ItemsInList(Coverage); j+=1)
984             wave_rate="rate_"+num2str(j)
985             wave_temp="temp_"+num2str(j)
986             duplicate /d /o rate $wave_rate
987             duplicate /d /o temp $wave_temp
988             wave cur_rate = $Wave_rate
989             wave cur_temp = $wave_temp
990             rescoverage = str2num(StringFromList(j-1,coverage))
991             T=Tstart
992             for(i=0; i<numpnts(cur_rate); i+=1)
993                 cur_rate[i] =
                    rescoverage^Rorder*exp(Nu+NuVar*rescoverage)*exp(-(Edes-rescoverage*lin-re
                    scoverage^2*quad)/(R*T))/Hrate
994                 if (resCoverage<0)
995                     cur_rate[i]=0
996                 elseif (cur_rate[i]*Tstep > 0)
997                     resCoverage -= cur_rate[i]*Tstep
998                 else
999                     cur_rate[i]=0
1000                endif
1001                cur_temp[i] = T
1002                T += Tstep
1003            endfor
1004        endfor
1005        //killwaves rate, temp
1006    end
1007
1008    //_____________________________________________________________________________
        _____________________________________________
1009
1010    static function Ratio(Int1, Temp1, Int2, Temp2)
1011        string Int1, Temp1, Int2, Temp2
1012        wave Intwave1 = $Int1
1013        wave Tempwave1 = $Temp1
1014        wave Intwave2 = $Int2
```

```
1015        wave Tempwave2 = $Temp2
1016        make /d /n=(numpnts(intwave1)) /o Ratios
1017
1018        variable i
1019        for (i=0; i<numpnts(Intwave1); i+=1)
1020            Ratios[i]=areaxy(tempwave1, intwave1, tempwave1[i], inf)/areaxy(tempwave2,
                intwave2, tempwave2[i], inf)
1021        endfor
1022    end
1023
1024    //_____________________________________________________________________________________
    _____________________________________________
1025
1026    static function SumNEXAFS(BaseString, NumSpec, [Start])
1027        string BaseString
1028        variable NumSpec, Start
1029        Start = paramIsDefault(Start) ? 1 : Start
1030
1031        variable i
1032        string wNameF,wNameI, WaveTag
1033
1034        for(i=Start; i<(Start+NumSpec); i+=1)
1035            wNameF = BaseString+num2str(i)+"_Flrscnc"
1036            wNameI = BaseString+num2str(i)+"_Ioncur"
1037            wave Fwave = $wNameF
1038            wave Iwave = $wNameI
1039
1040            if(i==Start)
1041                WaveTag = BaseString + "_sum"
1042                duplicate /d /o Fwave $WaveTag
1043                wave SumWave = $WaveTag
1044                SumWave = Fwave/Iwave
1045            else
1046                Sumwave+=Fwave/Iwave
1047            endif
1048        endfor
1049        Sumwave/=WaveMax(Sumwave)
1050        //Sumwave/=NumSpec
1051    end
1052
1053    //_____________________________________________________________________________________
    _____________________________________________
1054
1055    static function GA_TPD()
1056        //simtpd(1, 100*(1+enoise(0.3)), 20*enoise(0.5), 20*enoise(0.3),
            35*(1+enoise(0.3)), "1.0", 1, 100, 600)
1057        wave rate_1 = rate_1
1058        duplicate /o /d rate_1 testwave
1059        wave testwave = testwave
1060        wave wtemp = temp_1
1061
1062        variable individuals = 1000
1063        variable generations = 2000
1064        variable mutationProbability = 0.1
1065        variable survivors = 0.20    //meaning the best x% are taken
1066
1067        variable i,j,k,l
1068        variable Rows = numpnts(wtemp)
1069        variable heatingrate = 1.0 //get this later from input
1070        variable Tstart=wtemp[0]
1071        variable Tend=wtemp[numpnts(wtemp)-1]
1072        variable dT = (Tend-Tstart)/Rows
1073        variable coverage=1.0
1074        variable T, rescov
1075        make /d /n=(Rows) /o Rate
1076        wave Rate = Rate
1077        make /d /n=(Rows) /o Temperature
1078        wave Temperature = Temperature
1079
1080        //we have three parameters for the optimization
1081        //set up genome
1082        make /d /n=(individuals) /o DesorptionEnergy
1083        wave E0 = DesorptionEnergy
```

```
1084
1085        make /d /n=(individuals) /o FrequencyFactor
1086        wave nu = FrequencyFactor
1087
1088        make /d /n=(individuals) /o LinearE
1089        wave linE = LinearE
1090
1091        make /d /n=(individuals) /o SquareE
1092        wave sqrE = SquareE
1093
1094        make /d /n=(individuals) /o NuVariation
1095        wave NuVar = NuVariation
1096
1097        make /d /n=(individuals) /o ROrder
1098        wave Rord = ROrder
1099
1100        make /d /n=(individuals) /o Deviation
1101        wave deviation = Deviation
1102
1103        make /d /n=(generations) /o errorOverGenerations
1104        wave errorOverGenerations = errorOverGenerations
1105
1106        //the genes can take those values
1107        variable E0Low = 150        //Currently tested for Nt/Ag,Cu(111)
1108        variable E0Spread = 30
1109
1110        variable nuLow=36
1111        variable nuSpread =4
1112
1113        variable linELow=5
1114        variable linESpread =15
1115
1116        variable sqrELow=0
1117        variable sqrESpread =5
1118
1119        variable NuVarLow=0
1120        variable NuVarSpread =4.6
1121
1122        variable ROrdLow=0.7
1123        variable ROrdSpread =0.6
1124
1125        //populate with gene values
1126        for (i = 0; i < individuals; i += 1)
1127            E0[i] = E0Low + E0Spread * ( 0.5+enoise(0.5) )
1128            nu[i] = nuLow + nuSpread * ( 0.5+enoise(0.5) )
1129            linE[i] = linELow + linESpread * (0.5+enoise(0.5) )
1130            sqrE[i] = sqrElow + sqrESpread * (0.5+enoise(0.5) )
1131            NuVar[i] = NuVarLow + NuVarSpread * (0.5+enoise(0.5) )
1132            ROrd[i] = ROrdlow + ROrdSpread * (0.5+enoise(0.5) )
1133            //print E0[i], nu[i]
1134        endfor
1135
1136        //get its fitness and sort it
1137
1138        variable errorSum
1139
1140        // go through all individuals, and for each one get the error
1141
1142        for ( i = 0; i < individuals; i += 1 )
1143            errorSum = 0
1144
1145            Rate = 0
1146            Temperature = 0
1147            T=Tstart
1148            rescov=coverage
1149
1150            for (l = 0; l < Rows; l += 1)
1151                Rate[l] =
                    (1/heatingRate)*exp(nu[i]+NuVar[i]*rescov)*(rescov)^ROrd[i]*exp(-(E0[i]-li
                    nE[i]*rescov-sqrE[i]*(rescov^2))/(R*T))
1152                if (resCov<0)
1153                    Rate[l]=0
1154                elseif (Rate[l]*dT > 0)
```

```
1155                resCov -= Rate[l]*dT
1156            else
1157                Rate[l]=0
1158            endif
1159            Temperature[l] = T
1160            T += dT
1161            errorSum += abs(Rate[l] - testWave[l])
1162            endfor
1163        deviation[i] = errorSum
1164    endfor
1165
1166    sort deviation, deviation, E0, nu, linE, sqrE, NuVar, Rord
1167    errorOverGenerations[0] = deviation[0]
1168
1169    // generation 0 has finished now, start the next generations
1170
1171    for ( k =1; k < generations; k += 1)
1172        variable randomParentIndex
1173
1174        // set up the next generation
1175        //now overwrite the not-fit part of the population with the offspring of the
          fit fraction
1176
1177        for (j = ceil(survivors*individuals); j < individuals; j += 1)   //every
          index below survivors*individuals is untouched - the good ones are allowed
          to survive
1178            //draw a random index between 0 and floor(0.1*individuals) ... just take
              a value which was present in the fit population
1179            randomParentIndex = floor( floor(survivors*individuals) * (0.5 +
                enoise(0.5)))
1180            E0[j] = E0[randomParentIndex]
1181            //add a little mutation
1182            if ( ( 0.5+enoise(0.5) ) < mutationProbability)
1183                //E0[j] = (k < floor(generations/2)) * ( E0Low + E0Spread * (
                  0.5+enoise(0.5) ) ) + (k >= floor(generations/2))*(E0[j]*( 1
                  +enoise(0.4) ) )
1184                E0[j] = E0Low + E0Spread * ( 0.5+enoise(0.5) )
1185            endif
1186
1187
1188            randomParentIndex = floor( floor(survivors*individuals) * (0.5 +
                enoise(0.5)))
1189            nu[j] = nu[randomParentIndex]
1190            if ( ( 0.5+enoise(0.5) ) <  mutationProbability)
1191                //nu[j] = (k < floor(generations/2)) * (nuLow + nuSpread * (
                  0.5+enoise(0.5) ) ) +  (k >= floor(generations/2))*(nu[j]*( 1
                  +enoise(0.4) ) )
1192                nu[j] =nuLow + nuSpread * ( 0.5+enoise(0.5) )
1193            endif
1194
1195            randomParentIndex = floor( floor(survivors*individuals) * (0.5 +
                enoise(0.5)))
1196            linE[j] = linE[randomParentIndex]
1197            if ( ( 0.5+enoise(0.5) ) <  mutationProbability)
1198                //linE[j] = (k < floor(generations/2)) * (linELow + linESpread * (
                  0.5+enoise(0.5)) ) +  (k >= floor(generations/2))*(linE[j]*( 1
                  +enoise(0.4) ) )
1199                linE[j] = linELow + linESpread * ( 0.5+enoise(0.5))
1200            endif
1201
1202            randomParentIndex = floor( floor(survivors*individuals) * (0.5 +
                enoise(0.5)))
1203            sqrE[j] = sqrE[randomParentIndex]
1204            if ( ( 0.5+enoise(0.5) ) <  mutationProbability)
1205                //sqrE[j] = (k < floor(generations/2)) * (sqrELow + sqrESpread *
                  (0.5+enoise(0.5)) ) +  (k >= floor(generations/2))*(sqrE[j]*( 1
                  +enoise(0.4) ) )
1206                sqrE[j] = sqrELow + sqrESpread * (0.5+enoise(0.5))
1207            endif
1208
1209            randomParentIndex = floor( floor(survivors*individuals) * (0.5 +
                enoise(0.5)))
1210            NuVar[j] = NuVar[randomParentIndex]
```

```
1211                if ( ( 0.5+enoise(0.5) ) <  mutationProbability)
1212                    //NuVar[j] = (k < floor(generations/2)) * (NuVarLow + NuVarSpread *
                        ( 0.5+enoise(0.5)) ) +  (k >= floor(generations/2))*(NuVar[j]*( 1
                        +enoise(0.4) ) )
1213                    NuVar[j] = NuVarLow + NuVarSpread * ( 0.5+enoise(0.5))
1214                endif
1215
1216                randomParentIndex = floor( floor(survivors*individuals) * (0.5 +
                    enoise(0.5)))
1217                ROrd[j] = ROrd[randomParentIndex]
1218                if ( ( 0.5+enoise(0.5) ) <  mutationProbability)
1219                    //ROrd[j] = (k < floor(generations/2)) * (ROrdLow + ROrdSpread *
                        (0.5+enoise(0.5)) ) +  (k >= floor(generations/2))*(ROrd[j]*( 1
                        +enoise(0.4) ) )
1220                    ROrd[j] = ROrdLow + ROrdSpread * (0.5+enoise(0.5))
1221                endif
1222
1223            endfor
1224            //now analyze the new generation
1225            for ( i = 0; i < individuals; i += 1 )
1226                errorSum = 0
1227
1228                Rate = 0
1229                Temperature = 0
1230                T=Tstart
1231                rescov=coverage
1232
1233                for (l = 0; l < Rows; l += 1)
1234                    Rate[l] =
                        (1/heatingRate)*exp(nu[i]+NuVar[i]*rescov)*(rescov)^ROrd[i]*exp(-(E0[i
                        ]-linE[i]*rescov-sqrE[i]*(rescov^2))/(R*T))
1235                    if(resCov<0)
1236                        Rate[l]=0
1237                    elseif (Rate[l]*dT > 0)
1238                        resCov -= Rate[l]*dT
1239                    else
1240                        Rate[l]=0
1241                    endif
1242                    Temperature[l] = T
1243                    T += dT
1244                    errorSum += abs(Rate[l] - testWave[l])
1245                    endfor
1246                deviation[i] = errorSum
1247            endfor
1248
1249            sort deviation, deviation, E0, nu, linE, sqrE, NuVar, Rord
1250            errorOverGenerations[k] = deviation[0]
1251
1252        endfor
1253
1254
1255        // final number of generations reached,plot the best one
1256        Rate = 0
1257        Temperature = 0
1258        T=Tstart
1259        rescov=coverage
1260
1261        for (l = 0; l < Rows; l += 1)
1262            Rate[l] =
                (1/heatingRate)*exp(nu[0]+NuVar[0]*rescov)*(rescov)^ROrd[0]*exp(-(E0[0]-linE[0
                ]*rescov-sqrE[0]*(rescov^2))/(R*T))
1263            if (resCov<0)
1264                Rate[l]=0
1265            elseif (Rate[l]*dT > 0)
1266                resCov -= Rate[l]*dT
1267            else
1268                Rate[l]=0
1269            endif
1270            Temperature[l] = T
1271            T += dT
1272        endfor
1273        print "E0 ", E0[0], "-  Nu ", nu[0], "-  LinE ", linE[0], "-  SquareE ",
            sqrE[0], "-  NuVar ", NuVar[0], "-  Order ", Rord[0]
```

```
1274
1275  end
1276
1277  //_____________________________________________________________________________
      ____________________________________________
1278
1279  static function GA_TPD_multi(Coveragelist)
1280      string Coveragelist
1281
1282      variable individuals = 1000
1283      variable generations = 100
1284      variable mutationProbability = 0.75
1285      variable survivors = 0.15
1286
1287      variable i,j,k,l
1288      variable heatingrate = 1.0
1289      variable Rows, Tstart, Tend, dT, coverage, T, rescov
1290      string wavetag, xwavetag
1291
1292      make /d /n=(individuals) /o DesorptionEnergy
1293      wave E0 = DesorptionEnergy
1294
1295      make /d /n=(individuals) /o FrequencyFactor
1296      wave nu = FrequencyFactor
1297
1298      make /d /n=(individuals) /o LinearE
1299      wave linE = LinearE
1300
1301      make /d /n=(individuals) /o SquareE
1302      wave sqrE = SquareE
1303
1304      make /d /n=(individuals) /o NuVariation
1305      wave NuVar = NuVariation
1306
1307      make /d /n=(individuals) /o ROrder
1308      wave Rord = ROrder
1309
1310      make /d /n=(individuals) /o Deviation
1311      wave deviation = Deviation
1312
1313      make /d /n=(generations) /o errorOverGenerations
1314      wave errorOverGenerations = errorOverGenerations
1315
1316      variable E0Low =60
1317      variable E0Spread =10
1318
1319      variable nuLow=34
1320      variable nuSpread =4
1321
1322      variable linELow=0
1323      variable linESpread =30
1324
1325      variable sqrELow=-10
1326      variable sqrESpread =20
1327
1328      variable NuVarLow=0
1329      variable NuVarSpread =5
1330
1331      variable ROrdLow=1.0
1332      variable ROrdSpread =0.0
1333
1334      for (i = 0; i < individuals; i += 1)
1335          E0[i] = E0Low + E0Spread * ( 0.5+enoise(0.5) )
1336          nu[i] = nuLow + nuSpread * ( 0.5+enoise(0.5) )
1337          linE[i] = linELow + linESpread * (0.5+enoise(0.5) )
1338          sqrE[i] = sqrElow + sqrESpread * (0.5+enoise(0.5) )
1339          NuVar[i] = NuVarLow + NuVarSpread * (0.5+enoise(0.5) )
1340          ROrd[i] = ROrdlow + ROrdSpread * (0.5+enoise(0.5) )
1341      endfor
1342
1343      variable errorSum
1344      variable curveIndex
1345
```

```
1346        for (curveIndex = 1; curveIndex <= ItemsInList(coveragelist); curveIndex += 1)
1347            coverage = str2num(StringFromList(curveIndex-1,coverageList))
1348            waveTag = "rate_" + num2str(curveIndex)
1349            XwaveTag =  "temp_" + num2str(curveIndex)
1350            wave testwave = $waveTag
1351            wave Temp = $XwaveTag
1352
1353            Rows = numpnts(temp)
1354            Tstart=temp[0]
1355            Tend=temp[numpnts(temp)-1]
1356            dT = (Tend-Tstart)/Rows
1357
1358            make /d /n=(Rows) /o Rate
1359            wave Rate = Rate
1360            make /d /n=(Rows) /o Temperature
1361            wave Temperature = Temperature
1362
1363            for ( i = 0; i < individuals; i += 1 )
1364                errorSum = 0
1365
1366                Rate = 0
1367                Temperature = 0
1368                T=Tstart
1369                rescov=coverage
1370
1371                for (l = 0; l < Rows; l += 1)
1372                    Rate[l] =
                        (1/heatingRate)*exp(nu[i]+NuVar[i]*rescov)*(rescov)^ROrd[i]*exp(-(E0[i
                        ]-linE[i]*rescov-sqrE[i]*(rescov^2))/(R*T))
1373                    if (resCov<0)
1374                        Rate[l]=0
1375                    elseif (Rate[l]*dT > 0)
1376                        resCov -= Rate[l]*dT
1377                    else
1378                        Rate[l]=0
1379                    endif
1380                    Temperature[l] = T
1381                    T += dT
1382                    errorSum += abs(Rate[l] - testWave[l])
1383                endfor
1384                deviation[i] += errorSum
1385            endfor
1386        endfor
1387
1388        sort deviation, deviation, E0, nu, linE, sqrE, NuVar, Rord
1389        errorOverGenerations[0] = deviation[0]
1390        deviation = 0
1391
1392        for ( k =1; k < generations; k += 1)
1393            variable randomParentIndex
1394
1395            if(k==generations/2)
1396                print "Half Time!"
1397            endif
1398
1399            for (j = ceil(survivors*individuals); j < individuals; j += 1)
1400                randomParentIndex = floor( floor(survivors*individuals) * (0.5 +
                    enoise(0.5)))
1401                E0[j] = E0[randomParentIndex]
1402                if ( ( 0.5+enoise(0.5) ) < mutationProbability)
1403                    //E0[j] = (k < floor(generations/2)) * ( E0Low + E0Spread * (
                        0.5+enoise(0.5) ) ) + (k >= floor(generations/2))*(E0[j]*( 1
                        +enoise(0.4) ) )
1404                    E0[j] = E0Low + E0Spread * ( 0.5+enoise(0.5) )
1405                endif
1406
1407
1408                randomParentIndex = floor( floor(survivors*individuals) * (0.5 +
                    enoise(0.5)))
1409                nu[j] = nu[randomParentIndex]
1410                if ( ( 0.5+enoise(0.5) ) <  mutationProbability)
1411                    //nu[j] = (k < floor(generations/2)) * (nuLow + nuSpread * (
                        0.5+enoise(0.5) ) ) +  (k >= floor(generations/2))*(nu[j]*( 1
```

```
                    +enoise(0.4) ) )
1412                nu[j] =nuLow + nuSpread * ( 0.5+enoise(0.5) )
1413            endif
1414
1415            randomParentIndex = floor( floor(survivors*individuals) * (0.5 +
                enoise(0.5)))
1416            linE[j] = linE[randomParentIndex]
1417            if ( ( 0.5+enoise(0.5) ) <  mutationProbability)
1418                //linE[j] = (k < floor(generations/2)) * (linELow + linESpread * (
                    0.5+enoise(0.5)) ) +  (k >= floor(generations/2))*(linE[j]*( 1
                    +enoise(0.4) ) )
1419                linE[j] = linELow + linESpread * ( 0.5+enoise(0.5))
1420            endif
1421
1422            randomParentIndex = floor( floor(survivors*individuals) * (0.5 +
                enoise(0.5)))
1423            sqrE[j] = sqrE[randomParentIndex]
1424            if ( ( 0.5+enoise(0.5) ) <  mutationProbability)
1425                //sqrE[j] = (k < floor(generations/2)) * (sqrELow + sqrESpread *
                    (0.5+enoise(0.5)) ) +  (k >= floor(generations/2))*(sqrE[j]*( 1
                    +enoise(0.4) ) )
1426                sqrE[j] = sqrELow + sqrESpread * (0.5+enoise(0.5))
1427            endif
1428
1429            randomParentIndex = floor( floor(survivors*individuals) * (0.5 +
                enoise(0.5)))
1430            NuVar[j] = NuVar[randomParentIndex]
1431            if ( ( 0.5+enoise(0.5) ) <  mutationProbability)
1432                //NuVar[j] = (k < floor(generations/2)) * (NuVarLow + NuVarSpread *
                    ( 0.5+enoise(0.5)) ) +  (k >= floor(generations/2))*(NuVar[j]*( 1
                    +enoise(0.4) ) )
1433                NuVar[j] = NuVarLow + NuVarSpread * ( 0.5+enoise(0.5))
1434            endif
1435
1436            randomParentIndex = floor( floor(survivors*individuals) * (0.5 +
                enoise(0.5)))
1437            ROrd[j] = ROrd[randomParentIndex]
1438            if ( ( 0.5+enoise(0.5) ) <  mutationProbability)
1439                //ROrd[j] = (k < floor(generations/2)) * (ROrdLow + ROrdSpread *
                    (0.5+enoise(0.5)) ) +  (k >= floor(generations/2))*(ROrd[j]*( 1
                    +enoise(0.4) ) )
1440                ROrd[j] = ROrdLow + ROrdSpread * (0.5+enoise(0.5))
1441            endif
1442
1443        endfor
1444
1445        for (curveIndex = 1; curveIndex <= ItemsInList(coveragelist); curveIndex += 1)
1446            coverage = str2num(StringFromList(curveIndex-1,coverageList))
1447            waveTag = "rate_" + num2str(curveIndex)
1448            XwaveTag =  "temp_" + num2str(curveIndex)
1449            wave testwave = $waveTag
1450            wave Temp = $XwaveTag
1451
1452            Rows = numpnts(temp)
1453            Tstart=temp[0]
1454            Tend=temp[numpnts(temp)-1]
1455            dT = (Tend-Tstart)/Rows
1456
1457            make /d /n=(Rows) /o Rate
1458            wave Rate = Rate
1459            make /d /n=(Rows) /o Temperature
1460            wave Temperature = Temperature
1461            for ( i = 0; i < individuals; i += 1 )
1462                errorSum = 0
1463
1464                Rate = 0
1465                Temperature = 0
1466                T=Tstart
1467                rescov=coverage
1468
1469                for (l = 0; l < Rows; l += 1)
1470                    Rate[l] =
                        (1/heatingRate)*exp(nu[i]+NuVar[i]*rescov)*(rescov)^ROrd[i]*exp(-(
```

```
                    E0[i]-linE[i]*rescov-sqrE[i]*(rescov^2))/(R*T))
1471                if(resCov<0)
1472                    Rate[l]=0
1473                elseif (Rate[l]*dT > 0)
1474                    resCov -= Rate[l]*dT
1475                else
1476                    Rate[l]=0
1477                endif
1478                Temperature[l] = T
1479                T += dT
1480                errorSum += abs(Rate[l] - testWave[l])
1481            endfor
1482        deviation[i] += errorSum
1483        endfor
1484    endfor
1485
1486    sort deviation, deviation, E0, nu, linE, sqrE, NuVar, Rord
1487    errorOverGenerations[k] = deviation[0]
1488    deviation = 0
1489  endfor
1490
1491  for (curveIndex = 1; curveIndex <= ItemsInList(coveragelist); curveIndex += 1)
1492    coverage = str2num(StringFromList(curveIndex-1,coverageList))
1493    waveTag = "rate_" + num2str(curveIndex)
1494    XwaveTag =  "temp_" + num2str(curveIndex)
1495    wave testwave = $waveTag
1496    wave Temp = $XwaveTag
1497
1498    Rows = numpnts(temp)
1499    Tstart=temp[0]
1500    Tend=temp[numpnts(temp)-1]
1501    dT = (Tend-Tstart)/Rows
1502
1503    make /d /n=(Rows) /o $(wavetag+"_GA")
1504    wave Rate = $(wavetag+"_GA")
1505    make /d /n=(Rows) /o $(Xwavetag+"_GA")
1506    wave Temperature = $(Xwavetag+"_GA")
1507
1508    Rate = 0
1509    Temperature = 0
1510    T=Tstart
1511    rescov=coverage
1512
1513    for (l = 0; l < Rows; l += 1)
1514        Rate[l] =
            (1/heatingRate)*exp(nu[0]+NuVar[0]*rescov)*(rescov)^ROrd[0]*exp(-(E0[0]-li
            nE[0]*rescov-sqrE[0]*(rescov^2))/(R*T))
1515        if (resCov<0)
1516            Rate[l]=0
1517        elseif (Rate[l]*dT > 0)
1518            resCov -= Rate[l]*dT
1519        else
1520            Rate[l]=0
1521        endif
1522        Temperature[l] = T
1523        T += dT
1524    endfor
1525  endfor
1526  print "E0 ", E0[0], "-  Nu ", nu[0], "-  LinE ", linE[0], "-  SquareE ",
      sqrE[0], "-  NuVar ", NuVar[0], "-  Order ", Rord[0]
1527
1528  end
1529
1530  //_____________________________________________________________________________
      _____________________________________
1531
1532  static function Reducepoints(Specnum, intbasis, tempbasis, Pointsnum, [Startpoint])
1533    variable Specnum, pointsnum, Startpoint
1534    string intbasis, tempbasis
1535    Startpoint = paramIsDefault(Startpoint) ? 1 : Startpoint
1536
1537    variable i, j
1538    variable startposition_i = strsearch(intbasis, num2str(Startpoint),0)
```

```
1539        variable startposition_t = strsearch(tempbasis, num2str(Startpoint),0)
1540
1541        string WaveTag
1542        string XWaveTag
1543
1544        for(i=Startpoint; i<=SpecNum; i+=1)
1545            waveTag = intbasis[0,startposition_i-1] + num2str(i) +
                intbasis[startposition_i+1,strlen(intbasis)-1]
1546            XwaveTag = tempbasis[0,startposition_t-1] + num2str(i) +
                tempbasis[startposition_t+1,strlen(tempbasis)-1]
1547            averageTPD(WaveTag,XWaveTag,pointsnum)
1548        endfor
1549    end
1550
1551    //_____________________________________________________________________________
    ____________________________________
1552
1553    static function averageTPD(yWaveTag, xWaveTag, numPointsRed)
1554        //This function reduces the numbers in a spectrum, consisting of the
1555        //two given waves, one for the energy and one for the intensity values
1556        //the output is a scaled wave, containing the intensity.
1557        // 3 points get averaged to one point.
1558        //To start this function, you have to give a intensity and energy wave
1559
1560        string xWaveTag
1561        string yWaveTag
1562        variable numPointsRed    //number of points for averaging e.g. 3
1563
1564
1565        variable SuitingLength, residual, i , newpoints
1566        variable oldStart, oldStep
1567        variable offsetFactor    //important for proper energy position
1568        string newYwaveTag
1569
1570        newYwaveTag = yWaveTag + "_R"+num2istr(numPointsRed) //give a name to the new wave
1571
1572        WaveStats /Q $yWaveTag  //get information about the input-wave
1573
1574        if (V_npnts <= numPointsRed)
1575            print "not enough data points in the given wave, setting the number of
                points to average to 3"
1576            numPointsRed = 3
1577        endif
1578
1579        residual = mod(V_npnts,numPointsRed)  //Modulo Division -- here is the residual
1580        SuitingLength = V_npnts - residual   //truncate to a number of points, dividable
        by numPoints
1581
1582        newpoints = SuitingLength / numPointsRed  // number of points in the 'reduced'
        wave
1583
1584        make /w /o /d /n = (newpoints)  $newYwaveTag  //create a new wave with the
        appropriate length
1585        //create waves, as kind of local variables
1586        //the next lines are crucial for the function of the script
1587        //do not get confused by the $ formalism , in doubt take look
1588        //at the help-files
1589        wave refName = $newYwaveTag
1590        wave refOrigName = $yWaveTag
1591        wave xrefOrigName = $xWaveTag
1592
1593        //find the starting-energy and the size of the energy steps in the input spectrum
1594        oldStart = xrefOrigName[0]
1595        oldStep = xrefOrigName[1]- xrefOrigName[0]
1596
1597        //start the calculation
1598        // look at the explanation at the file end, concerning the next few lines
1599        for ( i = 0; i< newpoints; i += 1)
1600                refName[i] =( sum (refOrigName,numPointsRed*i,numPointsRed*i +
                    (numPointsRed-1)) )/numPointsRed
1601        endfor
1602
1603        offsetFactor = (numPointsRed -1) / 2
```

```
1604        SetScale /P x, oldStart+offsetFactor*oldStep, numPointsRed*oldStep, refName
1605
1606        //draw the results //rename them properly for display
1607        duplicate /o /d refOrigName, yDuplWave
1608        duplicate /o /d xrefOrigName, xDuplWave
1609        duplicate /o /d refName, yDuplCor
1610
1611        averageSingleTPD(xwavetag,numPointsRed)
1612    end
1613
1614    //_____________________________________________________________________________________
    _____________________________________________
1615
1616    static function averageSingleTPD(WaveTag,numPointsRed)
1617        //This function reduces the number of points in a given wave
1618        // and creates a new wave with the averaged values of the input wave
1619        string WaveTag
1620        variable numPointsRed
1621
1622        string newWaveTag
1623        variable SuitingLength, residual, i , newpoints
1624        variable oldStart, oldStep
1625        variable offsetFactor
1626        string DWave1Tag = "displayCurve1"
1627        string DWave2Tag = "displayCurve2"
1628
1629        newWaveTag =  WaveTag  + "_R" + num2istr(numPointsRed)   //give a name to the
        new wave
1630
1631        WaveStats /Q $WaveTag   //gather information about the 'input-wave'
1632
1633        if (V_npnts <= numPointsRed)
1634            print "not enough data points in the given wave, setting the number of
            points to average to 3"
1635            numPointsRed = 3
1636        endif
1637
1638        residual = mod(V_npnts,numPointsRed)  //Modulo Division -- here is the residual
1639        SuitingLength = V_npnts - residual   //truncate to a number of points that is
        dividable by 3
1640        newpoints = SuitingLength / numPointsRed  // number of points in the 'reduced'
        wave
1641
1642        make /w /o /d /n = (newpoints)  /d $newWaveTag
1643        //create waves, as kind of local variables
1644        //the next lines are crucial for the function of the script
1645        //do not get confused by the $ formalism , in doubt take look
1646        //at the help-files
1647        wave refName = $newWaveTag
1648        wave refOrigName = $WaveTag
1649        wave DispWave = $DWave1Tag
1650        wave DispWave2 = $DWave2Tag
1651        //find the old starting point, i.e. the respective energy value,
1652        //this is possible, because the wave originates from an igor text file
1653        //and the leftx() command the assigns to the calculated x-Axis value
1654        //in the case of a normal x-y file leftx(y) would give the point index of
1655        //the first element, i.e. 0.
1656        oldStart = leftx(refOrigName)
1657        oldStep = deltax(refOrigName)
1658
1659
1660        //start the calculation
1661        for ( i = 0; i< newpoints; i += 1)
1662                refName[i] =( sum (refOrigName,pnt2x(refOrigName,numPointsRed
                *i),pnt2x(refOrigName,numPointsRed*i + (numPointsRed-1) )) ) /
                numPointsRed
1663        endfor
1664        //  ... huh, what a code mutant! This is hard stuff what does that mean?Look at
        the explanation at the file end
1665        //print pnt2x(refOrigName,0)     //uncomment this, to check the output
1666
1667
1668
```

```
1669        offsetFactor = (numPointsRed -1) / 2
1670        SetScale /P x, oldStart+offsetFactor*oldStep, numPointsRed*oldStep, refName
1671
1672
1673        duplicate /o  refOrigName, DispWave
1674        duplicate /o  refName, DispWave2
1675    end
```

D.3 Import-Procedures

```
#pragma TextEncoding = "UTF-8"
#pragma rtGlobals=3     // Use modern global access method and strict wave access.
#pragma modulename = Import

Menu "Macros"
    "Load AES Spectra from TPD", Import#AES_TPD()
    "Load Surveys from TPD", Import#Survey_TPD()
    "Load NEXAFS Spectra from HIKE", Import#NEXAFS_HIKE()
End

static function AES_TPD()
    Variable refNum
    String message = "Select one or more files"
    String outputPaths
    String fileFilters = "Data Files (*.txt,*.dat,*.csv,*.aes):.txt,.dat,.csv,.aes;"
    fileFilters += "All Files:.*;"
    String path, Exp_Name, ColumnInfoStr

    Open /D /R /MULT=1 /F=fileFilters /M=message refNum
    outputPaths = S_fileName

    if (strlen(outputPaths) == 0)
        Print "Cancelled"
    else
        Variable numFilesSelected = ItemsInList(outputPaths, "\r")
        Variable i
        for(i=0; i<numFilesSelected; i+=1)
            path = StringFromList(i, outputPaths, "\r")
            Printf "%d: %s\r", i, path
            Exp_Name = path
            Exp_Name = RemoveEnding(Exp_Name,".aes")
            Exp_Name =
            Exp_Name[StrSearch(Exp_Name,":",strlen(Exp_Name)-1,3)+1,strlen(Exp_Name)-1
            ]
            ColumnInfoStr = "N="+Exp_name+"_Enrg; N="+Exp_Name+"_Int;"
            LoadWave/A/B=ColumnInfoStr/D/G path
        endfor
    endif
End

static function NEXAFS_HIKE()
    Variable refNum
    String message = "Select one or more files"
    String outputPaths
    String fileFilters = "Data Files (*.txt,*.dat,*.csv):.txt,.dat,.csv;"
    fileFilters += "All Files:.*;"
    String path, Exp_Name, ColumnInfoStr

    Open /D /R /MULT=1 /F=fileFilters /M=message refNum
    outputPaths = S_fileName

    if (strlen(outputPaths) == 0)
        Print "Cancelled"
    else
        Variable numFilesSelected = ItemsInList(outputPaths, "\r")
        Variable i
        for(i=0; i<numFilesSelected; i+=1)
            path = StringFromList(i, outputPaths, "\r")
            Printf "%d: %s\r", i, path
            Exp_Name = path
            Exp_Name = RemoveEnding(Exp_Name,".txt")
            Exp_Name =
            Exp_Name[StrSearch(Exp_Name,":",strlen(Exp_Name)-1,3)+1,strlen(Exp_Name)-1
            ]
            ColumnInfoStr = "N="+Exp_name+"_Enrg; N="+Exp_Name+"_Ioncur;
            N="+Exp_Name+"_Samplecur; N="
            ColumnInfoStr = ColumnInfoStr+Exp_Name+"_Ringcur; N="+Exp_Name+"_Flrscnc;"
            LoadWave/A/B=ColumnInfoStr/D/G path
        endfor
    endif
End

static function Survey_TPD()
```

```
69      string str_int, str_mass, str_temp
70      prompt str_int, "Insert intensity wavename: "
71      prompt str_mass, "Insert mass wavename: "
72      prompt str_temp, "Insert temp wavename: "
73      DoPrompt "Enter Wavenames for Import", str_int, str_mass, str_temp
74
75      wave intensity = $str_int
76      wave mass = $str_mass
77      wave temp = $str_temp
78
79      variable i, j
80      variable massrange, massstart, massend
81      string wavetag, wavetag2, datafolder
82
83      //datafolder = getdatafolder(1)
84      newdatafolder/O Surveys
85      newdatafolder/O TPDs
86
87      massstart=mass[0]
88      massend=mass[numpnts(mass)-1]
89      massrange=numpnts(mass)/numpnts(temp)
90
91      make /o /d /n=(massrange) int_integral
92      wave integral=int_integral
93
94      make /o /d /n=(massrange, numpnts(temp)) intensity_2D
95      wave wave2D=intensity_2D
96
97      for(i=0;i<(numpnts(intensity)/massrange); i+=1)
98          wavetag="survey_"+num2str(temp[i])+"_K"
99          make /o /d /n=(massrange) $wavetag
100         wave runwave=$wavetag
101         for (j=0;j<numpnts(runwave);j+=1)
102             runwave[j]=intensity[j+i*massrange]
103             integral[j]+=intensity[j+i*massrange]
104             wave2D[j][i]=intensity[j+i*massrange]
105         endfor
106     endfor
107
108     make /o /d /n=(massrange) mzratio
109     for (j=0;j<numpnts(runwave);j+=1)
110         mzratio[j]=mass[j]
111     endfor
112
113     for(i=0;i<massrange; i+=1)
114         wavetag="TPD_"+num2str(mzratio[i])+"_u"
115         make /o /d /n=(numpnts(temp)) $wavetag
116         wave runwave=$wavetag
117         for (j=0;j<numpnts(runwave);j+=1)
118             runwave[j]=wave2D[i][j]
119         endfor
120     endfor
121 end
122
123
```

E List of Figures

Curriculum Vitae

Der Lebenslauf wurde aus Datenschutzgründen aus der publizierten Version entfernt.

Attended Conferences

- Bessy-User-Meeting 2019 in Berlin, Poster title: Reactive Metal-Organic Interfaces Studied with HAXPES: Modifying Reaction Depth and Interphase Formation
- Bunsen-Meeting 2019 in Jena, Poster title: Functional Structural Elements in Carbon-Based Nanomaterials: Alternant vs. Non-Alternant Topology and Interface Chemical Bond
- DPG Spring Meeting 2019 in Regensburg, Lecture title: Low-Dimensional Hybrid Interfaces Between Acenes and TMDCs: Pentacene and Perfluoropentacene on MoS_2, Poster title: Reactive Metal-Organic Interfaces Studied with HAXPES: Modify Reaction Depth and Interphase Formation
- SFB Winter School 2019 in Hirschegg, Lecture title: Technical Challenges in TPD and Investigations of PEN and PFP on MoS_2
- Tongji – UMR Summer Schools, Interdisciplinary and Intercultural Symposium on Chemistry, Medicine and Life Sciences, Shanghai 2018, Lecture title: Temperature-Programmed Desorption Studies of Azulene and Naphthalene on Cu(111) and Ag(111)
- Joint Seminar SFB 1083 2018 in Volkenroda, Lecture title: HAXPES on Metal/Organic Interfaces
- DPG Spring Meeting 2018 in Berlin, Poster title: Intermolecular Repulsion at Metal/Organic Interfaces: Azulene and Naphthalene on Cu(111) and Ag(111)

- Tongji – UMR Summer Schools, Interdisciplinary and Intercultural Symposium on Chemistry, Medicine and Life Sciences, Marburg 2017, Lecture title: Temperature-Programmed Desorption Studies of Azulene and Naphthalene on Cu(111) and Ag(111)
- DPG Spring Meeting 2017 in Dresden, Poster title: Topology Dependent Molecule-Substrate Interactions: Azulene vs. Naphthalene in Temperature-Programmed Desorption
- SFB Winter School 2017 in Rauischholzhausen